Advances in Quantum Chemistry

Volume 54

Advances in
QUANTUM CHEMISTRY

DV-Xα FOR INDUSTRIAL–ACADEMIC COOPERATION

VOLUME **54**

Editors

JOHN R. SABIN
Quantum Theory Project
University of Florida
Gainesville, Florida

ERKKI BRÄNDAS
Department of Quantum Chemistry
Uppsala University
Uppsala, Sweden

Founding Editor

PER-OLOV LÖWDIN
1916–2000

Guest Editors

JUN KAWAI
Department of Materials Science and Engineering
Kyoto University
Kyoto 606-8501, Japan

YANG-SOO KIM
Sunchon Branch, Korea Basic Science Institute
Sunchon, Jeonnam 540-742
Republic of Korea

HIROHIKO ADACHI
Department of Materials Science and Engineering
Kyoto University
Kyoto 606-8501, Japan

ELSEVIER

Amsterdam • Boston • Heidelberg • London
New York • Oxford • Paris • San Diego
San Francisco • Singapore • Sydney • Tokyo
Academic Press is an imprint of Elsevier

Academic Press is an imprint of Elsevier
84 Theobald's Road, London WC1X 8RR, UK
Radarweg 29, PO Box 211, 1000 AE Amsterdam, The Netherlands
Linacre House, Jordan Hill, Oxford OX2 8DP, UK
30 Corporate Drive, Suite 400, Burlington, MA 01803, USA
525 B Street, Suite 1900, San Diego, CA 92101-4495, USA

First edition 2008

ISBN: 978-0-12-373926-1
ISSN: 0065-3276

For information on all Academic Press publications
visit our website at books.elsevier.com

Printed and bound in USA

08 09 10 11 12 10 9 8 7 6 5 4 3 2 1

CONTRIBUTORS

Numbers in parenthesis indicate the pages where the authors' contributions can be found.

H. Adachi (255)
Fukui Institute for Fundamental Chemistry, Kyoto University, Kyoto 606-8103, Japan

Naoko Aizawa (35)
Department of Advanced Materials Science, Kagawa University, 2217-20, Hayashicho, Takamatsu 761-0396, Japan

Hideki Araki (161)
Department of Materials and Manufacturing Science, Graduate School of Engineering, Osaka University, 2-1 Yamada-oka, Suita, Osaka 565-0871, Japan; Center for Atomic and Molecular Technologies, Graduate School of Engineering, Osaka University, 2-1 Yamada-oka, Suita, Osaka 565-0871, Japan

Takeshi Baba (145)
Department of Chemistry, School of Science and Engineering, Waseda University, Tokyo 169-8555, Japan

Erkki J. Brändas (115)
Department of Quantum Chemistry, Uppsala University, Box 518, S-751 20 Uppsala, Sweden

Wanuk Choi (23)
Energy 3 Team, Energy R&D Center, CTO, Samsung SDI Co. Ltd., South Korea

Jonathan D. Denlinger (219)
Lawrence Berkeley National Laboratory, 1Cyclotron Road, Berkeley, CA 94720, USA

Yukikazu Fuke (35)
Department of Advanced Materials Science, Kagawa University, 2217-20, Hayashicho, Takamatsu 761-0396, Japan

Kimichika Fukushima (47, 341)
AITEL Corporation, 8, Shinsugita-cho, Isogo-ku, Yokohama 235-8523, Japan

Yoshinori Hayafuji (89, 103, 133, 325)
Graduate School of Science and Technology, Kwansei Gakuin University, 2-1 Gakuen, Sanda, Hyogo 669-1337, Japan

Yoshitsune Higashiguchi (89)
Graduate School of Science and Technology, Kwansei Gakuin University, 2-1 Gakuen, Sanda, Hyogo 669-1337, Japan

Yuka Igarashi (227)
Shonan Institute of Technology, 1-1-25, Tsujido Nishikaigan, Fujisawa, Japan

Kazuyuki Igei (89)
Graduate School of Science and Technology, Kwansei Gakuin University, 2-1 Gakuen, Sanda, Hyogo 669-1337, Japan

Takeshi Inoue (325)
Graduate School of Science and Technology, Kwansei Gakuin University, 2-1 Gakuen, Sanda, Hyogo 669-1337, Japan

Tomohiko Ishii (35)
Department of Advanced Materials Science, Kagawa University, 2217-20, Hayashicho, Takamatsu 761-0396, Japan

Keisuke Ishizumi (103, 133)
School of Science and Technology, Kwansei Gakuin University, 2-1 Gakuen, Sanda, Hyogo 669-1337, Japan

Hironori Kawanishi (103,133)
School of Science and Technology, Kwansei Gakuin University, 2-1 Gakuen, Sanda, Hyogo 669-1337, Japan

Sung-Soo Kim (23)
Energy 3 Team, Energy R&D Center, CTO, Samsung SDI Co. Ltd., South Korea

Yang-Soo Kim (23, 81, 271)
Sunchon Branch, Korea Basic Science Institute, 315 Maegok, Sunchon, Jeonnam 540-742, Korea

Heejin Kim (23)
Department of Materials Science and Engineering, Korea Advanced Institute of Science and Technology, Daejeon 305-701, Korea

Sung Kwan Kim (81)
Department of Materials Science and Engineering, Korea Advanced Institute of Science and Technology, Daejeon 305-701, Korea

Yusuke Kinoshita (325)
Graduate School of Science and Technology, Kwansei Gakuin University, 2-1 Gakuen, Sanda, Hyogo 669-1337, Japan

S. Kishino (13)
Department of Electrical Engineering, Fukui University of Technology, 3-6-1, Gakuen, Fukui 910-8505, Japan

Kenji Komiya (245)
Department of Materials Science and Engineering, Graduate School of Engineering, Nagoya University, Furo-cho, Chikusa-ku, Nagoya 464-8603, Japan

L. Kövér (175)
Institute of Nuclear Research of the Hungarian Academy of Sciences, 18/c Bem tér, H-4026 Debrecen, Hungary

Y. Kowada (255)
Hyogo University of Teacher Education, Hyogo 673-1494, Japan

Tsutomu Kurisaki (315)
Department of Chemistry, Faculty of Science, Fukuoka University, 8-19-1 Nanakuma, Jonan-ku, Fukuoka, 814-0180, Japan

Yasutomo Matsumoto (1)
Graduate Student, University of Hyogo, 2167 Shosha, Himeji, Hyogo 671-2201, Japan

Shuji Matsuo (193, 315)
Physical Analysis and Evaluation Department, Electronics Division, KOBELCO Research Institute, Inc., 1-5-5 Takatsukadai, Nishi-ku, Kobe, Hyogo 651-2271, Japan

Qiang Miao (271)
School of Chemistry and Chemical Engineering, Nanjing University, Nanjing 210093, China

T. Minami (255)
Osaka Prefecture University, Sakai 599-8531, Japan

Masataka Mizuno (161)
Department of Materials and Manufacturing Science, Graduate School of Engineering, Osaka University, 2-1 Yamada-oka, Suita, Osaka 565-0871, Japan;

Center for Atomic and Molecular Technologies, Graduate School of Engineering, Osaka University, 2-1 Yamada-oka, Suita, Osaka 565-0871, Japan

Kentaroh Morikawa (227)
Shonan Institute of Technology, 1-1-25, Tsujido Nishikaigan, Fujisawa, Japan

Masahiko Morinaga (145, 245)
Department of Materials Science and Engineering, Graduate School of Engineering, Nagoya University, Furo-cho, Chikusa-ku, Nagoya 464-8603, Japan

Masao Morishita (1)
Department of Materials Science and Chemistry, University of Hyogo, 2167 Shosha, Himeji, Hyogo 671-2201, Japan

Yasuji Muramatsu (209, 219)
Graduate School of Engineering, University of Hyogo, 2167 Shosha, Himeji, Hyogo 671-2201, Japan

Toshio Nakagiri (61)
Advanced Nuclear System Research and Development Directorate, Japan Atomic Energy Agency, 4002 Narita-cho, O-Arai-machi, Ibaraki-ken, 311-1393, Japan

Hiromi Nakai (145)
Department of Chemistry, School of Science and Engineering, Waseda University, Tokyo 169-8555, Japan

Ryo Nakao (103)
School of Science and Technology, Kwansei Gakuin University, 2-1 Gakuen, Sanda, Hyogo 669-1337, Japan

Yuichi Nakazono (315)
Department of Chemistry, Faculty of Science, Fukuoka University 8-19-1 Nanakuma, Jonan-ku, Fukuoka, 814-0180, Japan

Koujiroh Nishiyama (227)
Shonan Institute of Technology, 1-1-25, Tsujido Nishikaigan, Fujisawa, Japan

Kwang-soo No (81)
Department of Materials Science and Engineering, Korea Advanced Institute of Science and Technology, Daejeon 305-701, Korea

Takayuki Noguchi (325)
Graduate School of Science and Technology, Kwansei Gakuin University, 2-1 Gakuen, Sanda, Hyogo 669-1337, Japan

Hiroaki Ochiai (89)
Graduate School of Science and Technology, Kwansei Gakuin University, 2-1 Gakuen, Sanda, Hyogo 669-1337, Japan

Kazuyoshi Ogasawara (297)
Department of Chemistry, Kwansei Gakuin University, 2-1 Gakuen, Sanda, Hyogo 669-1337, Japan

Kengo Ohmori (89)
Graduate School of Science and Technology, Kwansei Gakuin University, 2-1 Gakuen, Sanda, Hyogo 669-1337, Japan

Shinichi Orimo (245)
Institute for Materials Research, Tohoku University, Katahira, Sendai 980-8577, Japan

Rupert C.C. Perera (315)
EUV Technology, 6680 Alhambra Avenue #187, Martinez, CA 94553, USA

Liang Pu (271)
School of Chemistry and Chemical Engineering, Nanjing University, Nanjing 210093, China

Yoshifumi Shinzato (145, 245)
Department of Materials Science and Engineering, Graduate School of Engineering, Nagoya University, Furo-cho, Chikusa-ku, Nagoya 464-8603, Japan

Yasuharu Shirai (161)
Department of Materials and Manufacturing Science, Graduate School of Engineering, Osaka University, 2-1 Yamada-oka, Suita, Osaka 565-0871, Japan; Center for Atomic and Molecular Technologies, Graduate School of Engineering, Osaka University, 2-1 Yamada-oka, Suita, Osaka 565-0871, Japan

K. Sueoka (13)
Department of System Engineering, Okayama Prefectural University, 111 Kuboki, Soja 719-1197, Japan

Sunao Sugihara (227)
Shonan Institute of Technology, 1-1-25, Tsujido Nishikaigan, Fujisawa, Japan

Kazuki Sugita (161)
Department of Materials and Manufacturing Science, Graduate School of Engineering, Osaka University, 2-1 Yamada-oka, Suita, Osaka 565-0871, Japan

Chikashi Suzuki (61)
Advanced Nuclear System Research and Development Directorate, Japan Atomic Energy Agency, 4002 Narita-cho, O-Arai-machi, Ibaraki-ken, 311-1393, Japan

Isao Takahashi (103, 133)
School of Science and Technology, Kwansei Gakuin University, 2-1 Gakuen, Sanda, Hyogo 669-1337, Japan

Yoshitaka Takahashi (245)
Department of Materials Science and Engineering, Graduate School of Engineering, Nagoya University, Furo-cho, Chikusa-ku, Nagoya 464-8603, Japan

M. Tatsumisago (255)
Department of Applied Chemistry, Osaka Prefecture University, Sakai 599-8531, Japan

Hikaru Terauchi (103, 133)
School of Science and Technology, Kwansei Gakuin University, 2-1 Gakuen, Sanda, Hyogo 669-1337, Japan

Takumi Tomita (325)
Graduate School of Science and Technology, Kwansei Gakuin University, 2-1 Gakuen, Sanda, Hyogo 669-1337, Japan

Satoshi Ueda (219)
Graduate School of Engineering, University of Hyogo, 2167 Shosha, Himeji, Hyogo 670-2201, Japan

James H. Underwood (315)
EUV Technology, 6680 Alhambra Avenue #187, Martinez, CA 94553, USA

Hisanobu Wakita (193, 315)
Department of Chemistry, Faculty of Science, Fukuoka University, 8-19-1 Nanakuma, Jonan-ku, Fukuoka 814-0180, Japan

Qing Wang (271)
School of Chemistry and Chemical Engineering, Nanjing University, Nanjing 210093, China

Shinta Watanabe (297)
Department of Chemistry, Kwansei Gakuin University, 2-1 Gakuen, Sanda, Hyogo 669-1337, Japan

Hiroaki Yamamoto (1)
Department of Materials Science and Chemistry, University of Hyogo, 2167 Shosha, Himeji, Hyogo 671-2201, Japan

Masahiro Yamashita (35)
Department of Chemistry, Tohoku University, Aoba, Aramaki, Aoba-ku, Sendai 980-8578, Japan

Ri-Zhu Yin (23)
Energy 3 Team, Energy R&D Center, CTO, Samsung SDI Co. Ltd., South Korea

H. Yoshida (13)
Graduate School of Engineering, University of Hyogo, 2167 Shosha, Himeji 671-2280, Japan

Hiroshi Yukawa (145, 245)
Department of Materials Science and Engineering, Graduate School of Engineering, Nagoya University, Furo-cho, Chikusa-ku, Nagoya 464-8603, Japan

Yong Zhang (271)
Chemistry Department, Boston University, Boston, MA 02215, USA

Zhibing Zhang (271)
School of Chemistry and Chemical Engineering, Nanjing University, Nanjing 210093, China

FOREWORD

This volume is a collection of the papers presented at the 4th International Conference on DV-Xα Method (DV-Xα 2006). This conference was organized by the Society for Discrete Variational Xα (Japan) and Sunchon National University (Korea). A subtitle set to the conference was the Industrial–Academic Cooperation Symposium and the 19th DV-Xα Annual Meeting. The primary objective of the conference was the promotion and development of science and technology on the basis of the DV-Xα molecular orbital method.

DV-Xα 2006 was held in Jeju Island, South Korea, on August 3–5, 2006, and 76 participants attended from various countries including Sweden, Hungary, Russia, China, Japan, and Korea. The scientific program included 4 plenary talks, 17 invited talks, and 34 poster presentations. DV-Xα 2006 has been one of the most important events in the calendar of the worldwide community, providing the participants with great opportunities for meeting their colleagues, sharing scientific and technical knowledge, and strengthening their friendship.

In the past, the Society for Discrete Variational Xα organized three international conferences. The first conference was held in 1996 at ATOMKI, Debrecen, Hungary, the second was held in 1998 at Seoul University, Korea, and the third was held in 2001 at RIKEN, Wako, Japan. The scientific papers presented in these three conferences were published in three volumes: Vol. 29, Vol. 37, and Vol. 42 of *Advances in Quantum Chemistry*.

We believe that research activities in the DV-Xα method have increased rapidly throughout the world. The key issues treated at the 4th conference were materials science, surfaces, grain boundaries, lattice defects, metals, ceramics and organic materials, and X-rays and electrons spectroscopy as well as fundamental quantum theory. Thus, the research fields of DV-Xα method are very wide and still maturing, while keeping a high potential for building up new computational materials science and also for developing new advanced products that are needed to be supplied in the 21st century in order to solve important issues connected with the environment, energy, and health and welfare of human-beings.

The conference was held under the auspices of many organizations, Sunchon National University, Nagoya University, The Korean Institute of Metals and

Materials, The Japan Institute of Metals, The Japan Society for the Promotion of Science (JSPS), and others. We sincerely acknowledge our great debt to all of them.

August 20, 2007
Byung-Il Kim
Masahiko Morinaga
DV-Xα 2006 Chairmen
The 4th International Conference on DV-Xα Method (DV-Xα 2006):
Industrial–Academic Cooperation Symposium
and the 19th DV-Xα Annual Meeting

PREFACE

We are pleased to present the proceedings of the 4th International Conference on the DV-Xα Method, which was organized jointly by the Korean Industrial–Academic Cooperation Symposium and the 19th DV-Xα Japanese Annual Meeting. Further details about this conference are described in the Foreword of this volume by the co-chairs of the conference, two very distinguished and renowned professors from Korea and Japan.

The conference program is summarized below to give the reader an overview of the activities of the symposium. The very active scientific atmosphere can be recognized from the conference photo; the younger researchers were in the majority, as they also are among the authors of the present volume.

Several important sources of conference support have already been acknowledged in the Foreword; in addition we like to mention the contribution from a bilateral research cooperation project between the Hungarian Academy of Science (MTA) and the Japan Society for the Promotion of Science (JSPS).

The editorial process was unfortunately delayed due to illness (an attack of apoplexy but now recovered) in the family of one of the guest editors (JK). The Guest Editors would like to thank *Advances in Quantum Chemistry* Editor, Professor Erkki Brändas for his patience in connection with the long editorial process.

Jun Kawai
Yang-Soo Kim
Hirohiko Adachi
Guest Editors


The 4th International Conference on DV-Xα Method(DV-Xα 2006)
Industrial-Academic Cooperation Symposium and the 19th DV-Xα Annual Meeting
August 3~5, 2006, CROWNE PLAZA HOTEL, JEJU, KOREA

The 4th International Conference on DV-Xα Method (DV-Xα 2006)—Industrial–Academic Cooperation Symposium and the 19th DV-Xα Annual Meeting—Program

Crowne Plaza Hotel, Jeju, South Korea, 3–5 August 2006

August 3rd, Thursday

Chair: Y.S. Kim
9:00 Opening Ceremony (B.I. Kim and M. Morinaga)

Chair: M. Morinaga
9:15 Plenary 1. Erkki Brändas (Uppsala University): Quantum Mechanics and the Theory of Relativity

Chair: Y.J. Kim
9:55 Invited 1. Kazuyoshi Ogasawara (Kwansei Gakuin University): Current Situation and Future Development of Discrete Variational Multielectron (DVME) Method

Industrial-Academic Cooperation Talk
10:15 Invited 2. Dong-Yoon Lee, Won-Jae Lee, Jae-Sung Song and Yang-Soo Kim (Korea Electrotechnology Research Institute, Corporate R&D Center Samsung SDI): Chemical Bonding State of Iodide Adsorbed on Surface of Carbon Nanotube

10:35–11:05 Coffee Break

Chair: Qiang Miao
11:05 Invited 3. Masahito Yoshino (Nagoya University): 1.5 μm Luminescence and Electronic Structures in Er-Containing Compounds

11:25 Invited 4. Tatiana Nedoseykina, Ri-Zhu Yin, Joo-Han Song and Sung-Soo Kim (Samsung SDI Co. Ltd.): Lithium Insertion/Removal Mechanism of $Li_{1.1}V_{0.9}O_2$ Negative Electrode in Lithium Ion Cell

11:45 Invited 5. Bin Song and Pei-Lin Cao (Zhejiang University): Density Functional Investigation of Geometrical and Electronic Structures of Atomic Clusters

12:05–13:30 Lunch

Chair: S. Matsuo, M. Morishita and M. Yoshino
13:30 Short Presentation for Posters (3 min each)
13:30 Poster 1. Shino Tsuboi, Akito Takashima, Tomohiko Ishii and Genta Sakane (Kagawa University, Okayama University of Science): Controlling of the Ligand Field Splitting and the Solid State Properties of the Metal Complexes by DV-Xα Method

13:33 Poster 2. Akito Takashima, Shino Tsuboi, Tomohiko Ishii and Genta Sakane (Kagawa University, Okayama University of Science): Mechanism of the RGB Color in the Porphyrin Derivatives by DV-Xα Calculation

13:36 Poster 3. Tsutomu Kurisaki and Hisanobu Wakita (Fukuoka University): Development and Performance Evaluation of Laboratory Ultra Soft X-Ray Absorption Spectrometer

13:39 Poster 4. Shinta Watanabe, Takugo Ishii and Kazuyoshi Ogasawara (Kwansei Gakuin University): First-Principles Calculation for f^n–$f^{n-1}d^1$ Transition Absorption Spectra of Trivalent Lanthanides and Actinides in $LiYF_4$

13:42 Poster 5. K. Sugita, M. Mizuno, H. Araki and Y. Shirai (Osaka University): Electronic Structure and Bonding in Amorphous $Zr_{67}Ni_{33}$ and $Zr_{67}Cu_{33}$

13:45 Poster 6. M.G. Brik and K. Ogasawara (Kwansei Gakuin University): First-Principles Calculations of Optical Spectra for Transition Metal Ions in Crystals

13:48 Poster 7. Yang-Soo Kim, Ri-Zhu Yin, Wan-Wook Choi and Sung-Soo Kim (Samsung SDI Co. Ltd.): Lithium Vanadium Oxide as Next Generation Negative Material for Advanced Li-Ion Batteries: Structure, Analysis, and First-Principles Calculation

13:51 Poster 8. Yoshiki Inoue, Hisao Yamashige, Tsutomu Kurisaki and Hisanobu Wakita (Fukuoka University): Characterization of Various Tetraaza Macrocycles using X-Ray Spectroscopy

13:54 Poster 9. Kazuhiro Fujikawa, Hisashi Yoshida and Kazuyoshi Ogasawara (Kwansei Gakuin University, NEC Lighting. Co. Ltd.): First Principles Calculation of Multiplet Structures and Absorption Spectra of ns^2-type Ions

13:57 Poster 10. Young-Ah Jeon, Yang-Soo Kim and Kwangsoo No (Korea Advanced Institute of Science and Technology, Korea Basic Science Institute): Theoretical Study of Lithium Intercalation in Titanium Sulfides and Titanium Oxides

14:00 Poster 11. Ryusuke Teramoto, Hidenari Kai, Shinta Watanabe, Hisashi Yoshida and Kazuyoshi Ogasawara (Kwansei Gakuin University): First-Principles Calculation of Multiplet Structures of Ln^{3+} in $YAl_3(BO_3)_4$

14:03 Poster 12. Yoshifumi Shinzato, Kenji Komiya, Yoshitaka Takahashi, Hiroshi Yukawa, Masahiko Morinaga and Shinichi Orimo (Nagoya University, Tohoku University): Characteristics of Chemical Bond in Perovskite-Type Hydrides for Hydrogen Storage

14:06 Poster 13. Satoshi Ueda and Yasuji Muramatsu (University of Hyogo): Soft X-Ray Emission Spectral Analysis of Graphite Fluoride $(CF)_n$ using DV-Xα Calculations

14:09 Poster 14. Hironori Kawanishi, Keisuke Ishizumi, Isao Takahashi, Hikaru Terauchi and Yoshinori Hayafuji (Kwansei Gakuin University): Electronic Structure Calculation of $ATiO_3$ Perovskite Oxides (A=Ba, Sr, and Pb)

14:12 Poster 15. Keisuke Ishizumi, Hironori Kawanishi, Ryo Nakao, Isao Takahashi, Hikaru Terauchi, Kaoru Miura and Yoshinori Hayafuji (Kwansei Gakuin University): Particle Size and Surface Effects on Critical Thickness for Ferroelectricity of $BaTiO_3$ by First-Principles Calculation

14:15 Poster 16. Sung Kwan Kim, Yang-Soo Kim and Kwangsoo No (Korea Advanced Institute of Science and Technology): The Electronic Structures and Optical Properties of Hf–O–N Thin Films as a Phase Shift Mask for ArF Laser Lithography

14:18 Poster 17. Yoshitsune Higashiguchi, Hiroaki Ochiai, Kazuyuki Igei and Yoshinori Hayafuji (Kwansei Gakuin University): Theoretical Study of the Stability of XB_{12} and XB_6 Clusters, X=H–Br

14:21 Poster 18. Koichi Nakagawa, Setsuko Matsumoto and Hironaga Matsumoto (Meiji University): Analysis of VUV Reflection Spectra of KDP, RDP and KDA by DV-Xα Method

14:24 Poster 19. Yusuke Kinoshita, Atsushi Nakamura, Takayuki Noguchi, Takeshi Inoue, Takumi Tomita and Yoshinori Hayafuji (Kwansei Gakuin University): Electronic Structures of ZnO Doped by Various Atoms (from Li to Bi without Radioactive Atoms)

14:27 Poster 20. Sunao Sugihara, Shunsuke Naitoh, Koujiroh Nishiyama, Yuka Igarashi and Kentaroh Morikawa: Thermoelectric Properties of the Oxide and Electronic Structures

14:30 Poster 21. Takeshi Mukoyama (Kansai Gaidai University): Chemical Effect on K_β/K_α X-ray Intensity Ratios for Potassium Compounds

14:33 Poster 22. Hiroshi Tsutsumi, Manabu Fuziwara, Tsutomu Kurisaki and Hisanobu Wakita (Fukuoka University): Electronic Structure Analyze of Various Types of Lithium Compounds using an X-ray Absorption Spectroscopic Analysis Method

14:36 Poster 23. Chikashi Suzuki, Toshio Nakagiri and Kazumi Aoto (Japan Atomic Energy Agency): Sulfur Trioxide Adsorption on Pt Electrode

14:39 Poster 24. Shoichi Takayama, Takeshi Tanigaki and Jun Kawai (Kyoto University): On Plasmon and Bremsstrahlung

14:42 Poster 25. Masanori Sakaguchi, Rie Endo and Masahiro Susa (Tokyo Institute of Technology): Synthesis of New Coloured Alloys Based upon Colour Specification and Density of States

14:45 Poster 26. Y. Shinzato, H. Yukawa, M. Morinaga, T. Baba and H. Nakai (Nagoya University, Waseda University): New Expression of the Chemical Bond in Hydrides Using Atomic Energy Densities

14:48 Poster 27. W. Takahara and F. Minami (Osaka University): Chemical Nature of Si–O Bonds in Silica-Based Clusters-Linking for Element Selection Rules in Biological System

Chair: H. Yoshida and T. Ishii
Industrial-Academic Cooperation Poster
14:51 Poster 28. Hidenari Kai, Hisashi Yoshida and Kazuyoshi Ogasawara (Kwansei Gakuin University, NEC Lighting): First-Principles Calculations for Phosphorescent Molecule $Ir(ppy)_3$ used in Organic Light Emitting Diodes

Industrial-Academic Cooperation Poster
14:54 Poster 29. M. Morinaga, Y. Murata, R. Hashizume, A. Yoshinari and T. Kiyono (Nagoya University, The Kansai Electric Power Company, Inc., Hitachi Co. Ltd.): Design and Development of Ni-Based Single Crystal Superalloys for Gas Turbine Blades Using the Alloying Parameters Obtained by DV-Xα Method

Industrial-Academic Cooperation Poster
14:57 Poster 30. Young-Ah Jeon, Sung-Kwan Kim, Yang-Soo Kim and Kwangsoo No (Korea Advanced Institute of Science and Technology, Korea Basic Science Institute): Comparison the Electronic Structures between $Li(Ni_{0.5}Mn_{0.5})O_2$ and $Li(Ni_{1/3}Mn_{1/3}M_{1/3})O_2$ (M=Al and Co) for Lithium Battery Cathode Materials

Industrial-Academic Cooperation Poster
15:00 Poster 31. Masataka Mizuno, Teruo Kihara, Hideki Araki, Yasuharu Shirai and Takashi Onishi (Osaka University, Kobe Steel Ltd.): Theoretical Calculation of Positron Lifetimes of Vacancy Clusters in Cu

Industrial-Academic Cooperation Poster
15:03 Poster 32. B.S. Kim, D.Y. Lee, M.W. Oh, S.D. Park, H.W. Lee, W.S. Chung and T. Ishii (Korea Electrotechnology Research Institute, Pusan National University, Kagawa University): Comparison of Electronic State Calculation and Experimental Results of Electrical Conductivity of Mn-X(transition elements) Oxide by Anodic Deposition

Industrial-Academic Cooperation Poster
15:06 Poster 33. Akira Kubo, Shinta Watanabe, Hiroki Moriwake and Kazuyoshi Ogasawara (Kwansei Gakuin University, Japan Fine Ceramics Center): An Approach for Design of Magnetic Materials Based on Spinel Ferrites using First-Principles Calculations

15:09 Poster 34. Seigo Kishno, Koji Sueoka and Haruhiko Yoshida (Fukui University of Technology, Okayama Prefectural University, University of Hyogo): Energy Band Structure of Strained Semiconductor Studied by DV-Xα Calculation using Madelung Potential

15:30–18:00 Coffee and Poster Session

19:00 Welcome Reception

August 4th, Friday

Chair: S.S. Kim
9:00 Plenary 2. Laszlo Kövér (Institute of Nuclear Research of the Hungarian Academy of Sciences): Local Electronic Structures from Analyzing and Modeling High Energy Auger and Photoelectron Spectra of Solids

Chair: Y. Hayafuji
9:40 Invited 6. Yasuji Muramatsu (University of Hyogo): Soft X-ray Spectral Analysis of Industrial Carbon Materials using DV-Xα Calculations

10:00 Invited 7. Young-Min Kim, Jin-Kyu Kim and Youn-Joong Kim (Korea Basic Science Institute): Electron Spectroscopy by Energy-Filtered High Voltage Electron Microscopy

10:20–10:50 Coffee Break

Chair: J. Kawai

10:50 Invited 8. Shuji Matsuo (Kobe Steel, LTD.): X-ray Absorption Spectroscopic Study on Polymerization of Aqueous Aluminate and Theoretical Analysis by DV-Xα MO Method

11:10 Invited 9. Hisao Yamashige, Shuji Matsuo, Tsutomu Kurisaki and Hisanobu Wakita (Fukuoka University): Local Structure Analyses of Nitrogen Atoms in a Porphine Ring of *meso*-Phenyl Substituted Porphyrin and Related Compounds with an Electron-Withdrawing Group Using X-ray Photoelectron Spectroscopy and X-ray Absorption Spectroscopy

11:30 Invited 10. Qiang Miao, Chun-gen Liu, Hirohiko Adachi and Isao Tanaka (Nanjing University, Kyoto University): DV-Xα Study on Quantum Mirages and Quantum Corrals in Non-Metal Systems

11:50 Invited 11. H. Yukawa, M. Maeda, M. Morinaga and S. Inoue (Nagoya University, Numazu National College of Technology): Alloying Effects on the Electronic Structures of Tungsten

12:10 Lunch

13:45 Conference Photo

Chair: H. Wakita
14:00 Plenary 3. Yuichi Ikuhara (The University of Tokyo): Grain Boundary Atomic Structures in Oxide Ceramics
15:00–19:00 Excursion

20:00 Banquet

August 5th, Saturday

Chair: T. Mukoyama
9:00 Plenary 4. S. Nasu (Osaka University): Hyperfine Interaction Study of Materials and Related DV-Xα Calculations

Chair: D.Y. Lee
9:40 Invited 12. Masao Morishita and Hiroaki Yamamoto (University of Hyogo): Thermal Spectroscopy of $Mg_{48}Zn_{52}$, Mg_2Zn_3, $MgZn_2$ and Mg_2Zn_{11} from Near Absolute Zero Kelvin: Electronic Term Contributing to Heat Capacity, Electric Resistivity and Thermal Conductivity

10:00 Invited 13. Y. Kowada (Hyogo University of Teacher Education): Chemical Bonding of Mobile Cations in Superionic Conductors

10:20 Invited 14. Katsumi Nakagawa (Canon Inc.) Trial of Non-LCAO DVXα Method

10:40–11:00 Coffee Break

Chair: Y. Kowada
11:00 Invited 15. Kimichika Fukushima (AITEL Corporation): First-Principle Analysis of Metal Oxides and Investigation of Catalytic Properties for Dimethyl Ether Steam Reforming

11:20 Invited 16. Tomohiko Ishii, Yuya Yamaoka, Daisuke Kudo, Genta Sakane and Masataka Mizuno (Kagawa University, Okayama University of Science, Osaka University): Electronic Structures and Magnetic Properties of Single-Molecule Magnets (SMMs)

Industrial–Academic Cooperation Talk
11:40 Invited 17. Hisashi Yoshida and Kazuyoshi Ogasawara (NEC Lighting, Ltd., Kwansei Gakuin University): A Novel Study of Phosphors using Relativistic DV-Xα Method

Chair: J. Kawai
12:00 DV-Xα Award Ceremony (K. Fukushima), Closing Address (H. Adachi)

12:15 DV-Xα Association Assembly (M. Morinaga),
Non-members are welcome to attend the Assembly as an observer.

CHAPTER 1

Thermal Spectroscopy of Magnesium–Zinc Binary Compounds Near Absolute Zero Kelvin: Coefficient of the Electronic Contribution to Heat Capacity and Density of States in the Vicinity of the Fermi Level

Masao Morishita[*], **Hiroaki Yamamoto**[*] and **Yasutomo Matsumoto**[**]

Contents

[*] Department of Materials Science and Chemistry, University of Hyogo, 2167 Shosha, Himeji, Hyogo 671-2201, Japan
Corresponding author. E-mail: morisita@eng.u-hyogo.ac.jp
[**] Graduate Student, University of Hyogo, 2167 Shosha, Himeji, Hyogo 671-2201, Japan

Advances in Quantum Chemistry, Vol. 54
ISSN 0065-3276, DOI 10.1016/S0065-3276(07)00001-9

Abstract The electronic states for the intermetallic compounds, $Mg_{48}Zn_{52}$, Mg_2Zn_3, $MgZn_2$ and Mg_2Zn_{11} in the Mg–Zn binary system were investigated by measuring the coefficients γ of the electronic contribution to the heat capacities and calculating the densities of states (DOS) in the vicinities of the Fermi levels (E_F) by the DV-Xα molecular orbital method. The γ value of Mg_2Zn_{11} was found to be nearly equal to that of pure Zn while the γ value of $Mg_{48}Zn_{52}$ and Mg_2Zn_3 was similar to that of pure Mg. The γ value of $MgZn_2$ was comparable to the simple compositional average of the γ values of pure Mg and Zn. Such γ values probably result from the localization or de-localization of valence electrons, consistent with the DOS theoretically calculated by the DV-Xα molecular orbital method. The combined use of the measured γ and the calculated DOS is expected to provide an important method to clarify electronic states of substances as thermal spectroscopy.

1. INTRODUCTION

In the field of not only traditional metallurgy but also recently developed nano-technology, it is very interesting and important what change is introduced when it is surrounded by other atoms. Such a change in electronic states has been investigated as chemical shift detected by X-ray (XPS) and UV (UPS) photoemission spectroscopy [1] as well as X-ray emission and absorption spectroscopy [2,3]. Also, such a chemical shift has been simulated by theoretical calculation [4]. However, many problems have been unsolved. In the case of XPS and UPS, since the most outer layers of substances are analyzed, the spectra are easily affected by absorbed gaseous molecules. Also, with the X-ray emission and absorption spectroscopy it is difficult to analyze the complicated X-ray transition states for substances composed of heavy metal elements. Therefore, a complementary method has been demanded for the spectroscopy such as XPS, UPS and X-ray emission and absorption spectroscopy. The coefficient γ of the electronic contribution to heat capacity, C_p, near absolute zero Kelvin reflects the density of states (DOS) in the vicinity of Fermi level (E_F) [5]. Therefore, the measurement of γ is expected to be one of the useful methods to clarify the electronic states of substances composed of heavy metal elements.

Recently a relaxation method [6,7] has been developed to measure C_p at very low temperature. As the method can change a sample temperature rapidly due to the use of a very small amount (5–30 mg) of sample for the measurement, the C_p values at the temperature can be determined rapidly and precisely from near absolute zero to 400 K [8–14]. In the present study, we have attempted to determine the γ values of the intermetallic compounds of the Mg–Zn binary system by using the relaxation method.

In the Mg–Zn binary system, as the composition goes from magnesium- to zinc-side, there are stoichiometric compounds of $Mg_{48}Zn_{52}$, Mg_2Zn_3, $MgZn_2$ and Mg_2Zn_{11}. Their valence bands are composed of Mg electrons spread over the crystal as if they are nearly free electrons in pure magnesium and localized Zn-3d electrons. Therefore, it is very important to know how the de-localization or the localization of their valence electrons is caused as a function of magnesium

or zinc content. Also, they are interesting compounds from view of lattice vibration states, since they have the long-range periodic structures with large-sized unit cell.

In the present study, the γ values of the compounds were determined by measuring the C_p values at very low temperatures. Also, the γ values obtained were compared with the DOS calculated by the DV-Xα molecular orbital method [4]. In addition, the Debye temperature, the standard entropy of formation, the electric resistivity ρ and the thermal conductivity κ were further determined for each compounds. The physico-chemical properties of the compounds were discussed from both views of the electronic and lattice vibration states.

2. EXPERIMENTAL

2.1 C_p

Figure 1.1 shows the phase diagram of the Mg–Zn binary system. $Mg_{48}Zn_{52}$, Mg_2Zn_3, $MgZn_2$ and Mg_2Zn_{11} were prepared by melting in a high-frequency induction furnace in Ar, followed by heat treatment as described in our previous studies [8,10,11,13]. Each specimens of the compounds was cut into $2.5 \times 2.5 \times 1\,mm^3$ and diameter 6 mm and thickness 1.5 mm for the measurement of the heat capacity C_p at low and high temperatures, respectively.

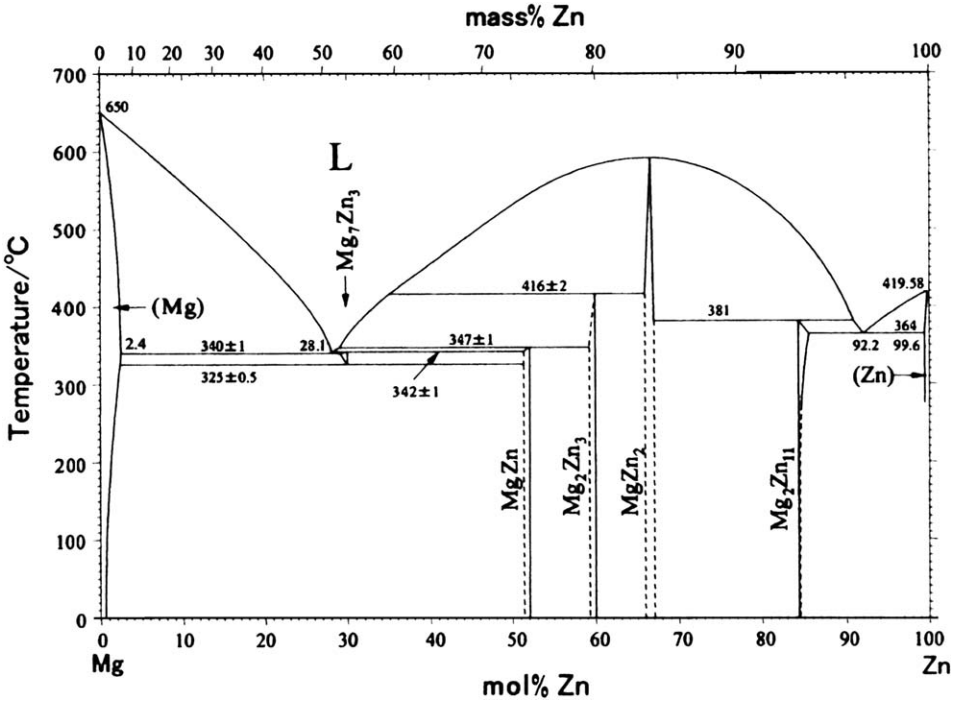

Figure 1.1 Phase diagram of the Mg–Zn binary system. Reproduced by permission from Ref. [15].

The entropy of a material S_T, based on the third law of thermodynamics is given by,

$$S_T = \int_0^T \left(\frac{C_p}{T}\right) \mathrm{d}t. \tag{1}$$

The C_p values of $Mg_{48}Zn_{52}$, Mg_2Zn_3, $MgZn_2$ and Mg_2Zn_{11} were measured from 2 K to 400 K by the relaxation method [6,7–14] and at 400–680 K by a heat-flow stabilized differential scanning calorimeter (DSC) [9,13]. Since C_p is negligibly small below 2 K, S_T can be determined from the data measured over 2 K. The measurements for determining the low-temperature C_p were repeated six times, and their average values were adopted. The measurements for determining the high-temperature C_p were repeated five times, and their average values were adopted.

The entropy of formation $\Delta_f S_T^\circ$ of Mg_XZn_Y is given by

$$\Delta_f S_T^\circ(Mg_XZn_Y) = S_T(Mg_XZn_Y) - XS_T(Mg) - YS_T(Zn) \quad [J\,K^{-1}\,mol^{-1}]. \tag{2}$$

Here, S_T(Mg) and S_T(Zn) are the third law entropies of pure magnesium and pure zinc, respectively. The values of S_T(Mg) and S_T(Zn) were taken from the NIST data [16,17]. In the present study, thermodynamic values are expressed as the formulation for 1 mole atom.

2.2 γ

At low temperatures, almost all lattice vibrations cease to contribute, leaving the thermal excitations of the electrons dominant [5]. The electronic term contributing to the constant volume heat capacity C_v is proportional to temperature T and the vibrational term is proportional to T^3. Consequently, C_v is expressed as [5],

$$C_v = \gamma T + AT^3, \tag{3}$$

where γ and A are defined as the coefficients of the electronic and the vibrational terms, respectively. Since C_v and C_p are very similar at low temperatures [5], C_p can be approximately used instead of C_v. The quantity γ reflects the DOS in the vicinity of the Fermi level, E_F [5]. Dividing both sides of Eq. (3) by T and substituting C_p into C_v, Eq. (3) can be rewritten as,

$$\frac{C_p}{T} = \gamma + AT^2. \tag{4}$$

The γ values of $Mg_{48}Zn_{52}$, Mg_2Zn_3, $MgZn_2$ and Mg_2Zn_{11} were determined from the measured low-temperature C_p values.

Also, their Debye temperatures Θ_D were determined by inserting γ and A into Eq. (5) [18],

$$\Theta_D = \left[\frac{\{(12/5)\pi^4 R\}}{A}\right]^{1/3}, \tag{5}$$

where R is the gas constant.

2.3 κ and ρ

The thermal conductivity κ was measured at 298 K by the laser-flush method for each compounds with the specimen shape of diameter 6 mm and thickness 1.5 mm. The electric resistivty ρ was measured from 2 to 300 K by the four terminal method for each compounds with the specimen shape of $2 \times 4 \times 7\,mm^3$.

3. CLUSTER MODELS FOR THE DV-Xα MOLECULAR ORBITAL CALCULATION

The long-range crystal structures of $MgZn_2$ [19] and Mg_2Zn_{11} [20] are composed of the assembly of hcp zinc cells, judging from its lattice parameter. Although the atomic configurations in the unit cell have been unsolved, their chemical formula indicate that the magnesium atoms are basically surrounded by the zinc atoms in their lattice. In the present study, a cluster model of $Zn_{18}Mg$ was approximately adopted to investigate the electronic states for $MgZn_2$ and Mg_2Zn_{11}, in which the centered magnesium atom was surrounded by 12 first-neighbor zinc atoms and 6 second-neighbor zinc atoms in a hexagonal zinc lattice.

$Mg_{48}Zn_{52}$ [21] and Mg_2Zn_3 [22] have been found to have a very long range periodic structure according to their X-ray diffraction patterns [21,22] although their atomic configurations are still unknown. Especially the crystal structure of $Mg_{48}Zn_{52}$ [21] is composed of at least one hundred atoms. Since both of the crystal structures of pure magnesium and pure zinc are hcp, it is supposed that the long-range periodic structures of $Mg_{48}Zn_{52}$ and Mg_2Zn_3 are composed of the assembly of hcp cells. Also, Mg–Mg bonding should be formed in $Mg_{48}Zn_{52}$ and Mg_2Zn_3, from their chemical formula. A hexagonal cluster model of Mg_{19} was adopted to investigate the local electronic states around such an Mg–Mg bonding. Furthermore, a cluster model of Zn_{19} was adopted to clarify the DOS for the zinc atom in an hcp zinc lattice.

The lattice parameter of pure zinc, that is $a = 0.26650$ nm and $c = 0.49470$ nm [23], was approximately adopted for the cluster models of $Zn_{18}Mg$ and Zn_{19}. The lattice parameter of pure magnesium, that is $a = 0.32095$ nm and $c = 0.52107$ nm [23], was also adopted for the cluster models of Mg_{19}.

4. RESULTS AND DISCUSSIONS

4.1 C_p and γ

Figure 1.2 shows the C_p values of Mg_2Zn_3 [11]. The C_p values increased over 10 K as a function of temperature due to the lattice vibration. A peak near 560 K was detected, indicating that polymorphic transformation took place in it [11]. The C_p values below 10 K are very important for investigating the electronic states. The γ was determined from the low-temperature C_p values on the basis of Eq. (4).

Figure 1.3 shows the relationships between (C_p/T) and (T^2) near absolute zero Kelvin ($T^2 < 14\,K^2$) for Mg_2Zn_3 [11]. In the same way, the C_p values of $Mg_{48}Zn_{52}$

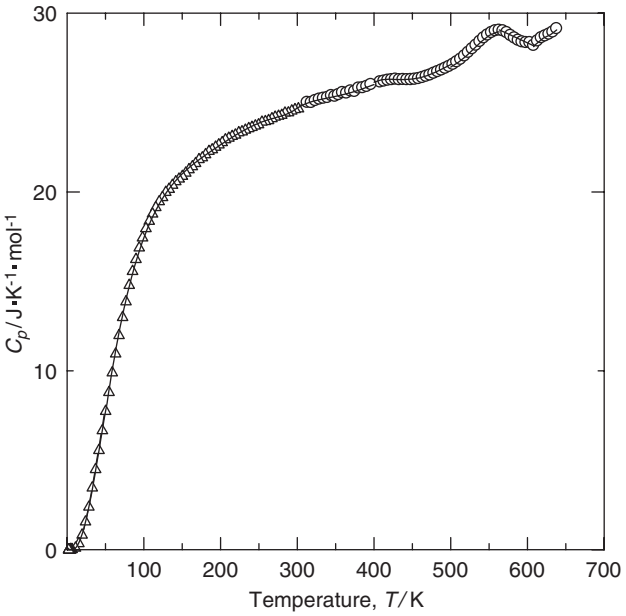

Figure 1.2 Measured C_p values of Mg_2Zn_3, reproduced by permission from Ref. [11]. In the temperature range of 2–400 K, C_p values were measured by the relaxation method, and in the temperature range of 400–500 K, C_p values were measured by DSC.

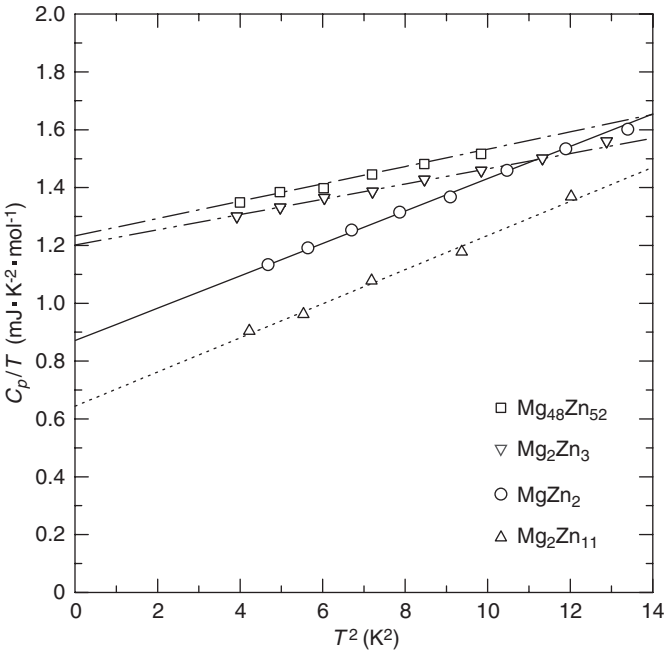

Figure 1.3 C_p/T vs. T^2 for $Mg_{48}Zn_{52}$ [10], Mg_2Zn_3 [11], $MgZn_2$ [13] and Mg_2Zn_{11} [8]. Reproduced with permission from Refs. [8] (p. 969, Figure 2); [10] (p. 894, Figure 2); [11] (p. 35, Figure 3); and [13] (p. 3159, Figure 8).

Table 1.1 Experimental coefficients γ ($mJ\,K^{-2}\,mol^{-1}$) of the electronic contribution and coefficients A ($mJ\,K^{-4}\,mol^{-1}$) of the vibrational contribution of $Mg_{48}Zn_{52}$, Mg_2Zn_3, $MgZn_2$ and Mg_2Zn_{11}

	Mg	$Mg_{48}Zn_{52}$	Mg_2Zn_3	$MgZn_2$	Mg_2Zn_{11}	Zn
γ	1.3 [24]	1.233 [10]	1.201 [11]	0.871 [13]	0.644 [8]	0.64 [24]
A	–	0.030 [10]	0.026 [11]	0.056 [13]	0.059 [8]	–

Note: References are given in square brackets.

[10], $MgZn_2$ [13] and Mg_2Zn_{11} [8] have been measured in our previous studies [8,10,13]. The relationships between (C_p/T) and (T^2) for $Mg_{48}Zn_{52}$ [10], $MgZn_2$ [13] and Mg_2Zn_{11} [8] are also shown in Figure 1.3 for comparison. Since linear relationships were observed in all compounds, their γ and A values were determined from the intercept at $T = 0$ and the slope, respectively.

Table 1.1 shows the γ and A values of $Mg_{48}Zn_{52}$ [10], Mg_2Zn_3 [11], $MgZn_2$ [13] and Mg_2Zn_{11} [8], together with those of pure magnesium and pure zinc [24]. The γ values of $Mg_{48}Zn_{52}$ [10] and Mg_2Zn_3 [11] were found to be similar to that of pure magnesium [24]. The γ of Mg_2Zn_{11} [8] was nearly equal to that of pure zinc [24]. Also, γ of $MgZn_2$ [13] was found to be similar to the simple composition average of the γ values of pure magnesium and pure zinc: $1.3 \times 0.333 + 0.64 \times 0.667 = 0.86\,mJ\,K^{-2}\,mol^{-1}$.

The γ of pure Mg is high since the DOS for the conduction band being composed of 3s and 3p components is spread approximately following the free-electron parabolic law. On the other hand, in pure Zn, the DOS for the conduction band being composed of 4s and 4p components appears to be deviated from the free-electron parabolic law due to the trapping by the strongly localized 3d components in it. Thus, the γ of pure Zn is lower than that of pure Mg. Such a localization or de-localization of the valence electrons state also appears in the Mg–Zn binary compounds depending on the composition. The DOS for the cluster models were calculated, in order to obtain better understanding the electronic states for de-localization or localization of the Mg–Zn binary compounds.

4.2 DOS

Figure 1.4 shows the DOS for the sum of 3s, 3p and 3d components of the magnesium atom located at a center of the cluster model of $Zn_{18}Mg$. Also, the DOS is shown in Figure 1.4 for the sum of 3d, 4s and 4p components of the zinc atom located at a center of the cluster model of Zn_{19}. From the DOS for Zn, the strong localization of the 3d component was found as peak ''a'' shown in Figure 1.4. Peaks A and A′ in the DOS for Mg corresponded to the trapped state of electrons by the 3d component of Zn. Also, the peaks B–G in the DOS for Mg are overlapped with the peaks b–g in the DOS for Zn. Namely, the electronic state DOS for Mg localized by the presence of Zn in the neighborhood, resulting in the deviation from the free-electron parabolic law. It is likely that such electronic states for the

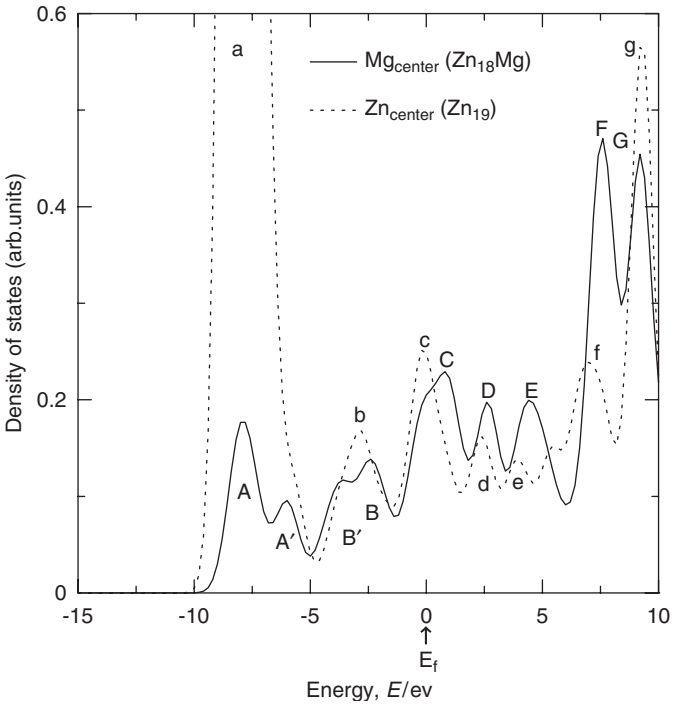

Figure 1.4 DOS for sum of 3s, 3p and 3d components for Mg centered in $Zn_{18}Mg$ cluster model and DOS for sum of 3d, 4s and 4p components for Zn centered in Zn_{19} cluster model.

magnesium atom surrounded by the zinc atoms result in the γ of Mg_2Zn_{11} which is nearly equal to the value of pure zinc.

Figure 1.5 shows DOS for the sum of 3s, 3p and 3d components of the magnesium atom located at a center of the cluster model of Mg_{19}. The DOS for Mg was found to change approximately following a free-electron parabolic law. This indicates that valence electrons of the magnesium atom appear to spread along the Mg–Mg bond. Such an Mg–Mg bond should be formed in $Mg_{48}Zn_{52}$ and Mg_2Zn_3, according to their chemical formula. In such a case, the 3s and 3p components for Mg are released from the trapped state by the 3d components for Zn in $Mg_{48}Zn_{52}$ and Mg_2Zn_3 and then the nearly free-electron parabolic law is satisfied. As a result, the γ values of $Zn_{48}Mg_{52}$ and Mg_2Zn_3 are similar to that of pure magnesium, as shown in Table 1.1.

The DOS for the magnesium and zinc atoms in $MgZn_2$ appears to be hybridized altogether. As a result, the γ of $MgZn_2$ appears to be close to the simple composition average of the γ values of pure magnesium and pure zinc. The Mg content is 6.7 mol% lower in $MgZn_2$ than in Mg_2Zn_3. It is likely that such a decrease of Mg content in the unit cell prevents the spreading of the valence electrons along the Mg–Mg bond. The atomic configurations in the unit cell of the compounds should be further investigated by using Rietveld analysis.

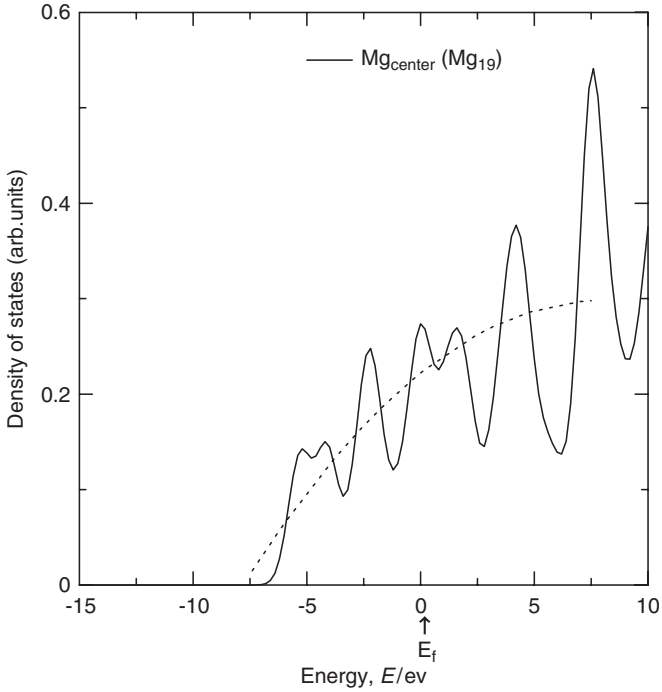

Figure 1.5 DOS for sum of 3s, 3p and 3d components for Mg centered in Mg_{19} cluster model.

4.3 Entropy of formation and the Debye temperature

Table 1.2 shows the entropies of formation of $Mg_{48}Zn_{52}$ [10], Mg_2Zn_3 [11], $MgZn_2$ [13] and Mg_2Zn_{11} [8] at 100, 298 and 500 K. The physical meaning of the entropy of formation is the entropy of vibration [25]. The entropy of formation was higher in $Mg_{48}Zn_{52}$ than in the other compounds. Its large-sized unit cell, that is constructed by at least one hundred atoms, is considered to induce complicated lattice vibrations in it. As a result, its entropy of formation becomes high.

Also, the crystal structure of Mg_2Zn_3 is a very long range periodic structure [22]. However, its entropy of formation was lower than that of $Mg_{48}Zn_{52}$. Since the entropy of vibration decreases as the cohesive energy increases, it is likely that the lattice vibration states of Mg_2Zn_3 are not so complicated but instead its cohesive energy is high.

The Debye temperatures of $Mg_{48}Zn_{52}$, Mg_2Zn_3, $MgZn_2$ and Mg_2Zn_{11} are also shown in Table 1.2. The Debye temperatures of $Mg_{48}Zn_{52}$ and Mg_2Zn_3 are high. It is well known that the Debye temperature of substance is generally high when its lattice vibration is complicated or its cohesive energy is high. Therefore, a high Debye temperature of $Mg_{48}Zn_{52}$ appears to be due to the complicated lattice vibration, and a high Debye temperature of Mg_2Zn_3 appears to be due to the high cohesive energy.

Table 1.2 Entropies of formation $\Delta_f S_T^\circ$ (J K^{-1} mol^{-1}) and Debye temperatures Θ_D (K) of $Mg_{48}Zn_{52}$, Mg_2Zn_3, $MgZn_2$ and Mg_2Zn_{11}

	$Mg_{48}Zn_{52}$	Mg_2Zn_3	$MgZn_2$	Mg_2Zn_{11}
$\Delta_f S_{100}^\circ$	−0.80	−1.42	−1.49	−0.70
$\Delta_f S_{298}^\circ$	−1.23 [10]	−2.19 [11]	−2.01 [13]	−1.73 [8]
$\Delta_f S_{500}^\circ$	−1.26	−2.37	−2.17	−2.08
Θ_D	401	421	326	320

Note: References are given in square brackets.

Table 1.3 Thermal conductivities κ (W m^{-1} K^{-1}) of $Mg_{48}Zn_{52}$, Mg_2Zn_3, $MgZn_2$ and Mg_2Zn_{11}

	$Mg_{48}Zn_{52}$	Mg_2Zn_3	$MgZn_2$	Mg_2Zn_{11}
κ	20.8	27.5	46.2	42.0

4.4 κ

Table 1.3 shows the κ values at 298 K of $Mg_{48}Zn_{52}$, Mg_2Zn_3, $MgZn_2$ and Mg_2Zn_{11}. The thermal conductivity κ was found to be lower in $Mg_{48}Zn_{52}$ than in other compounds. The reason for such a low κ of $Mg_{48}Zn_{52}$ appears to result from its complicated lattice vibration as explained by the entropy of formation and the Debye temperature. Also, κ of Mg_2Zn_3 was found to be low. The reason for such a low κ of Mg_2Zn_3 appears to be resulted from its high cohesive energy as explained by the entropy of formation and the Debye temperature.

4.5 ρ

Figure 1.6 shows the ρ values from 2 to 300 K of $Mg_{48}Zn_{52}$, Mg_2Zn_3, $MgZn_2$ and Mg_2Zn_{11}. The electric resistivity ρ was found to be higher in $Mg_{48}Zn_{52}$ than in the other compounds due to the complicated lattice vibration. The ρ of Mg_2Zn_3 was lower than that of $Mg_{48}Zn_{52}$ and close to $MgZn_2$ and Mg_2Zn_{11} near 300 K. It is possible that such a low ρ of Mg_2Zn_3 is not attributable to the complicated lattice vibration as shown by its entropy of formation and de-localized component as given by its γ. Thus, Mg_2Zn_3 has a contradicting property, that is, low ρ but low κ. Such a contradicting property is materialized from its very long range periodic structure.

A contradicting property, that is, low ρ but low κ, is generally necessary for materials used for thermoelectric modules. Consequently we conclude that the study for the electronic states and lattice vibration states for the substances with very long range periodic structure like Mg_2Zn_3 is important to the development of novel materials.

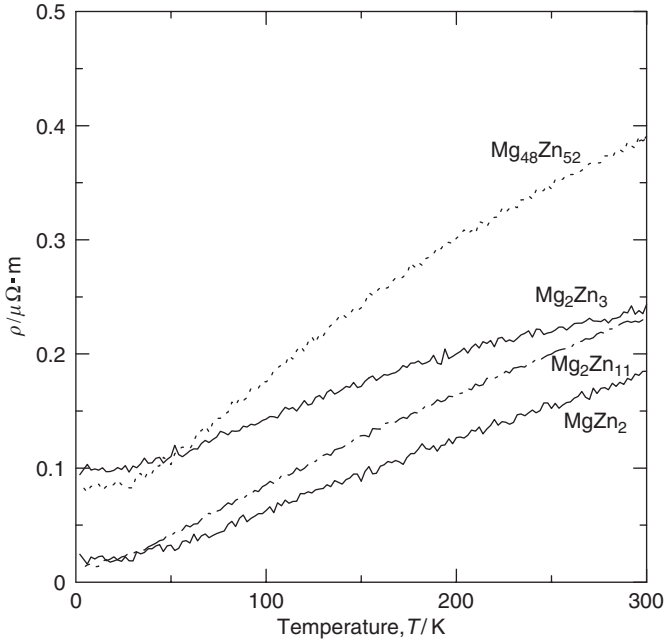

Figure 1.6 Electric resistivities ρ ($\mu\Omega \cdot$ m) of $Mg_{48}Zn_{52}$, Mg_2Zn_3, $MgZn_2$ and Mg_2Zn_{11} at 2–300 K.

5. CONCLUSION

The physico-chemical properties of the magnesium–zinc binary compounds were discussed from both views of the electronic and lattice vibration states. The coefficients of an electronic term γ contributing to the heat capacities were measured for the intermetallic compounds, $Mg_{48}Zn_{52}$, Mg_2Zn_3, $MgZn_2$ and Mg_2Zn_{11} in the Mg–Zn binary system. The γ value of Mg_2Zn_{11} was found to be nearly equal to that of pure Zn, while the γ of $Mg_{48}Zn_{52}$ and Mg_2Zn_3 were similar to that of pure Mg. The γ value of $MgZn_2$ was similar to the simple composition average of the γ values of pure Mg and pure Zn. Such γ values were resulted from the localization or de-localization of the valence electrons, consistent with the DOS calculated theoretically by the DV-Xα molecular orbital method. The Debye temperature and the thermal conductivity κ of Mg_2Zn_3 were high and low, respectively, indicating a complicated atomic configuration and a high cohesive energy. However, electric resistivity ρ of Mg_2Zn_3 was comparatively low due to the de-localized components of the valence electrons. Such contradicting properties appear to be materialized from its long-range periodic structure. Consequently we conclude that the study for the electronic states and lattice vibration states for substances composed of very long range periodic structure is important to develop new frontier materials.

REFERENCES

[1] B. Fisher, R.A. Pollak, T.H. DiStefano, W.D. Grobman, *Phys. Rev.* **15B** (1977) 3193.
[2] J. Kawai, *Adv. Quantum Chem.* **29** (1997) 329.
[3] K. Ogasawara, I. Tanaka, H. Adachi, *Adv. Quantum Chem.* **29** (1997) 441.
[4] H. Adachi, *Adv. Quantum Chem.* **37** (2000) 1.
[5] T.H.K. Barron, G.K. White, *Heat Capacity and Thermal Expansion at Low Temperatures*, Plenum, New York, 1999, p. 234.
[6] J.S. Hwang, K.J. Lin, C. Tien, *Rev. Sci. Instrum.* **68** (1997) 94.
[7] J.C. Lashely, M.F. Hundley, A. Migliori, A.J.L. Sarrao, P.G. Pagliuso, T.W. Darling, M. Jaime, J.C. Cooley, W.L. Hults, L. Morales, D.J. Thoma, J.L. Smith, J. Boerio-Goates, B.F. Woodfield, G.R. Stewart, R.A. Fisher, N.E. Phillips, *Cryogenics* **43** (2003) 369.
[8] M. Morishita, K. Koyama, *Z. Metallkd.* **94** (2003) 967.
[9] M. Morishita, A. Navrotsky, *J. Am. Ceram. Soc.* **86** (2003) 1927.
[10] M. Morishita, K. Koyama, S. Shikada, M. Kusumoto, *Met. Mater. Trans.* **35B** (2004) 891.
[11] M. Morishita, K. Koyama, S. Shikada, M. Kusumoto, *Z. Metallkd.* **96** (2005) 32.
[12] M. Morishita, K. Koyama, *J. Alloys Compd.* **398** (2005) 12.
[13] M. Morishita, H. Yamamoto, S. Shikada, M. Kumoto, Y. Matsumoto, *Acta Mater.* **54** (2006) 3151.
[14] M. Morishita, H. Yamamoto, K. Tsuboki, Y. Matsumoto, *Mater. Trans.* **47** (2006) 1555.
[15] J.B. Clark, L. Zabdyr, Z. Moser, Binary Alloy Phase Diagram, In: T. B. Massalski (Ed.), Second ed., ASM OH, **3** (1990) 2571.
[16] M.W. Chase, NIST-JANAF Thermochemical Tables (1998) p. 1530.
[17] M.W. Chase, NIST-JANAF Thermochemical Tables (1998) p. 1936.
[18] N.E. Phillips, *Phys. Rev.* **134** (1964) A385.
[19] JCPDS X-ray Reference Data No. 1-1211 (2001).
[20] JCPDS X-ray Reference Data No.6-0665 (2001).
[21] JCPDS X-ray Reference Data No. 40-1334 (2001).
[22] JCPDS X-ray Reference Data No. 08-0196 (2001).
[23] B.D. Cullity, *X-Ray Diffraction*, second ed., Agne, Tokyo, 1997, p. 467 [Translated to Japanese].
[24] C. Kittel, *Introduction to Solid State Physics*, seventh ed., Maruzen, Tokyo, 1998, p. 173 [Translated to Japanese].
[25] R.A. Swalin, *Thermodynamics of Solids*, Corona, Tokyo, 1974, p. 42 [Translated to Japanese].

CHAPTER 2

First-Principles Calculation of Energy Band Structure of Gallium Arsenide Crystals Using Madelung Potential

S. Kishino*, K. Sueoka** and **H. Yoshida*****

Contents

Abstract

Energy band structure of gallium arsenide crystals is calculated by the discrete variational (DV)-Xα molecular orbital method using a Madelung potential. By the use of the Madelung potential technique we found a possibility to be able to obtain energy band gaps close to the intrinsic values in the case of GaAs crystal. We then applied the technique to Zn-doped GaAs crystal with external strain and investigated an acceptor level as a function of the magnitude of external strain induced. By this investigation, we found a possibility that the acceptor level becomes shallower by the introduction of the external strains. The application of the Madelung potential to the semiconductor crystals is the first trial and the related technical procedures have not yet been established. Therefore, further investigations on this technique are to be continued.

1. INTRODUCTION

Regarding the calculation of an energy band structure of the semiconductor crystals there is a problem of dangling bond formation followed by the resultant

* Department of Electrical Engineering, Fukui University of Technology, 3-6-1, Gakuen, Fukui 910-8505, Japan
Corresponding author. E-mail: sg-kishino@fukui-ut.ac.jp
** Department of System Engineering, Okayama Prefectural University, 111 Kuboki, Soja 719-1197, Japan
*** Graduate School of Engineering, University of Hyogo, 2167 Shosha, Himeji 671-2280, Japan

Advances in Quantum Chemistry, Vol. 54
ISSN 0065-3276, DOI 10.1016/S0065-3276(07)00002-0

introduction of localized states in energy band gap. The problem has been usually solved using hydrogen termination technique [1]. Besides the problem, we have another difficulty in which energy band gaps calculated are considerably large in comparison with the intrinsic value. This difficulty could be eliminated if a large sized cluster with atoms more than 1000 is used. However, this is not practical because of long time consumption for calculation.

As a solution to this problem we have tried the application of Madelung potential [2] to the semiconductor crystals. Till now, the trial has not been carried out in the semiconductor crystals to our knowledge except our presentation at the fourth international conference on DV-Xα method (2006) [3]. The difficulty in the application to the semiconductor crystals might be related with a kind of a sea with $\pm$ electronic charges used in the Madelung potential technique. This is partly so because the semiconductor crystals such as Si and diamond are of covalent bond structure and these crystals are composed of a single element. These two difficulties make the application of a Madelung potential to the semiconductor crystals difficult.

After finding some application technique of Madelung potential to the semiconductor crystals, we applied the Madelung potential technique to the strained GaAs crystals. A technique of strain introduction to semiconductor crystal has been prevailing in the field of Si devices [4,5]. This technique is aimed for a higher mobility of carrier in order to develop a higher speed device. The technique will be applied to GaAs crystal in the future. With these circumstances as a background, we calculated the energy band structures of strained p-type GaAs crystals doped with Zn and investigated an acceptor energy level as a function of the magnitude of induced strain.

2. APPLICATION OF MADELUNG POTENTIAL TO SEMICONDUCTOR CRYSTALS

Regarding the application of a Madelung potential to the semiconductor crystals we obtained a beneficial hint from a GaAs crystal which is of zinc blend structure. As is well known, diamond structure is the same in structure except the composite elements. Therefore, it is conjectured that the application technique of Madelung potential is similarly applicable to Si and diamond crystals if an application technique to the GaAs crystal is established. Firstly, we applied the Madelung potential technique to an undoped GaAs cluster model with 87 atoms using the electronic charge of ± 3. This is because Ga has a valence of +3 charge. Besides the +3 charge a -3 charge was added to maintain electric neutrality of the model cluster. After the calculation we focused our attention to a value of band gap E_G as shown in Table 2.1. In Table 2.1 calculation results of Si and diamond crystals are also tabulated in which electric charges of ± 4 are used in these crystals because Si and C have a valence of 4 charges. Data on Si and diamond crystals were reported at the fourth international conference on DV-Xα method (2006) held at Jeju [3].

Table 2.1 Energy band gap E_G of Si, diamond, and GaAs calculated using Madelung potential [3]

Cluster	Si (eV)		C (Dia) (eV)		GaAs (eV)	
	H.T.	M.P.	H.T.	M.P.	H.T.	M.P.
87 atoms	3.01	1.17	8.73	5.76	2.97	1.78
Intrinsic	1.12		5.47		1.42	
Value (0 K)	(1.17)		(5.48)		(1.52)	

Note: H.T. and M.P. show hydrogen termination technique and Madelung potential technique, respectively.

Subsequently, we doped p-type impurity (Zn) to GaAs crystals and obtained about 0.3 eV [3] above valence band as an acceptor level. This value was too large in comparison with the intrinsic value (0.031) [6]. However, we were not able to decrease the value of acceptor level from this value with electric charge of 3. Then, we tried to decrease the electric charges of Madelung potential from ± 3 to ± 1. This change was carried out by the consideration of ionic feature of GaAs crystal. GaAs crystals are not ionic by nature and so ± 3 electric charges were too large for the GaAs crystals from the beginning. By this procedure we obtained an energy band as shown in Figure 2.1(a). The comparison of the energy band in the case of ± 3 electric charge is shown in Figure 2.1(b).

The energy band gap and the acceptor level obtained by the calculation are shown in Table 2.2, where the previous results using ± 3 electric charges are also shown for comparison. Next, we investigated a sectional contour plot of wave function for the present GaAs cluster model with and without the Madelung potential. In this case two cross sections of the model cluster were used. One cross section was composed of three atomic coordinates, some of which included dangling bonds. The other was also composed of three atomic coordinates, but these atomic coordinates had no relation to the dangling bonds. Namely, the latter three atomic coordinates were composed of perfect atomic coordinates without dangling bonds. As to the contour plot of the wave function in the cross section composed of three perfect coordinates, we could not find any notable difference between the case with and without the electric charges for Madelung potential. However, we found some difference in the contour plot of the wave function when the cross section was composed of the atomic coordinates, some of which contained the dangling bonds.

In Figure 2.2(a) and (b), we showed the contour plots of the wave function in the cross section of the GaAs cluster. Here we compared the two contour plots of the wave function in the cross section with and without the dangling bonds. Figure 2.2(a) and (b) show contour plots of wave function of highest occupied molecular orbit (HOMO) level for the GaAs cluster with and without Madelung potential, respectively. Strictly speaking, the contour plot of the cluster model without Madelung potential was not the wave function of HOMO level because the HOMO level without the Madelung potential became one of a localized state due to the dangling bonds existing in the cluster. From these two plots we can see that some rearrangement of the wave functions occurred by the application of the Madelung potential to the GaAs model cluster.

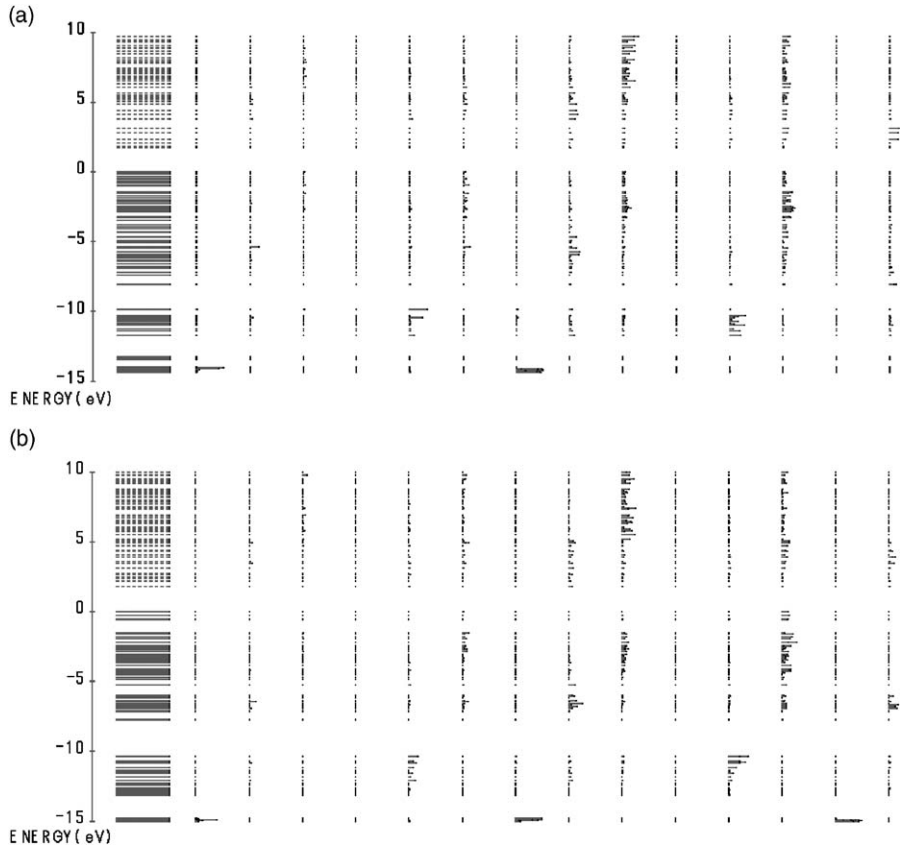

Figure 2.1 (a) Energy band when the electronic charges for Madelung potential are ± 1. (b) Energy band when the electronic charges for Madelung potential are ± 3.

Table 2.2 Variation of energy band gap E_G and acceptor level E_A by the change of number of electronic charge for Madelung potential

Electronic charge	± 3	± 1	Intrinsic value
Band gap (eV)	1.78	1.34	1.52
Acceptor level (eV)	0.37	0.11	0.031

Regarding the acceptor level we investigated the dependence of the energy values on the number of electric charges surrounding the model cluster. The results are shown in Table 2.3, where the dependence of energy gap on the number of electronic charges is also shown. From Table 2.3, the acceptor level was gradually decreased by the increase in the number of electric charges surrounding the model cluster. On the other hand, the energy gap was gradually increased.

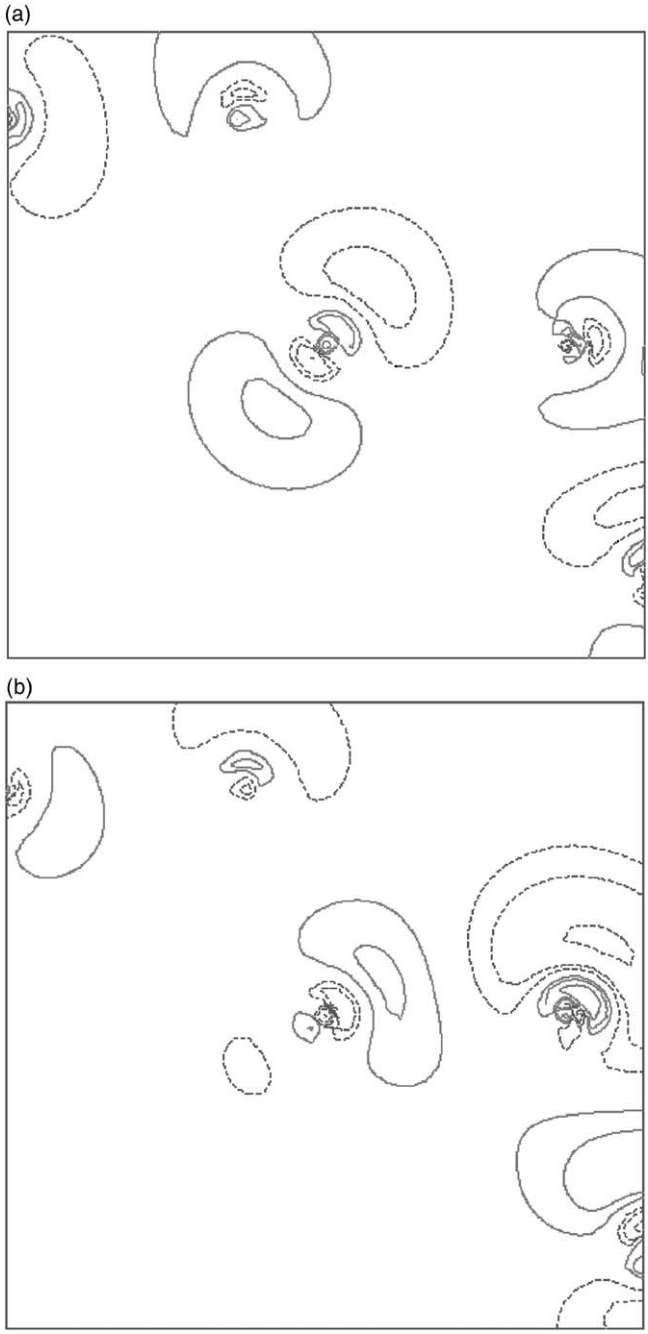

Figure 2.2 (a) Contour plot of the wave function of HOMO level for GaAs cluster model with Madelung potential. (b) Contour plot of wave function for GaAs cluster model without Madelung potential in which the energy level corresponds to the HOMO level in the case using Madelung potential.

Table 2.3 Dependence of acceptor level E_A and energy band gap E_G on the number of electronic charges surrounding GaAs cluster model

Number of electronic charge	E_G	E_A
640	1.258	0.1131
5,376	1.339	0.1066
10,560	1.346	0.1062
43,520	1.353	0.1059
98,560	1.356	0.0984

Through this procedure we obtained a shallower acceptor level in comparison with the previous one (about 0.4 eV) when Zn impurity was doped into GaAs crystals, but the reduced value (about 0.1 eV) was still large in comparison with the intrinsic value. Regarding the value of acceptor level we must continue to investigate the calculation method to obtain a shallower value. Anyway, in the present report we have studied the strained GaAs crystal using the conditions of electronic charge of ± 1.

3. APPLICATION TO STRAINED GaAs CRYSTAL

As is mentioned in the previous section, the Madelung potential technique is very useful for the calculation of energy band structure of GaAs crystal. As an application of this technique, we applied the Madelung potential technique to a strained GaAs crystal. As is well known, the GaAs crystals have been prevailing as materials for high-frequency devices [7]. This means that the GaAs crystals are beneficial materials for high switching speed devices. For obtaining the higher switching devices the strain semiconductor techniques will be also applied to the GaAs crystals as is now prevailing in the field of Si LSI devices.

With these circumstances as a background we investigated a p-type strained GaAs crystal doped with Zn using the Madelung potential technique. In order to introduce strain into GaAs crystal uni-axial stress was used where tension was applied to the crystal in the x-direction and compression was made in the z-direction. No stress was applied in the y-direction. In the actual cluster model the x-coordinates were increased, whereas the z-coordinates were decreased, and the y-coordinates were unchanged. Regarding the z-coordinates the values of the coordinate were decreased by the same absolute values as x-coordinates. The x-coordinates were varied as shown in Table 2.4 from 0.03 to 10% in a suitable step. We mainly investigated a variation of an acceptor level by strain introduction. We used a cluster model with 87 atoms.

Calculated results are shown in Table 2.4 and Figure 2.3. In Table 2.4 the calculated band gaps are a little bit smaller. This is due to the difference of calculation technique. In the data shown in Table 2.4, the degree of symmetry for the calculation was lower than the case shown in Table 2.2. In Figure 2.3 both the

Table 2.4 Change of acceptor level by external strain

Strain (%)	Band gap (eV)	Acceptor level (eV)
0	1.280	0.1090
0.03	1.281	0.1090
0.1	1.282	0.1093
0.3	1.284	0.1086
0.45	1.276	0.1036
0.6	1.275	0.1042
1.0	1.265	0.1034
3.0	1.213	0.1013
10.0	1.051	0.2342

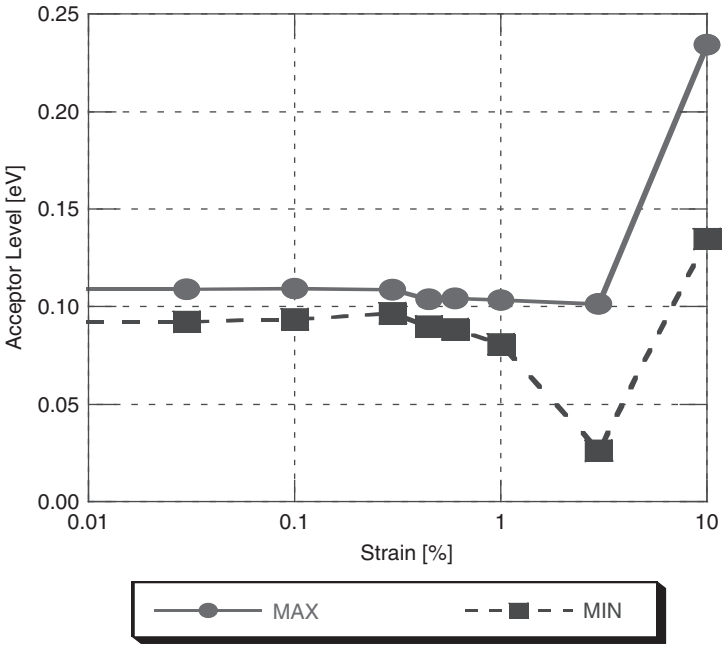

Figure 2.3 Variation of acceptor level by introduction of external strain.

maximal and minimal acceptor level are shown because of the band splitting induced by the external strain. However, in Table 2.4 only the maximal acceptor value is shown. From Table 2.4 we can see energy band gaps are almost of the same values (1.28 eV) although an energy band gap value decreased to 1.05 eV in the case of 10% strain. On the other hand, an acceptor level is varied depending on the size of induced strain and has a minimal value at the induced strain of about 3%.

4. DISCUSSIONS

As to the band gap reduction obtained by the use of the Madelung potential technique, we investigated the effect of the electric charges surrounding a model cluster. As a result, we found that the smaller electric charge is more suitable as the electric charge for the Madelung potential in the case of the GaAs crystal. This might be due to the ionic feature of the GaAs crystal. However, it is thought that the present conditions used for the calculation are not the best method because of the deeper acceptor level obtained. Therefore, further investigations must be made.

In addition, up to now, we showed the calculation results obtained without using the atomic coordinates after the lattice relaxation. When the impurity atom is introduced into the crystal some lattice relaxation occurs in order to reduce the total energy of the crystal. Therefore, we checked whether the calculation for lattice relaxation is necessary or not. Namely, we recalculated both the energy band gaps and acceptor levels using *x*-, *y*-, and *z*-coordinates determined by the calculation for the lattice relaxation [8]. This result is shown in Table 2.5.

In Table 2.5 the values with parenthesis show the calculation results without the lattice relaxation. As is seen in Table 2.5, calculated band gap values are little changed whether the coordinates after the lattice relaxation are used or not. As to the acceptor level there is a small difference in value between after and before the lattice relaxation. However, this is a negligibly small difference. It is therefore acceptable that the acceptor level has a minimal strain value of about 3%. However, it is not yet clear whether the present results are physically reasonable or not. Therefore, in the present stage, it is suitable to say that there is a possibility that an acceptor level has a minimal value at a certain strain introduction.

Regarding the cause for which an acceptor level of the GaAs crystal has a minimal value at the strained crystal, we conjecture two origins. One is that the total energy of the doped crystal is lowered by the introduction of external strain. As to this case we are now carrying out further investigations, which will be reported, including detailed results concerning total energy, in a separate future paper.

Table 2.5 Acceptor level of strained GaAs after lattice relaxation

Strain (%)	Band gap	Acceptor level (maximal value)
0	1.307	0.1234
	(1.280)	(0.1090)
0.6	1.301	0.1207
	(1.275)	(0.1042)
1.0	1.282	0.1107
	(1.265)	(0.1034)
3.0	1.230	0.1051
	(1.213)	(0.1013)
10.0	1.051	0.2342
	(1.051)	(0.2342)

As another cause we must consider the effect of band splitting of the acceptor level since the crystal symmetry will be broken by the introduction of the uni-axial strain. As is well known, a band split occurs at the semiconductor crystals when the symmetry of the crystal is broken. On these grounds we have showed maximal and minimal values of an acceptor level in Figure 2.3. The effect of the band splitting to the acceptor levels is under investigation and will be reported in the near future.

5. CONCLUSIONS

The following conclusions are obtained:

i. By the application of the Madelung potential technique to a GaAs crystal we showed a possibility that the energy band gap close to the intrinsic value is obtainable by the DV-Xα calculation without using the model cluster of a large number of atoms. However, more detailed investigations are necessary for the final conclusion.
ii. Compared with a hydrogen termination technique, the troublesome formation work on *x*-, *y*-, and *z*-coordinates becomes simple. This is a big advantage when we perform the calculation of the semiconductor crystal in which the external strain is introduced.
iii. Using the Madelung potential technique, we further found possible that a shallower acceptor level is obtained in the GaAs crystals when the small external strain is induced.
iv. The conclusion that an acceptor level in the GaAs crystal has the minimal value is not changed even when the lattice relaxation is considered, though more detailed investigations, where relativistic effects should be considered, must be performed.

ACKNOWLEDGMENTS

This work has been financially supported by FUT Research Promotion Fund.

REFERENCES

[1] Y. Higashiguchi, T. Numata, K. Ohmori, H. Kawasaki, Y. Hayafuji, *Bull. Soc. DV-Xα* **18** (2005) 101.
[2] M. O'Keeffe, *Structure and Bonding in Crystal*, Vol. 1, Academic Press, New York, 1981.
[3] S. Kishino, K. Sueoka, H. Yoshida, *DV-Xα* **19** (2006) 210.
[4] T. Vogelsang, K.R. Hofman, *Appl. Phys. Lett.* **63** (1993) 186.
[5] S. Takagi, J.L. Hoyt, J.J. Welser, J.F. Gibbons, *J. Appl. Phys.* **80** (1996) 1567.
[6] S.M. Sze, *Physics of Semiconductor Devices*, Wiley, 1981, p. 849.
[7] J.B. Gunn, *Solid State Commun.* **1** (1963) 88.
[8] K. Sueoka, S. Ohara, S. Fukutani, *Trans. Jpn. Soc. Mech. Eng.* **71** (2005) 1103.

CHAPTER 3

Structural Analysis and First-Principles Calculation of Lithium Vanadium Oxide for Advanced Li-Ion Batteries

Ri-Zhu Yin*, Yang-Soo Kim, Wanuk Choi*, Sung-Soo Kim*** and **Heejin Kim*****

Contents

Abstract

The structural and theoretical possibility of lithium vanadium oxide as next generation negative material for advanced Li-ion batteries is discussed. The initial and charged $Li_{1.1}V_{0.9}O_2$ compounds show $R\bar{3}m$ and $P\bar{3}m_1$ hexagonal structures respectively from XRD analysis. The electronic structure and chemical bonding of the $Li_{2.1}V_{0.9}O_2$ and $Li_{1.1}V_{0.9}O_2$ are studied by two kinds of first-principles calculations, molecular orbital (MO) calculations by the DV-Xα method and the *ab initio* total-energy and molecular dynamics program VASP (Vienna Ab-initio Simulation Package). Strong V 3d and O 2p orbital mixing is found by both the DV-Xα calculation and XANES measurements in $Li_{1.1}V_{0.9}O_2$.

* Energy 3 Team, Energy R&D Center, CTO, Samsung SDI Co. Ltd., South Korea
** Sunchon Branch, Korea Basic Science Institute, Korea
Corresponding author. E-mail: yhyyx@hanmail.net; kimyangsoo@kbsi.re.kr
*** Department of Materials Science and Engineering, Korea Advanced Institute of Science and Technology, Daejeon 305-701, Korea

Advances in Quantum Chemistry, Vol. 54
ISSN 0065-3276, DOI 10.1016/S0065-3276(07)00003-2

1. INTRODUCTION

Since its introduction in 1990, the secondary rechargeable lithium-ion battery (LIB) with high energy density and power capability has become an important power source for portable electronic devices, such as cellular phones, laptop computers, and portable media players. Recently, LIB research has also widened to include the hybrid electric vehicles (HEV).

The Li-ion rechargeable batteries are presently made with Li transition metal oxide as the positive electrode material and carbonaceous material as the negative electrode material [1]. Li-ion rechargeable batteries can offer a higher energy density, higher average voltage, and a higher power density than existing rechargeable batteries such as Ni–MH or Ni–Cd.

However recent portable devices are becoming smaller, slimmer, lighter, and multi-functional and customers require a longer operating time. The energy density of currently available batteries is insufficient to meet this need. To overcome this situation, a number of researchers have recently focused on two activities: (i) improving the existing positive material like Co-, Ni-, or Mn-based oxides or searching for new ones, or (ii) searching for the alternatives to the carbonaceous negative electrode materials with large capacity and a strong reducing power. The second approach constitutes the issue of this paper.

Several types of negative material have been investigated for Li rechargeable batteries; Li metal [2], Li/Si/Sn-based alloys [3,4], carbonaceous materials [5], Sn-oxide based materials [6], nitride [7], and vanadates [8,9]. Li metal [2] has the most negative redox potential among the metallic elements. It also has a large capacity of 3860 mAh/g and 2060 mAh/cc. Batteries with metallic Li are expected to have a high energy density. However, Li dissolution and deposition are not fully reversible in a battery with a non-aqueous liquid electrolyte, and dendrite deposition during the charging shortens a battery's cycle life and threats a critical safety issue of battery's reliability. It is therefore necessary to control the growth of the dendrites, and improve safety and cycle performances.

Several vanadate materials have been reported that can be reversibly intercalated up to seven lithium atoms leading to 800–900 mAh/g capacities when charged down to 0.1 V, more than two times greater than commercial graphite. However, since the average voltage, when the vanadates react with Li, is around 1.5 V compared to 0.2 V for graphite, the energy density of the cell based on vanadate is not enhanced remarkably [8,9].

A unique feature of the vanadate material upon lithiation is their amorphization lower than 1 V, which leads to a different shape of voltage profile between first and second lithiation process. For the practical cell applications, having the different voltage profile between first and second cycle, it is required to accurately control the cell balance for the safety and reliability.

In the present work, we report the novel V-based material which can be negative potential material. The reaction mechanism of this V-based material is discussed through crystal and electronic structure analysis using the XRD Rietveld refinement, X-ray absorption near edge structure (XANES) and the

first-principles calculations, which were carried out to clarify its remarkable low reaction potential.

Two kinds of first-principles calculations were used. Molecular orbital (MO) calculations by the DV-Xα method using the program code SCAT have been performed in order to obtain the electronic structure and chemical bonding information of the lithium vanadium oxide. The *ab initio* total-energy and molecular dynamics program Vienna *ab-initio* simulation package (VASP) is also used to calculate the open-circuit voltage (OCV) and density of state (DOS), which is based on the density functional theory pseudo-potential plane wave method and the general gradient approximation (GGA) exchange.

2. EXPERIMENTAL DETAILS

2.1 Material preparation and cell assembly

Samples were prepared by conventional solid-state reaction. Stoichiometric amount of Li_2CO_3 (Aldrich Co.), V_2O_3 (High Purity Chemicals) were mixed and sintered at 1100°C for 10 h in a N_2 gas flow.

$Li_{1.1}V_{0.9}O_2$, PVDF, Super P were mixed together to be coated on a Cu foil to make the electrode, and commercial electrolyte (Samsung Electric Co.) was used in this system. Li metal was used as cathode and a thin pouch was used to seal the cell.

2.2 Structural characterization

The structure of samples, formulated as $Li_{1.1}V_{0.9}O_2$ and $Li_{2.1}V_{0.9}O_2$, were characterized by the X-ray diffraction (XRD) using a Philips X'pert Pro PW3123/00 powder diffractometer (Cu Kα radiation). The data was collected in the range of 15–100 degrees under step scanning mode with 40 kV/50 mA, 0.02°/step, and 10 s exposure time. Rietveld refinement of the collected data was done using the Cerius2 (Accelrys Inc. Ver. 4.8.1) Rietveld (DBWS) code.

The X-ray absorption (XAS) data were collected at 7C beamline in Pohang Accelerator Laboratory (Korea) with the ring current of 120–190 mA at 2.5 GeV. In order to eliminate higher harmonics, the crystals were detuned by 25% for the V K-edge measurement. The energy resolution $\Delta E/E$ was 2×10^{-4}. The spectra were recorded in transmission mode by nitrogen gas filled ion chambers as detectors.

3. COMPUTATIONAL PROCEDURE

The electronic structures and chemical bonding of lithium vanadium oxide were calculated by the DV-Xα method [10,11] using the program code [12]. The population analysis was made according to Mulliken [13]. The *ab initio* total-energy and molecular dynamics program VASP [14–16], based on the density

functional theory pseudo-potential plane wave method and the GGA exchange and correlation functional, were used to obtain the OCV.

First-principles calculation on lithium transition metal oxides of positive electrodes for lithium-ion batteries have been done by many researchers [17–20]. In general the open-circuit voltage $E_{OCV}(x)$ depends on the difference in the Li chemical potential between anode Li metal and cathode. In this paper, we have investigated the possibility of using the metal oxide powders for anodic electrode as active materials and find out their electrochemical performance through the calculation. The first-principles calculation in this paper for the voltages was carried out as follows:

$$\mathrm{OCV} = \frac{-\Delta G}{zF} = \frac{-(E^{\mathrm{Li}}_{\mathrm{cathode}} - E^{\mathrm{Li}}_{\mathrm{anode}})}{zF}. \tag{1}$$

Here F is the Faraday constant and z the ion transported charge in the electrolyte. In the LIB system, Li^+ is the ionic conductor, which means that z=1 for the LIB system.

4. RESULTS AND DISCUSSIONS

A perfect crystal structure model is very helpful for theoretical calculations, reaction mechanism analysis, and some physical property analysis such as conductivity, magnetic susceptibility, chemical potential, etc. Powder XRD (or neutron diffraction) Rietveld refinement is one of the most popular methods used to characterize crystal structure.

The Rietveld refinement of the $Li_{1.1}V_{0.9}O_2$ model gives here a satisfactory fit to the overall profile. The best-fit of the XRD patterns are shown in Figure 3.1.

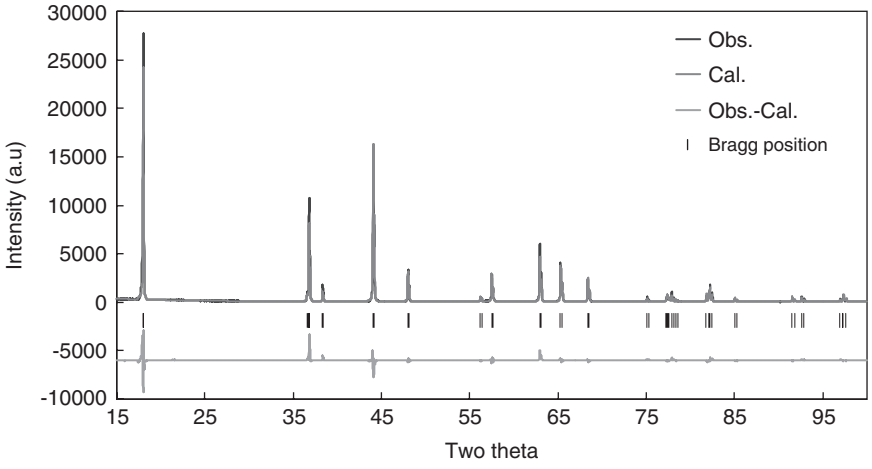

Figure 3.1 The XRD profiles of $Li_{1.1}V_{0.9}O_2$ after the Rietveld refinement (a) x=0.1, (b) 0.2, and (c) 0.3. For a colour version of this figure please see the colour plate section near the end of this book.

The sample exhibits hexagonal structure. The V^{3+} is coordinated by six oxygen atoms and located in the octahedral site, some Li^{+} is also located in the V^{3+} (3b) site. The fractional coordinates of the $Li_{1.1}V_{0.9}O_2$ at room temperature are listed in Table 3.1.

The refinement processes were carried out with several variations such as baseline correction, cell parameters, zero correction, scale factor, temperature factor, etc. $Li_{1.1}V_{0.9}O_2$ is assigned to the hexagonal system with an *R*-3*m* space group with cell parameter of a=2.853 Å, c=14.698 Å, and cell volume of V=103.62 Å^3. The best-fitted model is shown in Figure 3.2(a).

The structure of charged state $Li_{2.1}V_{0.9}O_2$ is characterized by XRD as shown in Figure 3.3, and assigned to *P*-3*m*1 space group with cell parameters of a=3.099 Å, c=5.212 Å, and cell volume of V=103.62 Å^3. The best-fitted model is shown in Figure 3.2(b). About 10% of V(1a) sites are substituted by lithium ions. Vanadium atom occupies the center of the octahedron. The fractional coordinates of the $Li_{2.1}V_{0.9}O_2$ at room temperature are listed in Table 3.1.

The calculation of the electronic states of lithium vanadium oxide is carried out using cluster models taken from bulk crystal. The model clusters which are

Table 3.1 Atomic coordinates of $Li_{1.1}V_{0.9}O_2$ and $Li_{2.1}V_{0.9}O_2$

	$Li_{1.1}V_{0.9}O_2$ (*R*-3*m*)				$Li_{2.1}V_{0.9}O_2$ (*P*-3*m*1)			
	Site	*x*	*y*	*z*	Site	*x*	*y*	*z*
Li	3a	0	0	0	2d	0.3333	0.6667	0.6490
Li	3b	0	0	0.5	1a	0	0	0
V	3b	0	0	0.5	1a	0	0	0
O	6c	0	0	0.2452	2d	0.3333	0.6667	0.2333

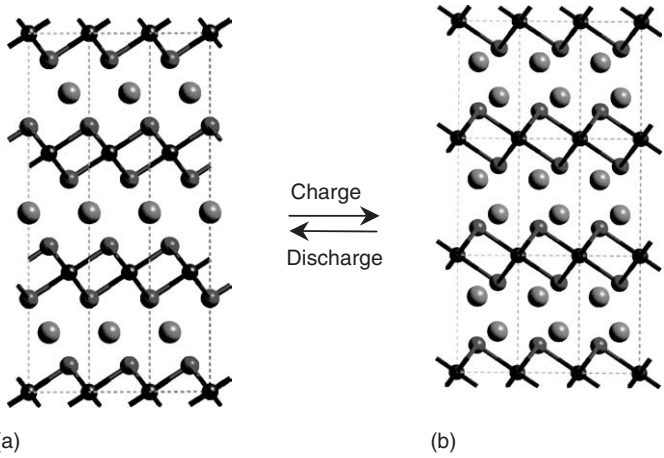

Figure 3.2 The structure of initial and charged state of lithium vanadium oxide: (a) initial state ($Li_{1.1}V_{0.9}O_2$), (b) charged state ($Li_{2.1}V_{0.9}O_2$).

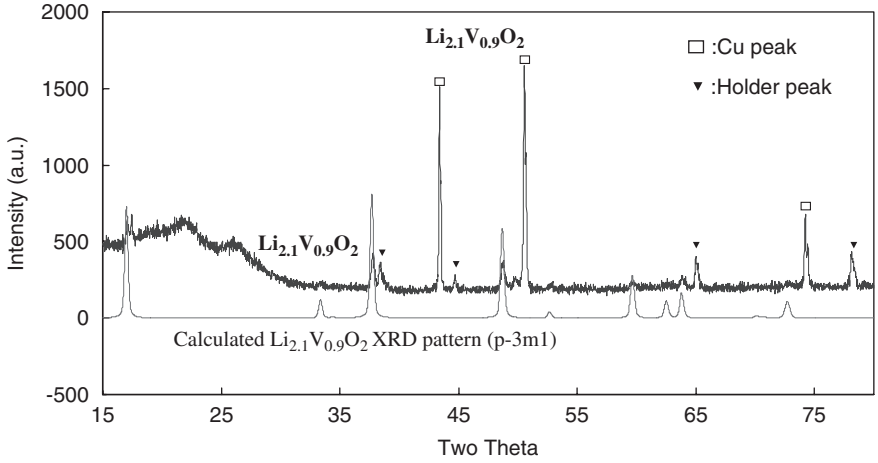

Figure 3.3 The XRD pattern of lithium vanadium oxide as charged state.

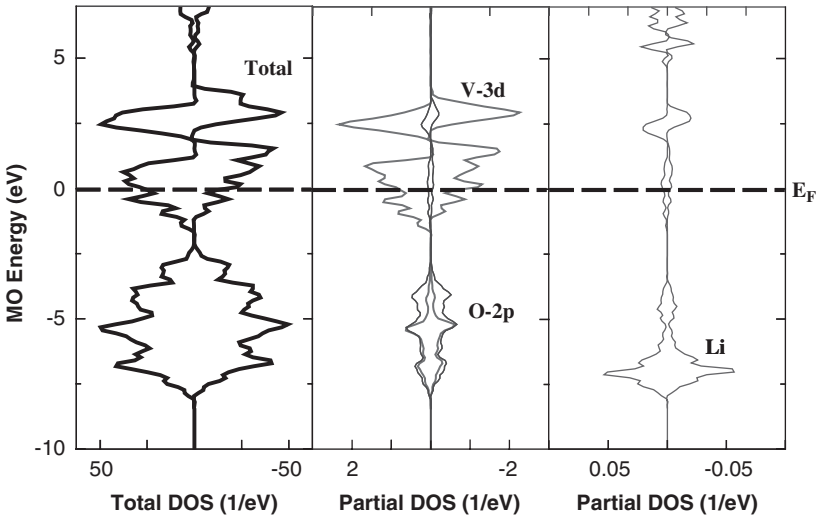

Figure 3.4 Calculated density of states (DOS) of $Li_{2.1}V_{0.9}O_2$ using VASP: (a) total DOS, (b) partial DOS of V 3d and O 2p, and (c) partial DOS of Li 2sp.

composed of (a) 51 atoms $(Li_{13}V_{12}O_{26})^{3-}$ for $Li_{1.1}V_{0.9}O_2$ and (b) 61 atoms $(Li_{24}V_{13}O_{24})^{2+}$ for $Li_{2.1}V_{0.9}O_2$ are employed for these purposes.

In order to discuss the valence electronic state and chemical bonding of lithium vanadium oxide we made calculations using cluster models. The density of states (DOS) and the partial density of states (PDOS) of $Li_{1.1}V_{0.9}O_2$ are obtained by this study as shown in Figure 3.4. The filled band located from −8 to −3 eV is mainly composed of O 2p orbital. The partially filled band located around −2 to 4 eV is mainly composed of V 3d orbital. Unoccupied band located above 5 eV is

made up of Li 2sp and V 4sp orbitals. Significant amounts of V 3d, 4sp states in the O 2p band are found. Strong covalent interaction between V and O is presented.

The bond overlap population diagrams or crystal overlap population (COP) for V–O and Li–O bonds are plotted, as shown in Figure 3.5. The interactions between V and O, and Li–O have been investigated individually. The values of bonding and the anti-bonding contributions to the overlap population (BOP) are also noted.

On the other hand, the Li–O bond overlap population is small, but not zero in Figure 3.5. This provides the evidence for the strong covalency between M and X (XS and O), as discussed in our previous report [21–23].

The V 3d band is located intensively around the E_F. The V 3d band also involves a considerably large amount of O 2p components making anti-bonding interactions for V–O bonds. It means that the lowest unoccupied molecular orbital (LUMO) V 3d has a strong p character rise from O 2p; induced significant absorption intensity of 1s–3d quadruple allowed transition in the XANES spectrum.

When the initial material $Li_{1.1}V_{0.9}O_2$ is charged up, the lithium layer in the $Li_{1.1}V_{0.9}O_2$ becomes a double layer with lithium intercalated. The total DOS and partial DOS of $Li_{2.1}V_{0.9}O_2$ are shown in Figure 3.6.

The bonding contribution of Li–O is almost same as that of V–O bonding, reflecting shorter Li–O distance (1.907 Å) than that of V–O (2.16 Å). Moreover, the anti-bonding contribution of V–O is greater than that of Li–O. As a result, the net bond overlap population is smaller in V–O than in Li–O as shown Figure 3.7.

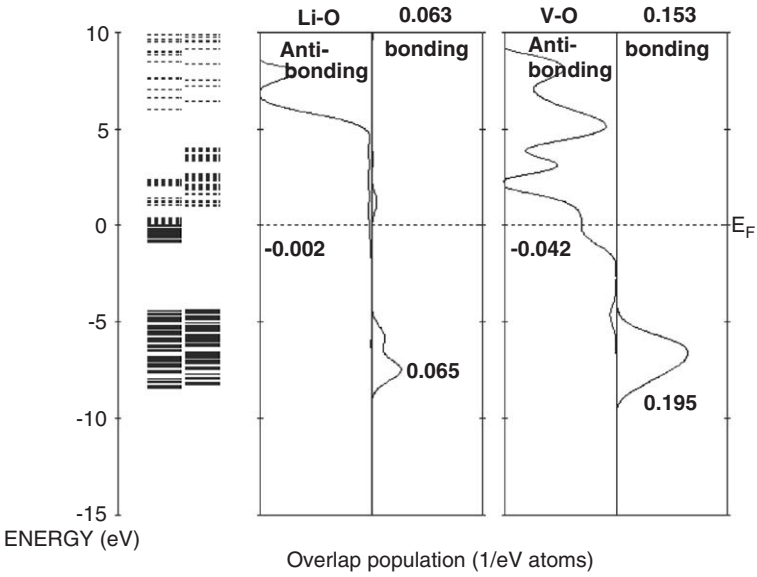

Figure 3.5 Energy diagram and overlap population of $Li_{1.1}V_{0.9}O_2$ with $(Li_{13}V_{12}O_{26})^{3-}$ cluster model.

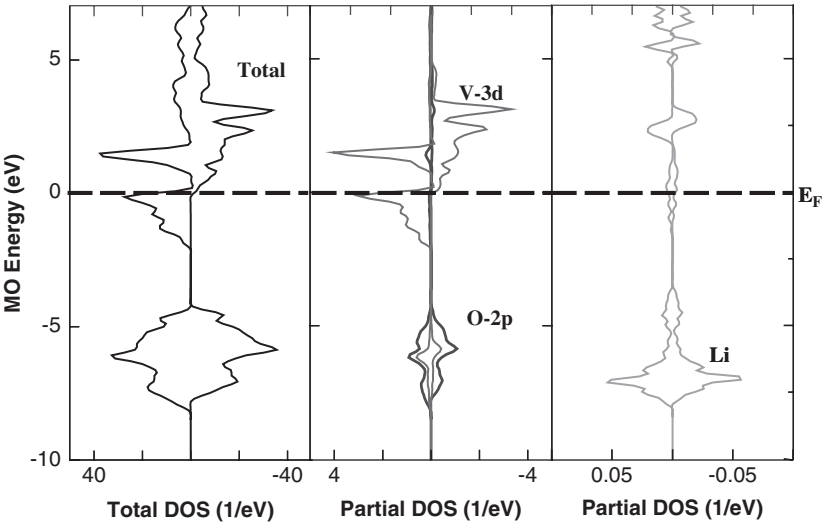

Figure 3.6 Calculated DOS of $Li_{2.1}V_{0.9}O_2$ using VASP: (a) total DOS, (b) partial DOS of V 3d and O 2p, (c) partial DOS of Li 2sp.

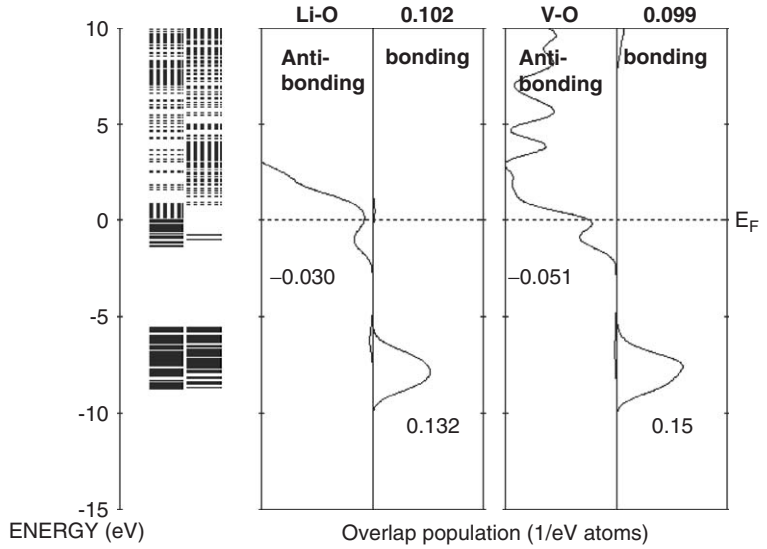

Figure 3.7 Energy diagram and overlap population of $Li_{2.1}V_{0.9}O_2$ with $(Li_{24}V_{13}O_{22})^{2+}$ cluster model.

Compared with those of $Li_{1.1}V_{0.9}O_2$, the covalent state between V 3d and O 2p orbitals is decreased. Since an electron is added to the V 3d anti-bonding orbital, the bond overlap population of V-O is decreased from 0.153 to 0.099 by the lithium intercalation. It is obvious that oxidation state of V changes during the charging or intercalation from V(III) to V(II).

This can be ascribed to the fact that Li atoms are virtually in the Li^+ state and make slight covalent interaction with the surrounding atoms. The location of Li^+ therefore does not affect the electronic states of the clusters significantly.

The LUMO V 3d has a weaker p character arising from O 2p of $Li_{2.1}V_{0.9}O_2$ than initial $Li_{1.1}V_{0.9}O_2$; it's induced absorption intensity of 1s–3d quadruple allowed transition in the XANES spectrum is lower than $Li_{1.1}V_{0.9}O_2$ as shown in Figure 3.8.

As expected from the Li-PDOS in Table 3.2, the net charge of Li is more than 0.7. This means that the nature of the V–O bond is hardly affected by the presence of Li. The fact that Mulliken's charge of Li is almost fully ionized is contrary to the widely accepted picture of Li-inserted compounds, and should be a very important factor in determining the high OCV for Li^+ ions. One of the parameters that determine the redox reaction energy is the covalent bonding of the electrons at a transition metal cation.

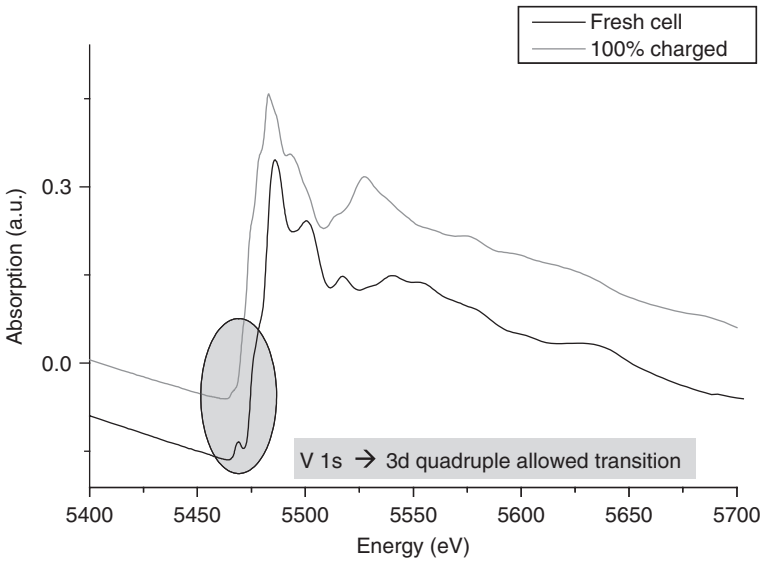

Figure 3.8 XANES spectra of initial (fresh) and full charged (100% charged) $Li_{1.1}V_{0.9}O_2$.

Table 3.2 Comparisons of BOP between $Li_{1.1}V_{0.9}O_2$ and $Li_{2.1}V_{0.9}O_2$ and OCV between calculational and experimental results

	Li–O		V–O		Ionicity of Li atom	*E** OCV
	BOP	Length (Å)	BOP	Length (Å)		
$Li_{1.1}V_{0.9}O_2$	0.063	2.0956	0.153	2.0115	0.73	0.93 V (calc.) vs. 0.3 V (exp.)
$Li_{2.1}V_{0.9}O_2$	0.102	1.9073	0.099	2.1634	0.55	

The averaged battery voltage of $Li_{2.1}V_{0.9}O_2/Li_{1.1}V_{0.9}O_2$ is given by:

$$E_{ave} = \int_{1.1}^{2.1} E_{ocv}(dx)dx \tag{2}$$

using $E_{OCV}(x)$ defined by Eq. (1). The following quantity E^* is often used as an approximated E_{ave} by the pseudo-potential calculation

$$E^* = -\frac{1}{F}\{E_{Li_{2.1}} - E_{Li_{1.1}} - E_{Li}\}, \tag{3}$$

where E is the total energy of the system. E^* is equal to E_{ave} when both entropy and volume-change terms are negligible in free-energy difference between $Li_{2.1}V_{0.9}O_2$ and $Li_{1.1}V_{0.9}O_2$. In the present study, the total energies per unit formula for $Li_{2.1}V_{0.9}O_2$, $Li_{1.1}V_{0.9}O_2$, and metallic Li (BCC) were computed independently, and E^* was obtained. The present E^* value is presented in Table 3.2, together with our experimental OCV for comparison.

Unfortunately our experimental and calculational data is not directly comparable. Nevertheless, the value E^*, which may be a good approximation of theoretical OCV, reproduces experimental OCV within an error. It is contrary to the widely accepted picture of Li-intercalated compounds, and should be a very important consideration for the determination of battery properties such as OCV. The information on these characteristics of these materials can be helpful to investigate another possibility as new practical materials.

5. CONCLUSION

V-based material was discussed through crystal and electronic structure using XRD, Rietveld analysis, and the first-principles calculation. The electronic structure and chemical bonding of the $Li_{2.1}V_{0.9}O_2$ and $Li_{1.1}V_{0.9}O_2$ are studied by two kinds of first-principles calculations, MO calculations by the DV-Xα method and the *ab initio* total-energy and molecular dynamics program VASP.

$Li_{1.1}V_{0.9}O_2$ is assigned to the hexagonal system with a *R*-3*m* space group with cell parameter of a=2.853 Å, c=14.698 Å and the structure of charged state $Li_{2.1}V_{0.9}O_2$ is assigned to *P*-3*m*1 space group with cell parameters of a=3.099, c=5.212.

Mulliken's population analysis has been thoroughly conducted to examine the net charge as well as the magnitude of covalent bondings. The author found that Mulliken's charge of Li in $Li_{2.1}V_{0.9}O_2$ and $Li_{1.1}V_{0.9}O_2$ and the BOP value for Li–O and V–O are different in their structure. It is contrary to the widely accepted picture of Li-intercalated compounds, and should be a very important consideration for the determination of battery properties such as OCV. The information should be helpful to investigate possibility of new electrode active materials.

ACKNOWLEDGMENTS

The authors thank Samsung SDI CAE team for providing Cerius2 program. We are also grateful for beam time allotment by PAL. The experiments at PLS were supported in part by MOST and POSTECH.

REFERENCES

[1] Sony lithium ion battery performance summary, *JEC Batt. Newslett.* **2** (1994) 31.
[2] T.C. Murphy, D.M. Cason-Smith, In: Proceedings of the 34th International Power Source Symposium, 1990, p. 176.
[3] A. Anani, S. Crouch-Baker, R.A. Huggins, In: A.N. Dey (Ed.), Proceedings of the ECS Symposium on Lithium Batteries, Pennington, NJ, 1987, p. 365.
[4] W. Choi, J.Y. Lee, B.H. Jung, H.S. Lim, *J. Power Sources* **136** (2004) 154–159.
[5] T. Zheng, J.S. Xue, J.R. Dahn, *Chem. Mater.* **8** (1996) 389–393.
[6] Y. Idota, T. Kubota, A. Matsufuji, Y. Maekawa, T. Miyasaka, *Science* **276** (1997) 1395–1397.
[7] M. Nishijima, N. Tadokoro, Y. Takeda, N. Imanishi, O. Yamamoto, *J. Electrochem. Soc.* **141** (1994) 2966–2971.
[8] S. Denis, E. Baudrin, M. Touboul, J.-M. Tarascon, *J. Electrochem. Soc.* **144** (1997) 4099–4109.
[9] S.-S. Kim, H. Ikuta, M. Wakihara, *Solid State Ionics* **139** (2001) 57–65.
[10] F.W. Averill, D.E. Ellis, *J. Chem. Phys.* **59** (1973) 6412–6418.
[11] D.E. Ellis, H. Adachi, F.W. Averill, *Surf. Sci.* **58** (1976) 496–510.
[12] H. Adachi, M. Tsukada, C. Satoko, *J. Phys. Soc. Jpn.* **45** (1978) 875–883.
[13] R.S. Mulliken, *J. Chem. Phys.* **23** (1955) 1833–1840.
[14] G. Kresse, J. Hafner, *Phys. Rev. B* **48** (1993) 13115–13118.
[15] G. Kresse, J. Furthmuller, *Comput. Mater. Sci.* **6** (1996) 15–50.
[16] G. Kresse, J. Furthmuller, *Phys. Rev. B* **54** (1996) 11669–11686.
[17] G. Ceder, M.K. Aydinol, A.F. Kohan, *Comput. Mater. Sci.* **8** (1997) 161–169.
[18] S.K. Mishra, G. Ceder, *Phys. Rev. B* **59** (1999) 6120–6130.
[19] J. Reed, G. Ceder, *Electrochem. Solid-State Lett.* **5** (2002) A145–A148.
[20] Y. Koyama, I. Tanaka, H. Adachi, Y. Makimura, T. Ohzuku, *J. Power Sources* **119–121** (2003) 664–668.
[21] Y.-S. Kim, Y. Koyama, I. Tanaka, H. Adachi, *Jpn. J. Appl. Phys.* **37** (1998) 6440–6445.
[22] Y. Koyama, Y.-S. Kim, I. Tanaka, H. Adachi, *Jpn. J. Appl. Phys.* **38** (1999) 2024–2027.
[23] Y. Koyama, I. Tanaka, Y.-S. Kim, S.R. Nishitani, H. Adachi, *Jpn. J. Appl. Phys.* **38** (1999) 4804–4808.

CHAPTER 4

Novel Theoretical Prediction Method of the Haldane Gap among the Azido-Bridged Compounds by DV-Xα Molecular Orbital Calculation

Tomohiko Ishii*, Yukikazu Fuke*, Naoko Aizawa* and **Masahiro Yamashita****

Contents

Abstract

The electronic structures of the Haldane gap compounds that include Ni^{II} ions having s=1 spin are reported. The azido-bridged Haldane gap compounds, such as NINAZ ($[Ni(NH_2(CH_2)_3NH_2)_2N_3]ClO_4$), NDMAZ ($[Ni(NH_2CH_2C(CH_3)_2CH_2NH_2)_2N_3]ClO_4$), and NDMAP ($[Ni(NH_2CH_2C(CH_3)_2CH_2NH_2)_2N_3]PF_6$) have been synthesized by substituting different in-plane ligands and counteranions. The most powerful advantage of the metal complex based Haldane gap compounds is to control the antiferromagnetic interaction by changing the combination of the counteranions and the in-plane and the bridging ligands. After carrying out a high-precision X-ray structural analysis of NINAZ, the differences of the molecular structures and the electronic structures among these three azido-bridged Haldane gap compounds can be compared in order to clarify the mechanism of the energy difference between the singlet ground state and the triplet excited state. From the result of the energy difference between the singlet and the triplet states using the DV-Xα calculation method, we have observed a trend that the compound having a large Haldane gap energy, such a NINAZ, has a

* Department of Advanced Materials Science, Kagawa University, 2217-20, Hayashicho, Takamatsu 761-0396, Japan
Corresponding author. E-mail: mail@tishii.com
** Department of Chemistry, Tohoku University, Aoba, Aramaki, Aoba-ku, Sendai 980-8578, Japan

Advances in Quantum Chemistry, Vol. 54
ISSN 0065-3276, DOI 10.1016/S0065-3276(07)00004-4

large energy difference between two spin states, implying the larger energy difference should be the harder spin inversion from anti-parallel singlet to the parallel triplet state. Our previous manifestation of the way to predict the value of the Haldane gap by using the analysis of the bond overlap population by means of a DV-Xα molecular orbital calculation was not so suitable for general Haldane gap compounds including the NO_2-bridged one-dimensional (1D) chain structure compounds. Therefore in this study the novel way using the analysis of the energy level structures should be reported.

1. INTRODUCTION

Study on molecular magnetism has established an important research field in physics and chemistry over the past several decades [1], including Haldane gap [2], single-molecule magnets (SMMs) [3], organic molecular magnets [4], and so on. Especially in the field of the low dimension system [5] many such un-resolved magnetic problems have been observed. The Haldane gap is one of the typical interesting topics in the field of the 1D magnetic susceptibility. Generally speaking the temperature dependence of the magnetic susceptibility of the one-dimensional Heisenberg antiferromagnet (1D-HAF) has been explained using the Bonner–Fisher theory [6], spin-dimer model (singlet–triplet model), and the alternating chain model [7]. The typical spin–spin interaction can be explained by using the Curie–Weiss law, or Curie constant, C, such as

$$C = \frac{Ng^2 s(s+1)\mu_B^2}{3k_B},$$

for $s = 1/2, 1, 3/2, 2, 5/2\ldots$ spins, where N, g, μ_B, and k_B denote the Avogadro's number, g factor (spectroscopic splitting factor), Bohr magneton, and the Boltzmann constant, respectively. Therefore there are no differences between the integer ($s = 1, 2, 3\ldots$) and half-integer ($s = 1/2, 3/2, 5/2\ldots$) of spin states. On the other hand, a very exciting hypothesis has been predicted by F.D.M. Haldane in 1983. He predicted that the ground state of the 1D Heisenberg model depends on the value of spin s. He predicted that half-odd-integer spin systems keep the features of the $s = 1/2$ spin, but in the case of integer spin chains have the following three features; (1) the ground state is unique, (2) there exists a large energy gap (called Haldane gap) between the ground state and the excited state, and (3) the spin correlation function decays quickly according to the exponential function. Among Haldane's three predictions about the integer spin system, the existence of the gap is the most surprising one. This is called the ''Haldane gap'' [8] for integer values of spin s ($s = 1, 2, 3\ldots$) the 1D-HAF exhibits singlet ground states, separated from the first triplet excited state by a finite energy gap (the Haldane gap E_g), as shown in Figure 4.1. This Haldane gap is also available for the half-odd integer s ($s = 1/2, 3/2, 5/2\ldots$). It is predicted that the 1D-HAF has a gap-less spectrum of excitations.

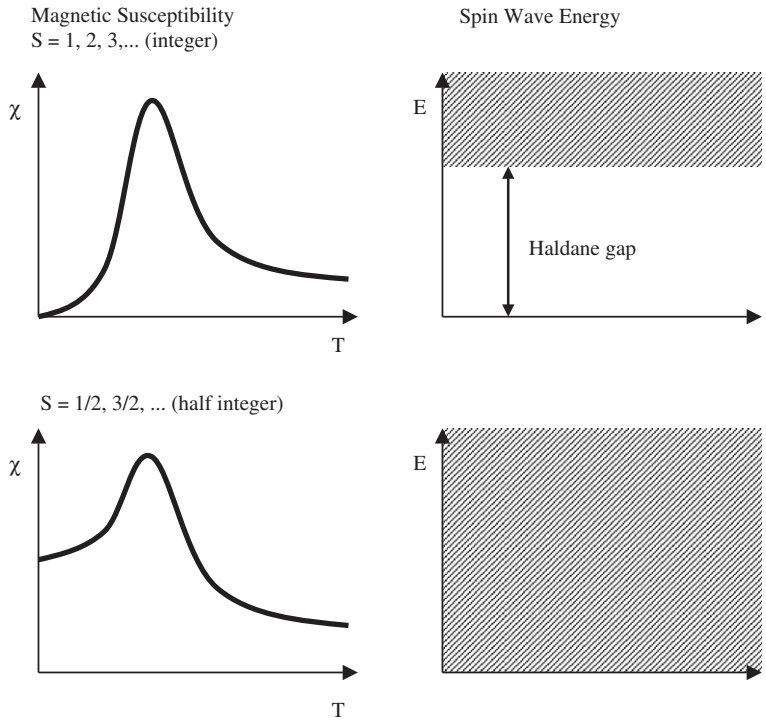

Figure 4.1 Magnetic susceptibilities and spin wave energies in the cases of the integer (top) and half-odd integer spin quantum numbers (bottom).

As is well known, there should be no difference between integer and half-odd-integer spins according to the theory of quantum physics, because a 1/2 spin is an elementary unit of the spin momentum. After Haldane predicted, no one believed such a strange magnetic phenomena. However, Haldane's prediction is now well supported by many theoretical works and by physical measurements not only in the inorganic compounds but also in the many metal complexes [9]. The relationship between the Haldane gap E_g and the magnetic spin interaction J to be $E_g \approx 0.41|J|$, which have been given by theoretical Monte-Carlo methods [10]. Especially in the 1D chain structure metal complexes are the typical materials having the Haldane gap observed in the magnetic susceptibilities. The typical Haldane gap materials are $[Ni(NH_2(CH_2)_2NH_2)_2NO_2]ClO_4$ (NENP) [11,12], $[Ni(NH_2(CH_2)_3NH_2)_2NO_2]ClO_4$ (NINO) [13], $[Ni(NH_2(CH_2)_3NH_2)_2N_3]ClO_4$ (NINAZ) [14], and $(CH_3)_4N[Ni(NO_2)_3]$ (TMNIN) [15].

In our previous work [16], we have reported the synthesis, X-ray structural analysis, and the magnetic property data on NINAZ, which has the largest value of both the Haldane gap E_g (= 41 K) and the strength of the antiferromagnetic interaction J (= −144 K) of all Haldane gap compounds. Among the other compounds exhibiting a Haldane gap that include Ni^{II} ions having $s = 1$ spin, the general chemical formula can be shown to be $[Ni(AA)_2X]Y$, (where $(AA)_2$ = $(diamines)_2$, tetramines; $X = N_3^-$ or NO_2^- and $Y = ClO_4^-$, PF_6^-). One particular

theory, known as the ''Valence-Bond-Solid (VBS) state'' may be used to explain the mechanism behind the Haldane gap, which comes from the presence of integer spins [17]. Until our previous work a high-precision X-ray structural analysis of NINAZ have not been reported.

Therefore after our previous research about the calculated Haldane gap energy [16] is also revealed the possibility of controlling the Haldane gap, E_g, by selecting particular combinations of in-plane ligand (AA), bridging ligands (X), and counteranions (Y). However, a clear reason why the Haldane gap E_g is changed by substituting between these ligands and anions, even though the large structural modification is not expected after substituting the ligands has not been reported up to now. For example, the energy differences between E_g and J are quite large among the N_3^- bridging compounds such as NINAZ ($E_g = 41\,K$, $J = -144\,K$), NDMAZ ($E_g = 21.6\,K$, $J = -70.6\,K$) [18], and NDMAP ($E_g = 5\,K$, $J = -31\,K$), although the structural differences are quite small.

For high-accuracy DV-Xα molecular orbital calculations, high-precision absolute structures by X-ray diffraction analysis are required. We have already observed the exact three azido-bridged crystal structures [16]. Therefore the electronic structures of the corresponding Haldane gap compounds have been investigated by means of the DV-Xα method. From the result of the DV-Xα calculations, we have discovered that the overlap population of the bridging N_3^- molecule is an important factor and that this differs significantly among these three N_3^- bridged compounds. The differences among the overlap populations of three N_3^- bridged compounds are significantly small. In addition, our previous way to predict the value of the Haldane gap by considering the bond overlap population by means of the DV-Xα method was not suitable for general Haldane gap compounds including the NO_2-bridged 1D chain structure compounds.

Therefore in the present paper, we report that the energy difference between the singlet ground state and the triplet excited state is more important than the differences among the overlap populations mentioned above. Therefore a new theoretical way to predict the value of the Haldane gap using the DV-Xα method should be discussed.

2. EXPERIMENTAL RESULTS AND CLUSTER MODELS FOR DV-Xα CALCULATION

Haldane gap compounds that include a Ni^{II} d^8 ion, such as not only NINAZ, NDMAZ, and NDMAP, but also the compounds $[Ni(NH_2(CH_2)_3NH_2)_2NO_2]PF_6$ (NINOP), $[Ni(NH_2(CH_2)_3NH_2)_2N_3]PF_6$ (NINAP), and $[Ni(NH_2(CH_2)_2NH_2)_2N_3]PF_6$ (NDMAPen) were prepared by substituting between combinations of in-plane and bridging ligands and counteranions. The magnetic susceptibility measurement was performed using a Quantum Design MPMS-4 SQUID susceptometer operating at a magnetic field of 0.01 T between 2 and 300 K. A purple block ($0.2 \times 0.2 \times 0.2$ mm) single crystal was selected and mounted on a RIGAKU IP-Rapid diffractometer as well as a RIGAKU AFC-7R diffractometer.

Detailed structural data from the X-ray structure analysis diffraction data was used in the construction of the cluster model for the DV-Xα calculation.

In our previous work, the X-ray structure of single crystal NINAZ has been reported, whose 1D molecular structure is shown in Figure 4.2. Our structural analysis has shown that the crystal structure of NINAZ was identical with that of NDMAP, as Monfort et al. reported previously [19]. The structure consists of 1D nickel-azido chain propagating along the *a*-axis, isolated by ClO_4^- anions, found in the inter-chain spaces. In the chain structure, the Ni(II) atom is coordinated by two bidentate 1,3-diaminopropane and two azido ligands in a distorted octahedral *trans*-arrangement. This is formed by two N atoms of the azido bridging ligands at 2.11 Å and four N atoms of the two bidentate amine ligands at the same distance,

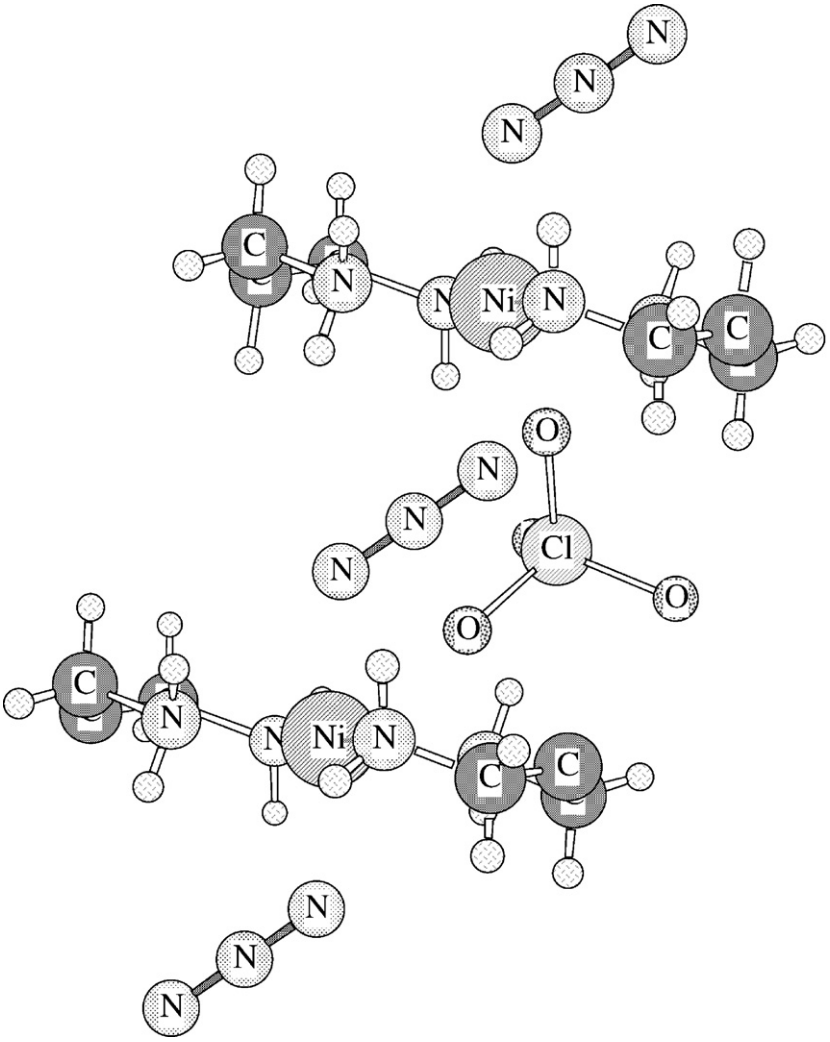

Figure 4.2 Crystal structure of the 1D chain unit in $[Ni(NH_2(CH_2)_3NH_2)_2N_3]ClO_4$ (NINAZ).

2.09 Å, giving a local D_{4h} symmetry. The direct antiferromagnetic interaction between two adjacent nickel ions is not expected in the 1D chain unit, because the Ni–Ni distance along the chain is 5.856 Å.

In the case of these isotropic 1D systems with $s = 1$, the temperature dependence of the susceptibility, extrapolated from calculations performed on ring chains of increasing length, has been given by Weng [20]. To reproduce Weng's results, Kahn et al. [11] introduced the following empirical function:

$$\chi = \frac{N\beta^2 g^2}{k_B T}\left[\frac{2 + 0.0194X + 0.777X^2}{3 + 4.346X + 3.232X^2 + 5.834X^3}\right],$$

where β denotes the Bohr magneton, $X = |J|/kT$. The Haldane gap E_g can be given by the following relation,

$$\chi(T) = \chi(0) + C\exp\left(-\frac{E_g}{k_B T}\right).$$

We have summarized the correlation of the antiferromangetic interaction constant, J, and the Haldane gap, E_g, in the compounds with the particular counteranions, in-plane and bridging ligands in Figure 4.3 and in Table 4.1. The Haldane energy gap E_g is almost proportional to the intra-chain exchange energy $|J|$. The Haldane gaps of the N_3-bridged compounds (closed circles) are quite

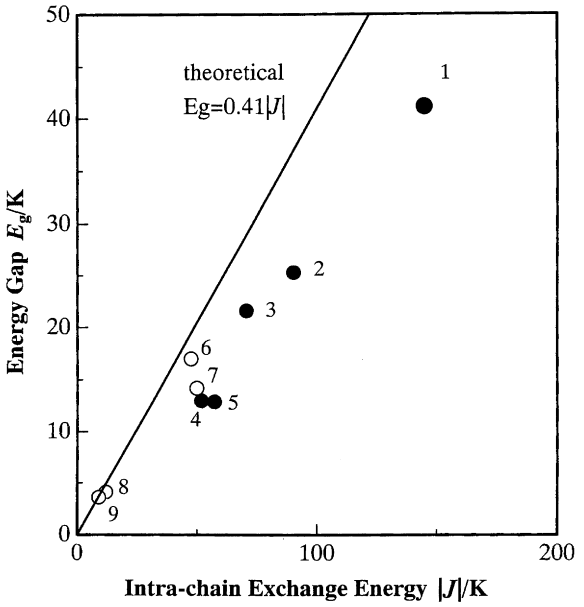

Figure 4.3 Relation between E_g and J for the Haldane gap compounds. 1, $[Ni(tn)_2N_3]ClO_4$ (NINAZ); 2, $[Ni(3,2,3\text{-tet})N_3]ClO_4$; 3, $[Ni(dmpn)_2N_3]ClO_4$ (NDMAZ); 4, $[Ni([15]aneN_4)N_3]ClO_4$; 5, $[Ni(Me_6[14]aneN_4)N_3]ClO_4$; 6, $[Ni(en)_2(NO_2)]ClO_4$ (NENP); 7, $[Ni(tn)_2(NO_2)]ClO_4$ (NINO); 8, $(CH_3)_4N[Ni(NO_2)_3]$ (TMNIN); 9, $[Ni(dmpn)_2(NO_2)]PF_6 \cdot H_2O$ (NDMAPNO2) (excerpted from *Polyhedron* **20** (2001) 1297–1304).

Table 4.1 Intra-chain exchange energy, J, and the Haldane gap, E_g, of several Haldane gap compounds with particular in-plane and bridging ligands and counteranions

	Counteranions			
	ClO_4^-		PF_6^-	
	In-plane ligands		In-plane ligands	
Bridging ligands	dmpn	tn	dmpn	tn
N_3^-	(NDMAZ) $J = -70.6\,K$ $E_g = 21.6\,K$	(NINAZ) $J = -144\,K$ $E_g = 41\,K$	(NDMAP) $J = -31\,K$ $E_g = 5\,K$	 $J = -83.4\,K$ $E_g = 23\,K$

larger than those of the NO_2-bridged ones (open circles). As a consequence, we can reveal a possible mechanism for controlling the Haldane gap by substituting the bridging ($N_3^- > NO_2^-$) and in-plane (tn > en > linear-tetramines > dmpn > Me_6 [14] aneN_4 > [15] aneN_4) ligands and counteranions ($ClO_4^- > PF_6^-$). From the X-ray structural analysis, it is shown that the differences in the structure among the Haldane gap materials are very small. Therefore a discussion based only on the combination of the bridging and in-plane ligands and counteranion is not appropriate to deduce the electronic structure of the Haldane gap compound.

The crystallographic data of NINAZ, NDMAZ, and NDMAP we have obtained are completely consistent with those reported previously [2]. The cluster model of each compound we have used for the DV-Xα calculation is extracted from the X-ray structural data of the single crystal. Cluster models of the same formula N_3–Ni$(AA)_2$–N_3–Ni$(AA)_2$–N_3 are used in the DV-Xα calculation in order to compare both the electronic structure and the Haldane gap directly.

From the preliminary calculations, using smaller sized cluster models, we have realized the importance of using the larger size of in-plane ligand cluster models, which do not suffer from the influence of the terminal effects in the DV-Xα calculation. In order to investigate the effect of the extended cluster size, calculations which involve the complete structure of the in-plane tn (tn = $NH_2(CH_2)_3NH_2$) and dmpn (dmpn = $NH_2CH_2C(CH_3)_2CH_2NH_2$) ligands were carried out. As a result, we require the cluster model (N_3–Ni$(AA)_2$–N_3–Ni$(AA)_2$–N_3) on the basis of these preliminary calculations, in order to clarify the subtle differences in the electronic structure among these three N_3^- bridged compounds, as shown in Figure 4.4.

The non-relativistic DV-Xα calculation [21] was performed with the Slater exchange parameter, $\alpha = 0.7$, for all atoms and with 50,000 DV sampling points, which provided a precision of less than 0.1 eV for valence electron energy eigenvalues. We employed the basis functions of the central nickel atom 1s–4p orbitals, while those of the nitrogen and carbon atoms were used 1s–2p orbitals. The calculations were carried out self-consistently until the difference in the orbital populations between the initial and final states of the iteration was less

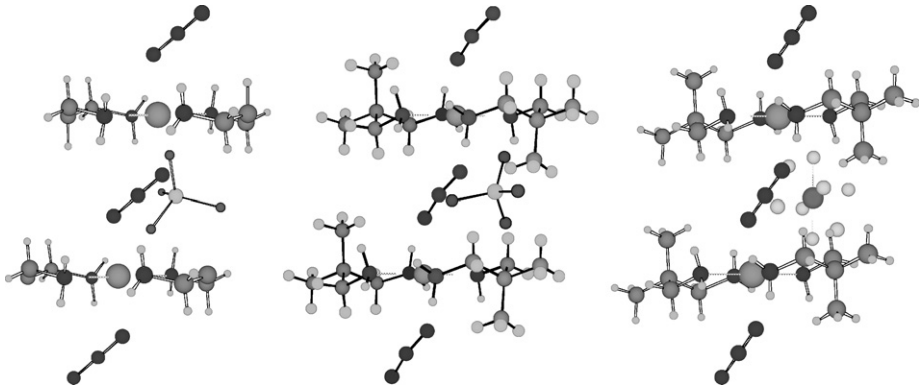

Figure 4.4 Cluster model N_3–Ni(tn)$_2$–N_3–Ni(tn)$_2$–N_3 of NINAZ (left), N_3–Ni(dmpn)$_2$–N_3–Ni(dmpn)$_2$–N_3 of NDMAZ (center) and N_3–Ni(dmpn)$_2$–N_3–Ni(dmpn)$_2$–N_3 of NDMAP (right). Counter anions ClO_4^- and PF_6^- are excluded for the DV-Xα calculations. For a colour version of this figure please see the colour plate section near the end of this book.

than 0.01 electron/orbital. The computation details of the non-relativistic (DV-HFS) method used in the present work have been described elsewhere [22].

3. DISCUSSION

In the N_3^- bridged compounds, there is a stronger electron–electron interaction through the N_3^- bridging molecule between two adjacent Ni spins, than between the NO_2^- bridged compounds. A cluster model constructed on the basis of the accurate structure determined by X-ray diffraction is used in the DV-Xα calculation for NINAZ, NDMAZ, and NDMAP. These are typical Haldane gap materials, which include the N_3-bridging ligand.

The Haldane gaps are estimated from magnetic measurements to be 41, 22, and 5 K (see Table 4.1) for NINAZ, NDMAZ, and NDMAP, respectively. From the analysis of the X-ray diffraction data, the distance between two adjacent Ni ions along the Haldane 1D chain is about 6 Å, which we suggest is too far to allow any antiferromagnetic interaction directly between them. The typical interatomic distance between two antiferromagnetic interaction spins is about 2–3 Å. In addition, the structural differences between these three compounds are very small, suggesting that there is no possibility for the strong super-exchange interaction between two Ni ions through N_3^- bridging ligands to take place.

In this study, the DV-Xα calculations including the spin polarized effect have been required for these three compounds, in order to reveal the correlation of the Haldane gap and the electronic structures, and the energy difference between singlet ground state and the triplet excited state, as shown in Figure 4.5. The calculated electronic level structure around the Fermi energy level of each cluster model is shown in Figure 4.6. The features of the energy level structures are very

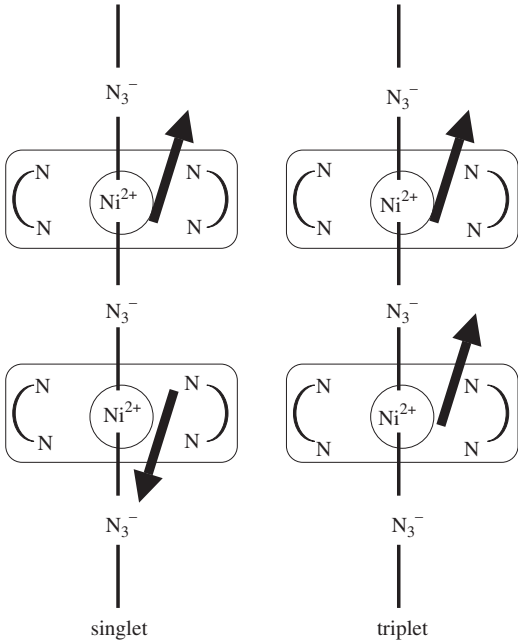

Figure 4.5 Schematic expression of the singlet (left) and the triplet (right) spin states between two adjacent Ni^{2+} ions having S=1 spin in the 1D metal complex chain of the Haldane gap compound. The energy barrier of the spin inversion from the anti-parallel singlet to the parallel triplet state has the relationship with the energy difference between them.

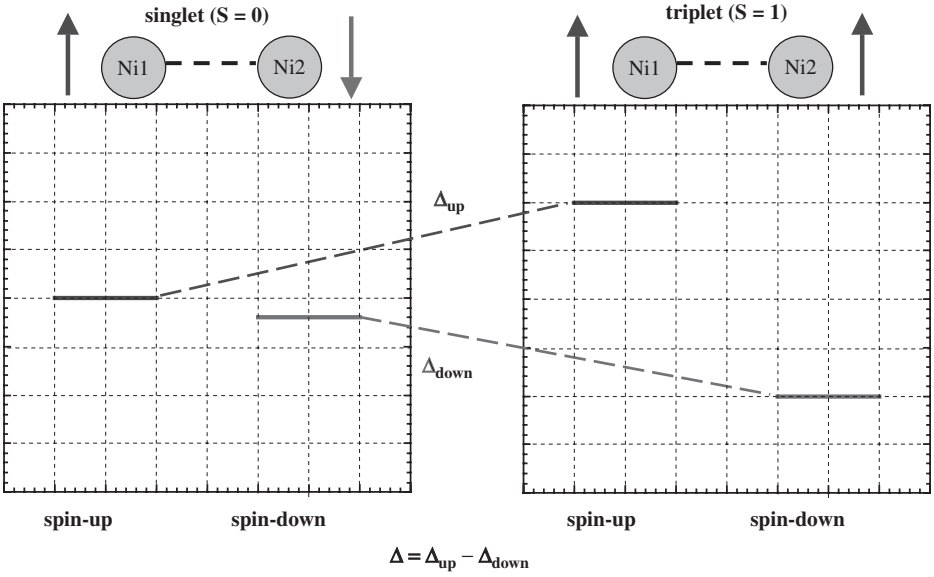

Figure 4.6 Energy level structures and the energy shifts between the singlet ground state (left) and the triplet excited state (right). The parameters Δ_{up} and Δ_{down} denote the energy differences between two spin states of spin-up and spin-down electrons, respectively. The total energy difference Δ can be determined as $\Delta=\Delta_{up}-\Delta_{down}$.

Table 4.2 Energy levels around at the Fermi energy levels of the spin-up and the spin-down electrons in the cases of the singlet ground state and the triplet excited state

	NINAZ	NDMAZ	NDMAP
E_g	41.0 K	21.6 K	5.0 K
Singlet (spin-up)	−1.91 eV	−1.76 eV	−1.81 eV
Singlet (spin-down)	−1.91 eV	−1.73 eV	−1.85 eV
Triplet (spin-up)	−1.70 eV	−1.65 eV	−1.69 eV
Triplet (spin-down)	−1.97 eV	−1.83 eV	−1.84 eV
Δ_{up}	0.21 eV	0.12 eV	0.12 eV
Δ_{down}	−0.06 eV	−0.09 eV	0.00 eV
$\Delta = \Delta_{up} - \Delta_{down}$	0.27 eV	0.21 eV	0.12 eV

Note: The parameters Δ_{up} and Δ_{down} can be determined by the difference between these two spin states of spin-up and spin-down electrons, respectively.

similar to each other, reflecting the very similar X-ray diffraction data. On the other hand, the number of electrons in Ni 3d orbitals is known to be larger in the large Haldane gap materials from the results of Mulliken population analysis [23]. The energy difference between the singlet ground state and the triplet excited state in each compound has been calculated in order to clarify the correlation between the electronic structure and the Haldane gap more precisely. The results are summarized in Table 4.2. It has been postulated that the Haldane gap may be larger when there is a large value of the energy difference between the singlet ground state and the triplet excited state, supporting the VBS state theory of Haldane gap compound. A trend is found in the results of the energy level structural analysis. The larger Haldane gap compounds, such as NINAZ, have a larger energy difference between singlet and the triplet states, whereas the smaller Haldane gap compounds such as NDMAP have a smaller energy difference between them, as shown in Table 4.2. The results are explained as follows. The Haldane gap material exhibits a strong spin–spin coupling between two neighboring spins of opposite sign ($S = \pm 1$) along the 1D chain by means of the valence bond on the basis of the VBS state. The strong coupling between these two spins causes the antiferromagnetic interaction, which is the origin of the Haldane gap. In the case of the N_3^- bridged Haldane gap compounds, such as NINAZ, NDMAZ, and NDMAP, the N_3^- molecule between two adjacent Ni^{II} ions in the 1D chain plays a role as the coupler of the VBS state between two neighboring spins of opposite sign ($S = \pm 1$). In the case of NINAZ, the energy difference between the singlet ground state and the triplet excited state is very large, suggesting that there is a large energy barrier for spin inversion from the anti-parallel singlet spin pair to the parallel triplet spin pair. As a result, the largest value of the Haldane gap is observed to be 41 K in the case of NINAZ. On the other hand, the energy difference of NDMAP is inclined in the N_3^- molecule, giving rise to a small value for the measured Haldane gap of 5 K. In our preliminary calculation, we can reveal the correlation of the Haldane gap and the

energy difference in the case of not only the N_3^- bridged compounds such as NINAZ, NDMAZ, and NDMAP but also the NO_2^- bridged compounds such as NENP and NINO. Therefore such a computational calculation can be used for predicting the Haldane gaps not only qualitatively but also quantitatively.

By using only X-ray structural analyses, it would be very difficult to predict these energy difference in the 1D chain of the Haldane gap compounds. Additional information on the electronic structure is required in order to understand the correlation between the magnetic properties and the electronic structure, through the energy level structure analysis. As a result, we can reveal a reliable method to predict the value of the Haldane gap by means of analysis of the energy difference between the singlet ground state and the triplet excited state using detailed DV-Xα molecular orbital calculations.

4. CONCLUSION

We have shown the possibility of controlling the Haldane gap through substitution of the in-plane and bridging ligands and counteranions. The value of the Haldane gap may then be predicted by using DV-Xα molecular orbital calculations. The correlation of the observed Haldane gap, E_g, is in good agreement with the dependence of the energy difference between the singlet ground state and the triplet excited state of each cluster model calculated by the DV-Xα molecular orbital method.

ACKNOWLEDGMENTS

The authors express their gratitude to Professor H. Adachi (Kyoto University) for permission to use a computational program. The authors also thank Professor R. Sekine (Shizuoka University) and Dr. G. Sakane (Okayama University of Science) for fruitful discussions and useful technical advice.

REFERENCES

[1] O. Kahn (Ed.), *Magnetism: A Supramolecular Function*, NATO ASI Series C484, Kluwer Academic Publishers, Dordrecht, 1996, ISBN-13: 978-0792341536;
J.S. Miller, A.J. Epstein, *Angew. Chem. Int. Ed. Engl.* **33** (1994) 385;
E. Coronado, P. Delhaés, D. Gatteschi, J.S. Miller (Eds.), *Molecular Magnetism: From Molecular Assemblies to the Devices*, NATO ASI Series E321, Kluwer Academic Publishers, Dordrecht, 1996, ISBN-13: 978-0792341307;
H. Iwamura, *Adv. Phys. Org. Chem.* **26** (1990) 179.
[2] M. Yamashita, T. Ishii, H. Matsuzaka, *Coord. Chem. Rev.* **198** (2000) 347.
[3] R. Sessoli, D. Gatteschi, A. Caneschi, M.A. Novak, *Nature* **365** (1993) 141;
R. Sessoli, H.-L. Tsai, A.R. Sxchake, J.B. Wang, K. Folting, D. Gatteschi, G. Christou, D.N. Hendrickson, *J. Am. Chem. Soc.* **115** (1993) 1804;
L. Thomas, F. Lionti, R. Ballou, D. Gatteschi, R. Sessoli, B. Barbara, *Nature* **383** (1996) 145;
D. Gatteschi, A. Caneschi, L. Pardi, R. Sessoli, *Science* **265** (1994) 1054;
D. Gatteschi, R. Sessoli, *Angew. Chem. Int. Ed.* **42** (2003) 268;
D. Gatteschi, R. Sessoli, A. Cornia, *Chem. Commun.* (2000) 725.

[4] O. Kahn, Molecular Magnetism, VCH Publishers (1993), ISBN-13: 978-1560815662. C.J. O'Connor, ''Research Frontiers in Magnetochemistry'', World Scientific (1993), ISBN-13: 978-9810212469; P.M. Lahti, ''Magnetic Properties of Organic Materials'', Marcel Dekker (1999), ISBN-13: 978-0824719760.
[5] J.S. Miller (Ed.), *Extended Linear Chain Compounds*, Plenum, New York and London, 1982, Vol. I–III, ISBN-13: 978-0306407123.
[6] J.C. Bonner, M.E. Fisher, *Phys. Rev.* **135(3A)**, (1964) A640.
[7] W. Duffy, K.P. Barr, *Phys. Rev.* **165** (1968) 647;
J.W. Hall, W.E. Marsh, R.R. Weller, W.E. Hatfield, *Inorg. Chem.* **20** (1981) 1033.
[8] F.D.M. Haldane, *Phys. Lett.* **A93** (1983) 464.
[9] K. Katsumata, H. Tasaki, *Haldane Gap – Macroscopic Quantum Phenomena in Spin Systems*, Selected Papers in Physics VIII, The Physical Society of Japan (1997).
[10] M.P. Nighttingal, H.W.J. Blote, *Phys. Rev.* **B33** (1986) 659;
T. Sakai, M. Takahashi, *Phys. Rev.* **B42** (1990) 1090.
[11] A. Meyer, A. Gleizes, J.-J. Girerd, M. Verdaguer, O. Kahn, *Inorg. Chem.* **21** (1982) 1729.
[12] J.P. Renard, M. Verdaguer, L.P. Regnault, W.A.C. Erkelens, J.R. Mignod, W.G. Stirling, *Europhys. Lett.* **3** (1987) 945.
[13] T. Yoshida, M. Fukui, *J. Phys. Soc. Jpn.* **61** (1992) 2304.
[14] J.-P. Renard, L.P. Renault, M. Verdaguer, *J. Phys.* **49** (1988) C8;
T. Takeuchi, H. Hori, T. Yoshida, A. Yamagishi, K. Katsumata, J.-P. Renard, V. Gadet, M. Verdaguer, M. Date, *J. Phys. Soc. Jpn.* **61** (1992) 3262.
[15] V. Gadet, M. Verdaguer, V. Briois, A. Gleizes, J.-P. Renard, P. Beauvillain, C. Chappert, T. Goto, K. Le Dang, P. Vellet, *Phys. Rev.* **B44** (1991) 705;
L.-K. Chou, K.A. Abboud, D.R. Talham, W.W. Kim, M.W. Meisel, *Physica* **B194–196** (1994) 311;
T. Kobayashi, A. Kohda, K. Amaya, M. Ito, H. Deguchi, K. Takeda, A. Asana, Y. Ajiro, M. Mekata, *J. Phys. Soc. Jpn.* **63** (1994) 1961.
[16] T. Ishii, N. Aizawa, H. Hara, M. Yamashita, H. Matsuzaka, *Polyhedron* **20(11–14)** (2001) 1297–1304.
[17] I. Affleck, T. Kennedy, E.H. Lieb, H. Tasaki, *Phys. Rev. Lett.* **59** (1987) 799.
[18] M. Yamashita, K. Inoue, T. Ohishi, H. Miyamae, T. Takeuchi, T. Yoshida, *Synth. Met.* **71** (1995) 1961;
T. Takeuchi, T. Yoshida, K. Inoue, M. Yamashita, T. Kumada, K. Kinda, S. Merah, M. Verdaguer, J.-P. Renard, *J. Mag. Mag. Mat.* **140** (1995) 1633;
Z. Honda, K. Katsumata, H.A. Katori, K. Yamada, T. Ohishi, T. Manabe, M. Yamashita, *J. Phys: Condens. Matter.* **9** (1997) L83.
[19] M. Monfort, J. Ribas, X. Solans, M.F. Bardia, *Inorg. Chem.* **35** (1996) 7633.
[20] C.Y. Weng, Ph.D. Thesis, Carnegie Institute of Technology (1968).
[21] A. Rosen, D.E. Ellis, *Chem. Phys.* **62** (1975) 3039.
[22] H. Adachi, M. Tsukada, C. Satoko, *J. Phys. Soc. Jpn.* **45** (1978) 875;
H. Nakamatsu, H. Adachi, T. Mukoyama, *Bull. Inst. Chem. Res. Kyoto Univ.* **70** (1992) 16.
[23] R.S. Mulliken, *J. Chem. Phys.* **23** (1955) 1833; *J. Chem. Phys.* **23** (1955) 1841; *J. Chem. Phys.* **23** (1955) 2338; *J. Chem. Phys.* **23** (1955) 2343.

CHAPTER 5

First-Principles Analysis of the Antiferromagnetic State

Kimichika Fukushima

Contents

Abstract

This paper examines the mechanism of the antiferromagnetic state. The study used the Xα molecular orbital theory, which has been successfully applied to analyze material properties. The author found a non-empirical method to describe the antiferromagnetic state of hydrogen clusters with a relatively long H–H distance and transition metal oxides like copper oxides, where a composing H atom as well as a metal atom of metal oxide octahedron have one localized conducting electron. The antiferromagnetic state of the former hydrogen clusters is partially due to energy difference between atomic orbitals with the same spin on atoms adjacent to each other. It was also shown that the delocalization of electrons on the oxygen in metal oxides leads to the decrease in overlap between metal *d* orbital and oxygen *p* orbital, and results in the localization of metal *d* electron.

1. INTRODUCTION

The present author found a non-empirical method to describe the antiferromagnetic state of transition metal oxides and hydrogen clusters with a relatively long H–H distance [1–3]. The study used the discrete variational (DV)-Xα molecular orbital theory, which has been successfully applied to analyze properties of

AITEL Corporation, 8, Shinsugita-cho, Isogo-ku, Yokohama 235-8523, Japan
E-mail: kimichika1a.fukushima@glb.toshiba.co.jp; km.fukushima@mx2.ttcn.ne.jp

Advances in Quantum Chemistry, Vol. 54
ISSN 0065-3276, DOI 10.1016/S0065-3276(07)00005-6

metals, semiconductors, and so on [4]. In a typical antiferromagnetic state, the spin direction of electrons on adjacent atoms is opposite to each other. (As is known, the spin concept was born around 1925 when Schrödinger formulated the theory of quantum mechanics, and the initial picture of spin was a rotation of electron. Pauli had thought that spin should be a pure mathematical object, and presented the theory where electron has two internal degrees of freedom, that is, electron is described by the wave function with two components. The theoretical intrinsic magnetic moment of electron was determined from the further extension of this Pauli theory of spin.) Around 1950, Shull and Smart made a groundbreaking discovery of the antiferromagnetic state in a real material of MnO with a neutron diffraction experiment [5]. The antiferromagnetic state is a fundamental concept of the condensed matter physics, and the theoretical description of the antiferromagnetic state was rendered an important quest. Theoretical approaches [6,7] were performed before and after the experimental discovery of the antiferromagnet. Hubbard extensively examined a model of the semi-empirical theory, which was based on the band theory, and the model is called Hubbard model today. This model consists of the transfer integral term and the on-site Coulomb repulsion term. When number of localized conductive electron (or hole) per atom is unity and the transfer integral is larger than the on-site Coulomb repulsion term, the system becomes a metal. Whereas, when the transfer integral is smaller than the on-site Coulomb repulsion term, the system becomes an antiferromagnetic insulator.

However, it seems that the research of the antiferromagnetic state by the non-empirical theory was not enough. In fact, when copper oxide superconductors were discovered in 1986 [8], a naïve non-empirical band structure calculation indicated that the host material with a single localized conductive electron per atom is a metal, contrary to the followed experimental result that the host material is an antiferromagnetic insulator. This missing of the antiferromagnetic state in the naïve band structure calculation was partially caused by the fact that the energy difference between Cu-3*d* orbital and O-2*p* orbital was not so large, and the overlap between these orbitals did not seem to be small enough for strong localization of the localized conductive electron. To overcome this difficulty, some improvements [9–11] were presented in band structure calculations by the self-interaction correction and by the LDA+*U* method, where *U* is the strong on-site Coulomb repulsion. Although these improvements proceeded to some extent, there remain problems. Concerning non-empirical molecular orbital method, calculations of the antiferromagnetic state had not been fully reported.

Doubly ionized oxygen, O^{2-}, which appears in Cu oxides, emits electron in a vacuum, but is stabilized in a crystal, and the author found a non-empirical method to describe the antiferromagnetic state. It was indicated that the delocalization of electrons on the oxygen site causes the antiferromagnetic moment on the metal site. It was also shown that, in hydrogen clusters with a relatively long H–H distance, the antiferromagnetic state appears clearly, where a composing H atom as well as a metal atom of metal oxide octahedron have one localized conducting electron. The antiferromagnetic state in the latter hydrogen

cluster is partially due to difference in energy between atomic orbitals with the same spin on atoms adjacent to each other. The low-energy atomic orbital contributes larger to the molecular orbital compared to the high-energy atomic orbital on the nearest-neighbor atomic site, and this tendency is enhanced by the Xα potential. This paper examines the effect of the delocalization of electrons on the oxygen atom in metal oxides on overlap between metal *d* orbital and oxygen *p* orbital as well as the localization of metal *d* electron. The relatively long Cu–Cu distance in Cu oxides is suitable for the antiferromagnetic state, since, in hydrogen clusters with a relatively long H–H distance, the antiferromagnetic state appears clearly. Molecular orbital calculational method used here has flexibilities and makes it easy to extract essential properties of the electronic state simply compared to band structure calculational methods. For the non-empirical Xα method, time-consuming process for the exchange interaction is carried out without difficulty. Additionally, the present method does not need experimental data unlike semi-empirical molecular orbital methods. Furthermore, by means of small number of numerical basis set, accurate calculations are performed.

The author finally describes in this introduction that quasi two-dimensional layered Cu oxides have a pure antiferromagnetic spin arrangement in plane, however, MnO is antiferromagnetic along a specific axis and is ferromagnetic along another axis. From technological viewpoints, Cu oxide superconductors made it unnecessary to replenish liquid helium in the case of small superconducting magnets. In the ferrimagnet case, a set of ferromagnetic moments does not cancel the other set of ferromagnetic moments, and practical permanent magnets like ceramic ferrite magnets have been applied to magnetic devices such as hard disk, magnetic head, and so on.

In this paper, Section 2 will be devoted to describe spin-polarized first-principles calculational method, and Section 3 will examine the mechanism of the antiferromagnetic state. Section 4 will summarize the results.

2. SPIN-POLARIZED FIRST-PRINCIPLES CALCULATIONAL METHOD OF ELECTRONIC STATE

To investigate the spin state of electron systems, the first principles spin-polarized Xα molecular orbital theory is used, where this non-empirical theory does not need parameters to be determined from experimental data. Based on the Pauli theory of spin, electron is described in terms of two wave functions. In quantum mechanics, magnetic moment observed is a component along the considered *z*-axis, in which magnetic field is applied. (If necessary, we may consider the limiting case, where the applied magnetic field strength approaches zero.) Two spin states of an electron with $s = 1/2$ (s is spin) are distinguished by $\sigma = \uparrow$ (up spin) for $s_z = 1/2$ (s_z is spin z-component), and by $\sigma = \downarrow$ (down spin) for $s_z = -1/2$. The intrinsic magnetic moment of electron,

$$\mu_e = \gamma_e \hbar s, \tag{1}$$

was determined by Dirac, where the magnetic moment is parallel to the spin direction. We use atomic units in this paper, where $\hbar = 1$ (Plank constant), $m_e = 1$ (mass of electron) and $e = 1$, where charge of electron is $-e$.

The total energy of electron system in the scheme of spin-polarized Xα method is expressed as

$$E_{\mathrm{t}} = \int d\boldsymbol{r} \sum_{\sigma i} n_{\sigma i} \psi^*_{\sigma i}(\boldsymbol{r}) \left[-\frac{1}{2}\nabla^2 + V_{\mathrm{N}}(\boldsymbol{r}) + \frac{1}{2} V_{\mathrm{C}}(\boldsymbol{r}) + \frac{3}{4} V_{\mathrm{X}\alpha\sigma}(\boldsymbol{r}) \right] \psi_{\sigma i}(\boldsymbol{r}), \tag{2}$$

where $\psi_{\sigma i}(\boldsymbol{r})$ is the wave function of electron with spin σ at a space point $\boldsymbol{r}$, and the other quantities are as follows:

$$V_{\mathrm{N}}(\boldsymbol{r}) = -\sum_{v} \frac{Z_v}{|\boldsymbol{r} - \boldsymbol{R}_v|}, \tag{3}$$

with Z_v being charge of nucleus at a space position $\boldsymbol{R}_v$.

$$V_{\mathrm{C}}(\boldsymbol{r}) = \int d\boldsymbol{x} \frac{\rho(\boldsymbol{x})}{|\boldsymbol{r} - \boldsymbol{x}|}, \tag{4}$$

where

$$\rho(\boldsymbol{x}) = \sum_{\sigma} \rho_{\sigma}(\boldsymbol{x}), \tag{5}$$

with

$$\rho_{\sigma}(\boldsymbol{x}) = \sum_{\sigma i} n_{\sigma i} |\psi_{\sigma i}(\boldsymbol{x})|^2, \tag{6}$$

where $n_{\sigma i}$ is the number of electrons, which occupy $\psi_{\sigma i}(\boldsymbol{r})$. The Xα potential is given by

$$V_{\mathrm{X}\alpha\sigma}(\boldsymbol{r}) = -3\alpha \left(\frac{3}{4\pi} \right)^{1/3} [\rho_{\sigma}(\boldsymbol{r})]^{1/3}, \tag{7}$$

where α is the parameter, which usually is set to a value of 0.7.

The variational of the total energy, under the condition that the wave function is normalized to unity, leads to the wave equation as

$$\left[-\frac{1}{2}\nabla^2 + V_{\mathrm{N}}(\boldsymbol{r}) + V_{\mathrm{C}}(\boldsymbol{r}) + V_{\mathrm{X}\alpha\sigma}(\boldsymbol{r}) \right] \psi_{\sigma i}(\boldsymbol{r}) = \varepsilon_{\sigma i} \psi_{\sigma i}(\boldsymbol{r}), \tag{8}$$

where $\varepsilon_{\sigma i}$ is the energy. The magnetic moment density of electrons is denoted as

$$\mu_{\rho}(\boldsymbol{r}) = \gamma_e s [\rho_{\uparrow}(\boldsymbol{r}) - \rho_{\downarrow}(\boldsymbol{r})] \tag{9}$$

where $\rho_{\uparrow}(\boldsymbol{x})$ and $\rho_{\downarrow}(\boldsymbol{x})$ are the electron densities with up and with down spins, respectively.

For atoms, the wave function has, in a spherical coordinate (r, θ, ϕ), a form

$$\chi_{\sigma j}(\boldsymbol{r}) = R_{\sigma j}(r) Y_{lm}(\theta, \phi), \tag{10}$$

where $Y_{lm}(\theta, \phi)$ is the spherical harmonic function and a radial function $R_j(r)$ satisfies

$$\left[\frac{1}{r^2}\frac{d}{dr}(r^2)\frac{d}{dr} - \frac{l(l+1)}{r^2} + 2\left(\varepsilon_{\sigma j} - V_{\mathrm{N}}(r) - V_{\mathrm{C}}(r) - V_{\mathrm{X}\alpha\sigma}(r)\right)\right] R_{\sigma j}(r) = 0, \tag{11}$$

where $V_{\mathrm{C}}(r)$ in the spherical coordinate is rewritten as

$$V_{\mathrm{C}}(r) = \frac{4\pi}{r}\int_0^r dr' r'^2 \rho(r') + 4\pi \int_r^\infty dr' r' \rho(r'). \tag{12}$$

The radial wave function has $(n - 1 + l)$ nodes, where n and l are the quantum numbers. To solve the radial atomic wave equation above, the Herman–Skillman method [12] is usually used. The equation above may be rewritten in a logarithmic coordinate of radius. The radial wave equation is first expressed in terms of low-power polynomials near the origin at the nucleus [13]. With the help of the derived polynomials near the origin, the equation is then numerically solved step by step outward from the origin to satisfy the required node number. At the same time, the radial wave equation is solved numerically from a point far away from the origin, where the radial wave function decays exponentially. The inner and outer solutions are required to be connected smoothly including derivative at a connecting point.

Concerning molecules, the wave function (molecular orbital) for a hydrogen-like molecule, for instance, is expanded in terms of hydrogen-like atomic orbitals $\chi_{\sigma j}(\boldsymbol{r})$ belonging to hydrogen-like atoms $j = 1, 2$, respectively, as

$$\psi_{\sigma i}(\boldsymbol{r}) = c_{\sigma i1}\chi_{\sigma 1}(\boldsymbol{r}) + c_{\sigma i2}\chi_{\sigma 2}(\boldsymbol{r}). \tag{13}$$

The wave equation in a molecule is expressed by

$$h_\sigma[c_{\sigma i1}\chi_{\sigma 1}(\boldsymbol{r}) + c_{\sigma i2}\chi_{\sigma 2}(\boldsymbol{r})] = \varepsilon_{\sigma i}[c_{\sigma i1}\chi_{\sigma 1}(\boldsymbol{r}) + c_{\sigma i2}\chi_{\sigma 2}(\boldsymbol{r})], \tag{14}$$

where

$$h_\sigma(\boldsymbol{r}) = -\frac{1}{2}\nabla^2 + V_{\mathrm{N}}(\boldsymbol{r}) + V_{\mathrm{C}}(\boldsymbol{r}) + V_{\mathrm{X}\alpha\sigma}(\boldsymbol{r}). \tag{15}$$

By multiplying $\chi^*_{\sigma j}(\boldsymbol{r})$ to the wave equation, and by space integrating, the following secular equation in the matrix form, which is common for all wave functions, is derived:

$$\boldsymbol{H}_\sigma \boldsymbol{C}_\sigma = \varepsilon_\sigma \boldsymbol{S}_\sigma \boldsymbol{C}_\sigma. \tag{16}$$

Here, $\boldsymbol{C}_\sigma$ is a vector whose element is $c_{\sigma j}$. The matrix element (of the Hamiltonian) of $\boldsymbol{H}_\sigma$ is denoted as

$$\mathrm{H}_{\sigma ij} = \int d\boldsymbol{r}\chi^*_{\sigma i}(\boldsymbol{r}) h_\sigma(\boldsymbol{r})\chi_{\sigma j}(\boldsymbol{r}); \tag{17}$$

and the matrix element (overlap integral) of S_σ is given by

$$S_{\sigma ij} = \int d\boldsymbol{r}\chi^*_{\sigma i}(\boldsymbol{r})\chi_{\sigma j}(\boldsymbol{r}). \tag{18}$$

By diagonalization of the secular equation above, molecular orbitals in terms of $c_{\sigma j}$ and associated orbital energy are derived.

To evaluate chemical bonds and ionic states, the Mulliken populations are useful [14]. The overlap charge between atomic orbitals is defined as

$$q_{\sigma i12} = 2n_{\sigma i}c_{\sigma i1}c_{\sigma i2}\int d\boldsymbol{r}\chi^{*}_{\sigma 1}(\boldsymbol{r})\chi_{\sigma 2}(\boldsymbol{r}). \tag{19}$$

The orbital charge belonging to the atom labeled with j=1 is denoted by

$$q_{\sigma i11} = n_{\sigma i}[c_{\sigma i1}c_{\sigma i1}\int d\boldsymbol{r}\chi^{*}_{\sigma 1}(\boldsymbol{r})\chi_{\sigma 1}(\boldsymbol{r}) + c_{\sigma i1}c_{\sigma i2}\int d\boldsymbol{r}\chi^{*}_{\sigma 1}(\boldsymbol{r})\chi_{\sigma 2}(\boldsymbol{r})]. \tag{20}$$

The DV-Xα molecular orbital calculational method used here utilizes basis sets of numerically calculated atomic orbitals, as well as those of analytical atomic orbitals such as Slater orbitals. Matrix element of the Hamiltonian and the overlap integral are calculated numerically by summing integrand at sampling points $\boldsymbol{r}_k$, the Diophantine points, which are distributed according to the weighted function, and expressed as.

$$H_{\sigma ij} = \sum_k \omega_S(\boldsymbol{r}_k)\chi_{\sigma i}(\boldsymbol{r}_k)h_\sigma(\boldsymbol{r}_k)\chi_{\sigma j}(\boldsymbol{r}_k), \tag{21}$$

$$S_{\sigma ij} = \sum_k \omega_S(\boldsymbol{r}_k)\chi_{\sigma i}(\boldsymbol{r}_k)\chi_{\sigma j}(\boldsymbol{r}_k). \tag{22}$$

The weighted function employed is the Fermi distribution-like function. Namely, sampling point density is dense around a nucleus and decay exponentially beyond the atomic radius. Then, the weighted volume $\omega_S(\boldsymbol{r}_k)$ is derived.

3. MECHANISM EXAMINATION OF THE ANTIFERROMAGNETIC STATE

In this section, we consider mechanism of the antiferromagnetic state by using the non-empirical Xα method. The author showed that the antiferromagnetic state appears for layered hydrogen clusters at a relatively long H–H distance, even for large hydrogen clusters shown in Figure 5.1. Elongated hydrogen clusters (a set of atoms) were employed for consideration based on the fact that metal oxides such as La_2CuO_4 in the antiferromagnetic state are composed of octahedrons with a metal atom and surrounding oxygen atoms, and the metal atom is similar to a hydrogen atom of elongated hydrogen clusters as follows: Both the hydrogen atom and the metal atom have one localized conductive electron, and the Cu–Cu interatomic distance is rather long, where an influence of oxygen atoms was investigated in this study. We may then investigate essential properties of the antiferromagnetic state by hydrogen cluster calculations more simply compared to the Cu oxides case.

We examine reasons why the antiferromagnetic state appears in hydrogen clusters even by the molecular orbital theory. The spin-polarized calculational method uses wave function consisting of two components describing spin-up and spin-down electrons, as mentioned in the previous section. A molecular orbital energy level diagram for the antiferromagnetic hydrogen molecule at a

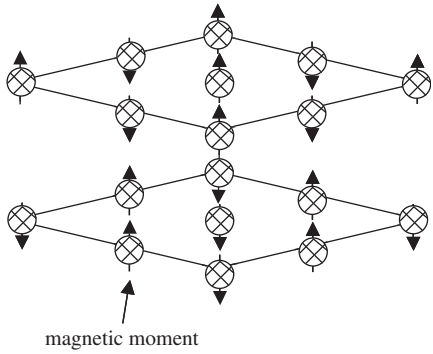

Figure 5.1 Antiferromagnetic state of layered H_{18} with a relatively long H–H in-plane distance.

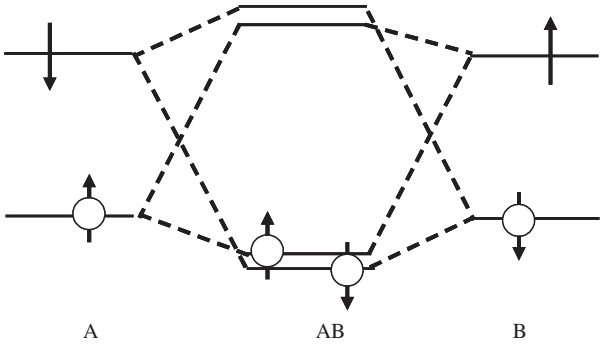

Figure 5.2 Schematic orbital energy diagram for H_2 with a relatively long H–H distance.

relatively long interatomic distance is shown in Figure 5.2, where degenerate orbital energies for hydrogen molecule AB consisting of hydrogen atom A and hydrogen atom B are separated for eye guide. The wave function of H_2 with spin σ is expressed as

$$\psi_\sigma(\boldsymbol{r}) = c_{\sigma A}\chi_{\sigma A}(\boldsymbol{r}) + c_{\sigma B}\chi_{\sigma B}(\boldsymbol{r}), \tag{23}$$

where $\chi_{\sigma A}(\boldsymbol{r})$ and $\chi_{\sigma B}(\boldsymbol{r})$ are 1s atomic orbitals on atom A and atom B, respectively. When the energy of atomic orbital with specified spin on atom A is equal to the energy of atomic orbital with opposite spin on atom B, and the energy of atomic orbital with up spin on atom A is lower than the energy of atomic orbital with the opposite down spin on the same atom A, the contribution of atomic orbital with up spin on atom A to the molecular orbital is larger than that of the atomic orbital with the same spin on atom B. By letting the A–B interatomic distance large enough, the antiferromagnetic state appears, where electron with up spin is localized on atom A and electron with down spin is localized on atom B. In other word, the higher energy atomic orbital with down spin on atom A and that with up spin on atom B contribute largely to the molecular orbital unoccupied by electron. The unoccupied molecular orbital, localized on a specified atom site

with a specified spin, gives rise to an opposite spin on the same atom. Even if the unoccupied molecular orbital is composed of many localized atomic orbitals with different (atomic) orbital energy like metal oxides, the situation is same. Namely, an atomic orbital localized on a specified atom site with a specified spin, whose contribution to the unoccupied molecular orbital is dominant, helps to give rise to an opposite spin on the same atom site. This antiferromagnetic state is stabilized by elongation of the interatomic distance. The antiferromagnetic state becomes stronger as parameter α in the Xα potential increases appropriately from a value of zero. The calculated dependence of the antiferromagnetic moment on the overlap integral and on α in the Xα potential will be shown below.

We here study the electronic state and the parameter dependence of the antiferromagnetic state for a layered H_8 cluster shown in Figure 5.3. In the cluster, positions of H atoms were $(\pm a_H, \pm a_H, \pm 1.25 a_H)$, where 0.126 nm was set to a_H. The H–H interatomic distance was made shorter up to 0.7 times a_H. A set of basis functions of 1s atomic orbitals was calculated numerically by adding a well potential, which was -2.0 a.u. in depth and was 0.8 time the interatomic distance in radius, to the potential for electrons. Integration points for matrix elements of the Hamiltonian and the overlap integral were 1000 per H atom. Point group for molecular orbitals was not taken into account, but atomic charges were set to be identical for atoms located at equivalent points. Figure 5.4 shows molecular orbital energy level diagram calculated by the spin-polarized method in an antiferromagnetic electron configuration for the layered H_8 cluster. The H–H interatomic distance was 0.8 times a value of a_H. In order to compare the orbital energy level diagram, we calculated in case of the non-spin polarized electron configuration the layered H_8 cluster. The difference in energy between highest occupied molecular orbital (HOMO) and lowest unoccupied molecular orbital (LUMO) is made larger the antiferromagnetic case in Figure 5.4 compared to the non-magnetic case in Figure 5.5, due to the antiferromagnetic interaction. Figure 5.6 shows the dependence of the magnetic moment on the parameter α of the Xα potential for the layered H_8 cluster. Figure 5.7 is the dependence of the

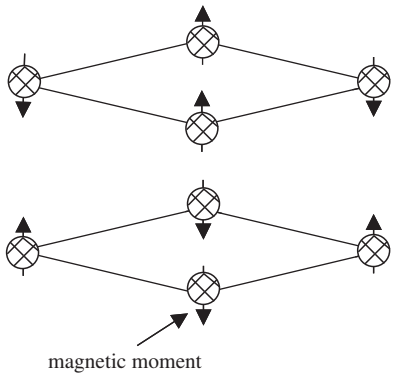

Figure 5.3 The H_8 cluster and a spin arrangement with a relatively long H–H in-plane distance.

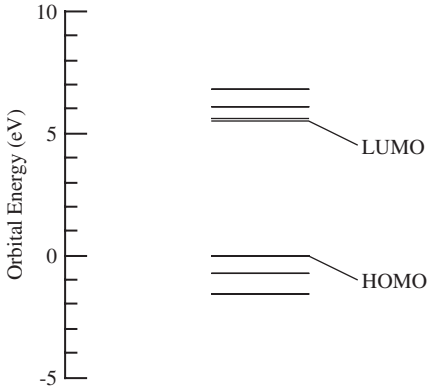

Figure 5.4 Molecular orbital energy levels calculated in the antiferromagnetic states for the layered H_8 cluster.

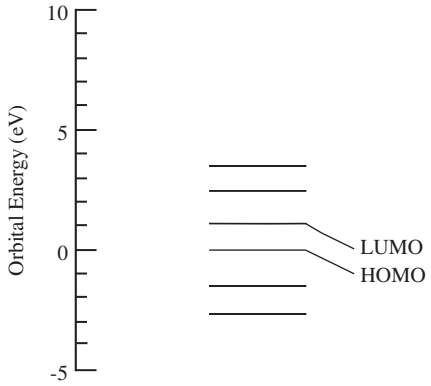

Figure 5.5 Molecular orbital energy levels calculated in the non-spin polarized electron configuration for the layered H_8 cluster.

HOMO–LUMO gap on the parameter α of the Xα potential for the layered H_8 cluster. As is seen, the magnetic moment of the H atom and the HOMO–LUMO gap get larger with the increase in α of the Xα potential. Figure 5.8 shows the dependence of the magnetic moment on the H atom site on the overlap integral between atomic orbitals of the A and B atoms, where the H–H interatomic distances were 1.0, 0.8, and 0.7 times a value of a_H. The magnetic moment decreases as the overlap integral becomes larger due to the compression of the cluster. Figure 5.9 shows the corresponding HOMO–LUMO energy gaps, ΔE_S and ΔE_N, for the antiferromagnetic and the non-magnetic spin configuration cases, respectively. The difference $\Delta E_S - \Delta E_N$ becomes smaller with decrease of H–H interatomic distance.

It was further difficult to derive the antiferromagnetic state in the case of transition metal oxides like Cu oxides. One of typical Cu oxides is La_2CuO_4, in the K_2NiF_4-type crystal structure, we displayed in Figure 5.10. The Cu oxide of

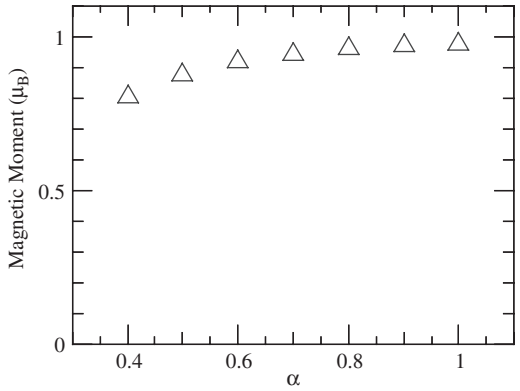

Figure 5.6 Dependence of the magnetic moment on the parameter α of the Xα potential for the layered H_8 cluster.

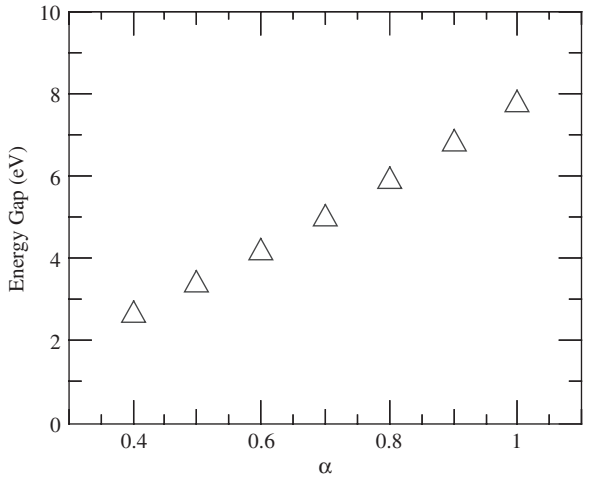

Figure 5.7 Dependence of the HOMO–LUMO gap on the parameter α of the Xα potential for the layered H_8 cluster.

La_2CuO_4 was experimentally shown to be in the antiferromagnetic state at low temperatures, after the groundbreaking discovery of the high-temperature superconductor of $La_{1.85}Ba_{0.15}CuO_4$. In La_2CuO_4, the ionic states of copper and oxygen are Cu^{2+} and O^{2-}, and electron configurations are mainly $(3d_{xz})^2(3d_{yz})^2(3d_{xy})^2(3d_{z^2})^1(3d_{x^2-y^2})^1$ and $(2p_x)^2(2p_y)^2(2p_z)^2$, respectively. Due to these electron configurations, the Jahn–Teller effect occurs, resulting in that apical oxygen atoms are elongated and the crystal structure has a layered perovskite. For copper oxides, Cu-3*d* orbital energy is not so different from O-2*p* orbital energy, and Cu–O distance is not elongated from a usual value. Overlap between these orbitals then did not seem to be small, and a naïve non-empirical calculation did not predict the

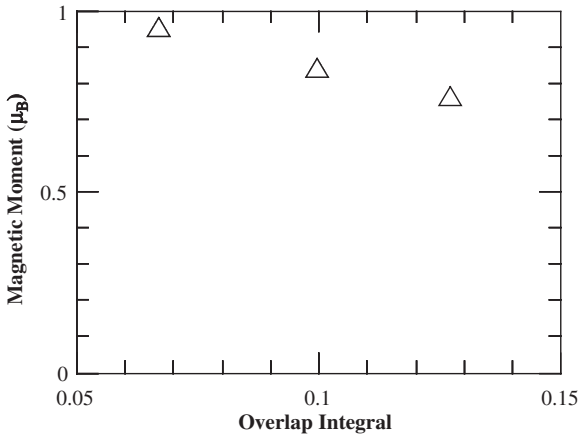

Figure 5.8 Dependence of the magnetic moment on the overlap integral for the layered H_8 cluster.

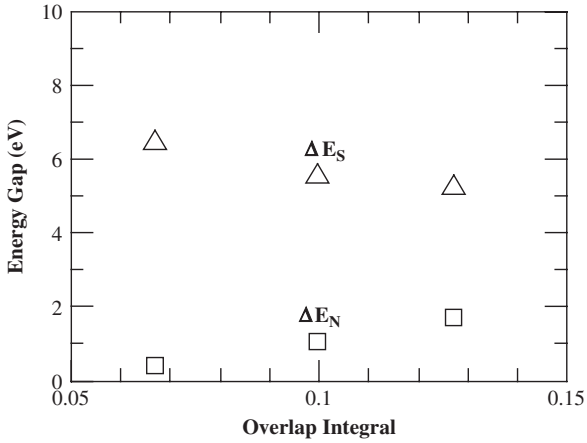

Figure 5.9 Dependence of the HOMO–LUMO gap on the overlap integral for the layered H_8 cluster.

expected state that Cu-3*d* electron would be localized on the Cu atomic site resulting in the antiferromagnetic state.

However, doubly ionized oxygen, O^{2-}, in Cu oxides, emits an electron in a vacuum, but is to be stabilized in an ionic crystal, and the author found that delocalization of electrons on the oxygen site causes the antiferromagnetic moment on the metal site. The analysis was performed by changing width and depth (including zero depth) of a well potential added to the potential for electrons of oxygen atom in deriving numerical trial basis functions (atomic orbitals). (The well potential was not added to copper atom.) The radial part of trial basis function was numerically calculated as described in the previous

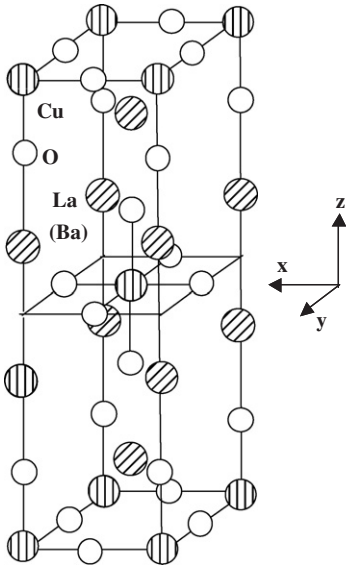

Figure 5.10 Crystal structure of La_2CuO_4.

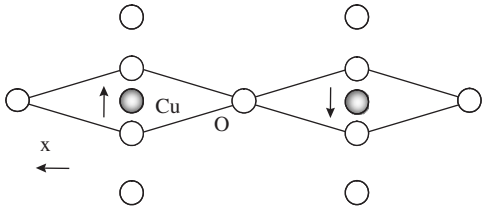

Figure 5.11 Model cluster of Cu oxide.

section. Since the trial basis function is interpolated locally in terms of polynomials with smooth derivative, inner and outer trial functions were connected smoothly. We further examine reasons why the antiferromagnetic state also appears in Cu oxides even with the molecular orbital theory, by using the same model depicted in Figure 5.11 with spin arrangement, and the same calculational procedures as those reported in the previous paper [2]. The positions of Cu atoms were $(\pm a_C, 0, 0)$, and those of O atoms were at $(\pm a_C, \pm a_C, 0)$, $(\pm 2a_C, 0, 0)$, (0,0,0) and $(\pm a_C, 0, \pm c_C)$, where 0.189 nm and 0.243 nm were set to a_C and c_C, respectively. A basis set used was 1*s*, 2*s*, 2*p*, 3*s*, 3*p*, and 3*d* numerical atomic orbitals for Cu atom, and 1*s*, 2*s* as well as 2*p* atomic orbitals for O atom. Number of numerical random points for the matrix elements was 18,000, and a value set to α of the Xα potential was 0.9. Formal charges assigned initially in self-consistent iterations were $+2e$ for Cu atom with the antiferromagnetic spin configuration and $-2e$ for O atom. The Madelung potential produced by atoms within the size of $4.02a_K \times 3.02a_K \times 2.74c_K$ in the *x*, *y*, and *z* directions in the

K_2NiF_4 structure was added to the potential for electrons in clusters, where a_K and c_K are the unit cell length along a and c axes with c_K being 1.33 nm.

In the case where we added the oxygen well potential of −2.0 a.u. in depth and 2.863 a.u. in radius, the system showed the metallic state. Whereas, in the case where the oxygen atom has no well potential, the copper atom had the antiferromagnetic moment of 0.98 μ_B. The overlap integral between Cu $3d_{x^2-y^2}$ and O $2p_x$ atomic orbitals for the latter antiferromagnetic case was about 0.73 times the corresponding value for the former metallic case. When another well potential was added to the oxygen atom, where the well depth was −0.5 a.u and the well radius was 2×2.863 a.u., respectively, the antiferromagnetic moment with a value of 0.54 μ_B appeared. In this antiferromagnetic case, the overlap integral takes 0.57 times the value for the metallic case. These results show that, when the overlap integral takes at least about 0.6–0.7 times that in the metallic case, the antiferromagnetic state appears. Additionally, the antiferromagnetic case, where the well potential is removed from the oxygen atom, the atomic orbital of oxygen is more delocalized compared to the antiferromagnetic case, where the well potential is added to the oxygen atom. The appearance of the antiferromagnetic moment on the Cu site is therefore due to the localization of Cu-3d electron caused by the delocalization of O-2p atomic orbital. Furthermore, even when O atoms exist between Cu atoms, electron transfers to the lower energy orbitals, and the localized 3d orbital, which is not occupied by electron with a specified spin, gives rise to an opposite spin on the same Cu atom, as mentioned previously for an elongated hydrogen atoms system. The relatively long Cu–Cu distance in Cu oxides is suitable for the antiferromagnetic state, since hydrogen clusters with a relatively long H–H distance shows a clear antiferromagnetic state.

We add a note concerning a calculational procedure that, in self-consistent iterations, an expected spin arrangement is specified initially. The initial spin arrangement has a tendency to be maintained in iterations, and the possibility to arrive finally at another spin arrangement may be small. The situation resembles to the following example: We consider a function of a variable u, where the function increases monotonically with the increase of $|u|$ for large $|u|$. When the function has two local minima around the origin of the u axis, by moving u slowly, the local minimum can be found from the sign change of slope. But, the local minimum point, which is found, depends on the initial u and the moving direction along the u axis. The molecular orbital is expanded in terms of basis functions and is expressed by a function of expansion coefficients. These coefficients correspond to the variable u in the example above. Total energy calculations may help to find a specific spin arrangement [15].

4. CONCLUSIONS

The author found a non-empirical method for describing the antiferromagnetic state of hydrogen clusters at a relatively long H–H distance and transition metal oxides. The Xα molecular orbital theory has been successfully applied to analyze

material properties. The clear antiferromagnetic state of the hydrogen clusters with a relatively long H–H distance is partially due to the difference in energy between atomic orbitals with the same spin on atoms adjacent to each other. The low-energy atomic orbital contributes larger to the molecular orbital, which is occupied by electron, than the high-energy atomic orbital on the nearest-neighbor atom, and this tendency is enhanced by the Xα potential. It was shown that the delocalization of electrons on the oxygen in metal oxides results in the decrease in overlap between metal *d* orbital and oxygen *p* orbital, and enhances the localization of metal *d* electron.

REFERENCES

[1] K. Fukushima, *J. Phys. Soc. Jpn.* **69** (2000) 1247.
[2] K. Fukushima, In: J.R. Sabin, E. Brändas (Eds.) [E. Brändas, H. Adachi, M. Uda, R. Sekine (Guest Eds.)], *Advances in Quantum Chemistry*, Vol. 42, 2003, p. 223.
[3] K. Fukushima, In: H. Adachi, T. Mukoyama, J. Kawai (Eds.), *Hartree–Fock–Slater Method for Material Science*, Springer, Berlin, Heidelberg, 2006, Chapter 5
[4] H. Adachi, M. Tsukada, C. Satoko, *J. Phys. Soc. Jpn.* **45** (1978) 875.
[5] C.G. Shull, J.S. Smart, *Phys. Rev.* **76** (1949) 1256.
[6] L. Néel, *Ann. Phys.* **17** (1932) 5.
[7] J. Hubbard, *Proc. Royal Soc. A* **276** (1963) 238.
[8] J.G. Bednorz, K.A. Müller, *Z. Phys. B* **64** (1986) 189.
[9] A. Svane, O. Gunnarson, *Phys. Rev. Lett.* **65** (1990) 1148.
[10] V.I. Anisimov, J. Zaanen, O.K. Andersen, *Phys. Rev. B* **44** (1991) 943.
[11] M. Arai, T. Fujiwara, *Phys. Rev. B* **51** (1995) 1477.
[12] F. Herman, S. Skillman, *Atomic Structure Calculations*, Prentice-Hall, Englewood Cliffs, NJ, 1963.
[13] J.C. Slater, *The Calculation of Molecular Orbitals*, Wiley, New York, 1979.
[14] R.S. Mulliken, *J. Chem. Phys.* **23** (1955) 1833.
[15] K. Fukushima, J. Mizuno, K. Fujima, H. Adachi, *J. Phys. Soc. Jpn.* **51** (1982) 4028.

CHAPTER 6

Sulfur Trioxide Adsorption on Pt Surface

Chikashi Suzuki and **Toshio Nakagiri**

Contents

Abstract

We studied the configuration of SO_3 adsorbed on Pt (111) surface using the first-principles calculations with a slab model in a periodic boundary condition. Based on the results from this study, we calculated the electronic states of the adsorbed SO_3 using the DV-Xα molecular orbital method. We found there were two stable configurations where the adsorbed SO_3 molecules were bound to the Pt surface. In one configuration (A), an S and two O atoms were bound to Pt surface atoms, and in the other configuration (B), all the three O atoms were bound to the Pt surface atoms. From the analysis with the DV-Xα molecular orbital method, it was found that in these SO_3 adsorption cases the component O 2p was blended with Pt 5d and became noticeably broad; it was also found that the components S 3p and O 2p in LUMO of SO_3 molecule moved into an occupied region. Besides, charge was transferred from surface Pt atom to an S atom, and S–O bond became weak in these adsorption states. In addition, it was assumed that the transfer of O atom to Pt surface was more restricted in configuration A than

Advanced Nuclear System Research and Development Directorate, Japan Atomic Energy Agency, 4002 Narita-cho, O-Arai-machi, Ibaraki-ken, 311-1393 Japan
Corresponding author. E-mail: suzuki.chikashi@jaea.go.jp

Advances in Quantum Chemistry, Vol. 54
ISSN 0065-3276, DOI 10.1016/S0065-3276(07)00006-8

in configuration B from the overlap population between O and Pt. From these calculations, we evaluated the electronic states of SO_3 adsorbed on Pt surface and also studied the interaction between SO_3 and Pt surface.

1. INTRODUCTION

High-efficiency hydrogen production system, utilizing the heat generation of multi-purpose small-sized Fast Breeder Reactor (FBR), is regarded as a promising technology for the future energy conversion systems. Among the various hydrogen production processes, thermo-chemical hydrogen production process has shown excellent characteristics, such as zero emission of CO_2 and high heat efficiency that can exceed 40%. So far many thermo-chemical hydrogen production processes have been proposed to produce hydrogen from water [1–3].

With one such thermo-chemical hydrogen production process, we are developing a hybrid version of such a system [4]. This hybrid thermo-chemical process is based on sulfuric acid (H_2SO_4) synthesis and decomposition processes, and where a decomposition process of sulfur trioxide (SO_3) is facilitated by electrolysis. With this process, we have succeeded in continuous production of hydrogen for up to 5 h; this has clearly demonstrated the practical applicability of the process [4]. However, in order to improve the energy efficiency of hydrogen production, it is necessary to reduce SO_3 electrolysis resistance, but the mechanism of SO_3 electrolysis has not yet been fully understood. The cell used in SO_3 electrolysis comprises of an YSZ electrolyte and a Pt electrode, which happens to be very similar to a solid oxide fuel cell (SOFC). We showed that the reaction rate during the SO_3 electrolysis depended not on the conductivity of O^{2-} through the electrolyte, but rather on the electrode reaction [5]. This electrode reaction consisted of SO_3 adsorption on Pt electrode and SO_3 decomposition on Pt electrode, $SO_3 \rightarrow SO_2$ (gas phase)$+O_{ad}$ (adsorbed on Pt electrode) [5]. To understand the electrode reaction, the SO_3 adsorption on the electrode has to be studied, although this area has not been pursued.

Recently, based on several spectroscopic data, an assumption was made regarding the SO_3 configuration on a metal surface [6]. On the basis of this assumption, Cao et al. performed the first-principles molecular orbital calculation for SO_3/Cu (111) system and found the results in good agreement with the results obtained from the spectroscopic experiments [7]. However, the SO_3 configuration on Cu was based on an assumption from the experimental result and was not optimized with the first-principles calculation. On the other hand, SO_3 configuration on Pt was investigated using theoretical methods [8]. Though SO_3 configuration on Pt surface was calculated in detail in this study, the electronic structure of SO_3 and Pt surface was not investigated [8].

In order to investigate the mechanism of SO_3 electrolysis, it was necessary to evaluate the electronic states of SO_3 adsorbed on Pt surface. For this purpose, by using the molecular orbital calculation with cluster models, we have evaluated the electronic states of SO_3 adsorbed on Pt (111) surface. Also, in order to

optimize adsorbed SO_3 configuration on Pt surface, we performed the first-principles calculations with a slab model in a periodic boundary condition. From these calculations, we evaluated the electronic states of SO_3 and studied the interaction between SO_3 and Pt surface by adsorption.

2. CALCULATION

2.1 Surface configuration

In order to calculate adsorbed SO_3 configuration on Pt surface, we used the first-principles calculation code PHASE [9] with a slab model in a periodic boundary condition along the surface plane to simulate the Pt (1 1 1) surface. A four-layer slab model was used for main calculations. In these calculations, the atoms at the bottom are fixed at a bond distance d=2.83 Å, which is the optimized value in Pt fcc crystal with PHASE. A p(4 × 4) lateral supercell was used for the computation of the most energetically stable configuration. The p(4 × 4) surface supercell has 16 Pt atoms per layer with a lateral lattice constant of 11.31 Å.

The core electrons of all atoms were treated via ultra-soft pseudo potentials [10,11] with a cut-off of 25 Ry for wave function, and 240 for electronic density. The PBE gradient-corrected exchange-correlation function was used in self-consistent DFT calculations. The geometry optimization was performed using a $1 \times 1 \times 1$ k-point mesh. Because of the natural paired electron occupancies of the adsorbates, spin polarization effects were not considered to be important and were not treated explicitly in this study.

2.2 Electronic states

To evaluate the electronic states of SO_3 adsorbed on Pt surface and to study the interaction between SO_3 and Pt surface, we calculated the electronic states using a relativistic DV-Xα molecular orbital method [12]. The model clusters we used were SO_3 (plane triangle), plane Pt_{12}, and SO_3Pt_{12} as the models of SO_3 molecule, which is a plane triangle, Pt (1 1 1) plane, and SO_3 adsorbed on Pt (1 1 1) surface; we did this in place of calculating infinite surface structure calculated with PHASE. Figure 6.1(a) and (b) shows the two cluster models of SO_3Pt_{12} representing configurations A and B, which are later explained in Section 3.1. The formations of SO_3 in both SO_3Pt_{12} clusters are similar to that in SO_3 trimer where tetrahedral SO_4 are polymerized. The atomic positions were determined by the results of the calculation with PHASE. The basis sets used were S 1s–3p, O 1s–2p, and Pt 1s–6p.

The number of random sampling points in the DV-Xα calculations was 8000 for SO_3 molecule and 24,000 for SO_3Pt_{12}. Slater's exchange parameter (α) was fixed at 0.7 for all the atoms in the cluster. All atoms were contained inside a potential well of radius 5.0 bohr (1 bohr=0.529 Å) and depth −1.0 hartree (1 hartree=27.2 eV).

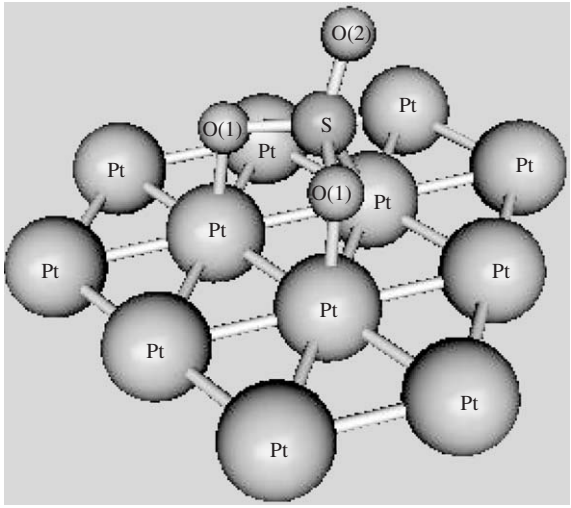

(a) Suzuki *et al.*

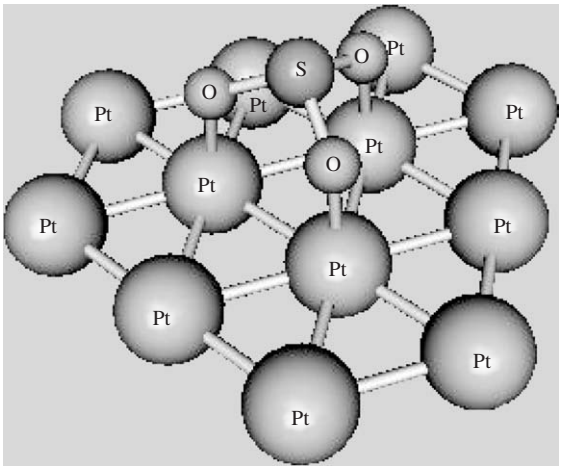

(b) Suzuki *et al.*

Figure 6.1 SO_3Pt_{12} cluster models used for the calculation with DV-Xα method. (a) Configuration A, (b) configuration B. For a colour version of this figure please see the colour plate section near the end of this book.

3. RESULTS AND DISCUSSIONS

3.1 SO_3 configuration on Pt surface

The configurations of SO_3 adsorbed on Pt (111) surface are shown in Figure 6.2, and its adsorption energy and geometric data are shown in Table 6.1. Figure 6.2 shows two such configuration A and B where three atoms from the molecule SO_3 are bound to Pt surface in both cases, and a fourth atom remains unbound to the Pt surface in each case. In configuration A, two O atoms and one S atom are bound to

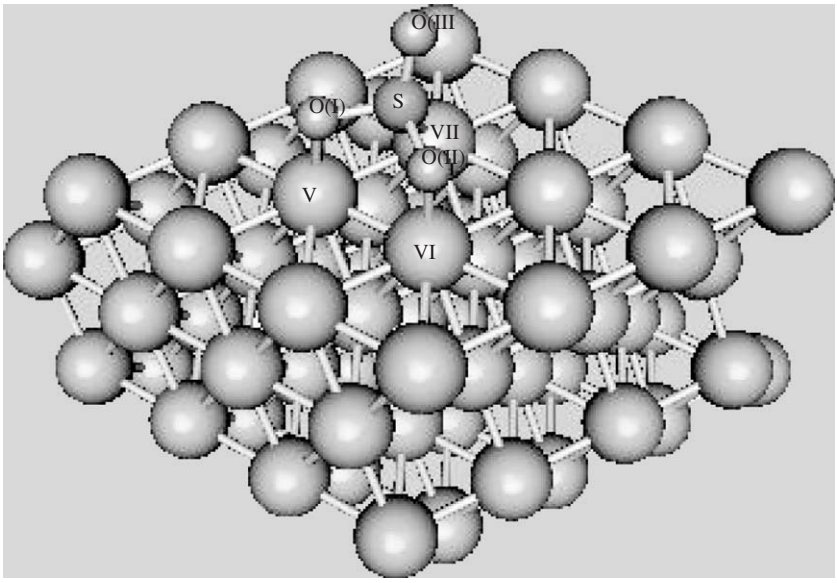

(a) Suzuki *et al.*

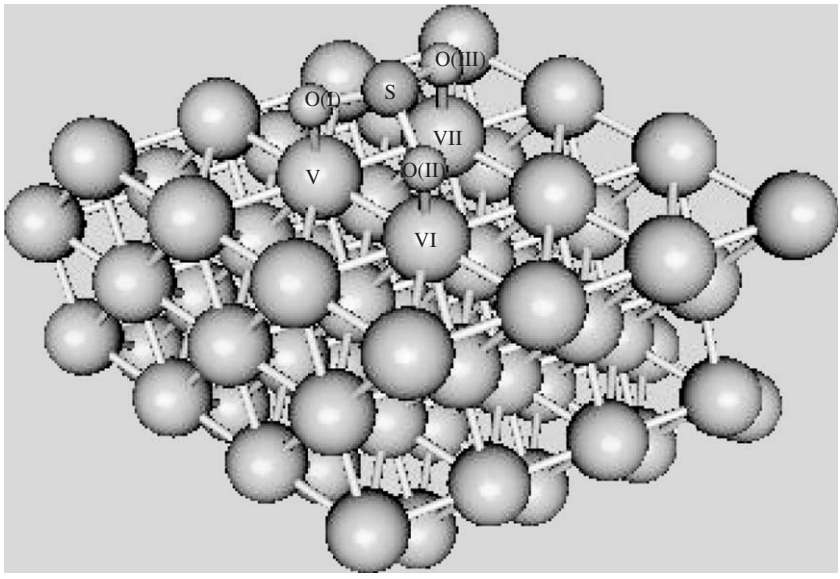

(b) Suzuki *et al.*

Figure 6.2 Calculated adsorbed SO_3 configuration on Pt surface. (a) Configuration A (b) configuration B. For a colour version of this figure, please see the colour plate section near the end of this book.

Table 6.1 Binding geometry of Pt (111)-SO_3

	Adsorption energy	Bond length (Å)			O–S–O Angle
		S–O	O–Pt	S–Pt	
Configuration A	1.75 eV	S–O(I): 1.690	O(I)-Pt: 2.133	2.414	O(I)-S-O(II): 103.1°
		S–O(II): 1.691	O(II)-Pt: 2.127		O(I)-S-O(III): 109.6°
		S–O(III): 1.545			O(II)-S-O(III): 109.9°
Configuration B	2.36 eV	S–O(I): 1.669	O(I)-Pt: 2.117		O(I)-S-O(II): 105.8°
		S–O(II): 1.669	O(II)-Pt: 2.117		O(II)-S-O(III): 105.8°
		S–O(III): 1.669	O(III)-Pt: 2.117		O(III)-S-O(I): 105.8°

the Pt surface and a fourth O atom remains unbound to the Pt surface. In the case of configuration B, the three O atoms from the molecule SO_3 are bound to Pt, while the S atom itself remains unbound to the Pt surface and is located right above a hollow site. The adsorption energy of configuration A is 1.75 eV, and that of configuration B is 2.36 eV. Although both these numbers are of the order of 2 eV, the configuration B is seen more stable than the configuration A. These molecules are primarily adsorbed above a threefold fcc site, as shown in Figure 6.2 by the locations of atoms marked V, VI, and VII. Similar to these, there are two stable configurations. Here the molecules are primarily adsorbed above a threefold hcp site. The adsorption energy in these configurations is a little smaller (approximately by 0.1 eV) than that of similar configurations. This means that these configurations are a little less stable than the other similar configurations. Unlike the planar gas-phase SO_3, the S center in configuration A is approximately tetrahedrally bound to three O atoms and one surface Pt atom. The O–S–O angle in the plane formed by the three surface-bound atoms is 103°. In addition, the O–S–O bond angles involving the O atom (unbound to the surface) are larger than O–S–O angle of the three directly bound atoms (110 vs. 103°). This difference is due to the geometric constraints imposed by the coordination to the surface metal atom. These angles are close to that of a tetrahedral configuration. The S–O bond with the non-surface bound is 1.545 Å, which is similar to that of the calculated S–O bond of the gas phase, 1.538 Å. The S–O bond with the surface bound is 1.69 Å, which is longer than that of the calculated S–O bond of the gas phase.

The S center in configuration B is approximately tetrahedrally bound to three O atoms and apart from surface Pt atom. Here the O–S–O angle is 106°. This angle is close to that of a tetrahedral configuration. Therefore the formations of adsorbed SO_3 in both configurations A and B are similar. The S–O bond with the surface bound is 1.669 Å, which is longer than that of the calculated S–O bond of the gas phase and is similar to that of the S–O bound to Pt surface in configuration A, 1.69 Å.

3.2 Analysis of density of states

3.2.1 SO_3 and Pt surface

To obtain a qualitative picture of the complex structure of SO_3 adsorbed on the Pt (1 1 1) surface, the density of states (DOS) was calculated from the DV-Xα molecular orbital method. The level width was broadened by a Gaussian function (1.0 eV FWHM) to mimic the solid state. The results of the studies are summarized in the following paragraphs. In each DOS, Fermi energy is set at 0. In configuration A, the adsorbed O atoms are classified as of two types. One is two O atoms bound to Pt surface atom (O(1)) and the other is one O atom unbound to Pt surface (O(2)).

The DOS of configuration A is shown in Figure 6.3(a) and that of configuration B is shown in Figure 6.3(b), which display direct comparison between Pt (1 1 1) surface and SO_3 molecule, and the components of Pt (1 1 1) and SO_3 in SO_3 adsorbed on Pt (1 1 1) surface. An important feature of Figure 6.3(a) is the broadening of SO_3 orbitals in the region from −6 eV to the Fermi level. Another important feature in this area is that LUMO of SO_3 molecule (which is an anti-bonding orbital at 0.90 eV) blends into the extended metallic occupied component and then disappears almost entirely by adsorption.

Figure 6.3(b) shows its characteristics similar to that of Figure 6.3(a) except for the broadening of SO_3 orbitals in the region from −6 eV to the Fermi level.

The projected DOS of S and O components in configurations A and B are shown in Figure 6.4(a) and (b), which display direct comparison between Pt (1 1 1) surface and SO_3 molecule, and SO_3 adsorbed on Pt (1 1 1) surface. In Figure 6.4(a), O components of SO_3 molecule are divided into two atoms and one atom in order to compare O(1) and O(2) with O component in SO_3 molecule. In Figure 6.3(a), the broadening of SO_3 orbitals in the region from −6 eV to the Fermi level is found as described above. This broadening is derived from the component of O(1). The components of S and O(2) do not contribute to this broadening in the region.

Figure 6.4(b) shows its characteristics similar to that of Figure 6.4(a). The shape of O component in Figure 6.4(b) is similar to that of the superimposition of the components of O(1) and O(2).

3.2.2 Atomic orbital components in SO_3

The projected DOS of S and O atomic orbital components in configurations A and B are shown in Figure 6.5(a) and (b), which display direct comparison between Pt (1 1 1) surface and SO_3 molecule, and SO_3 adsorbed on Pt (1 1 1) surface. In Figure 6.5(a), O component of SO_3 molecule is divided into two atoms and one atom in order to compare O(1) and O(2) with O component in SO_3 molecule.

From Figure 6.5(a), the broadening of SO_3 components in the region from −6 eV to the Fermi level is primarily due to 2p of O(1). The 2p component of O(2) in this region is similar to that of O in SO_3 molecule because O(2) is unbound to Pt surface atom. In addition, a small component of S 3p is involved in the occupied region from −5 to −2 eV, though S 3p is not involved in this region in SO_3 molecule.

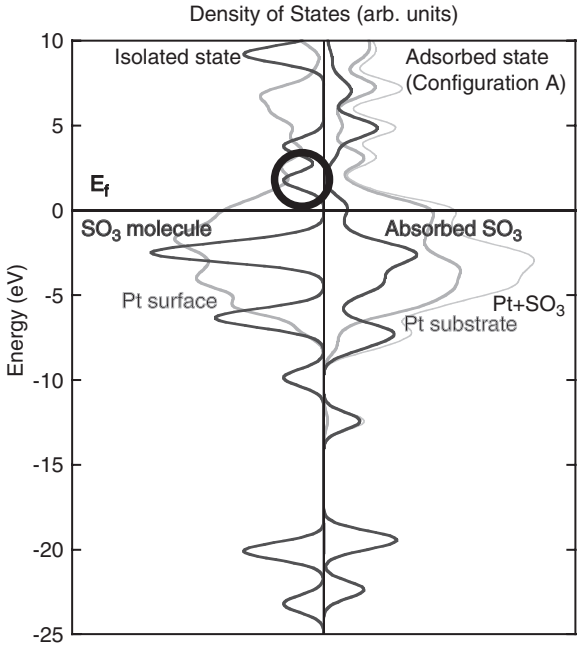

(a) Suzuki *et al*.

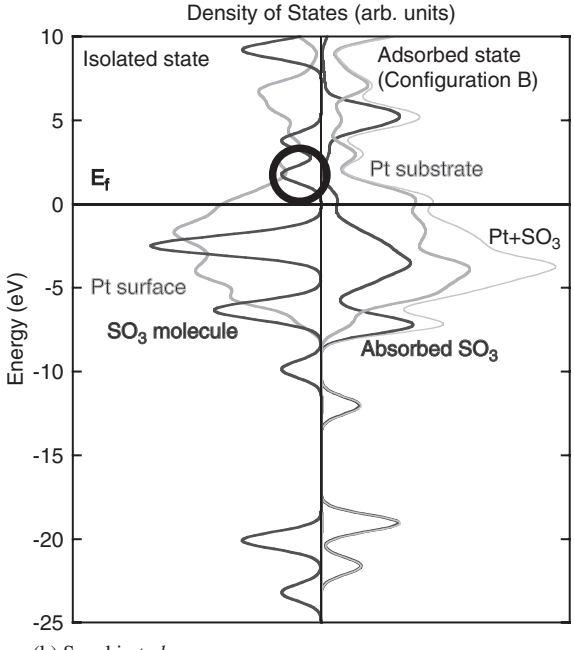

(b) Suzuki *et al*.

Figure 6.3 Comparison of the density of states (DOS) of adsorbed SO_3 and Pt surface with that of SO_3 molecule and clean Pt surface. (a) Configuration A, (b) configuration B.

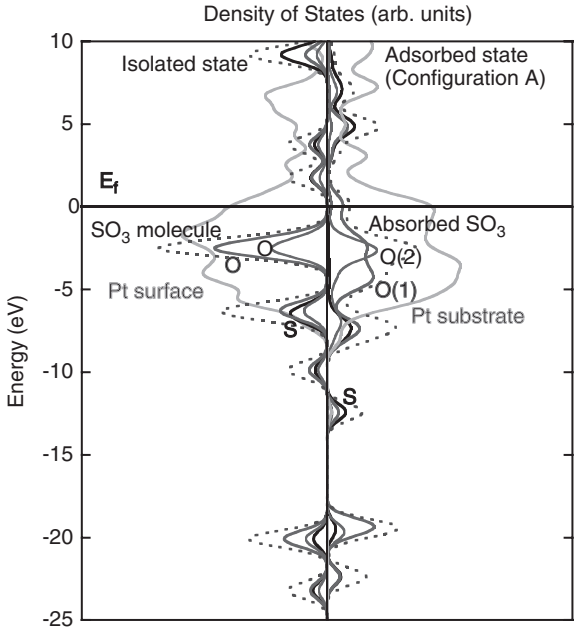

(a) Suzuki *et al*.

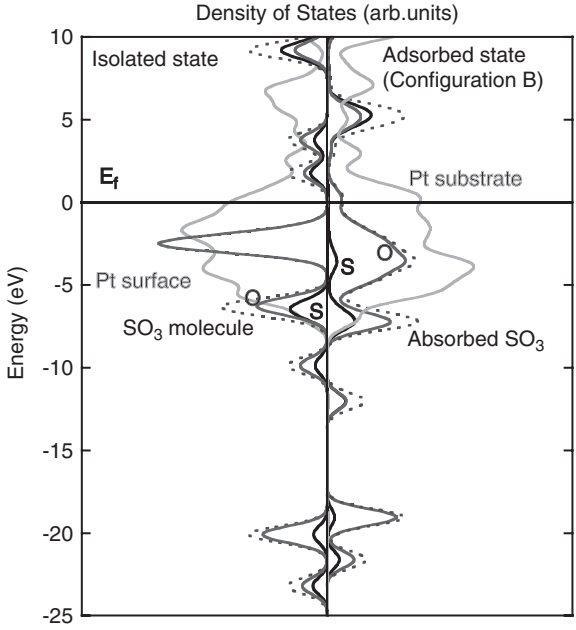

(a) Suzuki *et al*.

Figure 6.4 Comparison of p-DOS of S and O component of adsorbed SO_3 with that of SO_3 molecule. (a) Configuration A, (b) configuration B.

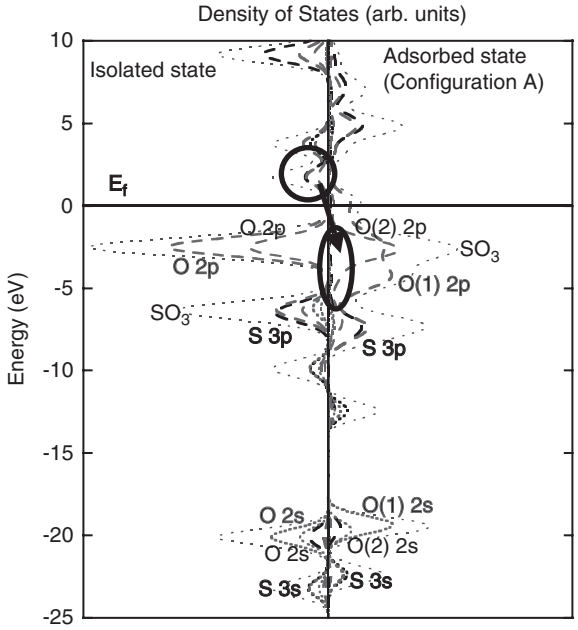

(a) Suzuki *et al*.

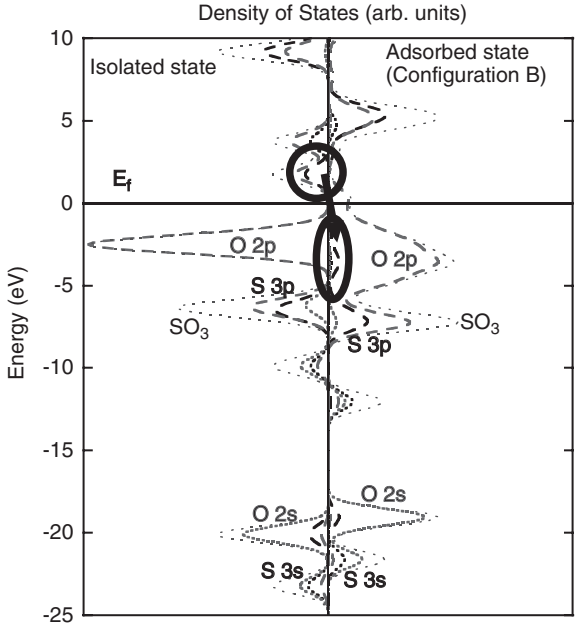

(b) Suzuki *et al*.

Figure 6.5 Comparison of p-DOS of S and O atomic orbital component of adsorbed SO_3 with that of SO_3 molecule. (a) Configuration A, (b) configuration B.

As shown in Figure 6.3(a), LUMO of SO_3 molecule blends into the extended metallic occupied component and then disappears almost entirely by adsorption. LUMO of SO_3 molecule consists of O 2p and S 3p and does not include O 2s or S 3s components. In Figure 6.5(a), this characteristic is shown only in the occupied region from −5 to −2 eV in configuration A. Therefore, S 3p and O 2p components in LUMO move into this occupied region by adsorption.

Figure 6.5(b) shows its characteristics similar to that of Figure 6.5(a). The shape of O component in Figure 6.5(b) is similar to the superimposition of the components of O(1) and O(2). However, a few of the characteristics here are also different from those of Figure 6.5(b). The S 3p component in the occupied region from −5 to −2 eV in Figure 6.5(b) is a little more apparent than that in Figure 6.5(a).

3.2.3 Interaction between S and Pt orbitals

The projected DOS of S and Pt atomic orbital components in configurations A and B are shown in Figure 6.6(a) and (b), which display direct comparison between Pt (111) surface and SO_3 molecule, and SO_3 adsorbed on Pt (111) surface.

From Figure 6.6(a), a small component of S 3p is involved in the occupied region from −5 to −2 eV as shown in Figure 6.5 and the S 3p component becomes broad in this region, which means some interaction between S 3p and Pt 5d takes place. However, except for this interaction, the interaction between S and Pt is very little and S component change only on the energy in the occupied region.

In the unoccupied region, LUMO of SO_3 molecule involving S 3p components disappears almost entirely by adsorption as shown in Figure 6.5(a). Above LUMO, the molecular orbitals involving both S 3s and 3p component are created in the two regions at the energy of 5.0 and 7.3 eV by adsorption from the orbitals of only S 3s at 3.8 eV or that of only S 3p component at 9.2 eV in SO_3 molecule in configuration A. From these results, it is found that the S component in unoccupied region change quite noticeably in configuration A.

Figure 6.6(b) shows its characteristics similar to that of Figure 6.6(a) although there is a little difference between the two. As regards to the difference from Figure 6.6(a), the molecular orbital involving both S 3s and 3p components is created only in the one region at the energy of 5.4 eV by adsorption from the orbitals of S 3s component at 3.8 eV, and by adsorption from the orbitals of S 3p component at 9.2 eV in SO_3 molecule in configuration B.

3.2.4 Interaction between O and Pt orbitals

The projected DOS of atomic orbital components of Pt and O bound to Pt in configuration A is shown in Figure 6.7(a) and that in configuration B is shown in Figure 6.7(b), which display direct comparison between Pt (111) surface and SO_3 molecule, and SO_3 adsorbed on Pt (111) surface.

From Figure 6.7(a), O(1) 2p, component is involved in the occupied region from −9 eV to the Fermi level in configuration A. In the region from −6 eV to the Fermi level, a remarkable interaction between O(1) 2p and Pt 5d is found.

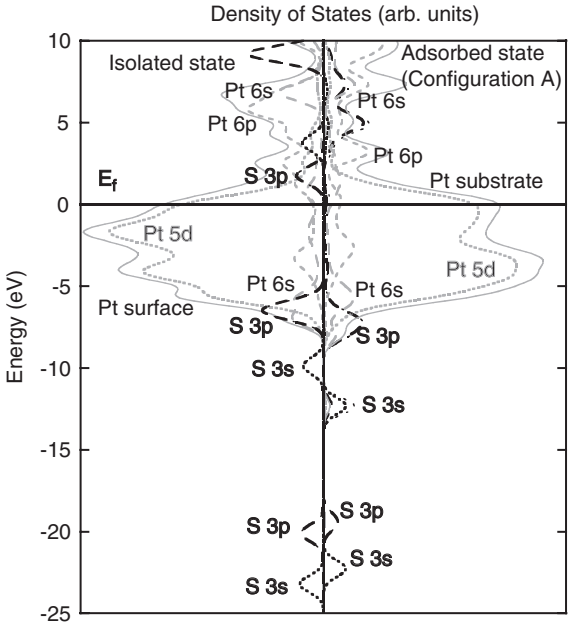

(a) Suzuki *et al*.

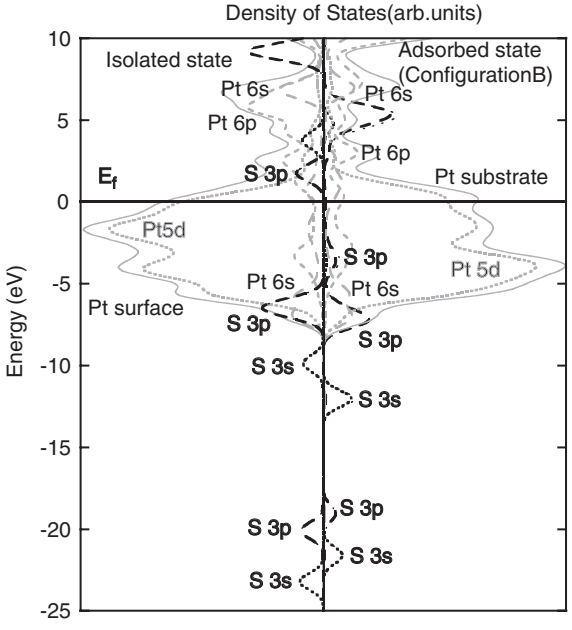

(b) Suzuki *et al*.

Figure 6.6 Comparison of p-DOS of Pt and S atomic orbital component of adsorbed SO_3 with that of SO_3 molecule. (a) Configuration A, (b) configuration B.

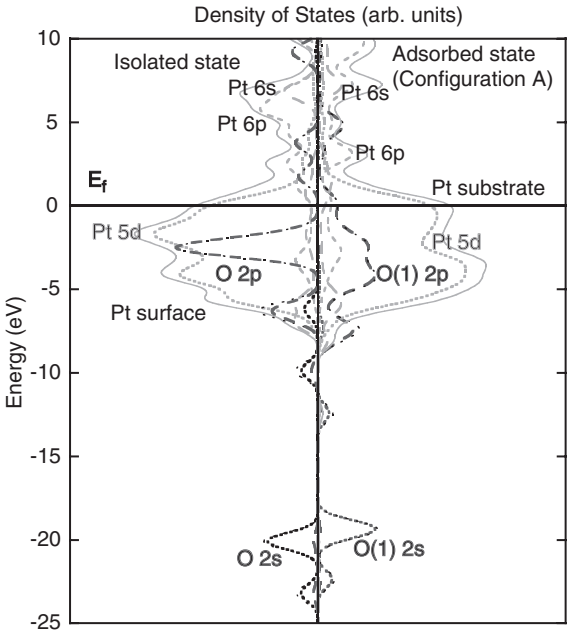

(a) Suzuki *et al*.

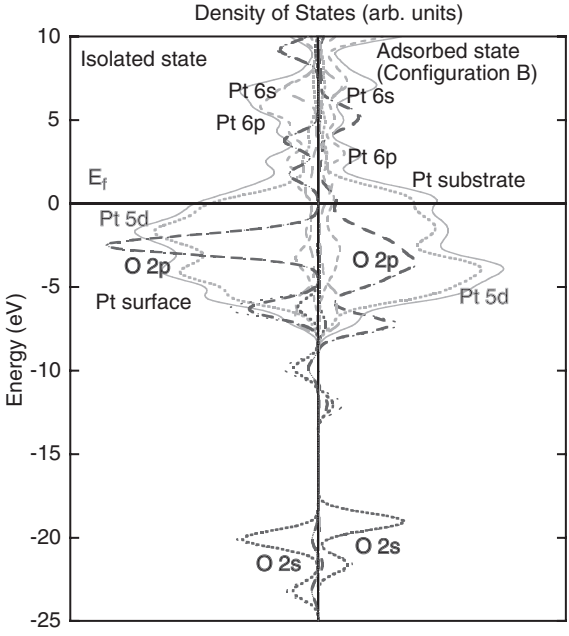

(b) Suzuki *et al*.

Figure 6.7 Comparison of p-DOS of Pt and S atomic orbital component of adsorbed SO_3 with that of SO_3 molecule. (a) Configuration A, (b) configuration B.

However, O(1) 2p component except for that in this region and O 2s component change only on the energy in the occupied region.

In the unoccupied region above LUMO in SO_3 molecule, O 2p components are situated in the two regions at the energies of 3.8 and 9.2 eV. By SO_3 adsorption on Pt surface, O 2p components are situated in the one region at the energy of 5.0 eV.

Figure 6.7(b) shows similar characteristics as of Figure 6.7(a) except for the shape of DOS of O 2p component in the region from −6 eV to the Fermi level.

3.3 Chemical bonding states

3.3.1 Effective charge

Table 6.2 shows the calculated effective charge of the atoms of SO_3 molecule and of SO_3 adsorbed on Pt surface. In SO_3 molecule, the effective charge of S atom is 1.83 and that of O atom is −0.61, which shows charge is polarized to O atom. In SO_3 adsorbed on Pt surface of configuration A, the effective charge of S atom is 1.60, that of O bound to Pt atom is −0.68, and that of O unbound to Pt atom is −0.74. The effective charge of O unbound to Pt atom is similar to that of one bound to Pt atom, although both atomic configurations are quite different. In both S and O atoms of configuration A, the effective charge is more negative than that of SO_3 molecule. In SO_3 adsorbed on Pt surface of configuration B, the effective charge of S atom is 1.42 and that of O atom is −0.80. In both S and O atoms of configuration B, the effective charge is more negative than that of SO_3 molecule. In particular, the effective charge of S atom is more negative than that of configuration A, though this atom is unbound to Pt atom. Total effective charge of SO_3 of configuration A and that of configuration B is −0.50 and −0.80, respectively, which means that more charge is transferred from Pt surface to SO_3 in configuration B than in configuration A. In both configurations A and B, charge transfer to S is remarkable compared with that to O.

3.3.2 Overlap population in SO_3 molecule

Table 6.3 shows an overlap population of the atoms of SO_3 molecule and SO_3 adsorbed on Pt surface. For SO_3 molecule the overlap population of S–O is 0.55, and that of O–O is −0.19. S–O bond shows bonding characteristics and O–O shows anti-bonding characteristics. As a result, the overlap population between one O atom and the other two O and S atoms is 0.18, which shows bonding characteristics.

Table 6.2 Effective charge of S, O, and SO_3

	SO_3 molecular	Configuration A	Configuration B
S	1.83	1.57	1.42
O	−0.61	O(1): −0.68 O(2): −0.74	−0.74
SO_3		−0.50	−0.80

Table 6.3 Overlap population of element at Pt surface

	SO_3 molecular	Configuration A	Configuration B
S–O	0.55	S–O(1): 0.33 S–O(2): 0.52	0.35
O–O	−0.18	O(1)–O(1): −0.14 O(1)-O(2): −0.15	−0.15
O–SO_2	0.19	O(1)–SO_2: 0.05 O(2)-SO_2: 0.22	0.05
S–Pt (nearest atom)		0.44	−0.08
S–Pt (2nd nearest atoms)		−0.26	
S–Pt_9 (outer)		–0.05	0.00
S–Pt surface		0.13	−0.24
O–Pt (nearest atom)		O(1)-Pt: 0.19 O(2)-Pt: −0.13	0.17
O–Pt_2 (2nd nearest atoms)		O(1)-Pt: −0.24 O(2)-Pt: 0.01	−0.08
O–Pt_9 (outer)		O(1)-Pt: −0.11 O(2)-Pt: 0.00	−0.15
O–Pt surface		O(1)-Pt: −0.16 O(2)-Pt: −0.12	−0.06
SO_3–Pt surface		−0.31	−0.42

3.3.3 Overlap population in configuration A

For SO_3 adsorbed on Pt surface of configuration A, the overlap population between S and O bound to Pt atom is 0.33. The overlap population between S and O that is apart from Pt atom is 0.52. The overlap population of O–O is −0.14 and −0.15, in cases where O atoms are bound to Pt atoms, and where they are apart from Pt atoms. The S–O bond shows bonding characteristics and O–O shows anti-bonding characteristics. For O–O bond, one O atom apart from Pt atom and two O atoms bound to Pt atoms look like equivalent. For S–O bond, the overlap population is same as that of SO_3 molecule; that is in case where O atom is apart from Pt atom. In case where O atom is bound to Pt atom, the overlap population is smaller than that of the SO_3 molecule. This result shows that S–O bond becomes weak by binding O atom to Pt surface atom. Therefore, the overlap population between one O atom (bound to Pt atom) and the other two O and S atoms is 0.05, which is a smaller number than that of SO_3 molecule, and thus shows a weak bond. From this result, we also see the overlap population between one O atom (apart from Pt surface) and other two O and S atoms is 0.22, which is a larger number than that of SO_3 molecule and thus shows a strong bond.

The overlap population between S and Pt, which is the nearest to S, is 0.44, which means that this bond is strong. The overlap population between S and the two second-nearest Pt atoms is −0.26, which is a negative value. The overlap population between S and the nine outer Pt atoms is −0.05, which is a small but of negative value. The total overlap population between S and Pt surface is 0.13.

The overlap population between Pt and O atom bound to this Pt is 0.19, which means that this bond is strong. The overlap population between this O and the two second-nearest Pt atoms is −0.24, which is a negative value. The overlap population between O and the nine outer Pt atoms is −0.11, which is a negative value. The total overlap population between this O and Pt surface is −0.16, which is a negative value and shows anti-bonding characteristic. The total overlap population between Pt surface and O apart from Pt surface is −0.12, which is a negative value and shows anti-bonding characteristic. From these results, the overlap population between SO_3 and Pt surface is −0.31, which shows an anti-bonding characteristic.

3.3.4 Overlap population in configuration B

In the case of configuration B, for SO_3 adsorbed on Pt surface, the overlap population of S–O is 0.35, and the overlap population of O–O is −0.15. S–O bond shows bonding characteristics and O–O shows anti-bonding characteristics. For S–O bond, the overlap population is smaller than that of SO_3 molecule. This result shows that S–O bond becomes weak by adsorbing O atom on Pt surface, which is the same as that in configuration A. Therefore, the overlap population between one O atom and the other two O and S atoms is 0.05, which is smaller than that of SO_3 molecule and shows a weak bond.

The total overlap population between S and Pt surface is −0.24. The overlap between Pt atom and O atom bound to this Pt atom is 0.17, which means that this bond is strong. The overlap population between O and the two second-nearest Pt atoms is −0.08, which is a negative value. The overlap population between O and the nine outer Pt atoms is −0.15, which is a negative value. The total overlap population between O and Pt surface is −0.06, which is a small and negative value. From these results, the overlap population between SO_3 and Pt surface is −0.42, which shows an anti-bonding characteristic.

3.4 Interaction between Pt surface and O atom

From the results of overlap population, by binding O atom to Pt surface atom, S–O bond becomes weak. It is assumed to be so, because LUMO of SO_3 molecule, which is anti-bonding orbital, moves into the occupied area by adsorption, and the charge is transferred to these anti-bonding orbitals by adsorption. On the other hand, by binding S atom to Pt surface atom, S–O bond does not become weak. Besides, even by binding either S or O atom to Pt atom, O–O bond is not much affected. From these results, it is found that the creation of O–Pt bond is important for dissociation between O and SO_2.

In configuration A, the bond between O and the nearest Pt atom shows bonding characteristic. However, the bond between O and Pt atom that is unbound to O atom show strong anti-bonding characteristic. This fact means Pt atom, which is unbound to O atom, has more influence on O atom than the Pt atom bound to O atom has. In other words, the bonds between Pt surface and O atom bound to Pt show both bonding and anti-bonding characteristics, but anti-bonding characteristics overcome bonding characteristic.

In the configuration B, the bond between O and the nearest Pt atom shows bonding characteristic, and the bond between O atom and Pt atom, which is unbound to O atom, shows anti-bonding characteristic. However, both bonding and anti-bonding characteristics between O and Pt surface atom in configuration B are not as strong as that in configuration A except for the effect of the outer nine Pt atoms. Therefore, it is assumed that the transfer of O atom to Pt surface is more restricted in configuration A than in configuration B near the adsorption site.

Generally, the energy barrier does not exist in the reaction of molecule adsorption on the surface. Therefore, at least, both configuration A and B exist in the process of SO_3 absorption reaction. In addition, it is assumed that the transfer of O atom to Pt surface is restricted and S atom is bound to Pt atom strongly in configuration A. From these facts, it is difficult that SO_3 absorbed on Pt surface in the configuration A is converted into SO_3 absorbed on Pt surface in the configuration B. Therefore, it is assumed that both the configurations A and B are formed on Pt surface.

3.5 Stabilization of SO_2 desorption

We assume that SO_3 electrolysis is performed under 500–550 C, which is near 800 K. As described above, S–O bond becomes weak by binding O atom to Pt surface atom. As a result, SO_3 is dissociated to SO_2 and adsorbed O atom. This adsorbed O atom is stable, but SO_2 may be unstable on Pt surface due to the entropy effect. In order to evaluate the stabilization of absorbed SO_2 on Pt surface, the entropy effect need be estimated. Calculated energy of SO_3 adsorption and that of SO_2 desorption from adsorbed SO_3 are shown in Table 6.4. The energy of SO_2 desorption from adsorbed SO_3 is 1.12 or 1.72 eV in configuration A or configuration B. In order to estimate the entropy effect of SO_2 desorption from solid phase to gas phase at 800 K, we investigate the SO_2 desorption reaction from solid phase to gas phase. We select the reaction of $SnSO_4 \rightarrow SnO_2 + SO_2$ and $PbSO_4 \rightarrow PbO_2 + SO_2$ as examples of such a reaction to roughly estimate it because thermodynamic data can be found in the literature. The standard reaction entropy is 150–168 J mol^{-1} K^{-1} at 800 K [13]. Therefore, the entropy effect ($T\Delta S$) is 120–134 kJ mol^{-1} at 800 K, corresponding to 1.25–1.39 eV for SO_2 desorption from solid phase to gas phase. In case where the entropy effect for SO_2 desorption from SO_3 adsorbed on Pt surface is of this value, it is larger than the energy of SO_2 desorption from adsorbed SO_3 in configuration A, and is smaller in configuration B. Therefore, it is assumed that SO_2 is stable in gas phase

Table 6.4 Calculated energy of SO_3 adsorption and that of SO_2 desorption from adsorbed SO_3 (eV)

	Configuration A	Configuration B
SO_3 adsorption energy	1.75	2.36
SO_2 desorption energy	1.12	1.72

and is desorbed from Pt surface in configuration A at 800 K, and that SO_2 is unstable in gas phase and is not desorbed from Pt surface in configuration B at 800 K.

4. CONCLUSIONS

We evaluated adsorbed SO_3 configuration on Pt (1 1 1) surface by using the first-principles calculations with a slab model in a periodic boundary condition. On the basis of the result of the calculations with a slab model, we evaluated the electronic states of SO_3 in detail using the relativistic DV-Xα molecular orbital method.

From the calculations with a slab model for SO_3 adsorption on Pt surface, it was found that there were two stable adsorbed SO_3 configurations on the Pt (1 1 1) surface, and three atoms were bound to Pt surface and one atom was unbound in both configurations, where one configuration formed S and two O atoms bound to Pt surface (configuration A), whose adsorption energy was 1.75 eV, and another formed three O atom bound to Pt surface (configuration B), whose adsorption energy was 2.36 eV.

From the DV-Xα molecular orbital method, it was found that in these SO_3 adsorption cases the component O 2p blended with Pt 5d and became noticeably broad and that the components S 3p and O 2p in LUMO of SO_3 molecule moved into the occupied region. In addition, charge was transferred from Pt surface to S atom and S–O bond became weak by adsorbing SO_3 on Pt surface. Besides, the interaction between Pt surface atoms and O atom bound to Pt surface showed both bonding and anti-bonding characteristics in configurations A and B. This interaction showed stronger characteristics of both bonding and anti-bonding in configuration A than in configuration B. Therefore it was assumed that the transfer of O atom to Pt surface was more restricted in configuration A than in configuration B. Moreover, comparing SO_2 desorption energy and the entropy effect of SO_2 desorption from solid phase to gas phase, it is assumed that SO_2 is stable in gas phase in configuration A and unstable in configuration B at 800 K at which SO_3 electrolysis is performed.

ACKNOWLEDGMENT

The authors thank Prof. K. Oagasawara and Mr. H. Yoshida for the development of the relativistic DV-Xα method code (RSCAT) and offering it to us.

REFERENCES

[1] IAEA, Hydrogen as an energy carrier and its production by nuclear power, IAEA-TECDO-1085, (1999).
[2] W. Weirich, K.F. Knoche F. Behr, et al., Thermochemical processes for water splitting: Status and outlook, *Nucl. Eng. Des.* **78** (1984) 285–291.
[3] M. Nomura, et al., Estimation of thermal efficiency to produce hydrogen from water through IS process, *ALChE* (2003).

[4] T. Nakagiri, T. Kase, S. Kato, K. Aoto, *JSME Int. J., Ser. B* **49** (2006) 302.
[5] C. Suzuki, T. Nakagiri, K. Aoto, *Int. J. Hydrogen Energy* **32** (2007) 1771.
[6] G.J. Jackson, S.M. Driver, D.P. Woodruff, N. Abrams, R.G. Jones, M.T. Butterfield, M.D. Crapper, B.C.C. Cowie, V. Formoso, *Surf. Sci.* **459** (2000) 231.
[7] S. Cao, J.-C. Tang, P. Zhu, L. Wang, S.L. Shen, *Phys. Rev. B* **66** (2002) 045403.
[8] X. Lin, K.C. Hass, W.F. Schneider, B.L. Trout, *J. Phys. Chem. B* **108** (2004) 250.
[9] The "PHASE" computer program was created by the members of the national project "Frontier Simulation Software for Industrial Science (FSIS)" and Advance soft Co., Ltd., has developed and released this software as "Advancesoft/PHASE" (http://www.advancesoft.jp/).
[10] D. Vanderbilt, *Phys. Rev. B* **41** (1990) 7892.
[11] K. Laasonen, A. Pasquqrello, R. Car, C. Lee, D. Vanderbilt, *Phys. Rev. B* **47** (1993) 10142.
[12] A. Rosen, D.E. Ellis, H. Adachi, F.W. Averill, *J. Phys. Chem.* **65** (1976) 3629.
[13] I. Barin (Ed.), *Thermochemical Data of Pure Substance*, 3th ed., VCH, Weinheim, 1995.

CHAPTER 7

X-Ray Absorption Near-Edge Structure and Optical Properties of Hafnium Oxynitride Thin Films

Sung Kwan Kim*, **Yang-soo Kim**** and **Kwang-soo No***

Contents

Abstract

Using the suggested local structures of HfO_2 (coordination number: 7.0), $Hf_4O_5N_2$ (6.25), and $Hf_4O_2N_4$ (5.5) in the previous research, we analyzed the effects of film composition on the X-ray absorption near-edge structure (XANES) spectra for O K-edge and N K-edge of hafnium oxynitride (Hf–O–N) thin films. The dispersion of optical constants for Hf–O–N thin films was analyzed using a four-phase model of ambient/graded/film/substrate for spectroscopy ellipsometry analysis. Two Cody–Lorentz models were applied for the spectroscopy ellipsometry analysis of films based on the XANES spectra. The effects of film composition on the dispersion of optical constants and on the surface degradation were analyzed.

1. INTRODUCTION

Hafnium oxynitride (Hf–O–N) thin films have attracted interest because of their unique properties, particularly their high dielectric constant, relatively large

* Department of Materials Science and Engineering, Korea Advanced Institute of Science and Technology, Daejeon 305-701, Korea
** Sunchon Branch, Korea Basic Science Institute 315 Maegok, Sunchon, Jeonnam 540-742, Korea
Corresponding author. E-mail: kimyangsoo@kbsi.re.kr

Advances in Quantum Chemistry, Vol. 54
ISSN 0065-3276, DOI 10.1016/S0065-3276(07)00007-X

band gap, and stability. Given their high dielectric properties, these films have been investigated as a potential replacement of dielectric to reduce the tunneling current through the gate-oxide of a field-effect transistor (FET) [1–3]. Hf–O–N thin films have also been considered as a substitute for the phase-shift mask (PSM). Because of their high refractive index, it is expected that Hf–O–N thin films with the thickness less than 70 nm can satisfy the requirements of transmittance and phase shift of PSM [4].

In the present study, to investigate the optical absorption of Hf–O–N thin films, we attempted to analyze the X-ray absorption near-edge structure (XANES) spectra for O and N K-edges of Hf–O–N thin films using first-principles calculations. In the comparison of the XANES spectra and the simulated transition states, the transition rate was suggested as one of reasons about the difference between the optical band gap and the simulated band gap. Based on the results of the XANES spectra, the models for spectroscopy ellipsometry (SE) analysis of Hf–O–N thin films were suggested. The effects of film composition on the optical constants (n and k) were analyzed using the suggested models.

2. EXPERIMENTAL PROCEDURE

In previous research [5], Hf–O–N thin films (50 ± 5 nm) were deposited using a planar circular RF magnetron reactive sputtering system with a 4″ Hf target with the different gas flow rates (Ar: 20 sccm, O_2: 0, 1 sccm, N_2: 10, 20 sccm). The O/Hf and N/Hf ratios of Hf–O–N thin films were 1.71 (± 0.04) and 0.08 (± 0.02) for sample S1, 1.36 (± 0.04) and 0.38 (± 0.07) for sample S2, and 0.20 (± 0.15) and 1.1 (± 0.1) for sample S3. The composition was determined by means of Rutherford backscattering spectroscopy (RBS) and Auger electron spectroscopy (AES).

3. RESULTS AND DISCUSSION

The absorbance of Hf–O–N thin films were measured in the range of 1.55–6.53 eV, and the $(\alpha hv)^{0.5}$ as a function of the photon energy hv were plotted in a previous report [5]. According to Tauc's formula [6], the extrapolation of the linear part to zero yields the optical band gap of 4.3 eV for S1, 3.98 eV for S2, and 2.04 eV for S3. Similar results of a decreasing band gap have been observed for metal oxynitrides as well [7]. The optical band gaps of Hf–O–N thin films were compared with the band gap (3.9 eV for S1, 2.28 eV for S2, and 1.1 eV for S3) simulated using first-principles calculations and the local structures of HfO_2 (coordination number (CN): 7.0) for S1, $Hf_4O_5N_2$ (CN: 6.25) for S2, and $Hf_4O_2N_4$ (CN: 5.5) for S3. The local structures of HfO_2 (CN: 7.0) for S1, $Hf_4O_5N_2$ (CN: 6.25) for S2, and $Hf_4O_2N_4$ (CN: 5.5) for S3 were determined by the analysis of the extended X-ray absorption fine structure (EXAFS) and of the structure optimization using first-principles calculations [8–10].

The optical band gap of S1 (4.3 eV) is larger than the simulated band gap (3.9 eV) of HfO_2 (CN: 7.0). The inherent error for the band gap calculation using DFT method is considered as reason about the difference (0.4 eV) between the optical band gap and the simulated band gap. However, the difference (1.7 eV) between the optical (3.98 eV) and simulated band gap (2.28 eV) of S2 is larger than that of S1. Considering the difference (0.8 eV) between the optical band gap and the simulated band gap of the crystallized monoclinic hafnium oxide with the thickness of 900 nm, the transition rate for the optical absorption is suggested as another reason for the band gap difference of S2.

For an indirect transition, the transition rate is expressed as follows [11]:

$$\alpha \propto |V^{\omega_k}|^2 |V^{\omega}|^2 \int_0^{\hbar\omega+\hbar\omega_k-E_G} \rho_v(E-\hbar\omega-\hbar\omega_k)\rho_c(E)dE \quad (1)$$

(The probability of the photon absorption ($|V^{\omega}|^2$) is nearly constant for the allowed transitions and α is the absorption coefficient.)

It indicates that the absorption coefficient for an indirect transition to energy E from an initial energy (see Eq. (1)) is proportional to the product of the initial density of states and the final density of states. When S3 absorbs a light having photon energy over the band gap, electrons in N 2p in the valence band are excited to Hf 5d related to Hf–N bonds in the conduction band. It is speculated that the increase of the absorption coefficient is low because the pDOS of Hf 5d and N 2p related to Hf–N bonds is small. When a photon with energy over 3.8 eV is absorbed, it is expected that the absorption coefficient increases abruptly because the pDOS of Hf 5d and N 2p related to Hf–N bonds is large.

To verify the effects of transition rates on the optical absorption, XANES for O and N K-edges were measured (Figure 7.1). The XANES spectra were measured using the 4B1 photoemission electron microscopy beam-line at the Pohang Accelerator Laboratory (PLS, Pohang, Korea) [12]. The absorption threshold (the inflection point) of O K-edge is constant regardless of film composition, even though the edge step decreased as the N/Hf ratio increased. For N K-edge, the absorption peak of S2 was formed at 399.4 eV, and the absorption peak was broadened and the absorption was formed at 395.0 eV.

The XANES spectra for N K-edge of S2 and S3 was compared with the calculated N K-edge of $Hf_4O_5N_2$ (CN: 6.25) for S2 and $Hf_4O_2N_4$ (CN: 5.5) for S3 (Figure 7.2). To calculate the N K-edge of Hf–O–N thin films, we used a program SCAT based on the discrete variational Xα (DV-Xα) method [13]. The nitrogen atom for the corresponding X-ray absorption is put at the center of the cluster models. Each cluster is embedded in point charges located at the external atomic sites so as to produce an effective Madelung potential. In the X-ray absorption process, an electron is promoted from a core level to an unoccupied state leaving a core hole. To reproduce the experimental spectrum, self-consistent calculation should be carried out including a core hole.

For N K-edge of S2 (Figure 7.2(a)) two absorption peaks were formed at the transition energy of 387.0 and 389.0 eV. They were related to the anti-bonding interaction of Hf 5d and N 2p. Considering the bond overlap population of Hf 5d and O 2p, the peak to the anti-bonding interaction of Hf 5d and O 2p is placed at

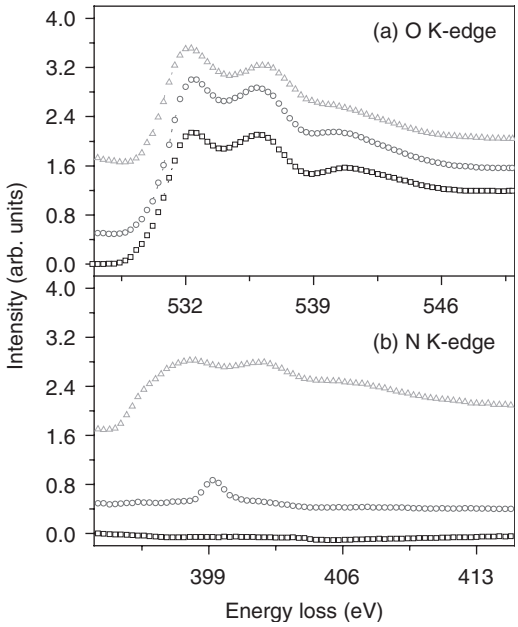

Figure 7.1 The XANES spectra for O K-edge (a) and N K-edge (b) of Hf–O–N thin films. (S1: square, S2: circle, and S3: triangle).

388.1 eV, which is higher than the transition energy (387.0 eV) of the peak to the anti-bonding interaction of Hf 5d and N 2p. Even though the difference between transition energies of two peaks is over 1.0 eV, the transition states are dependant on the O K-edge, because the intensity of K-edge is smaller than that of O K-edge. For N K-edge of S3 (Figure 7.2(b)), the first peak by the anti-bonding interaction of Hf 5d and N 2p was formed at the lower transition energy (385.0 eV) than the transition energy (387.5 eV) of the peak by the anti-bonding interaction of Hf 5d and O 2p. The difference between transition energies of two peaks is about the difference between the optical band gap of S1 and S3.

Using a four-phase model consisting of ambient/simple grade/film/substrate, we fit the data to obtain the dispersion of optical constants for each films in the range of 1.55–6.53 eV. The Cauchy model was used as a model for the substrate and fixed during the fitting. The Cody–Lorentz (CL) model [14] was used as a model for the film.

In the range of 1.55–6.35 eV, the absorption coefficient of S1 was represented by one CL model. Based on the assumptions that the Hf–N bonds and Hf–O bonds independently form the parabolic band structure, and that total absorption coefficient is the sum of the absorption coefficients related to the Hf–N bonds and the Hf–O bonds two CL models were used as models for S2 and S3 films. Due to the degradation of Hf–O–N thin films, the simple grade model was applied after the fitting of films.

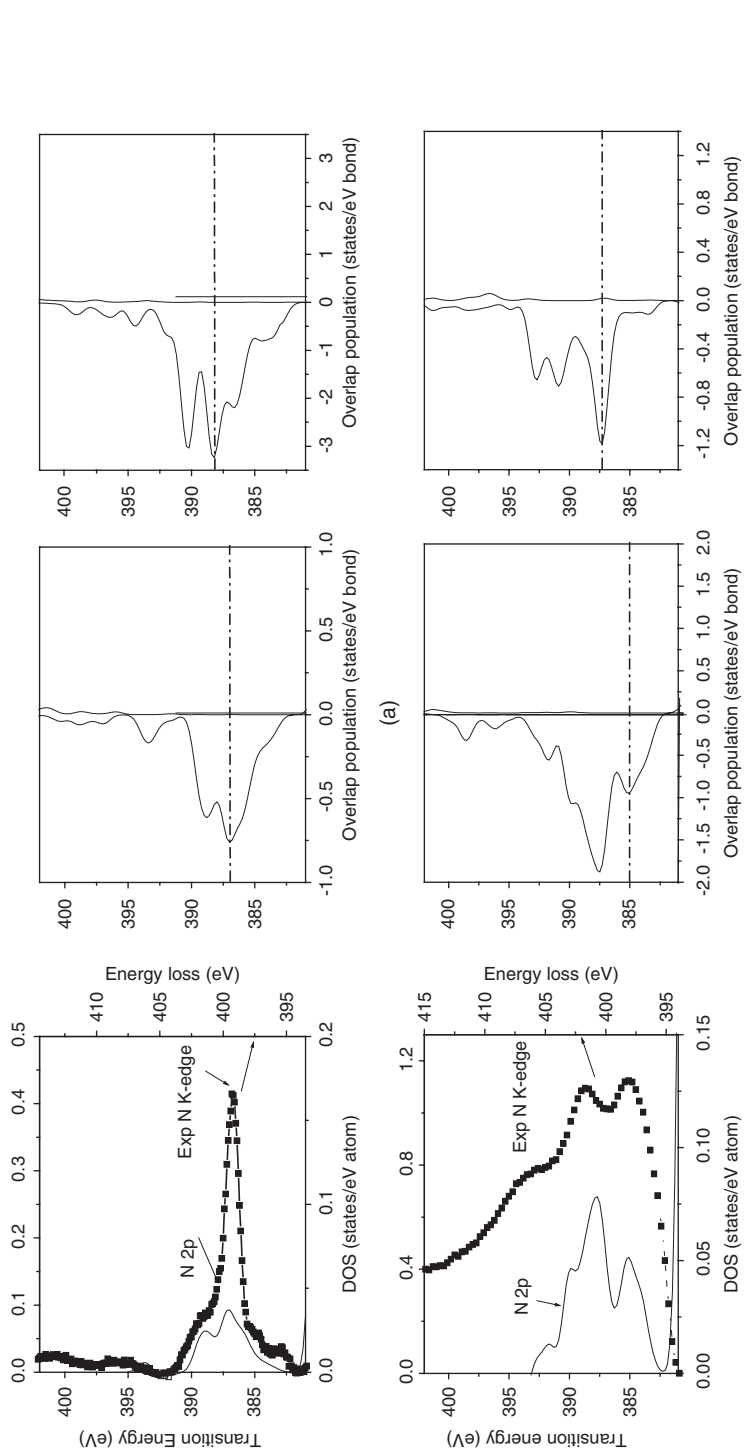

Figure 7.2 The comparison of experimental N K-edge and the calculated N K-edge PDOS (left), the bond overlap population (BOP) for Hf 5d–N 2p bonds (middle) and for Hf 5d–O 2p bonds (right) of S2 (a) and S3 (b).

Table 7.1 Compilation of the fitting results for Hf–O–N thin films using CL model with Urbach absorption

Hf–O–N thin films	Thickness (nm)	A_1/A_2	E_{g1}/E_{g2}	E_{01}/E_{02}	C_1/C_2	E_{p1}	E_{t1}	E_{u1}	MSE
S1	47.69±0.07	25.23	5.52	8.34	3.80	2.16	0.75	1.28	1.01
S3	51.93±0.08	13.66/2.50	2.51/5.75	6.22/6.63	2.28/0.85	4.38	1.73	1.30	1.57
S5	55.64±0.05	47.05/13.85	0.90/4.07	4.43/7.17	3.13/5.27	5.45	1.61	0.75	0.84

Note: A, E_g, E_0, C, E_p, E_t, and E_u have units of eV.

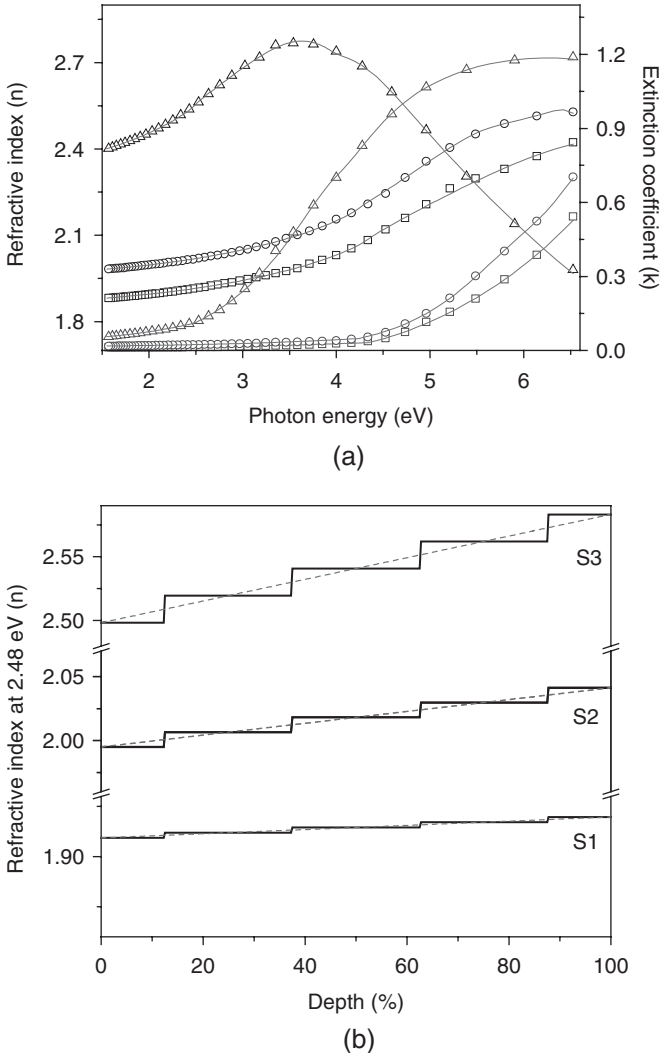

Figure 7.3 The $\langle n \rangle$ and $\langle k \rangle$ of pseudo optical constants obtained by the inversion technique (dot) and the best CL fitting (line) of Hf–O–N thin films (S1: square, S2: circle, and S3: triangle) (a) and the depth profile for the refractive index at 2.48 eV of Hf–O–N thin films (b).

With a four-phase model, the results are shown in Table 7.1 where the mean square error (MSE) represents the goodness-of-fit parameter. The uncertainties of the film thickness listed in Table 7.1 were obtained with a 90% confidence limit. To verify that the dispersion in the experimental spectral range (1.55–6.53 eV) is correct, we used the data inversion to obtain its pseudo-optical constants ($\langle n \rangle$ and $\langle k \rangle$). Theseconstants are calculated from the measured Ψ and Δ using the film thickness obtained from the fitting.

The dispersions of optical constants for Hf–O–N thin films are shown in Figure 7.3(a). Note that the optical constants of S1 and S2 are the normal dispersion in the experimental spectral range, and that the optical constants of S3 were the normal dispersion in the range of 1.55–3.70 eV and were the abnormal dispersion in the range over 3.70 eV. In the normal dispersion region, the refractive index of Hf–O–N thin films increased as the N/Hf ratio increased. However, the tendency of the refractive index was reversed from that at the intersecting point (5.2 and 5.5 eV). Figure 7.3(b) shows the depth profile of refractive index at 2.48 eV from the simple grade model of films. The refractive index at the film surface was lower than that at the interface between the film and the substrate. It was due to the surface degradation of Hf–O–N thin films by the oxygen in the air. The variations of the refractive index increased from 0.01 to 0.10 as the N/Hf ratio of Hf–O–N thin films increased. It indicates that surface degradation of S3 is more critical than that of S2 and S1 are.

4. CONCLUSION

Using the suggested local structures of HfO_2 (CN: 7.0), $Hf_4O_5N_2$ (CN: 6.25), and $Hf_4O_2N_4$ (CN: 5.5) in the previous research, we analyzed the effects of composition on the XANES spectra for O and N K-edges of Hf–O–N thin films. From the results of the XANES spectra, the transition rate for the direct transition was suggested as one of the reasons of the difference between the optical band gap and the simulated band gap of S3. The dispersion of optical constants for Hf–O–N thin films was analyzed using a four-phase model of ambient/graded/film/substrate for SE analysis. Two CL models were applied for the SE analysis of films based on the XANES spectra. As the N/Hf ratio increased, the refractive index in the normal dispersion region increased, and the tendency of the refractive index was reversed in the abnormal dispersion region. From the depth profile of refractive index in the simple grade model of films, the effects of the surface degradation on the optical constants were analyzed.

ACKNOWLEDGMENTS

The experiments at the Pohang Accelerator Laboratory were supported in part by MOST and Pohang Iron and Steel (POSCO). Special thank to Isao Tanaka for supporting the *ab initio* total-energy and molecular dynamics program VASP (Vienna *ab initio* simulation package).

REFERENCES

[1] T. Watanabe, M. Takayanagi, K. Kojima, et al., *IEDM Tech. Dig.* (2004) 507–510.
[2] Chao-Ching Cheng, Chao-Hsin Chien, Ching-Wei Chen, et al., *Microelectron. Eng.* **80** (2005) 30–33.
[3] D. Gui, Jinfeng Kang, Hongyu Yu, et al., *Appl. Surf. Sci.* **231–232** (2004) 590–593.
[4] S.K. Kim, M.A. Kang, J.M. Sohn, et al., *Opt. Mater.* **22** (2003) 361–377.
[5] S.K. Kim, Y. Kim and K. No, *X-Ray Spectrom.* **35** (2006) 287–295.
[6] J. Tacu, R. Grigorovici and A. Vancym, *Phys. Status Solidi* **15** (1996) 527.
[7] S. Venkataraj, D. Severin, S.H. Mohanmed, et al., *Thin Solid Films* **502** (2006) 228–234.
[8] Y. Wang and J.P. Perdew, *Phys. Rev. B* **44** (1991) 928.
[9] G. Kresse and J. Furthmüller, *Comput. Mater. Sci.* **6** (1996) 15.
[10] David Vanderbilt, *Phys. Rev. B* **41** (1990) 7892.
[11] F. Wooten, *Optical Properties of Solids*, Academic Press, Inc., New York, 1972, Chapter 5.
[12] Tai-Hee Kang, Ki-jeong Kim, C.C. Hwang, et al., *Nucl. Instrum. Methods Phys. Res., Sect. A* **467** (2001) 581.
[13] H. Adachi, *J. Phys. Soc. Japan* **45** (1978) 875.
[14] A.S. Ferlauto, G.M. Ferreira, J.M. Pearce, et al., *J. Appl. Phys.* **92** (2002) 2424.

CHAPTER 8

Atomic and Electronic Structures of Boron Clusters in Crystalline Silicon: The Case of $X@B_6$ and $X@B_{12}$, X=H–Br

Yoshitsune Higashiguchi, Hiroaki Ochiai, Kazuyuki Igei, Kengo Ohmori and **Yoshinori Hayafuji**

Contents

Abstract

Ultra-shallow junction formation in metal oxide semiconductor field effect transistor (MOSFET) fabrication has been one of the most controversial parts of the silicon process technology. In the present work, *ab initio* calculations of the atomic and electronic structures of crystalline silicon (c-Si) with $X@B_6$ and $X@B_{12}$ (X=H–Br) clusters have been performed to investigate carrier generation by doping atoms inside the cage of the boron clusters as a novel type dopants for shallow junction formation. We confirmed that octahedral B_6, cubo-octahedral B_{12} (B_{12}-co), and icosahedral B_{12} (B_{12}-ico) clusters can exist stably in c-Si and should act as double acceptors. We also found that H atoms can be settled in B_{12}-co cluster and the $H@B_{12}$-co cluster can introduce a very shallow single acceptor level whose activation energy is lower than those of B_6, B_{12} (-co, -ico), and substitutional boron atom (B_s). The structural stability of the clusters was discussed from the viewpoint of the covalency between atom X and surrounding boron atoms using the bond overlap population and of the charge distribution, and we found that, in c-Si,

Graduate School of Science and Technology, Kwansei Gakuin University, 2-1 Gakuen, Sanda, Hyogo 669-1337, Japan
Corresponding author. E-mail: hayafuji@ksc.kwansei.ac.jp

Advances in Quantum Chemistry, Vol. 54
ISSN 0065-3276, DOI 10.1016/S0065-3276(07)00008-1

the three-center bonding is not enough to account for their stability of the boron clusters. Among 96 trial models, $H@B_{12}$-co cluster is the most promising candidate as the cluster dopant for the formation of a high-performance, ultra-shallow junction.

1. INTRODUCTION

Ion implantation of boron atoms has been widely used in forming the extension region of source/drain of the field effect transistor (FET) in ultra large scaled integrated circuit (ULSI) technology. Conventionally, post-thermal annealing is required to achieve the electrical activation of implanted atoms and repair the implantation damages. However, as the size of the LSI devices are becoming smaller, the junction depth is required to be even shallower, and thermal diffusion of the implants caused by post-annealing has become more serious problem. In addition, the reduction of the concentration of the carrier at critical region of the metal oxide semiconductor field effect transistor (MOSFET) is also a crucial issue for the fabrication of shallow junctions. Thus, an ultra-shallow junction with a high-carrier-concentration layer is essential for future ULSI technology.

In 1993, a fascinating experimental result was reported by Mizushima et al. [1] that icosahedral B_{12} (B_{12}-ico) clusters should exist and acted as double acceptors to form the low-resistivity region in c-Si upon high-dose ion implantation of boron ($>1\times10^{16}$ atoms/cm^2) without any post-annealing. After that, some theoretical investigations were performed for the boron cluster in that curious phenomenon. Yamauchi et al. [2] showed that the B_{12}-ico cluster was energetically more stable than cubo-octahedral B_{12} (B_{12}-co) cluster on the basis of *ab initio* calculations of the total energy. Meanwhile, Okamoto et al. [3] concluded that the B_{12}-co cluster was more suitable in the silicon crystalline lattice because of its symmetry adaptation. Recently, Ohmori et al. [4] proposed an interesting model for cluster formation, which stated that in the relatively low-dose region ($1–3\times10^{16}$ atoms/cm^2), octahedral B_6 clusters were generated and acted as double acceptors, while in the higher-dose region ($>3\times10^{16}$ atoms/cm^2), this function was fulfilled by B_{12}-co clusters instead. In any case, boron clusters that can produce high-carrier-concentration layers without any post-annealing are sure to contribute to the advancement of silicon ULSI technology.

The above-mentioned three clusters, B_6, B_{12}-co, and B_{12}-ico in Figure 8.1, have a hollow at the center of the cluster cages, which can be occupied by another atom. Fujimori and Kimura [5] reported that the B_{12}-ico cluster with an additional B atom in its hollow site showed metallic bonding, instead of covalent bonding like the original B_{12}-ico. In addition, recently the electronic structure of $A@B_{12}$-ico (A=H–He) clusters was studied by Hayami [6]. Boron clusters have been studied extensively as components of new materials. However, these studies have all focused on bare clusters, i.e., there is no reports on the electronic structure of boron clusters in c-Si with another element inside its hollows.

Thus, we investigated the atomic and electronic structures of $X@B_6$ and $X@B_{12}$ (-co, -ico) (X=H–Br) clusters in c-Si using *ab initio* calculations in order to find a

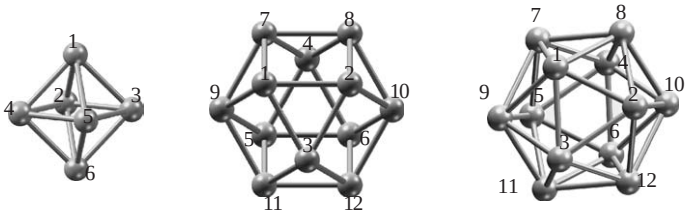

(a) B_6 (b) B_{12}-co (c) B_{12}-ico

Figure 8.1 Ideal structures of the boron clusters investigated in this study. The boron atoms in the clusters are marked by sequential numbers. (b) and (c) are viewed along the [111] direction of the cluster.

"cluster dopant" that can contribute to the formation of ultra-shallow junctions with a high-carrier-concentration layer.

2. COMPUTATIONAL METHOD

In the present calculation, we used two *ab initio* methods to investigate structural stability and the potential for carrier generation of $X@B_6$ and $X@B_{12}$ clusters in c-Si. Here X is from H to Br in the periodic table. The following two methodsused were: (i) plane wave ultrasoft pseudopotential method for the optimization of atomic structures and (ii) discrete variational-Xα (DV-Xα) molecular orbital method for the analysis of the fine electronic structures and activation energies of the clusters.

To optimize the structure and evaluate the formation energy, we have employed the Vienna *ab initio* simulation package (VASP) code [7], which implements the density functional theory with the Vanderbilt ultrasoft pseudopotential [8] and the generalized gradient approximation (GGA) [9] for the exchange correlation energy. The cutoff energy for the wave functions is 260 eV except for the four clusters (X=C, N, O, and F) whose default values given by VASP are higher than 260 eV. We adopted the default for these clusters. With a high implantation dose of up to 1×10^{17} atoms/cm^2, the concentration of implanted boron atoms in c-Si surpasses 1×10^{21} cm^{-3}. In order to model such a high-concentration system, we used the 64-silicon-atom simple cubic supercell whose experimentally determined lattice constant was 5.4308 Å, and introduced the $X@B_6$ and $X@B_{12}$ clusters into the divacancy site and the tetrahedral vacancy site, respectively. The Brillion zone sampling was performed using special *k*-points, generated by the Monkhorst–Pack scheme [10] with the parameters $4 \times 4 \times 4$. Structural optimizations were performed using the conjugate gradient method [11], with a convergence criterion of 0.01 eV/Å for the magnitude of the calculated Hellmann–Feynman forces on each atom. No atoms were fixed during structure optimization. A convergence criterion of 10^{-5} eV was used for the total energy at each step in the electronic iteration.

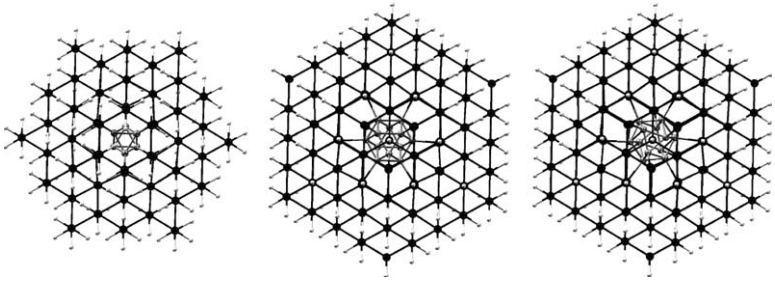

(a) $B_6Si_{108}H_{114}$ (b) B_{12}-co$Si_{160}H_{100}$ (c) B_{12}-ico$Si_{160}H_{100}$

Figure 8.2 Some model clusters used in the DV-Xα molecular orbital method. The effect of the structural optimization is taken into account. Gray atoms represent B, while the black and white ones are Si and H atoms, respectively. These arrangements are viewed along the [111] direction of the cluster.

To obtain the fine electronic structure, we carried out the first-principle DV-Xα molecular orbital method [12] with a linear combination of atomic orbitals expansion of molecular orbitals. After atomic optimization using VASP, we cut out the boron clusters and their first and second neighboring silicon atoms of supercells then embedded them in silicon-based model clusters. We used a $Si_{110}H_{114}$-based model cluster for B_6 and X@B_6 clusters and $Si_{165}H_{100}$ for B_{12} (-co, -ico) and X@B_{12} (-co, -ico). Figure 8.2 shows the model clusters with the optimized B_6, B_{12} (-co, -ico), and their neighboring silicon atoms. These model clusters are all based on the perfect silicon crystal, and hydrogen atoms were used as terminators of the dangling bonds on the Si surface.

3. RESULTS AND DISCUSSION

3.1 Structural stability

3.1.1 B_6, B_{12}-co, and B_{12}-ico clusters

We performed structural optimization using ideal B_6, B_{12}-co, and B_{12}-ico clusters (shown in Figure 8.1) with a 64-silicon-atom supercell. Table 8.1 shows the interatomic distances of these clusters and nearest-neighbor distances between boron and silicon atoms. The B_6 cluster kept its octahedral symmetry during optimization, and the structure of the B_{12}-co cluster was not altered appreciably; its symmetry was lowered from O_h to T_d following that of the bulk. In contrast, the B_{12}-ico cluster underwent distortion and its symmetry was reduced drastically from I_h to C_3.

We calculated the total energy of the optimized supercells with these clusters. We also obtained the total energy of the substitutional boron atom using the same supercell in order to evaluate the gain in total energy by the clustering of boron atoms. We defined the energy gain per boron atom ($\Delta E_{B_6}, \Delta E_{B_{12}}$) as

$$\Delta E_{B_6} = \frac{1}{6}\left\{(E_{B_6} + 5E_{Si_{64}}) - \left(6E_{B_s} + \frac{4}{64}E_{Si_{64}}\right)\right\}, \quad (1)$$

Table 8.1 Interatomic (B–B) and nearest-neighbor (B–Si) distances of the ideal and optimized structures of the B_6, B_{12}-co, and B_{12}-ico clusters

	Ideal structure (Å)		Optimized structure (Å)	
B_6	B–B	1.693	B–B	1.698
	B–Si	1.774	B–Si	1.925
B_{12}-co	B–B	1.751	B–B (Δ 1-2-3, 4-7-8, 5-9-11, 6-10-12)	1.731
			B–B (Δ 1-7-9, 2-8-10, 3-11-12, 4-5-6)	1.788
	B–Si	2.089	B–Si	2.028
B_{12}-ico	B–B	1.810	B–B (Δ 1-7-9, 2-8-10, 3-11-12, 4-5-6)	1.742
			B–B (Δ 1-2-3, 4-7-8, 6-10-12, 5-9-11)	1.799
			B–B (Δ 1-8, 2-12, 3-9, 4-10, 5-7, 6-11)	1.930
	B–Si	2.020	B–Si	2.073

$$\Delta E_{B_{12}} = \frac{1}{12}\left\{(E_{B_{12}} + 11E_{Si_{64}}) - \left(12E_{B_s} + \frac{7}{64}E_{Si_{64}}\right)\right\}, \quad (2)$$

where E_{B_6}, $E_{B_{12}}$, and E_{B_s} are the total energies of the supercells containing a B_6 or B_{12} (-co, -ico) cluster and substitutional boron atom, respectively, and $E_{Si_{64}}$ the total energy of the perfect 64-silicon-atom supercell. The last terms, $4/64E_{Si_{64}}$ and $7/64E_{Si_{64}}$, in Eqs. (1) and (2) are introduced to keep the number of Si atoms the same between the initial and final states. The calculated results of the energy gains are shown in Figure 8.3. As shown in this figure, the B_6, B_{12}-co, and B_{12}-ico clusters are energetically more favorable structures than substitution structure for the boron atom in crystalline silicon. These results indicate that boron atoms have a natural tendency to form B_6, B_{12}-co, and B_{12}-ico clusters in sufficiently high density in c-Si. With respect to the total energy of the supercell, the B_{12}-ico cluster is more stable than B_{12}-co. The energy difference between these supercells is 0.980 eV, however, the difference in the energy gain associated with the formation of a cluster between the two configurations is only 0.080 eV per boron atom. Thus, it is completely natural that B_{12}-co and B_{12}-ico clusters are simultaneously formed in c-Si by high-dose ion implantation of boron atoms.

3.1.2 X@B_6, X@B_{12}-co, and X@B_{12}-ico clusters

Structural stability of 26 models were investigated for X-doped clusters of X@B_6, X@B_{12}-co, and X@B_{12}-ico based on each of the optimized supercells with nondoped clusters, namely B_6, B_{12}-co, and B_{12}-ico. We introduced the atom X (X=H–Br) into the center of the optimized nondoped cluster, and optimized the atomic structure again, then we estimated the formation energy (E_f) of the X-doped clusters defined as:

$$E_f = E_{X-doped} - (E_{nondoped} + E_X), \quad (3)$$

where $E_{X-doped}$ is the total energy of the supercells containing X-doped clusters, and $E_{nondoped}$ is that of the supercell with a nondoped cluster, which is equal to E_{B_6} or $E_{B_{12}}$ in Eqs. (1) or (2), and E_X is that of the isolated atom X. To calculate E_X,

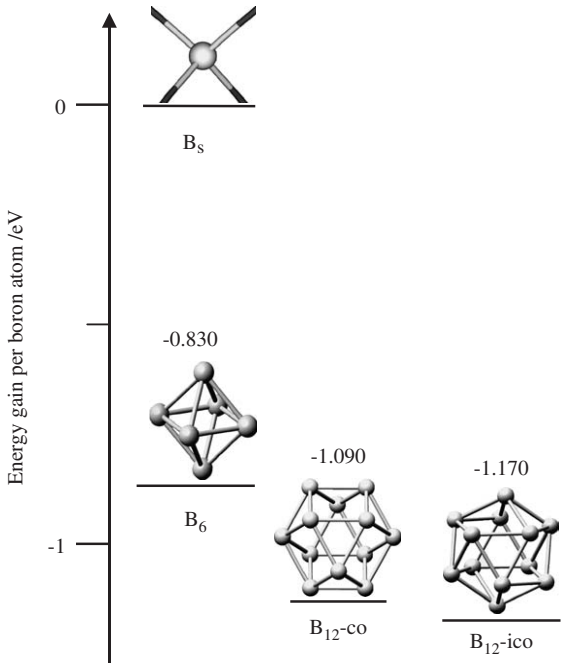

Figure 8.3 Gains in total energy per boron atom. B_s represents the substitutional boron atom model with structural optimization.

we used a simple cubic supercell with lattice parameter α=30.0 Å containing only an atom X in the center of the supercell. Figure 8.4 shows the calculated formation energies of all models except the collapsed models. In the case of the X@B_6 models, because of the limited space of the hollow of the B_6 cluster, all X-doped clusters except for H@B_6 were collapsed or deformed and lost their original octahedral structure. The B@B_6 cluster was the only one that showed a gain in total energy of the system (E_f=−0.908 eV), however, the B@B_6 cluster did not have an octahedral B_6 cage, either. Representative structures of the energetically stable X-doped clusters in c-Si are shown in Figure 8.5, and the corresponding interatomic distances and formation energies are listed in Table 8.2. In the X@B_{12}-co models, almost none of the X-doped clusters collapsed; the five elements H, Be, B, Cr, and Mn that settled in the center of the cage enhanced the stability of the clusters. On the other hand, in the X@B_{12}-ico models, half of the models collapsed and six X-doped clusters, viz. Be@, V@, Cr@, Mn@, Fe@, and Co@B_{12}-ico, stabilized the system with distortion. Twelve X@B_{12}-ico clusters (X=Li, Be, B, Na, Mg, Al, K, Ca, Ni, Cu, Zn, and Se) were transformed into the same cubo-octahedral structure as the X@B_{12}-co clusters; we represent these clusters without original symmetry symbols, such as Li@B_{12}, Be@B_{12}, and so on. We found that there were two types of the stable structure: strained co-type and strained ico-type, and that the strained ico-type clusters with some transition elements viz. V, Cr, Mn, Fe, and Co showed remarkable stability.

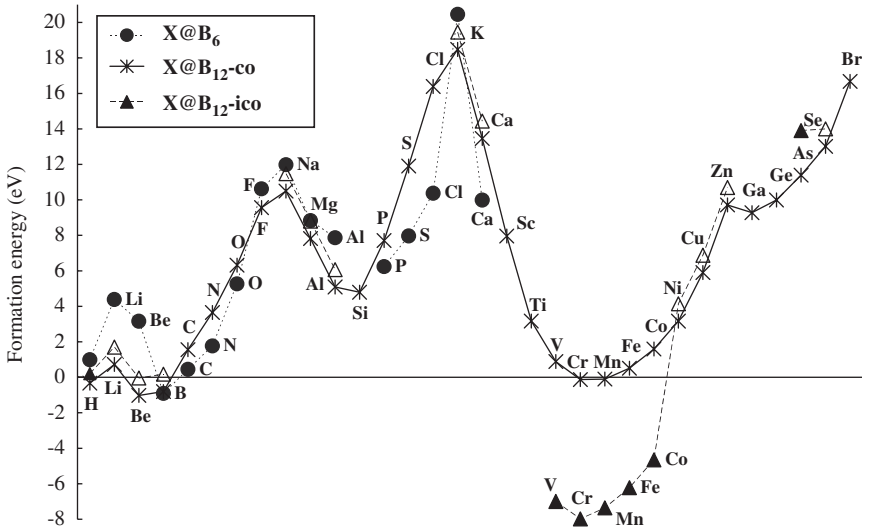

Figure 8.4 Calculated formation energies (E_f) of X-doped boron clusters. E_f is defined as $E_f = E_{X-doped} - (E_{nondoped} + E_X)$, where $E_{X-doped}$ is the total energy of the supercell with X-doped boron clusters and $E_{nondoped}$ is that of the undoped supercell. E_X is the total energy of the isolated atom X. Closed circle represents the value of the $X@B_6$ models and those of $X@B_{12}$-co and $X@B_{12}$-ico are denoted by an asterisk and triangle, respectively. Open triangle indicates the model having the same structure as the $X@B_{12}$-co model, and the common final structure is cubo-octahedral.

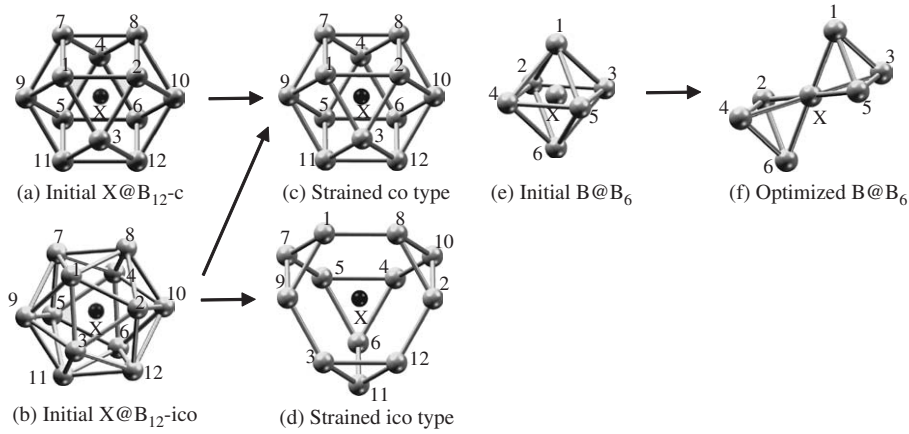

Figure 8.5 Representative structures of the $X@B_{12}$ (-co, -ico) clusters, and the structures of $B@B_6$ clusters. The initial and optimized structures are depicted. The number markings added to boron atoms are consistent before and after optimization. The H@, Cr@, and $Mn@B_{12}$-co clusters and the Be@ and $B@B_{12}$ clusters form structure (c). Meanwhile, the V@, Cr@, Mn@, Fe@, and $Co@B_{12}$-ico clusters have structure (d). The $B@B_6$ cluster undergoes great distortion and gains total energy. The optimized $B@B_6$ cluster should be called a B_7 cluster without the octahedral structure. The arrow represents the transformation of the cluster structure.

Table 8.2 Interatomic distances and formation energies of the energetically stable X@B_{12}-co and X@B_{12}-ico clusters with optimization

		Interatomic distance (Å)		E_f (eV)
		B–B (Δ1-2-3, 4-7-8, 5-9-11, 6-10-12)	B–B (Δ1-7-9, 2-8-10, 3-11-12, 4-5-6)	
(a)	B_{12}-co	1.731	1.788	0.000
(c)	H@B_{12}-co	1.756	1.815	−0.324
	Be@B_{12}	1.800	1.888	−1.023 (-co) −0.042 (-ico)
	B@B_{12}	1.791	1.870	−0.807 (-co)
	Cr@B_{12}-co	1.797	2.212	−0.123
	Mn@B_{12}-co	1.787	2.186	−0.098
		B–B (Δ1-7-9, 2-8-11, 3-10-12, 4-5-6)	B–B (1-8, 2-12, 3-9, 4-11, 5-7, 6-10)	
(b)	B_{12}-ico	1.742	1.930	0.000
(d)	V@B_{12}-ico	1.843–1.844	1.781	−6.997
	Cr@B_{12}-ico	1.822	1.760	−7.983
	Mn@B_{12}-ico	1.802	1.761	−7.358
	Fe@B_{12}-ico	1.786	1.771–1.772	−6.222
	Co@B_{12}-ico	1.778–1.780	1.782–1.784	−4.654

Note: The representation (a)–(d) in this table has the same meaning as in Figure 8.5.

3.2 Electronic structures

In this section, we discuss the electronic structures of the energetically stable clusters investigated in the previous section. First, we evaluate the energy diagrams and determine the activation energy for carrier generation. Second, we consider the source of the structural stability from the viewpoint of the chemical bonding and of the charge distribution in the clusters.

3.2.1 Energy diagrams

Figure 8.6 shows diagrams of the energy levels obtained for the optimized $B_6Si_{108}H_{114}$ and B@$B_6Si_{108}H_{114}$ model clusters and $Si_{110}H_{114}$ base model cluster as reference using the DV-Xα method. The band gap energies are 2.763, 2.936, and 2.793 eV for $Si_{110}H_{114}$, $B_6Si_{108}H_{114}$, and B@$B_6Si_{108}H_{114}$, respectively. These values are slightly larger than that of crystalline silicon because of the limited size of the model cluster. The $B_6Si_{108}H_{114}$ has a double acceptor level with activation energy of 0.254 eV above the top of the valence band. Assuming that the calculated band gap energy is equal to the experimental value of c-Si, i.e., 1.120 eV, activation energy for carrier generation of B_6 is 0.097 eV. The value obtained is relatively high as the dopant for c-Si. However, considering the electron-withdrawing

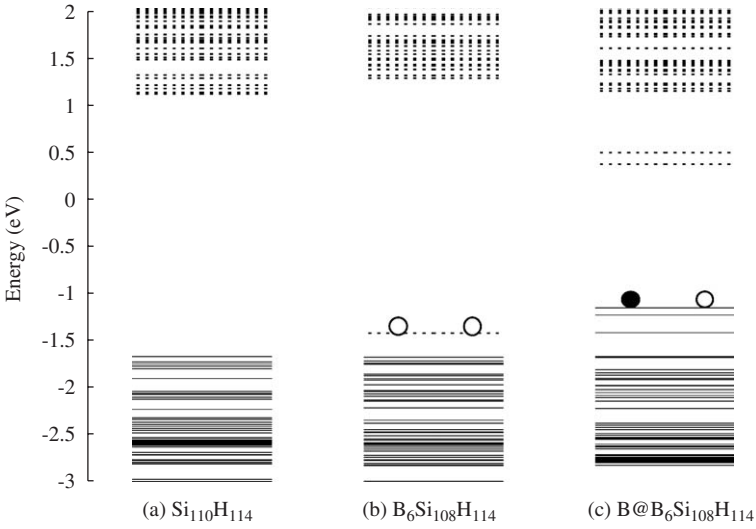

Figure 8.6 Calculated energy diagrams for the $Si_{110}H_{114}$, $B_6Si_{108}H_{114}$, and $B@B_6Si_{108}H_{114}$ model clusters with optimization. Unoccupied levels are denoted by broken lines and occupied levels are denoted by solid lines. Open and filled circles are unoccupied and occupied states, respectively. The $B_6Si_{108}H_{114}$ has a double acceptor level located immediately above the top of the valence band. $B@B_6Si_{108}H_{114}$ has many mid-gap levels localized to the $B@B_6$ cluster and may act as recombination centers.

character of the octahedral B_6 cluster caused by its three-center bonding [13], it is conceivable that the B_6 cluster can generate holes and play a role in the formation of the low-resistivity layers in the relatively low-dose region, as reported by Ohmori et al [4]. In contrast, $B@B_6Si_{108}H_{114}$ has many mid-gap levels that are localized to the $B@B_6$ cluster and may act as recombination centers, and work as carrier inhibitors, reducing the conductivity.

Figures 8.7 and 8.8 are calculated energy diagrams for the $X@B_{12}$ (-co, -ico) based on $Si_{165}H_{100}$ model clusters with optimization. The diagrams of $Si_{165}H_{100}$ and optimized $B_sSi_{164}H_{100}$ model clusters are also shown in Figure 8.7 as reference. It is confirmed that B_{12}-co and B_{12}-ico clusters have shallow double acceptor levels as reported in Refs. [1,2,4]. In addition, we found that $H@B_{12}$-co has an extremely shallow single acceptor level. The activation energy of the B_{12}-co, B_{12}-ico, and $H@B_{12}$-co clusters are 0.034, 0.066, and 0.029 eV, respectively, if we assume that the calculated energy of the substitutional boron atom is equal to the experimental value of 0.045 eV. The $H@B_{12}$-co cluster has an even shallower acceptor level than that of B_{12}-co, which in turn is shallower than that of substitutional boron. The B_{12}-ico cluster has higher activation energy (0.066 eV) for carrier generation than substitutional boron atom. These data imply that it is difficult to achieve a low resistivity using only the B_{12}-ico cluster, but possible using the B_{12}-co or $H@B_{12}$-co clusters alone, and assure the formation of the B_{12}-co cluster by high-dose ion implantation. Other X-doped clusters have

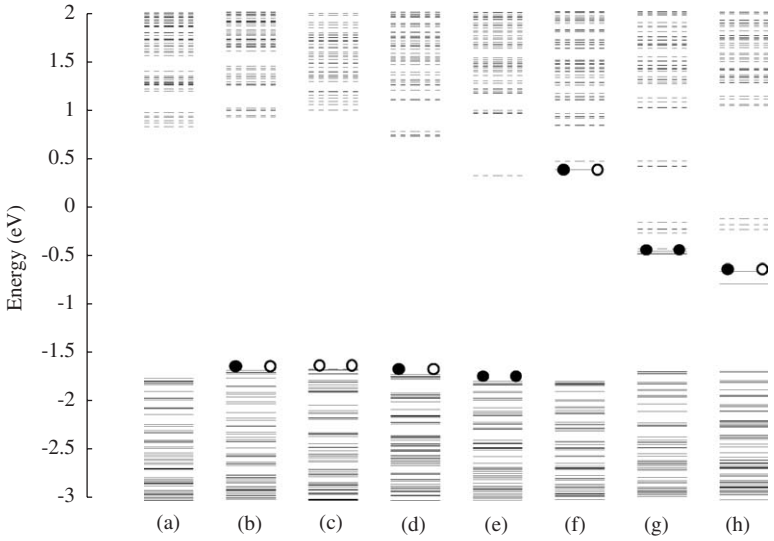

Figure 8.7 Calculated energy diagrams for (a) $Si_{165}H_{100}$, (b) $B_sSi_{164}H_{100}$, (c) B_{12}-co$Si_{160}H_{100}$, (d) H@, (e) Be@, (f) B@, (g) Cr@, and (h) Mn@B_{12}-co$Si_{160}H_{100}$ model clusters with optimization. The symbols and notations are the same as in Figure 6. From diagrams (c) and (d), B_{12}-co has a double acceptor level and H@B_{12} has a single acceptor level lying slightly above the top of the valence band. Diagrams (f–h) have many mid-gap levels that localize to X@B_{12}-co clusters.

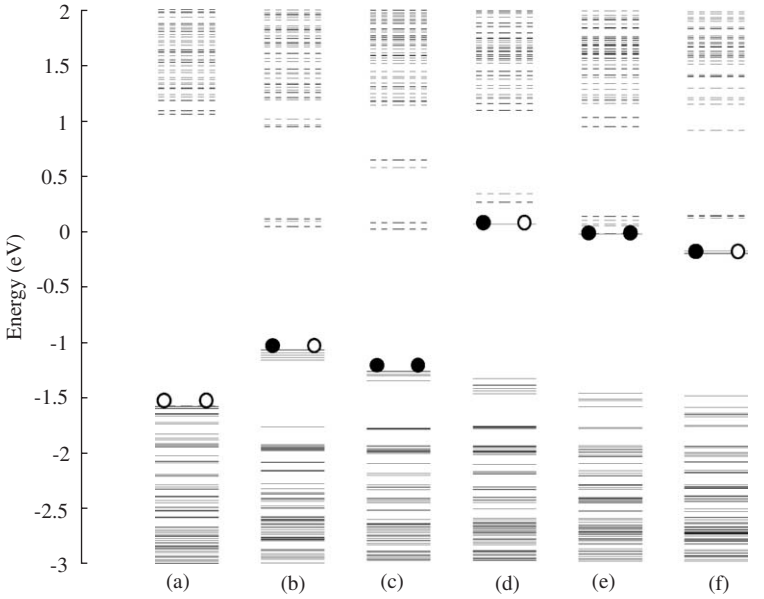

Figure 8.8 Calculated energy diagrams for (a) B_{12}-ico$Si_{160}H_{100}$, (b) V@, (c) Cr@, (d) Mn@, (e) Fe@, and (f) Co@B_{12}-ico$Si_{160}H_{100}$ model clusters with optimization. The symbols and notations are the same as in Figure 6. B_{12}-ico has a double acceptor level lying above the top of the valence band. Diagrams (b–f) have many mid-gap levels that localize to X@B_{12}-ico clusters.

neither shallow acceptor levels nor shallow donor levels and introduce many mid-gap levels that may be recombination centers for carriers. Hence, among the 78 kinds of X-doped clusters, only $H@B_{12}$-co has both the energetic stability and the electronic advantage, and can be the cluster dopant for high-concentration carrier generation.

3.2.2 Chemical features of the bonding

In order to analyze the chemical features of the interatomic bonding of the $X@B_{12}$-co clusters, we evaluate the bond overlap population (BOP) [12]. The BOP is based on Mulliken population analysis and is sometimes referred to as bond order. It can be used as a measure of the strength of covalent bonding, and its magnitude corresponds to the degree of covalency. Figure 8.9 displays the changes in the total BOP between the atom X and the surrounding boron atoms (X–B) and between boron atoms (B–B) of the $X@B_{12}$-co clusters. The BOP between boron atoms of the cluster cages change little through the whole clusters; by contrast, that between the atom X and the boron atoms shows the highly characteristic tendency that the position of local maxima corresponding to that of the local minima of the formation energy in Figure 8.4. This reveals that the degree of the covalency of bonding between the atom X and the surrounding boron atoms determines the stability of the cluster, and a stronger covalency leads to a more stable structure.

3.2.3 Charge distribution of the clusters

Figure 8.10 shows the iso-surfaces of electron densities (density level: $0.1/Å^3$) calculated for B_{12}-co, B_{12}-ico, $H@B_{12}$-co, and $B@B_{12}$ clusters with their nearest-neighbor silicon atoms. As we illustrated in Figure 8.10(a) and (c), both B_{12}-co and B_{12}-ico clusters have triangles of their cluster cages that form the three-center

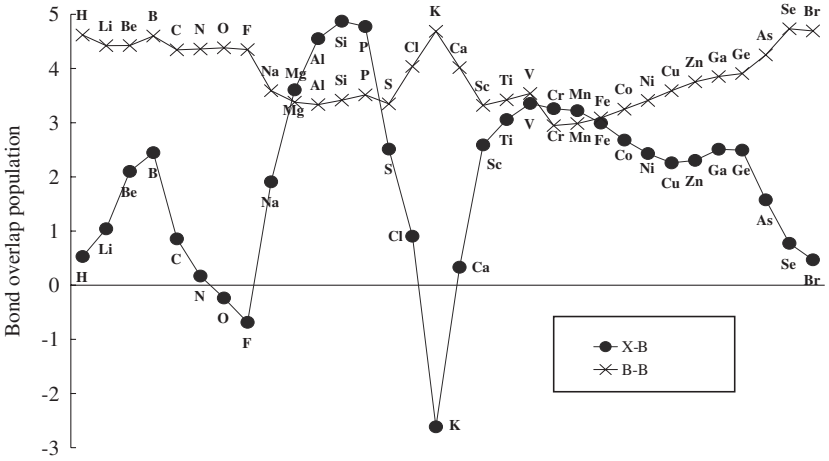

Figure 8.9 Bond overlap populations for $X@B_{12}$-co clusters. The filled circle denotes the value between the atom X and surrounding boron atoms and × -mark indicates that between boron atoms of the cluster cage.

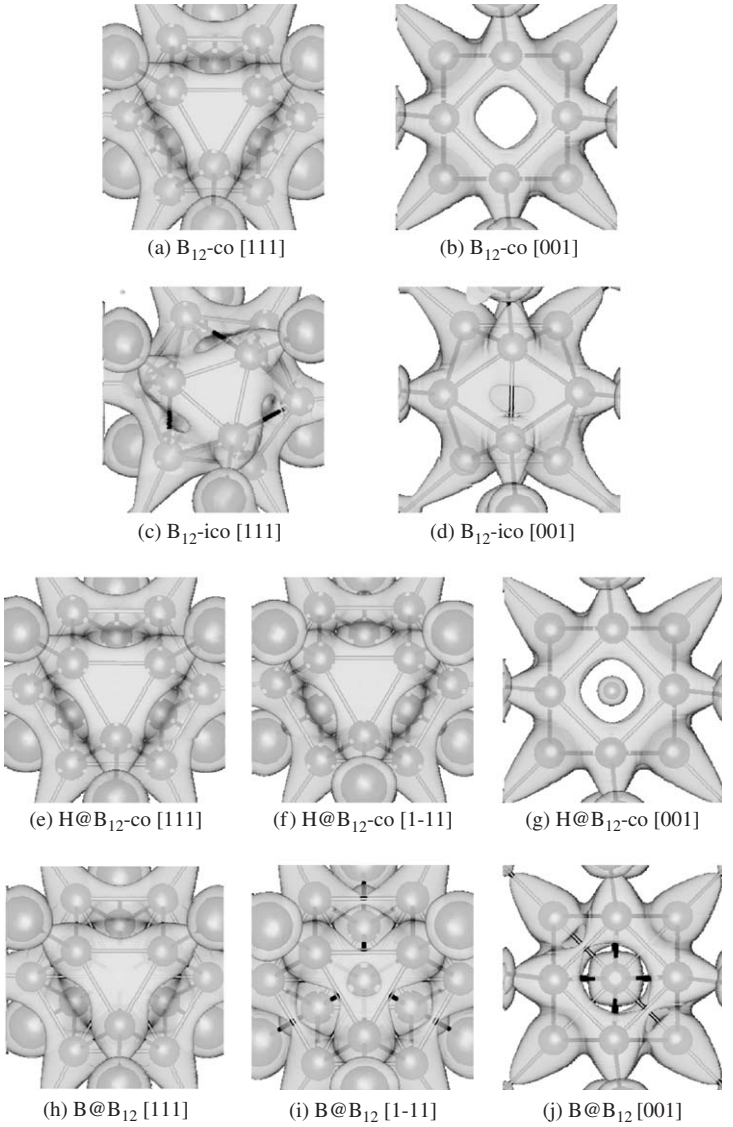

Figure 8.10 Iso-surfaces of electron densities (density level: 0.1/Å^3) calculated for (a, b) B_{12}-co, (c, d) B_{12}-ico, (e, f, g) H@B_{12}-co, and (h, i, j) B@B_{12} clusters with their nearest-neighbor silicon atoms. (a, c, e, and h) are viewed along the [111], (b, d, g, and j) are along the [0 0 1], and (f) and (i) are along the [1 –11] direction of the cluster. For a colour version of this figure please see the colour plate section near the end of this book.

bonding which contribute the structural stability and define the electron affinity of the clusters. The B_{12}-co cluster has also some squares of the cluster cage, and, as shown in Figure 8.10(b), the charge density around the center of the square is lower than that at the edge. While the B_{12}-co cluster had uniform charge

distribution around the center of all triangles and form three-center bonding, some triangles of the B_{12}-ico cluster showed high and nonuniform charge density as illustrated in Figure 8.10(d). Some previous reports [1,2] described that the stability of the cluster came from the number of the triangles, or three-center bonding. The B_{12}-co cluster consists of 8 triangles and 6 squares whereas the B_{12}-ico cluster consists of 20 triangles, and the number of triangles of the B_{12}-ico cluster is more than that of the B_{12}-co cluster. However, from comparison of the charge distribution of the two clusters, it was found that not all triangles form three-center bonding and they have the same number of three-center bonding, thus, we cannot determine the stability of these clusters only from the number of the triangles of them. Therefore, the superiority in structural instability of the B_{12}-ico cluster than B_{12}-co cluster is due not to just the number of triangles with three-center bonding but to high charge density at the rest of triangles without it.

In contrast with the H@B_{12} cluster that has almost the same tendency of the charge distribution as the B_{12}-co cluster, the B@B_{12} cluster showed the anisotropic aspect in the distribution at the triangles of the cage: half of the triangles have lower electron densities than that of the others as shown in Figure 8.10(h) and (i). The structural stability of the B@B_{12} cluster came from the covalent bond between the center B atom and the surrounding boron atoms discussed in previous section, and we can make sure that from the result that the relatively spreading charge density around the center B atom illustrated in Figure 8.10(j). Therefore, regardless of the presence of the dopant atom inside the cluster, the three-center bonding is not enough in discussion about the stability of the boron clusters in crystalline silicon, and it is necessary to consider the effect of other factors, such as the covalency or the charge distribution of non-three-center bonding.

4. CONCLUSION

We have investigated the atomic and electronic structures of boron clusters with an atom X (X=H–Br) incorporated in their hollows in c-Si using *ab initio* calculations. We confirmed that octahedral B_6, B_{12}-co, and B_{12}-ico were energetically favorable clusters and act as double acceptors. It was found that the H@B_{12}-co cluster could be formed and introduce an extremely shallow acceptor level. The structural stability of the clusters was discussed from the viewpoint of the covalency between atom X and surrounding boron atoms using BOP and of the charge distribution around the clusters. We also found that, in c-Si, it is not enough by three-center bonding to account for their stability of the boron clusters. Thus, we conclude that, from the standpoint of the structural and the electronic advantages, the H@B_{12}-co cluster is one of the most promising candidates as a cluster dopant for the formation of a high-performance ultra-shallow junction.

REFERENCES

[1] I. Mizushima, M. Watanabe, A. Murakoshi, M. Hotta, M. Kashiwagi, M. Yoshiki, *Appl. Phys. Lett.* **63** (1993) 373;
I. Mizushima, A. Murakoshi, M. Watanabe, M. Yoshiki1, M. Hotta, M. Kashiwagi, *Jpn. J. Appl. Phys.* **33** (1994) 404.
[2] J. Yamauchi, N. Aoki, I. Mizushima, *Phys. Rev. B* **55** (1997) R10245.
[3] M. Okamoto, K. Hashimoto, K. Takayanagi, *Appl. Phys. Lett.* **70** (1997) 978.
[4] K. Ohmori, N. Esashi, D. Sato, Y. Hayafuji, *Appl. Phys. Lett.* **87** (2005) 112101.
[5] M. Fujimori, K. Kimura, *J. Solid State Chem.* **133** (1997) 310.
[6] W. Hayami, *Phys. Rev. B* **60** (1999) 1523.
[7] G. Kresse, J. Furthmüller, *Comput. Mater. Sci.* **6** (1996) 15; G. Kresse, J. Furthmüller, *Phys. Rev. B* **54** (1996) 11169.
[8] D. Vanderbilt, *Phys. Rev. B* **41** (1990) 7892.
[9] J.P. Perdew, *Phys. Rev. B* **46** (1992) 6671.
[10] H.J. Monkhorst, J.D. Pack, *Phys. Rev. B* **13** (1976) 5188.
[11] M.C. Payne, M.P. Teter, D.C. Allen, T.A. Arias, J.D. Joannopoulos, *Rev. Mod. Phys.* **64** (1992) 1045.
[12] H. Adachi, M. Tsukada, C. Satoko, *J. Phys. Soc. Jpn.* **45** (1978) 875;
H. Adachi, S. Shiokawa, M. Tsukada, C. Satoko, S. Sugano, *J. Phys. Soc. Jpn.* **47** (1979) 1528;
H. Adachi, *Introduction to Quantum Materials Chemistry – Approach with DV-Xα Method*, Sankyo Press, Tokyo, 1991.
[13] D. Emin, *Phys. Today* (January, 1987) 55.

CHAPTER 9

Particle Size and Surface Effects on Critical Thickness for Ferroelectricity of $BaTiO_3$ by *ab initio* Calculations

Keisuke Ishizumi, Hironori Kawanishi, Ryo Nakao, Isao Takahashi, Hikaru Terauchi and **Yoshinori Hayafuji**

Contents

Abstract

The particle size and surface effects of the critical thickness for ferroelectricity of nanoscale $BaTiO_3$ particles is investigated using a first-principles molecular orbital (MO) method and population analysis for net charge and overlap population. A series of models composed of a $Ba_8Ti_7O_6$ cluster and point charges surrounding the cluster are employed for the calculations of the electronic structures of the $BaTiO_3$ particles, with the size of the model defined by the size of the point charge array. The calculation results show that the critical thickness for the ferroelectric-to-paraelectric transition of nanoscale $BaTiO_3$ particles decreases with decreasing basal area of the rectangular particles. We conclude that in the ferroelectric phase of $BaTiO_3$ particles, ferroelectricity still exists extremely close to the surface.

School of Science and Technology, Kwansei Gakuin University, 2-1 Gakuen, Sanda, Hyogo 669-1337, Japan
Corresponding author. E-mail: hayafuji@ksc.kwansei.ac.jp; z99014@ksc.kwansei.ac.jp

Advances in Quantum Chemistry, Vol. 54
ISSN 0065-3276, DOI 10.1016/S0065-3276(07)00009-3

1. INTRODUCTION

Ferroelectric materials have attracted widespread attention for various applications, including use in gate capacitors of nonvolatile semiconductor memories such as the ferroelectric random access memory (FeRAM) [1,2]. A ferroelectric material exhibits a spontaneous electric dipole moment that can be easily reversed by applying an electric field. Typical ferroelectric materials that are used for nonvolatile memories have a perovskite crystal structure with the chemical structure ABO_3, where A is a relatively large cation located at the corners of the unit cell, B a relatively small cation located at the center, and O an oxygen anion located at the face-centered position. Since the concept of MOSFET device scaling was introduced, it has been predicted that MOSFET device scaling will eventually reach a lower limit. The scaling of ferroelectric devices is related to the minimum thickness of the ferroelectric layer. There is experimental and theoretical evidence that the Curie temperature of a thin film ferroelectric material may be different from that of the bulk ferroelectric material, and that ferroelectricity may disappear at a certain nanoscale size of the ferroelectric material [3–12]. Using X-ray diffraction experiments at room temperature, Dudkevich et al. [4], Uchino et al. [6], and Yamamoto et al. [11] reported a critical size of about 100 nm for ferroelectricity for $BaTiO_3$ powder samples. Schlag et al. [9,10] found a critical size of about 49 nm in a study of the size dependence of the phase transition temperature of $BaTiO_3$ particles. Frey and Payne [8] also reported a limiting size of well below 100 nm and commented that the large critical size reported by other researchers was due to a dead layer produced during sample preparation. Using a phenomenological approach in the scheme of the Ginzburg–Landau theory, Shih and Shih [7] showed that, with a 7.5–50 nm thick Schottky space-charge layer, the polar phase became unstable for cubic particles smaller than 200–500 nm at room temperature, depending on the space-charge layer thickness, and that the polarization of small particles at a constant temperature decreases with decrease in the particle size. Junquera and Ghosez [12] showed that $BaTiO_3$ films between two metallic $SrRuO_3$ electrodes in a short circuit lost their ferroelectric properties below a critical thickness of about 2.4 nm by first-principles calculations. However, Mayer and Vanderbilt [13] reported theoretically the absence of a critical size for the disappearance of ferroelectricity in $BaTiO_3$ particles.

Cohen [14] and one of the present authors [15–17] reported the origins of ferroelectricity in ferroelectric perovskite oxides $ATiO_3$ (A=Ba, Pb) and the origin of Ti ion displacement induced ferroelectricity in $PbTiO_3$ by first-principles calculations. They pointed out that the covalent interaction between the Ti 3d and O 2p orbitals and between the O 2p and Pb 6s orbitals in $PbTiO_3$, and the interaction between the Ti 3d and O 2p orbitals in $BaTiO_3$ were essential for ferroelectricity. They provided an atomistic explanation for the appearance of ferroelectricity in terms of hybridization due to covalent interactions. The present authors recently reported [18] a study of the critical thickness for ferroelectricity in $BaTiO_3$ particles by first-principles calculations by using model clusters with a well-defined size of 20.36 nm length, 20.36 nm width, and 4.5–60 nm thickness for

future devices according to International Technology Roadmap for Semiconductors 2003 edition (Semiconductor Industry Association, San Jose, 2003). We concluded that the critical thickness was about 12 nm for ferroelectricity of $BaTiO_3$ particles with a $20.36 \times 20.36\,nm^2$ base area, based on the analysis of the overlap population between the Ti 3d and O 2p orbitals and the net charge of the O ion as a function of the particle thickness. In the present paper, we report more details on the critical thickness and surface effects on the ferroelectric-to-paraelectric transition of nanoscale rectangular shaped $BaTiO_3$ particles with various basal areas and an analysis of covalent interactions through a first-principles computational examination of electronic structures and an analysis of covalent interactions.

2. MODEL AND CALCULATION DETAILS

First-principles calculations of electronic structures were performed using a series of models composed of a $Ba_8Ti_7O_6$ cluster, as shown in Figure 9.1, located at the center and a three dimensional (3D) array of point charges surrounding the $Ba_8Ti_7O_6$ cluster. The $Ba_8Ti_7O_6$ cluster is constructed on the basis of the crystal structure of the $BaTiO_3$ ferroelectric phase. Point charges are typically used to create a Madelung potential for a model of ionic crystals in first-principles calculations. In this study, the dimensions of the 3D point charge array were used to define the dimensions of the model in order to study the particle size dependence on ferroelectricity. Junquera and Ghosez [12] pointed out that the thickness dependence of ferroelectricity of a $BaTiO_3$ film between two metallic electrodes can be explained by simple electrostatic arguments. Based on the above statement of Junquera and Ghosez [12], we can state that our calculations, considering all possible electrostatic interactions but neglecting items relating to lattice dynamics, are valid. The initial charge states of the ions are Ba^{+2}, Ti^{+4},

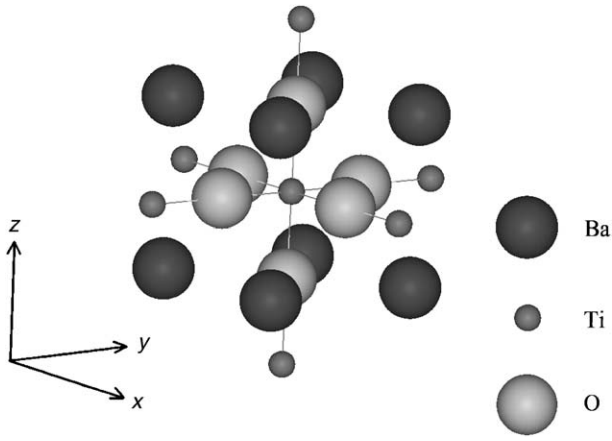

Figure 9.1 A $Ba_8Ti_7O_6$ cluster shown embedded at the center of a three-dimensional point charge array.

and O^{-2}. The lattice constants used were the experimental values at room temperature [19] of a=3.992 Å and c=4.036 Å for a tetragonal structure in a tetragonal ferroelectric phase, and all of our calculations were assumed at room temperature. The coordinates of the ions in a distorted tetragonal structure were taken to be (0, 0, ΔTi) for the Ti ions, ($\pm a/2$, 0, $+\Delta O_{xy}$), (0, $\pm a/2$, $+\Delta O_{xy}$), and (0, 0, $\pm c/2+\Delta O_z$) for the $O_{\pm x}$, $O_{\pm y}$, and $O_{\pm z}$ ions, and ($\pm a/2$, $\pm a/2$, $\pm c/2$) for the Ba ions, where ΔTi, ΔO_{xy}, and ΔO_z are displacements of +0.05, −0.05, and −0.09 Å for the Ti, O_{xy}, and O_z ions, respectively [20]. Here, we denote the oxygen ions located at the ($\pm$1,0,0), (0,$\pm$1,0), and (0,0,$\pm$1) planes as $O_{\pm x}$, $O_{\pm y}$, and $O_{\pm z}$, respectively. The coordinates of the ions in our cluster models correspond to the coordinates of modeling the electrical boundary conditions fixed by putting the electrodes in a short-circuit. The model sizes used were basal areas of 9.98 × 9.98, 16.37 × 16.37, 20.36 × 20.36, 32.34 × 32.34, 40.32 × 40.32, and 44.31 × 44.31 nm^2 and thicknesses of 4.5–60 nm to represent rectangular-shaped $BaTiO_3$ particles for the study of the particle thickness dependence.

The electronic structures of a series of models were calculated using the first-principles discrete variational-$X\alpha$ (DV-$X\alpha$) molecular orbital (MO) method with a linear combination of atomic orbitals (LCAO) expansion of MOs [21]. In the DV-Xα method based on the Hartree–Fock–Slater method, the exchange-correlation potentials are approximated by the simple Slater form [22] $V_{xc}(\mathbf{r})=-3\alpha\{3\rho(\mathbf{r})/4\pi\}^{1/3}$, where the coefficient α is a scaling parameter, fixed at 0.7 in the present study, and $\rho(\mathbf{r})$ is the local electron density at a position $\mathbf{r}$. Using the simple form for the potentials, high-speed calculations were iterated until $\rho(\mathbf{r})$ reached a constant value by the self-consistent-charge method. The basis function for the MO calculation consisted of atomic orbital wave eigenfunctions obtained in a numerical form, including 1s–6s orbitals for the Ba ions, 1s–4p for Ti, and 1s–2p for O. To evaluate the ionicity and covalency of a chemical bond between H and K ions, Mulliken overlap population analysis [23] was used to analyze the covalent bonding between pairs of atoms in a model, giving the net charge of each atom (ΔQ_H for ion H) and the bond overlap population between each pair of atoms in a model (Q_{HK} between ions H and K), as defined by the following equations:

$$\Delta Q_H = Z_H - Q_H, \tag{1}$$

$$Q_H = \sum_H Q_i, \tag{2}$$

$$Q_i = \sum_l Q_i^l, \tag{3}$$

$$Q_i^l = \sum_j Q_{ij}^l, \tag{4}$$

$$Q_{HK} = 2\sum_{H,K} Q_{ij}, \tag{5}$$

$$Q_{ij} = \sum_l Q_{ij}^l. \tag{6}$$

Here, the quantity Q_{ij} is the overlap population. In these equations, $\sum_H$, $\sum_K$, $\sum_l$, $\sum_i$, and $\sum_j$ represent the sum of the populations of the H ions, the K ions, the MO φ_l, and the atomic orbitals χ_i and χ_j, respectively. Both ΔQ_H and Q_{HK} are obtained from the sum of Q_{ij}^l, expressed by

$$Q_{ij}^l = n_l c_{il} c_{jl} S_{ij}, \tag{7}$$

Here, Q_{ij}^l is the partial overlap population, namely, the electron population of the overlap region between the atomic orbitals χ_i and χ_j in the MO φ_l, which is the product of n_l, the number of electrons in MO φ_l (usually $n_l = 2$); c_{il} and c_{jl}, the contributions of atomic orbitals χ_i and χ_j in the MO φ_l; and S_{ij}, the overlap integral between atomic orbitals χ_i and χ_j. Q_H is the gross atomic population or the gross atomic charge on atom H and is given by the sum of the atomic orbital populations Q_i. The net charge ΔQ_H is obtained from the difference between Q_H and the atomic number Z_H, namely, the number of electrons in the neutral atom.

Figure 9.2 shows the bond overlap population Q_{TiX} (X=O, Ba, Ti) between the center Ti ion and the first nearest neighbor O, the second Ba, or the third Ti ions in the $Ba_8Ti_7O_6$ cluster. The bond overlap population is appreciable only between the center Ti and the first nearest neighbor O ions. The value of 0.17 for Q_{TiO} represents the average of Q_{TiO+z}, Q_{TiO-z}, $Q_{TiO\pm x}$, and $Q_{TiO\pm y}$. The bond overlap population Q_{BaY} (Y=O, Ti, Ba) between the Ba and surrounding ions of the first nearest neighboring O, the second Ti, or third Ba ions was negligibly small. These comparisons showed that the Ti ion orbitals were slightly hybridized with the O ion orbitals in the $Ba_8Ti_7O_6$ cluster, while none of the Ba ion orbitals were hybridized with the orbital composing the cluster. This validated our assumption that the bonding in $BaTiO_3$ is predominantly ionic with a fractional covalent interaction [18].

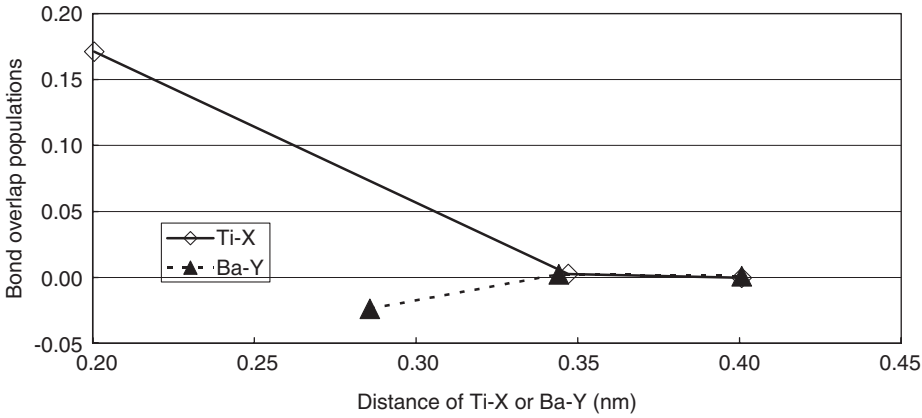

Figure 9.2 Bond overlap populations Q_{TiX} (X = O, Ba, Ti) between the central Ti ion and the first nearest neighboring O, the second Ba, or the third Ti ions, and Q_{BaY} (Y = O, Ti, Ba) between the Ba ion and the first nearest neighboring O, the second Ti, or third Ba ions.

3. RESULTS AND DISCUSSION

3.1 Dependence of the critical thickness for ferroelectricity on basal area

We first studied the dependence of the critical thickness of ferroelectricity as a function of the basal area of nanoscale rectangular $BaTiO_3$ particles. The base areas of the models used were 9.98×9.98, 16.37×16.37, 20.36×20.36, 32.34×32.34, 40.32×40.32, and $44.31 \times 44.31\,nm^2$. Figure 9.3 shows the change of the overlap population $Q_{Ti3dO2p}$ between the Ti 3d orbital and the O 2p orbital of the O_{+z} ion as a function of the thickness of the rectangular $BaTiO_3$ in the range of 4.5–60 nm. The six plots shown in Figure 9.3 have a similar shape, all exhibiting two essential features: a decrease in $Q_{Ti3dO2p}$ with decreasing thickness and a constant value of $Q_{Ti3dO2p}$ of about 0.099 at small thicknesses. The curved $Q_{Ti3dO2p}$ thickness dependence reached the constant value at different critical thicknesses for each cluster. In a previous paper [18], we demonstrated that this critical thickness corresponds to the critical thickness for ferroelectricity of the rectangular $BaTiO_3$. In the thickness range above the critical thickness, $Q_{Ti3dO2p}$ is dominated by a long-range Coulomb interaction that favors a ferroelectric distortion, while in the thickness range below the critical thickness, a short-range repulsive interaction that stabilizes a paraelectric phase is predominant. These calculations are assumed at room temperature, therefore the electronic instability in this study is much larger than lattice vibrations with changing thickness. Hence, whether $Q_{Ti3dO2p}$ has a value above about 0.099 is a fairly good measure

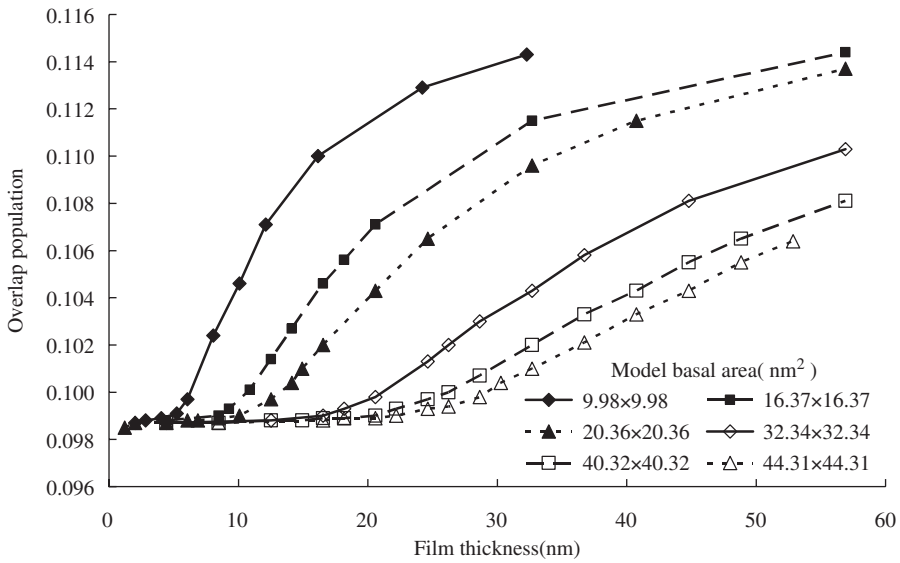

Figure 9.3 Change in $Q_{Ti3dO2p}$ (overlap population between Ti 3d and O 2p orbitals of the O_{+z} ion) as a function of the thickness of rectangular $BaTiO_3$ in the range of 4.5–60 nm for models with basal areas.

for the occurrence of ferroelectricty. As shown in Figure 9.3, the critical thickness for ferroelectricity is thinner in models with a smaller basal area. The general relationship between $Q_{Ti3dO2p}$ and a dimensionless normalized thickness, i.e., the thickness divided by the square root of the basal area, is shown in Figure 9.4. The calculated data were obtained for widely varying conditions of thickness and basal areas, however, as can be seen in Figure 9.4, all the data points trace out a single curve. Figure 9.4 shows that the normalized critical thickness for ferroelectricity can be determined to be about 0.60. We can use this normalized critical thickness to estimate a critical thickness corresponding to a specific basal area. Figure 9.5 shows the dependence of the critical thickness on the basal area of a model, plotted as a function of the square root of the basal area. Surprisingly, the critical thickness is almost directly proportional to the square root of the basal area. A least-squares curve fit using the linear equation

$$t_{crit} = h \cdot \sqrt{S} + k \tag{8}$$

yields h=0.533 and k=1.623 nm, where t_{crit} [nm] represents the critical thickness and $\sqrt{S}$ [nm] is the square root of the basal area. There are two important consequences of this linear relationship between the critical thickness and the square root of the basal area. One is that since the parameter h is less than unity, a spherical $BaTiO_3$ particle may have no critical thickness for ferroelectricity. The other is that although the linear relationship expressed by Eq. (8) is valid for nanoscale particles, it is expected to be invalid for particles larger than the nanoscale, in other words, the range of validity or applicability of Eq. (8) with regard to particle size is still under consideration.

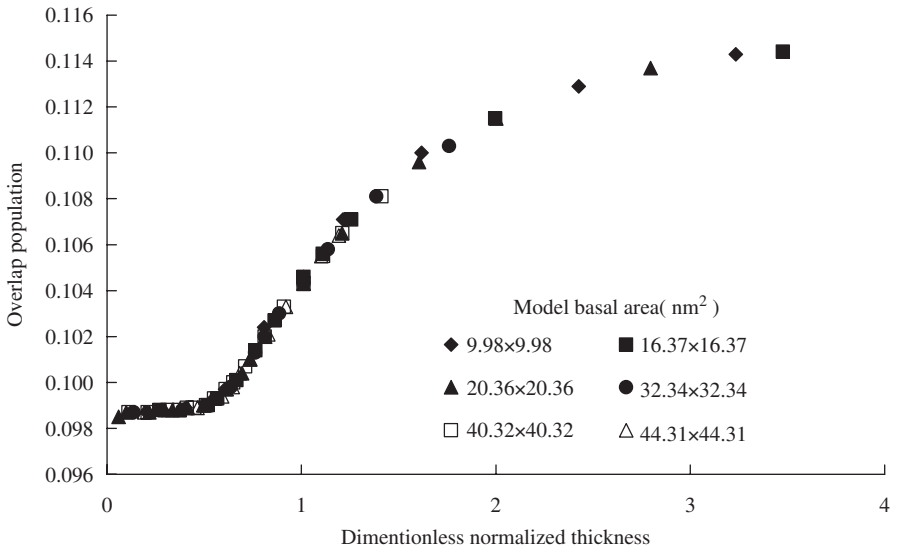

Figure 9.4 General relationship between $Q_{Ti3dO2p}$ and the dimensionless normalized thickness (thickness divided by the square root of the basal area) with calculated data obtained for widely varying conditions of thickness and basal area.

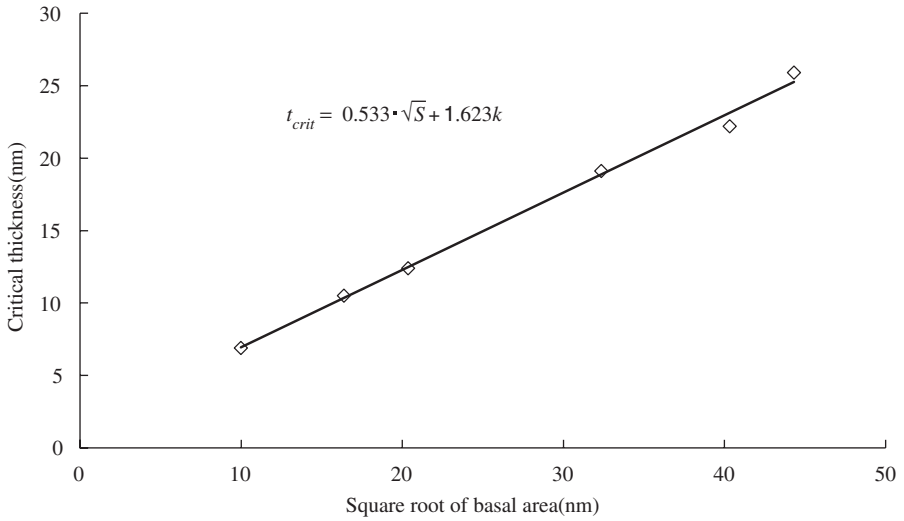

Figure 9.5 Dependence of critical thickness on the basal area of the model, plotted as a function of the square root of the basal area.

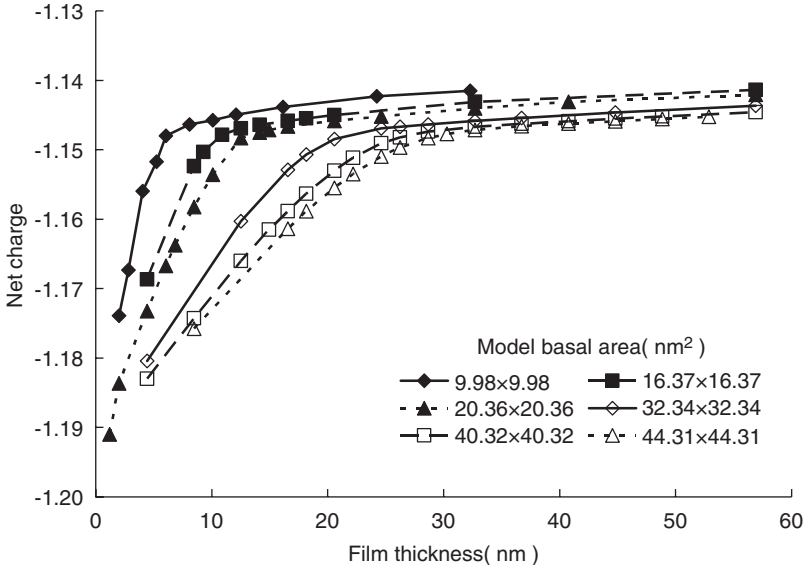

Figure 9.6 Change of ΔQ_{O+z} of the O_{+z} ion in six models with different basal areas.

The *change of* ΔQ_{O+z} for the O_{+z} ion with thickness for the six models with different basal areas is presented in Figure 9.6, as an example of the thickness dependence of the net charge of the constitutive ions of the models. As noted in our previous paper [18], the critical thickness in the change of ΔQ_{O+z} can be

defined as the thickness at which a further decrease in thickness induces a rapid decrease in ΔQ_{O+z}. Each plot of ΔQ_{O+z} in Figure 9.6 clearly shows such a critical thickness for ferroelectric transition. Comparing Figure 9.6 with Figure 9.3, it is found that the critical thickness for the change of $Q_{Ti3dO2p}$, shown in Figure 9.3, coincides with the critical thickness for the change of ΔQ_{O+z}, shown in Figure 9.6, in the corresponding model.

3.2 Surface effect on ferroelectricity

The $Ba_8Ti_7O_6$ cluster exists within a Madelung potential and its electronic structure is strongly influenced by the arrangement of point charges surrounding the cluster that interact with the cluster by long-range Coulomb forces. Because of this, the $Ba_8Ti_7O_6$ cluster can be used to monitor the electronic state at different positions within the point charge array. To examine the surface effect on ferroelectricity, we calculated the degree of hybridization, i.e., the overlap population Q_{ij} between two orbitals using models with the $Ba_8Ti_7O_6$ clusters at different positions in the 3D point charge array. The basal area of the 3D point charge array was $20.36 \times 20.36\,nm^2$ and the thicknesses used were 4.44, 14.13, 24.40, 32.69, 56.91, and 129.56 nm, for rectangular $BaTiO_3$. In the model, the location of the $Ba_8Ti_7O_6$ cluster was shifted step by step from the center to the upper and lower surfaces of the charge array. Figure 9.7 shows the change of the overlap population $Q_{Ti3dO2p}$ with distance of the $Ba_8Ti_7O_6$ cluster from the center of the model. Interestingly, $Q_{Ti3dO2p}$ is not constant, but is different changes throughout the model. For all seven models, $Q_{Ti3dO2p}$ gradually decreases with increasing distance from the center. However, even at the surface $Q_{Ti3dO2p}$ does not reach a value of 0.099, which indicates that ferroelectricity still

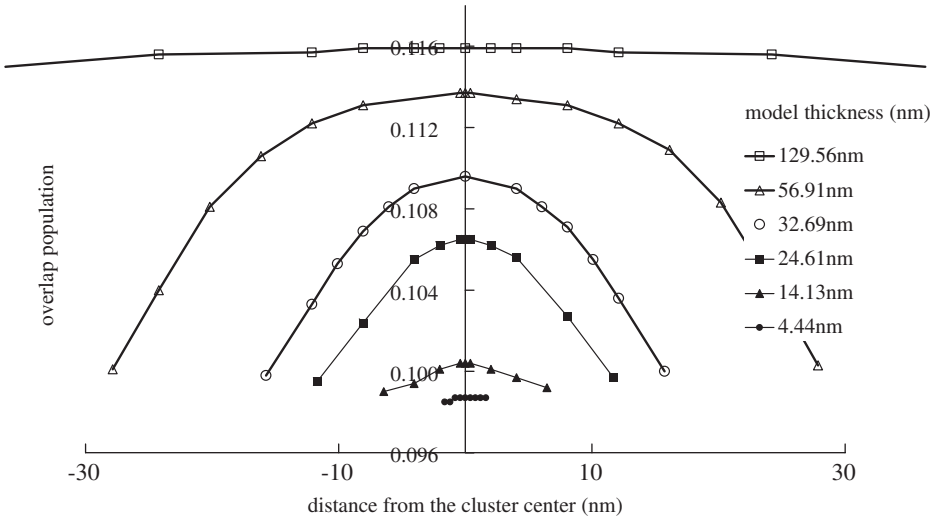

Figure 9.7 Change of $Q_{Ti3dO2p}$ with distance of the $Ba_8Ti_7O_6$ cluster from the center of the model.

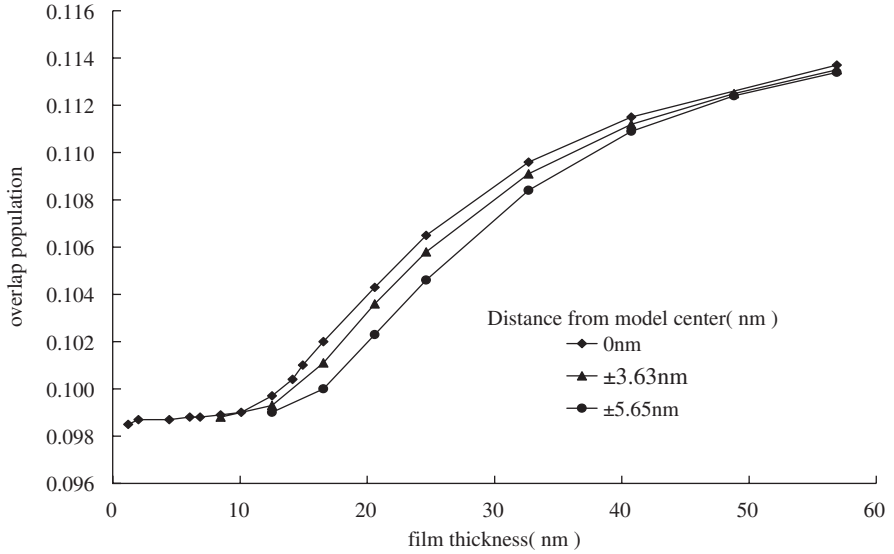

Figure 9.8 $Q_{Ti3dO2p}$ against model thickness for a $Ba_8Ti_7O_6$ cluster located at different positions away from the center of the model.

exists, even extremely near the surface and hence there is no reason to suppose that spontaneous polarization due to ferroelectric distortion vanishes near the surface region. It is interesting that $Q_{Ti3dO2p}$ at the surface of the thicker models is slightly larger than that of the thinner ones. It is supposed that spontaneous polarization at the surface depends on the particle size, i.e., on the basal area and the thickness, and that the smaller $Q_{Ti3dO2p}$ at the surface is not caused by a particulate surface effect, but is an effect of the entire particle volume at the surface.

The change in $Q_{Ti3dO2p}$ throughout the model suggests that the critical thickness for ferroelectricity changes at different locations in the model. Figure 9.8 shows $Q_{Ti3dO2p}$ as a function of model thickness for the $Ba_8Ti_7O_6$ cluster located at three different positions, 0, $\pm$3.63, and $\pm$5.65 nm from the center of the model. The figure shows critical thicknesses for the position of 0, $\pm$3.63, and $\pm$5.65 nm of 12.47, 14.60, and 16.89 nm, respectively. From this we can conclude that as the thickness decreases, the spontaneous polarization due to a ferroelectric distortion vanishes successively from the surface to the center.

4. SUMMARY

The effects of particle size on the critical thickness for ferroelectricity of nanoscale $BaTiO_3$ particles were investigated using a first-principles method and population analysis. Models composed of a small $Ba_8Ti_7O_6$ cluster and a point charge array surrounding the cluster were used for the calculations, with the size of each

model defined by the size of the point charge array. The calculation results show that the critical thickness for ferroelectricity of rectangular $BaTiO_3$ particles decreases with decreasing basal area of the particles and that the critical thickness is almost directly proportional to the square root of the basal area. From these results, we expect that a spherical $BaTiO_3$ particle will not have a critical thickness for ferroelectricity. $Q_{Ti3dO2p}$ gradually decreases with increasing distance from the center of the model. However, even at the surface $Q_{Ti3dO2p}$ does not reach a value of 0.099, which corresponds to the paraelectric phase, and hence we conclude that ferroelectricity still exists even extremely near the surface. The smaller $Q_{Ti3dO2p}$ at the surface is not caused by a particulate surface effect, but is due to an effect of the entire particle volume at the surface.

ACKNOWLEDGMENTS

The authors express their gratitude to Professor H. Adachi and associate K. Sakaue for technical assistance and helpful discussions.

REFERENCES

[1] J.F. Scott, C.A. Paz de Araujo, *Science* **246** (1989) 1400.
[2] J.T. Evans, R. Womack, *IEEE J. Solid State Circuits* **23** (1988) 1171.
[3] I.P. Batra, B.D. Silverman, *Solid State Commun.* **11** (1972) 291.
[4] V.P. Dudkevich, V.A. Bukreev, V.M. Mukhortov, Y.I. Golovko, Y.G. Sindeev, E.G. Fesenko, *Phys. Status Solidi A* **65** (1981) 463.
[5] D.R. Tilley, B. Zeks, *Solid State Commun.* **49** (1984) 823.
[6] K. Uchino, E. Sadanaga, T. Hirose, *J. Am. Ceram. Soc.* **72** (1989) 1555.
[7] W.Y. Shih, W.H. Shih, I.A. Aksay, *Phys. Rev. B* **50** (1994) 15575.
[8] M.H. Frey, D.A. Payne, *Phys. Rev. B* **54** (1996) 3158.
[9] S. Schlag, H.F. Eicke, *Solid State Commun.* **91** (1994) 883.
[10] S. Schlag, H.F. Eicke, W.B. Stern, *Ferroelectrics* **173** (1995) 351.
[11] T. Yamamoto, H. Nioiri, H. Moriwake, *Jpn. J. Appl. Phys.* **39** (2000) 5683.
[12] J. Junquera, P. Ghosez, *Nature* **422** (2003) 506.
[13] B. Mayer, D. Vanderbilt, *Phys. Rev. B* **63** (2001) 205426.
[14] R.E. Cohen, *Nature* **358** (1992) 136.
[15] K. Miura, M. Tanaka, *Jpn. J. Appl. Phys.* **35** (1996) 2719.
[16] K. Miura, M. Tanaka, *Jpn. J. Appl. Phys.* **35** (1996) 3488.
[17] K. Miura, M. Tanaka, *Jpn. J. Appl. Phys.* **36** (1996) 226.
[18] R. Nakao, K. Ishizumi, I. Takahashi, H. Terauchi, Y. Hayafuji, K. Muira, *Appl. Phys. Lett.* **86** (2005) 222901.
[19] R.G. Rhodes, *Acta Crystallogr.* **4** (1951) 105.
[20] G. Shirane, F. Jona, R. Pepinsky, *Proc. IRE* **43** (1955) 38.
[21] H. Adachi, M. Tsukada, C. Satoko, *J. Phys. Soc. Jpn.* **45** (1978) 874.
[22] J.C. Slater, *Phys. Rev.* **81** (1951) 385.
[23] R.S. Mulliken, *J. Chem. Phys.* **23** (1955) 1841.

CHAPTER 10

Quantum Mechanics and the Special and General Theory of Relativity

Erkki J. Brändas

Contents

Abstract

The old dilemma of quantum mechanics versus the theory of relativity is reconsidered. A first principles relativistically invariant theory will be provided through a model, which is basically quantum mechanical. Moreover, by analytically extending quantum mechanics into the complex plane, it is possible to include dynamical features such as time-, length-, and temperature-scales into the theory. The flexibility of including complex symmetric interactions will in the same way support a transition from firmly quantum mechanical non-local behaviour to a decidedly classical-local appearance. Furthermore, the extended formulation gives rise to so-called Jordan blocks. They will be shown to appear logically in the present generalized dynamical picture and a compelling interpretation is microscopic self-organization (MSO). Not only have the manifestation of quantum–thermal correlations, and the emergence of generic time scales been established, but the present viewpoint also appears to throw new light on the age-old problem of quantum mechanics versus relativity. To bring all these ideas together, we will demonstrate that our model (i) displays the simple occurrence of such a degenerate unit, (ii) demonstrates the link with the Klein–Gordon–Dirac relativistic theory and (iii) provides dynamical features of both special and general relativity theory.

Department of Quantum Chemistry, Uppsala University, Box 518, S-751 20 Uppsala, Sweden
E-mail: Erkki.Brandas@kvac.uu.se

Advances in Quantum Chemistry, Vol. 54
ISSN 0065-3276, DOI 10.1016/S0065-3276(07)00010-X

1. INTRODUCTION

In this study, we will re-examine the old dilemma of quantum mechanics versus the theory of relativity. One obvious problem has been and still is that quantum mechanics in its traditional formulation does not provide apposite scale dimensions. In a recent popular book by E.B. Bolles [1] one can read:

> Einstein granted that the (Dirac) equation was ''the most logically perfect presentation'' of quantum mechanics yet found, but not that it got us any closer to the ''secret of the Old One''. It neither described the real world phenomena that he wanted to understand nor proposed new concepts that would make the real world accessible to understanding. Furthermore, Dirac's unification of quantum mechanics with special theory of relativity left out Einstein's later success with general relativity and the gravitational field.

To give further details on the subject of this theme, we repeat that although the Dirac and Klein–Gordon equations, despite giving an almost perfect description of microscopic quantum effects, do not account for dynamical effects like the time- and length-scale contractions in the special theory of relativity or could be rigorously integrated with the general gravitational theory. A first-principles quantum many-body relativistically invariant theory is furthermore still lacking although excellent practical and useful schemes exist today [2]. An additional bonus from such a general integration would be to obtain the famous Schwarzschild solution (or rather the correct Schwarzschild radius) along the way or to deduce the correct law for the gravitational deviation of light.

We will here, to begin with, recognize as a background setting, that quantum mechanics today has evolved from the very abstract to the materialization of an entirely new research area, viz. quantum technology. However, even if early-thought experiments now have become experimentally achievable still the fundamental problem of understanding and interpretation remains [3]. In what follows, we will arrive at a representation that will throw new light on the problems mentioned above.

The model to be presented below is basically a quantum mechanical model. However, the theory behind the description to be given has an additional generalization. By analytically extending the quantum method into the complex plane, there is augmented an important quality, i.e. the possibility to include dynamical features such as time-, length- and temperature-scales into the theory. Using well-known rigorous mathematical theorems on so-called dilatation analytic interactions, Aguiar, Balslev and Combes [4,5] proved important spectral properties of many-body Schrödinger operators. The ''permission'' to include complex symmetric interactions actually supports a transition from firmly quantum mechanical non-local behaviour to a decidedly classically local appearance. In this generalized picture, a supposed class of resonance states can be defined, computed and analysed; compare, for instance, the illustrious

Gamow waves, even though standard quantum mechanical states remain embedded [6]. Although general Hamiltonians may not subscribe to dilatation analyticity, complex symmetric perturbations, as the specific situation dictates, have an additional appeal. In the forthcoming description, basic quantum mechanical physical law will rule; at the same time classical mechanics takes over where and when appropriate.

Before we continue one should conceivably mention parallel developments concerning so-called complex systems and their quantum equivalent. Here the subject matter is, for example the system-environment partitioning, entanglement and/or dissipation, non-adiabaticity, off-diagonal long-range order (ODLRO), the approach to the classical limit and appropriate coherence–decoherence mechanisms. In this picture, there appears naturally certain well-defined quantum–thermal correlations. The latter are significant as a result of an established relationship between the temperature and the phenomenological relaxation time leading up to the emergence of a generic time scale. For a description of this work see, for example Refs. [7,8].

One of the challenges in the formulation of these so-called coherent-dissipative systems is to clarify, if possible, the mechanism of microscopic self-organization (MSO). It has been put forward (see e.g. [9]) that MSO may be approached through the formation of certain degenerate units identified as classical Jordan blocks turning up in the generalized dynamical picture. It has also been remarked that the present approach can be linked back to a relativistic origin [10]. To bring all these ideas together, we will, as explained above, present a very simple model that (i) displays the simple occurrence of such a degenerate unit, (ii) demonstrates the link with the Klein–Gordon–Dirac relativistic theory and (iii) provides dynamical features of both special and general relativity theory.

2. THE MODEL

As promised we will present a simple model that displays both the fundamental nature of the concept of resonances as well as the quality of relativistic principles. A Klein–Gordon-like equation will be derived with specific restrictions and interpretations. Although the representation turns up somewhat naïve and *ad hoc*, we will appreciate some general and surprising features that reveal the underlying fundamental principles.

We will start by setting up a simple 2×2 matrix that (without interaction) displays perfect symmetry between the particle and its antiparticle image. Note that it is well known that the Klein–Gordon and the Dirac equation can be written formally as a standard self-adjoint secular problem (see e.g. [11,12]), based on the simple Hamiltonian matrix (in mass units)

$$\mathbf{H} = \begin{pmatrix} m_0 & p/c \\ p/c & -m_0 \end{pmatrix}. \tag{1}$$

Here c the velocity of light and p is the momentum of the particle. The velocities of the particles are relative a system in rest, wherever the rest masses of the particles involved are m_0 and $-m_0$ respectively.

It is also straightforward to generalize the off-diagonal interaction to incorporate the previously mentioned resonance picture of unstable states by using a complex symmetric operator. For general discussions on this issue, we refer to the proceedings of the Uppsala-, Lertorpet- and the Nobel-Satellite workshops and references therein [13–15]. Thus one may arrive at a complex symmetric secular problem (note that the same matrix construction may be derived from a suitable hermitean matrix in combination with a non-positive definite metric [9]; see also below), which surprisingly leads to a comparable secular equation as the one obtained from Eq. (1). To be more specific we write

$$\mathbf{H} = \begin{pmatrix} m & -iv \\ -iv & -m \end{pmatrix}, \tag{2}$$

where (in mass units) the diagonal elements are the energies associated with the particle and the antiparticle states (which may be fermionic), respectively, and $-iv$ is the complex symmetric interaction to be determined later (the minus sign is merely convention, see further below). We also observe that H_{11} describes a quantum particle with mass m and H_{22} a corresponding antiparticle assigned with a negative energy $-m$ corresponding to a hole or void. For zero interaction, the diagonal elements are $\pm m_0$, i.e. the correspondent to the particle rest mass. Also the quantum vectors $|m_0\rangle$ and $|\bar{m}_0\rangle$ will be chosen orthonormal. Note also the difference with Eq. (1), where m_0 occur in the diagonal of a self-adjoint problem while the insertion of $-i$ instead of unity creates a complex symmetric ansatz; see more on this further below.

Let us now diagonalize the matrix in Eq. (2); compare, for instance, the one equivalent to Eq. (1) obtaining for the roots $\lambda_\pm$ (equal to $\pm m_0$)

$$\lambda^2 = m^2 - v^2 \tag{3}$$

or identifying the diagonal matrix with the energies corresponding to the rest mass m_0

$$m_0^2 = m^2 - v^2 \tag{4}$$

and further by recognizing the choice of kinematical perturbation to be $v = p/c$ that

$$m^2c^4 = m_0^2c^4 + p^2c^2. \tag{5}$$

Although we have not introduced in detail the character of the wave function and the structure of the associated spaces we may, for example associate $p = mv$ for a free particle. In general, however, one needs to take into account that p is an operator, which in its extended form may not be self-adjoint. Hence our secular equation yields well-known relations and by standard operator identification one may obtain a familiar Klein–Gordon type equation. We will, however, proceed by looking further at the secular equation. In an obvious notation one obtains for the

eigenvalues inserted in the secular equation associated with Eq. (2) above

$$\begin{aligned} |m_0\rangle &= c_1|m\rangle + c_2|\overline{m}\rangle; \quad \lambda_+ = m_0 \\ |\overline{m}_0\rangle &= -c_2|m\rangle + c_1|\overline{m}\rangle; \quad \lambda_- = -m_0 \end{aligned} \tag{6}$$

or

$$\begin{aligned} |m\rangle &= c_1|m_0\rangle - c_2|\overline{m}_0\rangle \\ |\overline{m}\rangle &= c_2|m_0\rangle + c_1|\overline{m}_0\rangle \end{aligned} \tag{6'}$$

with

$$\begin{aligned} c_1 &= \sqrt{\frac{1+X}{2X}} \\ c_2 &= -i\sqrt{\frac{1-X}{2X}} \end{aligned} \quad m = \frac{m_0}{X}; \quad c_1^2 + c_2^2 = 1 \tag{7}$$

and where $X = \sqrt{1-\beta^2}$; $\beta = p/mc =$ (classical particles) $= \upsilon/c$. We emphasize that the matrix $\mathbf{H}$ is complex symmetric and hence the eigenvectors are bi-orthogonal instead of orthogonal. If one wants to make a "quasi-probability" interpretation of the weights $|c_1|^2$ and $|c_2|^2$ one multiplies Eq. (7) with $\sqrt{X}$. Note that $\upsilon/c \to 1$ implies $|c_1|^2/|c_2|^2 \to 1$.

Even if the equations arrived at seem familiar there are some obvious fundamental differences. First of all, the ansatz singles out two mirror spaces, where the particle and its mirror image may be located, respectively. Second, the expanded complex symmetric representation takes into account complex resonance states. Note also, as said above, that the complex symmetry can be obtained from the hermitean representation via a non-positive definite metric, i.e.

$$\mathbf{H} = \overline{\mathbf{H}}\mathbf{D}^{-1}; \quad \overline{\mathbf{H}} = \begin{pmatrix} m & iv \\ -iv & m \end{pmatrix}; \quad \mathbf{D} = \begin{pmatrix} 1 & 0 \\ 0 & -1 \end{pmatrix} \tag{8}$$

The representation further implies that the kinematical interaction $-ip/c$, where (originally) $p = p^+$, in addition to the particle's response to its mirror copy, must be bounded by $p/m \leq c$ (see further below). Additionally, since we are now working in an extended complex symmetric representation including a resonance picture of unstable states, m may be continued to complex values leading to a non-self-adjoint p and the appearance of generic time- and length-scales (see the next section). One may also define the following general symmetry operations (compare, e.g. the celebrated CPT theorem), namely

$$m \to -m, \ \mathrm{P}_{12}, \ \mathrm{K} = *, \tag{9}$$

i.e. substituting m with $-m$, exchanging index 1 and 2 and taking the complex (hermitean) conjugate. We also remark that the choice $cv = (\sigma \cdot \mathbf{p})$ where σ are the 2×2 Pauli matrices corresponds to a Dirac-like equation for a free fermion in an analogous 4×4 setting.

To examine the restriction $p/m \leq c$, we consider the degenerate matrix for $v = m$, for m finite.

$$\mathbf{H}_{\text{deg}} = \begin{pmatrix} m & -im \\ -im & -m \end{pmatrix}. \tag{10}$$

It follows that $\mathbf{H}_{\text{deg}}$ under the (unitary for m_0) transformation (note that the vectors $|m_0\rangle$ and $|\overline{m}_0\rangle$ are orthonormal while $|m\rangle$ and $|\overline{m}\rangle$ are biorthogonal)

$$\begin{aligned} |0\rangle &= \frac{1}{\sqrt{2}}|m\rangle - \frac{i}{\sqrt{2}}|\overline{m}\rangle \\ |\bar{0}\rangle &= \frac{1}{\sqrt{2}}|m\rangle + \frac{i}{\sqrt{2}}|\overline{m}\rangle \end{aligned} \tag{11}$$

becomes

$$\overline{\mathbf{H}}_{\text{deg}} = \begin{pmatrix} 0 & 2m \\ 0 & 0 \end{pmatrix} \tag{12}$$

Also, taking the complex conjugate of Eq. (10) (time reversal in this simple picture) yields under the same transformation

$$\overline{\mathbf{H}}^{+}_{\text{deg}} = \begin{pmatrix} 0 & 0 \\ 2m & 0 \end{pmatrix} \tag{13}$$

Similarly one obtains analogous formulas for $m \to -m$. The Jordan form obtained here describes the vacuum as a ''particle–antiparticle superposition''. Obviously there appear no particle states corresponding to the diagonal of Eqs. (12) and (13). The energy is hidden, i.e. ''bound up'' in the transition between the states defined in Eq. (11). One should observe that the transformation (Eq. (11)) is fundamentally different from the one obtained from the corresponding limit in Eq. (7).

3. THE SPECIAL THEORY

We will not analyse the situation further here except pointing that the present resonance model, under appropriate environmental perturbations, admits primary complex resonance energies commensurate with rigorous mathematics and precise boundary value conditions, i.e.

$$\begin{aligned} mc^2 &\to mc^2 - i\frac{\Gamma}{2}; \quad \tau = \frac{\hbar}{\Gamma} \\ m_0c^2 &\to m_0c^2 - i\frac{\Gamma_0}{2}; \quad \tau_0 = \frac{\hbar}{\Gamma_0} \end{aligned} \tag{14}$$

where Γ and τ are, respectively, the half width and lifetime of the resonance state and $\hbar$ is Planck's constant divided by 2π. We find directly from insertion into the

secular Eq. (2), separating real and imaginary parts, that

$$\Gamma_0 = \Gamma\sqrt{1-\beta^2}; \quad \tau = \tau_0\sqrt{1-\beta^2} \tag{15}$$

or that the time scale τ is also subject to an appropriate relativistic contraction. By comparing times in the two scales, we obtain

$$\frac{t}{\tau_0} = \frac{t_0}{\tau}$$

i.e. the time t, measured in the ''moving system'' in relation to the τ_0-scale should equal the time t_0 in relation to the contracted τ-scale. Hence

$$t = \frac{t_0}{\sqrt{1-\beta^2}}$$

Enforcing Lorentz-invariance, analogous relations for length scales are realized. Hence we find the well-known contraction formulas of the special theory of relativity

$$l = \frac{l_0}{\sqrt{1-\beta^2}}; \quad t = \frac{t_0}{\sqrt{1-\beta^2}}; \quad m = \frac{m_0}{\sqrt{1-\beta^2}}. \tag{16}$$

The simple model presented here is quite surprising and yet the interpretation and explanation is very different compared to the classical one. First, the particle and its image are represented by different vector subspaces. Next, the scale contractions are due to a superposition of the particle and its antiparticle image. The particle is thus weakly coupled to its mirror image and vice versa. The image is not directly experienced, unless the adherent is explicitly excited. Instead there is the indirect recognition through the well-known relativity law contained in the Lorentz transformations owing to the kinematical interaction v. We also note that for ''classical particles'' $v \to c$ implies $m \to \infty$ if m_0 is finite. Within the present picture, we mention that the general (operator) restriction $p/m \leq c$ may be difficult to analyse. Instead of exercising Ehrenfest's theorem, which may apply to a certain class of (classical) particles, we will instead look at the consequences inflicted by a sufficiently large energy fluctuation that may exhaust the inequality above. We point out that one can easily modify the model to include appropriate electromagnetic fields, for example

$$(E_{\text{op}} - e\mathrm{A}_0)^2 = m_0^4c^4 + \left(p - \frac{e}{c}\vec{\mathrm{A}}\right)^2 c^2 \tag{17}$$

where above $(\mathrm{A}_0, \vec{\mathbf{A}})$ are the usual vector and scalar potentials (and similarly for the Dirac equation). Since the present resonance model allows a general complex symmetric interaction between particles of a positive and a negative (image) mass, one may in principle also (see next section) incorporate a gravitational field. The question of gauge invariance in connection with analytic extensions of quantum mechanics will not be considered explicitly here except for some comments in the concluding remarks.

Hence, as described above, one might realize the degenerate situation, Eq. (10), via a sufficiently large fluctuation without any singular behaviour in m

as would be expected from the ''classical'' analysis. Assuming that such a degenerate state might be ''produced'' from, let us say, $\beta = 0.98$, or $m = 5m_0$, 80% of the mass content in the hidden-off diagonal part of the matrix in Eq. (12) is kinetic energy.

It is of course appealing to associate the ''structures'' in Eqs. (11) and (12) with the vacuum. It is also tempting to associate the limiting behaviour of an expanding universe with the occurrence of black holes with unique properties and related predicting power. The adiabatic limit discussed above should be different from the sudden onset of a degeneracy, i.e. obtaining Eq. (9) for $m = m_0$. To verify the latter, we find that taking the antisymmetrized product of the vectors corresponding to the ''vacuum'', we obtain

$$|0\rangle \wedge |\bar{0}\rangle = i|m_0\rangle \wedge |\overline{m}_0\rangle \tag{18}$$

It follows that if the particle (and the antiparticle) is a fermion, then Eq. (18) implies antisymmetry also under the exchange of the particle with its antiparticle image (including spin degrees of freedom). Note that the sudden (high energy) onset of a degenerate situation leading to the unitary transformation, Eq. (11) for $m = m_0$, is different from the adiabatic limit discussed in Eqs. (6) and (7). The general many-body theory outlined in Refs. [7–9] would hence apply. We will return to this issue in subsequent sections.

4. THE GENERAL THEORY

Before discussing general issues related to the gravitational field in more detail, we will mention the following aspects of the development identified above. To formulate a consistent many-body approach, which rests on Eq. (18), we will review some prerequisites. We start with a brief analysis of the many-particle fermion density matrix.

The N particle (and its p-reduced companions) representable density matrix $\Gamma^{(p)}$ can be defined as follows in the Löwdin normalization (x_i is a combined space-spin coordinate)

$$\Gamma^{(p)}(x_1 \ldots x_p | x'_1 \ldots x'_p) = \binom{N}{p} \int \Psi^*(x_1 \ldots x_p,\ x_{p+1} \ldots x_N) \times \Psi(x'_1 \ldots x'_p,\ x_{p+1} \ldots x_N) dx_{p+1} \ldots dx_N \tag{19}$$

where, the (normalized) wave function $\Psi(x_1 \ldots x_N)$ represents a fermionic many-body quantum mechanical system. We emphasize that the representation is valid in the present general complex symmetric setting. We will now focus on $p = 2$.

Let us first mention the notion of ODLRO, a fundamental concept introduced by Yang [16] in connection with his celebrated proof of the largest bound for $\Gamma^{(2)}$. He demonstrated that the manifestation of a macroscopically large eigenvalue $\lambda_L^{(2)}$ in the second-order (fermion) density matrix may lead to a new physical order (cf. the theories of superconductivity and superfluidity). For additional information regarding these issues see Refs. [17–19].

To connect with the previous section, we start by employing a set of n localized pair functions $\mathbf{h} = (h_1,\ h_2,\ \ldots h_n)$ also called geminals, here obtained from appropriate pairings of the particle–antiparticle basis spin functions in Eq. (18).

For future use, we incorporate the subsequent transformations

$$\mathbf{B} = \frac{1}{\sqrt{n}} \begin{pmatrix} 1 & \omega & \omega^2 & . & \omega^{n-1} \\ 1 & \omega^3 & \omega^6 & . & \omega^{3(n-1)} \\ . & . & . & . & . \\ . & . & . & . & . \\ 1 & \omega^{2n-1} & \omega^{2(2n-1)} & . & \omega^{(n-1)(2n-1)} \end{pmatrix}; \quad \omega = \mathrm{e}^{i\pi/n} \tag{20}$$

by introducing a coherent and a correlated basis $\mathbf{g}$ and $\mathbf{f}$, respectively, through

$$\begin{aligned} |\mathbf{h}\rangle\mathbf{B} &= |\mathbf{g}\rangle = |g_1,\ g_2, \cdots g_n\rangle \\ |\mathbf{h}\rangle\mathbf{B}^{-1} &= |\mathbf{f}\rangle = |f_1,\ f_2, \ldots f_n\rangle \end{aligned} \tag{21}$$

We note that the functions in $\mathbf{g}$ are completely delocalized over the region of sites defined by the ''localized'' particle–antiparticle basis $\mathbf{h}$. The $\mathbf{f}$-basis contains all possible phase shifted contributions from each site in accordance with Eqs. (20) and (21) above.

Some interconnections can be mentioned here. The first concerns Coleman's so-called extreme state (17) (cf. the theories superconductivity and superfluidity). If $\mathbf{h}$ is a set of two particle determinants and the wave function is constructed from an antisymmetric geminal power, based on g_1, then the reduced density matrix can be expressed as

$$\Gamma^{(2)} = \Gamma^{(2)}_{\mathrm{L}} + \Gamma^{(2)}_{\mathrm{S}} = \lambda_{\mathrm{L}} |g_1\rangle\langle g_1| + \lambda_{\mathrm{S}} \sum_{k=2}^{n} |g_k\rangle\langle g_k| \tag{22}$$

For the exact condition for the extreme state of the two-particle reduced density matrix including the ''tail contribution'' (not displayed here) resulting from remaining pair configurations, see Coleman [17]. The eigenvalues in Eq. (22) may exhibit the (possibly) large eigenvalue λ_{L} and the degenerate small one λ_{S} given by ($2n \geq N$)

$$\begin{aligned} \lambda_{\mathrm{L}} &= \frac{N}{2} - (n-1)\lambda_{\mathrm{S}} \\ \lambda_{\mathrm{S}} &= \frac{N(N-2)}{4n(n-1)} \end{aligned} \tag{23}$$

Since we have n basis pair functions or geminals and $2n$ spin orbitals (or particle and antiparticle functions), the number of fermion pairings and pair configurations is

$$\binom{N}{2},\ \binom{2n}{2},$$

respectively. The dimension of the ''box contribution'' defined in Eq. (22) is n and consequently the dimension of the left out ''tail contribution'' is $2n(n-1)$.

One can prove that the eigenvalue associated with the missing "tail" is identical to λ_S [17]. For the extreme state one obtains the eigenvalue λ_L and the $(n-1)(2n+1)$ degenerate eigenvalues λ_S. Under specific circumstances, one may find that λ_L grows to macroscopic size, i.e. approach the number of pairs, $N/2$ (in the Löwdin normalization) developing Yang's ODLRO. Rather than focusing on this particular transition, we will further consider the precursor level of the extreme state and the importance played by the full basis **g**.

As shown previously analogous equations can be derived in a statistical framework both for localized fermions in a specific pairing mode and/or for bosons subject to a quantum transport environment [7]. The second interconnection regarding the relevance of the basis **f** is related to the fact that a transformation of form (20) connects canonical Jordan blocks to convenient complex symmetric forms. This will not be explicitly discussed and analysed here except pointing out the possible relationship between temperature scales and Jordan block formation by thermal correlations (see e.g. [7–9,14], for more details).

Consider, for example a finite number of fermion or particle–antiparticle pairs in a vacuum or particle-like environment as defined in Eq. (18) (cf. Cooper pairs in a superconductor. Using Eqs. (22) and (23), we obtain for the associated (many-body potential) energy

$$W = \mathrm{Tr}\{H_{12}\Gamma^{(2)}\} \tag{24}$$

where H_{12} is the general two-body potential between the constituent parts, i.e. the particle–antiparticle combinations based on the pairing $|0\rangle \wedge |\bar{0}\rangle$. It is easy to show that Eq. (25) below may be simplified as follows. From Eq. (24), one obtains straightforwardly (note that the one-body contribution vanishes!)

$$W = \lambda_L \langle g_1|H_{12}|g_1\rangle + \lambda_S \sum_{k=2}^{n} \langle g_k|H_{12}|g_k\rangle. \tag{25}$$

If the localized basis **h** is "sufficiently" localized so that

$$\langle h_k|H_{12}|h_l\rangle = \langle h_k|H_{12}|h_k\rangle\delta_{kl} \tag{26}$$

then for large n

$$\begin{aligned} W &\approx \frac{N}{2} w \\ w &= \frac{1}{n}\sum_{k=1}^{n} \langle h_k|H_{12}|h_k\rangle \end{aligned} \tag{27}$$

We now assume that the pairing is based on a *fundamental interaction* with all matrix elements $\langle h_k\,|H_{12}\,|h_l\rangle = w_{LS}$, being constant provided that the localization centres are all inside a fundamental radius (later to be connected with the Schwarzschild radius). Note that the second term in Eq. (25) vanishes rigorously here. From Eq. (25), we will achieve remarkable energy stabilization (cf. Eq. (27) (for $n \gg N/2$))

$$W = \lambda_L \langle g_1|H_{12}|g_1\rangle = \lambda_L n w_{LS} = \frac{N}{2}\overline{n} w_{LS}; \quad (n-1) < \overline{n} < n \tag{28}$$

Note that $n = N/2$ corresponds to the independent particle model analogous to the celebrated Hartree–Fock equations in atomic and molecular physics. We also observe that the fundamental interaction mentioned above is unitarily connected with the electromagnetic interactions between the particle m_0 and the antiparticle $-m_0$. Since we do not make any distinctions between the Klein–Gordon and the Dirac equation, we are not able here to integrate the electro-weak theory although in principle this should be possible.

The large energy stabilization as a consequence of the fundamental interaction above is indicative of the possible existence of a black hole. To give an interpretation of this phenomenon, we envisage that the ''big bang'' through e-doubling (see more below) generates matter from the condensation of a sufficient amount of particle–antiparticle pairs.

Conversely, we predict fermion pairs located in the setting of a particle–antiparticle or vacuum-like environment. Here one can refer to general mirror theorems valid for the quantum mechanical description of such situations [8,20]. Hence the basis **h** is defined by localizing each function at associated ''nuclear'' sites. If these sites are appropriately condensed, so that the stabilization (28) occurs, we may have ODLRO. The emergence of a black hole is somewhat analogous to a Bose condensate. We may thus picture a set of fermion pairs, system I, as separated from the ''large particle'' system II. From Eq. (28), we note that the stabilization energy W is proportional to the product of the number of the particles of system I and the ones of system II with the proportionality factor given by the matrix element w_{LS} depending on the fundamental interaction H_{12} between the particle–antiparticle pair and the local properties (cusps, etc.) of h_k at a site k. An equivalent situation appears by exchanging the systems I and II, using the mirror theorem [8,20]. Hence we are able to associate the energy W with a macroscopically large system of mass M interacting with N particles of mass m and $-m$, respectively. Note that the condensate will contain an equal amount of particles and antiparticles. It also appears natural to connect Yang's concept of ODLRO in this situation with the (false) vacuum state of QED (cf. the Higg's mechanism). We will not dwell on this question here or the related analysis of appropriate order parameters as well as relevant thermodynamic limits.

We will now extend the present model to include gravitational interactions by augmenting the model presented in the previous section with a general scalar interaction as follows in the basis $|m, \overline{m}\rangle$:

$$\mathbf{H} = \begin{pmatrix} m - W/c^2 & -iv \\ -iv & -(m - W/c^2) \end{pmatrix} \tag{29}$$

with $v = p/c$ as before. We will assume that the particles and the antiparticles are sufficiently far away from the system II, characterized by M and that electromagnetic fields are not important here, although they in principle could be included in analogy with Eq. (17). By making use of conventional decompositions of p^2 in terms of spherical variables (more general symmetries

could of course be analysed here if needed) we obtain

$$p^2 = p_r^2 + \frac{\mathbf{J}^2}{r^2} \tag{30}$$

where $\mathbf{J}$ is the total angular momentum operator, which may, if needed, incorporate appropriate spin components. In a more detailed analysis, one might include a vector interpretation of the momentum operator $\boldsymbol{p}$ but for our purpose a scalar representation suffices. For simplicity we write

$$\frac{W}{c^2} = m\kappa(r) \tag{31}$$

where $\kappa(r) \geq 0$ depends on M, the coordinate r of the particle m (with origin in the centre of mass of M) and various fundamental constants. Eq. (29) then becomes converted into

$$\begin{aligned} \mathbf{H} &= \begin{pmatrix} m(1-\kappa(r)) & -iv \\ -iv & -m(1-\kappa(r)) \end{pmatrix} \\ \lambda^2 &= m^2(1-\kappa(r))^2 - \frac{p^2}{c^2} \\ \lambda &= m_0(1-\kappa(r)); \qquad v = \frac{p}{c} \end{aligned} \tag{32}$$

with the eigenvalue λ properly scaled as shown above. One gets further

$$\begin{aligned} m_0^2 &= \frac{m^2 - p^2}{(1-\kappa(r))^2 c^2} \\ \frac{\lambda_\pm}{(1-\kappa(r))} &= \pm m_0 = \pm\sqrt{m^2 - \frac{p^2}{(1-\kappa(r))^2 c^2}} \\ m &= \frac{m_0}{\sqrt{1-\beta'^2}}; \qquad \beta' \leq 1; \qquad 1 > \kappa(r) \\ \beta' &= \frac{p}{mc(1-\kappa(r))} = \frac{v}{c}(1-\kappa(r)) \end{aligned} \tag{33}$$

Note that the secular equation above can also be written in the dynamic representation

$$\mathbf{H} = \begin{pmatrix} m & -ip'/c \\ -ip'/c & -m \end{pmatrix}; \qquad p' = \frac{p}{(1-\kappa(r))} \tag{34}$$

where the particle of mass m is subject to the gravitationally modified momentum p'.

Let us first consider the case of a zero rest mass particle, i.e. $\lambda = m_0 = 0$. It follows

$$m^2c^4(1-\kappa_0(r))^2 = p^2c^2 \tag{35}$$

where the index "0" in κ_0 indicates that the gravitational interaction concerns the zero rest mass particle. Eq. (34) then becomes, see (10)

$$\mathbf{H}_{\text{deg}} = \begin{pmatrix} m & -im \\ -im & -m \end{pmatrix}$$

Using the decomposition (30) implies that the universal function $\kappa(r)$ (or $\kappa_0(r)$) may be written as

$$\begin{aligned} \kappa(r) &= \frac{\mu}{r} \\ \kappa_0(r) &= \frac{\mu_0}{r} \end{aligned} \tag{36}$$

where **J** for, for example a photon may be related to the polarization, and μ is independent of r.

For a particle with a non-zero mass (and possibly also a non-integer spin) one finds that for diminishing r the diagonal parts of the matrix in Eq. (32) get smaller in absolute magnitude, while the off-diagonal ones grow. A degeneracy occurs for $r = R_{\text{LS}}$, provided the mass M is entirely localized inside a sphere with radius R_{LS}

$$\frac{m}{2} = \frac{p}{c} = \frac{m\upsilon}{c} = m\kappa(r) = \frac{h\sqrt{j(j+1)}}{2\pi r}; \quad r = R_{\text{LS}} \tag{37}$$

where R_{LS}, see above, can now be identified with the Schwarzschild radius (note that $J = j(j+1)^{1/2}$ is the absolute magnitude of the total angular momentum of the particle (antiparticle)). Hence $\upsilon = c\kappa(r) = c\mu/r$; $r = R_{\text{LS}} = 2\mu$. With μ identified as the gravitational radius, R_{LS} is indeed the famous Schwarzschild radius of general relativity.

From Eq. (33) one has

$$\frac{\upsilon^2}{(1-\kappa(r))^2 c^2} \leq 1; \tag{38}$$

Hence one concludes, identifying μ with the gravitational radius and f with the gravitational constant, i.e.

$$R_{\text{LS}} = 2\mu; \quad \mu = \frac{f \cdot M}{c^2} \tag{39}$$

that $\upsilon/c = \mu/r$ corresponds to a singularity in Eq. (33) since $\beta' = 1$ (cf. also Eq. (47) below and a more general discussion at the end of this section).

Let us now consider the case with $p_r = 0$ implying that the particle (and similarly for the antiparticle) either orbits the system M or is so far away from the large system that there is no "gravitational" interaction between m and M. In this situation, we realize, see Eqs. (52) and (53) further below, that the kinematical interaction p/c equals $m\kappa(r)$ for a given value of r or

$$\frac{p}{c} = m\kappa(r) = \frac{m\mu}{r} = \frac{h\sqrt{j(j+1)}}{2\pi rc} \tag{40}$$

From Eq. (30) it follows

$$\begin{aligned} pr = J = \frac{h}{2\pi}\sqrt{j(j+1)}; \quad p = \frac{h}{\lambda} \\ \kappa(r) = \frac{\mu}{r} = \frac{h\sqrt{j(j+1)}}{2\pi m r} \end{aligned} \tag{41}$$

where λ is the wavelength of the particle. Eq. (41) embodies a Bohr-like quantum condition and a relationship between the angular momenta and the gravitational radius. It would be interesting to further analyse the linkage between the wavelength and the angular momentum in Eq. (41). Note also the difference between the coordinate r (and t) of a flat Euclidean space and the corresponding scales defining the curved space.

Returning now to the zero mass case, we note that we have a Jordan block situation irrespective of the value of r in Eq. (35). For a non-zero mass particle Eq. (39) determines the correct Schwarzschild radius. Hence consistency between Eqs. (35) and (36) and Eq. (39) requires

$$\kappa_0 = \frac{\mu_0}{r} = 2\kappa = \frac{2\mu}{r} \tag{42}$$

This means that a zero mass particle, like a photon, interacts ''twice as much'' with a gravitational field as a non-zero mass particle. This is of course in full agreement with the observations that lead to the original predictions and confirmations of the theory of general relativity.

In summary, the solution of the secular equations, Eqs. (32)–(34), corresponding to non-zero mass particles, may be written in analogy with Eqs. (2)–(7) as

$$\begin{aligned} \mathbf{H} = \begin{pmatrix} m(1-\mu/r) & -ip/c \\ -ip/c & -m(1-\mu/r) \end{pmatrix}; \quad \mu = \frac{f\cdot M}{c^2} \\ \lambda^2 = m^2\Big(1-\frac{\mu}{r}\Big)^2 - \frac{p^2}{c^2} \\ \lambda = m_0\Big(1-\frac{\mu}{r}\Big); \quad v = \frac{p}{c} \end{aligned} \tag{43}$$

and further

$$\begin{aligned} \lambda^2 = m^2\Big(1-\frac{\mu}{r}\Big)^2 - \frac{p^2}{c^2} \\ m_0^2 = \frac{m^2 - p^2}{(1-\mu/r)^2 c^2} \\ \frac{\lambda_\pm}{(1-\mu/r)} = \pm m_0 = \pm\sqrt{m^2 - \frac{p^2}{(1-\mu/r)^2 c^2}} \\ m = \frac{m_0}{\sqrt{1-\beta'^2}}; \quad r > \mu \\ \beta' = \frac{p}{mc(1-\mu/r)} = \frac{v}{c(1-\mu/r)} \end{aligned} \tag{44}$$

and finally

$$\begin{gathered}\lambda_+ = m_0; \quad |m_0\rangle = c_1|m\rangle + c_2|\overline{m}\rangle \\ \lambda_- = -m_0; \quad |\overline{m}_0\rangle = -c_2|m\rangle + c_1|\overline{m}\rangle \\ c_1 = \sqrt{\frac{1+X}{2X}}; \quad c_2 = -i\sqrt{\frac{1-X}{2X}}; \quad c_1^2 + c_2^2 = 1 \\ X = \sqrt{1-\beta'^2}; \quad \beta' = \frac{p'}{mc} = \frac{\upsilon}{c(1-\mu/r)}\end{gathered} \tag{45}$$

and

$$\begin{aligned}|m\rangle &= c_1|m_0\rangle - c_2|\overline{m}_0\rangle \\ |\overline{m}\rangle &= c_2|m_0\rangle + c_1|\overline{m}_0\rangle\end{aligned} \tag{46}$$

We note that if $\upsilon/c = \mu/r$ (see also Eqs. (52) and (53) below) then

$$\begin{gathered}\beta' = \frac{\upsilon}{c(1-\mu/r)} = \frac{\mu}{r-\mu} = 1 \\ r = R_{\mathrm{LS}} = 2\mu\end{gathered} \tag{47}$$

(cf. the zero-mass situation). At $r = R_{\mathrm{LS}}$ Eq. (32) may also be written

$$\begin{gathered}\mathbf{H}_{\mathrm{deg}} = \frac{1}{2}\begin{pmatrix} m & -im \\ -im & -m \end{pmatrix} \rightarrow \mathbf{H}_{\mathrm{deg}} = \begin{pmatrix} 0 & m \\ 0 & 0 \end{pmatrix} \\ |0\rangle = \frac{1}{\sqrt{2}}|m\rangle - i\frac{1}{\sqrt{2}}|\overline{m}\rangle \\ |\bar{0}\rangle = \frac{1}{\sqrt{2}}|m\rangle + i\frac{1}{\sqrt{2}}|\overline{m}\rangle\end{gathered} \tag{48}$$

Finally, we note that the following ''classical consistency'' relations hold. For particles with a non-zero rest mass, the energy law gives, using Eqs. (32) and (33)

$$\begin{gathered}d(mc^2(1-\kappa(r))) = d\mathbf{r}\cdot\frac{d\mathbf{p}'}{dt} + mc^2\frac{\kappa(r)}{r^2}\mathbf{r}\cdot d\mathbf{r} = 0 \\ p' = m\upsilon'; \quad \upsilon' = \frac{\upsilon}{(1-\kappa(r))}\end{gathered} \tag{49}$$

and assuming that we have central forces that

$$\mathbf{f}' = \frac{d\mathbf{p}'}{dt} = \mathbf{n}\cdot\frac{\kappa}{r}mc^2; \quad \mathbf{n} = -\frac{\mathbf{r}}{r}\mathbf{f}' = \frac{d\mathbf{p}'}{dt} = \mathbf{n}\frac{\kappa(r)}{r}mc^2; \quad \mathbf{n} = -\frac{\mathbf{r}}{r} \tag{50}$$

Note that the condition: $r > \mu = r\kappa(r) = (f\cdot M/c^2)$ follows from the definition of p'. Quantum conditions further yield $r \geq 2\mu$. Note the incompatibility between the force defined in Eq. (50) and the energy law defined by the theory of special theory of relativity. One should note here that Einstein, in his studies of the general theory of relativity, started from the force law

$$\mathbf{f} = \frac{d\mathbf{p}}{dt} = \mathbf{n}\frac{\kappa(r)}{r}mc^2; \quad \mathbf{n} = -\frac{\mathbf{r}}{r} \tag{51}$$

which gives a different result. However, it is important to recognize that the Hamiltonian behind Eq. (49) refers to an open system, where the degrees of

freedom associated with the mass M are left out. Hence in a quantum mechanical setting the variational principle corresponding to Eq. (49) becomes a stationary one without extremum properties. Noting that the angular momentum, $m\upsilon r$, for a particle under the influence of a central force is a constant of motion, we obtain (here $m = \hat{m}_{\mathrm{op}}$ has the eigenvalue m_0) Eq. (52) where the constant is evaluated for the limiting velocity c and the limiting distance being the gravitational radius, i.e.

$$m_0 \upsilon r = m_0 c \mu \tag{52}$$

From this follows the relation

$$\upsilon = \kappa(r)c = \frac{\mu c}{r} \tag{53}$$

generalizing the discussion in connection with the relations (37)–(41).

5. CONCLUSIONS

The present model is quite surprising in its simplicity and yet the interpretation is very different compared to classical and quantum mechanical pictures. The ansatz Eq. (2) implies that every fundamental quantum particle will occupy one of two quantum states. When the choice is made the associated antiparticle will be indirectly recognized through the kinematical interaction v and the appearance of the length- and time-scale contractions. We do not, therefore, directly experience mirror- (anti-)particles, unless they are bodily excited. Within the present description, we have proposed a generalized quantum description, which transcends classical features as the contraction of scales mentioned above, including also a dynamical formulation of gravitational interactions.

We have also pointed out that one can include without contradiction the electromagnetic field. As already mentioned in Section 3, the embedding of standard quantum mechanics in the complex symmetric description in general breaks gauge invariance. Howland [21] has discussed the question of gauge transformations in connection with analytic extensions (complex scaling) of quantum mechanics including the electromagnetic field showing that the essential spectrum of Floquet Hamiltonians rotate about a certain set of thresholds when subject to a suitable gauge. Nevertheless the present simplified description is still commensurate with Klein–Gordan–Dirac theories.

The appealing association of the "structures" in Eqs. (10)–(13) with the properties of the vacuum has been observed. It is further tempting to connect the limiting behaviour of an expanding universe with the occurrence of black holes with unique properties and related predicting power. It is anticipated that the present Jordan block representations will throw additional light on the properties of general QED-like structures, so as to give additional information on broken symmetry issues, the mass generation puzzle etc.

It has been demonstrated that a strongly correlated, including ODLRO, many-body theory based on particles (and antiparticles) will lead to immense energy stabilization provided a *fundamental interaction* operates inside a principal radius.

Our initial model, including the gravitational field, displays a dynamical formulation where velocities and momenta are appropriately scaled. It is further established that for non-zero rest mass particles a discontinuous behaviour in the mass eigenvalue occurs at the Schwarzschild radius. This irregularity stems from the appearance of a so-called Jordan block. To be consistent zero rest mass particles interact ''twice as much'' with the gravitational field. Precise relations are given between the gravitational interaction and the corresponding angular momenta. Whether these characteristics have anything to do with the dark-energy-matter problem should be an inviting possibility.

We have previously observed that the repeated use of Eqs. (12) and (13), after diagonalization, followed by a new degenerate Jordan block state, yields e-doubling. The expansion of the universe, i.e. Hubble's law, possibly due to a distant hidden black hole-like structure, could in principle lead to amplified contractions of time and length dimensions. From Eq. (34), i.e. reassigning $p \to p' = p(1 - \kappa(r))$ follows the interpretation that the momentum will be r-dependent.

In summary, the model allows for two types of interactions between the mirror spaces, the weak kinematical perturbation and the adiabatic and sudden limits equivalent to Eq. (17) or Eqs. (29)–(34). The overwhelming rate of particles over antiparticles in the Universe is inferred in this picture once the particular particle state has been selected. The Minkowski metric of the special theory of relativity is represented here by a non-positive definite metric, Eq. (8), bringing about a quantum model with a complex symmetric ansatz. Although the latter permits general symmetry violations, it is nevertheless surprising that fundamental transformations between complex symmetric representations and canonical forms come out unitary.

It also remains to be seen whether the present picture would allow for gravitational waves as predicted by the Einstein's general theory of relativity. On one hand, the present quantum model would not be against ''action at a distance''; on the other hand, a different, perhaps a soliton-like mechanism, would be needed to produce the latter.

There is finally the possibility of decay-like leakages between the particle–antiparticle spaces, and further that there could be an overall escape out of the presently defined spaces. If so associated Jordan blocks naturally appearing would decelerate this decay via the polynomial delay mechanism described earlier [7–10] with implications to subject matters like problems related to size of the cosmological constant. Also, the account given here should consider a more general decomposition of p^2 into curvilinear coordinates (cf. Eq. (30)) in order to yield a more appropriate analysis (see e.g. [22] and references therein).

ACKNOWLEDGMENTS

I gratefully acknowledge financial support from the The Japan Society for the Promotion of Science (JSPS). I am further particularly indebted to the Chairmen of the International DV-Xα Symposium, Profs. M. Morinaga and B.I. Kim for generous hospitality and support.

REFERENCES

[1] E.B. Bolles, *Einstein Defiant. Genius versus Genius in the Quantum Revolution*, Joseph Henry Press, Washington, DC, 2004, pp. 286.
[2] I.P. Grant, H.M. Quiney, Application of relativistic theories and quantum electro-dynamics to chemical problems, *Int. J. Quant. Chem.* **80** (2000) 283–297.
[3] E.B. Karlsson, E.J. Brändas, Modern studies of basic quantum concepts and phenomena, *Phys. Scr.* **T76** (1998) 7–15.
[4] J. Aguiar, J.M. Combes, A class of analytic perturbations for one-body Schrödinger Hamiltonians, *Commun. Math. Phys.* **22** (1971) 269–279.
[5] E. Balslev, J.M. Combes, Spectral properties of many-body Schrödinger operators with dilatation: Analytic interactions, *Commun. Math. Phys.* **22** (1971) 280–294.
[6] B. Simon, Resonances in *n*-body quantum systems with dilatation analytic potentials and the foundations of time-dependent perturbation theory, *Ann. Phys.* **97** (1973) 247–274.
[7] E. Brändas, Dynamics during spectroscopic transitions, In: E. Lippert, J.D. Macomber (Eds.), *Relaxation Processes and Coherent Dissipative Structures*, Springer Verlag, Berlin, 1995, pp. 148–193.
[8] E.J. Brändas, Quantum concepts and complex systems, *Int. J. Quant. Chem.* **98** (2004) 78–86.
[9] E.J. Brändas, Are Jordan blocks necessary for the interpretation of dynamical processes in nature? *Adv. Quant. Chem.* **47** (2004) 93–106.
[10] E.J. Brändas, Some theoretical problems in chemistry and physics, *Int. J. Quant. Chem.* **106** (2006) 2836–2839.
[11] M. Stanke, J. Karwowski, Recent advances in the theory of chemical and physical systems, In: J.-P. Julien, J. Maruani, S. Wilson, G. Delgado-Barrio (Eds.), *Non-Standard Representations of the Dirac Equation and the Variation Method*, Springer, Dordrecht, The Netherlands, 2006, pp. 217–228.
[12] J. Karwowski, G. Pestka, M. Stanke, F.E. Harris, Representation of the Dirac equation and the variational principle, *Int. J. Quant. Chem.* **106** (2006) 3129–3139.
[13] E.J. Brändas, Introduction to the concept of resonances, *Int. J. Quant. Chem.* **31** (1987) 699–705.
[14] E.J. Brändas, N. Elander, Resonances-the unifying route towards the formulation of dynamical processes-foundations and applications in nuclear, atomic and molecular physics, In: E. Brändas, N. Elander (Eds.), *Introduction*, Springer Verlag, Lecture Notes in Physics, 1989, Vol. 325, pp. iii–viii.
[15] E.J. Brändas, Resonances and microscopic irreversibility: An introduction, *Int. J. Quant. Chem.* **46** (1993) 339–341.
[16] C.N. Yang, *Rev. Mod. Phys.* **34** (1962) 694.
[17] A.J. Coleman, *Rev. Mod. Phys.* **35** (1963) 668.
[18] F. Sasaki, Technical Report 77, Uppsala Quantum Chemistry Group (1962);
F. Sasaki, *Phys. Rev.* **138B** (1965) 1338.
[19] A.J. Coleman, V.I. Yukalov, *Reduced Density Matrices Coulson's Challenge, Lecture Notes in Chemistry*, Vol. 72, Springer-Verlag, Berlin, 2000.
[20] E. Schmidt, Math. Ann. Phys. **63** (1907) 433; B.C. Carlson, J.M. Keller, Phys. Rev. **121** (1961) 659.
[21] J.S. Howland, Complex scaling of ac Stark Hamiltonians, *J. Math. Phys.* **24** (1983) 1240–1244.
[22] T. Levitina, E.J. Brändas, On the Schrödinger equation in ellipsoidal coordinates, *Comp. Phys. Commun.* **126** (2000) 107–113.

CHAPTER 11

Electronic Structures of $ATiO_3$ Perovskite Oxides (A = Ba, Sr, and Pb): Comparative First-Principles Study

Hironori Kawanishi, Keisuke Ishizumi, Isao Takahashi, Hikaru Terauchi and **Yoshinori Hayafuji**

Contents

Abstract

A comparative study of the electronic structures of $BaTiO_3$, $SrTiO_3$, and $PbTiO_3$ is carried out in order to specify the atomistic factors distinguishing the type of phase transition, whether ferroelectric or antiferrodistortive (rotating-type), in $ATiO_3$ perovskite oxides. The electronic structures of $BaTiO_3$, $SrTiO_3$, and $PbTiO_3$ in a cubic lattice are investigated using the discrete variational-Xα molecular orbital method. The changes in the strength of the A–O (A = Ba, Sr, and Pb) and Ti–O covalent interactions are evaluated as a function of the rotation angle of TiO_6 octahedron, the ferroelectric displacement of Ti and O, and the lattice constant. Comparison of the calculated results indicates that the rotation of TiO_6 octahedron and the ferroelectric displacement are dominated by the A–O and Ti–O

School of Science and Technology, Kwansei Gakuin University, 2-1 Gakuen, Sanda, Hyogo 669-1337, Japan
Corresponding author. E-mail: hayafuji@ksc.kwansei.ac.jp

Advances in Quantum Chemistry, Vol. 54
ISSN 0065-3276, DOI 10.1016/S0065-3276(07)00011-1

covalent interactions, and that the type of phase transition that occurs (ferroelectric or antiferrodistortive) in these perovskite oxides is governed by the delicate balance between the strength of the A–O and Ti–O covalent interactions.

1. INTRODUCTION

Perovskite oxides represented by the chemical formula ABO_3 have attracted much interest for many technological applications such as electro-optical, piezoelectric, and ferroelectric devices. Therefore, it is important to understand the physical property of ABO_3 perovskite oxides, and these oxides have been the subject of extensive investigation. The physical behavior of ABO_3 perovskite oxides is strongly influenced by the replacement of A- or B-site atoms. For example, the phase transitions displayed by $ATiO_3$ perovskite differ depending on the kind of atom at the A-site. At high temperature, $ATiO_3$ perovskite oxides (A = Ba, Sr, and Pb) form a paraelectric phase with a cubic structure. As the temperature is reduced, $BaTiO_3$ and $PbTiO_3$ display a ferroelectric phase transition from the cubic paraelectric phase to the tetragonal ferroelectric phase, while $SrTiO_3$ undergoes an antiferrodistortive (rotating-type) phase transition [1] from the cubic paraelectric to the tetragonal antiferrodistortive phase (rotating phase), involving the rotation of TiO_6 octahedron around the z-axis so as to maintain the TiO_6 octahedral shape.

The physical property of ABO_3 perovskite oxides with various A- and B-site atoms have been reported extensively. Cohen [2], and Cohen and Krakauer [3] reported the origin of ferroelectricity in $ATiO_3$ perovskite oxides (A = Ba and Pb) by a first-principles full-potential linear augmented plane-wave (FLAPW) approach, and pointed out that the covalent interaction between Ti 3d and O 2p orbitals is essential for the appearance of ferroelectricity. Miura and Tanaka [4,5] also reported the origins of ferroelectricity in $PbTiO_3$ based on a first-principles linear combination of atomic orbitals (LCAO) method, and concluded that the spatial change in O 2p electrons due to the covalent interaction between O 2p and Pb 6s orbitals is one of the origins of ferroelectricity in $PbTiO_3$. Yoshino et al. [6] also calculated the electronic structure of $SrZrO_3$ by a first-principles LCAO method, and showed that the phase transition in $SrZrO_3$ takes place by the successive rotation or tilting of ZrO_6 octahedron so as to maintain the strength of the Zr–O and Sr–O bonds. Kuroiwa and co-workers [7,8] investigated the effect of atomic replacement on the phase transition by determining the electronic distributions for cubic $BaTiO_3$, $SrTiO_3$, and $PbTiO_3$ from synchrotron X-ray powder diffraction data, and showed that the electronic distributions around O atoms and the covalency of A–O bonds (A=Ba, Sr, and Pb) differ among the cubic $BaTiO_3$, $SrTiO_3$, and $PbTiO_3$ phases.

A tolerance factor [9,10] can be used to determine the phase transition in ABO_3 perovskite oxides, as given by $t = (r_A + r_O)/\sqrt{2}(r_B + r_O)$, where r_A, r_B, and r_O are the ionic radii [11] of the A, B, and O ions, respectively. This indicates that the spatial margin relates to the type of phase transition. However, the atomistic explanation has not been given for the factor in order to distinguish between ferroelectric and antiferrodistortive phase transitions in ABO_3 perovskite oxides.

In this paper, the electronic structures of $BaTiO_3$, $SrTiO_3$, and $PbTiO_3$ are calculated by a first-principles approach, and the atomistic factors governing the occurrence of the ferroelectric or antiferrodistortive phase transition in $ATiO_3$ perovskite oxides are discussed on the basis of comparative chemical bond strength. The change in the strength of the A–O covalent interaction is determined as a function of the rotation angle of TiO_6 octahedron, and the strength of the Ti–O covalent interaction is evaluated as a function of the ferroelectric displacement of Ti and O. Also, the changes in the strength of the A–O and Ti–O covalent interactions are evaluated as a function of the lattice constant.

2. DETAILS OF MODEL AND CALCULATIONS

First-principles calculations of electronic structures were carried out using a series of model clusters composed of an $A_8Ti_7O_{36}$ cluster (A = Ba, Sr, and Pb), as shown in Figure 11.1, embedded at the center of a three-dimensional (3D) point charge array. Point charges were used to create a Madelung potential for a model of ionic crystals in first-principles calculations. The initial charge states of the ions were set as A^{2+} (A = Ba, Sr, and Pb), Ti^{4+}, and O^{2-}. Except for the calculations in Section 3.3, the lattice constants were fixed at the experimental values for the cubic phase: $a = 4.011$ Å [12], 3.905 Å [13], and 3.968 Å [14] for $BaTiO_3$, $SrTiO_3$, and $PbTiO_3$, respectively.

The electronic structures of a series of models were calculated using the first-principles discrete variational-Xα (DV-Xα) molecular orbital (MO) method with a

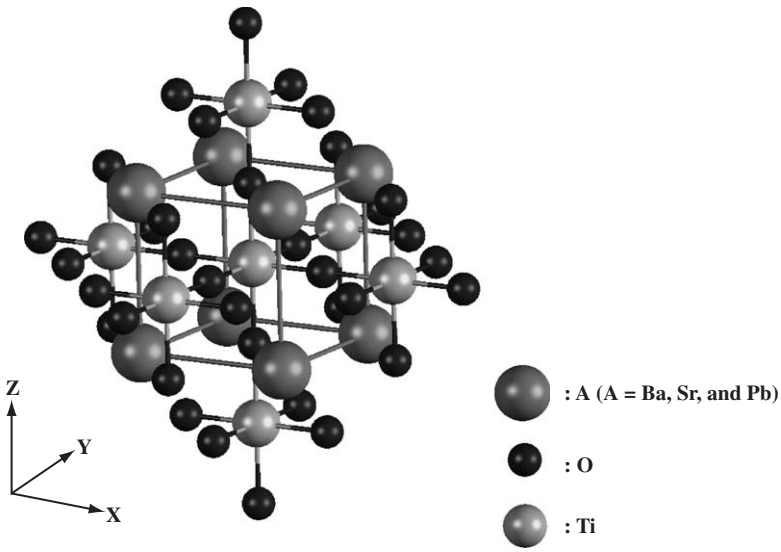

Figure 11.1 $A_8Ti_7O_{36}$ cluster (A = Ba, Sr, and Pb) embedded at the center of a 3D point-charge array.

LCAO expansion of the MOs [15]. In the DV-Xα MO method based on the Hartree–Fock–Slater approach, the exchange-correlation potential is approximated by the simple Slater form [16] $V_{xc}(\mathbf{r}) = -3\alpha\{3\rho(\mathbf{r})/4\pi\}^{1/3}$, where the coefficient α is a scaling parameter (fixed at 0.7 in the present study) and $\rho(\mathbf{r})$ is the local electron density at a position $\mathbf{r}$. The basis functions for the MO calculation consisted of atomic orbital wave eigenfunctions obtained in numerical form, which included the 1s–6s, 1s–5s, 1s–6p, 1s–4p, and 1s–2p orbitals for Ba, Sr, Pb, Ti, and O ions, respectively.

Mulliken overlap population analysis [17] was employed to analyze the covalent bonding between pairs of atoms. The covalency of a chemical bond between G and H ions was evaluated from the bond overlap population (BOP), as given by $Q_{GH} = 2\sum_{G,H} Q_{ij}$ $(Q_{ij} = (\sum_k Q_{ij}^k))$, where Q_{ij}^k is the partial overlap population, that is, the electron population of the overlapped region between the atomic orbitals χ_i and χ_j in the MO φ_k. The magnitude of BOP corresponds to the strength of the covalent interaction. In this study, the change of A–O_{x+} BOP is evaluated as a function of the rotation of TiO_6 octahedron around the z-axis, and that of Ti–O_{z+} BOP is determined as a function of the ferroelectric displacement of Ti and O along the z-axis. Also, the changes in A–O_{x+} and Ti–O_{x+} BOPs are evaluated as a function of the lattice constant. Here, O_{x+} and O_{z+} denote the oxygen ions neighboring Ti in the center of the cluster on the $+x$ and $+z$ sides, respectively. Also, Ti refers to the Ti ion at the center of the cluster, and A (A = Ba, Sr, or Pb) denotes an A ion neighboring O_{x+}.

3. RESULTS AND DISCUSSION

3.1 Changes in four A–O_{x+} bond overlap populations as a function of TiO_6 rotation around the z-axis

The changes in four A–O_{x+} BOPs as a function of the rotation of TiO_6 octahedron around the z-axis in $BaTiO_3$, $SrTiO_3$, and $PbTiO_3$ are shown in Figure 11.2, where four A–O_{x+} BOPs are divided into two near (in the direction of O_{x+} displacement) and two far (opposite direction to O_{x+} displacement) BOPs, namely two A_{near}–O_{x+} and two A_{far}–O_{x+} BOPs, respectively. In $BaTiO_3$ and $SrTiO_3$, sum of two A_{near}–O_{x+} BOPs decreases monotonically with increasing TiO_6 rotation, while sum of two A_{far}–O_{x+} BOPs increases. The opposite trend is observed for $PbTiO_3$. The magnitude of the changes in A–O_{x+} BOPs is larger in $PbTiO_3$ than in $SrTiO_3$, and smaller in $PbTiO_3$ than in $BaTiO_3$.

In the cubic lattice forms of $BaTiO_3$, $SrTiO_3$, and $PbTiO_3$, the TiO_6 octahedron normally displays zero rotation. The changes in A–O_{x+} BOPs as a function of TiO_6 octahedron rotation are, therefore, expected to reflect increases in the forces acting to return the TiO_6 octahedron to zero rotation, resulting in more unstable in the antiferrodistortive phase. The more stable in the antiferrodistortive phase, the more easily antiferrodistortive phase transition can take place. Therefore, the present results suggest a higher probability of the antiferrodistortive phase transition in $PbTiO_3$ than in $BaTiO_3$, and a lower probability compared to $SrTiO_3$.

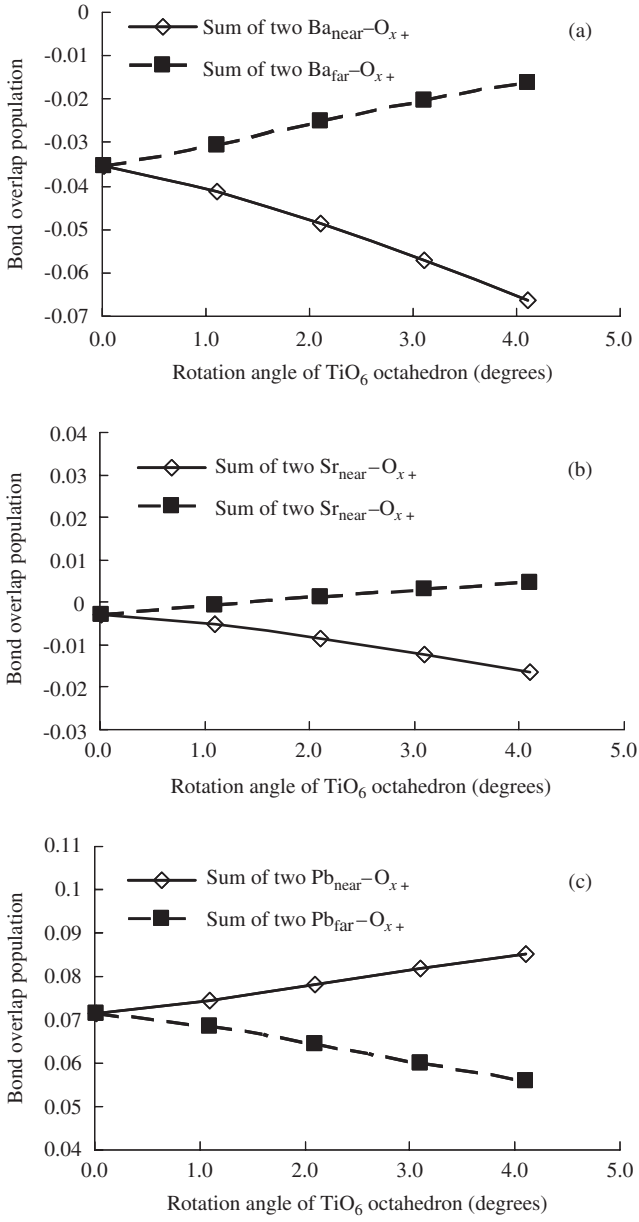

Figure 11.2 Changes in sum of two A_{near}–O_{x+} BOPs and sum of two A_{far}–O_{x+} BOPs (A = Ba, Sr, and Pb) as a function of the rotation angle of TiO_6 octahedron in (a) $BaTiO_3$, (b) $SrTiO_3$, and (c) $PbTiO_3$.

Because of the fixed cubic lattice, in this study, the TiO_6 octahedron is slightly elongated in the directions of the *x*- and *y*-axes by TiO_6 rotation. But, it is believed that such a distortion of TiO_6 octahedron does not affect the probability of the antiferrodistortive phase transition.

Munkholm et al. [18] revealed the antiferrodistortive reconstruction of the $PbTiO_3$ (0 0 1) surface through grazing incidence X-ray scattering measurements. Bungaro and Rabe [19], based on the first-principles plane-wave pseudopotential calculations, reported enhancement of the antiferrodistortive instability at the PbO termination on the $PbTiO_3$ surface, but no such enhancement of antiferrodistortive distortion on the $BaTiO_3$ surface. The results of these reports are in agreement with the present result that the possibility of the antiferrodistortive phase transition is higher in $PbTiO_3$ than in $BaTiO_3$, although there are the differences in electrostatic potential and bonding state between the surface and the bulk.

3.2 Change in Ti–O_{z+} bond overlap population as a function of ferroelectric displacement of Ti and O along the *z*-axis

The change in Ti–O_{z+} BOP as a function of the ferroelectric displacement of Ti and O along the *z*-axis in $BaTiO_3$, $SrTiO_3$, and $PbTiO_3$ is shown in Figure 11.3. Ti and O are displaced toward the $+z$ and $-z$ directions, respectively. As indicated by the arrows in Figure 11.3(a) and (c), Ti–O_{z+} BOP reaches the maximum at a ferroelectric displacement of approximately 0.025 Å in $BaTiO_3$ and $PbTiO_3$. The ferroelectric phase transition is believed to be caused by the motive force moving Ti and O atoms toward the positions corresponding to the maximum BOP. On the other hand, Ti–O_{z+} BOP in $SrTiO_3$ reaches the maximum at a ferroelectric displacement of zero for both Ti and O (Figure 11.3(b)), indicating that the $SrTiO_3$ lattice does not impart motive force to displace Ti and O atoms from the respective intrinsic positions. This lack of motive force allows the paraelectric phase to be retained.

Miura and Tanaka [4,5] reported that Ti–O_{z+} BOP is correlated with the total energy with respect to Ti displacement along the [0 0 1] direction in $PbTiO_3$, and the maximum Ti–O_{z+} BOP occurs at the minimum total energy. It has also been reported [2,3,20] that the potential surface of Ti displacement or the coupled displacement of Ti and O along the [0 0 1] direction is a double-well potential in $BaTiO_3$ and $PbTiO_3$, and a single-well potential in $SrTiO_3$. Hence, in consideration of these previous reports, the present results are considered to show that the minimum energy of $BaTiO_3$ and $PbTiO_3$ corresponds to the ferroelectric phase with a double-well potential, while the minimum-energy phase of $SrTiO_3$ is the paraelectric phase with a single-well potential. The occurrence of the ferroelectric phase transition with the displacement of Ti and O is thus concluded to be possible in $BaTiO_3$ and $PbTiO_3$, but not in $SrTiO_3$.

3.3 Changes in A–O_{x+} and Ti–O_{x+} bond overlap populations with zero rotation of TiO_6 octahedron and zero displacement of Ti and O as a function of the lattice constant

The changes in A–O_{x+} and Ti–O_{x+} BOPs with zero rotation of TiO_6 octahedron and zero displacement of Ti and O as a function of the lattice constant in $BaTiO_3$, $SrTiO_3$, and $PbTiO_3$, which are evaluated in the range of 3.58–4.62 Å without

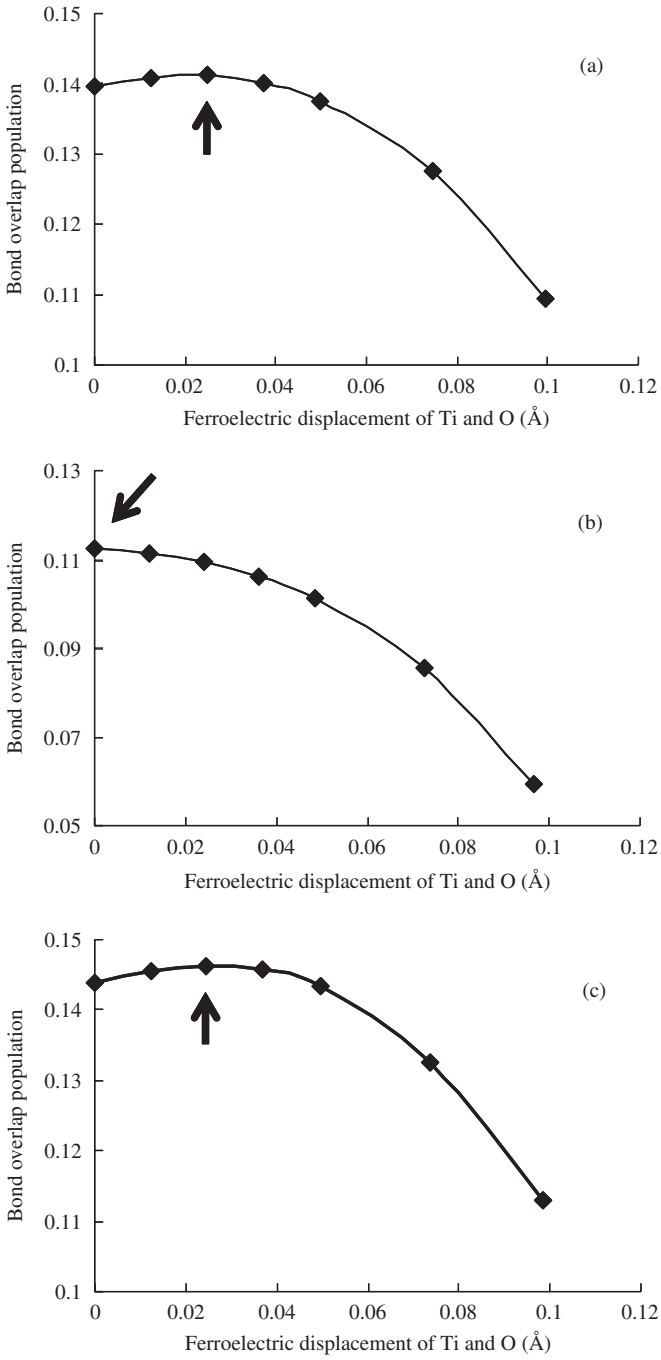

Figure 11.3 Change in $Ti–O_{z+}$ BOP as a function of the ferroelectric displacement of Ti and O in (a) $BaTiO_3$, (b) $SrTiO_3$, and (c) $PbTiO_3$. Arrows indicate the positions of maximum $Ti–O_{z+}$ BOPs.

considering the occurrence of phase transition and changing into a tetragonal lattice, are shown in Figures 11.4 and 11.5, respectively. The four pairs of A–O_{x+} BOPs are equivalent in this state. Ti–O_{x+} BOP shows an analogous decreasing tendency with decreasing the lattice constant in the three perovskite oxides although the magnitude of Ti–O_{x+} BOP is slightly different among the three perovskite oxides. A–O_{x+} BOP also decreases with decreasing the lattice constant in the three perovskite oxides, but the nature of A–O_{x+} BOP is much different among $BaTiO_3$, $SrTiO_3$, and $PbTiO_3$. Pb–O_{x+} BOP is positive at the lattice constant above 3.64 Å, and changes above zero. Sr–O_{x+} BOP decreases in the vicinity of zero with decreasing the lattice constant. The tendency of the change in Ba–O_{x+} BOP is different from the case of Pb–O_{x+} and Sr–O_{x+} BOPs, and Ba–O_{x+} BOP greatly decreases with decreasing the lattice constant. It is notable that Ba–O_{x+} BOP is negative with a repulsive sense at the lattice constant below 4.22 Å.

Next, the magnitude of A–O_{x+} and Ti–O_{x+} BOPs, and the relationship between A–O_{x+} and Ti–O_{x+} BOPs with zero rotation of TiO_6 octahedron and zero displacement of Ti and O at the three lattice constants, which are $a = 4.011$ Å ($BaTiO_3$ lattice), 3.905 Å ($SrTiO_3$ lattice), and 3.968 Å ($PbTiO_3$ lattice), are evaluated

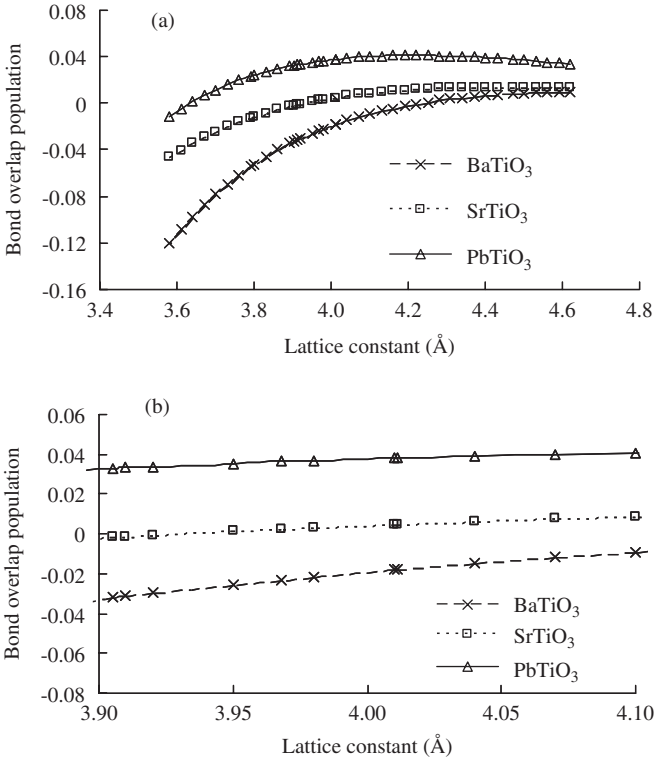

Figure 11.4 (a) Change in A–O_{x+} BOP (A = Ba, Sr, and Pb) with zero rotation of TiO_6 octahedron and zero displacement of Ti and O as a function of the lattice constant in $BaTiO_3$, $SrTiO_3$, and $PbTiO_3$. (b) Extended figure in (a).

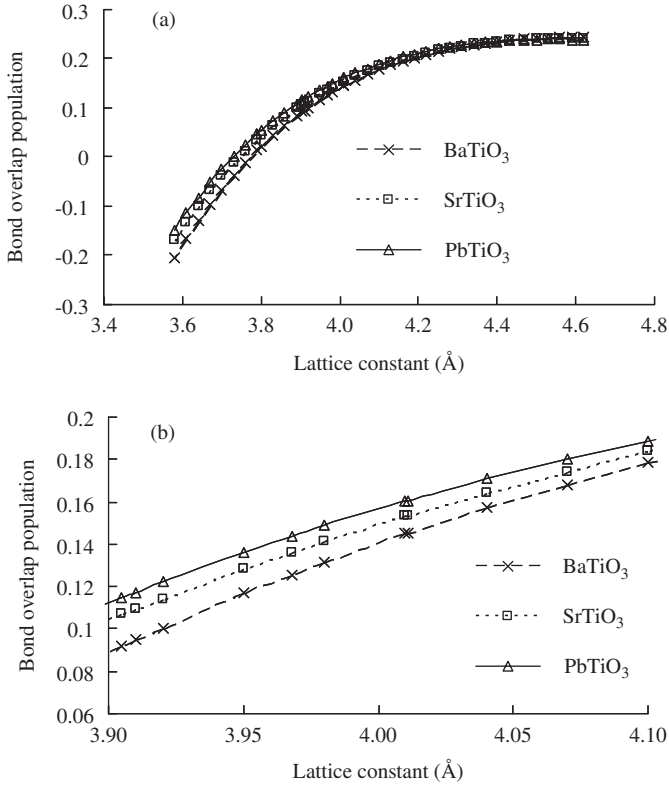

Figure 11.5 (a) Change in Ti–O_{x+} BOP with zero rotation of TiO_6 octahedron and zero displacement of Ti and O as a function of the lattice constant in $BaTiO_3$, $SrTiO_3$, and $PbTiO_3$. (b) Extended figure in (a).

in $BaTiO_3$, $SrTiO_3$, and $PbTiO_3$ (Table 11.1). Through comparison on the material-specific lattice constant, the present results show that Ti–O_{x+} BOP is much larger in $PbTiO_3$ than in $SrTiO_3$, and a little smaller in $PbTiO_3$ than in $BaTiO_3$. These differences are considered to be much affected by the Ti–O distance. As for A–O_{x+} BOP, the present results show that the Ba–O and Pb–O covalent interactions have repulsive antibonding and attractive bonding character, respectively. It remains controversial whether the Ba–O bond is entirely ionic [2,3] or involves some covalent interaction [21–24]. However, the present result shows that the Ba–O bond has some degree of covalent interaction with repulsive antibonding sense. The present result also shows that Sr–O BOP is almost zero, and the Sr–O bond hardly exhibits either a repulsive or attractive covalent interaction.

It has been reported based on the analysis of synchrotron X-ray powder diffraction data that the electronic distribution around the O atom is elongated in the directions perpendicular to the Ti–O covalent bond in $SrTiO_3$, but not in $BaTiO_3$ or $PbTiO_3$ [8]. Such a result may be associated with the present finding that the Ba–O and Pb–O bonds involve covalent interactions with repulsive and

Table 11.1 A–O_{x+} (A = Ba, Sr, and Pb) and Ti–O_{x+} BOPs in the zero-rotation and zero-displacement cubic phase of $BaTiO_3$, $SrTiO_3$, and $PbTiO_3$

		$BaTiO_3$ lattice 4.011 (Å)	$PbTiO_3$ lattice 3.968 (Å)	$SrTiO_3$ lattice 3.905 (Å)
$BaTiO_3$	Ba–O_{x+} BOP	−0.0177	−0.0230	−0.0321
	Ti–O_{x+} BOP	0.1454	0.1258	0.0922
$SrTiO_3$	Sr–O_{x+} BOP	0.0050	0.0026	−0.0016
	Ti–O_{x+} BOP	0.1539	0.1363	0.1068
$PbTiO_3$	Pb–O_{x+} BOP	0.0381	0.0363	0.0329
	Ti–O_{x+} BOP	0.1607	0.1438	0.1150

Note: A–O_{x+} and Ti–O_{x+} BOPs are evaluated at the three lattice constants: $a = 4.011$, 3.968, and 3.905 Å.

attractive senses, while the interaction related to the Sr–O bond has no attractive/repulsive nature because the A–O covalent interaction affects the electronic distribution of the O atom. Thus, $BaTiO_3$ and $PbTiO_3$, which undergo a ferroelectric phase transition, have A–O bonds involving either repulsive or attractive covalent interaction, while $SrTiO_3$, which displays an antiferrodistortive phase transition, involves no such interaction.

Through comparison on the same lattice constant at each of the three lattice constants, it is shown that Ti–O_{x+} BOP is larger in $SrTiO_3$ than in $BaTiO_3$, and smaller in $SrTiO_3$ than in $PbTiO_3$, and the same trend is observed for A–O_{x+} BOP. Hence, the present results suggest that the A–O covalent interaction affects the Ti–O covalent interaction, and the A–O covalent bond plays an important role on the physical behavior although the A–O covalent interaction is much weaker than the Ti–O covalent interaction. The effect of the A-site atom on the Ti–O covalent bond can be seen clearly through comparison on the same lattice constant.

4. CONCLUSION

A comparative study of the electronic structures of $BaTiO_3$, $SrTiO_3$, and $PbTiO_3$ was carried out to identify the atomistic factors distinguishing the ferroelectric and antiferrodistortive (rotating-type) phase transitions in $ATiO_3$ perovskite oxides. The study was performed through analyses of the strength of chemical bonds by the DV-Xα MO method.

The changes in the four A–O_{x+} covalent interactions were evaluated as a function of the rotation of TiO_6 octahedron around the z-axis in the three perovskite oxides, and it was concluded that the probability of the antiferrodistortive phase transition is higher in $SrTiO_3$ than in $PbTiO_3$, and lower in $BaTiO_3$ than in $PbTiO_3$.

Evaluation of the change in the Ti–O_{z+} covalent interaction as a function of the ferroelectric displacement of Ti and O along the z-axis revealed that the

occurrence of a ferroelectric phase transition with the displacement of Ti and O is possible in $BaTiO_3$ and $PbTiO_3$, but not in $SrTiO_3$.

The changes in the A–O_{x+} and Ti–O_{x+} covalent interactions were evaluated as a function of the lattice constant. Ti–O_{x+} BOP showed an analogous decreasing tendency with decreasing the lattice constant in the three perovskite oxides. A–O_{x+} BOP also decreased with decreasing the lattice constant in the three perovskite oxides, but the tendency of the change in A–O_{x+} BOP was much different among $BaTiO_3$, $SrTiO_3$, and $PbTiO_3$. Through comparison on the material-specific lattice constant, it was shown that $BaTiO_3$ and $PbTiO_3$, which display a ferroelectric phase transition, have A–O bonds with a repulsive or attractive covalent interaction, whereas $SrTiO_3$, which undergoes an antiferrodistortive phase transition, does not exhibit repulsion or attraction in the interaction. Through comparison on the same lattice constant, the present results indicate that the A–O covalent interaction affects the Ti–O covalent interaction. Although the A–O covalent interaction is much weaker than the Ti–O covalent interaction, the strength of the A–O covalent interaction is considered to profoundly influence the physical behavior related to the phase transition. The present results thus suggest that the type of phase transition is governed by the delicate balance between the strength of the A–O and Ti–O covalent interactions.

REFERENCES

[1] H. Unoki, T. Sakudo, *J. Phys. Soc. Jpn.* **23** (1967) 546.
[2] R.E. Cohen, *Nature* **358** (1992) 136.
[3] R.E. Cohen, H. Krakauer, *Ferroelectrics* **136** (1992) 65.
[4] K. Miura, M. Tanaka, *Jpn. J. Appl. Phys.* **35** (1996) 2719.
[5] K. Miura, M. Tanaka, *Jpn. J. Appl. Phys.* **37** (1998) 6451.
[6] M. Yoshino, H. Yukawa, M. Morinaga, *Mater. Trans.* **45** (2004) 2056.
[7] Y. Kuroiwa, S. Aoyagi, A. Sawada, J. Harada, E. Nishibori, M. Takata, M. Sakata, *Phys. Rev. Lett.* **87** (2001) 217601.
[8] Y. Kuroiwa, S. Aoyagi, A. Sawada, E. Nishibori, M. Takata, M. Sakata, H. Tanaka, J. Harada, *J. Korean Phys. Soc.* **42** (2003) S1425.
[9] K. Uchida, S. Tsuneyuki, T. Schimizu, *Phys. Rev. B* **68** (2003) 174107.
[10] M. Ghita, M. Fornari, D.J. Singh, S.V. Halilov, *Phys. Rev. B* **72** (2005) 054114.
[11] R.D. Shannon, *Acta Crystallogr. A* **32** (1976) 751.
[12] L.A. Shebanov, *Phys. Status Solidi A* **65** (1981) 321.
[13] F.W. Lytle, *J. Appl. Phys.* **35** (1964) 2212.
[14] G. Shirane, S. Hoshino, *J. Phys. Soc. Jpn.* **6** (1951) 265.
[15] H. Adachi, M. Tsukada, C. Satoko, *J. Phys. Soc. Jpn.* **45** (1978) 875.
[16] J.S. Slater, *Phys. Rev.* **81** (1951) 385.
[17] R.S. Mulliken, *J. Chem. Phys.* **23** (1955) 1841.
[18] A. Munkholm, S.K. Streiffer, M.V. Ramana Murty, J.A. Eastman, C. Thompson, O. Auciello, L. Thompson, J.F. Moore, G.B. Stephenson, *Phys. Rev. Lett.* **88** (2002) 016101.
[19] C. Bungaro, K.M. Rabe, *Phys. Rev. B* **71** (2005) 035420.
[20] Z.X. Chen, Y. Chen, Y.S. Jiang, *J. Phys. Chem. B* **106** (2002) 9986.
[21] L.T. Hudson, R.L. Kurtz, S.W. Robey, D. Temple, R.L. Stockbauer, *Phys. Rev. B* **47** (1993) 1174.
[22] P. Ghosez, X. Gonze, P. Lambin, J.P. Michenaud, *Phys. Rev. B* **51** (1995) 6765.
[23] P. Ghosez, J.P. Michenaud, X. Gonze, *Phys. Rev. B* **58** (1998) 6224.
[24] Z.X. Chen, Y. Chen, Y.S. Jiang, *J. Phys. Chem. B* **105** (2001) 5766.

CHAPTER 12

New Expression of the Chemical Bond in Hydrides Using Atomization Energies

Yoshifumi Shinzato*, **Hiroshi Yukawa***, **Masahiko Morinaga***, **Takeshi Baba**** and **Hiromi Nakai****

Contents

Abstract

Atomization energy diagram is proposed for analyzing the chemical bond in the hydrides including perovskite-type hydrides, metal hydrides and complex hydrides. The atomization energies of hydrogen and metal atoms in them are evaluated theoretically by the energy density analysis (EDA) of the total energy, and used for the construction of the atomization energy diagram. Every hydride can be located on such an energy scaled diagram, although there are significant differences in the nature of the chemical bond

* Department of Materials Science and Engineering, Graduate School of Engineering, Nagoya University, Furo-cho, Chikusa-ku, Nagoya 464-8603, Japan
Corresponding author. E-mail: shinzato@silky.numse.nagoya-u.ac.jp
** Department of Chemistry, School of Science and Engineering, Waseda University, Tokyo 169-8555, Japan

Advances in Quantum Chemistry, Vol. 54
ISSN 0065-3276, DOI 10.1016/S0065-3276(07)00012-3

among various hydrides. When the hydrides have a resemblance in the chemical bond, their locations are close to each other on the diagram. This diagram reflects characteristics of the chemical bond, since the atomization energy of hydrogen changes largely with the covalent or ionic interactions. Also, the roles of constituent elements in the hydrides are understood well with the aid of the atomization energy diagram.

1. INTRODUCTION

In 1955, Wigner and Seitz [1] predicted that if one had a great calculating machine, one might apply it to the problem of solving the Schrödinger equation for each metal and obtain the interesting physical quantities, such as the cohesive energy, lattice constant and similar parameters. It is not clear, however, that a great deal would be gained by this. Presumably the results would agree with the experimentally determined quantities and nothing vastly new would be learned from the calculation. This prediction made by two pioneers of solid-state physics appears true in these days, even though the computational science has made great progress.

In addition, the Mulliken population analysis [2] is common in the field of molecular orbital calculations, and the nature of the chemical bond between atoms has been treated well by using a standard concept of covalent or ionic bond. However, with this analysis it is still difficult to compare quantitatively the chemical bond strength among a variety of materials. To solve this problem, the chemical bond should be estimated quantitatively in an energy scale.

Recently, Nakai [3] has proposed a new analyzing technique called energy density analysis (EDA). In this method, the total energy of a system, computed by using the Kohn–Sham type density functional theory (DFT) [4], is partitioned into atomic energy densities, and the characteristics of the chemical bond are understood in terms of each atomic energy density instead of using the total energy. In this paper, special attention is directed toward hydrides such as perovskite-type hydrides, metal hydrides and complex hydrides. For comparison, the approach is further extended to the perovskite-type oxides.

2. CALCULATION PROCEDURE

2.1 Geometry optimization

The positions of hydrogen in hydrides are sometimes difficult to be determined experimentally. So, in this study, the crystal structures of hydrides are optimized by the total energy minimization using the plane-wave pseudopotentital method. For this purpose, the first-principle calculations based on the DFT are performed with a generalized gradient approximation (GGA) by Perdew et al. [5]. The implementation of DFT employed here combines a plane-wave basis set with the total energy pseudopotential method, as is embodied in the CASTEP code [6].

The present calculations used are based upon the ultrasoft pseudopotentials proposed by Vanderbilt [7]. The plane-wave cutoff energy is chosen to be 380 eV, because this cutoff energy is found to achieve the convergence of the total energies within 0.03 eV, as compared to the results with the cutoff energies up to 600 eV. The sampling in the reciprocal space is done with the *k*-point grids. For example, $5 \times 5 \times 2$ for tetragonal $NaAlH_4$, $6 \times 6 \times 6$ for cubic $KMgH_3$, $5 \times 5 \times 9$ for monoclinic $TiFeH_2$.

2.2 Energy density analysis

The electronic structures for optimized crystal lattice of hydrides are obtained by the DFT calculations under the periodic boundary condition (PBC) using Gaussian03 program package [8]. The adopted functional is the BLYP functional, which consists of the Slater exchange [9], the Becke (B88) exchange [10], the Vosko–Wilk–Nusair (VWN) correlation [11] and the Lee–Yang–Parr (LYP) correlation functionals [12]. The following modified Gaussian basis sets are adopted: (i) the correlation-consistent polarization plus the valence double zeta (cc-pVDZ) basis sets of Dunning [13,14] without d-type functions for H, Li, B, N, Na, Mg and Al, (ii) the Ahlrichs TZV basis set [15] without the outer *s* function for K, (iii) the Huzinaga basis sets [16] without the outer *s* function and constructed to be double-zeta class for V, Fe, Co, Ni, Rb, Zr, Nb and Pd, (iv) the 6-31G basis sets [17,18] without outer *s* function for O, Ti and Ca, and (v) the 3-21G basis set [19] without outer *s* function for Sr. In this study, the EDA calculations under PBC [20] are performed by linking the original code for the EDA with Gaussian03.

Following the EDA, the atomic energy density of atom A is evaluated by,

$$E^{\mathrm{A}} = E^{\mathrm{A}}_{\mathrm{NN}} + T^{\mathrm{A}}_{\mathrm{S}} + E^{\mathrm{A}}_{\mathrm{Ne}} + E^{\mathrm{A}}_{\mathrm{CLB}} + E^{\mathrm{A}}_{\mathrm{XC}}, \tag{1}$$

where $E^{\mathrm{A}}_{\mathrm{NN}}$ is the nuclear–nuclear repulsion energy density, $T^{\mathrm{A}}_{\mathrm{S}}$ the non-interacting kinetic energy density, $E^{\mathrm{A}}_{\mathrm{Ne}}$ the nuclear-electron attraction energy density, $E^{\mathrm{A}}_{\mathrm{CLB}}$ the Coulomb energy density and $E^{\mathrm{A}}_{\mathrm{XC}}$ the exchange-correlation energy density.

In Eq. (1), for example, $E^{\mathrm{A}}_{\mathrm{XC}}$ is evaluated by the partial sum for the numerical quadrature technique,

$$E^{\mathrm{A}}_{\mathrm{XC}} = \sum_{g}^{\mathrm{grid}} \omega_g p_{\mathrm{A}}(r_g) F_{\mathrm{XC}}(r_g), \tag{2}$$

where $\omega_g(r_g)$ is the weighting factor, $p_{\mathrm{A}}(r_g)$ the partition function and $F_{\mathrm{XC}}(r_g)$ the exchange-correlation functional. Other terms in Eq. (1), which are evaluated by the analytical integration with the Kohn–Sham orbitals, are partitioned into their energy densities on the analogy of Mulliken population analysis [2].

2.3 Atomization energy

The EDA analysis is performed with the geometry optimized by the plane-wave pseudopotential method. For binary hydrides, MH_n, the respective atomic energy densities of M and H are related closely to the nature of the chemical bond

relevant to M and H atoms in MH_n. When the energy of the isolated neutral atom, E_M^{atom} (or E_H^{atom}), is taken as a reference, the atomization energy, ΔE_M (or ΔE_H) is defined as,

$$\Delta E_M = \frac{(E_M^{atom} - E_M^{hydride})}{n}, \tag{3}$$

$$\Delta E_H = E_H^{atom} - E_H^{hydride}, \tag{4}$$

where $E_M^{hydride}$ and $E_H^{hydride}$ are the atomic energy densities for M and H in MH_n, respectively. Then, the cohesive energy, E_{coh}, of the hydride per hydrogen atom is expressed as,

$$\Delta E_M + \Delta E_H = E_{coh}. \tag{5}$$

Thus, ΔE_M and ΔE_H are the component of E_{coh}. In case of ternary hydrides, $(M1M2)H_n$, ΔE_M is defined as $(\Delta E_{M1} + \Delta E_{M2})/n$, that is the average atomization energy of M1 and M2 to be counted per hydrogen atom. Even in the other type of ternary hydrides, ΔE_M is defined in a similar way.

By setting that $y = \Delta E_H$ and $x = \Delta E_M$, we obtain a relation, $y = -x + E_{coh}$. So, E_{coh} is expressed as a point of intersection of this line and y-axis at $x = 0$.

3. RESULTS AND DISCUSSION

3.1 Heat of formation and cohesive energy for binary hydrides

First, to show the reliability of the present calculation, the heat of formation, ΔH, for binary hydrides, MH_n, is calculated assuming that $M+(n/2)H_2 \rightarrow MH_n$, and then compared with the experiment [21]. A satisfactory agreement is found between the calculated and experimental values as shown in Figure 12.1.

The cohesive energy, E_{coh}, is a measure of the electronic stability of hydrides. As shown in Table 12.1, the difference between the calculated and the experimental values for E_{coh} lies within 0.44 eV [22]. Thus, the present calculation is performed in a reasonable manner.

3.2 Binary hydrides

For binary hydrides, a ΔE_H vs. ΔE_M diagram is constructed in an energy scale as shown in Figure 12.2. This ΔE_H vs. ΔE_M diagram is hereafter called ''atomization energy diagram''. As a whole, there is a clear trend that ΔE_H increases with decreasing ΔE_M. ΔE_H is positive, but ΔE_M is negative in most cases. Thus, the hydrogen state is more stabilized in the hydride than in an isolated atomic state and instead the M state is destabilized. In other words, the stabilized H state emerges in compensation for the destabilized M state in most hydrides.

Needless to say, when the hydrides have a resemblance in the chemical bonding state, their locations are close to each other in the diagram. For example, any binary hydrides of transition elements appear in the higher ΔE_H region than those of typical elements. This indicates that transition elements could

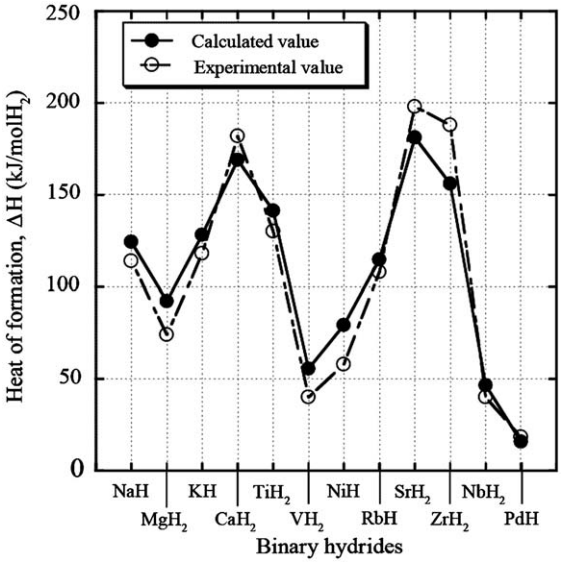

Figure 12.1 Calculated and experimental heat of formation for binary hydrides.

Table 12.1 Calculated and experimental cohesive energy for binary hydrides (units: eV)

	E_{coh} (Calculated)	E_{coh} (Experimental)
NaH	4.39	3.96
MgH_2	3.34	3.41
AlH_3	3.22	3.56
KH	3.38	3.78
CaH_2	4.27	4.12
RbH	3.34	3.64
SrH_2	3.76	4.04
TiH_2	5.52	5.38
VH_2	5.08	5.13
NiH	7.20	7.32
ZrH_2	6.13	6.29
NbH_2	6.48	6.20
PdH	6.17	6.58

stabilize the hydrogen state remarkably in the binary hydrides probably owing to the covalent interaction operating between hydrogen and transition elements. On the other hand, binary hydrides of typical elements have a lower ΔE_H, probably owing to the ionic interaction mainly operating between hydrogen and typical elements in them. As a result, binary hydrides of transition elements have larger cohesive energy, E_{coh}, than those of typical elements, as listed in Table 12.1.

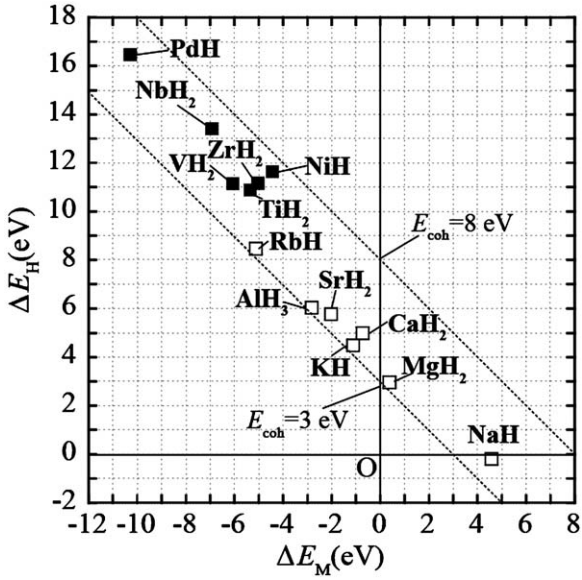

Figure 12.2 Atomization energy diagram for binary hydrides.

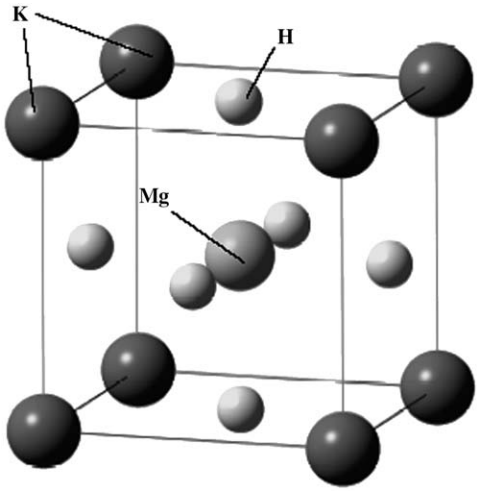

Figure 12.3 Crystal structure of perovskite-type hydride, $KMgH_3$.

3.3 Perovskite-type hydrides

For any perovskite-type hydrides, $M1M2H_3$, (e.g., $KMgH_3$, as shown in Figure 12.3), it is known that the M1–H and M2–H interactions are rather ionic in character, even though covalent character still remains to some extent in the M2–H bond because of the shorter M2–H distance than the M1–H distance. The covalent character further increases in case when M2 is a transition metal. As shown in Figure 12.4, the atomization energy diagram for perovskite-type

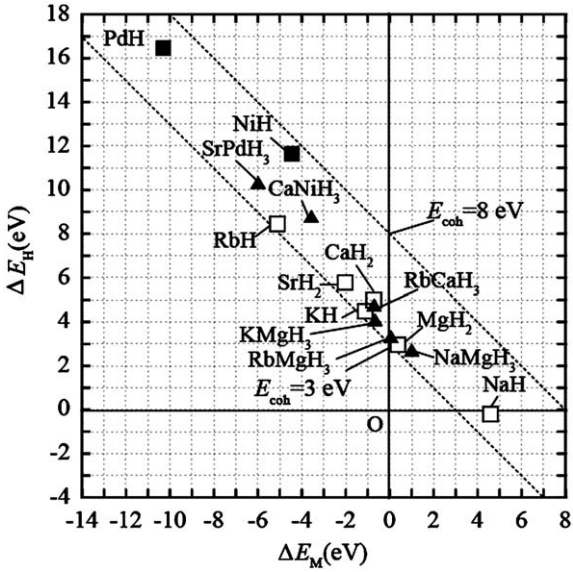

Figure 12.4 Atomization energy diagram for perovskite-type hydrides and binary hydrides.

hydrides is shown in an enlarged scale together with the results for binary hydrides. The chemical reaction for the formation of perovskite-type hydrides is understood with the aid of this diagram. For example, for a chemical reaction, $KH+MgH_2 \rightarrow KMgH_3$, it is found that $KMgH_3$ is located just in between KH and MgH_2 in this diagram. This indicates that $KMgH_3$ inherits the nature of the chemical bond from KH and MgH_2 to some extent. This trend is also seen in the other perovskite-type hydrides as shown in Figure 12.4.

Among the Mg-based perovskite-type hydrides, $M1MgH_3$ (M1 = Na, K, Rb), $NaMgH_3$ and $RbMgH_3$ are located near MgH_2 rather than NaH or RbH. This implies that the chemical bond in $NaMgH_3$ and $RbMgH_3$ has a resemblance to the chemical bond in MgH_2 to some extent. On the other hand, $KMgH_3$ is located near KH rather than MgH_2. So, there is a resemblance in the chemical bond between $KMgH_3$ and KH. However, fine adjustment to the chemical bond still takes place in these hydrides, as explained later.

A ΔE_{M1} vs. ΔE_{M2} diagram is also constructed on the basis of the present calculation to understand the role of metal elements in the formation of the chemical bond in the hydride. The results are shown in Figure 12.5. ΔE_{M1} (or ΔE_{M2}) is a measure of the M1 (or M2) contribution to the cohesive energy of the perovskite-type hydride. A line of showing a relation, $\Delta E_{M1} = \Delta E_{M2}$, is drawn in Figure 12.5. All the pervoskite-type hydrides except for $SrPdH_3$ are located along this line. This implies that the M1 and M2 metallic states are well balanced in the perovskite-type hydrides, and their contribution to the cohesive energy is nearly equal. However, such a balance is no longer present in $SrPdH_3$ containing Pd, where the strong covalent interaction between Pd and H atoms breaks the balance, resulting in a large, negative ΔE_{Pd} and in a large, positive ΔE_H, while showing a small, negative ΔE_{Sr}.

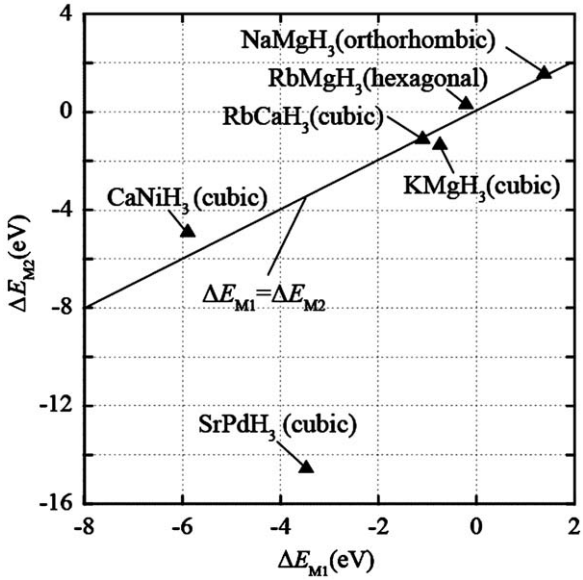

Figure 12.5 ΔE_{M1} vs. ΔE_{M2} diagram for perovskite-type hydrides.

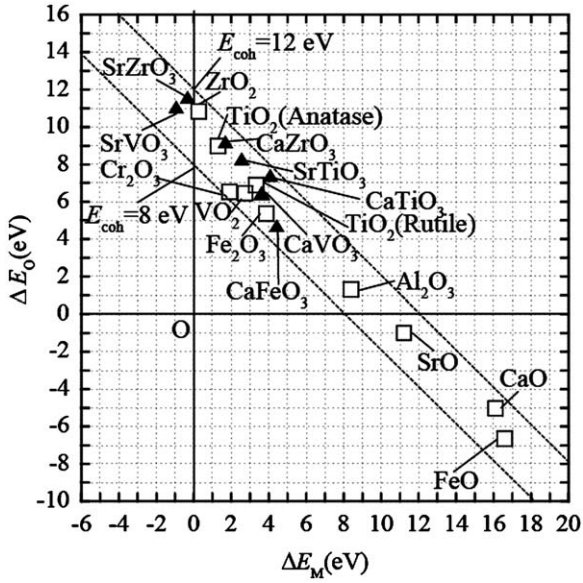

Figure 12.6 Atomization energy diagram for perovskite-type oxides and binary oxides.

3.4 Perovskite-type oxides

For comparison, the atomization energy diagram is shown in Figure 12.6 for the binary oxides and the perovskite-type oxides, $M1M2O_3$, where M2 are the

transition elements such as Ti, V, Fe and Zr. As a whole, there is a trend that ΔE_M and ΔE_O are both positive in most cases. This is in contrast with the trend of negative ΔE_M and positive ΔE_H observed in the perovskite-type hydrides as shown in Figure 12.4. In addition, there is a trend that ΔE_O decreases with increasing ΔE_M. As a result, E_{coh} lies in the range of 8–12 eV, which is larger than the value for binary hydrides listed in Table 12.1 and than that for the perovskite-type hydrides shown in Figure 12.4. Also, most of the binary oxides containing transition elements except for FeO appear in the higher ΔE_O region than the oxides containing typical elements, which is also found in the perovskite-type hydrides and in the binary hydrides as explained above. In addition, it is stressed here that the perovskite-type oxides, $M1M2O_3$, are located near the binary oxides, $M2O_n$, in the diagram, indicating that the perovskite-type oxide, $M1M2O_3$ inherits the nature of the chemical bond mainly from $M2O_n$.

For $CaM2O_3$ (M2 = Ti, V, Fe, Zr) and $SrM2O_3$ (M2 = Ti, V, Zr), a ΔE_{M1} vs. ΔE_{M2} diagram is shown in Figure 12.7. A line of showing a relation, $\Delta E_{M1} = \Delta E_{M2}$, is drawn in the figure. All the oxides are, however, located above this line, so ΔE_{M2} is larger than ΔE_{M1} in $M1M2O_3$, where M1 is a typical element and M2 is a transition element. Thus, the M2 contribution to the cohesive energy is larger than the M1 contribution in these oxides. Furthermore, $CaM2O_3$ (M2 = Ti, V, Fe, Zr) are located along a $CaM2O_3$-line, and $SrM2O_3$ (M2 = Ti, V, Zr) are located near a $SrM2O_3$-line even though the data is somewhat scattered. This implies that M1 (i.e., Ca and Sr) plays an important role in balancing between ΔE_{M1} and ΔE_{M2}, and the balanced relation changes depending on M1. As compared to the $CaM2O_3$-line, the $SrM2O_3$-line is positioned in the lower ΔE_{M1} region. This is interpreted as due to the fact that the Sr–O distance is longer than

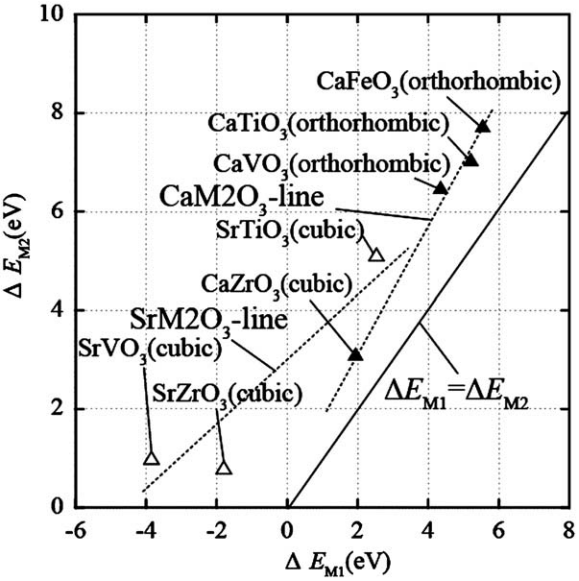

Figure 12.7 ΔE_{M1} vs. ΔE_{M2} diagram for perovskite-type oxides.

the Ca–O distance since the ionic radius is larger in Sr than in Ca, resulting in the relation of inequality, $\Delta E_{Sr} < \Delta E_{Ca}$. Owing to this ionic radius effect, $SrM2O_3$ keeps a cubic crystal structure, whereas $CaM2O_3$ changes from cubic to orthorhombic crystal structure with M2, as shown in Figure 12.6. It is stressed here that the oxides with non-cubic crystal structure possess larger ΔE_{M1} (and ΔE_{M2}), but smaller ΔE_O (see Figure 12.5) than the oxides with cubic crystal structure. This is also true in the perovskite-type hydrides as shown in Figure 12.7. The hydrides with non-cubic crystal structure possess larger ΔE_{M1} (and ΔE_{M2}), but smaller ΔE_H (see Figure 12.6). Thus, crystal structures are reflected well on the respective atomization energy of the perovskite-type hydrides and oxides.

3.5 Metal hydrides

For metal hydrides, $M1M2H_n$ (e.g., $TiFeH_2$, as shown in Figure 12.8), the M2-H covalent interaction is important since H is located in the neighborhood of M2 (e.g., Fe). As shown in Figure 12.9, this is also true in Mg_2NiH_4, where H is located in the neighborhood of Ni, and the strong covalent interaction is operating between Ni and H in it. In agreement with this, Mg_2NiH_4 is located near the position of NiH in the atomization energy diagram shown in Figure 12.9. However, the ΔE_H value is smaller in Mg_2NiH_4 than in NiH, indicating that the H state is destabilized by the presence of Mg in Mg_2NiH_4. On the other hand, $TiFeH_2$ is located well above TiH_2, so that the ΔE_H value is larger in $TiFeH_2$ than in TiH_2, indicating that H state is further stabilized by the presence of Fe in the neighborhood instead of Ti. Among metal hydrides, $TiFeH_2$ that absorbs and desorbs hydrogen at room temperature has the largest cohesive energy, 8.3 eV. Among the Mg-based metal hydrides, Mg_2FeH_6 is located near MgH_2, so there is a resemblance in the chemical bond between Mg_2FeH_6 and MgH_2. On the other hand, Mg_2NiH_4 is located near NiH rather

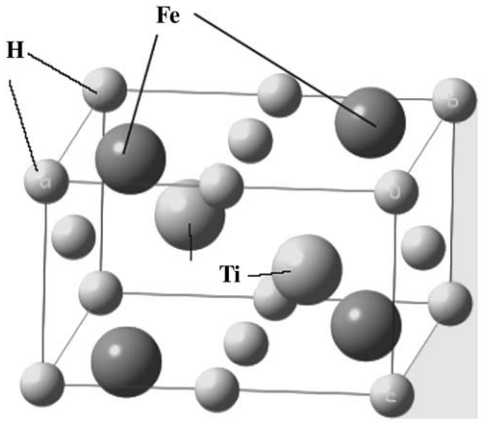

Figure 12.8 Crystal structure of metal hydride, $TiFeH_2$.

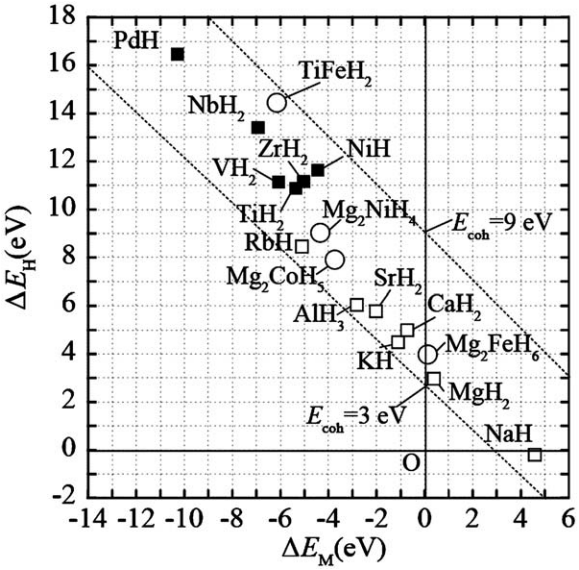

Figure 12.9 Atomization energy diagram for metal hydrides.

than MgH_2 as described earlier. Mg_2CoH_5 is located in-between Mg_2FeH_6 and Mg_2NiH_4.

Mg_2NiH_4 and $TiFeH_2$ are formed by the hydrogenation of intermetallic compounds, Mg_2Ni and TiFe, respectively. Therefore, the further analyses are carried out with these compounds. The value of ΔE_{M1} (M1 = Ti or Mg) and ΔE_{M2} (M2 = Fe or Ni) are shown in Figure 12.10 for TiFe and Mg_2Ni, together with the values for $TiFeH_2$ and Mg_2NiH_4. ΔE_{Ti} for TiFe and ΔE_{Mg} for Mg_2Ni are negative, whereas ΔE_{Fe} for TiFe and ΔE_{Ni} for Mg_2Ni are positive. By hydrogenation, the atomization energy decreases for both M1 and M2. However, the decrement is more remarkable in ΔE_{M2} than in ΔE_{M1}. This is because hydrogen exists in the neighborhood of M2 and strongly interacts with M2 (M2 = Fe or Ni) in the hydrides. As a result, most of the energy of M2 transfers to the hydrogen and the H state becomes stable. It is interesting to note that in either system of TiFe and Mg_2Ni there is a large difference between ΔE_{M1} and ΔE_{M2}, indicating that both TiFe and Mg_2Ni have the strong chemical bond between M1 and M2. This is a reason why the hydrogenation and dehydrogenation take place smoothly without changing the alloy composition in them.

3.6 Complex hydrides

For complex hydrides, $M1M2H_n$ (e.g., $NaAlH_4$, as shown in Figure 12.11), it is known that strong covalent interactions are operating between H and M2 (e.g., M2 = Al) to form complex ions, $(M2H_n)^{-1}$ (e.g., $(AlH_4)^-$) and that ionic interactions are operating between the complex ion and the M1 cation (e.g., Na^+) in them. As shown in Figure 12.12, complex hydrides are located in the

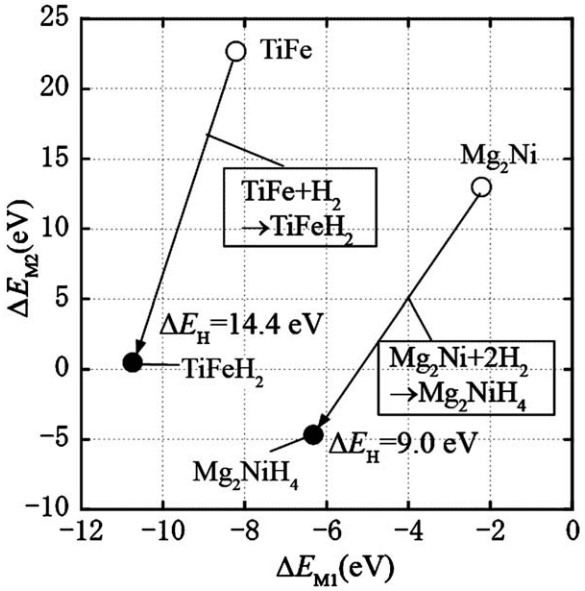

Figure 12.10 ΔE_{M1} vs. ΔE_{M2} diagram for metal hydrides.

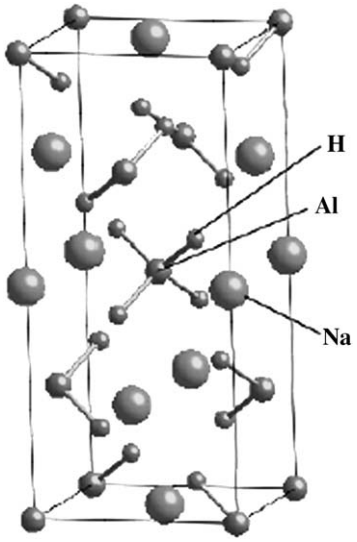

Figure 12.11 Crystal structure of complex hydride, $NaAlH_4$.

narrow and small ΔE_M range ($-2.2\,eV < \Delta E_M < -0.3\,eV$), but in the wide ΔE_H range of 4.2–8.5 eV. ΔE_H changes in the order, $Mg(AlH_4)_2 < M1AlH_4$ (M1 = Li, Na, K) $< M1BH_4$ (M1 = Li, Na, K) $< LiNH_2$. The cohesive energy changes in the same order. Thus, the H state is well stabilized in compensation for the destabilized M state. In particular, as shown in Figure 12.13, the destabilization of

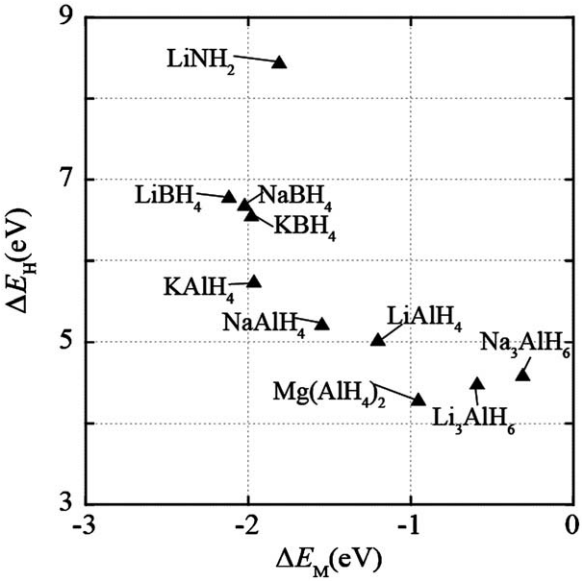

Figure 12.12 Atomization energy diagram for complex hydrides.

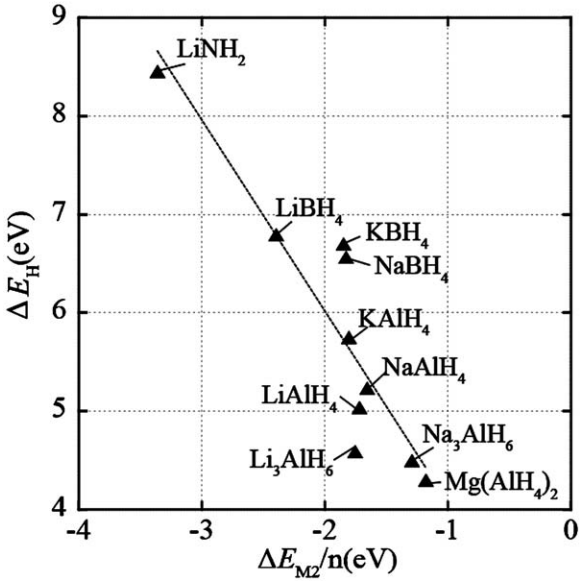

Figure 12.13 $\Delta E_{M2}/n$ vs. ΔE_H diagram for complex hydrides, n is the number of hydrogen atoms in the chemical formula.

the M2 state contributes mainly to the stabilization of the H state by forming the strong covalent bond between M2 and H atoms. As shown in Figure 12.14, ΔE_{M1} is either positive or negative, indicating that the ionic interaction between the ($M2H_n$) complex ion and M1 cation is not so strong as the M2–H covalent

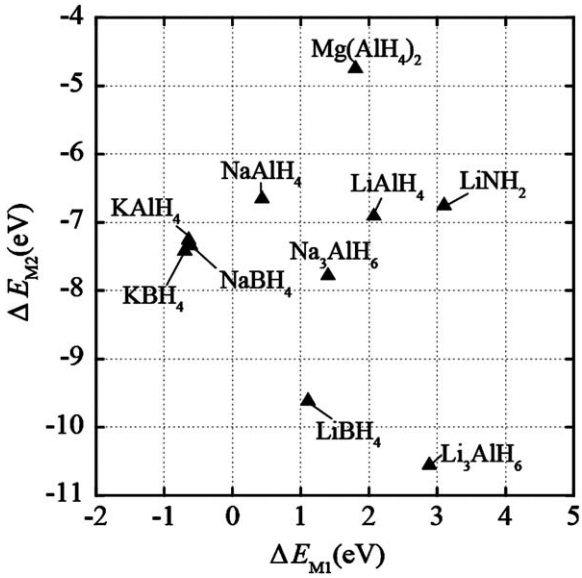

Figure 12.14 ΔE_{M1} vs. ΔE_{M2} diagram for complex hydrides.

interaction. So, there are not any clear correlations between ΔE_{M1} and ΔE_{M2}. For $M1AlH_4$ and $M1BH_4$, where M1 is the 1A group element, ΔE_{M1} changes in the order, K < Na < Li, that is the same order of elements in periodic table.

In case of alante (Al)-type complex hydrides, the magnitude of ΔE_H changes in the order, $Mg(AlH_4)_2 < LiAlH_4 < NaAlH_4 < KAlH_4$ as shown in Figure 12.12. Hence, the H state in $Mg(AlH_4)_2$ is least stable among them, as is found experimentally. In addition, the coordination number effect can be understood by using the atomization energy diagram. In Na_3AlH_6 (or Li_3AlH_6), an Al atom is surrounded by six hydrogen atoms, whereas in $NaAlH_4$ (or $LiAlH_4$) an Al atom is surrounded by four hydrogen atoms. As shown in Figure 12.12, ΔE_H is lower in Na_3AlH_6 (or Li_3AlH_6) than in $NaAlH_4$ (or $LiAlH_4$). Thus, the H state is less stable in Na_3AlH_6 (or Li_3AlH_6) than in $NaAlH_4$ (or $LiAlH_4$), as might be expected from the coordination number. In addition to these local parameters such as the coordination number and the interatomic distance, it is known that material density affects the atomization energy [23].

3.7 Atomization energy diagram for hydrides

For a variety of hydrides, including binary hydrides, perovskite-type hydrides, metal hydrides and complex hydrides, atomization energy diagram is constructed in an energy scale as shown in Figure 12.15. It is stressed here that every hydride can be shown in one figure, although there are significant differences in the nature of the chemical bond among the hydrides as described above. The role of constituent elements, chemical reaction, crystal structure and coordination number effect can be understood with the aid of this atomization energy diagram.

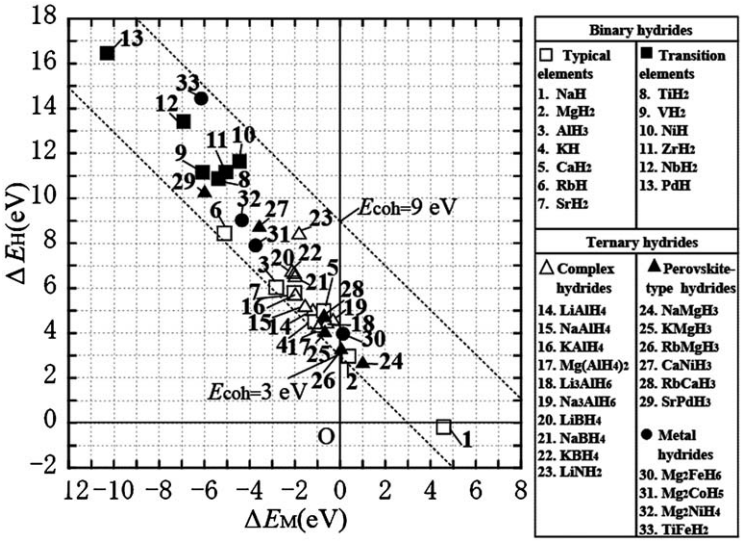

Figure 12.15 Atomization energy diagram for hydrides.

4. CONCLUSION

An atomization energy diagram, which is obtained by the EDA is constructed for the first time to treat the chemical interaction in hydrides and oxides in an energy scale. All the hydrides can be located in this diagram, although there are significant differences in the nature of the chemical bond among the hydrides. This diagram reflects well characteristics of the chemical bond between atoms, for example, the atomization energy of hydrogen (or oxygen) changes largely with covalent or ionic interactions.

Since the sum of the atomization energy equals the cohesive energy, each of atomization energies is a measure of the chemical bonding effect of the element on the stability of the hydrides. So, the role of constituent elements in the hydrides is also understood well with the aid of this diagram. It is interesting to note that there is a balance in the atomization energy among the constituent elements in hydrides and oxides. Also, crystal structure and other properties probably reflect on the atomization energy. It is concluded that the atomization energy diagram provides us a tool for the fundamental understanding of the chemical bond in hydrides and oxides.

ACKNOWLEDGMENTS

The authors would like to express sincere thanks to the staffs of the Computer Center, Institute for Molecular Science, Okazaki National Institute for the use of super-computers. This study was supported by a grant-in-aid for scientific research from the Ministry of Education, Culture, Sports, Science and Technology of Japan, and by the Japan Society for the Promotion of Science, and also by the 21st Century COE program ''Nature-Guided Materials Processing'' of the Ministry of Education, Culture, Sports, Science and Technology of Japan.

REFERENCES

[1] E.P. Wigner, F. Seitz, *Solid State Phys.* **1** (1955) 97–126.
[2] R.S. Mulliken, *J. Chem. Phys.* **23** (1955) 1833–1840.
[3] H. Nakai, *Chem. Phys. Lett.* **363** (2002) 73–79.
[4] W. Kohn, L.J. Sham, *Phys. Rev.* **140** (1965) A1133–A1138.
[5] J.P. Perdew, K. Burke, Y. Wang, *Phys. Rev. B* **41** (1970) 7892–7895.
[6] V. Milman, B. Winkler, J.A. White, C.J. Pickard, M.C. Payne, E.V. Akhmatsukaya, R.H. Nodes, *Int. J. Quant. Chem.* **77** (2000) 895–910.
[7] D. Vanderbilt, *Phys. Rev. B* **41** (1990) 7892–7895.
[8] M.J. Frisch, G.W. Trucks, H.B. Schlegel, G.E. Scuseria, M.A. Robb, J.R. Cheeseman, J.A. Montgomery, Jr., T. Vreven, K.N. Kudin, J.C. Burant, J.M. Millam, S.S. Iyengar, J. Tomasi, V. Barone, B. Mennucci, M. Cossi, G. Scalmani, N. Rega, G.A. Petersson, H. Nakatsuji, M. Hada, M. Ehara, K. Toyota, R. Fukuda, J. Hasegawa, M. Ishida, T. Nakajima, Y. Honda, O. Kitao, H. Nakai, M. Klene, X. Li, J.E. Knox, H.P. Hratchian, J.B. Cross, V. Bakken, C. Adamo, J. Jaramillo, R. Gomperts, R.E. Stratmann, O. Yazyev, A.J. Austin, R. Cammi, C. Pomelli, J.W. Ochterski, P.Y. Ayala, K. Morokuma, G.A. Voth, P. Salvador, J.J. Dannenberg, V.G. Zakrzewski, S. Dapprich, A.D. Daniels, M.C. Strain, O. Farkas, D.K. Malick, A.D. Rabuck, K. Raghavachari, J. B. Foresman, J.V. Ortiz, Q. Cui, A.G. Baboul, S. Clifford, J. Cioslowski, B.B. Stefanov, G. Liu, A. Liashenko, P. Piskorz, I. Komaromi, R.L. Martin, D.J. Fox, T. Keith, M.A. Al-Laham, C.Y. Peng, A. Nanayakkara, M. Challacombe, P.M.W. Gill, B. Johnson, W. Chen, M.W. Wong, C. Gonzalez, J.A. Pople, Gaussian, Inc., Wallingford, CT, 2004.
[9] J.C. Slater, *Phys. Rev.* **81** (1951) 385–390.
[10] A.D. Becke, *Phys. Rev. A* **38** (1988) 3098–3100.
[11] S.H. Vosko, L. Wilk, M. Nusair, *Can. J. Phys.* **58** (1980) 1200–1211.
[12] C. Lee, W. Yang, R.G. Parr, *Phys. Rev. B* **37** (1988) 785–789.
[13] T.H. Dunning, Jr., *J. Chem. Phys.* **90** (1989) 1007–1023.
[14] D.E. Woon, T.H. Dunning, Jr., *J. Chem. Phys.* **98** (1993) 1358–1371.
[15] A. Schafer, C. Huber, R. Ahlrichs, *J. Chem. Phys.* **100** (1994) 5829–5835.
[16] S. Huzinaga, J. Andzelm, M. Klobukowski, E. Radzioandzelm, Y. Sakai, H. Tatewaki, *Gaussian Basis Sets for Molecular Calculation*, Elsevier, New York, 1984.
[17] V.A. Rassolov, J.A. Pople, M. Ratner, T.L. Windus, *J. Chem. Phys.* **109** (1998) 1223–1229.
[18] W.J. Hehre, R. Ditchfield, J.A. Pople, *J. Chem. Phys.* **56** (1972) 2257–2261.
[19] K.D. Dobbs, W.J. Hehre, *J. Comput. Chem.* **7** (1986) 359–378.
[20] H. Nakai, Y. Kurabayashi, M. Katouda, T. Atsumi, *Chem. Phys. Lett.* **438** (2007) 132–138.
[21] Y. Fukai, *The Metal–Hydrogen System*, Springer-Verlag, Berlin, New York, 1994.
[22] R.C. Weast, M.J. Astle, W.H. Beyer, *CRC Handbook of Chemistry and Physics: A Ready-Reference Book of Chemical and Physical Data*, 84th ed., CRC Press, Boca Raton, 2003.
[23] Y. Shinzato, Y. Saito, H. Yukawa, M. Morinaga, T. Baba, H. Nakai, *Material Science Forum* **561–565** (2007) 823–1826.

CHAPTER 13

Electronic Structure and Bonding in Amorphous $Zr_{67}Ni_{33}$ and $Zr_{67}Cu_{33}$

Kazuki Sugita*, Masataka Mizuno, Hideki Araki**** and **Yasuharu Shirai****

Contents

Abstract

The electronic structures and the bonding properties in amorphous $Zr_{67}Ni_{33}$ and $Zr_{67}Cu_{33}$ alloys have been calculated by the discrete variational (DV)-Xα molecular orbital method to investigate the chemical bonding in the amorphous structures. The calculations about Zr_2Ni and Zr_2Cu and β-Zr crystals were also performed for comparison. The broad agreement between the DOSs for the amorphous $Zr_{67}Ni_{33}$ alloy and the Zr_2Ni crystal implies the structure similarity. The calculated DOSs and the bond overlap population analyses suggest that the amorphous structures are significantly influenced by the tight binding pair (Zr–Ni in the Zr–Ni systems and Cu–Cu in the Zr–Cu systems). The glass-formation abilities reflect the bonding properties in the amorphous and crystal structures.

* Department of Materials and Manufacturing Science, Graduate School of Engineering, Osaka University, 2-1 Yamada-oka, Suita, Osaka 565-0871, Japan
Corresponding author. E-mail: kazuki.sugita@mat.eng.osaka-u.ac.jp

** Center for Atomic and Molecular Technologies, Graduate School of Engineering, Osaka University, 2-1 Yamada-oka, Suita, Osaka 565-0871, Japan

Advances in Quantum Chemistry, Vol. 54
ISSN 0065-3276, DOI 10.1016/S0065-3276(07)00013-5

1. INTRODUCTION

Zr-based bulk amorphous alloys have been studied because of their superior character in mechanical properties [1–5], corrosion resistance [1,6] and micro-formability [7], and are of great interest for various applications [1]. Zr-based bulk amorphous alloys have been formed in many systems such as Zr–Cu–Ni–Al [1,2], Zr–Ti–Be–Ni–Cu [3], Zr–Nb–Cu–Ni–Al [4], Zr–Ti–Ni–Cu [5]. In most of the systems, Zr, Cu, Ni are essential elements for the glass formation [8]. Then we focus on the basic binary Zr–Ni and Zr–Cu systems. The radial density functions (RDFs) of amorphous $Zr_{70}Ni_{30}$ and $Zr_{70}Cu_{30}$ alloys are completely different in the first peaks [9]. These RDFs suggest that these amorphous alloys have different local structures in spite of the similar atomic radii of Ni and Cu. These results imply that bonding properties greatly influence the amorphous structures. The glass-formation abilities may also be influenced by the different amorphous structures. Therefore, we aim to investigate the bonding properties in amorphous $Zr_{67}Ni_{33}$ and $Zr_{67}Cu_{33}$ (a-$Zr_{67}Ni_{33}$ and a-$Zr_{67}Cu_{33}$) by the discrete variational (DV)-Xα molecular orbital method [10,11]. However, the three-dimensional atomic structures of Zr-based amorphous alloys have not been determined even in binary systems. The structure models have been proposed by reverse Monte-Carlo simulations based on the RDFs measured by X-ray and neutron diffraction experiments. The information deduced from RDFs is, however, not enough to construct three-dimensional atomic structures.

In the present study, we have determined the three-dimensional atomic structures of amorphous $Zr_{67}Ni_{33}$ and $Zr_{67}Cu_{33}$ alloys by molecular dynamics simulations. The short-range order structures were discussed by the RDFs obtained by the simulated amorphous structures. The electronic states of these alloys are calculated by the DV-Xα molecular orbital method. The bonding properties are discussed in view of the bond order (BO) parameters calculated by the Mulliken overlap population analysis [12]. For comparison, the calculations for Zr_2Ni and Zr_2Cu crystals (c-Zr_2Ni, c-Zr_2Ni), β-Zr, and the structure models fully substituted between Ni and Cu were also performed as described later.

2. COMPUTATIONAL PROCEDURE

2.1 Molecular dynamics simulation

The three-dimensional arrangement of atoms in the amorphous structure was calculated by a molecular dynamics simulation. The embedded-atom-method potential [13] and the alloying model [14] were employed in this simulation. Each cubic supercell for a-$Zr_{67}Ni_{33}$ and a-$Zr_{67}Cu_{33}$ contained 100 atoms. Though the number of the atoms may be insufficient to discuss the long-range order structures, we focus on the short-range order structures because the chemical bonding significantly depends on the short-range order structure. The liquid structures were obtained by the molecular dynamics simulations at 1500 K, which

is higher than the melting points of c-Zr_2Ni and c-Zr_2Cu. The initial coordinates were selected randomly, but the coordinates were selected again when the nearest-neighbor distance was below 2 Å. The amorphous structures were quenched to 100 K. The lengths of the cubic supercells were optimized at 1500 and 100 K to minimize the total energies. The calculated amorphous structures are analyzed by the RDFs and pair distribution functions.

2.2 DV-Xα cluster method and cluster model

The molecular orbital calculations were performed using a SCAT program code [10,11] based on the DV-Xα method. In this method, one-electron Schrödinger equations are iteratively solved to obtain the self-consistent electronic structure of model structures. The molecular orbitals are constructed by a linear combination of the atomic orbitals that are numerically obtained by solving the Schrödinger equation for the atoms in the model structures. At respective iterations, the charge densities of atoms are renewed using atomic orbital populations calculated by the Mulliken's scheme. The matrix elements of Hamiltonian and the overlap integrals were calculated by the three-dimensional diophantine numerical integration with 1000 integration points per atom.

The structure models for a-$Zr_{67}Ni_{33}$, a-$Zr_{67}Cu_{33}$, c-Zr_2Ni, c-Zr_2Cu, and β-Zr are shown in Figure 13.1. The compositions are (a) $Zr_{45}Ni_{22}$ for a-$Zr_{67}Ni_{33}$, (b) $Zr_{40}Cu_{27}$ for a-$Zr_{67}Cu_{33}$, (c) $Zr_{40}Ni_{21}$ for a-$Zr_{67}Ni_{33}$, (d) $Zr_{42}Cu_{21}$ for a-$Zr_{67}Cu_{33}$, and (e) Zr_{59} for β-Zr crystal respectively. The excess content of Cu atoms in the structure model of a-$Zr_{67}Ni_{33}$ may cause some problems, but the central region within a radius of 6 Å consists of 32 Zr and 17 Cu atoms, and this ratio is similar to the composition of $Zr_{67}Ni_{33}$.

The structure models fully substituted between Ni and Cu atoms (a-$Zr_{67}Ni_{33}$ substituted, a-$Zr_{67}Cu_{33}$ substituted, c-Zr_2Ni substituted, c-Zr_2Cu substituted) were also calculated to compare the bonding properties and the structural effects. The descriptions of the structure models are summarized in Table 13.1.

In order to evaluate the strength of the bonding between two atoms, the BO is calculated by the Mulliken population analysis. The atomic bond order BO_{AB} between atoms A and B is defined as

$$BO_{AB} = \sum_{l} n_l \sum_{m' \in B} \sum_{m \in A} \alpha_{lm'} \alpha_{lm} S_{m'm} \tag{1}$$

where α_{lm} and $\alpha_{lm'}$ are the coefficients of the atomic orbitals m and m′ in the molecular orbital l, $S_{m'm}$ is an overlap matrix element between two atomic orbitals m′ and m. n_l is the occupied charge of the molecular orbital l. In the amorphous alloys, the total BOs were corrected by using the coordination numbers calculated from the RDF because the coordination number of the structure models is not consistent with that of the amorphous structures obtained by a molecular dynamics simulation in a precise sense.

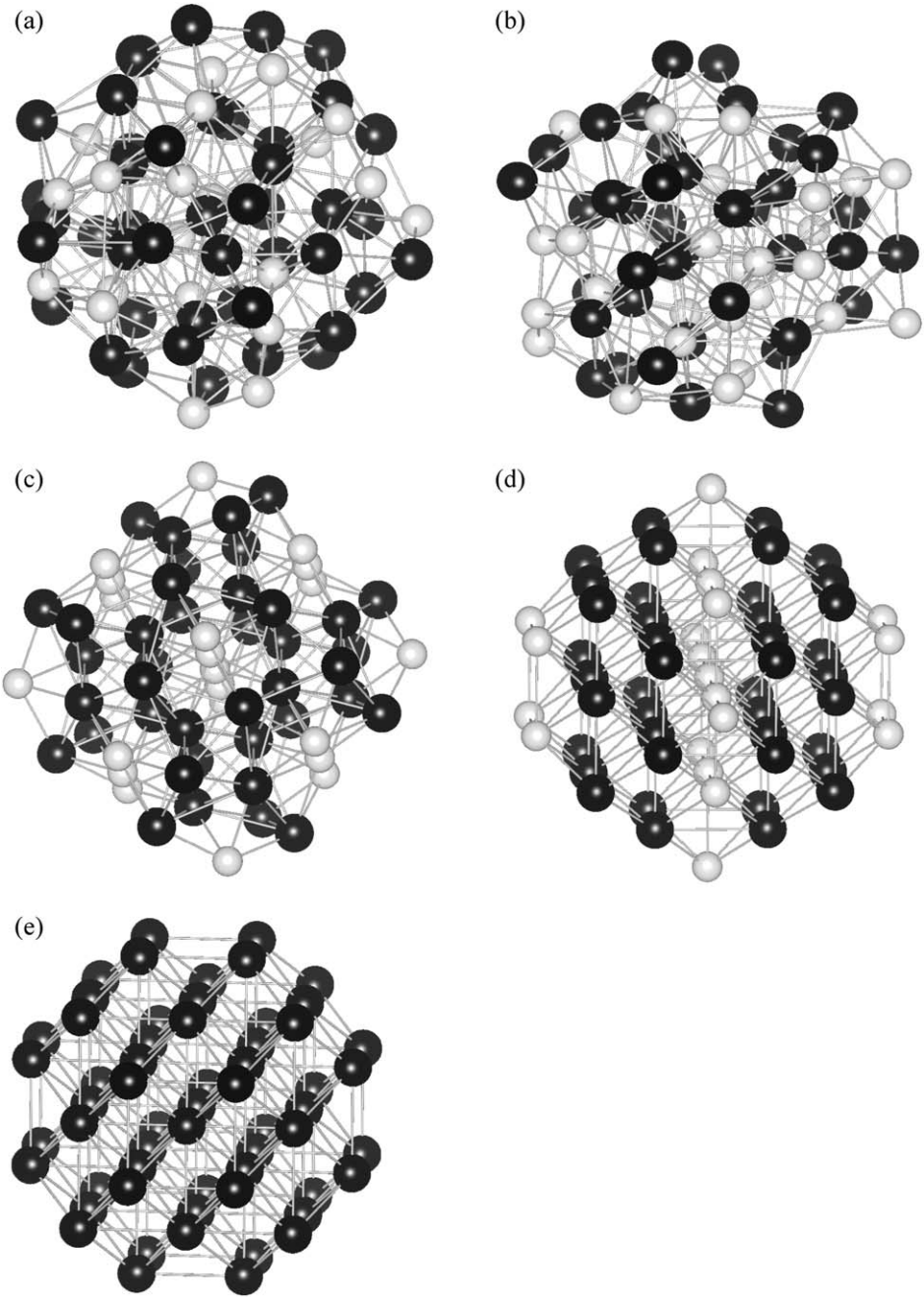

Figure 13.1 Structure models of (a) amorphous $Zr_{67}Ni_{33}$ alloy, (b) amorphous $Zr_{67}Cu_{33}$ alloy, (c) Zr_2Ni crystal, (d) Zr_2Cu crystal and (e) β-Zr crystal. Filled and open circles denote Zr and Ni or Cu atoms, respectively.

Table 13.1 Descriptions of the structure models in this study

	c-Zr_2Ni	c-Zr_2Cu substituted	c-Zr_2Cu	c-Zr_2Ni substituted	a-$Zr_{67}Ni_{33}$	a-$Zr_{67}Cu_{33}$ substituted	a-$Zr_{67}Cu_{33}$	a-$Zr_{67}Ni_{33}$ substituted
Structure type	Crystal Zr_2Ni	Crystal Zr_2Ni	Crystal Zr_2Cu	Crystal Zr_2Cu	Amorphous $Zr_{67}Ni_{33}$	Amorphous $Zr_{67}Ni_{33}$	Amorphous $Zr_{67}Cu_{33}$	Amorphous $Zr_{67}Cu_{33}$
Composition	Zr_2Ni	Zr_2Cu	Zr_2Cu	Zr_2Ni	$Zr_{67}Ni_{33}$	$Zr_{67}Cu_{33}$	$Zr_{67}Cu_{33}$	$Zr_{67}Ni_{33}$

3. RESULTS

3.1 Amorphous structure of a-$Zr_{67}Ni_{33}$ and a-$Zr_{67}Cu_{33}$

The short-range order structures in a-$Zr_{67}Ni_{33}$ and a-$Zr_{67}Cu_{33}$ calculated by a molecular dynamics simulation were examined with RDF analyses. As shown in Figures 13.2 and 13.3, the calculated RDFs for a-$Zr_{67}Ni_{33}$ and a-$Zr_{67}Cu_{33}$ agree with an X-ray diffraction measurement [9]. There are some differences especially in the first peaks. The first peak in the RDF of a-$Zr_{67}Ni_{33}$ is clearly separated into two peaks (Figure 13.2(a)), which correspond to the components of Zr–Zr and Zr–Ni pair. In order to estimate the bonding preferences, the amount of pairs is calculated (Figure 13.4). The number of Cu–Cu pairs in a-$Zr_{67}Cu_{33}$ is larger than that of Ni–Ni pairs in a-$Zr_{67}Ni_{33}$, however there are no apparent differences in the number of Zr–Zr pairs in both alloys. The amount of the Ni–Ni pairs is smaller than that estimated by a randomly arranged structure model, meanwhile the amount of the Zr–Ni pairs is larger. These results imply that Zr–Ni bonding has a strong chemical affinity as compared to the Ni–Ni bonding in a-$Zr_{67}Ni_{33}$. Additionally the Ni–Zr–Ni structures are found in a-$Zr_{67}Ni_{33}$, this is related to the small amount of Ni–Ni pairs and the significant increase around the atomic distance (4.5 Å in Figure 13.2(a)). On the other hand, a-$Zr_{67}Cu_{33}$ has an almost randomly arranged structure, which implies little bonding preferences. The differences in the local structures cannot be simply explained by the atomic radius of Ni and Cu.

3.2 Density of states

The total density of states (DOS) are obtained by summing of the partial DOS for the atoms in the central part of the structure models in order to reproduce the electronic structure of the bulk alloys as appropriately as possible. The number of the sampled atoms for the calculation of the amorphous alloys is typically 6 for one element. In case of crystals, a few atoms are sampled for calculation.

Total DOSs for a-$Zr_{67}Ni_{33}$, a-$Zr_{67}Cu_{33}$, c-Zr_2Ni, and c-Zr_2Cu are shown in Figure 13.5. The calculated DOS for a-$Zr_{67}Ni_{33}$ is similar to the DOS for c-Zr_2Ni (Figure 13.5(a)). The local structure of a-$Zr_{67}Ni_{33}$ may be close to that of c-Zr_2Ni. But there is a distinctive difference between a-$Zr_{67}Cu_{33}$ and c-Zr_2Cu around −3.0 eV in the molecular orbital energy (Figure 13.5(b)). The energy level corresponds to the Cu 3d orbital as shown in Figure 13.6(b), hence the bonding

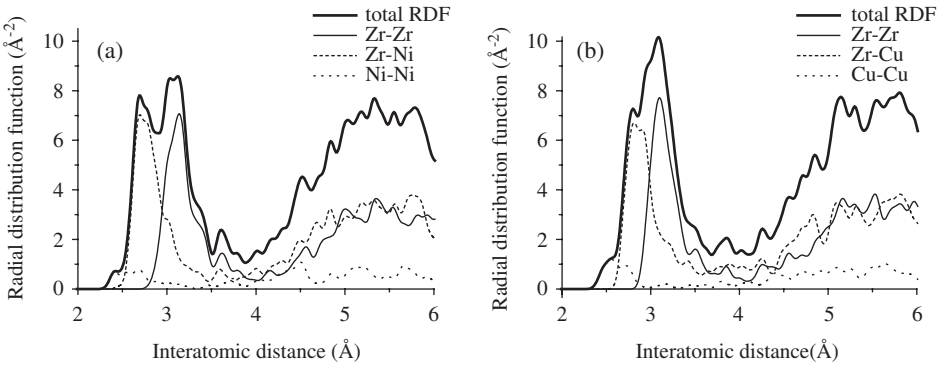

Figure 13.2 Calculated RDFs for (a) a-$Zr_{67}Ni_{33}$ and (b) a-$Zr_{67}Cu_{33}$.

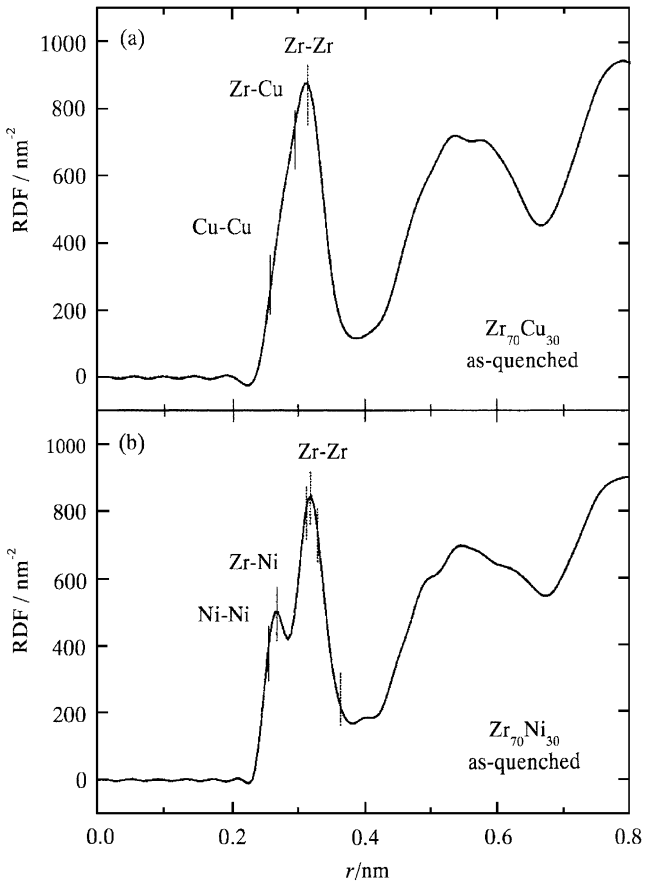

Figure 13.3 RDFs in a-$Zr_{70}Cu_{30}$, a-$Zr_{70}Ni_{30}$. (Reprinted from Ref. [9] with permission.)

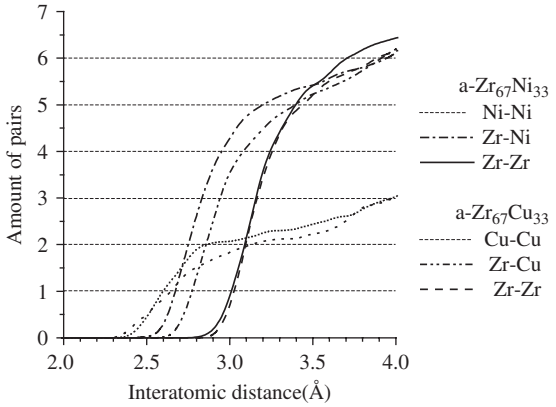

Figure 13.4 Pair distributions in a-$Zr_{67}Ni_{33}$ and a-$Zr_{67}Cu_{33}$.

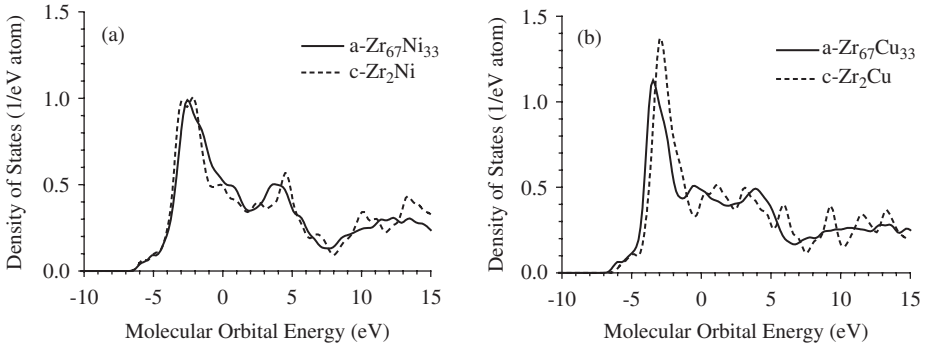

Figure 13.5 Total DOSs for (a) a-$Zr_{67}Ni_{33}$, a-$Zr_{67}Cu_{33}$, (b) c-Zr_2Ni, and c-Zr_2Cu.

states between Cu atoms are quite different. The bond distance between Cu atoms in c-Zr_2Ni is 3.2 Å, which is considerably longer than in a-$Zr_{67}Cu_{33}$. The increase in the bond distance shifts the molecular orbital energy level of Cu 3d upward. These results show that the bonding properties and the electronic structures interact with each other.

In order to understand why the amorphous and crystal structures are similar in the Zr–Ni system but not in the Zr–Cu system, the DOSs in the structure models substituted between Ni and Cu atoms are examined (Figure 13.7(a)–(d)). As shown in Figure 13.7(a), the substitution of Cu for Ni in the c-Zr_2Ni model decreases the molecular orbital energy levels of Ni 3d. The same tendencies are found in c-Zr_2Cu, a-$Zr_{67}Ni_{33}$, and a-$Zr_{67}Cu_{33}$ (Figure 13.7(b)–(d)). These results show that the energy level of Cu 3d orbital is deeper than Ni 3d in general.

Then the structural effect on the DOS was examined (Figure 13.8(a)–(d)). We focused on the energy shift in the molecular orbital energies for c-Zr_2Ni and c-Zr_2Cu. As shown in Figure 13.9, the energy shifts are caused by the differences in the orbital energies of Ni 3d and Cu 3d. The energy shift of the Cu 3d orbital

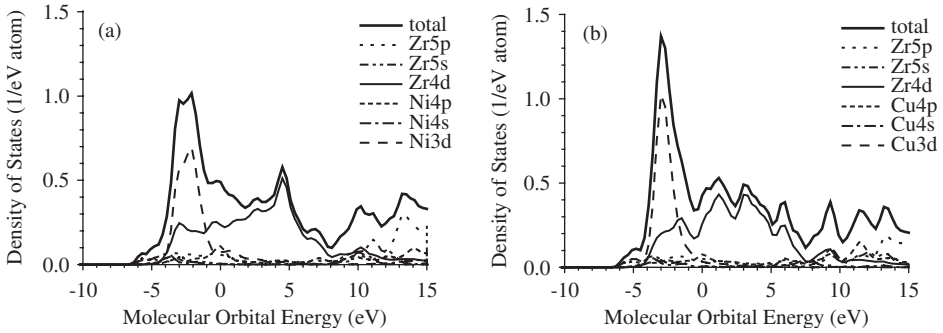

Figure 13.6 Partial DOSs for (a) c-Zr_2Ni and (b) c-Zr_2Cu.

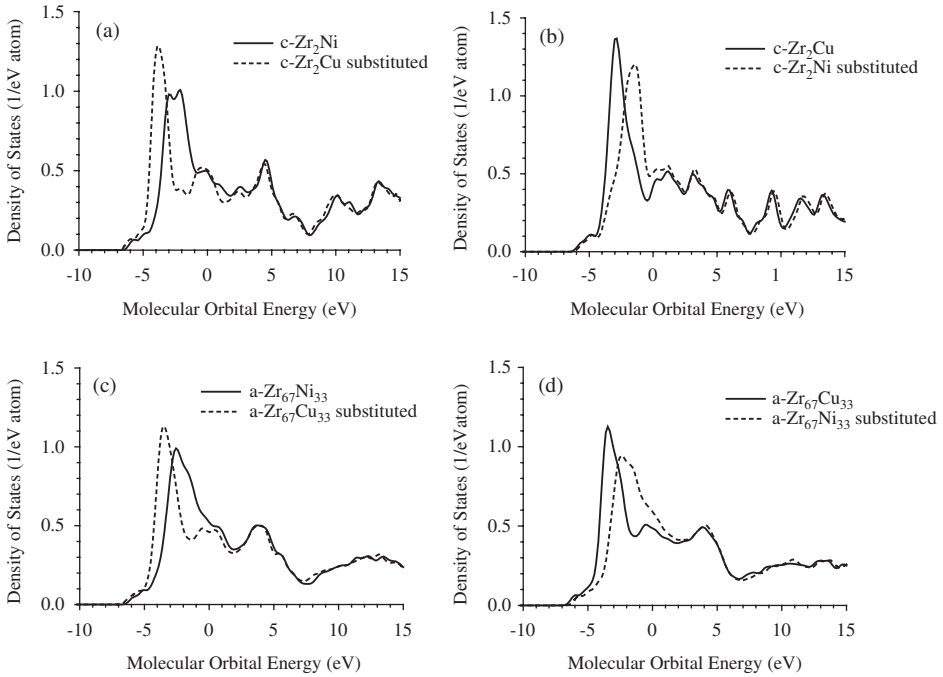

Figure 13.7 Substitutional effect on the total DOSs for (a) c-Zr_2Ni, (b) c-Zr_2Cu, (c) a-$Zr_{67}Ni_{33}$, and (d) a-$Zr_{67}Cu_{33}$.

is explained well by the weak Cu–Cu bonding in c-Zr_2Cu type structures. On the other hand, the structural effect is quite limited in the amorphous alloys (Figure 13.8(c) and (d)). The short-range order structures and the bonding distances in the amorphous alloys are not expected to be so different as compared to the crystals.

These results seem to conflict each other. Despite the Cu–Cu bonding in the Zr–Cu system being stronger than the Ni–Ni bond in Zr–Ni system, in the

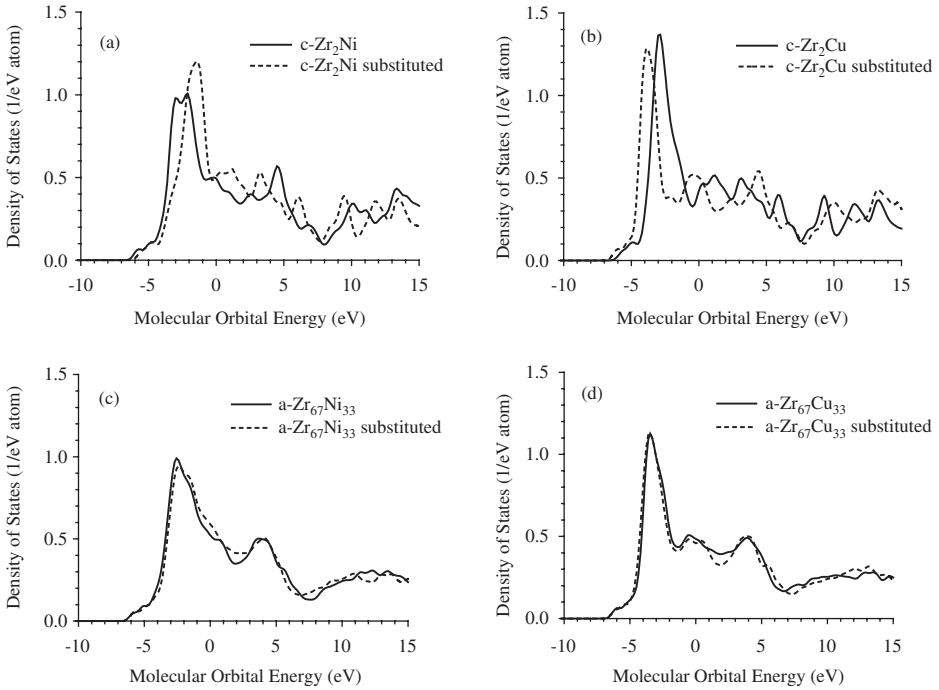

Figure 13.8 Structural effect on the total DOSs in (a) c-Zr_2Ni, (b) c-Zr_2Cu, (c) a-$Zr_{67}Ni_{33}$, and (d) a-$Zr_{67}Cu_{33}$.

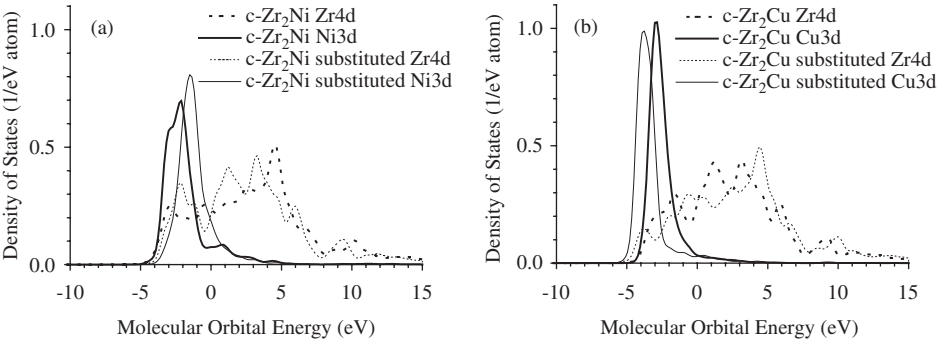

Figure 13.9 Structural effect on the partial DOSs for Zr4d, Cu3d, and Ni3d in (a) c-Zr_2Ni and (b) c-Zr_2Cu.

c-Zr_2Cu the Cu–Cu bond is quite weak because of its long bond distance. The properties of Zr–Zr bonding should be also investigated. However the energy level of the Zr 4d orbital is too wide to discuss the strength of the Zr–Zr bonds. Therefore, we discuss the strength of the bonds in the viewpoint of the bond overlap population in the next section.

3.3 Bond overlap population

The total BOs between the elements E_1 and E_2 are calculated by using the formula defined as

$$BO_{E_1E_2}^{total} = \sum_{\substack{A \in E_1, B \in E_2, \\ R_{AB} \le R_{cutoff}}} BO_{AB} \tag{2}$$

where R_{AB} is the distance between atoms A and B and R_{cutoff} the cutoff distance. The BOs for each pair in c-Zr_2Ni, c-Zr_2Cu substituted, c-Zr_2Cu, c-Zr_2Cu substituted, β-Zr, a-$Zr_{67}Ni_{33}$, a-$Zr_{67}Cu_{33}$ substituted, a-$Zr_{67}Cu_{33}$, and a-$Zr_{67}Ni_{33}$ substituted are listed in Table 13.2. For the calculations of the crystals, R_{cutoff} was fixed to 3.5 Å. In case of the amorphous alloys, R_{cutoff} for Ni–Ni and Cu–Cu pair was 3.0 Å and R_{cutoff} for Zr–Zr, Zr–Ni, and Zr–Cu pair was 3.5 Å. These cutoff distances were determined by RDFs in Figure 13.2.

First we focus on the effect of the substitution between Ni and Cu atoms. Comparing between c-Zr_2Ni and c-Zr_2Cu substitution, the substitution of Cu for Ni weakens the Zr–Ni and Ni–Ni bonds, whereas it slightly strengthens the Zr–Zr bonds. The substitution in a-$Zr_{67}Ni_{33}$ and a-$Zr_{67}Cu_{33}$ shows the same tendency, however the Ni–Ni bonds in c-Zr_2Ni substitution are strengthened by the substitution. The Zr–Ni bonds in c-Zr_2Ni substitution are strengthened instead of the Ni–Ni bonds because bond distances of Ni–Ni and Cu–Cu pairs are quite different. The bond distance of Cu–Cu in c-Zr_2Cu is significantly longer than those in other structures.

Second we focus on the structural effect. The structural effect on the BOs is rather smaller than the substitutional effect. In order to discriminate between the contributions of the number of the pair and the bonding strength, the BOs for each bond are calculated by using the following definition:

$$BO_{E_1E_2}^{bond} = \frac{1}{n_{E_1E_2}} BO_{E_1E_2}^{total} \tag{3}$$

Table 13.2 Total bond orders between each element

	Around Ni or Cu		Around Zr	
	Ni or Cu	Zr	Ni or Cu	Zr
c-Zr_2Ni	0.60	1.55	0.77	1.93
c-Zr_2Cu substituted	0.55	1.41	0.71	1.95
c-Zr_2Cu	0.55	1.53	0.76	1.89
c-Zr_2Ni substituted	0.49	1.64	0.82	1.84
β-Zr	–	–	–	2.04
a-$Zr_{67}Ni_{33}$	0.50	1.57	0.77	1.53
a-$Zr_{67}Cu_{33}$ substituted	0.48	1.39	0.69	1.58
a-$Zr_{67}Cu_{33}$	0.49	1.37	0.68	1.64
a-$Zr_{67}Ni_{33}$ substituted	0.54	1.51	0.74	1.51

Table 13.3 Bond orders for each bond

	Ni–Ni or Cu–Cu	Zr–Ni or Zr–Cu	Zr–Zr
c-Zr_2Ni	0.30	0.19	0.18
c-Zr_2Cu substituted	0.28	0.18	0.18
c-Zr_2Cu	0.14	0.19	0.24
c-Zr_2Ni substituted	0.12	0.21	0.23
β-Zr	–	–	0.26
a-$Zr_{67}Ni_{33}$	0.27	0.19	0.19
a-$Zr_{67}Cu_{33}$ substituted	0.26	0.17	0.20
a-$Zr_{67}Cu_{33}$	0.23	0.17	0.21
a-$Zr_{67}Ni_{33}$ substituted	0.26	0.19	0.19

where $n_{E_1E_2}$is the number of E_1–E_2 bonds. The results are listed in Table 13.3. In case of the crystals, the BOs for each pair are very different in the comparison between c-Zr_2Ni and c-Zr_2Cu type structures, although the total BOs are similar for each element. The result shows that the bond strength and the number of pairs are quite different in the crystal structures. In case of the amorphous alloys, the BOs strongly depend on the numbers of the bonding pair, because there are little differences between the BOs for each bond. The BOs for each pair in the amorphous alloys listed depend not on the structures but on the constitutional elements.

4. DISCUSSION

4.1 Bonding preference and structural stability

The calculated BOs listed in Tables 13.2 and 13.3 show that Zr–Zr bond in Zr–Cu system is stronger than that in the Zr–Ni systems and that the opposite trend is observed for Zr–Ni and Ni–Ni bonds. These bonding preferences should have significant effects on the local structures. The concept is applicable to the cases of the amorphous alloys. The BOs for the strengthened pair in the amorphous alloys are significantly large. But in case of the crystals, they are not necessarily large. In the crystallization process of the amorphous alloys in Zr–Cu system, the weak Zr–Zr bonds should be strengthened to decrease the total free energy.

The BOs may be useful to evaluate the structural stability comprehensively, because the BO parameter depends on both the bonding distances and the number of the bonding pair. The total BOs for each structure shown in Figure 13.10 are calculated by using the following definition:

$$BO_{Structure} = \sum C_{E_1} BO^{total}_{E_1E_2} \tag{4}$$

where C_{E_1} is the atomic ratio in the alloy.

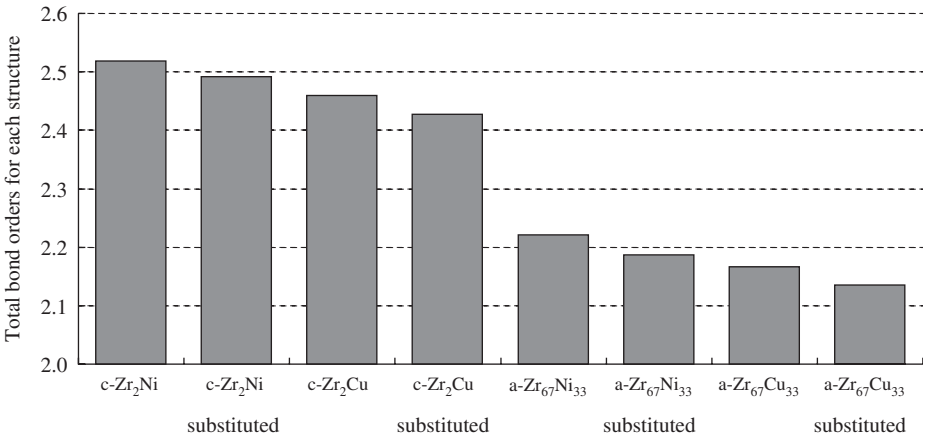

Figure 13.10 Total bond orders (BOs) for c-Zr_2Ni, c-Zr_2Ni substituted, c-Zr_2Cu, c-Zr_2Cu substituted, a-$Zr_{67}Ni_{33}$, a-$Zr_{67}Ni_{33}$ substituted, a-$Zr_{67}Cu_{33}$ and a-$Zr_{67}Cu_{33}$ substituted structures.

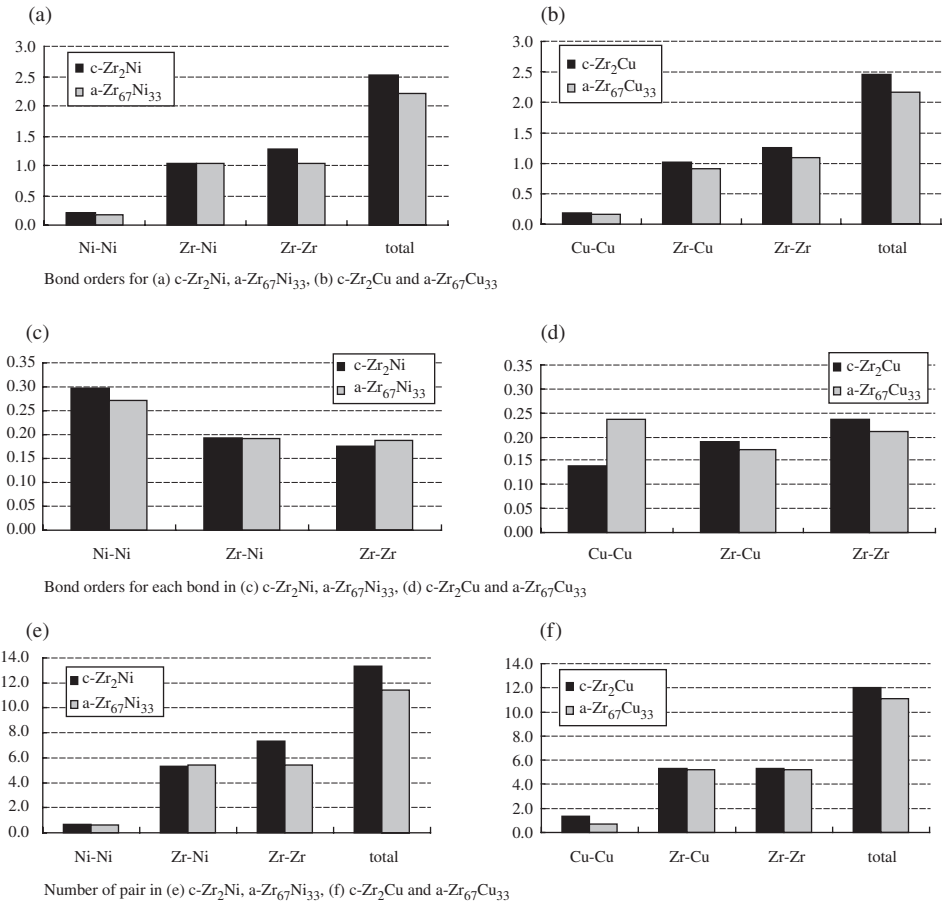

Figure 13.11 Comparison between the amorphous alloys and crystals in Zr–Ni and Zr–Cu systems.

The total BOs for each structure explain the structural stabilities in each system as well. The original structure models are more stable than replaced models. In the previous studies [15], the glass-formation abilities of the amorphous alloys were estimated by the calculation of the small representative clusters. However the glass-formation abilities depend not only on the stabilities of the amorphous alloys but also those of crystals. Moreover, the small clusters cannot cover the varieties of the bonds (the combinations and the distances of the pair).

4.2 Glass-forming ability

BOs and the numbers of each pair in c-Zr_2Ni, a-$Zr_{67}Ni_{33}$, c-Zr_2Cu, and a-$Zr_{67}Cu_{33}$ are summarized in Figure 13.11. The comparison between c-Zr_2Ni and a-$Zr_{67}Ni_{33}$ shows that the short-range order structures around Ni are almost the same in both and only the increase in the number of Zr–Zr pair is necessary for the crystallization of a-$Zr_{67}Ni_{33}$. On the other hand, the short-range order structures in Zr–Cu systems are very different. In the crystallization process of a-$Zr_{67}Cu_{33}$, the bond distances of strong Cu–Cu pair should be increased in order to strengthen the Zr–Zr bonds. The different binding mode between a-$Zr_{67}Cu_{33}$ and c-Zr_2Cu causes the difficulty in the structural changes in the crystallization process. The total and partial DOSs for a-$Zr_{67}Cu_{33}$ and c-Zr_2Cu show the large structural differences between the amorphous and crystal structures in Zr–Cu systems. These results imply that a-$Zr_{67}Cu_{33}$ has a higher glass-forming ability than a-$Zr_{67}Ni_{33}$. It is reported that the glass transition is observed in the $Zr_{70}Cu_{30}$ amorphous alloy but not in the $Zr_{70}Ni_{30}$ [9].

5. CONCLUSIONS

The conclusions derived from the present study are summarized as follows.

(1) The three-dimensional structures of a-$Zr_{67}Ni_{33}$ and a-$Zr_{67}Cu_{33}$ are calculated by a molecular dynamics simulation, the RDFs show a good agreement with the experiments.
(2) The total DOSs for c-Zr_2Ni, a-$Zr_{67}Ni_{33}$, c-Zr_2Cu, and a-$Zr_{67}Ni_{33}$ reflect the atomic orbital energies of the bonds, and imply that the local structures in c-Zr_2Ni are similar to those in a-$Zr_{67}Ni_{33}$ and that there are no similarities in Zr–Cu binary alloys. They are useful to understand the differences between the amorphous and crystal structures.
(3) The bonding preferences are examined by the BO parameters. The Ni–Ni and Zr–Ni bonds in Zr–Ni binary alloys are stronger than Cu–Cu and Zr–Cu bonds in the Zr–Cu alloys respectively. On the other hand, the Zr–Zr bonds in Zr–Cu binary alloys are stronger than in Zr–Ni binary alloys. The total BOs of each model explain the structure selectivity.
(4) The amorphous structures are significantly influenced by the bonding preference.
(5) The analysis of the BOs for the amorphous and crystal structures helps the estimation of the glass-forming abilities.

ACKNOWLEDGMENTS

This work was supported by "Priority Assistance of the Formation of Worldwide Renowned Centers of Research—The 21st Century COE Program (Project: Center of Excellence for Advanced Structural and Functional Materials Design)" from the Ministry of Education, Sports, Culture, Science, and Technology of Japan.

REFERENCES

[1] A. Inoue, *Acta Mater.* **48** (2000) 279.
[2] A. Inoue, T. Zhang, N. Nishiyama, et al., *Mater. Trans. JIM* **34** (1993) 1234.
[3] A. Inoue, T. Zhang, *Mater. Trans. JIM* **37** (1996) 185.
[4] A. Inoue, T. Zhang, *Mater. Trans. JIM* **36** (1995) 1420.
[5] X.H. Lin, W.L. Johnson, *J. Appl. Phys.* **78** (1995) 6514.
[6] A. Gebert, K. Buchholz, A. Leonhard, et al., *Mater. Sci. Eng. A* **267** (1999) 294.
[7] Y. Saotome, S. Miwa, T. Zhang, A. Inoue, *J. Mater. Process. Technol.* **113** (2001) 64.
[8] H. Yang, J.Q. Wang, Y. Li, *J. Non-Cryst. Solids* **352** (2006) 832.
[9] J. Saida, E. Matsubara, A. Inoue, *Mater. Trans.* **44** (2003) 1971.
[10] H. Adachi, M. Tsukada, C. Satoko, *J. Phys. Soc. Jpn.* **45** (1978) 875.
[11] D.E. Ellis, G.S. Painter, *Phys. Rev. B* **2** (1970) 2887.
[12] R.C. Mulliken, *J. Chem. Phys.* **23** (1955) 2343.
[13] X.W. Zhou, H.N.G. Wadley, R.A. Johnson, *Acta Mater.* **49** (2001) 4005.
[14] R.A. Johnson, *Phys. Rev. B* **39** (1989) 12554.
[15] X. Wang, M. Qi, C. Dong, *Mater. Sci. Eng. A* **375–377** (2004) 701.

CHAPTER 14

Local Electronic Structures from Analyzing and Modeling High-Energy Auger and Photoelectron Spectra of Solids

L. Kövér

Contents

Abstract

High energy resolution spectroscopy of energetic (up to 10 keV) Auger and photoelectrons excited by hard (2–10 keV) X-rays from clusters, nanostructures, surfaces, and interfaces of materials with high practical importance has started enjoying an increasing interest recently. The fast development of experimental technique and theoretical models in these days provides a possibility for a very detailed study of electronic structures of such systems including effects of solid environment on atomic transitions. Observing high-energy photoinduced electrons, surface effects on the spectra can be minimized, and the information depth is typically in the order of several times 10 nm, ensuring a new insight into the structure of "buried"

Institute of Nuclear Research of the Hungarian Academy of Sciences, 18/c Bem tér, H-4026 Debrecen, Hungary
E-mail: lkover@esca.atomki.hu

Advances in Quantum Chemistry, Vol. 54
ISSN 0065-3276, DOI 10.1016/S0065-3276(07)00014-7

interfaces, the local electronic structure surrounding atomic components of key functional importance, or the charge transfer between alloy components. Combining high energy resolution electron spectroscopies using hard X-rays and energetic electrons for excitation of Auger or photoelectrons and back-scattered electrons, as well as suitable models (including cluster molecular orbital type) for describing localized and collective electronic states, quantitative information can be obtained on local chemical and electronic structures around sites of key atoms even in the case of complex materials.

The aim of the paper is to give an insight into a recently fast-developing research field with promising practical applications, using examples for illustration such as solid-state and chemical effects on transitions in the deep atomic core, on initial- and final-state excitations, and on partial densities of electronic states obtainable from resonant Auger spectra. In addition, the role of the various electron energy loss processes, due to phenomena attributable to electron transport and to the sudden appearance of core holes, as reflected in the experimental electron spectra, will be discussed, together with suitable models for describing these processes.

1. INTRODUCTION

The local electronic structure surrounding atoms of functionally key elements in solids determines the macroscopic (mechanical, optical, electronic) properties of materials. The different electron spectroscopic methods, including X-ray photoelectron and Auger spectroscopy as well as electron energy loss spectroscopy, are well-suited and sensitive methods to provide information on the local electronic structure in various solid systems. High energy resolution spectroscopies of high-energy (2–10 keV) electrons are important tools for studying bulk, subsurface, and buried interface layers – elements of many systems of great practical importance. In this electron energy range, the mean free path of the electrons for inelastic scattering within the solid material is usually between 5 and 10 nm; therefore, photoelectrons excited from outer atomic shells or Auger electrons emitted following transitions between innermost atomic shells are probing bulk properties of solids, which is especially interesting for alloys and nanosized particles. In addition, photo- and Auger electrons excited from the deep atomic core can provide information on changes in the core potential and charge redistribution among components of alloys compared to the component metals [1]. For 1s photoelectron lines, exchange and spin-orbit splittings do not complicate the electron spectra.

2. SOLID-STATE AND CHEMICAL EFFECTS ON KLL AUGER SPECTRA (DIAGRAM TRANSITIONS) OF 3d TRANSITION METALS: EXPERIMENTS AND MODELS OF INTERPRETATION

A striking feature of the core Auger spectra is the multiplet structure of the diagram lines. Looking at the case of, for example, KLL Auger transitions in the

practically important 3d transition metal atoms, for estimating the respective multiplet energies, however, we can find mostly either semiempirical calculations for free atoms in the intermediate-coupling approach [2,3] or *ab initio* calculation without accounting for the complete configuration interaction (CI) [4]. In our recent work [5], the KLL multiplet energies for the 3d transition metals from chromium to copper ($Z = 24$–29) are calculated using a newly developed, fully relativistic (describes spin-orbit interactions) first-principles method with a complete CI (accounts for all interelectron interactions), based on the cluster molecular orbital (MO) model of solids. These calculations are compared to our high energy resolution (0.2 eV) experimental X-ray excited KLL Auger spectra in the $KL_{23}L_{23}$ region obtained from polycrystalline 3d metals by using synchrotron radiation at the Deutsches Elektronen Synchrotron (DESY), Hamburg, Germany [5]. The relativistic many-electron first-principles method applied for modeling the spectra is described in detail in Refs. [5,6]. Calculations were made both for free atoms and for clusters of 13–19 atoms, in order to study solid-state effects and including the CI with only $KL_{23}L_{23}$ configurations (model A) as well as including the CI with the KL_1L_1 configurations in addition (model B) [5]. Example results for the case of the $KL_{23}L_{23}$ Auger spectra of metallic Cr and Fe clusters of 15 atoms are shown in Figure 14.1. The calculated multiplet energies were derived by using model B for metal clusters [5]. The Auger energies in the figure are shifted to align the positions of the $^1D_2$ component facilitating the

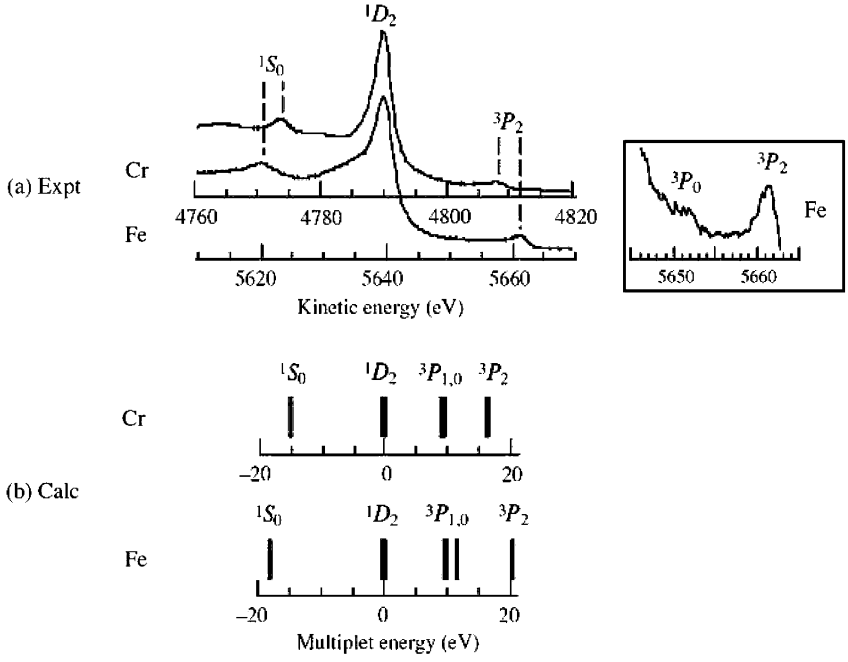

Figure 14.1 Experimental (a) and calculated (b) $KL_{23}L_{23}$ Auger spectra of Cr and Fe metals [5]. The inset shows a detail of the Fe spectrum.

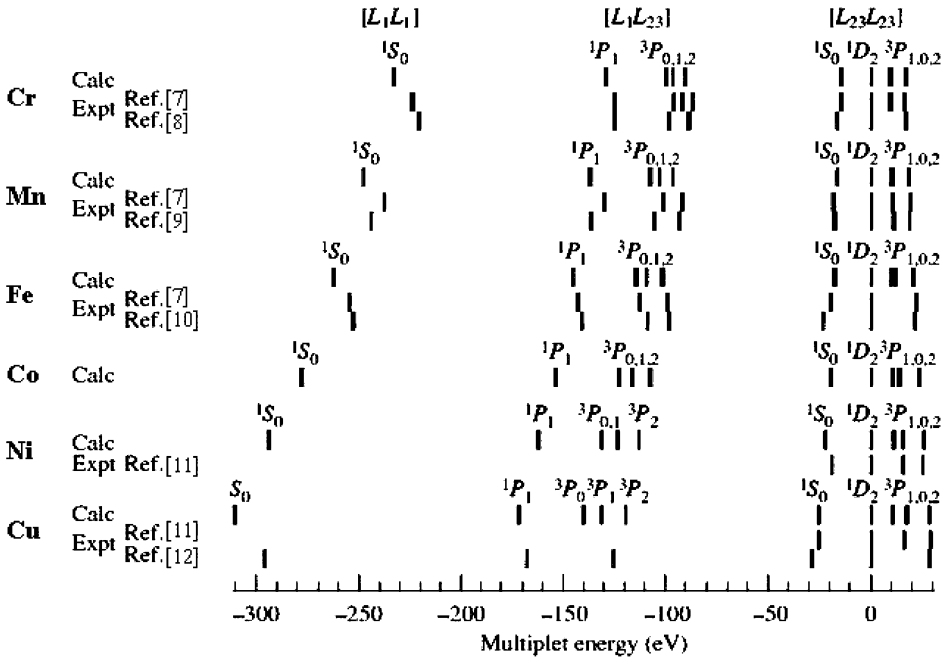

Figure 14.2 Multiplet energies in KLL Auger spectra of some 3d transition metals, calculated using configuration B for metal clusters, in comparison with experimental data published earlier. Reproduced with permission from Ref. [5].

comparison of the data. From the multiplet energies in Figure 14.1, a good agreement is seen between experiment and calculations; the weak peak in the KLL spectrum of Fe (see the inset) can unambiguously be assigned on the basis of the calculated results as due to the $^3P_0$ [L_3L_3] term. The calculations nicely reproduce the increase of the splittings in the case of Fe. Figure 14.2 shows the multiplet energies in the KLL Auger spectra (related to the energy position of the $^1D_2$ transition) of 3d transition metals from chromium to copper, calculated using configuration B for metal clusters [5], in comparison with experimental data published earlier [7–12]. As it can be seen in Figure 14.2, the respective energy separations due to the multiplet splittings increase with the increasing atomic number, and the increase is larger for the terms involving deeper atomic shells. The reason for this trend of increase in the multiplet splittings is the difference in the contraction of the respective orbitals as a consequence of the increase of the Coulombic repulsion between the electrons in those orbitals. Especially in the $KL_{23}L_{23}$ region, the agreement between the calculated and the more recently measured data is very good. For the metals Fe–Cu, the $^3P_1$ [L_3L_3] component is not observed in the experimental spectra due to parity conservation [13]. To illustrate the difficulties of accurate measurements of KLL Auger transition energies and intensities in the case of 3d transition metals, respective photoexcited KLL spectra of Cu polycrystalline metal are given in Figures 14.3 and 14.4. In Figure 14.3, the spectrum excited by bremsstrahlung (using a Mo(Cu) anode)

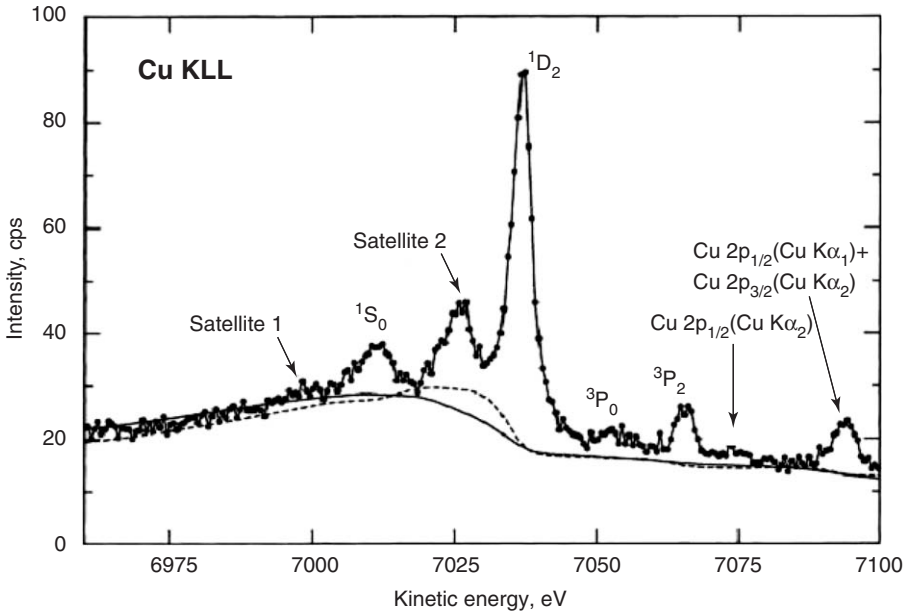

Figure 14.3 Experimental Cu $KL_{23}L_{23}$ Auger spectrum (dots) photoexcited from a approximately 100-nm thick polycrystalline layer using Mo bremsstrahlung [11]. The solid and dashed lines indicate the contributions from electrons scattered inelastically within the solid sample, estimated by different models [11].

from approximately 10-nm thick Cu layer [11] is shown. The intensity of the spectrum is rather low and in addition to the diagram Auger lines, strong satellites and photoelectron peaks excited by characteristic Cu K X-rays occur in the spectrum. In Figure 14.4, the experimental Cu $KL_{23}L_{23}$ Auger spectra photoexcited from (a) thick and (b) very thin (0.5 nm thick) polycrystalline Cu metal samples using monochromated synchrotron radiation of 9025 eV energy [14] are compared. In the case of the nanolayer sample, a near-grazing incidence irradiation was used [14]. A large contribution of the electrons scattered inelastically within the solid can be observed in the spectrum of the thick sample. The photoelectron peaks indicated by Ph1–3 appear due to the photoionization by the characteristic Cu K X-rays induced internally within the thick sample by the synchrotron radiation. In the spectrum of the nanolayer sample, the background caused by the inelastic electron scattering is largely diminished and the internally induced photopeaks are missing because the thickness of the nanolayer is too small compared to the inelastic mean free path of the Cu K X-rays. In Table 14.1 [5], theoretically and experimentally derived $KL_{23}L_{23}$ Auger energies are compared in the case of photoexcitation from Cu free atoms and Cu metal. The earlier calculations [2–4] were all performed for free atoms. The results in Table 14.1 and those given in [5] for other 3d metals show that the inclusion of the KL_1L_1 configuration in the CI (method B) leads to energy shifts improving the agreement with the more recent experiment and suggests

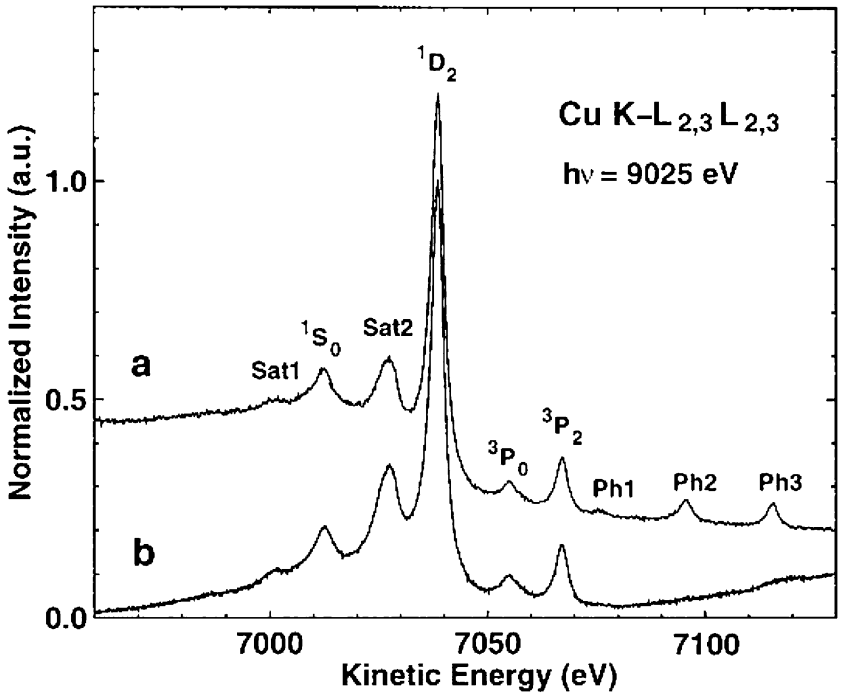

Figure 14.4 Experimental Cu $KL_{23}L_{23}$ Auger spectra photoexcited from (a) thick and (b) nanolayer (0.5 nm thick) polycrystalline Cu metal samples using monochromated synchrotron radiation of 9025 eV energy [14].

Table 14.1 Theoretical and experimental $KL_{23}L_{23}$ Auger multiplet energies in copper (in eV) [5]

Multiplets	Present theory				Previous theory			Experiment	
	Cu(A)	Cu_{19}(A)	Cu(B)	Cu_{19}(B)	Ref. [4]	Ref. [2]	Ref. [3]	Ref. [12]	Ref. [16]
$^3P_2$ [L_3L_3]	28.1	28.1	28.9	28.9	28.1	28.0	27.6	28.7	28.0
$^3P_0$ [L_3L_3]	15.3	15.3	17.1	17.2	15.3	15.0	16.3	15.9	
$^3P_1$ [L_2L_3]	10.8	10.8	10.8	10.7	11.1	–	10.6	–	–
$^1S_0$ [L_2L_2]	28.4	28.2	25.6	25.4	28.4	28.0	24.2	26.0	29.0

Note: The energies were shifted to take the energies of $^1D_2$[L_2L_3] term as the origin [5].

that accounting for CI among intermediate-coupling terms is necessary when using traditional semiempirical models. The present calculations for metal clusters and free atoms [5] indicate only a small (approximately 0.2 eV) solid-state effect, i.e., a slightly smaller multiplet splittings (and the respective peak positions in the KLL spectra) in metals than in free atoms. The results discussed above demonstrate that the applied cluster MO model is suitable to describe the diagram KLL Auger transitions in 3d transition metals in detail and indicate the

possibility of further applications of the method to describe other core Auger transitions in solids where covalency plays a greater role.

3. INITIAL- AND FINAL-STATE SHAKE UP EXCITATIONS IN KLL AUGER SPECTRA (PHOTOINDUCED NEAR THRESHOLD) OF Cu AND Ni METALS

Inner-shell hole production in atoms of 3d metals using X-ray photons can be accompanied by excitation processes leading to intense satellite structures in the corresponding photoinduced core Auger spectra. These satellites depend strongly on the local density of the unoccupied electronic states associated with the atom having the initial-state core hole. Such satellite peaks occur in the KLL Auger spectra of Cu and Ni metals [15–17], and following their evolution as a function of the exciting photon energy near the K-absorption threshold, unique information can be obtained on their origin and nature. From the detailed analysis and modeling of these satellite spectra, it is possible to determine whether they appear due to excitation processes localized to the atom with the initial-state core hole (intrinsic excitations) or as a consequence of inelastic electron scattering in the solid (extrinsic excitations). Furthermore, in the case of intrinsic excitations, it is possible to clarify the initial- or final-state character of the excitation processes. Observing the change in the intensity of the satellites at near-threshold photoexcitations as a function of photon energy is helpful not only for such clarification, but also for the decision whether the given process is a final-state excitation or a two-electron excitation in the initial state. On the basis of analysis and modeling the satellite-main diagram Auger peak energy separations only, these questions sometimes cannot be answered unambiguously.

The evolution of the satellite structure in the KLL Auger spectra photo-induced—using X-rays with energy near the K-absorption threshold—from polycrystalline Cu and Ni metals was observed with high energy resolution (0.2 eV) [17]. The measured spectra were corrected for background from inelastically scattered electrons, using experimental cross sections (derived from our REELS measurements [17]) for inelastic electron scattering [18]. The respective peaks in the background-corrected spectra were then fitted by asymmetric Lorentzian functions. Two different models were applied for interpretation of the experimental results: (i) for deriving the satellite-main diagram ($^1D_2$) energy separations, the discrete variational (DV)-Xα cluster MO model [19] using a simple cluster consisting of 13 atoms, the self-consistent charge method, a minimal basis set, and—in order to compensate for charges induced in the ionization/relaxation processes—charge neutralization of the clusters [2,17], (ii) for describing the photon energy (excess photon energy over the K-absorption threshold) dependence of the multiple-electron excitation probability (evolution of the intensity of the shake-up satellites), and the atomic generic model [17]. Figure 14.5 shows the obtained experimental KLL Auger spectra as a function of the excess photon energy from the K-threshold up to 46.5 eV, in the case of Cu metal [17]. Two distinct satellite structures, denoted by

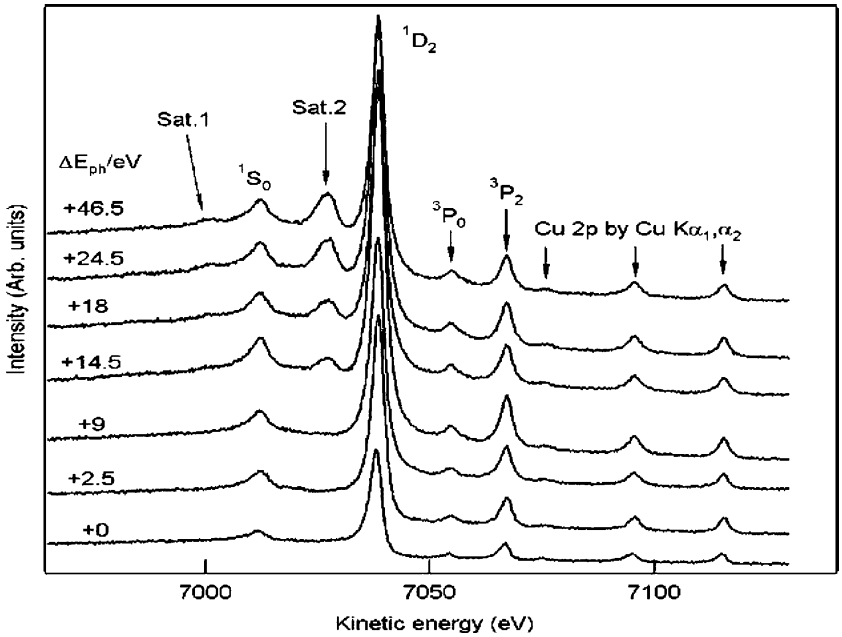

Figure 14.5 Experimental Cu $KL_{23}L_{23}$ Auger spectra photoinduced from the polycrystalline Cu metal sample, presented as a function of the excess photon energy (ΔE_{ph}) above the K-absorption threshold. The spectra are normalized to absolute intensity (in arb. units) [17].

Table 14.2 $KL_{23}L_{23}$ Auger satellite–$^1D_2$ (KL_2L_3) peak separations (eV) [17]

	Cu		Ni	
	Sat. 1	Sat. 2	Sat. 1	Sat. 2
XAES [20]	39.0	11.9	31.7	6.4
SR-XAES [17]	35.7	11.4	31.3	7.3
DV-Xα results				
$8e_g \rightarrow 15e_g$	37.2	10.2 [16]	30.9	5.7 [16]
$8t_{2g} \rightarrow 16t_{2g}$	35.8	10.6 [16]	30.4	6.4 [16]

Sat. 1 and Sat. 2, occur in the spectra. As the detailed analysis indicates, the intensity of the Sat. 2 peak (most intense at off-threshold excitations) decreases quickly with decreasing excess photon energy, while the intensity of the Sat. 1 peak at larger energy separation from the main ($^1D_2$) diagram Auger line changes rather slowly. The energy separations of the satellites from the main Auger peaks, derived from the respective experimental spectra, are presented in Table 14.2 [17] for both Cu and Ni metals and compared to the corresponding energy separation values calculated using the DV-Xα cluster MO model and Slater-type transition state method. A good agreement can be seen between the experimental and

calculated data given in Table 14.2, i.e., the experimental data confirm the origin of the satellites assumed in the model calculations, i.e., Sat. 1 appears due to a final-state shake-up type excitation (when a 3d electron is excited to an unoccupied 4d state as a consequence of the appearance of the two final-state core holes of the KLL Auger transition) while Sat. 2 appears due to initial-state shake-up type excitation (when the 3d–4d state transition takes place as a consequence of the appearance of the initial-state 1s hole). In the case of both experiment and model calculations, the satellite-main peak energy separations are smaller for Ni metal than for Cu metal, due to screening effects [16]. From the variation of the satellite intensities as a function of the excess photon energy (the ''satellite evolution curve''), additional independent information can be gained on the character of the satellites. In the case of the initial-state shake-up type excitation, the satellite intensity is expected to decrease rapidly approaching photon energies lower than the threshold plus the required shake-up excitation energy, while in the case of the final-state shake-up type excitation, the satellite intensity is not expected to depend on the excess photon energy. In Figure 14.6(a) and (b) [17], the observed satellite evolution curves are shown for the cases of the Cu and Ni metals, respectively, and for both the Sat. 1 and Sat. 2 satellites, in comparison with different atomic models [17,21] describing the dynamics of the initial-state shake-up processes. These satellite intensity evolution curves provide results consistent with the conclusions from the energy separation data in Table 14.2: the Sat. 2 satellites correspond to a 3d–4d shake-up excitation accompanying the creation of the initial-state 1s core hole, while the Sat. 1 satellite can be attributed to the appearance of the two core holes in the final state of the KLL Auger transition. The atomic models are approximating quite well the tendency of the changes in the intensity of the initial-state shake-up satellites, especially in the case of Ni, while for Cu the generic model underestimates the value for the sudden limit [17].

4. AUGER RESONANT RAMAN PROCESSES: EFFECTS OF THE PARTIAL DENSITY OF UNOCCUPIED ELECTRONIC STATES ON RESONANT KLL AUGER SPECTRA IN Cu AND Ni METALS

Tuning the exciting monochromatic photon energy across the K-absorption threshold and using high energy resolution for analyzing the energy distribution of the Auger electrons from solids, for example 3d transition metals, spectral features characteristic of the Auger Resonant Raman (ARR) effects [22] can be observed. In this process an 1s electron is excited resonantly into an unoccupied 4p state and the phenomenon is monitored by the measurement of the Auger spectra emitted as a result of the following Auger decay. This ARR process indicates the single-step nature of the threshold Auger emission [22] and provides information on the 4p unoccupied density of electronic states (DOS), which is important because this partial DOS dominates the K absorption. One of the main advantage of the ARR spectroscopy is that it is more selective for a specific partial DOS than for example the X-ray absorption spectroscopy. In addition, the emitted electrons have characteristic mean free paths for inelastic

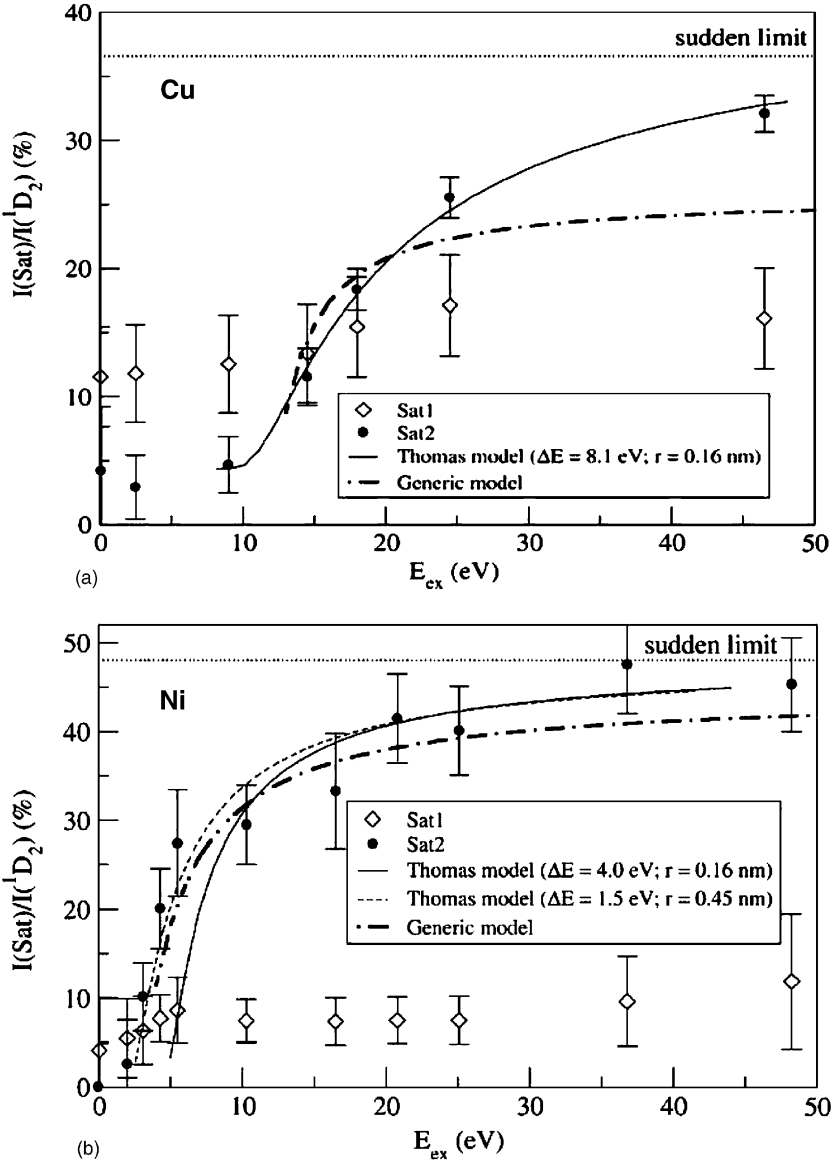

Figure 14.6 Evolution of the $KL_{23}L_{23}$ satellite intensities in (a) Cu and (b) Ni metals, related to the intensity of the $^1D_2$ main Auger line (Sat. 1: final-state shake up; Sat. 2: initial-state shake up), as a function of the excess photon energy above the K-absorption threshold [17]. For comparison, the predictions of the Thomas model [21] and the generic model [17] are also indicated.

scattering (IMFP) in the given solid, determining the depth of information. In the case of the KLL Auger transitions in 3d metals this depth can reach several tens of nanometers, allowing non-destructive studies of electronic structures at deeply buried interfaces. The following signatures of the ARR process can be observed in

the near-threshold Auger spectra: (i) asymmetry and lineshape distortion (e.g., the reduction of the energy width) at near-threshold excitations, (ii) linear dispersion of the energy position of the Auger line with photon energy at excitations using photons having lower energy than the threshold (sub-threshold excitations). These changes can be interpreted on the basis of the resonant scattering theory [23] and a simple model [24] describing the linear dispersion of the Auger peak position and the peak shape distortion as a function of the near-threshold photon energy using calculated partial DOS of the corresponding unoccupied electronic states. Considering only 1s–4p dipole transition, neglecting other channels and using the DOS of the unoccupied 4p states calculated in the transition (intermediate) state partially accounting for relaxation effects, the resonance formula originally given in [24] is derived for the resonant lineshape of the KL_2L_3 ($^1D_2$) Auger transition in Cu and Ni metals [25] for comparison with the experimental lineshape:

$$i(\varepsilon_A, \hbar\omega) = C \int_0^\infty \int_0^\infty \frac{\rho_p(\varepsilon) N_{ph}(\hbar\omega - \hbar\omega') d\varepsilon d\hbar\omega'}{[(\hbar\omega' - \varepsilon - E_K)^2 + (\Gamma_K^2/4)][(\hbar\omega' - \varepsilon - \varepsilon_A - E_{L_2L_3})^2 + (\Gamma_{L_2L_3}^2/4)]} \quad (1)$$

Here $i(\varepsilon_A, \hbar\omega)$ is the energy distribution of the $^1D_2$ Auger electrons having energy ε_A, $\hbar\omega$ the exciting photon energy, ε the energy of the unoccupied p state where the 1s electron is photoexcited, N_{ph} the photon energy distribution, $\rho_p(\varepsilon)$ the density of the unoccupied p-states, E_K the energy of the K-absorption edge position (defined as the inflection point of the leading absorption edge structure), $E_{L_2L_3} = E_K - E_A$ (where E_A is the measured energy of the $^1D_2$ line), Γ the lifetime width, and C is a scaling factor and includes all matrix elements.

For obtaining information on the 4p unoccupied DOS in Cu and Ni metals, as well as on the validity of the theoretical approach and Eq. (1) in the case of the resonant KLL Auger spectra in these metals, high energy resolution (0.2 eV) $KL_{23}L_{23}$ Auger spectra and X-ray absorption spectra excited by synchrotron radiation—using monochromatic photons with energies near the K-absorption threshold—from polycrystalline Cu and Ni foils, were measured [25] with the tunable high-energy XPS [26] equipment at the BW2 beamline of HASYLAB/DESY. The measured spectra then were background corrected, using experimental cross sections (derived from our REELS measurements [17,25]) for inelastic electron scattering within the solids [18]. The K-absorption spectra of Cu and Ni metals were measured detecting the total electron yield emitted from the samples as a function of the photon energy [25]. For interpreting the resonant Auger spectra, the resonant inelastic X-ray scattering model outlined above and the resonant formula in Eq. (1) was applied. The partial DOS for the unoccupied 4p states was calculated using the DV-Xα cluster MO model [19,25] with the self-consistent charge method, metal clusters of 79 atoms, basis sets including orbitals 1s–5p (Ni), 1s–4d (Cu), and Slater's transition state approach.

Figure 14.7 shows the resonantly photoexcited Ni $KL_{23}L_{23}$ Auger spectra using near-threshold– and sub-threshold–energy X-ray photons [25]. It can be clearly seen from the spectra that lowering the photon energy across the K-absorption threshold, the peaks shift on the energy scale, their shapes become more asymmetric, and the spectrum becomes more distorted compared to that

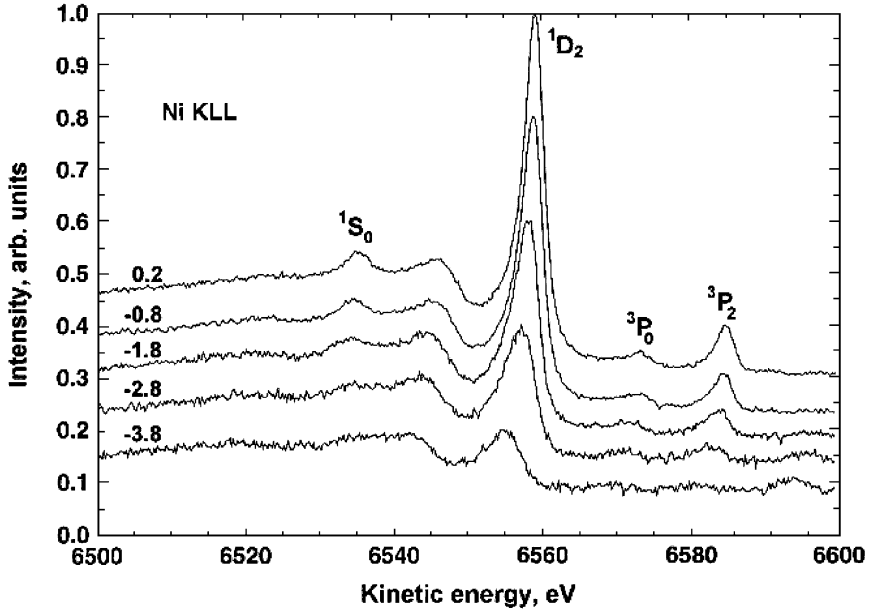

Figure 14.7 Resonant Ni $KL_{23}L_{23}$ Auger spectra excited from Ni metal foil using near-threshold– and sub-threshold–energy X-ray photons [25]. The energies of the photons related to the K-absorption threshold are indicated.

obtained at threshold (signatures of the ARR process). Similar trends can be observed in the resonant spectra of the Cu metal as well [25]. The linear dispersion of the energy positions of the main $^1D_2$ Auger peak is demonstrated in Figure 14.8. It is interesting that the ARR component of this peak starts to appear already at exciting photon energies a few electron volts above threshold [25]. In Figures 14.9 and 14.10, the near-threshold experimental spectra (corrected for contributions from electrons that suffered inelastic scattering and therefore energy loss within the samples) obtained for Cu (Figure 14.9) and Ni (Figure 14.10) are compared with the spectra using the models described above [25]. In the case of Cu the agreement between experiment and theory is rather good while for Ni the model provides a reasonable qualitative interpretation. In order to clarify the reason for the lower degree of agreement between theory and experiment in the case of Ni, the same calculated 4p partial DOS distributions were compared to the respective K-absorption spectra, yielding a quite good agreement, and in addition, these partial DOS distributions were compared to those derived using an *ab initio* self-consistent real-space multiple-scattering model, finding again a very good agreement between the DOS functions calculated with the different models [25]. Our further studies indicate that the difference between theory and experiment in the case of Ni (Figure 14.10) can be attributed most probably to the strong intrinsic type energy loss process; this excitation of collective nature occurs as a consequence of the sudden appearance of the core hole(s) [27].

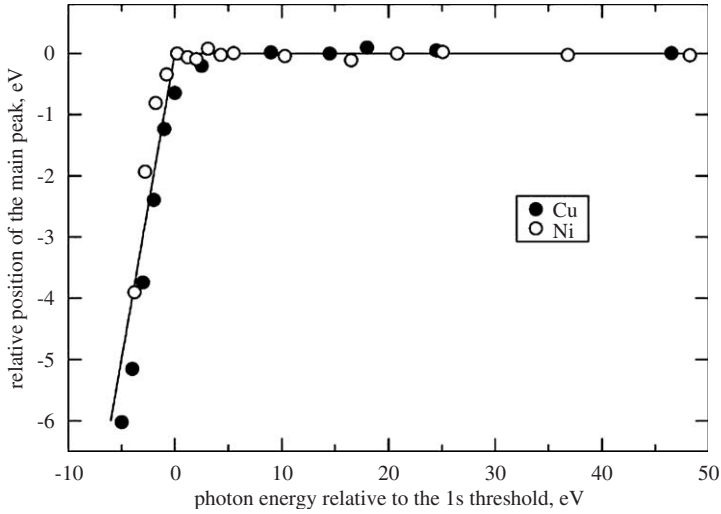

Figure 14.8 Relative energy positions of the maxima of the main $^1D_2$ peaks in the resonant $KL_{23}L_{23}$ Auger spectra of Cu and Ni metals as a function of the exciting X-ray photon energy related to the K-absorption threshold [25]. The linear dispersion and constant regions are indicated by the solid lines.

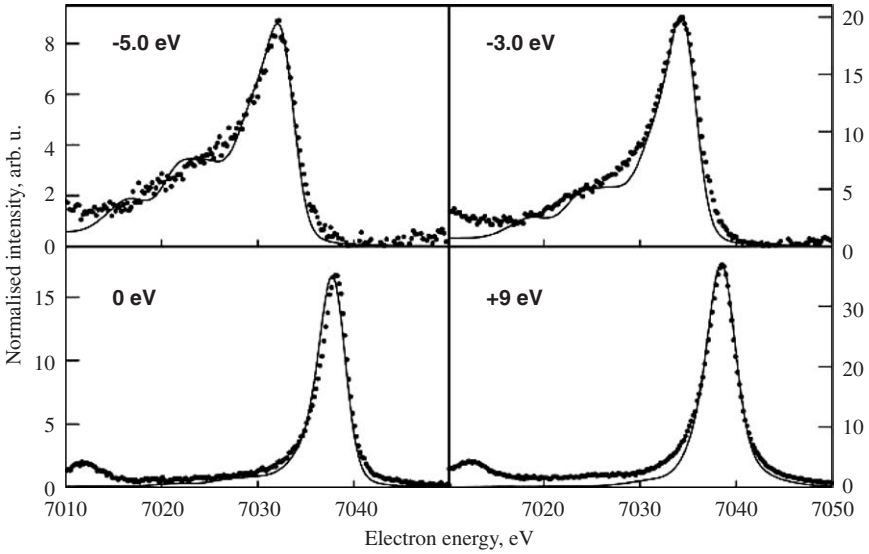

Figure 14.9 Resonant Cu $KL_{23}L_{23}$ Auger spectra excited from Cu metal foil using near-threshold– and sub-threshold–energy X-ray photons [25]. The energies of the photons related to the K-absorption threshold are indicated. Dots: experimental data corrected for inelastic electron scattering; solid line: calculated spectra using the resonant X-ray scattering theory and the DV-Xα cluster MO model.

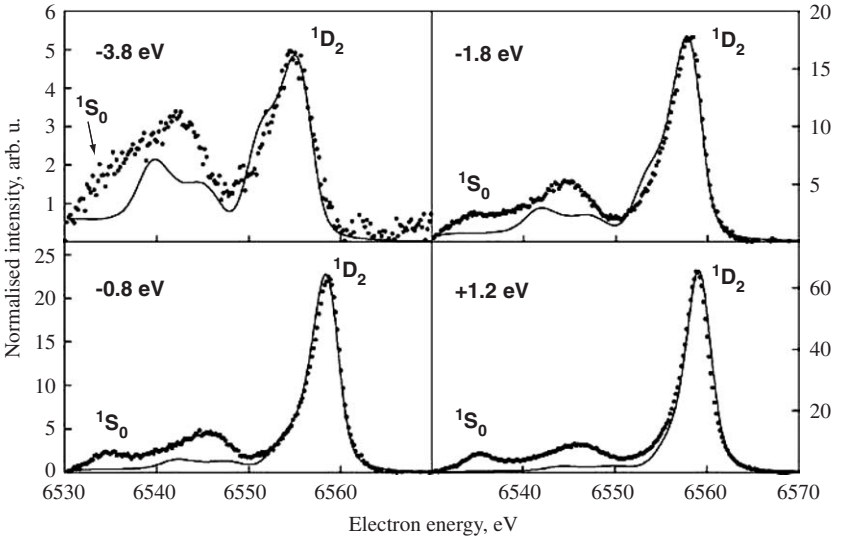

Figure 14.10 Resonant Ni $KL_{23}L_{23}$ Auger spectra excited from Ni metal foil using near-threshold– and sub-threshold–energy X-ray photons [25]. The energies of the photons related to the K-absorption threshold are indicated. Dots: experimental data corrected for inelastic electron scattering; solid line: calculated spectra using the resonant X-ray scattering theory and the DV-Xα cluster MO model.

5. FURTHER ELECTRON SPECTROSCOPIC METHODS FOR STUDYING LOCAL ELECTRONIC STRUCTURES IN SOLIDS

There are other, emerging electron spectroscopic methods applicable for revealing information on local electronic structures. For example, valence band XPS spectra reflect the valence electronic structure (initial-state DOS) of solids; however, it is difficult to separate unambiguously the symmetry-projected partial DOS distributions in these spectra. By the help of a recently developed method, the orbital determination from angular distribution (ODAD), the atomic orbitals constituting the valence band of a solid can be derived from the analysis of two-dimensional photoelectron intensity angular distributions of crystals [28,29]. Using linearly polarized synchrotron radiation and a display type analyzer [30], the two-dimensional intensity angular distribution of a given photoelectron line is observed. Selecting a proper direction of the emitted photoelectrons and then changing the polar or azimuthal angle of the crystalline sample, the analysis of the photoelectron intensity angular distributions measured in such a way provides a direct information on the different symmetry atomic orbitals, i.e., in the case of changing the polar angle, the maximum intensity for the different symmetry components occurs at different polar angles; therefore, these different symmetry components can be distinguished unambiguously [29].

Another emerging electron spectroscopic method for non-destructive determining local electronic structures at buried interfaces and nanostructures of high

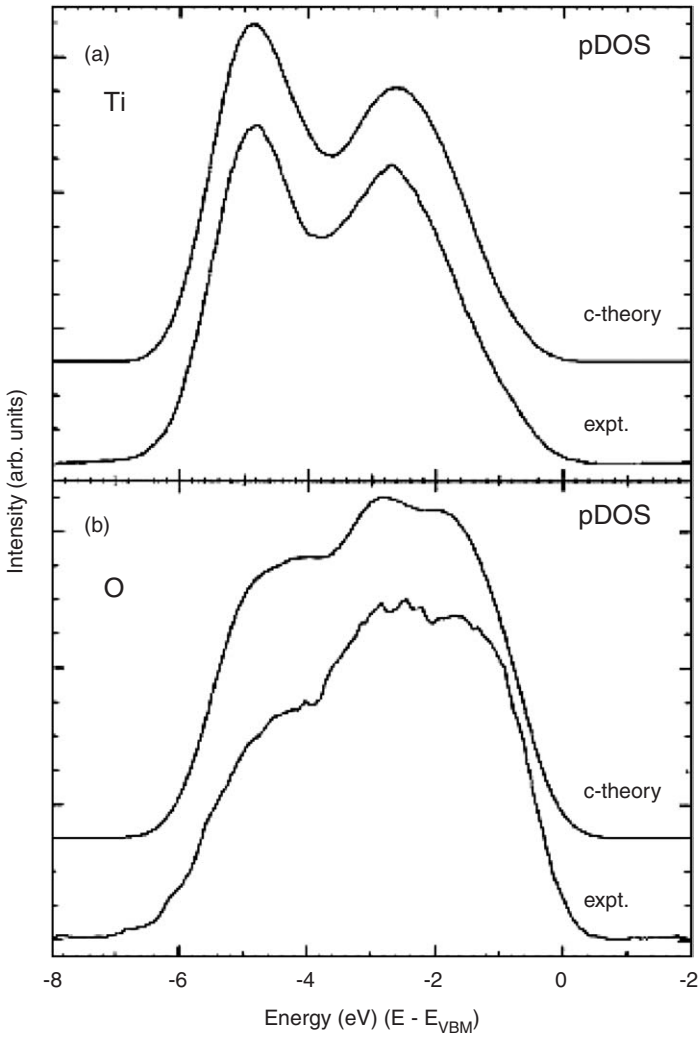

Figure 14.11 Site-specific experimental valence X-ray photoelectron spectrum of the rutile TiO_2 single-crystal sample, obtained using the XRSW technique, in comparison with the calculated partial density of states (corrected for individual angular-momentum–dependent photoionization cross sections) [32]. (a) Ti, (b) O. The spectra are normalized to equal peak height.

importance for the present semiconductor industry and information storage is the X-ray standing wave (XRSW) technique. Standing waves are generated by synchrotron radiation in Bragg reflection from a synthetic multilayer structure that serves as a substrate as well; on this substrate a wedge-shaped or tapered overlayer structure is deposited and the core photoelectrons, excited by the monochromatic, microfocused X-ray beam sledging through the slope, carry the depth-dependent (according to the depth-dependent periodic electric field

strength of the standing wave) analytical information [31]. Using a $[B_4C/W]_{40}$ multilayer standing wave generator and the magnetic circular dichromism in photoemission from the core levels of the Fe and Cr components of the wedge-shaped Fe/Cr bilayer grown on the top of this multilayer, from the analysis of the core photoelectron line intensities as a function of emission angle and X-ray beam position, the magnetic structure of the 1–2 atomic layer thick altered regions at the Fe/Cr interface was successfully revealed [31]. In a different study [32], a novel method, the site-specific valence band XPS, was applied for the case of the rutile TiO_2 single crystal for determining experimentally the partial DOS distributions at the Ti and O atoms, respectively. Site-specific valence band photoelectron spectra were measured tuning the standing wave electric field intensity on the atomic plane of Ti or O; the position of these planes were found by using the corresponding intensity maxima of the Ti 3p and O 2s core photoelectron lines as a function of photon energy (changing within the Bragg back-reflection peak) [32]. Figure 14.11 shows the Ti and O site-specific experimental valence band X-ray photoelectron spectrum of a rutile TiO_2 single crystal sample, obtained using the method utilizing the XRSW effect as described above, in comparison with the theoretical partial density of states (corrected for individual angular-momentum–dependent photoionization cross sections) calculated using *ab initio* local density approximation [32]. The agreement between theory and experiment is very good, i.e., the theory fully supports the experimental derivation of the site-specific DOS distributions.

6. SUMMARY

In summary, the selected examples clearly demonstrate that the applied cluster MO (DV-Xα, DV-multi-electron (ME)) approximations are capable of describing the high-energy Auger processes in detail and (in the case of resonant Auger spectra in combination with the resonant inelastic X-ray scattering model) show a very good agreement with the experimentally obtained resonant and non-resonant KLL Auger spectra of 3d metals such as Cu and Ni. The local electronic structure surrounding the selected atom (in a solid, e.g. at buried interfaces) with the initial-state core hole can be successfully revealed in detail using high energy, high energy resolution electron spectroscopies and the cluster MO theory.

ACKNOWLEDGMENTS

The authors acknowledge the financial support of the Grants OTKA T038016, K6783 and JSPS-MTA No. 97. This work was supported by the project IHP-Contract HPRI-CT-1999-00040/2001-00140 (EC).

REFERENCES

[1] L. Kövér, *Adv. Quantum Chem.* **42** (2003) 331.
[2] D.A. Shirley, *Phys. Rev.* **A7** (1973) 1520.

[3] F.P. Larkins, *Atomic Data Nucl. Data Tables* **20** (1977) 311.
[4] F.A. Gianturco, E. Semprini, F. Stefani, *Physica* **C80** (1975) 613.
[5] T. Ishii, L. Kövér, Z. Berényi, I. Cserny, H. Ikeno, H. Adachi, W. Drube, *J. Electron Spectrosc. Relat. Phenom.* **137–140** (2004) 451.
[6] K. Ogasawara, T. Iwata, Y. Koyama, T. Ishii, I. Tanaka, H. Adachi, *Phys. Rev.* **B64** (2001) 115413.
[7] A. Némethy, L. Kövér, I. Cserny, D. Varga, P.B. Barna, *J. Electron Spectrosc. Relat. Phenom.* **82** (1996) 31.
[8] A. Kovalík, M. Rysavy, V. Brabec, O. Dragoun, *Phys. Scr.* **37** (1988) 871.
[9] A. Kovalík, V. Brabec, J. Novák, O. Dragoun, A.F. Gorozhankin, V.M. Novgorodov, Ts. Vylov, *J. Electron Spectrosc. Relat. Phenom.* **50** (1990) 89.
[10] A. Kovalík, A.F. Inoyatov, A. Novgorodov, V. Brabec, M. Rysavy, Ts. Vylov, O. Dragoun, A. Minkova, *J. Phys.* **B20** (1987) 3997.
[11] L. Kövér, I. Cserny, J. Tóth, D. Varga, T. Mukoyama, *J. Electron Spectrosc. Relat. Phenom.* **114–116** (2001) 55.
[12] E. Sokolowski, C. Nordling, *Arkiv Fysik* **14** (1958) 557.
[13] R.M. Eisberg, *Fundamentals of Modern Physics*, Wiley, New York, 1963, p. 436.
[14] W. Drube, *Nucl. Instrum. Methods Phys. Res.* **547** (2005) 87.
[15] L. Kövér, Zs. Kovács, J. Tóth, I. Cserny, D. Varga, P. Weightman, S. Thurgate, *Surf. Sci.* **433** (1999) 833.
[16] I. Cserny, L. Kövér, H. Nakamatsu, T. Mukoyama, *Surf. Interface Anal.* **30** (2000) 199.
[17] L. Kövér, Z. Berényi, I. Cserny, L. Lugosi, W. Drube, T. Mukoyama, V.R.R. Medicherla, *Phys. Rev.* **B73** (2006) 195101.
[18] S. Tougaard, *Surf. Interface Anal.* **26** (1998) 249.
[19] H. Adachi, M. Tsukada, C. Satoko, *J. Phys. Soc. Jpn.* **45** (1978) 875.
[20] L. Kövér, D. Varga, I. Cserny, J. Tóth, Zs. Kovács, *J. Surf. Anal.* **5** (1999) 74.
[21] T.D. Thomas, *Phys. Rev. Lett.* **52** (1984) 417.
[22] T. Åberg, *Phys. Scr.* **T41** (1992) 72.
[23] T. Åberg, B. Craseman, In: G. Materlik, C.J. Sparks, K. Fischer (Eds.), *Resonant Anomalous X-Ray Scattering*, North-Holland, New York, 1994, p. 431.
[24] W. Drube, R. Treusch, G. Materlik, *Phys. Rev. Lett.* **74** (1995) 42.
[25] L. Kövér, W. Drube, Z. Berényi, I. Cserny, V.R.R. Medicherla, T. Ishii, H. Ikeno, H. Adachi, *Surf. Sci.* **601** (2007) 1085.
[26] W. Drube, T.M. Grehk, R. Treusch, G. Materlik, *J. Electron Spectrosc. Relat. Phenom.* **88–91** (1998) 683.
[27] L. Kövér, I. Cserny, W. Drube, F. Yubero, S. Tougaard, to be published.
[28] M. Kotsugi, H. Daimon, K. Nakatsuji, T. Okuda, T. Furuhata, M. Fujikawa, H. Takagi, Y. Tezuka, S. Shin, K. Kitahama, T. Kawai, S. Suga, *J. Electron Spectrosc. Relat. Phenom.* **88–91** (1998) 489.
[29] H. Daimon, M. Kotsugi, K. Nakatsuji, T. Okuda, K. Hattori, *Surf. Sci.* **438** (1999) 214.
[30] H. Daimon, *Rev. Sci. Instrum.* **59** (1988) 545.
[31] S.-H. Yang, B.S. Mun, N. Manella, S.-K. Kim, J.B. Kortright, J. Underwood, F. Salmassi, E. Arenholz, A. Young, Z. Hussain, M.A. Van Hove, C.S. Fadley, *J. Phys. Condens. Matter* **14** (2002) L407.
[32] J.C. Woicik, E.J. Nelson, L. Kronik, M. Jain, J.R. Chelikowsky, D. Heskett, L.E. Berman, G.S. Herman, *Phys. Rev. Lett.* **89** (2002) 077401.

CHAPTER 15

X-Ray Absorption Spectroscopic Study on Polymerization of Aqueous Aluminate by DV-Xα Molecular-Orbital Method

Shuji Matsuo* and **Hisanobu Wakita****

Contents

Abstract

Chemical species produced in the process of structural transition from aqueous aluminate to crystalline aluminum hydroxide (gibbsite) in 1.0 M aqueous solution and their ratios are examined by the curve fitting for the experimental Al K-edge XANES spectra using the calculated XANES curves derived from the results of the discrete variational (DV)-Xα molecular-orbital calculations and theoretical continuum curves as a baseline. The structural transform proceeds in order of: (I) decomposition of network structure of aluminate due to hydrolysis, (II) polymerization of hydrate ions, (III) precipitation of $Al(OH)_3$, and (IV) crystallization due to dehydration.

* Physical Analysis and Evaluation Department, Electronics Division, KOBELCO Research Institute, Inc., 1-5-5 Takatsukadai, Nishi-ku, Kobe, Hyogo 651-2271, Japan
Corresponding author. E-mail: matsuo.shuji@kki.kobelco.com

** Department of Chemistry, Faculty of Science, Fukuoka University, 8-19-1 Nanakuma, Jonan-ku, Fukuoka 814-0180, Japan

Advances in Quantum Chemistry, Vol. 54
ISSN 0065-3276, DOI 10.1016/S0065-3276(07)00015-9

The curve fittings for experimental XANES spectra corresponding to process (I)–(IV) during the transition are converged by $[Al(OH)_4]^-$ and $[Al(OH)_4(H_2O)_2]^-$ models for process (I), by $[Al(OH)_4]^-$, $[Al(OH)_4(H_2O)_2]^-$, and $[Al(H_2O)_6]^{3+}$ models for process (II), by $[Al(OH)_4(H_2O)_2]^-$, $[Al(H_2O)_6]^{3+}$, and gibbsite models for process (III), and by $[Al(H_2O)_6]^{3+}$ and gibbsite models for process (IV).

1. INTRODUCTION

1.1 Relationship between aluminate and $Al(OH)_3$

Aluminum alloys and materials are versatilely used in our life because of their lightness, strength, and plasticity. In addition, aluminum is an element out of the RoHS Directive and is a safe element for our health. The RoHS Directive stands for ''the restriction of the use of certain hazardous substances in electrical and electronic equipment''; it bans the placing on the EU market of new electrical and electronic equipment containing more than agreed levels of lead, cadmium, mercury, hexavalent chromium, polybrominated biphenyl, and polybrominated diphenyl ether flame retardants. Aluminum materials are generally manufactured through three major processes of: (I) the extraction of alumina components, (II) the products of Al metal by the electrolysis of the alumina in a melted cryolite, and (III) by rolling, pressing, founding, and forging. In particular, we have an interest in the structural transition from aqueous aluminate to crystalline aluminum hydroxide in the process (I) as described above.

In general, crystalline $Al(OH)_3$ (gibbsite) precipitates in the aqueous solution of aluminate [1], which is prepared by dissolving bauxites into aqueous solution of sodium hydroxide, in the process (I) because of the reduction of pH under atmosphere. The morphology of crystalline $Al(OH)_3$ is related with pH, viscosity, density, and refractivity of the aqueous solution of aluminate [2–4], and related with the rate of polymerization. Highly pure alumina obtained by sintering crystalline $Al(OH)_3$ are used for the pulverization of fine ceramic powders and pigment, and used as insulation materials and components for semiconductor devices. Accordingly, the morphology of $Al(OH)_3$ is an important factor in the formation of highly pure alumina, while it is related with the condition of the aqueous solution of aluminate. The structural transition from the aqueous aluminate to crystalline $Al(OH)_3$, therefore, can provide significant information on the crystallography and the morphology of $Al(OH)_3$ for high-purity alumina.

1.2 Spectroscopic study on aqueous solution of aluminate

The local structure of aluminate in aqueous solution has been found by Radnai et al. to be a fourfold coordination structure, $[Al(OH)_4]^-$, using a solution X-ray diffraction method [5]. We have spectroscopically examined the dynamic change in the structural transition from aluminate to $Al(OH)_3$ [6], which happens with the polymerization of aluminate due to the reduction of pH [7], using the *in situ* soft X-ray absorption spectroscopy we have developed [8,9]. The X-ray

absorption spectral measurements using the experimental tool were conducted at beamline 6.3.1 at the Advanced Light Source, Lawrence Berkeley National Laboratory. The result of X-ray absorption near-edge structure (XANES) measurements is shown in Figure 15.1. Figure 15.1 represent the elapsed time after the preparation of the 1.0 M aqueous solution of aluminate, where each spectrum was measured at about 3 min a scan [6]. The first scan was 23 min later, and the last scan was 103 min later. The absorption intensity in Figure 15.1(a) is shown by the total fluorescence yield measured, while that in Figure 15.1(b) is normalized by

$$I_{\mathrm{nor}} = \frac{I - I_{\mathrm{min}}}{I_{\mathrm{max}} - I_{\mathrm{min}}}, \tag{1}$$

where I_{nor}, I, I_{min}, and I_{max} are the normalized intensity, the intensity of each measured point in each spectrum, the minimum and maximum intensity in each spectrum, respectively. The intensity reduced until 54 min after the preparation, and increased after that as shown in Figure 15.1(a). The change indicates the beginning of the polymerization. The drastic change in the spectral shape can be seen between 76 and 85 min after the preparation as in Figure 15.1(b). The increase of the absorption intensity after that indicates the precipitate of $Al(OH)_3$ at a measured point. Therefore, the structural transition can be considered to happen between 76 and 85 min after the preparation.

Our aim of this study is to examine the chemical species and their ratios by analyzing Al K-edge XANES spectra in the aqueous solution of aluminate when the structural transformation happens. The selected experimental XANES spectra in this study are of 23 min later (first-scan), 76 min later (transform-beginning), 85 min later (transform-end), and 103 min later (last-scan) in Figure 15.1, and are analyzed using the calculated curves derived from the discrete variational (DV)-Xα molecular-orbital (MO) calculations.

2. COMPUTATIONAL METHOD

2.1 DV-Xα MO method and electron transition probability

The crystal models of β-aluminate (fourfold coordination) [10] and $Al(OH)_3$ [11] were based on the corresponding crystal data, respectively, and are shown in Figure 15.2. Note that the structure of $Al(OH)_3$ has two Al sites. The spectral shape of XANES for crystalline β-aluminate ($Al_2O_3 \cdot Na_2O$) was not similar to that of first-scan, while that of XANES for $Al(OH)_3$ was close to that of last-scan, as can be seen in Figure 15.1(b). Hence, the structure models for aluminate in aqueous solution were built up from the moiety of β-aluminate structure, and were 5Al_16(OH), Al_4(OH), Al_4(OH)_2(H_2O), Al_6(OH), and Al_6(H_2O) models, which were optimized by the Amsterdam Density Functional (ADF) program package [12–14], as shown in Figure 15.2. The interatomic distances between Al and O of each model are summarized in Table 15.1.

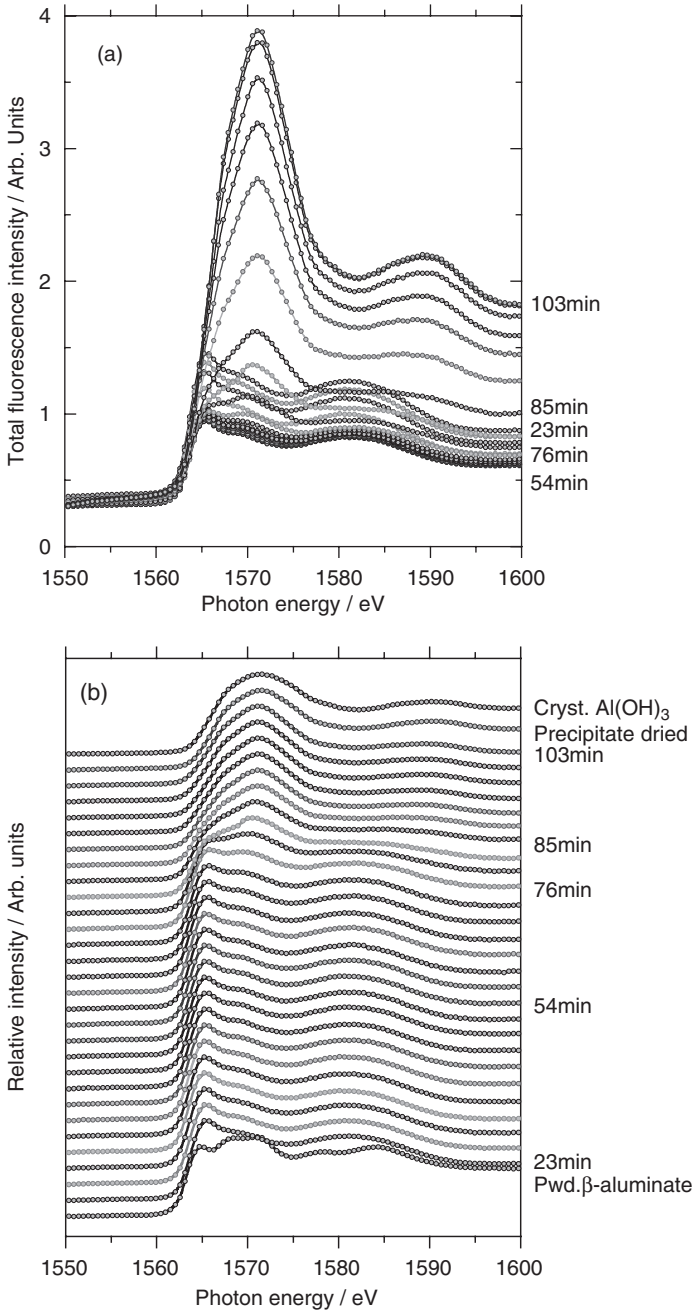

Figure 15.1 Time-dependent XANES spectra around Al *K* absorption edge for the 1.0 M aqueous solution of aluminate. Panels (a) and (b) show the spectra without and with normalization of absorption intensity, respectively. The times represent the elapsed time after the preparation of the 1.0 M aqueous solution of aluminate for the corresponding spectra.

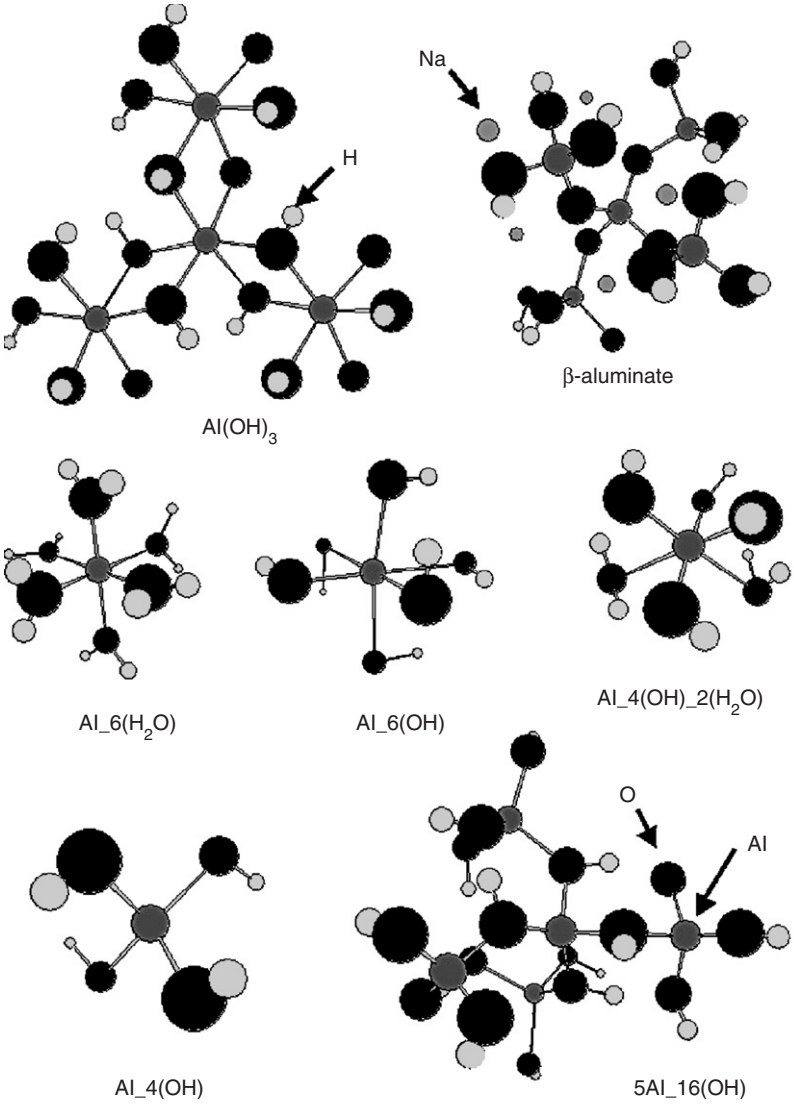

Figure 15.2 Structure models calculated by the DV-Xα MO method and used for the LC-XANES Fit analysis.

Computational details of the DV-Xα MO calculation have been described elsewhere [15]. Numerical atomic orbitals were used as basis sets for calculations as follows: 1s, 2s, 2p, 3s, 3p, 3d, 4s, 4p, and 4d for Al, 1s, 2s, 2p, 3s, and 3p for Na, 1s, 2s, and 2p for O, and 1s for H. Initial charges were set as follows: +3 for Al, −2 for O, −1 for O of OH, zero for O of H_2O, +1 for Na, and 0 for other atoms. The calculation considering a Madelung potential was carried out only for the $Al(OH)_3$ model. The calculations for the other models were conducted without

Table 15.1 The interatomic distances between Al and O of each model

Model	r(Al–O_b)[a] (Å)	r(Al–O_h)[b] (Å)	r(Al–O_w)[c] (Å)
β-aluminate	1.746, 1.773 1.777, 1.856	N/A[d]	N/A
5Al_16(OH)	N/A	1.738, 1.745 1.750, 1.911	N/A
Al_4(OH)	N/A	1.784, 1.787 1.791, 1.792	N/A
Al_4(OH)_2(H_2O)	N/A	1.863, 1.872 1.839, 1.881	2.127, 2.145
Al_6(OH)	N/A	1.951, 1.962 1.958, 1.975 1.902, 2.051	N/A
Al_6(H_2O)	N/A	N/A	1.890, 1.892 1.892, 1.896 1.898, 1.898
$Al(OH)_3$_site 1	N/A	1.831, 1.905 1.910, 1.918 1.922, 1.924	N/A
$Al(OH)_3$_site 2	N/A	1.861, 1.881 1.881, 1.922 1.929, 1.946	N/A

[a]Bridged oxygen atoms between aluminum atoms.
[b]Oxygen atoms of hydroxides.
[c]Oxygen atoms of water molecules.
[d]N/A = not available.

the potential. The DV-Xα MO calculations for all of the models were performed using the Slater's transition state method [16] with numerical integration of 1000 points per atom. Convergence of self-consistent-field iterations was set to 0.001 electrons.

Electron transition probabilities (hereafter ETPs) from the 1s orbital of Al to the unoccupied orbitals are calculated from the SXS code [17] on the basis of the dipole approximation using electron state data of MOs. The theoretical Al K-edge XANES spectra of the models were obtained from convoluting a Gauss function to ETPs.

2.2 Curve fit by least-squares procedure for XANES spectra

The calculated XANES curves of the structure models were used for the curve fits to the selected experimental XANES spectra of first-scan, transform-beginning, transform-end, and last-scan. However, it is hard to reproduce the feature of continuum region in XANES spectrum (hereafter, continuum feature) only using the calculated XANES curves. Continuum features are the result of excitation of

the inner electron to a continuum of final states. The intensity of continuum feature, I_{contin}, is approximated by an arctangent function,

$$I_{\text{contin}} = H\left[\frac{1}{\pi}\arctan 2\left(x - P, \frac{W}{2}\right) + \frac{1}{2}\right], \tag{2}$$

where H is the height of the step, P the position of the inflection point of the step, and W the FWHM of the rise [18]. The theoretical continuum curve obtained by equation (2) can thus represent the corresponding continuum feature in an experimental XANES spectrum, and plays an indispensable role in the fitting of a theoretical fitting curve into the corresponding experimental spectrum as a baseline. The theoretical fitting curve is represented by a linear combination of some calculated XANES curves (i.e., Gauss functions) and an arctangent curve obtained from equation (2). The curve fit of the theoretical fitting curve into the corresponding experimental XANES spectrum was performed by a least squares procedure. Peak position and component ratios of the calculated XANES curves and of theoretical continuum curve selected to make up the theoretical fitting curve are used for the curve fit by the least squares procedure as fitting parameters. The curve fit is evaluated by the residual, R, obtained from the following equation:

$$R(\%) = \frac{\sum_{x=1}^{N}(I_{\text{exp}}(x) - I_{\text{theor}}(x))}{\sum_{x=1}^{N} I_{\text{exp}}(x)} \times 100, \tag{3}$$

where x is a data point, N the number of data points, $I_{\text{exp}}(x)$ the intensity of an experimental XANES spectrum, and $I_{\text{theor}}(x)$ the intensity of a theoretical curve. In this study, the curve fits were performed using the ''LC-XANES Fit'' program [19] in WinXAS ver. 2.1 program package [20]. As a result, The LC-XANES Fit provide the peak positions and component ratios of the selected calculated XANES spectra and theoretical continuum curve.

3. RESULTS AND DISCUSSION

3.1 Calculated XANES curves

The calculated XANES curves for the structure models shown in Figure 15.2 are given in Figure 15.3, where the bars are ETPs from the 1s orbital of Al to the unoccupied orbitals, and the solid curves are obtained by convoluting a Gauss function to ETPs. For $Al(OH)_3$ model, the shape of calculated curve of Al in site 1 is different from that in site 2, so that the results of sites 1 and 2 are separately used for the curve fits. The peak positions for the fourfold coordination models appear at lower energy than those for sixfold coordination models. The difference in energy at the peak position is very important in the structural transition from aqueous aluminate to crystalline $Al(OH)_3$, and can be related with the interatomic distance and coordination number, i.e., when peak position moves

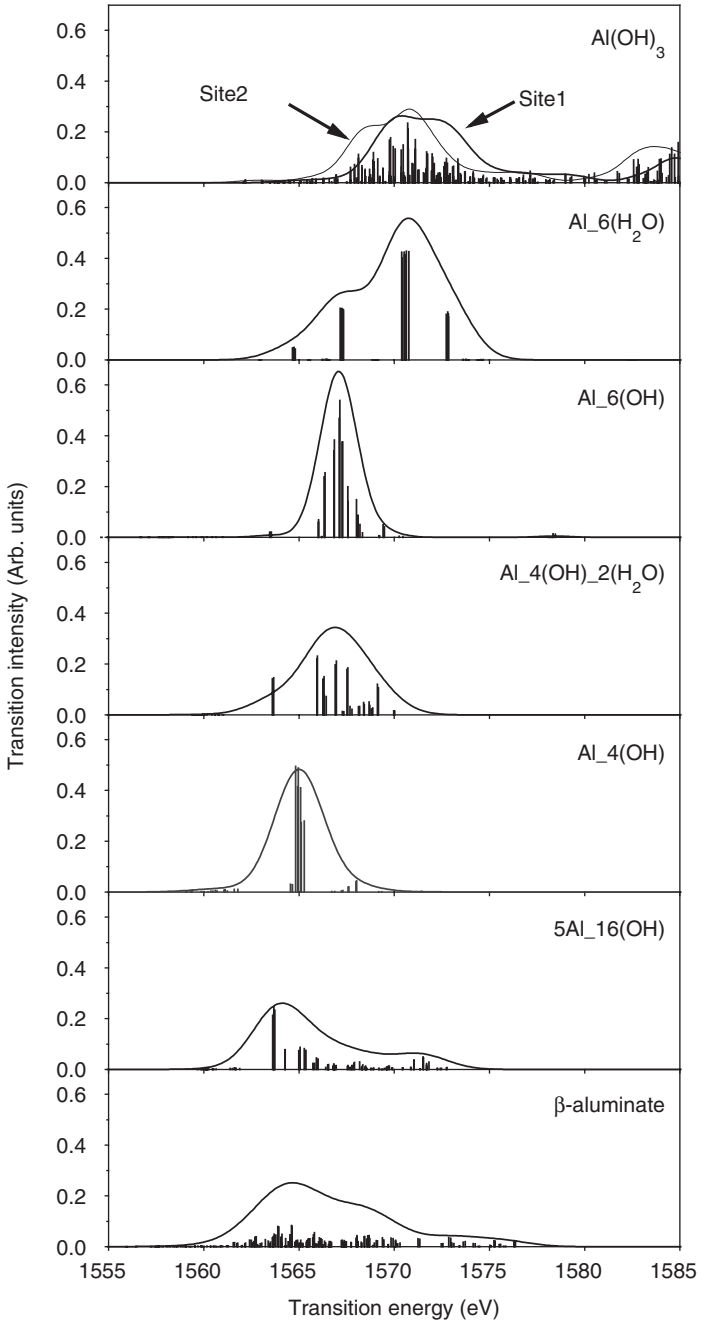

Figure 15.3 Electronic transition probabilities (bar) and calculated XANES curves (solid line) for each model in Figure 15.2.

to higher energy side, coordination number increases and interatomic distance is longer. The peak shapes of the structure models including H_2O molecules, Al_4(OH)_2(H_2O) and Al_6(H_2O), are broader and the peak positions move to higher energy, as compared with Al_4(OH) and Al_6(OH) models, respectively. The results indicate that the peak shapes of the structure models with H_2O molecules can be distinguished from those of the structure models with OH ions. Therefore, it can give important information on the hydration of Al complex species. The structure model of 5Al_16(OH) partly has the network structure like that of β-aluminate, although it has no Na ion. The spectral shape of 5Al_16(OH) model resembles that of β-aluminate model in broadening shape and a tail at the high-energy side.

As a result, we can predict the change of the chemical species on the structural transition by comparing the spectral shapes of the experimental XANES shown in Figure 15.1 with the calculated curves shown in Figure 15.3; at first, incompletely decomposed β-aluminate and aluminum hydroxide such as Al_4(OH) model predominate in the aqueous solution of aluminate after the

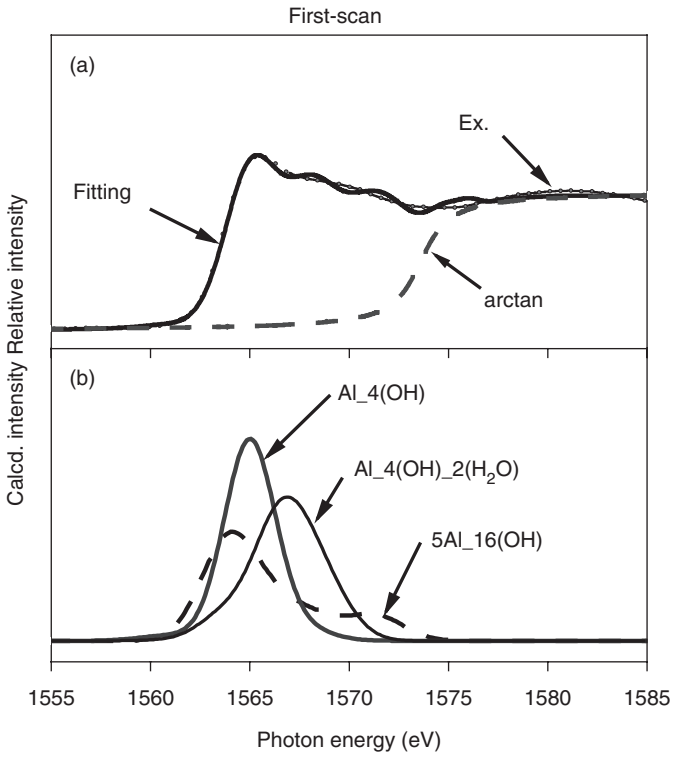

Figure 15.4 The results of LC-XANES Fit for the experimental Al K-edge XANES spectrum of first-scan. Panel (a) shows the corresponding experimental spectrum (thin solid line), the theoretical fitting curve (bold solid line), and the theoretical continuum curve (dashed line), and panel (b) shows the selected calculated XANES curves without adjustments for energy shift and intensity from the results shown in Figure 15.3.

preparation, and then Al hydrates such as Al_4(OH)_2(H_2O) and Al_6(H_2O) models increases with polymerization, and finally, $Al(OH)_3$ precipitates and crystallizes out.

3.2 Chemical species and their ratios during structural transition

The results of LC-XANES Fit for the selected four experimental Al K-edge XANES spectra of first-scan, transform-beginning, transform-end, and last-scan using the calculated XANES curves and theoretical continuum curves are shown in Figures 15.4–15.7, respectively, where each panel (a) shows the corresponding experimental spectrum (thin solid line), the theoretical fitting curve (bold solid line), and the theoretical continuum curve (dashed line) as one of the components of the theoretical fitting curve, and where each panel (b) shows the calculated XANES curves, which are the selected components for LC-XANES Fit, without adjustments for energy shift and intensity. The energy shift from the original peak

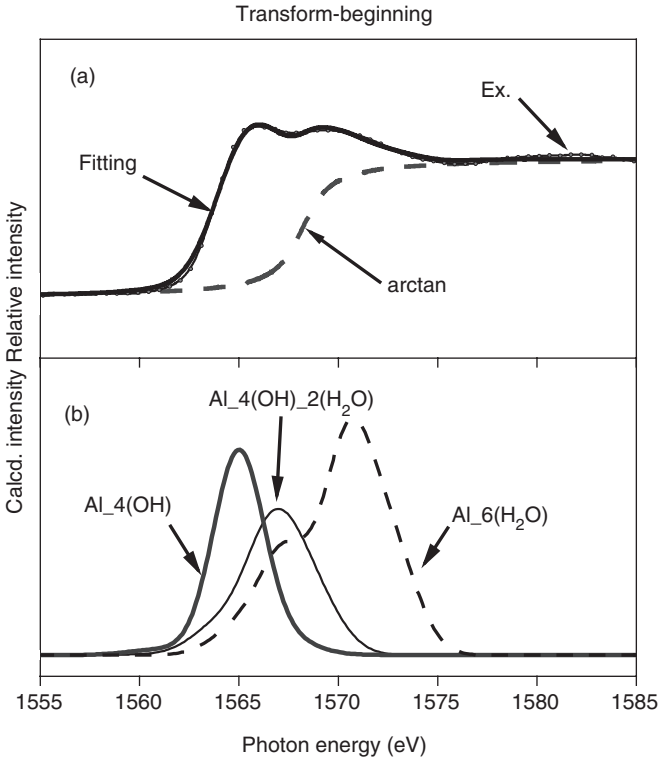

Figure 15.5 The results of LC-XANES Fit for the experimental Al K-edge XANES spectrum of transform-beginning. Panel (a) shows the corresponding experimental spectrum (thin solid line), the theoretical fitting curve (bold solid line), and the theoretical continuum curve (dashed line), and panel (b) shows the selected calculated XANES curves without adjustments for energy shift and intensity from the results shown in Figure 15.3.

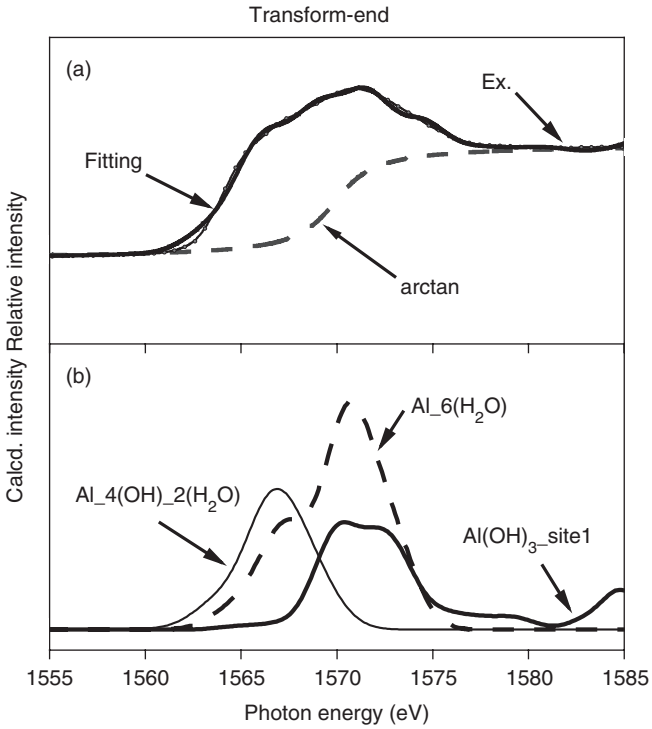

Figure 15.6 The results of LC-XANES Fit for the experimental Al K-edge XANES spectrum of transform-end. Panel (a) shows the corresponding experimental spectrum (thin solid line), the theoretical fitting curve (bold solid line), and the theoretical continuum curve (dashed line), and panel (b) shows the selected calculated XANES curves without adjustments for energy shift and intensity from the results shown in Figure 15.3.

position of each calculated XANES curve, the contribution ratios of the curves and theoretical continuum curve used the fitting for each experimental XANES spectrum, and the residual between the experimental spectra and the corresponding fitting curves are tabulated as shown in Table 15.2.

In Table 15.2, the parameter of the energy shift is likely related with the structural difference between the structure model and actual structure. As described above, coordination number to Al ions, coordination of H_2O molecules to Al ions, and interatomic distance between Al and O atoms usually affect the spectral shapes and the peak position of Al K-edge XANES spectra. The actual coordination structure of Al ions can be thus considered to be somewhat different in those points from the structure models used for the calculations.

For the experimental spectrum of first-scan, the result in Figure 15.4 indicates that the network structure of aluminate which consists of Al and O atoms partly remains, although aluminate dissolves in the water and is divided into aluminate complex anions and Na cations. Other chemical species in the aqueous solution is presumed to be $[Al(OH)_4]^-$ and the hydrated ions produced by the hydrolysis of aluminate. The XANES spectral shape of powder of β-aluminate has been

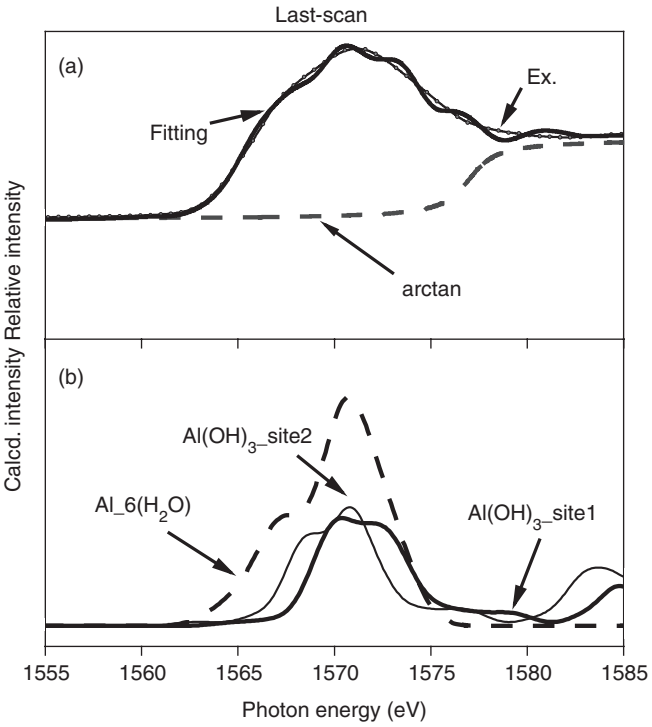

Figure 15.7 The results of LC-XANES Fit for the experimental Al K-edge XANES spectrum of last-scan. Panel (a) shows the corresponding experimental spectrum (thin solid line), the theoretical fitting curve (bold solid line), and the theoretical continuum curve (dashed line), and panel (b) shows the selected calculated XANES curves without adjustments for energy shift and intensity from the results shown in Figure 15.3.

deconvoluted using two components of α-aluminate (six-coordination structure) and β-aluminate [6]. Accordingly, the component of the sixfold coordination can also remain in the aqueous solution. The decomposition of the network structure can be therefore considered to proceed slowly.

For the experimental spectrum of transform-beginning, the result in Figure 15.5 indicates that the hydrated Al ions increase instead of the hydroxide ions after the decomposition of the network structure of aluminate. Although aluminum ions can stably form the monomer $[Al(H_2O)_6]^{3+}$ in acidic solution, the hydroxide-bridged dimmer, $[(H_2O)_{10}Al_2(OH)_2]^{4+}$, and the polymer exist over a wide range of pH [21]. Accordingly, the structure model of $[Al(H_2O)_6]^{3+}$ should be considered as the representative structure of the polymer. In another point of view, the formation of $[Al(H_2O)_6]^{3+}$ probably means the beginning of the polymerization.

For the experimental spectrum of transform-end, the result in Figure 15.6 indicates that the polymerization of aluminum hydrate proceeds and that the local structure around Al ions almost transforms from fourfold coordination to sixfold coordination. The contributable ratio of Al_6(H_2O) model increases more than that for the experimental spectrum of transform-beginning as shown in Table 15.2.

Table 15.2 The parameters of LC-XANES fit for each experimental spectrum and the result of the fitting

Experimental spectrum	Model	Energy shift (eV)	Ratio (wt%)	Residual (%)
First-scan	5Al_16(OH)	0.4	35.2	3.2
	Al_4(OH)	−3.6	26.4	
	Al_4(OH)_2(H_2O)	1.0	19.0	
	Arctangent	N/A[a]	19.4	
Transform-beginning	Al_4(OH)_2(H_2O)	0.0	33.3	2.3
	Al_4(OH)	0.0	22.3	
	Al_6(H_2O)	0.0	5.5	
	Arctangent	N/A	38.9	
Transform-end	Al_4(OH)_2(H_2O)	−0.3	26.2	2.7
	$Al(OH)_3$ site 1	1.7	21.4	
	Al_6(H_2O)	−1.5	20.3	
	Arctangent	N/A	32.1	
Last-scan	$Al(OH)_3$ site 1	3.6	36.1	4.9
	Al_6(H_2O)	−0.2	27.3	
	$Al(OH)_3$ site 2	−2.6	18.9	
	Arctangent	N/A	17.7	

[a]N/A = not available.

In addition, the contribution of $Al(OH)_3$_site 1 appears and the ratio is relatively large. The progress of the polymerization consequently brings the formation of $Al(OH)_3$ structure, that is, it probably means the beginning of crystallization.

For the experimental spectrum of last-scan, the result in Figure 15.7 indicates that the crystallization of $Al(OH)_3$ proceeds and precipitates. From the result of the fitting parameter in Table 15.2, the precipitates are presumed to have incomplete $Al(OH)_3$ structure like the ratio of the local structure of site 1 is larger than that of site 2 when it included moisture sufficiently. The crystallization of $Al(OH)_3$ can be thus predicted to proceed with dehydration and drying. For the spectral shape of XANES of crystalline $Al(OH)_3$, the components of site 1 and 2 occupy the ratios of 31.9 and 27.1% in the structure, respectively, and the component of Al_6(H_2O) is 27.3% (other component is theoretical continuum curve). The residual is 5.1% in this case. It suggests that the spectral shape is not sharp, or that the measured $Al(OH)_3$ reagent has not only the order structure, but also the disorder structure. The argument of the suggestion will be continued elsewhere because it is beyond the topic of this paper.

4. CONCLUSIONS

For understanding the structural transition from aqueous aluminate to crystalline $Al(OH)_3$, curve fits for Al K-edge XANES spectra have been performed using calculated curves and theoretical continuum curves. Coordination number to Al

ions, coordination of H_2O molecules to Al ions, and interatomic distance between Al and O atoms have been strongly related with the spectral shapes and the peak position.

The structure of aluminate in aqueous solution is gradually decomposed and the moiety of the network structure of aluminate, aluminum tetrahydroxide, and the hydrates occur as the predominant chemical species in the aqueous solution. The structure of chemical species in aqueous solution changes from fourfold coordination structure to sixfold coordination structure with H_2O molecules. At this time, polymerization begins to proceed. Hexaaquaaluminum cation serves as a core to form the network structure of $Al(OH)_3$ by the progress of polymerization. Finally, $Al(OH)_3$ precipitates and crystallizes.

The contributable ratios of calculated XANES curves and theoretical continuum curve used fitting for experimental XANES spectra can give information on the transition of chemical species, namely, intermediates through the process of a structural transition.

The analysis of spectral shape of XANES not only for Al, but also for other absorbing atoms using a curve fitting method will be therefore helpful to understanding not only the search of structural transition process, but also chemical species appearing in the process.

ACKNOWLEDGMENTS

This work is partly supported by the Grant-in-Aid for Scientific Research (B)(17350041) from Japan Society for the Promotion of Science, and the Advanced Materials Institute of Fukuoka University.

REFERENCES

[1] C.F. Base, R.E. Mesmer, *The Hydrolysis of Cations*, Wiley, New York, 1976.
[2] J. Li, C.A. Prestidge, J. Addai-Mensah, *J. Chem. Eng. Data* **45** (2000) 665.
[3] C. Sweegers, H.C. de Coninck, H. Meekes, W.J.P. van Enckevort, I.D.K. Hiralal, A. Rijkeboer, *J. Cryst. Growth* **223** (2001) 567.
[4] G. Lefèvre, V. Pichot, M. Fédoroff, *Chem. Mater.* **15** (2003) 2584.
[5] T. Radnai, P.M. May, G.T. Hefter, P. Sipos, *J. Phys. Chem. A* **102** (1998) 7841.
[6] S. Matsuo, P. Nachimuthu, D.W. Lindle, R.C.C. Perera, H. Wakita, *Adv. X-Ray Chem. Anal. Jpn.* **36** (2005) 303.
[7] R.C. Plumb, J.W. Swaine, *J. Phys. Chem.* **68** (1964) 2057.
[8] S. Matsuo, P. Nachimuthu, D.W. Lindle, H. Wakita, R.C.C. Perera, *J. Phys. Chem. B* **107** (2003) 12562.
[9] P. Nachimuthu, S. Matsuo, B. Farangis, D.W. Lindle, H. Wakita, R.C.C. Perera, *J. Alloys Compds.* **362** (2004) 124.
[10] J.A. Kaduk, S. Pei, *J. Solid State Chem.* **115** (1995) 126.
[11] H. Saalfeld, M. Wedde, *Z. Krist.* **139** (1974) 129.
[12] G. te Velde, F.M. Bickelhaupt, S.J.A. van Gisbergen, C.F. Guerra, E.J. Baerends, J.G. Snijders, T. Ziegler, *J. Comput. Chem.* **22** (2001) 931.
[13] C.F. Guerra, J.G. Snijders, G. te Velde, E.J. Baerends, *Theor. Chem. Acc.* **99** (1998) 391.
[14] E.J. Baerends, J. Autschbach, A. Bérces, C. Bo, P.M. Boerrigter, L. Cavallo, D.P. Chong, L. Deng, R.M. Dickson, D.E. Ellis, L. Fan, T.H. Fischer, C. Fonseca Guerra, S.J.A. van Gisbergen, J.A. Groeneveld, O.V. Gritsenko, M. Grüning, F.E. Harris, P. van den Hoek, H. Jacobsen, G. van Kessel, F. Kootstra, E. van Lenthe, D.A. McCormack, V.P. Osinga, S. Patchkovskii,

P.H.T. Philipsen, D. Post, C.C. Pye, W. Ravenek, P. Ros, P.R.T. Schipper, G. Schreckenbach, J.G. Snijders, M. Sola, M. Swart, D. Swerhone, G. te Velde, P. Vernooijs, L. Versluis, O. Visser, E. van Wezenbeek, G. Wiesenekker, S.K. Wolff, T.K. Woo, T. Ziegler, ADF2004.01 (Eds.), SCM, Amsterdam, 2004.

[15] H. Adachi, M. Tsukada, C. Satoko, *J. Phys. Soc. Jpn.* **45** (1978) 875.

[16] J.C. Slater, *Quantum Theory of Molecules and Solids*, McGraw-Hill, New York, 1974.

[17] H. Adachi, K. Taniguchi, *J. Phys. Soc. Jpn.* **49** (1980) 1944.

[18] J. Stöhr, *NEXAFS Spectroscopy*, Springer Series in Surface Science, 25, Springer, New York, 1992, pp. 211–238.

[19] T. Ressler, J. Wong, J. Roos, *J. Synchrotron Rad.* **6** (1999) 656.

[20] T. Ressler, *J. Synchrotron Rad.* **5** (1998) 118.

[21] A.W. Apblett, *Inorganic Aluminum Chemistry in Encyclopedia of Inorganic Chemistry*, In: R.B. King, R.L. Wells (Eds.), Wiley, Chichester, England, 1994, pp. 103–116.

CHAPTER 16

Soft X-Ray Absorption Spectral Analysis of Amorphous Carbon and Carbon Black Using the DV-Xα Method

Yasuji Muramatsu

Contents

Abstract

The discrete variational (DV)-Xα method was used to analyze the high-resolution soft X-ray absorption spectra (XAS) in the C *K*-region of sputtered amorphous carbon films and carbon black to elucidate their local structures. The measured XAS of amorphous carbon and carbon black were compared with those of reference compounds, and the fine structure in the XAS can be assigned by the calculated density of states of the reference compounds. Such a comparative analysis in the measured XAS and the calculated density of states of these carbon materials with reference compounds, which have been known their local or molecular structures, is a valid approach for elucidating the complex local structures of carbon materials.

1. INTRODUCTION

Carbon materials can be usually characterized by diffraction methods (XRD, ED), microscopic methods (TEM, SEM, STM, AFM), and spectroscopic methods

Graduate School of Engineering, University of Hyogo, 2167 Shosha, Himeji, Hyogo 671-2201, Japan
E-mail: murama@eng.u-hyogo.ac.jp

Advances in Quantum Chemistry, Vol. 54
ISSN 0065-3276, DOI 10.1016/S0065-3276(07)00016-0

(IR, Raman, NMR, ESR, UPS, XPS, AES, EELS, SIMS) [1]. However, some industrial carbon materials such as amorphous carbon films and carbon black cannot be easily characterized from the local-structure point of view by these methods, because these materials usually take amorphous and complex structures. Recently, soft X-ray emission and absorption spectroscopy using highly brilliant synchrotron radiation [2] has been utilized to characterize various carbon materials, because information on both the occupied and unoccupied orbitals, which directly reflect the local structure and chemical states, can be provided from the high-resolution soft X-ray measurements. We have applied the soft X-ray spectroscopy to elucidate the local structure and chemical states of various carbon materials [3]. Additionally, we have successfully used the discrete variational (DV)-Xα method [4] for the soft X-ray spectroscopic analysis of the carbon materials, because the DV-Xα method can easily treat complex carbon cluster models, which should be considered for the structural analysis of amorphous carbon materials.

We have recently found that some fine structures can be commonly observed in the C *K* edge X-ray absorption spectra (XAS) of various sputtered amorphous carbon (a-C) films [5,6] and carbon black (CB) [7]. To clarify the spectroscopic fine structures from the local-structure and chemical-state point of view, we have compared the XAS of a-C and CB with those of reference compounds, and estimated the local structures of a-C and CB from the spectroscopic analysis using the DV-Xα method. The present paper describes one of the approaches in determining the local structure of carbon materials using the soft X-ray spectroscopy as well as the DV-Xα method.

2. SPECTROSCOPIC MEASUREMENTS AND THE DV-Xα CALCULATION

Samples of a-C films were deposited on silicon wafer substrates by various sputtering methods such as RF-sputtering, ion-beam sputtering, and electron-cyclotron-resonance (ECR) sputtering. Powder samples of CB (high abrasion furnace (HAF), semi-reinforcing furnace (SRF), super abrasion furnace (SAF), fine thermal (FT)) and reference compounds (highly oriented pyrolytic graphite (HOPG), C_{60}, C_{70}, $C_{60}H_{36}$, anthracene) were commercially available. XAS in the C *K*-region of the samples were measured in the beamline BL-6.3.2 [8] at the advanced light source (ALS). XAS were obtained by measuring the sample photocurrent, which was a total electron yield (TEY) method. The estimated resolving power ($E/\Delta E$) of the TEY-XAS measurements was about 1600 using a 600 lines/mm variable-line-spacing grating and a 20-μm exit slit. The incident angle to the sample surface was fixed at 45° to average the orientation effect [9,10] on the spectral features resulted from oriented graphitic-structures. Energy calibration was achieved by tuning the π^* peak energy of HOPG to 285.5 eV [9].

The spectral analyses were performed using the DV-Xα software. The calculated unoccupied density of states (DOS) of adequate cluster models was

compared to the measured XAS. Molecular mechanics (MM2) [11] was used to optimize the cluster model structures.

3. RESULTS AND DISCUSSION

3.1 Sputtered amorphous carbon films

Figure 16.1 shows the XAS in the C *K*-region of various a-C films, deposited by RF-sputtering (denoted R1–4), ion-beam sputtering (I1–3), and ECR sputtering (E1–5) methods with various sputtering conditions, and reference compounds (HOPG, C_{70}, C_{60}, and *T* symmetry $C_{60}H_{36}$). The a-C exhibited two broad peaks around 285.5 and 293 eV, which corresponded to the π^* and σ^* peaks in HOPG, respectively. Additionally four fine structures were observed between the π^* and σ^* peaks; around 284.5 eV (denoted by *a*), 287 eV (*b*), 288 eV (*c*), and 289 eV (*d*). Although the relative peak intensities among these six structures (π^*, σ^*, *a*–*d*) depended on the deposition methods and conditions, they were observed at constant energy positions. This suggested that certain local structures existed in the a-C films, but that their ratios varied among the films.

Some of the fine structures in the XAS of a-C corresponded to some of the fine structures of C_{70}, C_{60}, and $C_{60}H_{36}$. Therefore, comparing the spectral fine structures of a-C to the reference compounds, whose molecular structures are known, appears to be a valid approach for assigning these unknown fine structures and for estimating the local structure of a-C. $C_{60}H_{36}$ is a useful compound for comparing the spectral fine structures of the a-C, because some of the fine structures (π^* *c*, *d*, and σ^*) in a-C are also observable in $C_{60}H_{36}$. Additionally $C_{60}H_{36}$ can be regarded as a fairly large cluster composed of sp^2- and sp^3-C atoms, which resembles a-C in the local structure composed of sp^2- and sp^3-C atoms. To analyze the fine structures in XAS of $C_{60}H_{36}$, the unoccupied DOS of the *T*-$C_{60}H_{36}$ cluster model was obtained by the DV-Xα method. The left panel in Figure 16.2 shows a cluster model of *T*-$C_{60}H_{36}$ and its local structure. *T*-$C_{60}H_{36}$ consists of 36 sp^3-C atoms, which are bonded to H atoms, while the remaining 24 sp^2-C atoms form 4 six-membered benzene rings, which are located at the tetrahedral positions of the cage. *T*-$C_{60}H_{36}$ has four types of carbon atoms. The 24 sp^2-C atoms (denoted by I) are identical, and each one is bonded to 2 sp^2-C atoms and 1 sp^3-C atom. There are three types of sp^3-C atoms: 24 of the sp^3-C atoms (II, III), each binds to 2 sp^3-C atoms, 1 sp^2-C atom, and 1 H atom, while the other 12 sp^3-C atoms (IV), each binds to 3 sp^3-C atoms and 1 H atom. The right panel of Figure 16.2 shows the unoccupied C 2p and 2s DOS of the individual sp^2- and sp^3-C atoms. The total C 2p DOS approximately reproduces the measured fine structures of the π^*, *c*, *d*, and σ^* peaks in the XAS. Consequently, the fine structures can be explained by the hybridization of the 2s and 2p orbitals in the sp^2- and sp^3-C atoms. Additionally, population analysis [12] indicates that the π^* peak originates from the π^* orbitals because the 2p orbitals of sp^2-C (I) account for approximately 90% of the population at peak π^*. For peaks *c*, *d*, and σ^*, their orbital populations are shared by the sp^2-C (I), sp^3-C

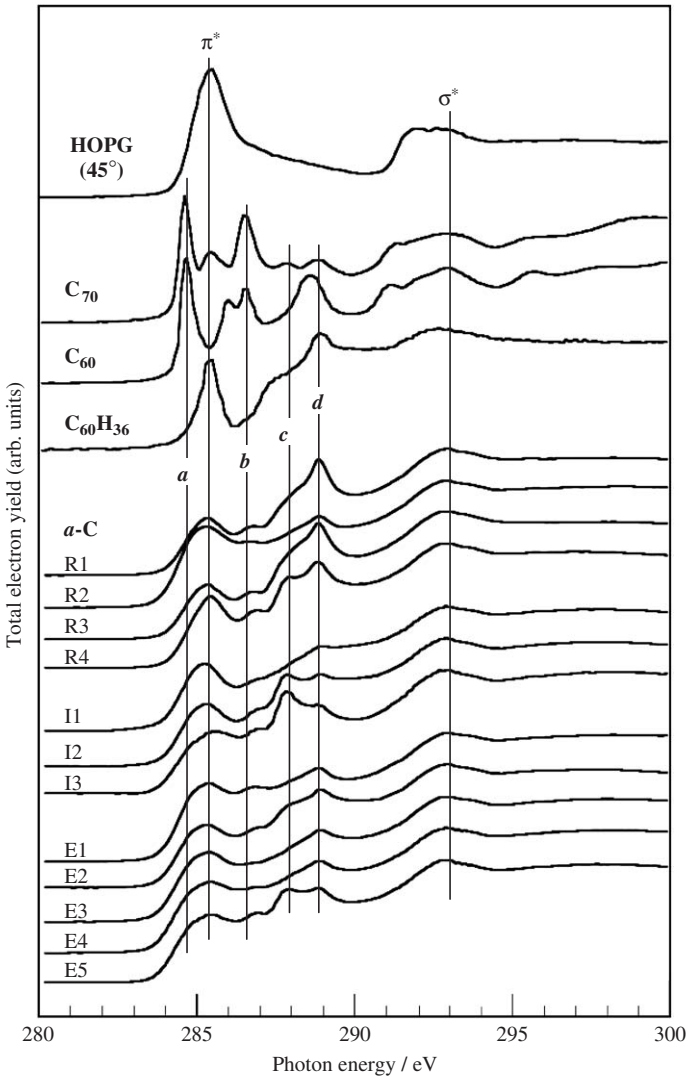

Figure 16.1 Soft X-ray absorption spectra (XAS) in the C *K*-region of amorphous carbon (a-C) films deposited by various methods (R1–4, I1–3, E1–5) and reference compounds of HOPG, C_{70}, C_{60}, and $C_{60}H_{36}$.

(II, III), and sp^3-C (IV) with 11–45% of 2p orbitals and up to about 11% of 2s orbitals. In particular, the 2p orbitals of both sp^2-C (I) and sp^3-C (II, III) account for more than 30% of the population at peak *c*, and the 2p orbitals of both sp^3-C (II, III) and sp^3-C (IV) account for more than 30% at peak *d*. These calculations show that peak *c* has more sp^2 character than peak *d*. Peak σ^* is mainly due to the σ^* orbitals, which are mostly sp^3-C (II, III) and sp^2-C (I). From this analogy, it can be rationalized that the fine structures of the π^*, *c*, *d*, and σ^* peaks in XAS of a-C are due to the hybridization of sp^2 and sp^3 carbon atoms. In addition, when a

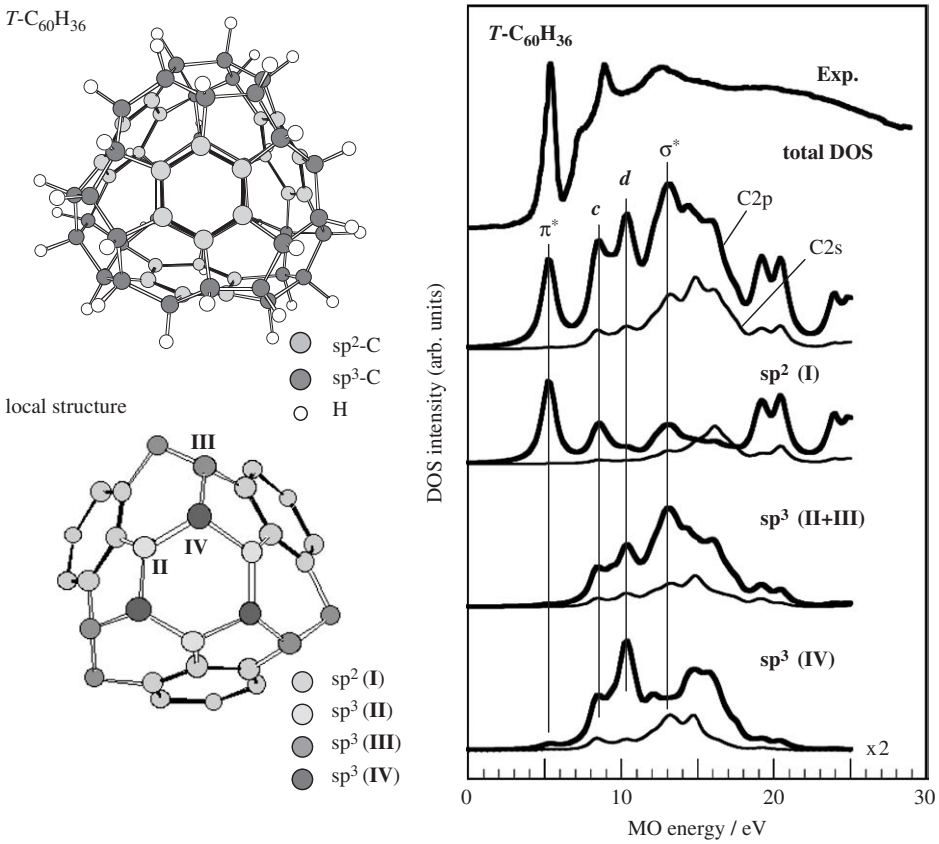

Figure 16.2 Left panel shows the molecular and local structure of *T*-$C_{60}H_{36}$. Right panel shows the unoccupied C 2s-DOS and C 2p-DOS of *T*-$C_{60}H_{36}$. The measured X-ray absorption spectrum (Exp.) of $C_{60}H_{36}$ is described on the total DOS. For a colour version of this figure please see the colour plate section near the end of the book.

hybridized carbon atom has the more sp^3 character in the local structure, the energy position of the fine structure peak becomes higher. One plausible explanation for the lower-energy portion (fine structure, *a*) in the broad π^* peak is discussed in the next section on carbon black, which can be estimated by nonbenzenoid structures or hydrogenated carbon atoms at the cluster edges.

3.2 Carbon black

Figure 16.3 shows the XAS in the C *K*-region of various CB samples and references of HOPG, C_{60}, and anthracene. Compared to HOPG, CB shows broad spectral features, especially in the π^* peak. In order to quantify the broadness of the spectral features, Figure 16.3 also shows the subtracted spectra, (CB)–(HOPG). The subtracted spectra of the CB clearly demonstrate the broad portion of the π^* peak, which has peak structures at 284.2 and 286.2 eV. The energy

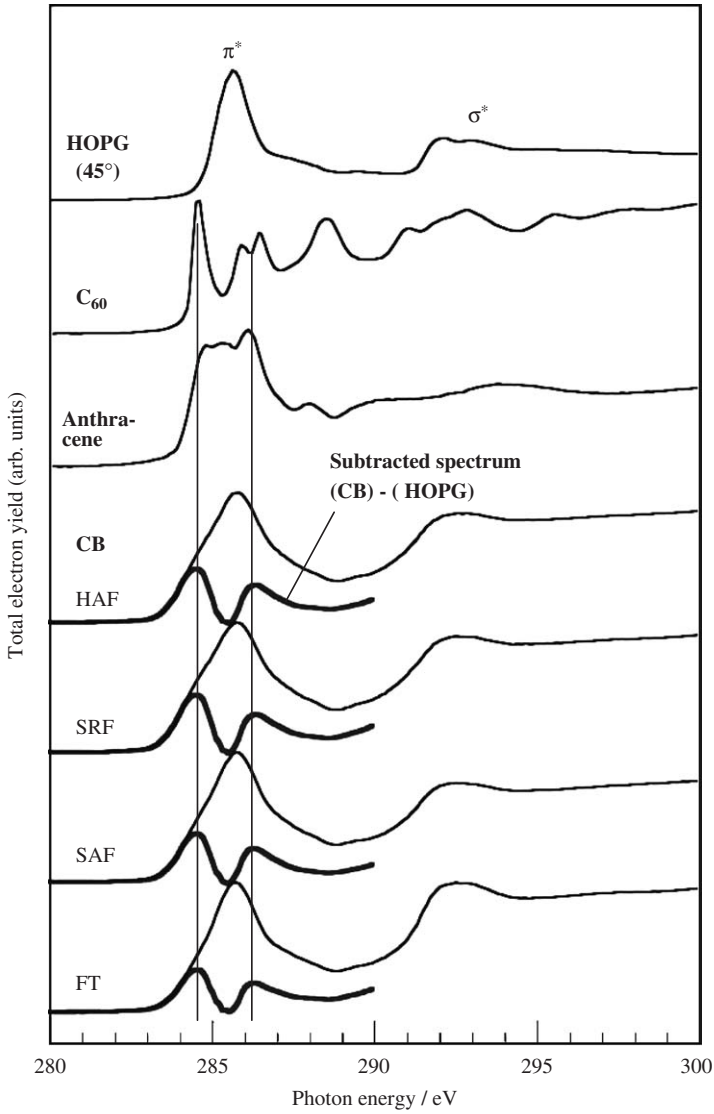

Figure 16.3 Soft XAS in the C *K*-region of various carbon black (CB) samples (HAF, SRF, SAF, FT) and reference compounds of HOPG, C_{60}, and anthracene. Subtracted spectra, (CB)–(HOPG), are also shown on the absorption spectra.

positions of these broad portions correspond to the π^* features of C_{60} and anthracene. It is well known that C_{60} has nonbenzenoid pentagonal rings with benzenoid hexagonal rings and that anthracene has hydrogenated sp^2-C atoms, which form hexagonal rings at the molecular edge. From this analogy, we hypothesize that the π^*-peak broadness in CB depends on the local structures such as nonbenzenoid structures and/or hydrogenated carbon atoms at graphitic cluster edges.

To verify this idea, we calculated the DOS of some benzenoid and nonbenzenoid cluster models using the DV-Xα method. Figure 16.4 shows the benzenoid ($C_{96}H_{24}$) and nonbenzenoid ($C_{80}H_{20}$, $C_{112}H_{28}$) cluster models, and their DOS in the unoccupied C 2p and C 2s orbitals from the centered carbon atoms (numbered as 1C) to the edged atoms (as 7C). In the nonbenzenoid cluster models, $C_{80}H_{20}$ and $C_{112}H_{28}$, the central 1C atoms form a pentagonal ring and a heptagonal, respectively. In the C 2p-DOS, the central 1C atoms in the nonbenzenoid pentagonal and heptagonal rings exhibit a lower-energy DOS at

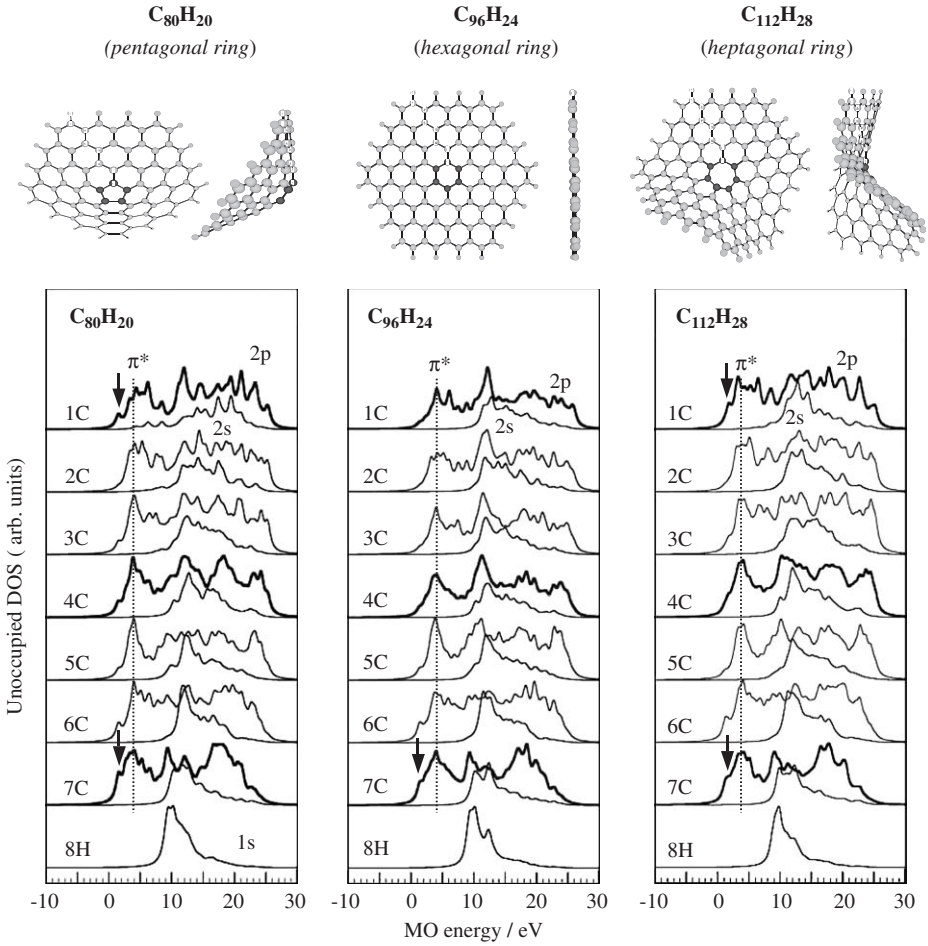

Figure 16.4 Upper panel shows a benzenoid cluster model ($C_{96}H_{24}$) and nonbenzenoid models ($C_{80}H_{20}$, $C_{112}H_{28}$). Lower panel shows the unoccupied C 2p-DOS and C 2s-DOS of carbon atoms in the cluster models. Carbon atoms from the centered atoms to the edged atoms are numbered as 1C–7C, respectively. Hydrogen atoms terminating the edged-carbon atoms are numbered as 8H. The lower-energy DOS portions at the π^* peak positions of 1C and 7C are denoted by arrows. For a colour version of this figure please see the colour plate section near the end of the book.

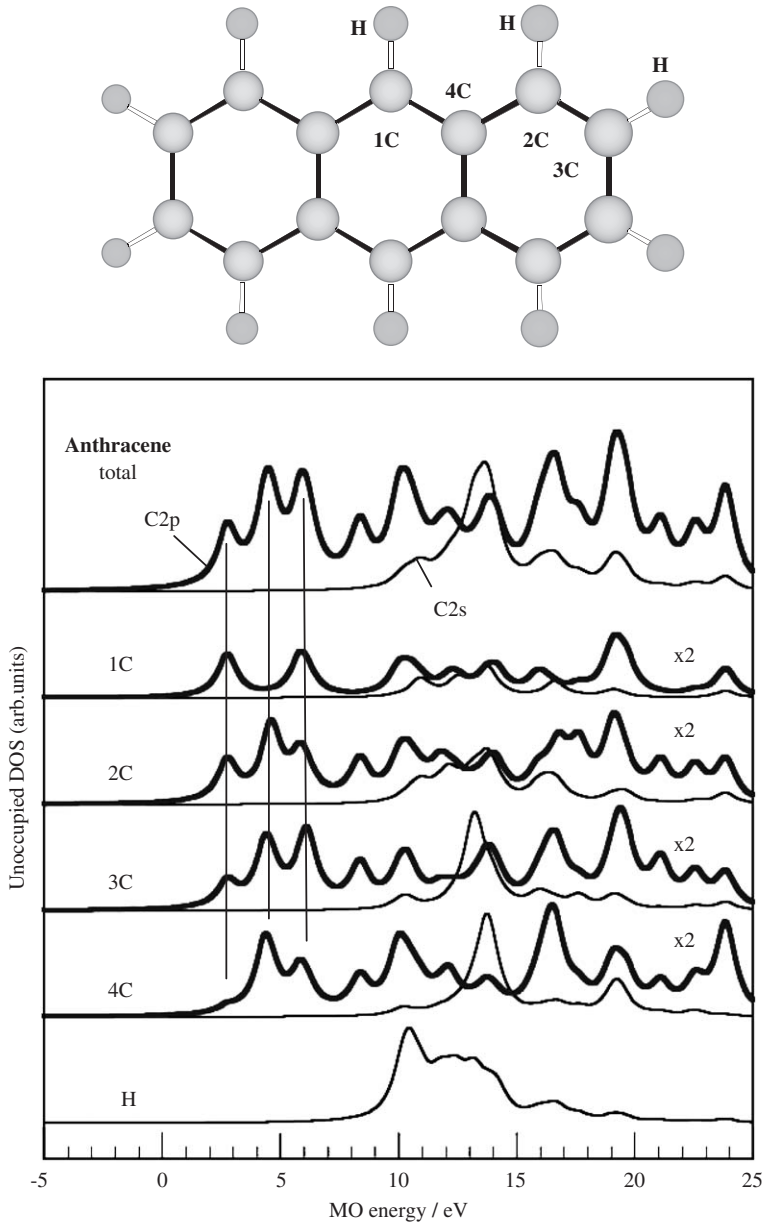

Figure 16.5 Upper panel shows a molecular model for anthracene ($C_{14}H_{10}$). Four types of C atoms are numbered as 1C–4C. Lower panels show the unoccupied C 2p-DOS and C 2s-DOS of the numbered carbon atoms and all carbon atoms.

the π^* positions compared to the hexagonal ring in the benzenoid cluster model. In addition, hydrogenated 7C atoms in both the benzenoid and nonbenzenoid cluster models exhibit similar lower-energy DOS at the π^* position compared to the center 1C atoms in the benzenoid cluster model. These lower-energy DOS portions, which are due to the nonbenzenoid structures and hydrogenated carbon atoms, correspond to the measured broad π^* peak features of CB; especially the 284.2 eV peak observed in the subtracted spectra of (CB)–(HOPG).

Figure 16.5 shows the molecular structure of anthracene and its DOS. In this model, the carbon atoms numbered as 1C, 2C, and 3C are hydrogenated atoms and the 4C atoms does not bond to hydrogen. Although the hydrogenated 1-3C atoms exhibit lower-energy DOS at the π^* positions, the 4C atoms does not exhibit the lower-energy DOS. These edged carbon atoms also exhibit a higher-energy DOS at the π^* position. This shows that the carbon atoms at cluster edges can results in the π^*-peak broadness, and especially the hydrogenated atoms can result in the lower-energy broadening at the π^* peak. These broad DOS features correspond to the measured broad portions of the π^* peak in the XAS of CB.

Consequently, it has been confirmed that the broad π^* peak features in the XAS of CB can provide local structure information, especially on the nonbenzenoid structure and/or hydrogenated cluster-edged carbon atoms.

4. CONCLUSION

To elucidate the local structures of sputtered a-C films and CB, we measured their high-resolution soft XAS in the C *K*-region and analyzed the spectral fine structures by the DV-Xα method. Sputtered a-C films exhibit fine structures between the π^* and σ^* peaks in the measured XAS. Some of the fine structures in the a-C correspond to those of $C_{60}H_{36}$. From the analogy between the a-C and $C_{60}H_{36}$, it can be considered that the fine structures in XAS of a-C results from the hybridization of the sp^2- and sp^3-C atoms and that the higher-energy structures between π^* and σ^* peaks has more sp^3 character and less sp^2 character than the lower-energy structures. CB exhibits the broad π^* features that correspond to some of the fine structures at the π^* peaks of C_{60} and anthracene. From the calculated DOS of the nonbenzenoid cluster models and anthracene, the broad π^* peak feature of CB can be explained by the nonbenzenoid structures and/or hydrogenated carbon atoms at the cluster edges.

Although the complex local structure of carbon materials cannot be easily or completely elucidated by conventional analysis methods, the high-resolution soft X-ray absorption spectroscopy and spectral analysis using the DV-Xα method are promising tools to analyze the local structure. In addition, comparative analysis of carbon materials with reference compounds that have been known their local and molecular structures is a valid approach for elucidating the local structure.

ACKNOWLEDGMENTS

The author would like to express his gratitude to Dr. Eric M. Gullikson and Dr. Rupert C. C. Perera of Lawrence Berkeley National Laboratory for their support in the spectroscopic measurements at ALS. This work has been supported by a Grant-in-Aid from the Ministry of Education, Culture, Sports, Science and Technology of Japan under contract No. 17550090.

REFERENCES

[1] For example, *Carbon Alloys* (Edition) by E. Yasuda, M. Inagaki, K. Kaneko, M. Endo, A. Oya, Y. Tanabe, Elsevier, 2003, pp. 145–414.
[2] For example, J. Nordgren, In: A.S. Schlachter and F.J. Wuilleumier (Eds.), *New Directions in Research with Third-Generation Soft X-Ray Synchrotron Radiation Sources*, Kluwer Academic Publisher, Dordrecht, The Netherlands, 1994, pp. 189–202; J. Stöhr, *NEXAFS Spectrosc.* (Springer, 1992).
[3] Y. Muramatsu, E.M. Gullikson, R.C.C. Perera, *Adv. X-Ray Chem. Anal. Jpn.* **35** (2004) 125–136.
[4] H. Adachi, M. Tsukada, C. Satoko, *J. Phys. Soc. Jpn.* **45** (1978) 875.
[5] Y. Muramatsu, T. Hayashi, *Adv. X-Ray Chem. Anal. Jpn.* **30** (1999) 41–53.
[6] Y. Muramatsu, Y. Ueno, S. Hirono, S. Umemura, T. Hayashi, M.M. Grush, E.M. Gullikson, R.C.C. Perera, In: The 5th International Conference on the Applications of Diamond Films and Related Materials, 1st International Conference on Frontier Carbon Technology, ADC/FCT, Tsukuba, 1999.
[7] Y. Muramatsu, R. Harada, E.M. Gullikson, In: Proceedings of AIP Conference, B. Hedman, P. Pianetta (Eds.), *X-Ray Absorption Fine Structure XAFS13*, Vol. 882, AIP, Melville, New York, 2007, pp. 511–513.
[8] J.H. Underwood, E.M. Gullikson, M. Koike, P.J. Batson, P.E. Denham, K.D. Franck, R.E. Tackaberry, W.F. Steele, *Rev. Sci. Instrum.* **67** (1996) 3372.
[9] P. Skytt, P. Glans, D.C. Mancini, J.-H. Guo, N. Wassdahl, J. Nordgren, *Phys. Rev. B* **50** (1994) 10457–10461.
[10] Y. Muramatsu, E.M. Gullikson, R.C.C. Perera, *Adv. X-Ray Chem. Anal. Jpn.* **34** (2003) 153–53163.
[11] U. Burkert, N.L. Allinger, *Molecular Mechanics*, ACS, Washington, DC, 1982.
[12] Y. Muramatsu, Y. Ueno, T. Hayashi, M.M. Grush, E.M. Gullikson, R.C.C. Perera, *J. Electron Spectrosc. Relat. Phenom.* **107** (2000) 177–184.

CHAPTER 17

Soft X-Ray Emission Spectral Analysis of Graphite Fluoride $(CF)_n$ Using the DV-Xα Calculations

Satoshi Ueda*, Yasuji Muramatsu* and **Jonathan D. Denlinger****

Contents

Abstract

We measured the soft X-ray emission spectra (XES) in the C and F *K*-regions of graphite fluoride $(CF)_n$ by suppressing sample decomposition due to synchrotron radiation (SR) excitation, and analyzed the X-ray spectral features using the DV-Xα method. The high-energy peak in the C *K*-spectra is assigned to the π transition due to the C 2p hybridized with the F 2p orbitals. The XES can be successfully reproduced by calculated C and F 2p density of states (DOS) of a stretched C–F bond model in which the C–F bond length is longer than the typical length of 1.397 Å.

1. INTRODUCTION

Graphite fluoride $(CF)_n$ has unique properties, which include heat-resistance, electrical capabilities, and solid lubrication. Numerous studies on $(CF)_n$ have been performed from the view points of electronic/crystal structures and chemical states/properties [1–5]. For example, Motoyama et al. [5] have

* Graduate School of Engineering, University of Hyogo, 2167 Shosha, Himeji, Hyogo 670-2201, Japan
Corresponding author. E-mail: murama@eng.u-hyogo.ac.jp
** Lawrence Berkeley National Laboratory, 1Cyclotron Road, Berkeley, CA 94720, USA

Advances in Quantum Chemistry, Vol. 54
ISSN 0065-3276, DOI 10.1016/S0065-3276(07)00017-2

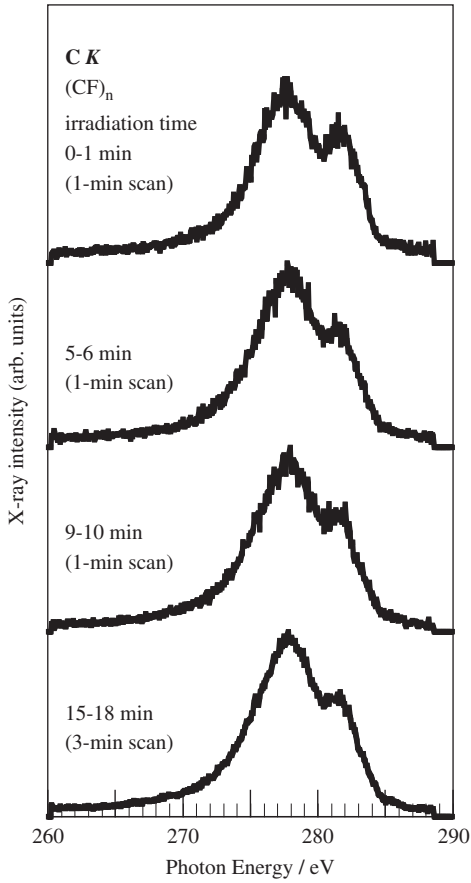

Figure 17.1 Irradiation-time dependence of the C *K* X-ray emission spectra (XES) of $(CF)_n$. Spectra with an irradiation time of 0–1, 5–6, and 9–10 min were taken with 1-min scans, while the spectrum with 15–18 min was taken with 3-min scans.

measured the C *K* X-ray emission spectra (XES) of $(CF)_n$ using electron probe microanalysis (EPMA). Their spectra were acquired by moving the sample position during electron-beam irradiation, because electron-beam irradiation easily decomposes $(CF)_n$. The observed C *K* X-ray emission spectral feature has a main peak with a high-energy peak. However, the X-ray spectral features have not been clearly analyzed by theoretical methods.

We have employed soft X-ray emission and absorption spectroscopy for chemical analysis of light-element materials using synchrotron radiation (SR) [6,7]. We have confirmed that soft X-ray spectral measurements by SR excitation have novel advantages for chemical analysis of organic materials, which include less damage to organic material samples by monochromatized-SR-irradiation. In order to obtain reliable soft XES of $(CF)_n$ and to investigate its electronic structure, we measured the XES of $(CF)_n$ using a monochromatized SR beam

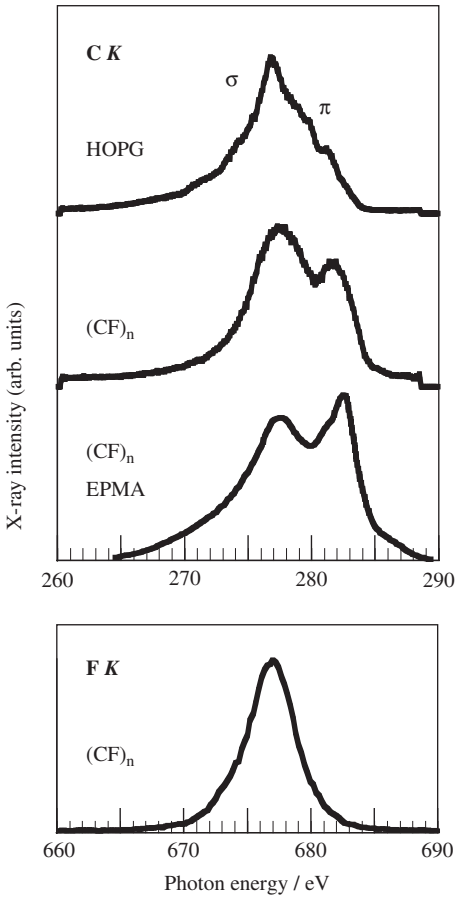

Figure 17.2 Soft XES in the C (upper panel) and F *K* (lower) regions of $(CF)_n$ and HOPG. C *K* spectrum of $(CF)_n$ measured with an EPMA [5] is also shown under the permissions for the use of the spectral data by Elsevier Ltd.

as the excitation probe and analyzed the spectral features using the discrete variational (DV)-Xα molecular orbital (MO) calculations [8].

In the present paper, we describe a reliable XES in the C *K* and F *K*-regions of $(CF)_n$, and compare the measured X-ray spectra to their density of states (DOS) calculated by the DV-Xα method.

2. EXPERIMENTAL

The samples were commercially available $(CF)_n$ powder and highly oriented pyrolytic graphite (HOPG) as a reference. Soft X-ray emission spectral measurements in the C and F *K*-regions were performed in the beamline BL-8.0.1 [9] at

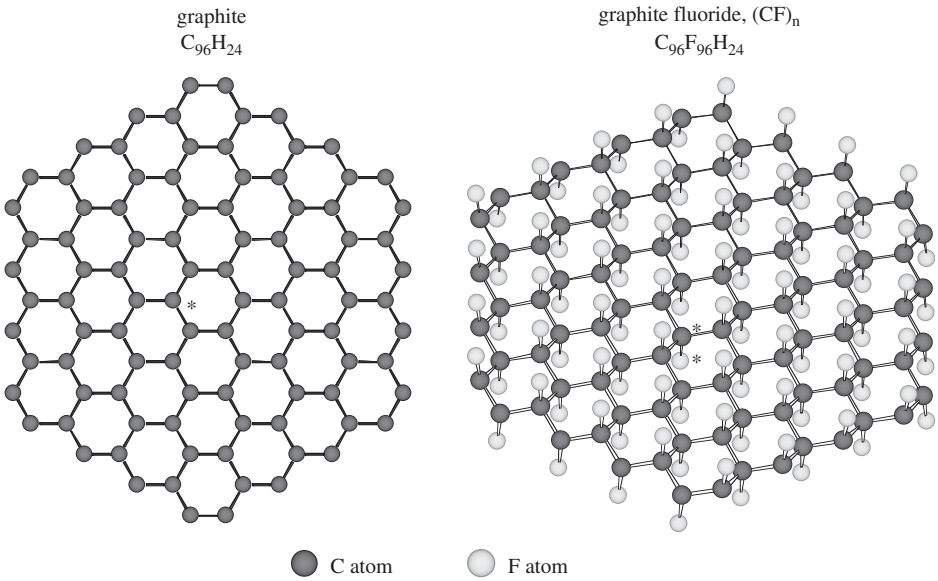

Figure 17.3 Cluster models of $C_{96}H_{24}$ for graphite and $C_{96}F_{96}H_{24}$ for $(CF)_n$ used in the DV-Xα calculations. Hydrogen atoms that terminate the carbon atoms at the cluster edges are not shown.

the Advanced Light Source (ALS). XES were obtained using a grating X-ray spectrometer equipped with 10-m curvature radius gratings (for a groove density of 600 lines/mm in the C *K*-region and 1500 lines/mm in the F *K*-region). The incident SR beam was tuned at 320 eV for the C *K* measurements and at 720 eV for the F *K* measurements. To determine the measurement conditions, the irradiation-time dependence on the C *K* XES of $(CF)_n$ was measured as shown in Figure 17.1. Although the spectral profile in the initial irradiation time of 0–1 min clearly demonstrated a high-energy peak at 282 eV, this peak intensity gradually decreased as the irradiation time increased; the high-energy peak become broader after irradiating between 5 and 6 min. To suppress the sample decomposition due to SR-irradiation, we measured each spectrum for 30 s and accumulated ten spectra taken at different sample positions.

3. RESULTS AND DISCUSSION

Figure 17.2 shows the XES in the C and F *K*-regions of $(CF)_n$, compared with the C *K*-spectra of HOPG and $(CF)_n$ measured by Motoyama et al. [5] using an EPMA. In the C *K*-spectra, $(CF)_n$ exhibits a main peak at 278 eV and a high-energy peak at 282 eV. To compare the spectral features of $(CF)_n$ to HOPG, the high-energy peak is assigned to the π peak. Although the relative intensity of the π-peak to the main peak of $(CF)_n$ excited by SR is slightly lower than that of $(CF)_n$ by an EPMA, the spectral features of the main peak and the π-peak

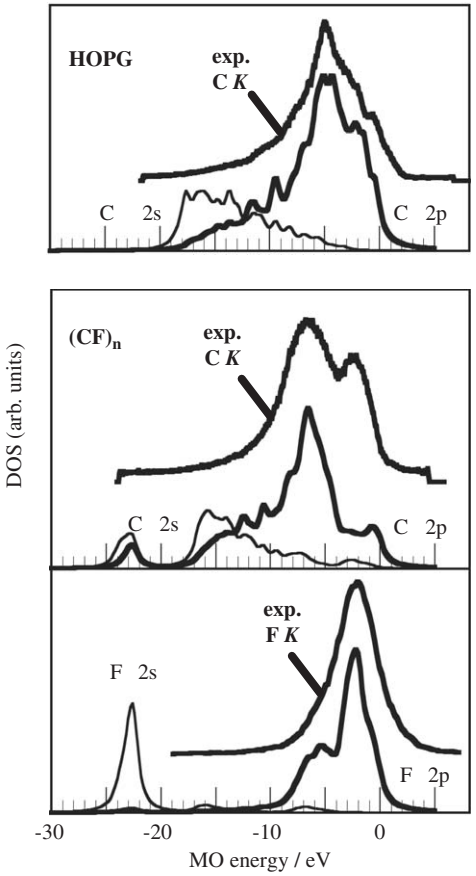

Figure 17.4 Comparison of the calculated DOS of $(CF)_n$ and HOPG with the measured XES in the C and F *K*-regions.

are similar to each other. A single peak feature is observed in the F *K* spectrum of $(CF)_n$.

To analyze the measured X-ray spectral feature of $(CF)_n$, we calculated the DOS using the DV-Xα method, and compared them to the X-ray spectra. Figure 17.3 shows the cluster models of $C_{96}H_{24}$ for graphite and $C_{96}F_{96}H_{24}$ for $(CF)_n$ in the DV-Xα calculations. In the DV-Xα calculations for these graphitic-structured materials, it has been confirmed that cluster models with nearly 100 atoms in the backbone were sufficient for spectral analysis [10]. Molecular mechanics (MM2) methods were used to optimize the structure of these cluster models. In the optimized basal $(CF)_n$ model, the C–F bond-length (denoted by L_{C-F}) is 1.397 Å. The calculation was performed in the ground-states with a basis set of 1s, 2s, and 2p orbitals for C and F atoms. Occupied DOS, which were broadened with a 0.5 eV wide Lorentzian functions, were obtained for the central

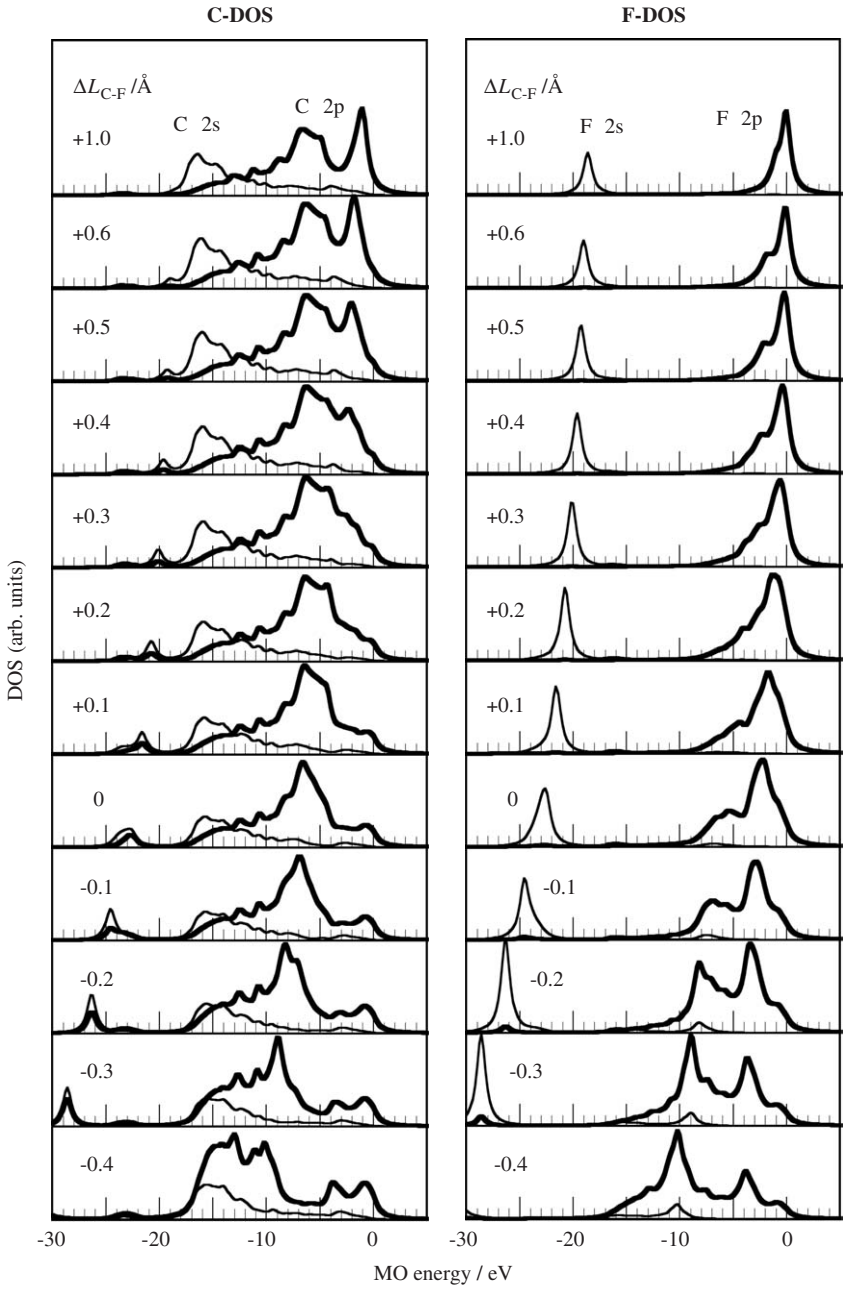

Figure 17.5 DOS of the C and F atoms in the $C_{96}F_{96}H_{24}$ cluster model where the basal C–F bond length in the center C and F atoms is varied from 0.997 Å (shortened, $\Delta L_{C-F} = -0.4$ Å) to 2.397 Å (stretched, $\Delta L_{C-F} = +1.0$ Å).

C and F atoms, which are denoted by asterisks in Figure 17.3. Figure 17.4 shows the calculated DOS of graphite (HOPG) and $(CF)_n$ compared to their X-ray spectra. In graphite, the calculated C 2p-DOS well reproduces the X-ray spectral features. Therefore, the DOS calculation using the 96-atom backbone cluster model is sufficiently reliable for spectral analysis. In $(CF)_n$, the C *K* X-ray spectral features, which consist of a main peak and a high-energy peak, can be roughly reproduced by the C 2p-DOS, while the F 2p-DOS can successfully reproduce the F *K* X-ray spectral features. In addition, the MO energy region of the F 2p-DOS corresponds to the high-energy portion of the C 2p-DOS. Hence, it is confirmed that the high-energy peak in the C *K*-XES is a π peak hybridized with F 2p orbitals.

However, the high-energy peak intensity cannot be sufficiently reproduced by the C 2p-DOS. To reproduce this peak intensity, we performed additional DOS calculations, focusing on the C–F bond-length (L_{C-F}) dependence of the C 2p-DOS. Figure 17.5 shows the DOS in the C and F atoms of the $C_{96}F_{96}H_{24}$ in which the basal C–F bond length in the center C and F atoms was varied from 0.997 Å (shortened, $\Delta L_{C-F} = -0.4$ Å) to 2.397 Å (stretched, $\Delta L_{C-F} = +1.0$ Å). In the shortened L_{C-F} models, the low-energy portion (σ) of the C 2p-DOS is enhanced as the L_{C-F} becomes shorter. On the other hand, in the stretched model, the high-energy portion (π) hybridized with F 2p orbitals is enhanced as the L_{C-F} become longer. The enhanced high-energy peak features of the C 2p-DOS in the stretched C–F bond models ($\Delta L_{C-F} = +0.4$–$+0.6$ Å) appear to be consistent with the measured C *K* X-ray spectral features. The F *K* X-ray spectra can also be reproduced by the stretched C–F bond models. It is therefore confirmed that the DOS calculations tuning the C–F bond length can successfully reproduce the X-ray spectra in C and F *K*-regions of $(CF)_n$.

4. CONCLUSIONS

To understand the soft X-ray emission spectral features of graphite fluoride $(CF)_n$, XES in the C and F *K*-regions of $(CF)_n$ were carefully measured using the monochromatized SR, and the spectral features were analyzed by the DV-Xα MO calculations. By comparing the measured X-ray spectra to the DOS of a $C_{96}F_{96}H_{24}$ cluster model, the measured high-energy peak in the C *K*-spectra is assigned to the π peak due to the hybridized C 2p with F 2p orbitals. However, the DOS of the basal cluster model with a typical C–F bond length of 1.397 Å cannot sufficiently reproduce the peak intensity of the π peak. From the further DOS calculations on the C–F bond length dependence, the X-ray spectral features can be reproduced with the stretched C–F bond models. It is therefore concluded that DOS calculations by the DV-Xα method can successfully reproduce the XES in the C and F *K*-regions of $(CF)_n$, and that the spectral features can be understood by the hybridization of valence orbitals between the C and F atoms.

ACKNOWLEDGMENTS

We thank Dr. Rupert C.C. Perera of Lawrence Berkeley National Laboratory for his support with the spectroscopic measurements in BL-8.0.1 at ALS. This work was supported by a Grant-in-Aid from the Ministry of Education, Culture, Sports, Science and Technology of Japan under contract No. 17550090.

REFERENCES

[1] Y. Sato, K. Itoh, R. Hagiwara, T. Fukunaga, Y. Ito, *Carbon* **42** (2004) 2897.
[2] E.Z. Kurmaev, A. Moewes, D.L. Ederer, H. Ishii, K. Seki, M. Yanagihara, F. Okino, H. Touhara, *Phys. Lett. A* **288** (2001) 340.
[3] J.-C. Charlier, X. Gonze, J.-P. Michenaud, *Phys. Rev. B* **47** (1993) 16162.
[4] S. Kim, J. Kawai, M. Motoyama, H. Adachi, S. Park, *Spectrochim. Acta B* **54** (1999) 179.
[5] M. Motoyama, T. Nakajima, N. Watanabe, *Soild State Ionics* **13** (1984) 227.
[6] Y. Muramatsu, M. Oshima, J. Kawai, H. Kato, *Nucl. Instr. Meth. B* **75** (1993) 559–562.
[7] Y. Muramatsu, E.M. Gullikson, R.C.C. Perera, *Adv. X-Ray Chem. Anal. Jpn.* **35** (2004) 125–136.
[8] H. Adachi, M. Tsukada, C. Satoko, *J. Phys. Soc. Jpn.* **45** (1978) 875.
[9] J.J. Jia, T.A. Callcott, J. Yurkas, A.W. Ellis, F.J. Himpsel, M.G. Samant, J. Stöhr, D.L. Ederer, J.A. Carlisle, E.A. Hudson, L.J. Terminello, D.K. Shuh, R.C.C. Perera, *Rev. Sci. Instrum.* **66** (1995) 1394.
[10] Y. Muramatsu, T. Hayashi, *Adv. X-Ray Chem. Anal. Jpn.* **30** (1999) 41–53.

CHAPTER 18

Functions of Metal Oxide for Thermoelectric Materials and Electronic Structures

Sunao Sugihara, Koujiroh Nishiyama, Yuka Igarashi and **Kentaroh Morikawa**

Contents

Abstract

We investigate metal oxides as thermoelectric (TE) materials and further as an additive for a certain purpose, i.e. from the view point of both theory, electronic structures, and experiment. The materials are ZnAlO, Fe_2O_3, and Sr_2FeMoO_6 (double perovskite). The oxides, Er_2O_3 and TiO_2 are the additives to ZnAlO and Fe_2O_3, respectively. ZnO has a large electrical resistivity, but the Al impurity level lies in an energy gap and becomes more semiconductive. We expect to reduce thermal conductivity by adding TiO_2 to Fe_2O_3. Lower electrical resistivity of $4 \times 10^{-5}\,\Omega$m was obtained by Er-addition to ZnAlO. TiO_2 addition to Fe_2O_3 reduced thermal conductivity by $4\,W\,m^{-1}K^{-1}$ which was a half as compared with non-additive. Sr_2FeMoO_6 was also calculated to find electronic structures depending on the state of spin to show the energy gap of 2.57 eV for spin-up and metallic structure for spin-down. Experimentally, electrical resistivity of $2 \times 10^{-4}\,\Omega$m was maintained up to 600 K, then increased like a metal. This material has a very small Seebeck coefficient less than $20\,\mu V\,K^{-1}$ which is not good for TE materials.

Shonan Institute of Technology, 1-1-25, Tsujido Nishikaigan, Fujisawa, Japan
Corresponding author. E-mail: sugihara@seaple.icc.ne.jp; sugihara@mate.shonan-it.ac.jp

Advances in Quantum Chemistry, Vol. 54
ISSN 0065-3276, DOI 10.1016/S0065-3276(07)00018-4

1. INTRODUCTION

Thermoelectricity is one of the methods for electric power generation of energy transformation from heat to electric power. For this purpose, one can use electron-movement in semiconductor by generating temperature difference between two substances or materials.

Thermoelectricity has been a key issue recently because of environmental problems and energy sources shortage. This is not a big energy generation but it is crucial in terms of energy security since thermoelectricity is a clean and local energy resource, in other words a personal or private energy source. However, the figure of merit of the thermoelectric (TE) material is small (10% at most) as compared with nuclear power generation and that of petroleum, and it has a rather lower efficiency than a solar power generation. Thermoelectricity [1] was invented as the Seebeck effect in 1821 and the Pertiel effect in 1834. Since then Bi_2Te_3 as reported by Goldsmidt [2], has been very popular and it is now the best TE material in the application field.

A variety of TE materials have been developed since 1990. The conventional ones are PbTe, SiGe besides BiTe. We can classify TE materials into two categories. One is the metal compound; skutterudite (CoSb, etc), clathrate (SrGaGe, etc), half Heusler (FeVSb, etc), and silicide (FeSi, MgSi, etc). Other ones are metal oxide-based, which consist of many types of compounds. Famous oxides are $NaCo_2O_4$ [3,4], Y_2O_3 [5], $Ca(Mn,In)O_3$ [6], (Zn,Al)O [7–9], and Fe_2O_3 [10]. Oxide research was established in Japan and now there are many active researchers as well as a large variety of materials studied (Table 18.1) [9].

Our approaches to improve the performances of TE material are of two kinds: one in which the oxide itself is used as TE material as shown above and the other utilizes an oxide as the additive to improve the properties of other TE materials. We discuss Fe_2O_3, (Zn,Al)O, and Sr_2FeMoO_6 as the oxide TE material and TiO_2 and Ta_2O_5 are further investigated as the additives to n- and p-$FeSi_2$ [11]. We also discuss their electronic structures of TE material and the system of TE material/additive.

Table 18.1 Effective charges of ZnO and substituted atoms

	Center atom	O (1)	O (2)	Another Zn
Original (Zn)	1.08	−1.10	−1.10	1.14
Al^{3+} substituted	1.41	−1.06	−1.08	1.12
Mn^{2+} substituted	1.17	−1.13	−1.14	1.16
Co^{2+} substituted	1.01	−1.07	−1.09	1.14
Ga^{3+} substituted	1.46	−1.07	−1.08	1.12
In^{3+} substituted	1.68	−1.13	−1.14	1.11

2. EXPERIMENT AND CALCULATION

2.1 Experimental procedure and calculation method

The experimental method is performed by conventional powder metallurgy to form (Zn,Al)O where the starting materials are ZnO and Al_2O_3 powders. These are mixed and pressed, followed by sintering at 1613 K for 2 h, leading to $(Zn_{0.98}Al_{0.02})O$, which is an n-type semiconductor. It is $5 \times 5 \times 14\,mm^3$ in size and the Seebeck coefficient and the electrical resistivity were measured with the high-temperature Seebeck probe equipment while increasing the temperature up to 900 K.

In the case of $FeSi_2$, Fe and Si are melted at 1803 K (1530°C) and annealed in vacuum to form the β-crystal of $FeSi_2$. Then, we need to form the n- and p-type $FeSi_2$, adding Co and Mn to the β crystal of $FeSi_2$, respectively. Another type of furnace (ULVAC Co. Ltd., Yokohama) is utilized to measure the Seebeck coefficient and the electrical resistivity in He atmosphere by increasing the temperature up to 900 K. The thermal conductivity is measured with the laser flash method (ULVAC Co. Ltd., Yokohama).

The calculation, using the DV-Xα technique as a first-principles method, was used to discuss metal oxide electronic structures which are exhibited in energy level structures (including energy gaps), in effective charges (including covalent bonding), and in the partial density of state. The calculation of the additive/oxide system is carried out by considering a cluster model (Figure 18.1 for ZnO [9], Figure 18.2 for Fe_2O_3, and Figure 18.12 for Sr_2FeMoO_6) of substituted atoms for one element of the TE material matrix. The symmetry of crystal is C_{3v} and C_3 for ZnO and Fe_2O_3, respectively.

The substituted elements are Al, Ga, In of 3A and Mn, Co of 3d.

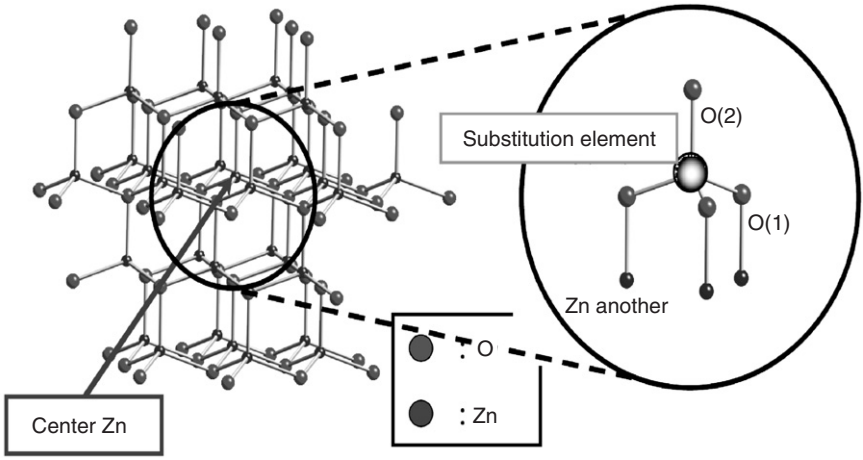

Figure 18.1 Cluster model of $(Zn_{32}O_{62})^{-60}$.

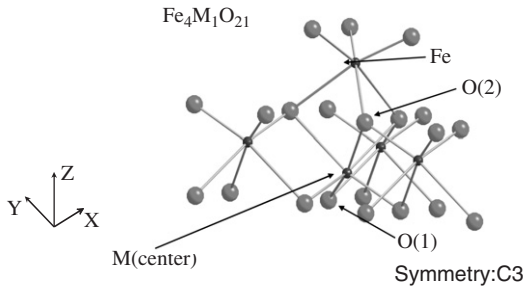

Figure 18.2 Cluster model of Fe_2O_3.

3. RESULTS AND DISCUSSION

3.1 Evaluation of TE material properties

We must make a compromise to obtain the following properties; the high TE power (Seebeck coefficient) α, the low electrical resistivity ρ, and the low thermal conductivity κ. These properties are an antinomy and a specialized semiconductor can play a role to satisfy these properties. The figure of merit, Z is shown in following equation:

$$Z = \frac{\alpha^2}{\rho\kappa}. \tag{1}$$

A thermocouple is a kind of TE material, but its TE power is usually very small (a few $10\,\mu V\,K^{-1}$). Therefore, a specialized semiconductor should be found as a proper TE material which can convert temperature differences to electric power, and electric current can generate temperature differences. The reasons why we select a metal oxide for the TE material are: (1) they are stable at high temperatures, (2) they have small mean free path of phonons leading to low thermal conductivity, and (3) usually their components are low-cost materials such as ZnO, Fe_2O_3, etc.

The Seebeck coefficient α relates to the energy gap between the Fermi level, E_F (or highest occupied molecular orbital) and the impurity level E_I (or lowest unoccupied molecular orbital) as shown in the following equation:

$$\alpha = \frac{k_B}{e}\left(\left|\frac{E_F - E_I}{k_B T}\right|\right), \tag{2}$$

where α is the TE power (Seebeck coefficient), e the electron charge, k_B the Boltzmann constant ($1.38 \times 10^{-23}\,J\,K^{-1}$), and T the temperature.

We are able to estimate a value of the entropy S from only the energy gap or the electronic structures around the Fermi level such as the electron density, the differential density of state, the degenerated state, etc.

Furthermore, the entropy is related to the TE power

$$S = -\frac{\mu}{e}\frac{1}{T}, \tag{3}$$

where μ is the chemical potential of the electron and where S can mainly be estimated from Eq. (2). According to Eq. (3),

$$\frac{\mu}{T} = -\left(\frac{dS}{dN}\right). \tag{4}$$

In consideration of the electrical resistivity, the energy gap, $E_F - E_I$, and the degenerated level in a gap it may also be important to evaluate κ. When $E_F - E_I$ becomes smaller, the electrical resistivity becomes smaller.

Thermal conductivity is the most difficult quantity to understand in terms of the electronic structure. Thermal energy can be stored in vibrational normal modes of the crystal, and one can transport thermal energy through the lattice of ions. These concepts seem to be macroscopic. Therefore, one can set up suitable wave packets to treat thermal conductivity as quantized matter. In particular, electron plus induced lattice polarization can be defined as polarons. For conduction electrons, the electrical conductivity and the thermal conductivity were first observed by Wiedemann and Franz as indicated in the following equation:

$$\frac{\kappa_e}{\sigma} = \frac{\pi^2}{3}\left(\frac{k_B}{e}\right)^2 T, \tag{5}$$

where κ_e is the thermal conductivity of electron, σ the electrical conductivity, k_B the Boltzmann's constant, e the electronic charge, and T the temperature.

The Lorenz number L is defined as follows:

$$L = \frac{\kappa_e}{\sigma T} = \frac{\pi^2}{3}\left(\frac{K_B}{e}\right)^2 = 2.45 \times 10^{-8}\ W\Omega\, K^{-2}, \tag{6}$$

(for electronic conduction only). Measured thermal conductivity κ is indicated as follows:

$$\kappa = \kappa_{ph} + \kappa_e. \tag{7}$$

Therefore, κ_{ph} which is the main component of thermal conductivity is calculated by a measured value κ and κ_e using Eqs. (5) and (6).

3.2 Experimental results and discussion

3.2.1 ZnO

The density of states and the TE properties such as the electrical resistivity; the thermal conductivity, and the Seebeck coefficient are discussed below.

The partial density of states for Al-doped ZnO is illustrated in Figure 18.3. One can find the impurity donor level of Al 3s orbital in the energy gap to obtain $E_g = 3.28$ eV. As a result, ZnO which is an insulator becomes an n-type semiconductor. Therefore, (Zn,Al)O can be a candidate for TE material. Actually, one can prepare $(Zn_{0.98}Al_{0.02})O$ using a powder metallurgical method from ZnO and Al_2O_3. As shown in the following equation, Al is apt to give electrons as compared with Zn which takes electrons with lower

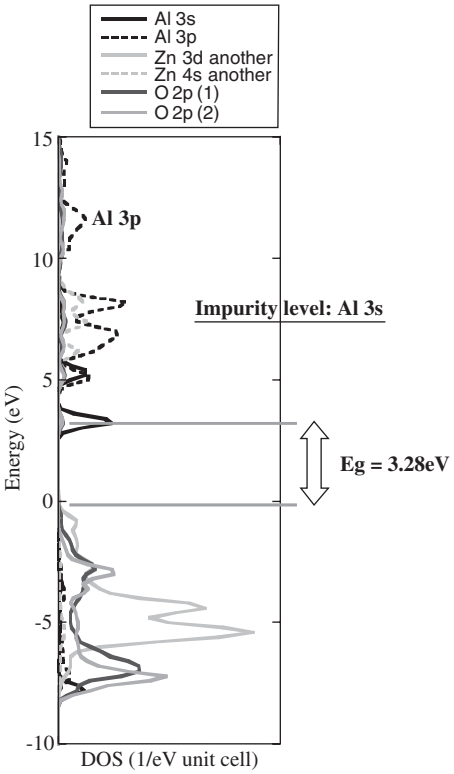

Figure 18.3 Density of state for Al-doped ZnO. Al 3s donor level appears in condution bands. Al 3p is a condution level.

energy

$$Al^{+3} + 3e \rightarrow Al - 1.68\,(\text{volts}),\ \text{and}\ Zn^{2+} + 2e \rightarrow Zn - 0.76\,(\text{volts})$$

This relationship between Al and Zn suggests that the electron moves easily which means lower electrical resistivity. The experimental electrical resistivity of this material is shown in Figure 18.4, and ZnO itself has $4 \times 10^6\,\Omega$m resistivity at 600 K, therefore the effect of Al is large enough to change ZnO into a more semiconductive material.

In considering the substitution of other elements, there is basically not much improvement although we obtained a lower value of $4 \times 10^{-5}\,\Omega$m by Er-substitution. It seems to show a slightly metallic behavior against the temperature. On the other hand, the thermal conductivity of $14\,W\,m^{-1}\,K^{-1}$ was high as shown in Figure 18.5. This value should be less than a few watts for the TE material. Figure 18.5 shows the thermal conductivity of $Zn_{0.98-X}Al_{0.02}M_XO$. In substitution of the elements, neither Cu nor Er helped in reducing the thermal conductivity. Cu-substitution rather caused a change for the worse. In general, thermal conductivity does not necessarily reflect electronic structures directly. The phonon has a rather large effect on thermal conductivity in macroscopic terms and the contribution of electron is fairly small in general as discussed in

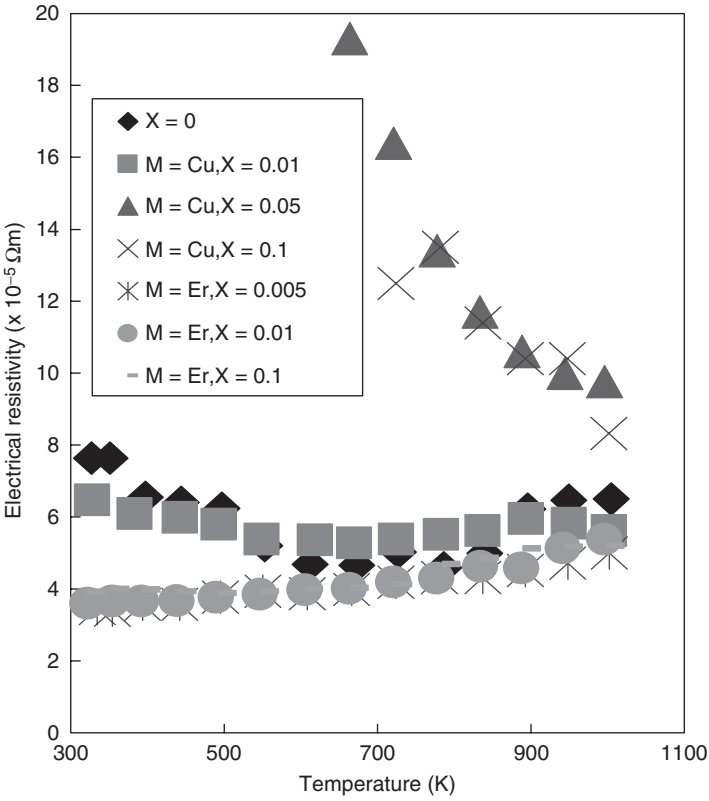

Figure 18.4 Electrical resistivity of Cu- and Er-doped (Zn,Al)O.

Section 3.1. Phonon scattering by impurity atoms, the grain boundary, defects, etc. should help to decrease the thermal conductivity.

Cu-substitution has the trend to increase thermal conductivity like a metal above 700 K. In the case of Er oxide addition, Er_2O_3 itself has a lower thermal conductivity of 2.2 $W\,m^{-1}\,K^{-1}$. Thus we need to develop the grain boundary, the impurity, and/or the defect in a crystal in order to generate phonon-scattering. It also seems to be true that one is not able to estimate the Seebeck coefficient by only the energy gap. One can see a large Seebeck coefficient of more than 150 $\mu V\,K^{-1}$ for small energy gaps (like 0.8 eV) in the BiTe series. In consideration of the TE properties, the Seebeck coefficient is referenced to entropy per electron which exists around the Fermi level in electronic structures. Moreover, the differential of the electron density against energy around the Fermi level is also important for the Seebeck coefficient.

The minus sign of the Seebeck coefficient indicates an n-type semiconductor as shown in Figure 18.6. The absolute values increase except for the specimen (M = Cu, $X = 0.1$), where the metallic Cu is supposed to exist in the crystal. The Seebeck coefficient in the specimen of Cu (0.01 mol%) increased against temperature although the electrical resistivity did not change much, implying a good characteristic for the TE material.

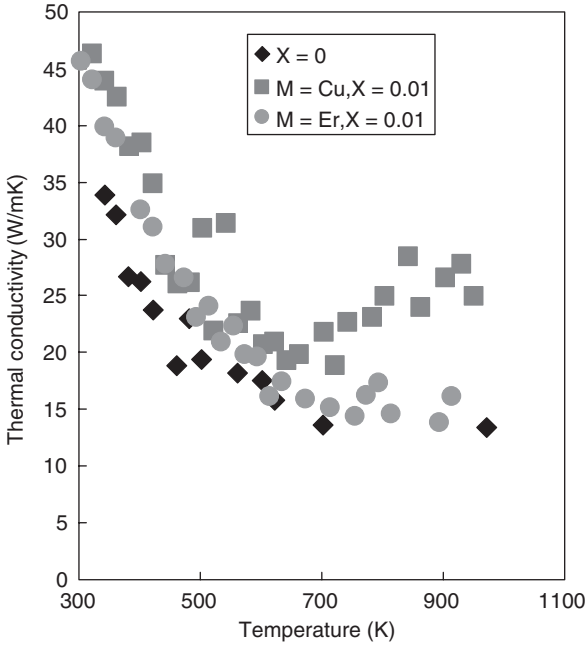

Figure 18.5 Thermal conductivity of $Zn_{0.98-x}Al_{0.02}M_xO$.

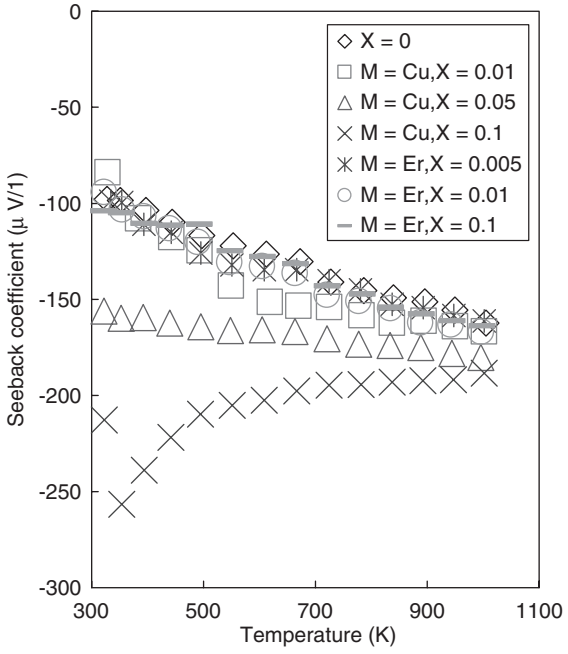

Figure 18.6 Seebeck coefficient of $Zn_{0.98-x}Al_{0.02}M_xO$.

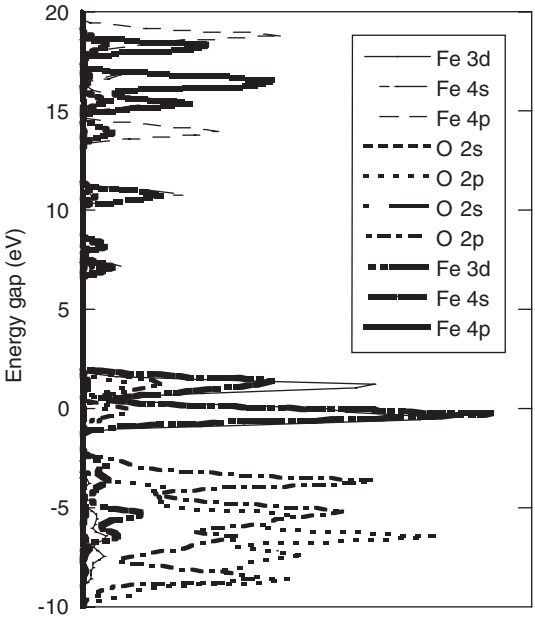

Figure 18.7 Density of state for $(Fe_{1-x}M_x)_2O_3$ ($x = 0$).

At 700 K, the Seebeck coefficient of this specimen (M = Cu, $X = 0.1$) was about 200 μV K^{-1}, although it was ca. 130 μV K^{-1} in the specimen (M = Er, $X = 0.1$). It is suggested that the former possessed electrical resistivity three times as large as the latter as shown in Figure 18.4 (Figure 18.7).

3.2.2 Fe_2O_3

Fe_2O_3 itself is an insulator. Ilmenite ($FeO \cdot TiO_2 = FeTiO_3$) is a starting material when fabricating TiO_2 and $NiO+ZnO+Fe_2O_3 \rightarrow (Ni_{0.3}Zn_{0.7})Fe_3O_4$ which is a piezoelectronic ceramics [12]. Iron oxide has usually been employed for electro ceramic materials as dielectrics of insulator. However, it can be rendered as a semiconductor by the substitution for a part of Fe, $Fe_{1-x}M_xO$. Fe_2O_3 has an energy gap of 3.1 eV and the Ti 3d orbital appeared in the gap by Ti-substitution as indicated in Figure 18.7 (X = 0 on $Fe_{1-x}M_x$) [13] and Figure 18.8 for $Fe_{1-x}M_x$ (M = Ti) [13].

The reduction of the gap decreased electrical resistivity by values smaller than two orders of the standard one. For instance, in experiment Ti 3 mol% substitution showed the value of 7×10^{-3} Ωm at 800 K.

In the compound $Fe_{1-x}M_xO$ (M = Ti), electron transportation occurs in the following chemical reaction; $Fe^{2+}+2e^- \rightarrow Fe$ −0.447 (V) and $Ti^{2+}+2e^- \rightarrow Ti$ −1.63 (V). It means that Fe takes electrons with a rather lower energy than Ti which gives electrons, resulting in larger effective charges in Ti of 2.42 than in Fe of 1.88 according to the calculations by the DV-Xα method. Thus the electron movement easily occurs in this system leading to result in lower electrical resistivity by the Ti substitution for Fe (Figure 18.9) [13].

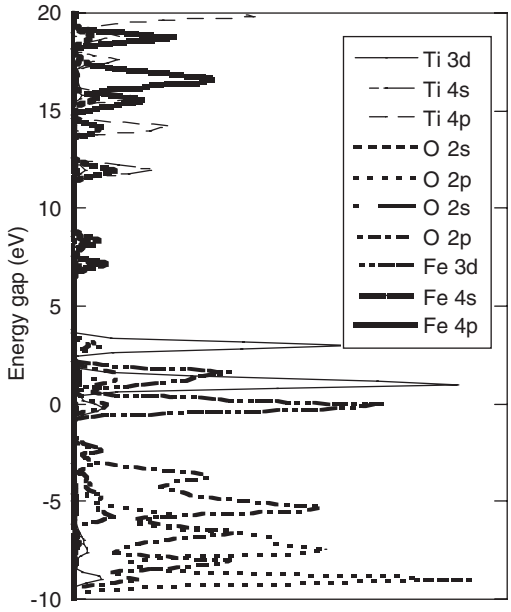

Figure 18.8 Density of state for $(Fe_{1-x}M_x)_2O_3$ (M = Ti).

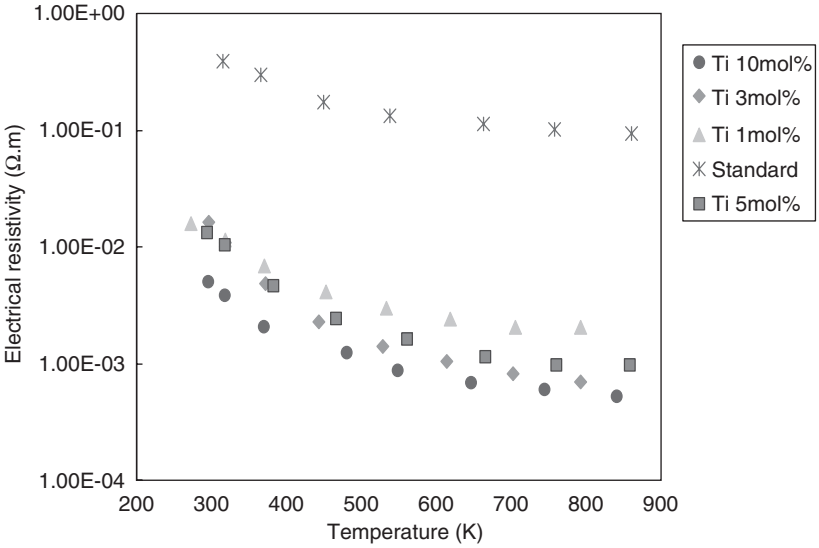

Figure 18.9 Electrical resistivity for $(Fe_{1-x}M_x)_2O_3$ (M = Ti).

We will now discuss the Seebeck coefficient in the system $Fe_{1-x}M_xO$ (M = Ti). The experimental result is shown in Figure 18.10. In the case of $X = 0$ the standard Seebeck coefficient is very high because of a large energy gap according to Eq. (2). The Ti-substitution decreases an absolute value of the Seebeck

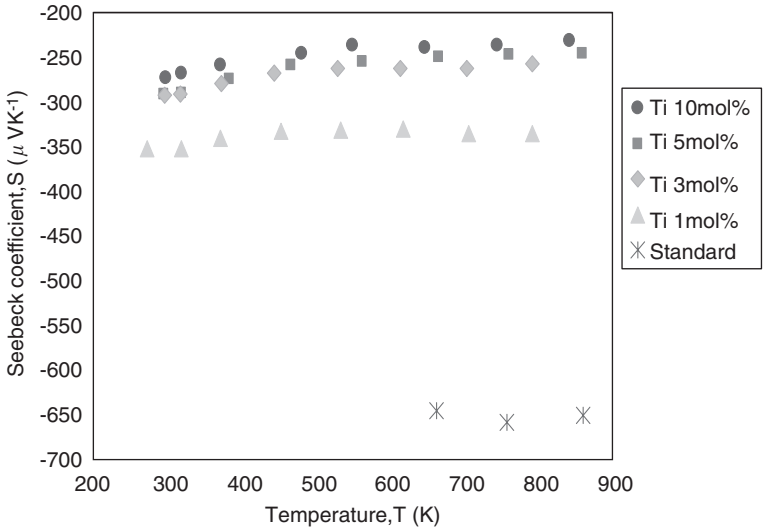

Figure 18.10 Seebeck coefficient for $(Fe_{1-x}M_x)_2O_3$ (M = Ti).

coefficient remarkably in agreement with the energy level structures in Figure 18.8, in which energy gaps become narrower by Ti 3d. Furthermore, there is a difference by 100 μV K^{-1} for the specimens of Ti 1 mol%- and 10 mol%-substitution.

Actually one can not express the Seebeck coefficient by definitive parameters, not only the energy gap but the interaction of electrons with phonons (polarons) also might play a role for thermo electric power. In an ionic lattice like an oxide, electrons are principally scattered by electromagnetic polar vibrations in which positive and negative ions move in opposite directions. This leads to the appearance of most powerful electric fields deflecting the moving electrons. Therefore, the free path length of electrons, ℓ, with a kinetic energy ε is indicated by following equation (S.I. Pekars model) [14]; $\ell_{\mathrm{pol}} \propto \varepsilon^2$. Pekar's theory is found to be well substantiated in the case of ionic semiconductors, when the electrons diffuse simultaneously with the polarization of the surrounding medium. Therefore, a larger amount of scattering center of impurity atoms such as 10 mol% Ti causes decrease of a small free path length of electrons leading to reduction of the Seebeck coefficient.

We also investigate thermal conductivity as discussed in Section 3.1 to evaluate TE materials. This physical factor seems to be difficult to take in the first-principle calculation. By analogy with diffusions and thermal conduction in gases, the phonon part of thermal conductivity κ_{ph} can be expressed as

$$\kappa_{\mathrm{ph}} = \frac{1}{3} c v \bar{\lambda}, \tag{8}$$

where c is the heat capacity per unit volume (J cm^{-3} K^{-1}), v the sound velocity (cm s^{-1}), and $\bar{\lambda}$ the mean phonon free path length (cm).

Let j denote the current of electrons through the boundary between substances; this current consists of a flow of electrons with all values of kinetic energy ε [15],

$$j = \int_0^\infty j(\varepsilon)d\varepsilon. \tag{9}$$

The average value of the energy of electron in the current is:

$$\bar{\varepsilon} = \frac{\int_0^\infty \varepsilon j(\varepsilon)d\varepsilon}{\int_0^\infty j(\varepsilon)d\varepsilon}. \tag{10}$$

Thus thermal conduction is described macroscopically. We can qualitatively suggest that the thermal conductivity decreases, not only with the increasing average atomic weight, but also in going over from a purely valence type to an ionic compound. In the case of the majority of semiconductors $c = 1.2$ to 1.6, $v = 2 \times 10^5$ to 5×10^5, and $(1/3)cv = 1 \times 10^5$ to 3×10^5. Taking the mean free path $\bar{\lambda} = 5 \times 10^{-8}$ cm, κ_{ph} is approximately 1.5 W [16]. Figure 18.11 shows the thermal

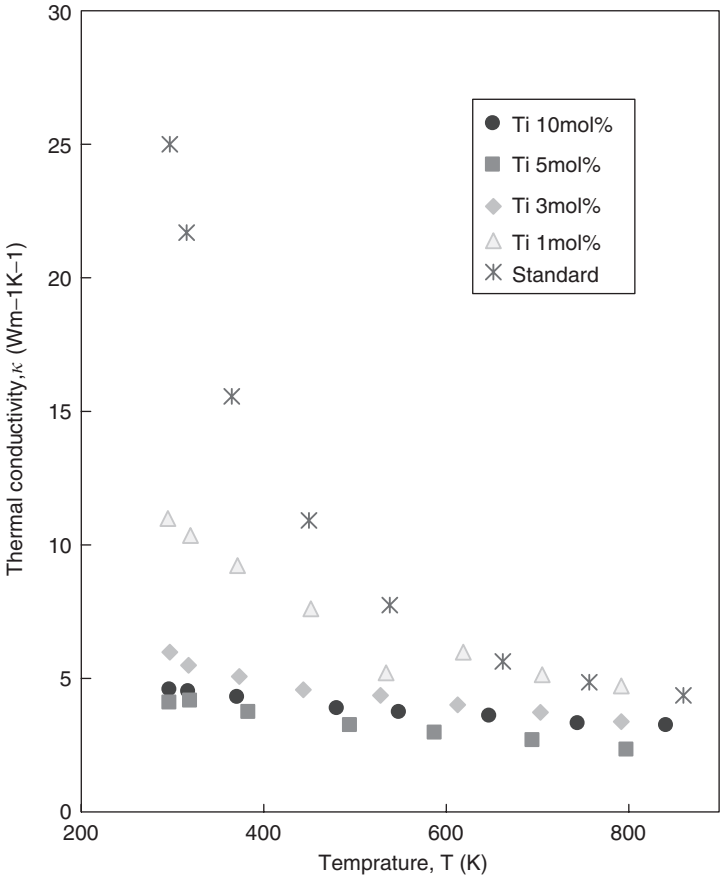

Figure 18.11 Measured thermal conductivity of TiO_2-added Fe_2O_3 against temperature. Standard means no addition of TiO_2.

conductivity of $Fe_{1-x}M_xO$ (M = Ti). As indicated in Figure 18.11, addition of TiO_2 decreased the thermal conductivity drastically. The more was the addition of TiO_2, the less was the resulting thermal conductivity. Furthermore, there is a lesser dependence of temperature when a larger amount of TiO_2 is added.

3.2.3 Sr_2FeMoO_6 (double perovskite)

This substance has mostly been studied on a colossal magnetic resistivity (CMR) in the function of the magnetic field [17]. Also the Mössbauer effect is interesting with respect to the magnetization [18]. The crystal structure is that of Fe and Mo in B-site arranged in order to make a sublattice. Furthermore, the substance possesses superexchange interaction in the midst of oxygen between Fe ($3d^5$) and Mo($4d^1$) with ferromagnetic characteristics. The band structure was reported by Kobayashi to show spin-up and spin-down structures, in which the former one relates to insulator or semiconductor and metallic to the latter one [16].

Basic features of calculation are as follows; space group $Fm\bar{3}m$.

Coordinate of atoms Fe (0, 0, 0), Mo (0, 0, 0.5), Sr (0.25, 0.25, 0.25), O (u, 0, 0), $u = 0.251$.

Lattice parameter $a = 7.89737$ Å.

According to our calculation, this substance is called a half-metal, and unusual electronic structures in which the spin-up electrons have an energy gap of 2.57 eV and the spin-down electrons show metallic property as described in Figure 18.12 [19].

We also fabricated Sr_2FeMoO_6 of specimen by $SrCO_3$, Fe_2O_3, and MoO_3, experimentally. Pelletizing is followed by calcinations and sintering at 1273 K for 24 h in the atmosphere of Ar+H_2. TE properties are measured by four-probe method up to 800 K.

Our calculation showed magnetic moment of 4.385 and $-0.673\,\mu_B$ for Fe and Mo, respectively, i.e. ferrimagnetism. The Seebeck coefficient (α) is related to entropy as the following equation:

$$\alpha = \frac{k_B}{e}\log G, \tag{11}$$

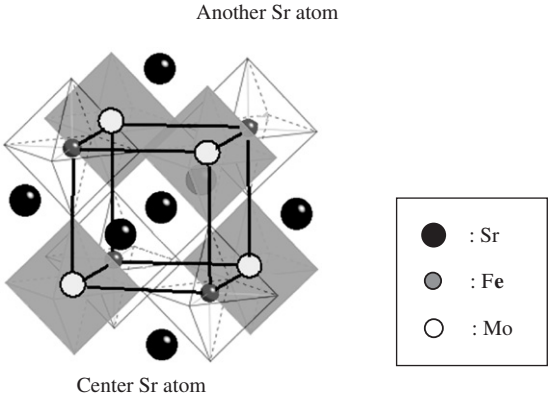

Figure 18.12 Cluster model of $(Sr_7Fe_4Mo_4O_{60})^{74-}$.

where the symbols have the usual nomenclature except for G which indicates any changes of states g_1 and g_2 as shown in Eq. (9)

$$G = |g_1 - g_2| \tag{12}$$

and g connects to quantum number of spin in the following Eq. (10)

$$g = 2S + 1. \tag{13}$$

We can calculate the Seebeck coefficient from these terms on the change of valence such as Fe^{2+} and Mo^{3+}.

Provided that the total spin of Fe was 2 with the degeneracy $2S+1 = 5$ and, the total spin of Mo was 3/2 with the degeneracy $2S+1 = 4$, the TE power was as follows:

$$Q = -\left(\frac{K_B}{e}\right)\ln\left(\frac{5}{4}\right) = -19\ \mu V. \tag{14}$$

If we take the total spin of 5/2 for Fe and 1 for Mo, $2S+1 = 6$ and 2, respectively. Then $Q = -95\,\mu V$ was obtained [20].

Now we discuss the covalence in the crystal.

The bonding of Sr–O is very weak covalent. Mo–O is the strongest covalent. In Fe–O–Mo covalent bonding appears as a whole resulting in strong electron correlation.

The charges of Fe and Mo fluctuate according to our calculation; the charge of Fe was 2.04 and Mo is 2.59 which is rather smaller than formative charge. This is because charges of Mo and Fe change through oxygen (Figures 18.13 and 18.14) [19].

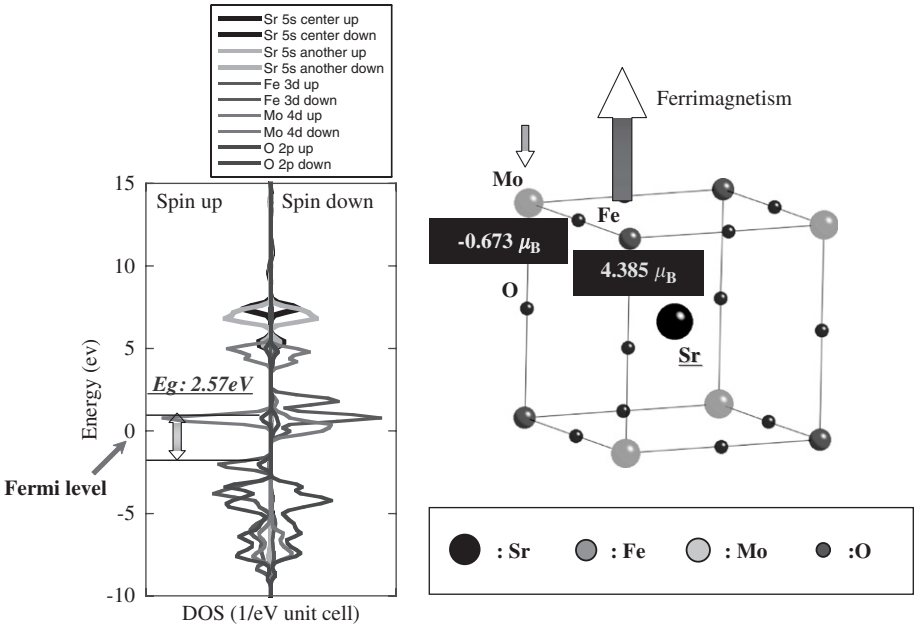

Figure 18.13 Density of state and magnetic state of Sr_2FeMoO_6.

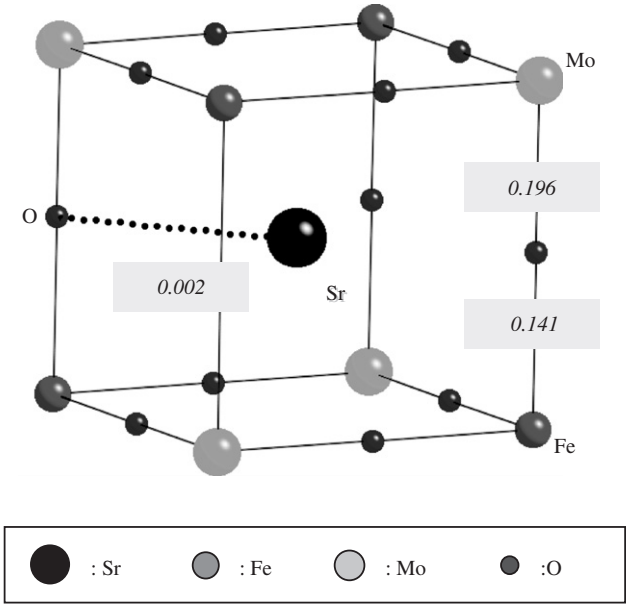

Figure 18.14 The strength of covalent bonding of Sr_2FeMoO_6; 0.196 between Mo and O, 0.141 between O and Fe, 0.002 between O and Fe.

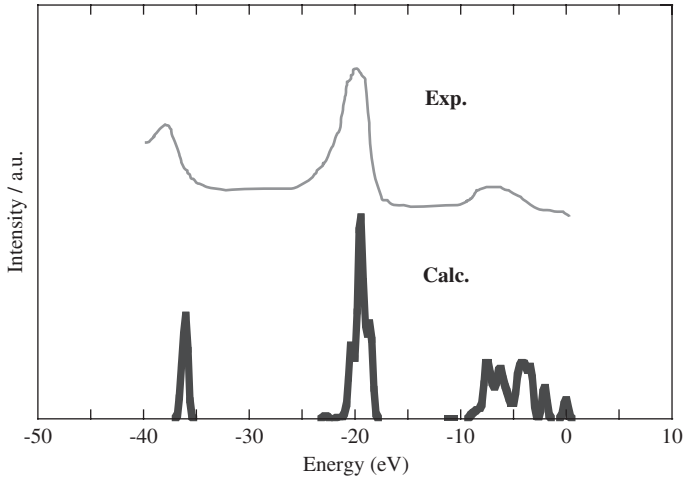

Figure 18.15 XPS for calculation and experiment.

Figure 18.15 shows the X-ray photoelectron spectrum of experimental result as compared with calculated one. As seen in this figure, the two spectra agreed with each other fairly well. This means that our calculation was appropriate with a cluster model. Experimentally, we could find a lower electrical resistivity of the order of $10^{-4}\Omega$m, which qualitatively suggested the electronic structures showing metallic

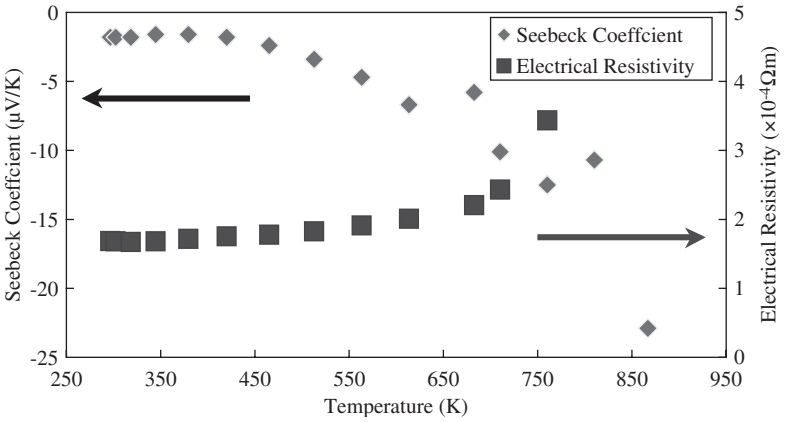

Figure 18.16 Seebeck coeffcient and electrical resistivity depending on temperature.

and/or semiconductor properties. However, one can not find the reason why electrical resistivity against temperature results in a metallic behavior (Figure 18.16) [19].

The experimental results are discussed below.

The electrical resistivity did not increase up to around 700 K. The resistivity of a metal containing impurities may usually be written as follows [21]:

$$\rho = \rho_i + \rho_L \tag{15}$$

where ρ_i is the resitivity caused by scattering the of electron waves by impurity atoms which disturb the periodicity of the lattice and ρ_L the resistivity caused by the thermal motion of the lattice. If the concentration of impurity atoms is small, ρ_i is independent of temperature. According to XRD (X-ray diffraction patterns) there were found some different substances from Sr_2FeMoO_6 due to vaporization of Mo oxide when it is heated above 600 K approximately. Thus, electrical resistivity increased around 600 K because of the lattice defect. The electrical resistivity was small for the semiconductor. However, the Seebeck coefficient was also very low just like the thermocouples which is not good for TE materials.

4. CONCLUSION

We have investigated metal oxides as TE materials and as an additive for a certain purpose from the view points of both electronic structures and experiment. The materials are ZnAlO, Fe_2O_3, and Sr_2FeMoO_6 (double perovskite). The oxides, Er_2O_3 and TiO_2 are the additive to ZnAlO and Fe_2O_3, respectively. ZnO has a large electrical resistivity, but Al impurity level in an energy gap became more semiconductive. We expect to reduce the thermal conductivity by adding TiO_2 to Fe_2O_3. Lower electrical resistivity of $4 \times 10^{-5}\,\Omega$m was obtained by Er-addition to ZnAlO. TiO_2 addition to Fe_2O_3 reduced thermal conductivity by $4\,W\,m^{-1}\,K^{-1}$ which was half as compared with the non-additive Fe_2O_3. Sr_2FeMoO_6 was also calculated to find electronic structures depending on

the state of spin to show the energy gap of 2.57 eV for spin-up and metallic structure for spin-down. Experimentally, electrical resistivity of $2 \times 10^{-4}\,\Omega$m was maintained up to 600 K and then increased like a metal. This material has very small Seebeck coefficient less than $20\,\mu V\,K^{-1}$ which is not good for TE materials. However, the double perovskite, Sr_2FeMoO_6 may be suggested as a good TE material by controlling the states of down-spin and up-spin.

REFERENCES

[1] A.F. Ioffe, *Semiconductor Thermoelements and Thermoelectric Cooling*, Inforsearch Limited, London, 1956.
[2] H.J. Goldsmidt, *Proc. Phys. Soc.* **71** (1958) 636–646.
[3] I. Terasaki, Y. Sasago, K. Uchinokura, *Phys. Rev. B* **56(20)** (1997) pp. R12685–R12687.
[4] H. Yakabe, K. Kikuchi, I. Terasaki ,Y. Sasago, K. Uchinokura, In: Proceedings of 16th Conference on Thermoelectrics, Dresden, Germany, 1997, pp. 523.
[5] K. Koumoto, W. Seo, S. Ozawa, *Appl. Phys. Lett.* **71** (1997) 1475.
[6] M. Ohtaki, H. Koga, T. Tokunaga, K. Eguchi, H. Arai, *J. Solid State Chem.* **120** (1995) 105.
[7] Y. Yoshida, T. Kurotori, S. Hiki, H. Yano, S. Sugihara, In: Proceedings of Thermoelectric Society Japan, 2004, pp. 136–137.
[8] H. Ohta, W.S. Seo, K. Koumoto, *J. Am. Ceram. Soc.* **79** (1996) 2193.
[9] Y. Yamamoto, M. Katayose, Y. Yoshida, S. Sugihara, In: Proceedings of Thermoelectric Energy Conversion, 2003, pp. 48–49.
[10] H. Muta, K. Kurosaki, M. Uno, S. Yamanaka, *J. Alloys Compounds* **335** (2002) 200–202.
[11] S. Sugihara, M. Fujita, S. Kawashima, H. Suzuki, I. Yonekawa, Electronic Structures of $FeSi_2$ and Thermoelectricity. In: P. Vincenzini (Ed.), Proceedings of 9th Cimtec-World Forum on New Materials Symposium, 1999, pp. 753–762.
[12] K. Okazaki, Ceramic Engineering for Dielectric, 4th ed., p. 160, Gakkennsha, Tokyo, 1992 (Japanese).
[13] S. Sugihara, K. Nishiyama, *J. Jpn. Powder Powder Metallurgy.* **54(5)** (2007) 362–365.
[14] A.F. Ioffe [1], p. 14.
[15] A.F. Ioffe [1], p. 47.
[16] C. Kittel [11], p. 139
[17] K.I. Kobayashi, T. Kimura, H. Sawada, K. Terakura, Y. Tokura, *Nature* **395** (1998) 677--680.
[18] J. Linden, T. Yamamoto, J. Nakamura, H. Yamauchi, K. Karrinen, *Phys. Rev. B* **66** (2002) 184408.
[19] Y. Yutoh, M. Yamamoto, H. Kuboya, S. Sugihara, H. Yamauchi, *IEICE Trans. Electron. (Jpn. Edn.)* **87-C(5)**, (2004) 452–458.
[20] S. Sugihara, M. Yamamoto, Y. Yutoh, H. Kuboya, H. Yamauchi, In: Proceedings of 22nd International Conference on Thermoelectrics, 2003, pp. 175–179.
[21] C. Kittel [11], p. 305.

CHAPTER 19

Characteristics of Chemical Bond in Perovskite-Type Hydrides

Yoshifumi Shinzato*, Kenji Komiya*, Yoshitaka Takahashi*, Hiroshi Yukawa*, Masahiko Morinaga* and **Shinichi Orimo****

Contents

Abstract

The electronic structure of typical perovskite-type hydrides, $MMgH_3$ (M = Na, K, Rb), $CaNiH_3$ and $SrPdH_3$, are simulated to understand the nature of the chemical bond between constituent ions in them using the DV-Xα molecular orbital method. For $MMgH_3$, it is found that the valence band consists mainly of the H 1s and Mg 3s, 3p components, and the M s, p components are distributed over the empty conduction band. Thus, the covalent bond still remains between Mg and H ions, but the ionic bond is rather strong between them. The chemical bond between M and H ions is further ionic in character. On the other hand, for $CaNiH_3$ and $SrPdH_3$, covalent bond is dominant between Ni (or Pd) and H ions.

Also, the enthalpy change in the dehydrogenation reaction, ΔH, is estimated for several reaction paths, using the plane-wave pseudopotential

* Department of Materials Science and Engineering, Graduate School of Engineering, Nagoya University, Furo-cho, Chikusa-ku, Nagoya 464-8603, Japan
Corresponding author. E-mail: shinzato@silky.numse.nagoya-u.ac.jp
** Institute for Materials Research, Tohoku University, Katahira, Sendai 980-8577, Japan

Advances in Quantum Chemistry, Vol. 54
ISSN 0065-3276, DOI 10.1016/S0065-3276(07)00019-6

method. For example, in the $NaMgH_3$ system, ΔH is estimated to be 72.9 kJ/molH_2 in the reaction, $NaMgH_3 \rightarrow NaH+Mg+H_2$, and 82.6 kJ/mol$H_2$ in the reaction, $NaH \rightarrow Na+1/2\,H_2$. In agreement with these calculated results, $NaMgH_3$ dehydrides in these two-step reactions at about 673 K according to recent experiments.

1. INTRODUCTION

There are many perovskite-type hydrides being composed mainly of the 1A group elements and the 2A group elements in the periodic table. The crystal structure of perovskite-type hydride, $KMgH_3$ is illustrated in Figure 19.1. In particular, the Mg-based perovskite-type hydrides, $MMgH_3$ (M = Na, K, Rb), are expected to be one of the materials for hydrogen storage because of their higher capacities of hydrogen than metal hydrides. However, any systematic investigations have not been carried out for the perovskite-type hydrides consisting of both the 1A group elements such as Li, Na, K, Rb, Cs and the 2A group elements such as Be, Mg, Ca, Sr, Ba in the periodic table. In addition, there are perovskite-type hydrides containing a transition metal (e.g., $CaNiH_3$), but detailed information on the chemical bond remains unknown in these hydrides.

The purpose of this study is to make clear the characteristics of the nature of the chemical bond in the perovskite-type hydrides, $MMgH_3$ (M = Na, K, Rb), $CaNiH_3$, and $SrPdH_3$, with the aid of electric structure calculations.

2. CALCULATION PROCEDURE

The hydrogen positions in the perovskite-type hydrides are sometimes difficult to be determined experimentally. So, in this study, the crystal structure of the perovskite-type hydrides are optimized by the total energy minimization.

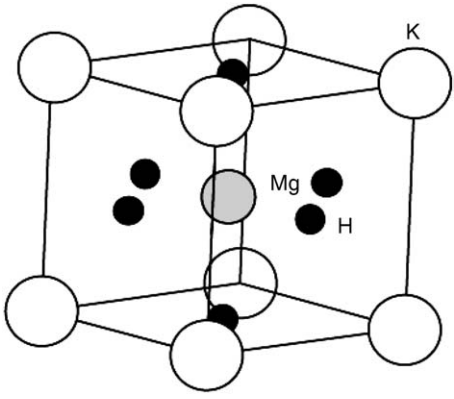

Figure 19.1 Schematic illustration of the perovskite-type hydride, $KMgH_3$.

For this purpose, the first-principles calculations based upon the density function theory (DFT) are performed with the generalized gradient approximation (GGA) [1]. The implementation of DFT employed here combines a plane-wave basis set with the total energy pseudopotential method, as is embodied in the CASTEP code [2]. The present calculations are based upon the ultrasoft pseudopotentials proposed by Vanderbilt [3]. The plane-wave cutoff energy is chosen to be 380 eV. This cutoff energy is found to achieve the convergence of the total energies within 0.03 eV/atom relative to the results with the cutoff energies up to 600 eV. The sampling in the reciprocal space is done with *k*-points grids of $6 \times 6 \times 6$ for orthorhombic $NaMgH_3$ [4], $6 \times 6 \times 6$ for cubic $KMgH_3$ [5], $5 \times 5 \times 2$ for orthorhombic $RbMgH_3$ [6], $8 \times 8 \times 8$ for cubic $CaNiH_3$ [7] and $8 \times 8 \times 8$ for cubic $SrPdH_3$ [8]. All the ions in the unit cell are allowed for full relaxation. The enthalpy change in the dehydrogenation reactions ΔH are also estimated by the total energy calculations, assuming several reaction paths for the dehydrogenation.

The DV-Xα cluster method [9,10] is used for investigating the nature of the chemical bond between ions in the perovskite-type hydrides. This is a molecular orbital method, assuming the Hartree–Fock–Slater (HFS) approximation. In this method, the exchange-correlation between electrons is given by the Slater's Xα potential. The matrix elements of Hamiltonian and the overlap integrals are calculated by a random sampling method. The molecular orbitals are constructed by a liner combination of numerically generated atomic orbitals (LCAO). The cluster models consisting of about 100 ions are constructed by using the optimized structure. For a characterization of the electronic structures and chemical bonding in the cluster, the bond order between ions and the ionicity (i.e., net charge) of each element in the cluster are estimated according to the Mulliken population analysis [11]. Here, the bond order is a measure of the strength of the covalent bond between ions in the hydride.

3. RESULTS AND DISCUSSION

3.1 Partial density of states

As an example of perovskite-type hydrides, the partial density of states is shown in Figure 19.2 for cubic $KMgH_3$. This is obtained after the geometry optimization using the pseudopotential method. It is found from this figure that the valence band consists mainly of the H 1s and Mg 3s, 3p components. The K 4s, 4p components are distributed over the empty conduction band. Thus, the covalent bond nature still remains between Mg and H ions. In Table 19.1, the result of the chemical bond for cubic $KMgH_3$ is compared with that for Mg–H and K–H diatomic molecules. It is apparent that the covalent bond between Mg and H ions is much weaker in cubic $KMgH_3$ than in the Mg–H diatomic molecule, instead the ionic bond is more enhanced. Additionally, the chemical bond between K and H ions is ionic in character. In other words, the ionic bonds between Mg and H ions and between K and H ions are stronger in $KMgH_3$ than the corresponding

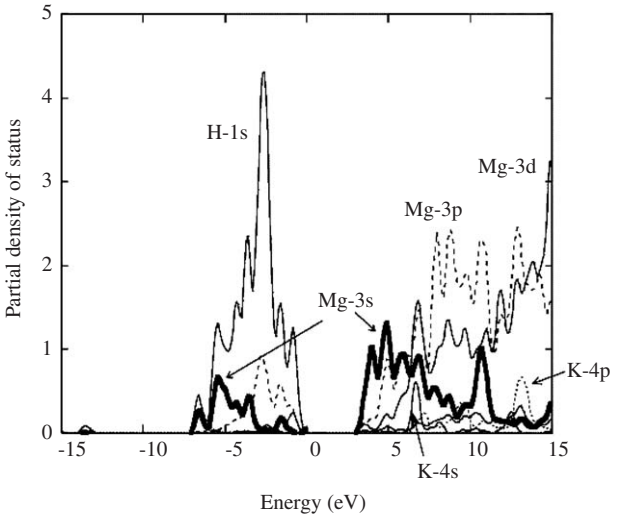

Figure 19.2 Partial density of state for cubic $KMgH_3$.

Table 19.1 Comparison of the bond order and ionicity of elements between $KMgH_3$ and diatomic molecules (K–H, Mg–H)

	Bond order		Ionicity	
$KMgH_3$	Mg–H (2.00 Å)	0.19	Mg	+1.08
	K–H (2.83 Å)	0.03	K	+0.70
Diatomic molecule	Mg–H (1.76 Å)	0.39	Mg	+0.55
	K–H (2.27 Å)	0.20	K	+0.75

bonds in the Mg–H and K–H diatomic molecules, owing to the differences in the interionic distance among them. Similar trends are also seen in other perovskite-type hydrides such as $NaMgH_3$ and $RbMgH_3$.

As an example of perovskite-type hydrides containing a transition element, the partial density of state for $CaNiH_3$ is shown in Figure 19.3. The Fermi energy level falls on the Ni 3d band and there is a large overlap between the Ni 3d band and the H 1s band, resulting in the strong covalent interaction operating between Ni and H ions.

3.2 Chemical bond

The DV-Xα molecular orbital calculations are performed with the cluster models constructed using the geometrically optimized crystal structures. The calculated

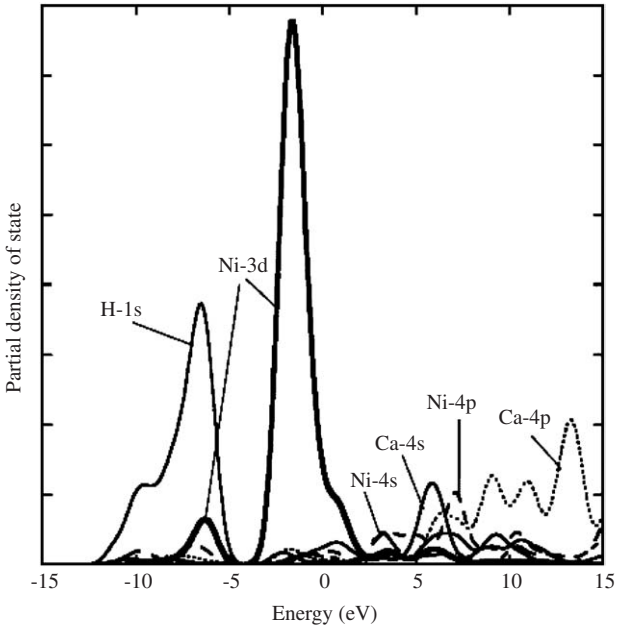

Figure 19.3 Partial density of state for cubic $CaNiH_3$.

lattice parameters agree with the experimental ones within 0.5% difference. Following the Mulliken population analysis, the ionicity of elements and the average bond order between ions in $MMgH_3$ (M = Na, K, Rb) are estimated and the results are shown in Figure 19.4a and b, respectively. The ionicitiy of H is similar among $MMgH_3$ (M = Na, K, Rb) and the value is about −0.6, which is negatively larger than the value of about −0.2 for H in typical metal hydrides. This means that the ionic character is more enhanced in the nature of the hydrogen–metal bond in $MMgH_3$ than in metal hydrides. Also, as shown in Figure 19.4b, the Mg–H bond order is much larger than the M–H bond order in $MMgH_3$ (M = Na, K, Rb), indicating that the Mg–H covalent bond is stronger than the M–H covalent bond in $MMgH_3$. By combining these results, it is evident that the Mg–H bond is rather ionic, but covalent interaction still remains. Also, the ionic interaction is dominant between K and H ions.

3.3 Enthalpy changes in the dehydrogenation reactions, ΔH

The enthalpy changes in the dehydrogenation reactions, ΔH, are calculated for the perovskite-type hydrides MXH_3 (M = Na, K, Rb, Li, X = Mg, Be). Here, $LiBeH_3$ is assumed to have a cubic perovskite-type structure. According to the total energy calculation, the lattice parameter of $LiBeH_3$ is about 3.15 Å, which satisfies the Westlake criterion that the H–H interaction should be longer than 2.1 Å.

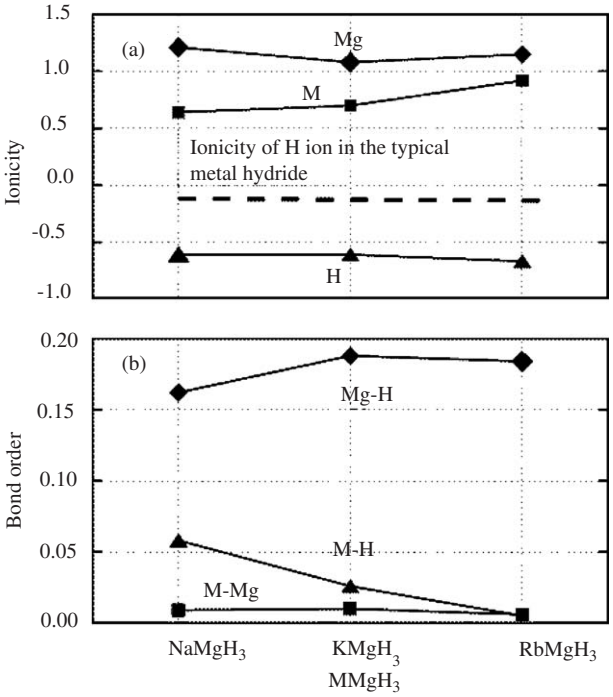

Figure 19.4 (a) Ionicity of elements and (b) the bond order in the perovskite-type hydrides, $MMgH_3$ (M = Na, K, Rb).

The calculated results are shown in Figure 19.5. In this figure, the desirable range of ΔH is indicated by a narrow band to control the dehydrogenation temperature to be less than 400 K. In most cases, the calculated ΔH is out of this range, so the dehydrogenation temperature must be high. Here, the three different dehydrogenation reactions are simulated for MXH_3. They are $MXH_3 \rightarrow MH+X+H_2$, $MXH_3 \rightarrow M+XH_2+1/2H_2$ and $MXH_3 \rightarrow M+X+3/2H_2$. For example, for the $NaMgH_3$ system, ΔH is estimated to be 72.9 kJ/molH_2 for the reaction (1): $NaMgH_3 \rightarrow NaH+Mg+H_2$, and 77.3 kJ/mol$H_2$ for the reaction (2): $NaMgH_3 \rightarrow Na+Mg+3/2H_2$. So, ΔH becomes 86.2 kJ/molH_2 for the reaction (3): $NaH \rightarrow Na+1/2H_2$. In agreement with these calculated results, $NaMgH_3$ dehydrides in the two-step reaction of (1) and (3) at 673 K according to recent experiments [12,13]. In the $KMgH_3$ system, ΔH is estimated to be 99.1 kJ/molH_2 for the reaction, $KMgH_3 \rightarrow K+Mg+3/2H_2$. In agreement with this calculated result, $KMgH_3$ dehydrides in the one-step reaction according to recent experiment [13]. For the $RbMgH_3$ system, ΔH is estimated to be 87.2 kJ/molH_2 for the reaction, $RbMgH_3 \rightarrow Rb+Mg+3/2H_2$. Judging from the calculation, $RbMgH_3$ is expected to dehydride in this one-step reaction, but $RbMgH_3$ dehydrides in two-step reactions and hence its dehydrogenation path is uncertain according to recent experiment [13].

Also, for the $LiBeH_3$ system, the enthalpy change in the dehydrogenation reaction, ΔH, is estimated to be 38.3 kJ/molH_2 for the reaction, $LiBeH_3 \rightarrow Li+Be+3/2H_2$,

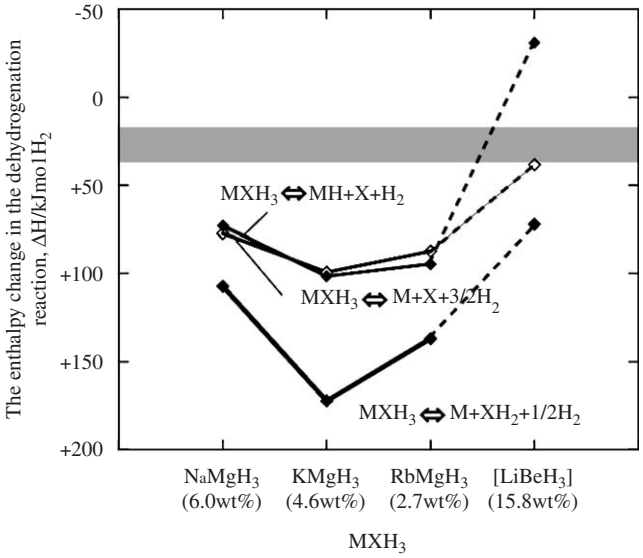

Figure 19.5 Enthalpy change in the dehydrogenation reaction, ΔH, for the perovskite-type hydrides, $MMgH_3$ (M = Na, K, Rb) and $LiBeH_3$. The number (wt%) in the parenthesis shown in the horizontal axis is the total amount of hydrogen to be release during dehydrogenation.

so its dehydrogenation is expected to occur in the one-step reaction at relatively low temperatures, if $LiBeH_3$ has the cubic perovskite-type structure. For the Li–Be–H ternary system, a few experimental data have been reported [14]. However, it remains still unclear whether it is the perovskite-type or not.

3.4 Relationship between enthalpy change of perovskite-type hydrides and binary hydrides

The relationship between ΔH_1 and ΔH_2 is shown in Figure 19.6, where ΔH_1 and ΔH_2 are the enthalpy change for the reactions, $MXH_3 \rightarrow M+X+3/2H_2$ and ($XH \rightarrow X+1/2H_2$ or $XH_2 \rightarrow X+H_2$), respectively. There is a clear trend that ΔH_1 increases with increasing ΔH_2 except for the pervoskite-type hydride containing transition elements such as $CaNiH_3$ and $SrPdH_3$. For example, $LiBeH_3$ has the lowest ΔH_1 because of the lowest ΔH_2 for BeH_2. In case of $CaNiH_3$ and $SrPdH_3$, ΔH_1 values are large, namely, 182 kJ/molH_2 for $CaNiH_3$ and 164 kJ/molH_2 for $SrPdH_3$, indicating that the strong covalent interaction between Ni (or Pd) and H atoms is operating in $CaNiH_3$ (or $SrPdH_3$) as explained earlier. This indicates that the hydrogen state in these hydrides is very stable. This result is supported by our recent calculation using energy density analysis [15]. Interionic Mg–H distances resembles between perovskite-type hydrides, $MMgH_3$ and MgH_2. For example, the optimized average Mg–H interionic distances are 1.95 Å for $NaMgH_3$, 2.00 Å for $KMgH_3$, and 2.02 Å for $RbMgH_3$, which are close to 1.96 Å for MgH_2. This trend is seen in $CaNiH_3$ and $SrPdH_3$.

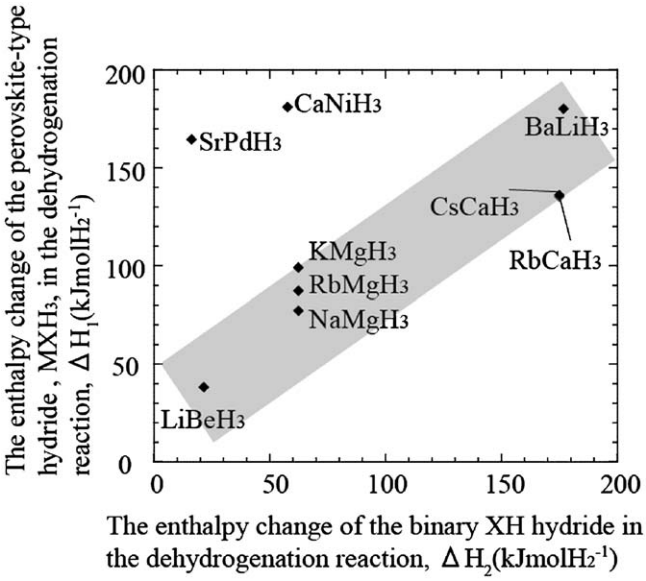

Figure 19.6 Correlation between enthalpy change of the perovskite-type hydrides, ΔH_1, and enthalpy change of the binary hydrides, ΔH_2, in the dehydrogenation reaction.

4. SUMMARY

The nature of the chemical bond between ions is investigated in the perovskite-type hydrides, $MMgH_3$ (M = Na, K, Rb), $CaNiH_3$, and $SrPdH_3$ by the DV-Xα molecular orbital method. Also, the enthalpy changes in the dehydrogenation reactions are calculated using the pseudopotential method. It is found that the Mg–H bond is rather ionic, but the covalent interaction still remains to some extent. On the other hand, the M–H bond is further ionic.

In the perovskite-type hydrides containing a transition element, $CaNiH_3$ and $SrPdH_3$, strong covalent interaction is operating between the transition element and hydrogen. So, their enthalpy changes are higher as compared to those of the other perovskite-type hydrides being composed of the 1A group element and the 2A group element.

ACKNOWLEDGMENTS

The authors express sincere thanks to the staffs of the Computer Center, Institute for Molecular Science, Okazaki National Institute for the use of super-computers. This study was supported by a Grant-in-Aid for Scientific Research from the Ministry of Education, Culture, Sports, Science and Technology of Japan, by the Japan Society for the Promotion of Science, and also by the 21st Century COE program ''Nature-Guided Materials Processing''.

REFERENCES

[1] J.P. Perdew, K. Burke, Y. Wang, *Phys. Rev. B* **54** (1996) 16533–16539.
[2] V. Milman, B. Winkler, J.A. White, C.J. Pickard, M.C. Payne, E.V. Akhmatskaya, R.H. Nobes, *Int. J. Quantum Chem.* **77** (2000) 895–910.
[3] D. Vanderbilt, *Phys. Rev. B* **41** (1990) 7892–7895.
[4] A. Bouamrane, J.P. Laval, J.-P. Soulie, J.P. Bastide, *Mater. Res. Bull.* **35** (2000) 545–549.
[5] J.P. Bastide, A. Bouamrane, P. Claudy, J.M. Letoffe, *J. Less-Common Metals* **136** (1987) L1–L4.
[6] F. Gingl, T. Vogt, E. Akiba, K. Yvon, *J. Alloys Compd.* **282** (1999) 125–129.
[7] T. Sato, D. Noreus, H. Takeshita, U. Häussermann, *J. Solid State Chem.* **178** (2005) 3381–3388.
[8] W. Bronger, G. Ridder, *J. Alloys Compd.* **210** (1994) 53–55.
[9] C. Satoko, M. Tsukada, H. Adachi, *J. Phys. Soc. Jpn.* **45** (1978) 1333–1340.
[10] M. Morinaga, N. Yukawa, H. Adachi, *J. Phys. Soc. Jpn.* **53** (1984) 653–663.
[11] R.S. Mulliken, *J. Chem. Phys.* **23** (1955) 1833–1840.
[12] K. Ikeda, Y. Kogure, Y. Nakamori, S. Orimo, *Scripta Mater.* **53** (2005) 319–322.
[13] K. Komiya, N. Morisaku, R. Rong, Y. Takahashi, Y. Shinzato, H. Yukawa, M. Morinaga, *J. Alloys Compd.* in press, doi: 10.1016/j.jallcom.2006.11.116.
[14] A. Zaluska, L. Zaluski, J.O. Strow-Clsen, *J. Alloys Compd.* **307** (2000) 157–166.
[15] Y. Shinzato, H. Yukawa, M. Morinaga, T. Baba, H. Nakai, *Adv. Quantum Chem.* **54** (2007) 145–160.

CHAPTER 20

Chemical Bonding of Mobile Cations in Superionic Conductors

Y. Kowada[a], M. Tatsumisago[b], T. Minami[c] and **H. Adachi[d]**

Contents

Abstract

Electronic states of monovalent ions in superionic conductors such as Li_3N, as well as the lithium sulfide superionic conducting glasses, were calculated by the DV-Xα cluster method. The movements of the cations were simulated by several model clusters with different positions of the moving cation. The net charge of the moving cation and the total bond overlap population (TBOP) between the moving cation and other ions were used for discussion of chemical bonding of the moving cation. In the Li_3N crystal, the TBOP of the moving cation along the conduction path changed less than those of the other paths. On the other hand, the changes of the net charges of the moving cations were similar in all paths. Furthermore, the relationship between ionic conductivity and the differential total bond overlap population (DBOP) was discussed in the lithium sulfide superionic conducting glasses. The cluster models were constructed by the coordination number reported by experimental methods and the bond length estimated from the ionic radii of each ion. Especially the relationship between ionic conductivity and the differential bond overlap population

[a] Hyogo University of Teacher Education, Hyogo 673-1494, Japan
Corresponding author. E-mail: ykowada@sci.hyogo-u.ac.jp
[b] Department of Applied Chemistry, Osaka Prefecture University, Sakai 599-8531, Japan
[c] Osaka Prefecture University, Sakai 599-8531, Japan
[d] Fukui Institute for Fundamental Chemistry, Kyoto University, Kyoto 606-8103, Japan

Advances in Quantum Chemistry, Vol. 54
ISSN 0065-3276, DOI 10.1016/S0065-3276(07)00020-2

was discussed for the sulfide-based lithium ion conducting glasses in the systems Li_2S–SiS_2–Al_2S_3 and Li_2S–SiS_2–P_2S_5. In these glasses, the DBOP with the movement of the lithium ion had good negative correlations with the ionic conductivity and positive correlations with the activation energy obtained by the experimental measurements. In any case, the smaller change of the TBOP of the moving cations played an important role in the fast ion movement in the superionic conducting glasses, rather than the change of the net charge of the moving cations. This bonding state of the moving cations is one of the characteristics of the electronic state in superionic conductors.

1. INTRODUCTION

In the recent 10 years, we have investigated the electronic state of the ion movement in solid-state materials [1–6]. In SiO_2–M_xO_y ($M_xO_y = P_2O_5$, TiO_2, and ZrO_2) gel films, the bonding state between the Na ions and the oxide ions was discussed. In this case the covalent bonding between Na and oxide ions was the reason for the movement of the Na ions. In the Li_2S–SiS_2–Li_4SiO_4 oxysulfide glasses, the Li ion conductivity of rapidly quenched glass was discussed from the viewpoint of the chemical bonding of the moving ions. The addition of Li_4SiO_4 lead to the formation of pyro-oxysulfide groups with the bridging oxygen and this unit had the same covalent interaction with the surrounding Li ions, which resulted in high ionic conductivity of the oxysulfide glass. We have also looked into the electronic state of the Ag ions in AgI-based superionic conducting materials. In this case we have proposed a method to simulate the movement of the ions in the molecular orbital calculations and discussed the change of the bonding state of the moving Ag ions. The result showed that the moving Ag ions had a very small change of the covalent bonding with movement through the conduction path rather than ionic interactions. This small change in the covalent bonding was one of the causes for the fast movement of the Ag ions in the AgI-based superionic conductors.

In these studies, we have paid attention on the bonding state of the moving ions from the viewpoint of an interaction named ''covalency and ionicity'' between the moving ions and the surrounding ions. Thus, the covalent bonding of the moving ions should support an important part of the ion movement in solid-state materials. In the present study the electronic states of the Li_3N crystal and sulfide-based superionic (or Li ion) conducting glasses were studied, in order to analyze the interaction of the moving ions in superionic conducting materials. These materials are the typical Li ion conductors and have high ionic conductivities. Furthermore the Li, N, and S ions usually have covalent interactions in the solid-state materials. We can expect that a relationship exists between the high ionic conductivity and the covalent interactions of the moving cations in these systems.

2. Li_3N Crystal

There are several studies on the high Li ion conductivity of Li_3N crystal that include experimental measurements and theoretical calculations [7–10]. Several experimental studies reported that the Li_3N crystal contained H^+ ion impurities in interstitial positions and they make a certain concentration of the Li ion vacancies. These vacancies yield on the planes, which contains both Li and N ions, called Li_2N plane. It was reported that the activation energy of the movement of the Li ion on Li_2N planes was 0.004 eV [10]. In the Li_3N crystal, there are another kind of Li ions on the planes containing only the Li ions, which connect between the Li_2N planes. This kind of Li ions hardly move compared with those on the Li_2N plane. In addition to this, the Li_3N crystal has the anisotropicity of the ionic conductivity and the Li ion conductivity along the *c*-axis is much smaller than those of the *a*- and *b*-axes.

Thus, the Li ion can move easily in the Li_2N plane and can hardly move in the Li plane. This is something strange from the viewpoint of chemical bonding. In the Li_2N plane, the moving Li ion might have a strong interaction with N ion compared with those on the Li plane. Generally, the larger interaction between the Li and N ions seems to impose constraints on the fast movement of the Li ion. The experimental results, however, suggest that the fast movement of the Li ion in the Li_3N crystal is not dependent on the smaller interaction between the Li and N ions. The chemical bonding of the Li ion should contribute to the fast movement of the Li ion in the Li_3N crystal.

2.1 Calculation method

The DV-Xα cluster method [11], which is one of the first principle molecular orbital calculation methods, was used for the calculation of the electronic state of the Li_3N crystal. In this method, Slater's exchange potential was used [12],

$$V_{\mathrm{XC}}(r_\uparrow) = -3\alpha\left[\frac{3}{4\pi}\rho_\uparrow(r)\right]^{1/3} \tag{1}$$

where ρ is the electron density and α a parameter. There are many studies in which $\alpha = 0.7$ is suitable for all elements [13,14]. So we have also adopted this value throughout this work.

The numerical basis functions were used. As a result, H and S matrices were evaluated by the weighted sum of each value on the sample points distributed in the three-dimensional space.

$$S_{ij} = \sum_k \omega(r_k)\phi_i^*(r_k)\phi_i(r_k) \tag{2}$$

$$H_{ij} = \sum_k \omega(r_k)\phi_i^*(r_k)h(r_k)\phi_i(r_k) \tag{3}$$

where ϕ_i are the basis functions, h the Hamiltonian, and ω the weight of each sample point.

We have obtained the bond overlap population (BOP) and net charge of the ions by the Mulliken population analysis in order to discuss the bonding state of the Li and N ions.

Several model clusters were constructed by the crystal structure of the Li_3N crystal [8]. This crystal is assigned to the space group of P6/mmm, and the lattice constants *a* and *c* are 3.65 and 3.88 Å, respectively. The schematic diagrams of the model clusters are shown in Figure 20.1. The Li_3N crystal has a layered structure of two kinds of planes: Li_2N and Li planes. On the Li_2N plane, Li and N ions form hexagons. On the Li plane, only Li ions that are bonding to N ions on the Li_2N plane exist and bridge between the two Li_2N planes. The conduction path of the

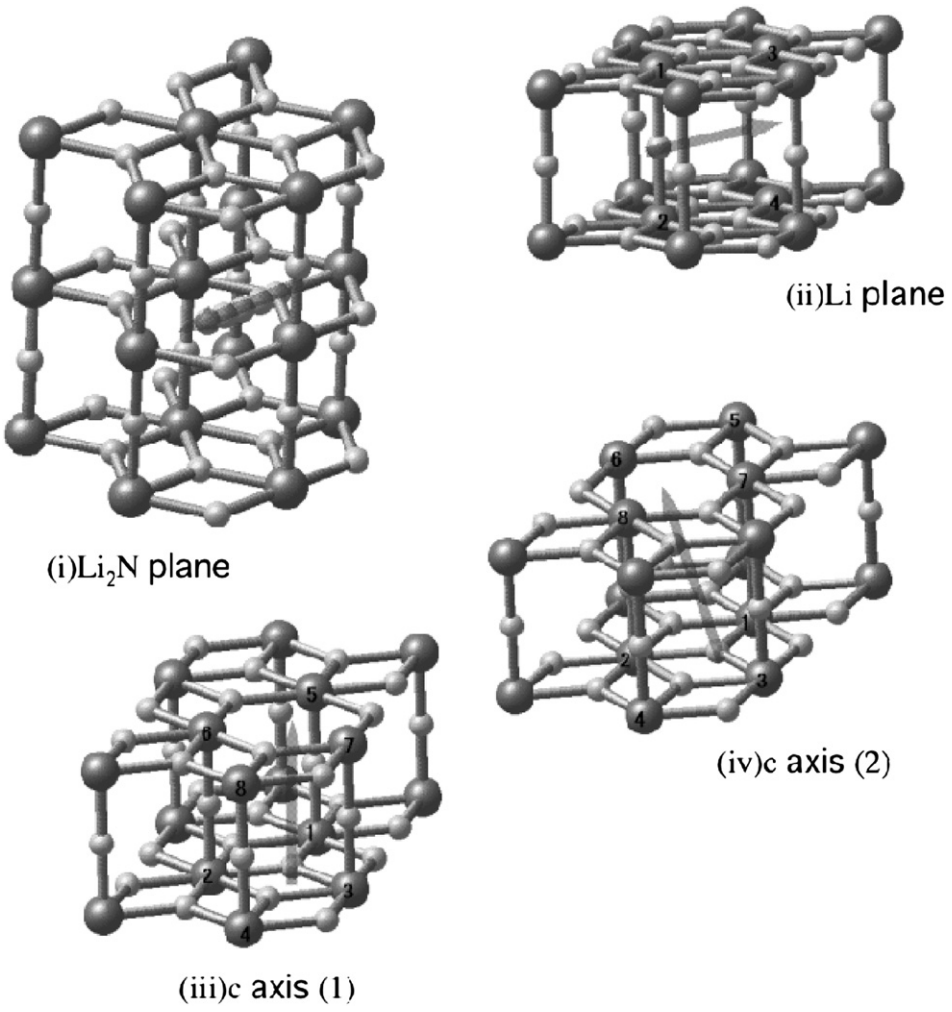

Figure 20.1 Schematic diagram of the Li_3N model clusters. For a colour version of this figure please see the colour plate section near the end of the book.

Li ions reported by several experimental studies is included in the Li_2N plane. Figure 20.1(i) shows a model cluster for the conduction path in Li_2N plane. In this model, one Li ion was removed from the Li_2N plane so that the neighboring Li ion can move to a vacant position. The movement of the Li ion was simulated by using several model clusters with different positions of the Li ion along the estimated conduction path, since it is fundamentally very difficult to manipulate the movement of the atoms and ions in the molecular orbital calculations. This method was already reported and was really very useful for the simulations of the movement of the Ag ions in the α-AgI crystal [4]. Figure 20.1(ii) shows the model cluster for the movement of the Li ions on the Li plane. In this model cluster one Li ion was moved to the neighboring vacancy of Li site. This path is not a suitable path for the Li ion in the Li_3N crystal reported by several experimental studies.

So we have used model clusters of the movement of the Li ion toward the *c*-axis as shown in Figure 20.1(iii) and (iv) for the comparison of the movement toward the different directions. Since several possibilities of the conduction path exist toward the *c*-axis, we have adopted two possible paths for the model clusters.

2.2 Results and discussion

Figure 20.2 shows net charge of the moving Li ions in clusters (i)–(iv). In this figure, the abscissa shows the relative position of the moving Li ion. Since the lengths of the conduction path in clusters (i)–(iv) are different, the value zero means the initial position and 1 means the final position of the moving Li ion so that the position of the moving lithium ion in each path was normalized.

In cluster (i), shown as closed circles, the net charge is 0.41 at initial position. It changes little with the movement of the Li ion and becomes 0.43 at the final position. The charge of the Li ion is almost the same and no obvious changes were observed in cluster (ii), as shown by closed squares. In case of α-AgI, the net charge of the moving Ag ion was changed and had a maximum at the middle position of the conduction path, called a saddle point. In the Li_3N crystal, however, there is no obvious change of the net charge of the Li ion during the movement. In the cases of clusters (iii) and (iv), shown as closed triangles and diamonds, respectively, the net charge of the Li ion at initial position is 0.28, which is clearly smaller than those in clusters (i) and (ii). The net charge of the Li ion was increased at $x = 0.25$ and was almost constant until $x = 0.75$. At the final position, the net charge again becomes smaller. This might be caused by the structures of the model clusters. In clusters (iii) and (iv), the initial and final positions are located on the surface of the model clusters. Though the surface atoms usually have larger electron density than the inner atoms, the net charges of the Li ions became smaller at the initial and the final positions in clusters (iii) and (iv). There were some difficulties in the calculation of conduction path along the *c*-axis because the cluster size became twice as large as clusters (i) and (ii) if all the Li ions around the conduction path through the *c*-axis were located inside of the model clusters. However, the net charge at the positions inside

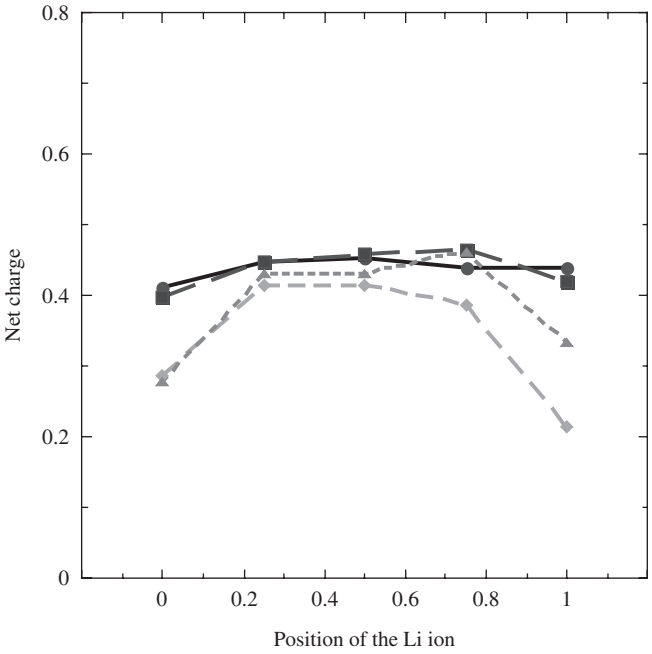

Figure 20.2 The relationship between the net charge and the position of the moving Li ion in the model clusters (i)–(iv). ●, cluster (i); ■, cluster (ii); ▲, cluster (iii); ◆, cluster (iv).

the clusters, from $x = 0.25$ to 0.75, shows similar values as those observed in clusters (i) and (ii).

Thus, the net charges of the moving Li ions in the different paths are very similar to each other, and we can conclude that there is no obvious change of the ionic interaction of the moving Li ion in the experimentally reported conduction path compared with other imaginary non-conduction paths.

Figure 20.3 shows the total bond overlap populations (TBOP) of the moving Li ion in the model clusters shown in Figure 20.1. The TBOP means the summation of all the BOPs between the moving Li ion and the surrounding ions, which shows the covalency of the bonding state of the moving Li ions.

In cluster (i), which is the model of the Li_2N plane, TBOP is 0.82 at the initial position and decreased slightly with the movement of the Li ion. A minimum exists at $x = 0.5$. The TBOP increased after $x = 0.5$ and becomes 0.79 at the final position. Basically a similar change is observed in the TBOP of the moving Li ion on the Li plane. In this plane the TBOP is 0.80 at the initial position and decreases with the movement of the Li ion. A minimum of TBOP is observed at $x = 0.5$ and finally the TBOP becomes 0.78. At the initial and the final positions the TBOP of the moving Li ion on the Li_2N plane is almost the same as that on the Li plane. However, at the middle position, $x = 0.5$, the TBOP on the Li_2N plane is almost 0.1 larger than that on the Li plane. As a result, the difference between the maximum and the minimum of the TBOP of the Li ion on the Li_2N plane is 0.077,

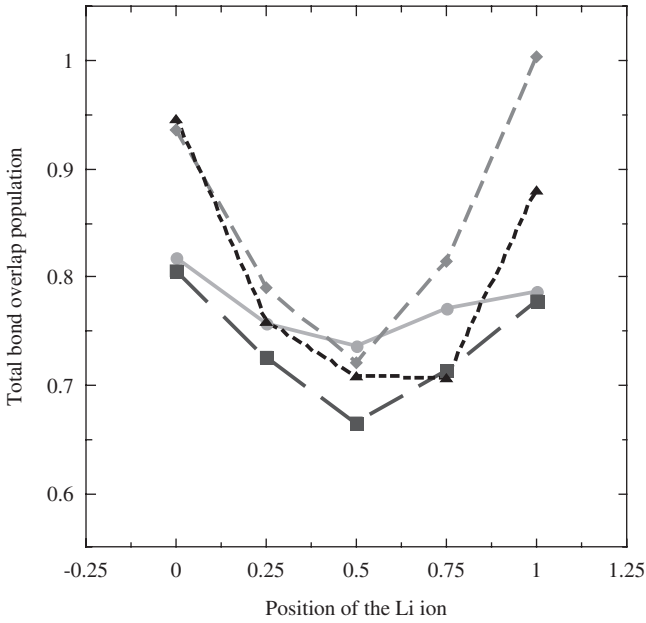

Figure 20.3 The relationship between the total bond overlap population (TBOP) and the position of the moving Li ion in the model clusters (i)–(iv). ●, cluster (i); ■, cluster (ii); ▲, cluster (iii); ◆, cluster (iv).

which is much smaller than that on the Li plane, i.e., 0.13. This small change of the TBOP through the path is a characteristic of the bonding nature of the moving Li ion on the Li_2N plane.

In the case of the movement of the Li ion toward the *c*-axis, another change was observed. In model cluster (iii) for the *c*-axis movement, the TBOP of the moving Li ion is 0.95 at the initial position. The TBOP of the moving Li ion decreases largely with the movement and becomes minimum, 0.72, at $x = 0.5$. The change of the TBOP with the movement of the Li ion through the path toward the *c*-axis is about 0.2, which is much larger than those in clusters (i) and (ii). The same tendency was observed in cluster (iv). The initial TBOP of the Li ion is 0.94 and the minimum is 0.70 at $x = 0.75$. The difference between the maximum and minimum is 0.35. In clusters (iii) and (iv), the initial and final positions of the moving Li ion are located on the surface of the clusters, since the cluster size becomes too large to calculate the electronic state of the Li ions if we take the extended model clusters for the *c*-axis movement of the Li ions. In general, the surface ions have relatively large interaction with the surrounding ions. This ''surface effect'' is the reason for the large change of the covalency in these model clusters. However, since the net charge of the moving Li ion is almost the same as those on the Li and Li_2N planes in the positions in the range from $x = 0.25$ to $x = 0.75$ as shown in Figure 20.2, the result suggests that surface effect of the bonding state of the moving Li ion could be neglected in these positions.

In the case of Li_3N crystal, the TBOP of the Li ion on the Li_2N plane changed less than those in other paths. This result suggests that the smaller change of the TBOP of the moving Li ion should play a very important role in the fast movement of the Li ion in the Li_3N crystal. To discuss this smaller change, the details of BOP of the moving Li ions are shown in Figures 20.4 and 20.5. Figure 20.4 shows the sum of the BOP between the moving Li and the surrounding N ions. On the Li_2N plane, for cluster (i), the BOP of Li–N is 0.64 at initial position and decreases with the movement of the Li ion. However, the change is very small and difference between the maximum and minimum is only 0.05. Contrary to this, the BOP changes largely on the Li plane for cluster (ii). In this case the initial value is 0.60 and decreases with the movement of the Li ion. The BOP has the minimum of 0.39, at $x = 0.5$. The difference is 0.21, which is considerably larger than that on the Li_2N plane. The similar results were obtained in the *c*-axis models of clusters (iii) and (iv). The BOP is 0.72 at the initial position and decreases largely with the movement of the Li ion. The minimum is observed at $x = 0.5$, where the value is 0.35 for cluster (iii) and 0.37 for cluster (iv). The changes in cluster (iii) and (iv) are more than 0.4. Especially in the positions from $x = 0.25$ to $x = 0.75$, which are inside the clusters, the change in BOP was still larger than that in cluster (i).

Figure 20.5 shows another component of BOP of the moving Li ion, Li–Li interaction. On the Li_2N plane, for cluster (i), the BOP of Li–Li is 0.19 at the initial position and decreases little with the movement of the Li ion. The BOP of the

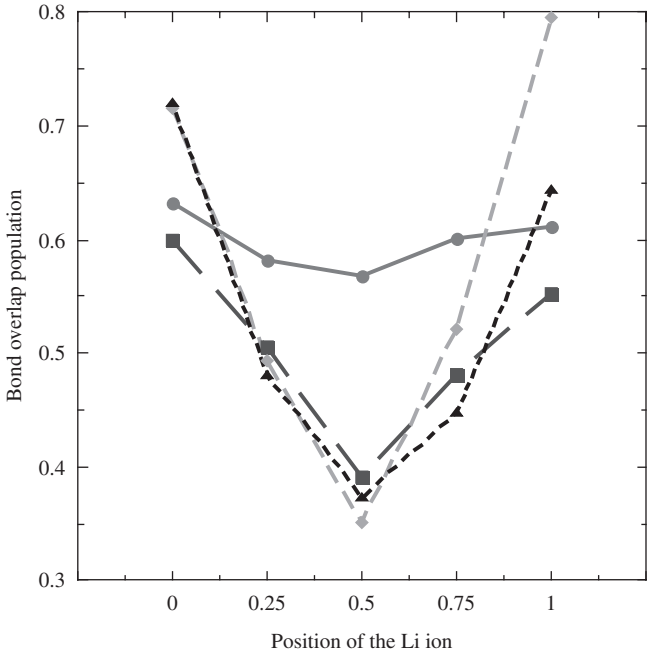

Figure 20.4 The position dependence of bond overlap population between the moving Li and the neighboring N ions. ●, cluster (i); ■, cluster (ii); ▲, cluster (iii); ◆, cluster (iv).

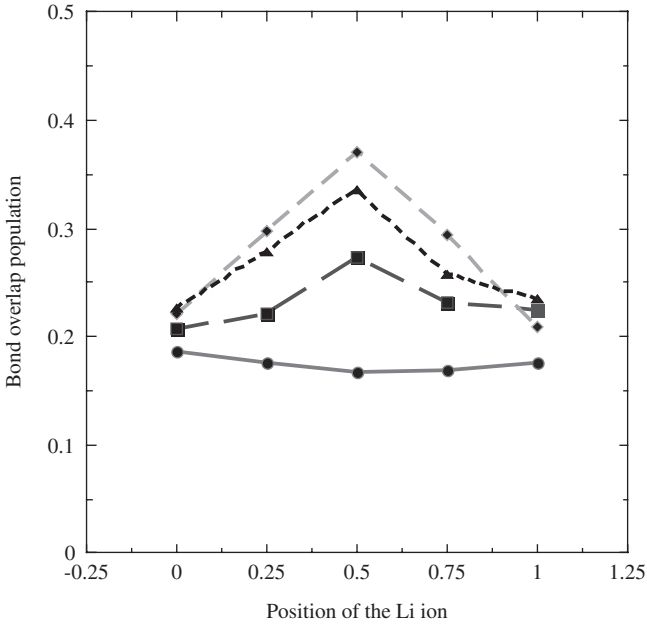

Figure 20.5 The position dependence of bond overlap population between the moving Li and the neighboring Li ions. ●, cluster (i); ■, cluster (ii); ▲, cluster (iii); ◆, cluster (iv).

moving Li ion is almost constant through the path. This "constant BOP" of the moving Li ion is the characteristic of the bonding state of the Li ion on the Li_2N plane. On the Li plane, for cluster (ii), the initial value of the BOP of the Li ion is 0.21, which is almost the same as that in the Li_2N plane. However, the BOP increases with the movement of the Li ion and has a maximum 0.27 at $x = 0.5$. In clusters (iii) and (iv), for the models of the movement along the *c*-axis, similar changes of the BOP of Li–Li were observed. That is, at the initial position the BOP is 0.22 and increases with the movement of the Li ion. There is a maximum at $x = 0.5$, and the value is 0.33 for cluster (iii) and 0.37 for cluster (iv), which are larger than that on the Li plane.

We have previously reported that the moving Ag ion in AgI-based superionic conducting materials had very small change of the covalent bonding with surrounding ions through the path. This small change depends on the covalent bonding between the moving Ag ion and the neighboring Ag ions, that is, Ag–Ag covalent interaction. Such cation–cation covalent interaction was the characteristic of the bonding nature of the mobile Ag ion. On the contrary, there are no obvious Li–Li covalent interactions of the moving Li ions in the conduction path on Li_2N plane, though the Li ions on other non-conduction paths have relatively larger Li–Li interactions. In the case of Li_3N the moving Li ion on the Li_2N plane has very small change of the covalent bonding of both Li–N and Li–Li through the movement along the path. This might be one of the origins of the fast movement of the Li ion in the Li_3N crystal.

3. SULFIDE-BASED Li ION CONDUCTING GLASSES

3.1 Model clusters

As described in the previous section, the smaller change of the TBOP of Li ion with the movement through the conduction path was observed in the Li_3N crystal. In this section, we have tried to estimate the relationship between the ionic conductivity and chemical bonding of the moving Li ions in the sulfide-based superionic conducting glasses.

In order to calculate the electronic state of the Li ion in the sulfide-based superionic conducting glasses, there is a hurdle to construct a model cluster, since it is difficult to obtain the detail of the structure around Li ions in the glasses by experimental methods. The coordination number of sulfide ions to the Li ion and the distances between the Li ion and the first neighboring ions were reported for several kinds of sulfide glasses [15–17]. Based on these studies, we have adapted tetrahedral structure and estimated the bond length from the ionic radius of each ion reported by Shannon [18], to calculate electronic state near Li ions. Figure 20.6 shows a schematic diagram of the model cluster to calculate the electronic state around the Li ion in the present work. In this model, a lithium ion is located in the center and is coordinated by four sulfide ions. Each sulfide ion is included in an SiS_4 unit, which has regular tetrahedron structure. The outside of the sulfide ions of SiS_4 units is terminated by lithium ions. The distances of Si–S, Li–S, P–S, and Al–S are 2.10, 2.43, 2.01, and 2.23 Å, respectively. Near the center of the tetrahedral unit, three lithium ions are located outside to keep the cluster neutral. The movement of the center Li ion was simulated by five clusters with different position of the ion. The SiS_2 content was changed with the exchange of Si in SiS_4 units with other elements, such as Al and P. In this case, the neutrality of the model clusters was adjusted by the number of the outside Li ions so that the contents of Al and P in the clusters could become 25, 50, 75, and 100 mol% in the present work. To compare the theoretical results with the experimental ones,

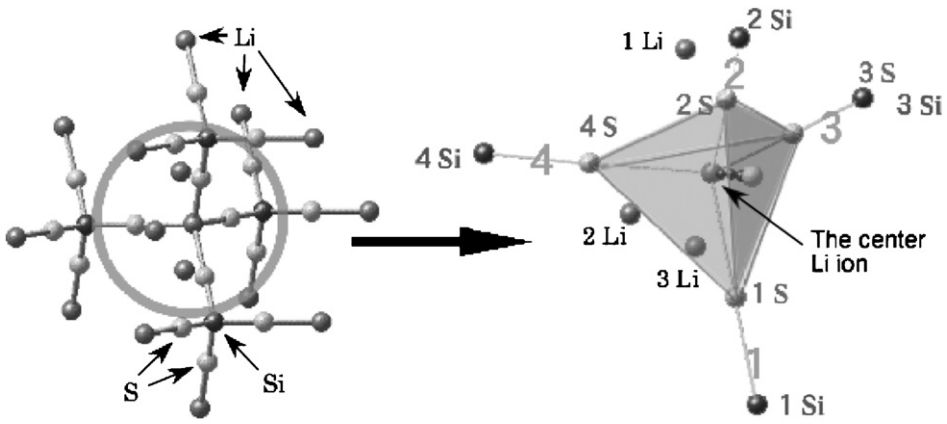

Figure 20.6 Schematic diagram of the $Li_{16}Si_4S_{16}$ model cluster. For a colour version of this figure please see the colour plate section near the end of the book.

the BOP of the composition corresponding to the experimental samples was obtained by interpolation of the results of these four compositions.

As previously reported, the covalency of bonding nature between the moving cations and surrounding ions were very important to realize the fast movement of the ions. We investigated the TBOP to estimate total of covalent interactions of moving cations, and it was suggested that the cations, which could move easily, had small change of the TBOP with the movement. In the present work we would like to introduce differential total bond overlap population (DBOP), to evaluate the relationship between the covalent interaction and the fast movement of the moving Li ions. DBOP is obtained by subtracting the minimum from the maximum of the TBOP with the movement of the lithium ion through the path. In this study the electronic state of the moving lithium ions was calculated in the systems Li_2S–SiS_2–Al_2S_3 and Li_2S–SiS_2–P_2S_5 to compare with the ionic conductivity.

3.2 Results and discussion

The composition dependences of the DBOP and the ionic conductivity at 25°C in the system Li_2S–SiS_2–Al_2S_3 are shown in Figure 20.7. In this figure, closed diamonds show the results of ionic conductivity reported in Ref. [19] and closed rectangles show DBOP in $60Li_2S \cdot 0.4(xAlS_{1.5}(100–x)SiS_2)$ glasses. The ionic conductivity is decreased with the increase of the compositional parameter x up to $x = 50$ and then gradually decreased with further increase of x. On the other hand, the DBOP shows opposite tendency with the Al_2S_3 content. The DBOP at $x = 0$ is 0.017 and shows increasing tendency with the Al_2S_3 content

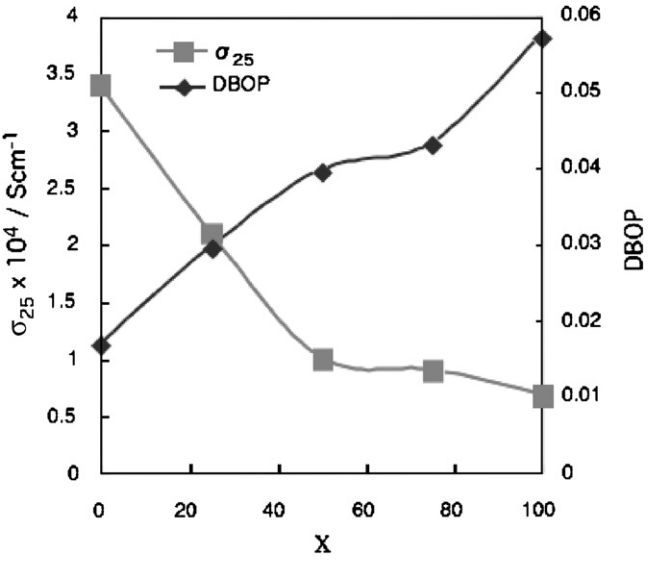

Figure 20.7 The composition dependence of ionic conductivity and DBOP in the $60Li_2S \cdot 0.4(xAlS_{1.5}(100–x)SiS_2)$ glasses.

to 0.057 at $x = 100$. As mentioned above, the faster movable cations in the superionic conducting glasses showed smaller DBOP with the movement. In this system, the DBOP becomes smaller at the composition with the higher ionic conductivity. Furthermore, there seems to be a correlation between the ionic conductivity and the DBOP.

Figure 20.8 shows the composition dependences of the activation energy for conduction and the DBOP. In this system, activation energy is increased with the Al_2S_3 content, corresponding to the decrease of the ionic conductivity. The DBOP is also increased with x and might be found to correlate with activation energy. Then, we have estimated correlations of the DBOP with the ionic conductivity and the activation energy. The ionic conductivity at 25°C and the activation energy for conduction in $60Li_2S \cdot 0.4(xAlS_{1.5}(100–x)SiS_2)$, as a function of the DBOP, are shown in Figure 20.9. It is noteworthy that the ionic conductivity decreases and the activation energy increases linearly with the increase of DBOP. The evaluated correlation coefficient between the ionic conductivity and DBOP is −0.91 and that between the activation energy and DBOP is 0.90. This result suggests that the DBOP significantly has a good positive correlation with the activation energy and a good negative correlation with the ionic conductivity in this system. This is very interesting because the model clusters for this calculation were constructed without any strict structural information obtained by experimental measurements. Furthermore, these good correlations of DBOP support quantitative relations between DBOP and ionic conductivity.

The results of the DBOP analysis in the system $Li_2S–P_2S_5–SiS_2$ are shown in Figure 20.10. This figure shows the composition dependence of DBOP and ionic

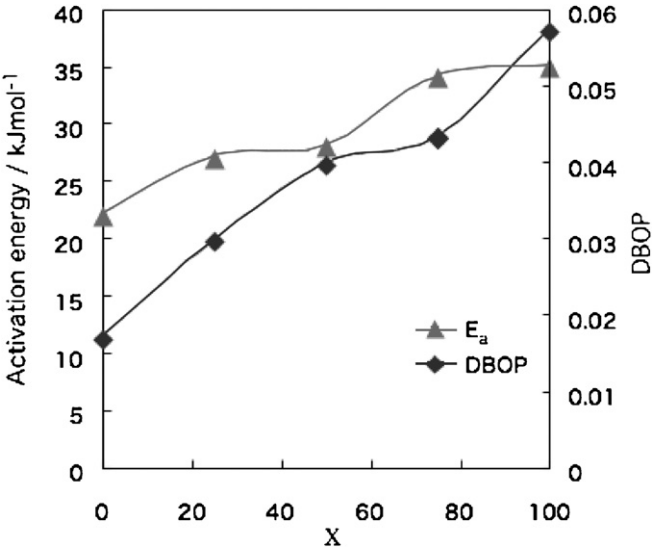

Figure 20.8 The composition dependence of the Ea of the ionic conductivity and DBOP in the $60Li_2S \cdot 0.4(xAlS_{1.5}(100–x)SiS_2)$ glasses.

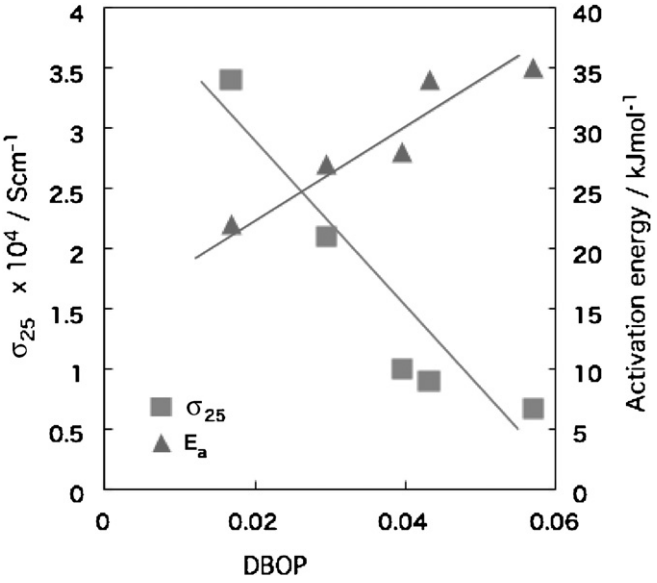

Figure 20.9 The relationship between the ionic conductivity, Ea and DBOP in the $60Li_2S \cdot 0.4(xAlS_{1.5}(100-x)SiS_2)$ glasses.

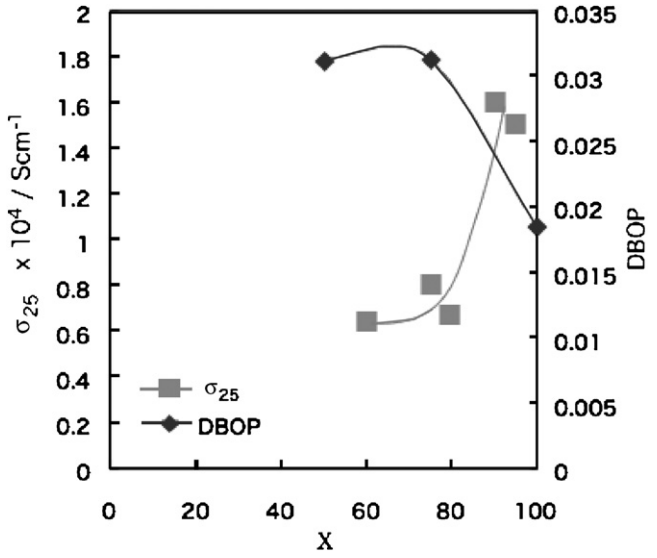

Figure 20.10 The composition dependence of ionic conductivity and DBOP in the $75Li_2S \cdot 0.25(xPS_{2.5}(100-x)SiS_2)$ glasses.

conductivity at 25°C in $75Li_2S \cdot 0.25(xPS_{2.5}(100–x)SiS_2)$ glass [20]. In this system, the ionic conductivity is $0.64 \times 10^{-4}\,S\,cm^{-1}$ at $x = 60$ and increases with the increase of the P_2S_5 content. The conductivity becomes $1.60 \times 10^{-4}\,S\,cm^{-1}$ at $x = 75$. Contrary to this, DBOP of the moving Li ion is 0.031 at $x = 50$ and

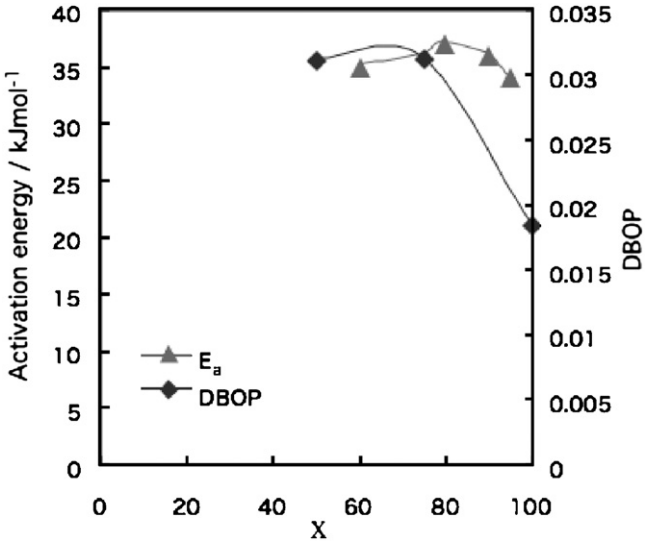

Figure 20.11 The composition dependence of the Ea of the ionic conductivity and DBOP in the $75Li_2S \cdot 0.25(xPS_{2.5}(100-x)SiS_2)$ glasses.

decreases with the P_2S_5 content. The composition dependence of the activation energy for conduction in this system is shown in Figure 20.11. The activation energy is 35.0 kJ mol^{-1} at $x = 60$ and is almost flat up to $x = 80$. Further increase in x results in a decrease in the activation energy. This change is corresponding to the increase of ionic conductivity. The DBOP of the Li ion shows similar variation with x, whereas the DBOP decreases in the range of x larger than 75. Since the change of the activation energy and the DBOP are again similar in this system, we have estimated the correlation between the experimental results and the DBOP.

Figure 20.12 shows the DBOP dependence of ionic conductivity at 25°C and activation energy for conduction. In this system the correlation of the DBOP with ionic conductivity and activation energy is very similar in the system $Li_2S-SiS_2-Al_2S_3$, that is to say, a positive correlation of the DBOP with activation energy and a good negative one with ionic conductivity are observed, while the increase of activation energy with the DBOP is smaller than that in the case of the addition of Al_2S_3. The correlation coefficient for the ionic conductivity is −0.92 and that for the activation energy is 0.51. The small correlation coefficient of activation energy would be due to the difference of the composition where the DBOP and the activation energy start to decrease. Nevertheless, there are good correlations of the DBOP with the ionic conductivity and the activation energy in both systems $Li_2S-SiS_2-Al_2S_3$ and $Li_2S-SiS_2-P_2S_5$. This result suggests that the DBOP calculated by the DV-Xα method has a certain relationship with the ionic conductivity and the activation energy in the sulfide-based superionic conducting glasses.

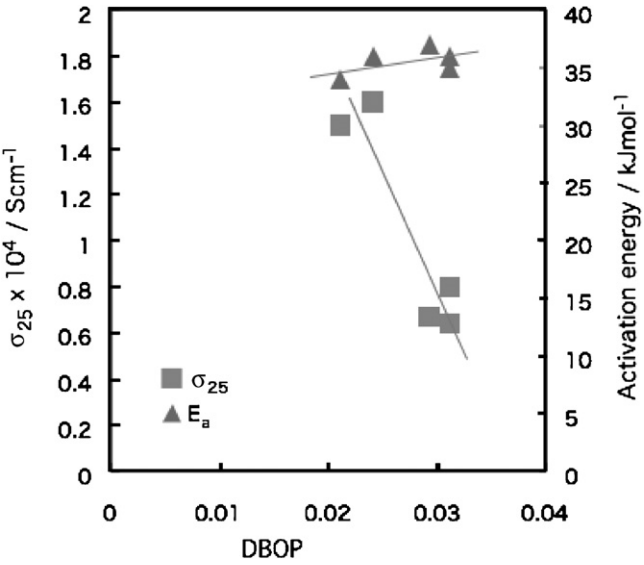

Figure 20.12 The relationship between the ionic conductivity, Ea and DBOP in the $75Li_2S \cdot 0.25(xPS_{2.5}(100-x)SiS_2)$ glasses.

4. CONCLUSION

Electronic states of monovalent ions in superionic conductors such as Li_3N, and sulfide-based superionic conducting glasses in the systems Li_2S–SiS_2–Al_2S_3 and Li_2S–SiS_2–P_2S_5, were calculated by the DV-Xα method. The DBOP was obtained from the model clusters constructed with no strict structural parameters by experimental measurements. The DBOP had good correlations with the ionic conductivity and activation energy in both systems. This result suggests that the covalent interaction of the moving Li ions is very important to understand the fast movement of the Li ions in the sulfide-based superionic conducting glasses. The DBOP estimated by the DV-Xα method could be applied to design a new sulfide-based superionic conducting glass.

REFERENCES

[1] Y. Kowada, H. Adachi, T. Minami, *J. Ceram. Soc. Jpn.* **101** (1993) 1330–1334.
[2] Y. Kowada, H. Adachi, M. Tatsumisago, T. Minami, *J. Non-Cryst. Solids* **232–234** (1998) 497–501.
[3] N. Imanaka, S. Tamura, G. Adachi, Y. Kowada, *Solid State Ionics* **130** (2000) 179–182.
[4] Y. Kowada, Y. Yamada, M. Tatsumisago, T. Minami, H. Adachi, *Solid State Ionics* **136–137** (2000) 393–397.
[5] R. Araki, A. Hayashi, Y. Kowada, M. Tatsumisago, T. Minami, *J. Non-Cryst. Solids* **288(1–3)** (2001) 1–7.
[6] Y. Kowada, M. Okamoto, I. Tanaka, H. Adachi, M. Tatsumisago, T. Minami, *J. Non-Cryst. Solids* **345/346** (2004) 489–493.
[7] J. Wahl, U. Holland, *Solid State Commun.* **27** (1978) 237.
[8] H. Schulz, K.H. Thiemann, *Acta Crystallogr. A* **35** (1979) 309.

[9] Y. Koyama, Y. Yamada, I. Tanaka, S.R. Nishitani, H. Adachi, M. Murayama, R. Kanno, *Mater. Trans.* **43(7)** (2002) 1460–1463.
[10] J. Sarnthein, K. Schwarz, P.E. Bloechl, *Phys. Rev. B: Condens. Matter* **53(14)** (1996) 9084–9091.
[11] H. Adachi, M. Tsukada, C. Satoko, *J. Phys. Soc. Jpn.* **45** (1978) 875.
[12] J.C. Slater, *Quantum Theory of Molecules and Solids*, Vol. 4, McGraw-Hill, New York, 1974.
[13] E.J. Baerends, P. Ros, *Chem. Phys.* **2** (1973) 52.
[14] E.J. Baerends, P. Ros, *Mol. Phys.* **30** (1975) 1735.
[15] C. Estournès, A.P. Owens, M. Ménétrier, A. Levasseur, K.J. Rao, S.R. Elliott, *J. Non-Cryst. Solids* **171** (1994) 80–86.
[16] A. Pradel, G. Taillades, M. Ribes, H. Eckert, *J. Non-Cryst. Solids* **188** (1995) 75–86.
[17] R. Prasada Rao, M. Seshasayee, *J. Non-Cryst. Solids* **352** (2006) 3310–3314.
[18] R.D. Shannon, *Acta Crystallogr. A* **32** (1976) 751.
[19] A. Hayashi, T. Fukuda, H. Morimoto, T. Minami, M. Tatsumisago, *J. Mater. Sci.* **39** (2004) 5125–5127.
[20] A. Hayashi, Y. Ishikawa, S. Hama, T. Minami, M. Tatsumisago, *Electrochem. Solid-State Lett.* **6(3)** (2003) A47–A49.

CHAPTER 21

Architecture of Hydrates and Local Structure of Acetic Acid Aqueous Solution: *Ab Initio* Calculations and Car–Parrinello Molecular Dynamics (CPMD) Simulations on Hydrogen-Bonding Rings, Network, and Intra-Hydrate Protonation in Multi-Hydrates of Acetic Acid Monomer

Liang Pu*, **Qing Wang***, **Yong Zhang*****, **Qiang Miao***, **Yang-soo Kim**** and **Zhibing Zhang***

Contents

* School of Chemistry and Chemical Engineering, Nanjing University, Nanjing 210093, China
Corresponding author. E-mail: cheminfo@nju.edu.cn
** Sunchon Branch, Korea Basic Science Institute, 315 Maegok, Sunchon, Jeonnam 540-742, Korea
*** Chemistry Department, Boston University, Boston, MA 02215, USA

Advances in Quantum Chemistry, Vol. 54
ISSN 0065-3276, DOI 10.1016/S0065-3276(07)00021-4

Abstract

The protonation and deprotonation phenomena and molecular association of solute molecule with water via intermolecular hydrogen bonding forming various hydration compounds are very common in aqueous solution and in biological cell in nature. In the aqueous solution, more complicated type of hydrogen bond, hydrogen-bonding rings, various kinds of hydration compounds (hydrates), and even hydrogen-bonding network can be expected. The nature of hydrogen bonding, the bonds networking, the rule in architecture of larger hydration compounds, deprotonation of acetic acid in solution, stability of the hydrated proton, and the local structure of its aqueous solution are the most fundamental problems to understanding solute molecule living style in aqueous solution.

Hydrogen-bonding rings and network in the multi-hydrates of acetic acid monomer have been investigated by *ab initio* calculations, and *ab initio* molecular dynamics (CPMD) simulations on acetic acid monomer–water system were also performed to explore the local structure of acetic acid aqueous solution. More than hundreds of multi-hydrates have been selected as candidates during our calculations. The structural optimizations and energy calculations have been performed at the MP2/6-31+g (d, p) and MP4/6-31+g (d, p) levels which are adequate for our large hydrates calculations with reliable results and reasonable cost as we stated in the Section 2. The most stable structure of the smallest hydration compound of acetic acid monomer, i.e., acetic acid water dimer, has a four-membered head-on ring with the smallest dipole moment. To verify the existence of it, the infrared spectra experiment data were collected in the dilute CCl_4/HAc and CCl_4/H_2O ratio condition. The hydroxyl (O–H) stretching vibrations in molecules of water, acetic acid, and the dimer are distinguished, for the dissolved species are isolated from each other by surrounded solvent molecules CCl_4. The calculated and measured vibration frequencies are almost lain in line with 0.872 scaling. The four-, five-, and six-membered head-on rings are the most favorable in the small multi-hydrates with a stable planar structure and the side-on ring with a weak hydrogen-bonding interaction of $\mathrm{C-H\cdots O_w-H}$. The six-membered ring is most important in the large multi-hydrates and in the local structure of dilute solution

also verified by our CPMD simulations. A larger ring of or more than seven-membered could no longer maintain the planar structure. Larger multi-hydrates of acetic acid monomer could be constructed from these basic building blocks. The strength order for the five kinds of bonds is in the descending order as $C-O-H\cdots O_w-H > O_w-H\cdots O_w-H > C=O\cdots H-O_w > O_w-H\cdots O_a-H \gg C-H\cdots O_w-H$. The three hydroxyl bonds O–H in the hydrated proton could be divided into two types: one of the hydroxyl bonds is hydrogen bonded to the deprotonated oxygen of the acetic acid, other two to waters in the hydrate. The larger the R_{O-H} becomes, the smaller the $R_{O\cdots H}$ and the stronger the associated hydrogen bond are. The hydrated proton is stable and liberated from the deprotonated acetic acid in the large multi-hydrate with more complicit head-on ring. In small hydrates, the protonating hydrogen is shared partly by the acetic acid.

1. INTRODUCTION

Molecular association of solute molecule with water via intermolecular hydrogen bonding forming various hydration compounds is very common in aqueous solution and in biological cell in nature. Architecture of the hydration compounds is the most fundamental problem to understanding solute molecule living style in aqueous solution. From the hydrogen bonding structural point of view, acetic acid molecule has two strong hydrogen acceptor sites (a hydroxyl oxygen and a carbonyl oxygen), one strong donor site (a hydroxyl hydrogen), and three weak donors of methyl hydrogen. In the vapor phase, pure liquid, and solid state, acetic acid forms simple self-associates (such as centro-symmetric cyclic dimer, side-on dimer, and chain cluster) containing $O-H\cdots O=C$ and $C-H\cdots O=C$ hydrogen bonds. While in the aqueous solution, various kinds of hydration compounds, more complicated type of hydrogen bond, and even hydrogen-bonding network can be expected. Through the study of progressively larger hydration compounds, it opens exciting possibilities for exploration of the local structure of acetic acid aqueous solution.

The pH measurements are widely in use in many basic investigations and detecting, since protonation and deprotonation phenomena are the ubiquity not only in aqueous solution but also in many organic liquids or even in solid states. The suggestion of aqueous solution chemistry in introductory texts gives a very simple picture of hydrolyzation for acetic acid as a popular example and has long been thought to play an essential role. The dominant species during its hydrolyzing are represented as a simplistic hydrated proton H_3O^+ (or alternative form of $H_5O_2^+$) and hydroxyl deprotonated acetic acid CH_3COO^- (Ac^-). However, there is still no clear molecular description for the hydrated proton and for the deprotonated hydrolysate presently.

Some hydration compounds of acetic acid have been reported by various experimental methods. The density measurements for acetic acid and water systems by Kipling [1] reveal the presence of mono-hydrated monomers. Ng and Shurvell [2,3] reported the species of hydrated acetic acid monomers and dimers

on dilute solution by applying factor analysis and band contour resolution techniques to the Raman spectra. Mass spectrometric analysis showed monomer, dimer hydrates [4,5], and even some larger size of aggregate hydrates, up to seven [6]. According to the analysis of UV spectra of acetic acid aqueous solutions, Ruderman et al. [7] suggested that the acetic acid molecule was hydrogen bonded with water molecules at 0.02 and 0.1 M. In concentrated solution, the acetic acid molecule associates with its own [8–10] and close to the neat liquid [8,11,12]. At lower concentrations, monomer hydrates signals were more dominant than dimer hydrates signals [4,5]. In dilute solution, interaction between molecules of acetic acid and water increases competitively [2,3,13]. Recently, the ATR-IR and Raman spectra of CH_3COOD and CD_3COOD in D_2O solution measured by Génin et al. [13] inferred the hydrated monomer is the only species in 0.1–1 M solutions.

Theoretically, very few of mono-hydrated acetic acid monomer compounds [14] and 1:2 and 1:3 HAc–water compounds [15] were reported by computational means for method examination or facilitating the interpretation of the experimental spectra purposes. The most favorable geometry of *syn*-acetic acid shows stronger interaction than that in the *anti*-acetic acid. More recently, the optimized structures and binding energies for acetic acid mono-hydrates and di-hydrates have been reported by DFT (B3LYP) method with three different basis sets [16]. From calculations for six mono-hydrates and di-hydrates, cyclic hydrogen bonding stable structures were found, with binding energies of $-39.941\,kJ\,mol^{-1}$ and $-86.166\,kJ\,mol^{-1}$ in mono- and di-hydrate, respectively. Studies on solvent effects on acetic acid dimers indicated that the formation dimer in strong polar solvent (water) was not favorable due to the very large disturbing effect in solvation [17,18]. The consistent suggestion was also inferred by Chocholoušová et al. [19] combining *ab initio* quantum chemical and molecular dynamics simulations.

Both the experimental and theoretical studies indicate that the interactions between acetic acid and water molecules are more competitive in dilute aqueous solution. However to our knowledge, the specific interactions between acetic acid and water molecules are still not well understood, especially in such as the nature of hydrogen bonding, the bonds networking, the rule in architecture of larger hydration compounds, deprotonation of acetic acid in solution, stability of the hydrated proton, the local structure of its aqueous solution, and so on. In the present work, we have performed *ab initio* calculations on multi-hydrates (rich water hydration compounds) of acetic acid, and *ab initio* Car–Parrinello molecular dynamics (CPMD) [20] simulations on acetic acid monomer and water system (at dilute aqueous solution condition) to find something helpful for interpreting the nature of acetic acid aqueous solution.

2. COMPUTATION DETAILS

Ab initio calculation and *ab initio* molecular dynamics simulation have been the trusted methods in the theoretical study of molecule structure and properties.

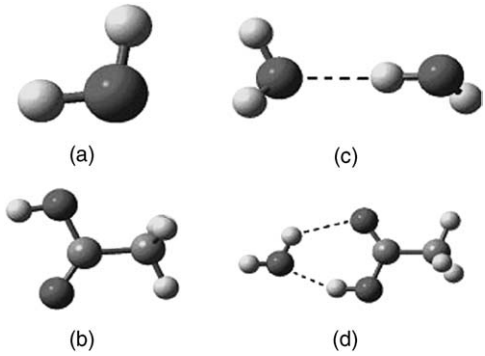

Figure 21.1 Four representative structures: (a) water monomer; (b) acetic acid monomer; (c) water linear dimer; (d) the most stable acetic acid water dimer (see text in Section 3.1).

The Gaussian 98 suite [21] is one of the major quantum chemistry programs and favorably used in the molecular science. Recently, owing to the landmark development of the density functional theory (DFT) in molecular dynamics contributed by Car and Parrinello [20], CPMD has been one of the *ab initio* molecular dynamics method and the most powerful tool used in solid and liquid simulations. In this section, we first focus ourselves on the levels and basis sets of comparison chosen for four small representative systems (denoted as a–d, as shown in Figure 21.1) by using Gaussian 98 before our large hydration compound structural optimization and energy calculations. CPMD simulation details for acetic acid water system simulations are given below.

2.1 *Ab initio* calculations

All the calculations were carried out using the Gaussian 98 suite [21]. Geometry optimizations were performed at MP2 and DFT levels using different basis sets. The basis set superposition error (BSSE) corrections for the association energy were estimated using the counterpoise method [22]. Before the calculation to our large hydration compounds, we first focus on choosing an economic, appropriate, and powerful level of theory to do it, i.e., methods and basis sets selection. For that purpose, water monomer (Figure 21.1(a)), acetic acid monomer (Figure 21.1(b)), water linear dimer (Figure 21.1(c)), and one of acetic acid water dimers (Figure 21.1(d)) were chosen to do pre-calculations for their representative structures. The OH bond length and dipole moment of monomers, as well as the binding energy, were taken as the parameters to assess the quality of prospective method.

The calculation results of the dipole moment, the OH bond length for the monomers, and the BSSE-corrected interaction energy for the dimers are listed in Table 21.1. Available experimental data are also listed for comparison.

We first check the OH bond length and the dipole moment of the water monomer. When d-type basis polarization functions were added to heavy atoms, and further, p-type polarization functions added to hydrogen atoms, both DFT

Table 21.1 Comparison of the energies, dipole moments, and geometrical parameters for monomers and dimers using MP2 and B3LYP with 10 basis sets

Method/basis set	Monomer				Dimer	
	W_{O-H}	A_{O-H}	μ_w	μ_A	ΔE_{WW}	ΔE_{WAt}
B3LYP/6-31g	0.97600	0.98220	2.3763	1.6283	−33.503	−58.579
6-31g (d)	0.96846	0.97570	2.0678	1.5803	−22.797	−49.733
6-31g (d, p)	0.96534	0.97220	2.0162	1.6079	−29.754	−48.360
6-31+g (d, p)	0.96507	0.97244	2.1633	1.7940	−21.853	−44.073
6-311g	0.97062	0.97691	2.4049	1.6568	−30.964	−64.330
6-311g (d, p)	0.96191	0.96877	2.0428	1.6011	−20.003	−45.185
6-311+g (d, p)	0.96209	0.96913	2.1287	1.7440	−21.193	−42.459
6-311+g (2d, p)	0.96310	0.97021	2.0486	1.7595	−20.270	−41.935
6-311++g (3df, 2p)	0.96081	0.96788	1.8744	1.7857	−20.005	−41.544
Aug-cc-PVTZ	0.96183	0.96861	1.8005	1.7894	−19.992	−48.398
MP2/6-31g	0.97495	0.98519	2.4443	1.3448	−28.272	−51.388
6-31g (d)	0.96871	0.97932	2.1743	1.4504	−21.431	−42.279
6-31g (d, p)	0.96141	0.97105	2.1116	1.4515	−32.749	−41.223
6-31+g (d, p)	0.96316	0.97263	2.2075	1.6278	−20.150	−38.700
6-311g	0.96878	0.97885	2.4358	1.3773	−25.725	−45.812
6-311g (d, p)	0.95776	0.96675	2.1006	1.4029	−17.639	−36.629
6-311+g (d, p)	0.95949	0.96802	2.1564	1.5432	−18.740	−35.298
6-311+g (2d, p)	0.96294	0.97197	2.0883	1.6031	−19.464	−39.432
6-311++g (3df, 2p)	0.95905	0.96772	1.9003	1.6627	−19.451	−41.431
Aug-cc-PVTZ	0.96137	0.96986	1.8136	1.6688	−19.869	−43.271
Exp.	0.9572[a]	0.97[c]	1.855[d]	1.70[d]		
	0.9572[b]					

Note: Bond length O–H are in Å, the interaction energies ΔE are in kJ mol^{-1}, dipole moments μ are in debye. W represents the water and A the acetic acid.
[a]From Ref. [25].
[b]From Ref. [27].
[c]From Ref. [26].
[d]From Ref. [28].

(B3LYP) and MP2 methods gave good descriptions on the OH bond length (with values of 0.960 ± 0.003 and 0.97 ± 0.01 for water). However, adding further polarization functions does not result in obviously improved results. As for the dipole moment, calculations at large basis sets (6-311++g (3df, 2p), Aug-cc-PVTZ) gave accurate results (less than 4.5%). The others all overestimated the experimental dipole moment of water by more than 10%. While for acetic acid, B3LYP/6-311+g (d, p) gave the best estimate. Results at 6-31+g (d, p) level were similar with that at 6-311++g (3df, 2p) and Aug-cc-PVTZ. Considering the cost of calculations, it is clear that using the largest basis set for the geometry optimization is too expensive for achieving the limiting value for the dipole moment. From this point of view, the basis set 6-31+g (d, p) is adequate for our later calculations.

Next we check the interaction energy of the water dimer. The experimental binding enthalpy of the water dimer has been reported as $15.1 \pm 2.1\,\mathrm{kJ\,mol^{-1}}$ [23]. Del Bene [24] has back-calculated an "experimental" electronic binding energy of $23.0 \pm 2.1\,\mathrm{kJ\,mol^{-1}}$ using the experimental data and *ab initio* calculations. The computational estimates are available, ranging from 20.5 to $22.2\,\mathrm{kJ\,mol^{-1}}$, fall within the experimental error bars [14]. Our calculations at 6-311++g (3df, 2p) and Aug-cc-PVTZ levels are in good agreement with the experiments and previous results of calculations [25–27]. Agreement with the best levels of theory was deemed the appropriate measure of suitability. That is why the results at 6-311++g (3df, 2p) and Aug-cc-PVTZ were adopted as the criteria for energy comparison.

Let us get back to the energy investigation. The results without polarization or diffuse functions are very poor. They all overestimate the interaction energy by more than $4.2\,\mathrm{kJ\,mol^{-1}}$. This also suggests that the polarization and diffuse functions should be involved in computing process so as to get reliable results. Both DFT (B3LYP) and MP2 methods at 6-31+g (d, p) level give good descriptions on the interaction energy of dimers. Since dispersion interactions are not accounted for in DFT, one should expect that DFT binding energy should always be less than the MP2 binding energy. Therefore, we carry out our later calculations on this chosen level, MP2/6-31+g (d, p), which produces reliable results with reasonable cost.

2.2 Modeling

In the present paper, structures are grouped and named as 1A*m*W-*n*. In which, *m* for the number of water molecules, $n = 1, 2, 3, \ldots$, for different structures, A and W for the abbreviations of acetic acid and water, respectively. In each group, more or less 10 structures have been optimized and only some relatively stabler ones will be presented. Calculations were first carried out on some simple structures constructed by referring to previous report [14]. And then larger and more complex ones were built upon step by step.

All the structures were first optimized at the MP2/6-31+g (d, p) level and improved energy were recalculated at the MP4/6-31+g (d, p) level except for some large hydrates. BSSE, which is corrected by the most common counterpoise method [22], was employed in the present work for the interaction energy calculations.

2.3 CPMD calculations details

The *ab initio* molecular simulation was carried out in the NPT ensemble with version 3.9.1 of CPMD [29]. In the calculation, 20 water and one acetic acid molecules were simulated in a periodic cubic cell under an ambient condition of a constant pressure 1 bar, a constant temperature 300 K, and density of $1.0\,\mathrm{g\,cm^{-3}}$. The starting structure was constructed in a simple flexible cubic cell with a length of 8.8794 Å, by randomly adding 11 water molecules to an optimized hydration compound composed of a single acetic acid molecule and 9 water molecules.

The Kohn–Sham orbitals were expanded in a plane wave basis set up to an energy cutoff of 70 Ry. A fictious mass of 1,100 a.u. was used in the thermostating equation of motion. A time step of 7 a.u. (0.169 fs) was used in the simulation. The trajectory data were collected every 10 steps during in the 16.9 ps production runs after its 1.69 ps initialization with an NPT ensemble.

The gradient-corrected Becke, Lee, Yang, and Parr (BLYP) [30,31] exchange correlation functional has been shown to give a good description of aqueous systems [32–34]; it was employed in our present simulation.

At post-processing, three radial distribution functions (RDFs), $g_{O(carbonyl)-H}(r)$, $g_{O(hydroxyl)-H}(r)$, and $g_{H(hydroxyl)-O}(r)$; three angle averages, $(C=)O\cdots H-O_w$, $(C-)O(H)\cdots H-O_w$, and $(C-)O-H\cdots O_w$; and one ring size (n-member of heavy atoms) averages were derived from the collected trajectories. In the present work, the upper limit of the distance of hydrogen bonding is defined as 2.30 Å from the three RDFs. This limit was also employed during the angle and ring average processing. A hydrogen bond angle was obtained from three distances of three atoms involved. And the hydrogen-bonding ring size was picked up and counted from hydrogen-bonding networks of the trajectories.

3. ACETIC ACID WATER DIMER ($HAc \cdot H_2O$)

A reasonable way of architecture hydration compound is constructing progressively larger hydrates from the simplest and the smallest. The acetic acid water dimer ($HAc \cdot H_2O$) is our starting point for structural understanding of hydration compound. In this section, we first discuss the hydrogen bonding and the lowest-energy configuration in the acetic acid water dimer candidates, and then the hydroxyl stretching vibration frequency compared with our infrared experimental spectra for the stable configuration.

3.1 Hydrogen bonding and low-energy configuration

3.1.1 Structural characters of hydrogen bonding

More than 10 acetic acid water dimer structures have been chosen as the candidates and been optimized at the MP2/6-31+g (d, p) level. The four most stable structures are selected as shown in Figure 21.2. The four acetic acid water dimer candidates are head-on cyclic ring structure 1A1W-1, side-on 1A1W-2 and 1A1W-3, and linear structure 1A1W-4. Both kinds of hydrogen bonding in the head-on 1A1W-1 are very strong. The oxygen at the carbonyl C=O of acetic acid molecule is a strong hydrogen acceptor and the H–O_w at water is a strong hydrogen donor in the hydrogen bonding $C=O\cdots H-O_w$. Another hydrogen bonding $H-O_w\cdots H-O-C$ exists between the hydrogen donor of hydroxyl of acetic acid and acceptor of the water oxygen. The four heavy atoms, one carbon, two oxygen atoms from acetic acid, and one oxygen atom from water, connected by the two hydrogen bonds in a ring upon the carboxylic head of acetic acid. The side-on structure 1A1W-2 has one strong and one weak hydrogen bond. The strong bonding of $C=O\cdots H-O_w$ is similar with that in the 1A1W-1 except for

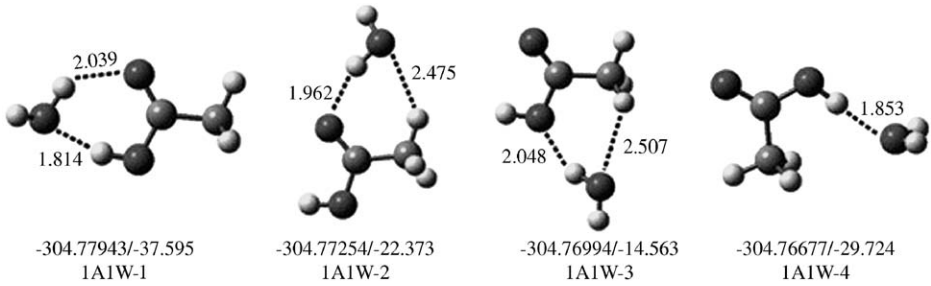

Figure 21.2 Four optimized candidates of acetic acid water dimer, denoted as 1A1W-*n*, 1A and 1W stand for one acetic acid and one water, respectively, *n* from 1 to 4 denotes for different structures. The distance O···H of hydrogen bond is shown on its side. The total energy (in Hartree)/interaction energy (in kJ mol^{-1}) is listed below the corresponding candidate.

the binding direction. In the weak bonding $H-O_w\cdots H-C$, the methyl is the hydrogen donor. Its binding energy is about one-fourth of strong hydrogen bonding. Similar with 1A1W-2, 1A1W-3 consists of four-membered hydrogen-bonding ring by one strong and one weak hydrogen bond. The strong hydrogen bonding $O_w-H\cdots O_a-H$ is different from that in the side-on 1A1W-2. The weak binding energy is also about one-fourth of strong hydrogen bonding (see text in Section 7). The simply linear structure 1A1W-4 has one strong hydrogen bonding $H-O_w\cdots H-O-C$, similar with that in the 1A1W-1. However, the binding is on the opposite direction and of a different trans-conformation.

3.1.2 Total energy and interaction energy

All the structural optimizations and energy calculations for the four candidates were performed at the MP2/6-31+g (d, p) and the MP4/6-31+g (d, p) level, respectively. Our calculation results of total energies and interaction energies for these acetic acid water dimers are similar to those reported by Gao [16]. From total energies, the relative stability of the four structures is in the order of 1A1W-1 > 1A1W-2 (18.077 kJ mol^{-1}) > 1A1W-3 (24.909 kJ mol^{-1}) > 1A1W-4 (33.227 kJ mol^{-1}), and evidently, 1A1W-1 is most stable in all. The interaction energies (ΔE) follow the trend as 1A1W-1 (-37.595 kJ mol^{-1}) > 1A1W-4 (-29.724 kJ mol^{-1}) > 1A1W-2(-22.373 kJ mol^{-1}) > 1A1W-3 (-14.563 kJ mol^{-1}). The four-membered hydrogen bonding connected by two strong hydrogen bonds $C=O\cdots H-O_w$ and $C-O-H\cdots O_w-H$ makes 1A1W-1 as the most favorable one.

3.1.3 Hydrogen bond length $R_{H\cdots O}$ and its strength

There are three kinds of strong hydrogen bonds in the four dimers as we have stated above. Among them, the distance $R_{H\cdots O}$ in the very strong bond $C-O-H\cdots O_w-H$ between the hydrogen of hydroxyl in carboxyl and the oxygen from water in 1A1W-1 and 1A1W-4 are 1.814 and 1.853 Å, respectively. The $R_{H\cdots O}$ in the hydrogen bonding $C=O\cdots H-O_w$ between the oxygen of carbonyl and hydrogen from water in 1A1W-1 and 1A1W-2 are 2.039 and 1.962 Å.

While in 1A1W-3, $R_{H\cdots O}$ in the $O_w-H\cdots O_a-H$ is 2.048 Å. Clearly, the strength of three kinds of strong hydrogen bonding has the order of $C-O-H\cdots O_w-H > C=O\cdots H-O_w > O_w-H\cdots O_a-H$. The distance of weak bonds of $H-O_w\cdots H-C$ is about 2.5 Å (2.475 Å in 1A1W-2 and 2.507 Å in 1A1W-3).

3.2 Hydroxyl (O–H) stretching vibration frequency calculations compared with infrared spectra

For verifying the existence of 1A1W-1, the most stable acetic acid water dimer we obtained in the above section, the infrared spectra experiment data were collected. The hydroxyl (O–H) stretching vibrations in molecules of water, acetic acid, and its hydration compounds can be affected (red shift in general) by the associated hydrogen bonds. The broadened infrared bands of acetic acid aqueous solution are due to the various hydration compounds involved and their complexity of hydrogen-bonding networks. Therefore, if acetic acid hydration compounds are complex enough and reveal bulk solution behavior, the O–H stretching vibrations will not be identified clearly one by one. In the present study, liquid carbon tetrachloride (CCl_4), a non-polar solvent, is used to extract the small dipole aggregate, the smallest hydration compound of acetic acid monomer, from acetic acid aqueous solution. At dilute CCl_4/HAc and CCl_4/H_2O ratios, the dissolved acetic acid monomer and its smallest hydration compound are isolated from each other by surrounded solvent molecules CCl_4, so that their characteristic O–H vibrations can be distinguished.

We first check the influence of water on the infrared spectrum of $HAc\cdot H_2O$–CCl_4 solution. In the absorption spectrum of CCl_4 with water (reference sample), the two free water modes ν_a and ν_s are located at 3,709 and 3,618 cm^{-1} respectively, and are in agreement with Bulmer [35]. In the lower panel (a) of Figure 21.3 we have shown the spectrum of $HAc\cdot H_2O$ in CCl_4 (solid line) and compared with that of reference sample (dotted line) in the whole measured region. The band shape of the reference is well suited to absorption background of the $HAc\cdot H_2O$ spectrum for correction at the present experimental condition.

The difference spectrum of the $HAc\cdot H_2O$ sample and the reference is given in Figure 21.3(b), where two free water modes have vanished. Except for O–H stretching region on the high-frequency side near 3,500 cm^{-1}, the main structure in the 2,000–3,750 cm^{-1} region is in good agreement with that of HAc/CCl_4 solution measured by Seifert et al. [36]. The feature at 3,537 cm^{-1} in the inset of Figure 21.3(c) (labeled 2) is assigned to the O–H stretching vibration of acetic acid monomer [36]. The most striking features in the difference spectrum, which are noticeably absent from the water-free acetic acid spectrum [36], are the two additional bands 3,675 and 3,460 cm^{-1} shown in the Figure 21.3(c) (labeled 1 and 3). The hydrogen bond in the acetic acid water dimer causes the red shift of water O–H stretching vibration. The band 3,675 cm^{-1} between the O–H stretching of acetic acid monomer 3,537 cm^{-1} and free water 3,709 cm^{-1} is uniquely assigned to ν_a of bounded water. The another bounded water O–H mode ν_s 3,460 cm^{-1} is on the red side of the bounded symmetrical O–H stretching of water dimer 3,573.6 cm^{-1} [37] (in Ar matrix cooled at 25 K, with Ar/H_2O ratio

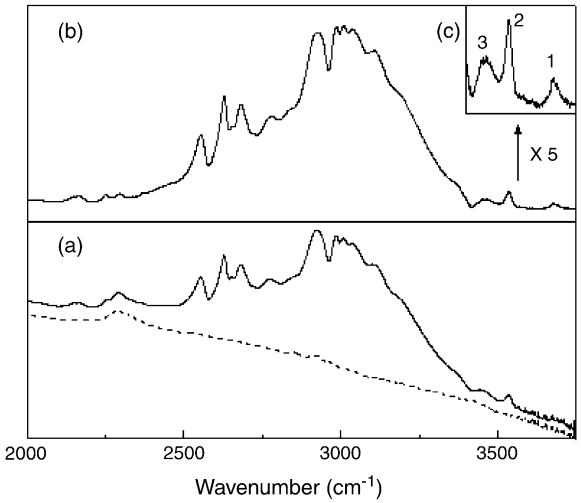

Figure 21.3 IR spectra of (a) acetic acid with saturated water CCl_4 solution (solid line) and CCl_4 with water (dotted line) at room temperature (about 5°C); (b) difference spectrum of the acetic acid and water sample; (c) striking features in the difference spectrum.

of 1,000/1 ~ 1,000/5), but on the high-frequency side of ν_s of acetic acid dimer 2,965 cm^{-1} [38] (gas phase). It indicates that the intermolecular interaction between acetic acid and water is stronger than that in water dimer, but weaker than acetic acid cycle dimer.

To confirm the above band assignments, frequency calculations have been carried out at mp2/6-311++g (3df, 2p) level. The calculated O–H stretching vibrations for acetic acid monomer, free water molecule, and the acetic acid water ring dimer are compared with the measurements in Figure 21.4. The calculated (in x-axis) and measured (in y-axis) vibration frequencies are almost lain in line with 0.872 scaling. Therefore, the absorption bands of 1, 3, and 2 shown in Figure 21.3(c) correspond to the O–H stretching modes of ν_a and ν_s in bounded water, the ring dimer and acetic acid monomer, respectively.

4. HYDROGEN-BONDING RINGS AND NETWORKING IN MULTI-HYDRATES OF ACETIC ACID MONOMER

The number of configuration and conformation in the multi-hydrated compounds of acetic acid monomer may become larger and larger and hydrogen-bonding ring and network may be more and more complex following one more water attached to it. Through constructing di-hydrates 1A2W, tri-hydrates 1A3W, and tetra-hydrates 1A4W of acetic acid monomer in this section, we analyze the nature of hydrogen bonding and discuss the rule of architecture of hydration compound of acetic acid to find a way approaching its larger multi-hydrates.

As we have stated in the above section, only the stable dimer has two strong hydrogen bonds. It suggests that the stronger the hydrogen bonds it contains, the

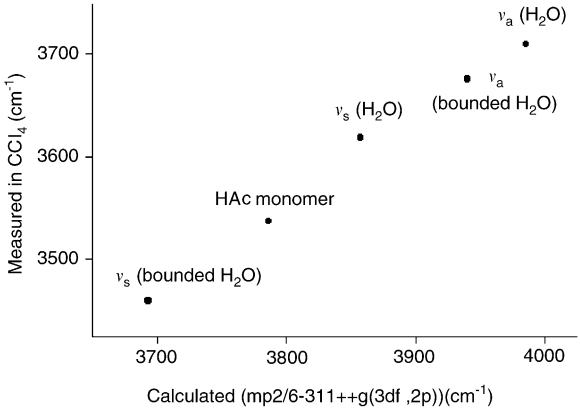

Figure 21.4 Comparison of the measured O–H stretching vibration frequencies with the calculations performed at the MP2/6-311++g (3df, 2p) level; ν_s (bounded H_2O) and ν_a (bounded H_2O) denote the symmetrical and asymmetrical O–H modes of the bounded water as shown in Figure 21.3(c), ν_s (H_2O), ν_a (H_2O), and HAc monomer denote the symmetrical and asymmetrical O–H modes of water monomer and the O–H mode of acetic acid monomer, respectively.

lower the energy configuration of the hydrate. Based on the principle, more than 10 candidates of each hydrate (1A2W, 1A3W, and 1A4W) have been selected and optimized at MP2/6-31+g (d, p) level. In the following section, only four or five most stable hydrates are presented for each group shown in Figure 21.5. The total energy and binding energy calculated at the MP4/6-31+g (d, p) level as well as the distances O···H in hydrogen bonding are also shown in the figure.

4.1 Di-hydrates of acetic acid HAc · $(H_2O)_2$ and the five-membered hydrogen-bonding ring

4.1.1 Structural characters of hydrogen-bonding ring

All of the four selected structures of 1A2W-n ($n = 1$–4) contain three strong hydrogen bonds building up from 1A1W. In the head-on 1A2W-1, the five-membered hydrogen-bonding ring is constructed by breaking the four-membered ring in the head-on dimer 1A1W-1 and then inserting one more hydrogen bonding $O_w-H\cdots O_w-H$ in it. All the five heavy atoms in the five-membered ring lay on the plane. The hydrogen-bonding structures in all the other di-hydrates, 1A2W-2, 1A2W-3, and 1A2W-4, could be simply regarded as one more water attached and bonded to the lowest configuration of acetic acid water dimer 1A1W-1 through a new hydrogen bonding. Both of the 1A2W-2 and 1A2W-3 have two four-membered hydrogen-bonding rings (multi-hetero-ring structure), the one is head-on with two strong bonds, and another is side-on with one strong and one weak bond. In the 1A2W-2, the two rings similar with those in the 1A1W-1 and 1A1W-2, while the 1A2W-3 seems to be combined by that in the 1A1W-1 and 1A1W-3. During the structural optimization of 1A2W-4, the attempt to construct a more stable oxygen-only-three-membered ring (only oxygen but no

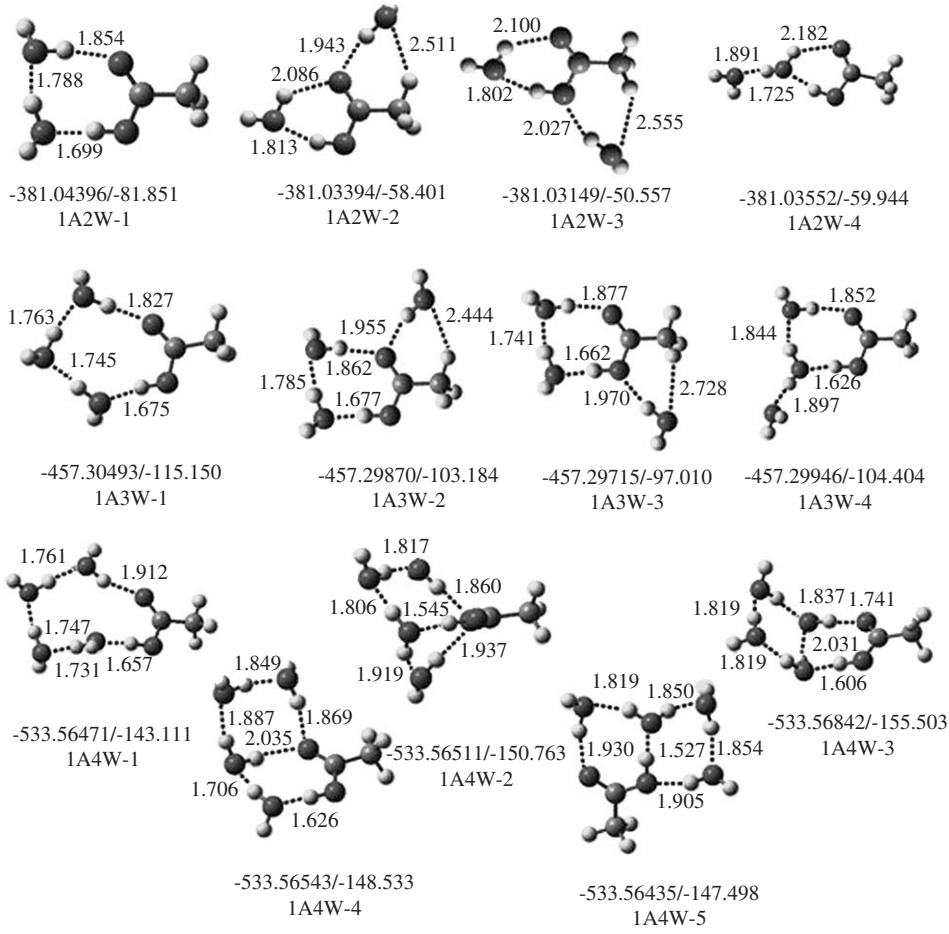

Figure 21.5 Selected and optimized structures of acetic acid di-, tri-, and tetra-hydrate are denoted as 1A*m*W-*n*. 1A stands for the one acetic acid molecule, W for water, *m* for the number of water molecules, and *n* from 1 to 4 or 5 for different structures. The hydrogen bond is represented as the dashed line, the distance of the hydrogen bond O···H is given on its side. The total energy/interaction energy below each corresponding structure is given in Hartree/kJ mol^{-1}.

any carbon atoms contained) has turned futile because of a large tension. The attached water binds to the head-on water of 1A1W-1 and still has only one four-membered ring in the final 1A2W-4.

4.1.2 Total energy and total interaction energy

Comparing the total energy for the four di-hydrates, the stability is in the order of 1A2W-1 > 1A2W-4 (22.164 kJ mol^{-1}) > 1A2W-2 (26.296 kJ mol^{-1}) > 1A2W-3 (32.741 kJ mol^{-1}). Therefore, the 1A2W-1 is of the lowest total energy and the favorable structure among the di-hydrates. The total interaction energy ΔE

between molecules in the di-hydrates has the same order, as 1A2W-1 ($-81.850\,kJ\,mol^{-1}$) > 1A2W-4 ($-59.944\,kJ\,mol^{-1}$) > 1A2W-2 ($-58.401\,kJ\,mol^{-1}$) > 1A2W-3 ($-50.557\,kJ\,mol^{-1}$). The larger interaction in the 1A2W-1 is owing to its bigger five-membered ring with less ring tension than that in the four-membered ring in the other di-hydrates (see text below) and that in the mono-hydrate 1A1W-1.

4.1.3 Hydrogen bond length $R_{H\cdots O}$ and its strength

From hydrogen-bonding distances $R_{H\cdots O}$ in Figure 21.5 one can see obvious difference between five- and four-membered rings. The $R_{H\cdots O}$ 1.699 and 1.854 Å of the strong hydrogen bonding $C-O-H\cdots O_w-H$ and $C=O\cdots H-O_w$ in the five-membered ring in the 1A2W-1 are about 0.1 and 0.2 Å smaller than those in four-membered ring in the other di-hydrates and in the mono-hydrate 1A1W-1. It implies larger bond interaction and less tension in the five-membered ring than those in small ring. Besides those bonds in acetic acid water dimers, there is a new kind of hydrogen bonding of $O_w-H\cdots O_w-H$. The bond distance $R_{H\cdots O}$ is 1.788 Å in the single head-on ring of 1A2W-1 and 0.1 Å smaller than that in the terminal bond in 1A2W-4 (1.891 Å). From average distance of $R_{H\cdots O}$, the strength order for the five kinds of bonds is evidently in the descending order: $C-O-H\cdots O_w-H > O_w-H\cdots O_w-H > C=O\cdots H-O_w > O_w-H\cdots O_a-H \gg C-H\cdots O_w-H$.

4.2 Tri-hydrates of acetic acid $HAc\cdot(H_2O)_3$ and the most stable six-membered ring

4.2.1 Structural characters of hydrogen-bonding ring

Similarly, we repeat the step stated in the above in Section 4.1 to construct the following stable tri-hydrates from the smaller one, di-hydrates 1A2W. All of the four selected structures of 1A3W-n ($n = 1$–4) contain four strong hydrogen bonds. In the 1A3W-1, the head-on six-membered hydrogen-bonding ring is constructed by breaking the head-on five-membered ring in the 1A2W-1 and inserting one more hydrogen bonding $O_w-H\cdots O_w-H$. The head-on six-membered ring keeps in a plane. In all the other tri-hydrates, 1A3W-2, 1A3W-3, and 1A3W-4, with the same viewpoint in building the 1A2W-n ($n = 2$–4), the lowest configuration 1A2W-1 is the building block here. That is, one more water attached and bonded to the lowest configuration of 1A2W-1 through a new hydrogen bonding. Both of the 1A3W-2 and 1A3W-3 are of multi-hetero-ring structure, and have one head-on five-membered ring with three strong bonds and one side-on four-membered ring. In 1A3W-2 and 1A3W-3, the four-membered ring similar with that in the 1A1W-2 and 1A1W-3, respectively, containing one strong and weak bonds. In the 1A3W-4, the attached water binds to either of the two waters in the five-membered head-on ring of 1A2W-1 and could not get another stable oxygen-only-three-membered ring with same reason as in the above Section 4.1.

4.2.2 Total energy and total interaction energy

The relative stability of the four tri-hydrates follows 1A3W-1 > 1A3W-4 ($14.362\,kJ\,mol^{-1}$) > 1A3W-2 ($16.354\,kJ\,mol^{-1}$) > 1A3W-3 ($20.407\,kJ\,mol^{-1}$) in descending order. The total interaction energy of the tri-hydrates has the same order as well, such that 1A3W-1 ($-115.150\,kJ\,mol^{-1}$) > 1A3W-4 ($-104.404\,kJ\,mol^{-1}$) > 1A3W-2 ($-103.184\,kJ\,mol^{-1}$) > 1A3W-3 ($-97.010\,kJ\,mol^{-1}$). The total energy and the total interaction energy of the single head-on ring structure are still competitive with other tri-hydrates. The six-membered planar ring is more favorable in constructing tri-hydrates from five-membered ring and 1A3W-1 is the most stable structure.

4.2.3 Hydrogen bond length $R_{H\cdots O}$ and its strength

In the six-membered head-on ring, all the distances $R_{H\cdots O}$ of the three kinds of hydrogen bonds are smaller than those in the five-membered ring in 1A2W-1. The $O_w-H\cdots O_w-H$ bonding is much longer at the terminal of the 1A3W-4 (1.897 Å and almost same that in the 1A2W-4) than in rings (from 1.741 Å in the 1A3W-3 to 1.785 Å in the 1A3W-2).

4.3 Hetero hydrogen-bonding rings and hydrogen-bond networking in $HAc\cdot(H_2O)_4$

4.3.1 Structural characters of hydrogen-bonding ring

Following the larger hydration compound and the choice of stabler rings, the more complex hydrogen-bonding network could be built up. For example, an oxygen-only-four-membered ring, such as in 1A4W-3, 1A4W-4, and 1A4W-5, is more favorable than a side-on four-membered ring as in the 1A3W-2 in constructing larger hydrates. Therefore, one cannot simply repeat the step as we do in the above section by attaching one water molecule to a tri-hydrate while finding all stable tetra-hydrates 1A4W. As seen from Figure 21.5, all the five stable structures of acetic acid mono tetra-hydrates have no weak hydrogen bonding. The 1A4W-1 has five hydrogen bonds in a single head-on seven-membered ring, but it no longer maintains the planer structure. All other 1A4W-n ($n = 2$–5) have six bonds. The 1A4W-2 can be built up by connecting two hydrogen bonds from the extra water molecule to the ring of the tri-hydrate 1A3W-1. The attaching water is above the six-membered ring, the one of its hydrogen atoms bonding to carbonyl oxygen and another to the water oxygen, which has bonded to hydroxyl in the ring. The two hydrogen bonds have compelled the original head-on planar six-ring bend and forming another five-membered out-of-plane head-on ring. The other three tetra-hydrates, 1A4W-3, 1A4W-4, and 1A4W-5, have the common building blocks of the five-membered head-on ring 1A2W-1 and a water dimer. The water dimer bound to the 1A2W-1 in three different direction by two new bonds result in the three tetra-hydrates. In these structures, a hydrogen bond is shared with the five-membered head-on ring and the oxygen-only-four-membered ring.

4.3.2 Total energy and total interaction energy

As we have stated, the seven-membered ring is too large and no longer a planar structure, and is less favorable. The total energies of the five tetra-hydrates given in the descending order of 1A4W-3 > 1A4W-4 ($7.86\,kJ\,mol^{-1}$) > 1A4W-2 ($8.69\,kJ\,mol^{-1}$) > 1A4W-1($9.74\,kJ\,mol^{-1}$) > 1A4W-5($10.69\,kJ\,mol^{-1}$). The total interaction energy ΔE between molecules in the tetra-hydrates has the order as 1A4W-3 ($-155.503\,kJ\,mol^{-1}$) > 1A2W-2 ($-150.763\,kJ\,mol^{-1}$) > 1A2W-4 ($-148.533\,kJ\,mol^{-1}$) > 1A2W-5 ($-147.498\,kJ\,mol^{-1}$) > 1A2W-1 ($-143.111\,kJ\,mol^{-1}$). The 1A4W-3 is more stable than the other four tetra-hydrates.

5. ARCHITECTURE OF HYDRATION COMPOUNDS

Thus, we can summarize briefly from the above discussion. The four-, five-, and six-membered head-on rings are the most favorable in the small multi-hydrates with a stable planar structure and the side-on ring with a weak hydrogen-bonding interaction of $C-H\cdots O_w-H$. The strength order for the five kinds of bonds is in the descending order as $C-O-H\cdots O_w-H > O_w-H\cdots O_w-H > C=O\cdots H-O_w > O_w-H\cdots O_a-H \gg C-H\cdots O_w-H$. Based on the knowledge, larger multi-hydrates of acetic acid monomer could be constructed from these basic building blocks. Figure 21.6 is a schematic architecture of selected hydrates built upon from the small four-membered head-on ring 1A1w-1. All of these have one or two side-on rings with weak bonds of $C-H\cdots O_w-H$. In the cases of 1A3W-5, 1A3W-6, 1A4W-6, and 1A4W-7, the five-membered side-on ring contains an extra strong $O_w-H\cdots O_w-H$ bond. While in Figure 21.7, the basic building block is 1A2W-1. Configurations 1A3W-7, 1A4W-6, 1A4W-7, and 1A4W-8 have two weak bonds in them.

6. INTRA-NETWORK HYDROXYL DEPROTONATION OF ACETIC ACID THROUGH HYDROGEN BONDING

During our calculations, many interesting structures have been obtained including intra-network protonation hydrates. To describe them, three selected protonation hydrates (1A4W-9, 1A6W-1, and 1A6W-2) and five relatives for helping discussion (1A, 1A1W-1, 1A2W-3, 1A2W-1, and 1A3W-3) are listed in Figure 21.8. The selected interesting distances of hydroxyl R_{O-H} and hydrogen bond $R_{O\cdots H}$ are listed as well on the side of the correspondent bond. The structural optimization for the protonation hydrates was also performed at the same level of MP2/6-31+g (d, p).

Structural characters of hydrogen bonding in the five related hydrates have been described in the above section. In the three selected protonation hydrates, the proton from hydroxyl of acetic acid transfers to the adjacent oxygen of inner water through hydrogen-bonding network. Therefore, the protonation hydrates is still neutral during the intra-network protonation. The structure of the 1A4W-9 is very similar with that of 1A4W5 except for the hydroxyl hydrogen of acetic

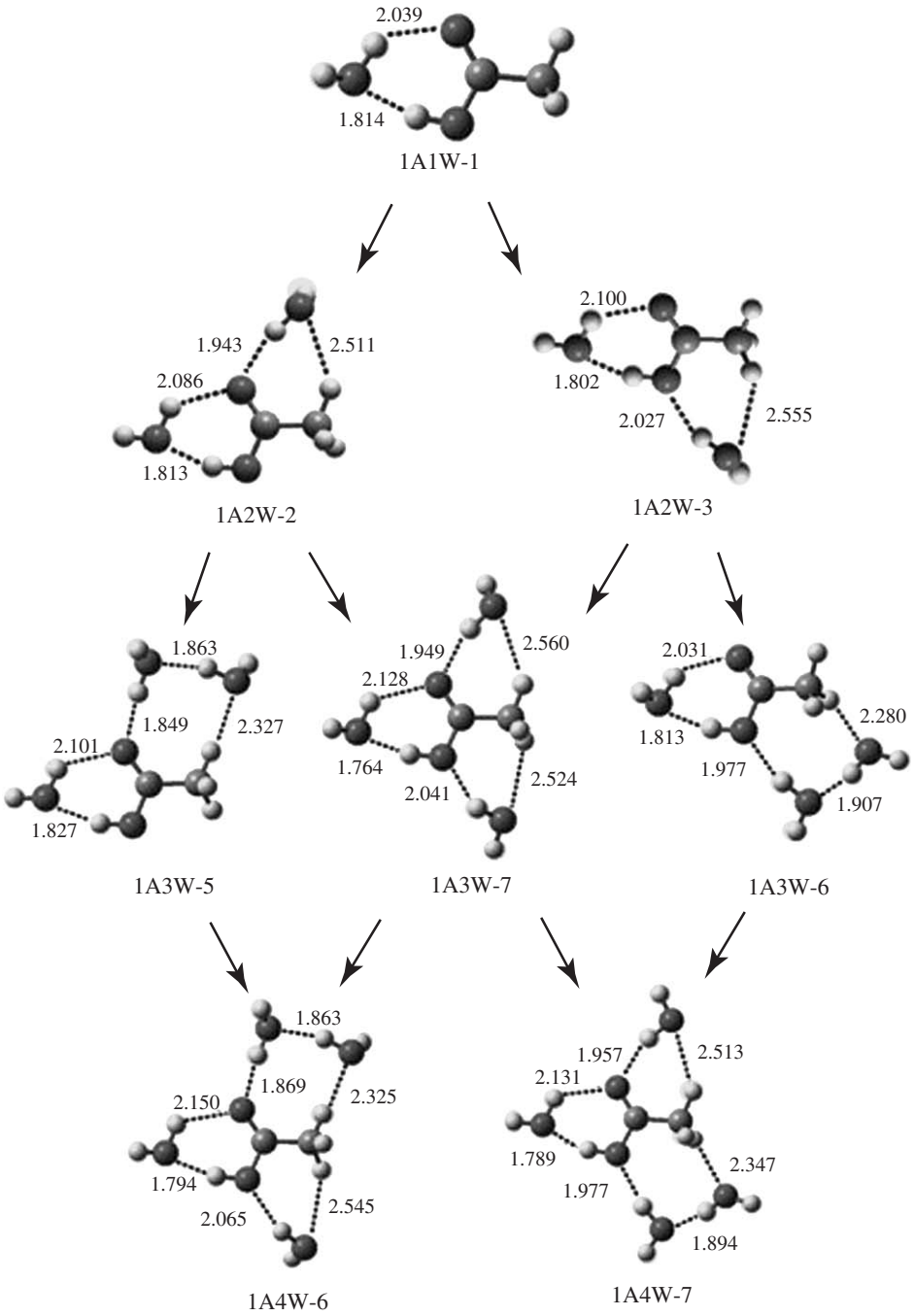

Figure 21.6 Architecture of multi-hydrates built upon from 1A1W-1, a 4-membered head-on ring. Following extra water molecule addition and hydrogen bonding forming, larger and larger hydrates are constructed. The hydrogen bond is denoted as the dashed line and the distance $R_{O\cdots H}$ is given on its side.

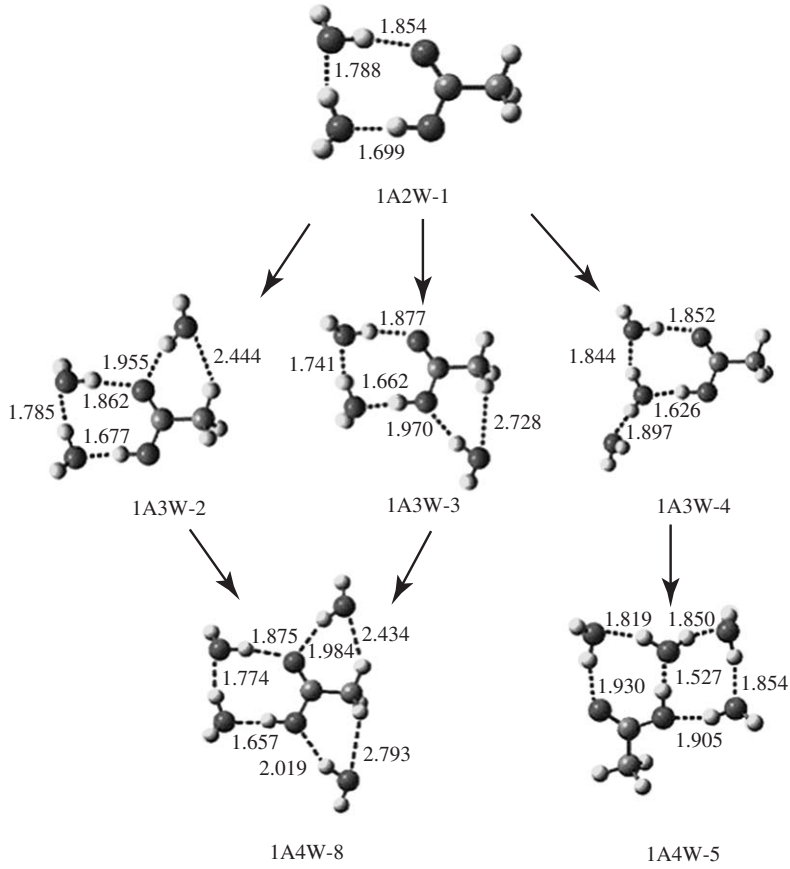

Figure 21.7 Architecture of multi-hydrates built upon from 1A2W-1, a five-membered head-on ring. Following extra water molecule addition and hydrogen bonding forming, larger and larger hydrates are constructed. The hydrogen bond is denoted as the dashed line and the distance $R_{O\cdots H}$ is given on its side.

acid deprotonated. The three bond rings in 1A6W-2 could be simply seen as those in 1A4W-4 and 1A4W-5 except for the protonation. The hydrogen-bond network in 1A6W-1 is complicated with six water and more head-on rings.

We first check the bond distances of hydroxyl R_{O-H} and hydrogen bond $R_{O\cdots H}$ for the five protonation free hydrates presented in Figure 21.8. Generally, the hydroxyl bond length R_{O-H} in the acetic acid can be affected by the hydrogen bonding associated with it as we have discussed in the Section 3.2. For none of the hydrogen bonds associated with it, the acetic acid free monomer has the smallest hydroxyl bond length R_{O-H} of 0.973 Å. About 0.1 Å larger of R_{O-H} is in the four-membered head-on ring 1A2W-3 (0.985 Å) and 1A1W-1 (0.987 Å). There is 0.1 Å still larger of R_{O-H} in 1A2W-1 (0.997 Å) and 1A3W-3 (1.001 Å) as we stated that less tension of head-on ring in the five-membered than in the four-membered. The larger the R_{O-H} becomes, the smaller the $R_{O\cdots H}$ and the stronger

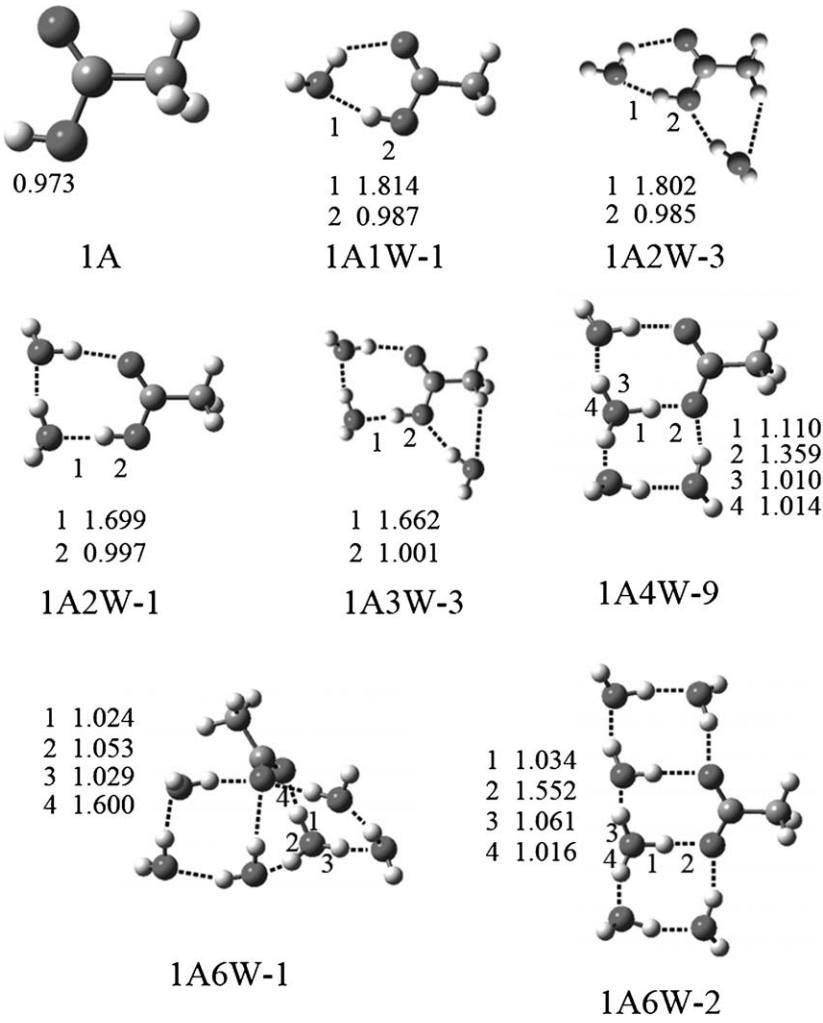

Figure 21.8 Optimized structures of three hydroxyl deprotonated hydrates (1A4W-9, 1A6W-1, and 1A6W-2) compared with five relatives (1A, 1A1W-1, 1A2W-3, 1A2W-1, and 1A3W-3). The dashed lines denote the hydrogen bonds and selected interesting distances of R_{O-H} and $R_{O\cdots H}$ are listed on the side of the correspondent bond.

the associated hydrogen bond becomes. There is about 0.1 Å or more difference of hydrogen bond $R_{O\cdots H}$ between that in the five-membered (1.699 Å in 1A2W-1, and 1.662 Å in 1A3W-3) and four-membered ring (1.814 Å in 1A1W-1 and 1.802 Å in 1A2W-3).

It could also be seen from the Figure 21.8, that there are three hydroxyl bonds O–H in the hydrated proton. These bonds could be divided into two types. One of the hydroxyl bonds is hydrogen bonded to the deprotonated oxygen of the acetic acid, other two to waters in the hydrate. The former bond length of R_{O-H} is 1.110 Å in 1A4W-9, and much smaller of 1.024 Å in 1A6W-1 and 1.034 Å in

1A6W-2. While the distance of the hydrogen bonding $R_{O\cdots H}$ associated with the hydrated proton and the deprotonated oxygen of the acetic acid has an inverse order. It is 1.359 Å in 1A4W-9, but much larger of 1.600 Å in 1A6W-1 and 1.552 Å in 1A6W-2. It implies that larger hydrogen-bonding interaction in 1A4W-9, and smaller in 1A6W-1 and 1A6W-2. Furthermore, the hydrated proton is of the most stable and has the largest freedom liberated from the deprotonated acetic acid in 1A6W-1. In 1A4W-9, the protonating hydrogen is also shared partly by the acetic acid.

7. CPMD SIMULATIONS

Three RDFs, $g_{O(carbonyl)-H}(r)$, $g_{O(hydroxyl)-H}(r)$, and $g_{H(hydroxyl)-O}(r)$ for the statistics of the three kinds of strong hydrogen bonding are presented in Figure 21.9(a–c). Three angle averages related to the hydrogen bonding $(C=)O\cdots H-O_w$, $(C-)O(-H)\cdots H-O_w$ and $(C-)O-H\cdots O_w$, are displayed in Figure 21.10. The simplest head-on rings were counted from configurations collected in the trajectory file and are given in Figure 21.11.

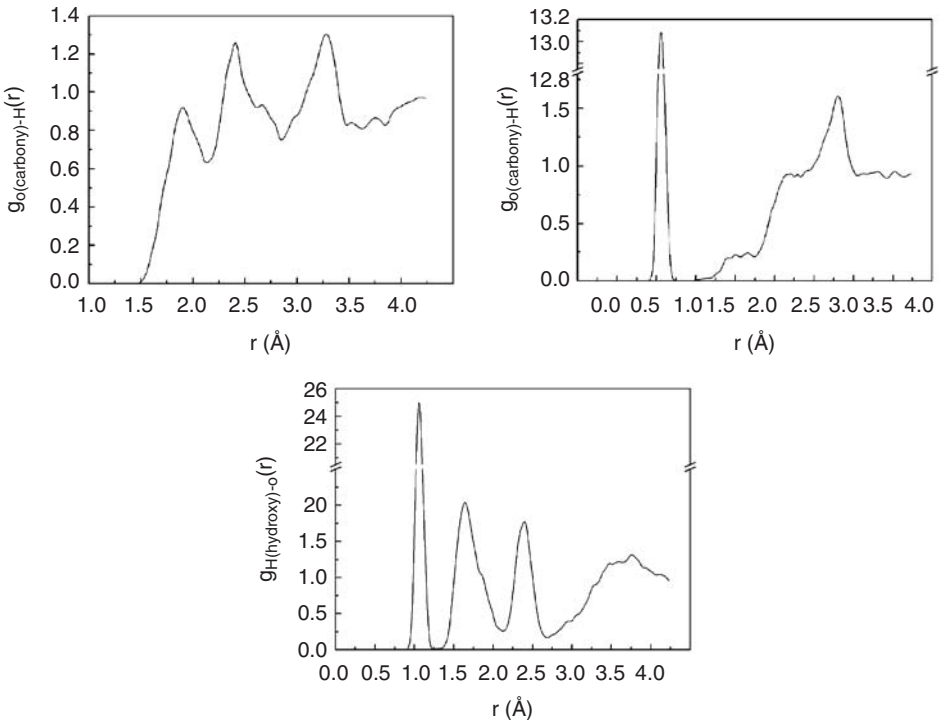

Figure 21.9 Simulated radial distribution functions (RDFs). The $g_{O(carbonyl)-H}(r)$ is for the carbonyl oxygen and all hydrogen atoms, the $g_{O(hydroxyl)-H}(r)$ for the hydroxyl oxygen and all hydrogen atoms, and the $g_{H(hydroxyl)-O}(r)$ for hydroxyl hydrogen and all oxygen atoms.

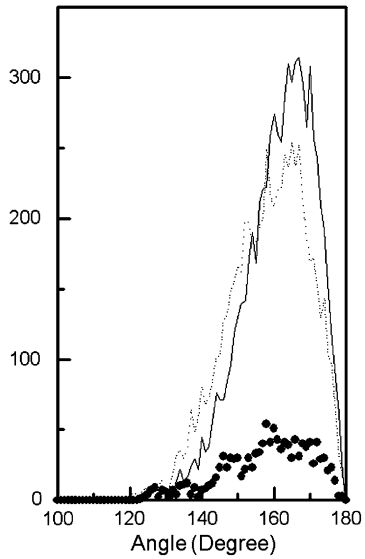

Figure 21.10 Three angle averages. The solid line is for the angle (C $=$)O$\cdots$H$-$O$_w$, the dotted line for (C$-$)O(H)$\cdots$H$-$O$_w$, and solid circles for (C$-$)O$-$H$\cdots$O$_w$.

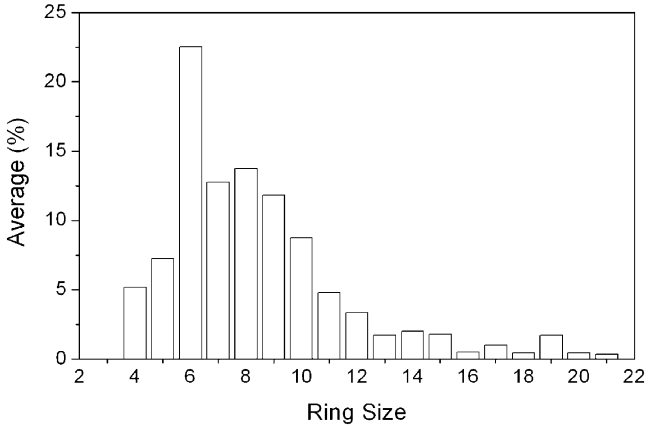

Figure 21.11 Statistics for the head-on hydrogen-bonding ring connected by the bonds C$-$O$-$H$\cdots$O$_w$$-$H, C $=$ O$\cdots$H$-$O$_w$ and O$_w$$-H\cdots$O$_w$$-$H. Evidently, the six-membered ring is the most favorable species.

7.1 Radial distribution functions

The sharp peak at 1.05 Å in Figure 21.9(b) and (c) shows the distance of hydroxyl O–H. The second peak at 1.64 Å in Figure 21.9(c) represents the strongest hydrogen bonding of O$_a$$-H\cdots$H$-O_w$. From the $g_{O(carbonyl)-H}(r)$ displayed in Figure 21.9(a), the distance of the second strong hydrogen bonding of

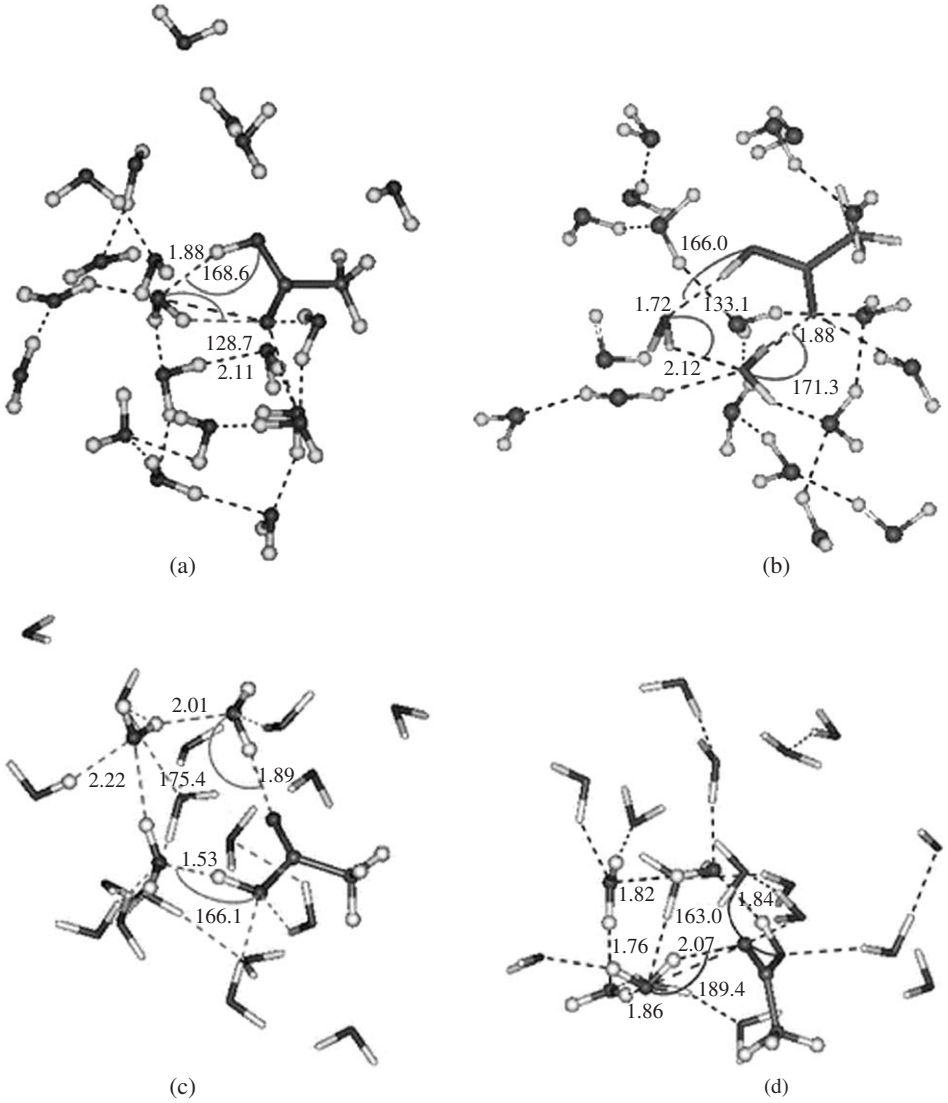

Figure 21.12 Snapshots obtained from 1A20W trajectory file. The hydrogen-bonding network and especially the head-on hydrogen-bonding rings, which are (a) four-membered ring, (b) five-membered ring, (c) six-membered ring, and (d) seven-membered ring, with the distance and some angles of hydrogen bonds involved.

$C=O\cdots H-O_w$ is around 1.90 Å. The second weak peak in Figure 21.9(b) ranging from 1.60 to 2.30 Å implies that the hydroxyl site is not a good hydrogen acceptor. The peak around 3.30 Å in Figure 21.9(a–c) shows the second coordination shell. The third is centered at 2.41 Å, which shows the intramolecular distance between the carbonyl oxygen and the hydroxyl hydrogen of acetic acid. Therefore, it is clear that the hydroxyl site is a very strong hydrogen

donor, less strong acceptor, and the carbonyl site is a strong hydrogen acceptor, which is consistent with the above *ab initio* calculations.

In Figure 21.9, the minima after the hydrogen-bonding peaks are around 2.15, 2.25, and 2.15 Å in the $g_{O(carbonyl)-H}(r)$, $g_{O(hydroxyl)-H}(r)$, and $g_{H(hydroxyl)-O}(r)$, respectively. According to this, 2.30 Å is selected as the upper limit of the distance of hydrogen bonding in the following sections of hydrogen-bonding ring averages.

7.2 Angle averages

From Figure 21.10, three favorable angles are around 165° for $(C=)O\cdots H-O_w$, 158° for $(C-)O(H)\cdots H-O_w$, and 167° for $(C-)O-H\cdots O_w$, respectively. The hydrogen-bonded linear angle about 180° in water dimer is rarely found.

7.3 Head-on ring averages

Head-on ring averages are displayed in Figure 21.11. It is shown that in dilute aqueous solution, at least 22.0% configurations contain head-on rings, in which 34.9% is of planar (four-, five-, and six-membered rings). As *ab initio* calculations predicted, planar ring structure always has small dipole moment. It implies that planar structures with relative small dipole moments are of significant importance even if in such a strong polar system. It is interesting that the six-membered ring is the most favorable as evident from similar results obtained from *ab initio* calculations. Another important planar five-membered ring has 7.2% significant occupation in all rings. The hydration compound with the smallest four-membered head-on ring is 5.2% of all ring structures. Larger and much more complicated spatial structures are not discussed in this paper for larger rings.

Four snapshots for the four-, five-, six-, and seven-membered head-on rings are displayed in Figure 21.12. The distance and angle of hydrogen bonding are involved.

8. CONCLUSIONS

The protonation and deprotonation phenomena and molecular association of solute molecule with water via intermolecular hydrogen bonding forming various hydration compounds are very common in aqueous solution and in biological cell in nature. In the aqueous solution, more complicated type of hydrogen bond, hydrogen-bonding rings, various kinds of hydration compounds (hydrates), and even hydrogen-bonding network can be expected. The nature of hydrogen bonding, the bonds networking, the rule in architecture of larger hydration compounds, deprotonation of acetic acid in solution, stability of the hydrated proton, and the local structure of its aqueous solution are the most fundamental areas to look into while understanding how a solute molecule exists in aqueous solution. In the present paper, we reported our *ab initio* calculations on hydrogen-bonding rings and hydrogen-bonding network in the

multi-hydrates of acetic acid monomer and *ab initio* molecular dynamics (CPMD) simulations on acetic acid monomer and water system for exploration of the local structure of acetic acid aqueous solution. More than hundreds of multi-hydrates have been selected as candidates during our calculations.

The structural optimizations and energy calculations have been performed at the MP2/6-31+g (d, p) and MP4/6-31+g (d, p) level, which are adequate for our large hydrates calculations with reliable results and reasonable cost as we stated in Section 2.

The most stable structure of the smallest hydration compound of acetic acid monomer, as well as the acetic acid water dimer, has a four-membered head-on ring with the smallest dipole moment. To verify the existence of it, the infrared spectra experiment data were collected in the dilute CCl_4/HAc and CCl_4/H_2O ratios condition. The hydroxyl (O–H) stretching vibrations in molecules of water, acetic acid, and the dimer are distinguished, for the dissolved species are isolated from each other by surrounded solvent molecules CCl_4. The calculated and measured vibration frequencies are almost lain in line with 0.872 scaling.

The four-, five-, and six-membered head-on rings are the most favorable in the small multi-hydrates with a stable planar structure and the side-on ring with a weak hydrogen-bonding interaction of $C-H\cdots O_w-H$. For small ring with tension, the six-membered ring is most important in the large multi-hydrates and in the local structure of dilute solution also verified by our CPMD simulations. A larger ring from seven-membered could no longer maintain the planar structure. Larger multi-hydrates of acetic acid monomer could be constructed from these basic building blocks. The strength order for the five kinds of bonds is in the descending order as $C-O-H\cdots O_w-H > O_w-H\cdots O_w-H > C=O\cdots H-O_w > O_w-H\cdots O_a-H \gg C-H\cdots O_w-H$.

The three hydroxyl bonds O–H in the hydrated proton could be divided into two types: one of the hydroxyl bonds is hydrogen bonded to the deprotonated oxygen of the acetic acid, other two to waters in the hydrate. The larger the R_{O-H} becomes, the smaller the $R_{O\cdots H}$ and the stronger the associated hydrogen bond becomes. The hydrated proton is stable and has the freedom liberated from the deprotonated acetic acid in the large multi-hydrate with more complicit head-on ring. In small hydrates, the protonating hydrogen is shared partly by the acetic acid.

ACKNOWLEDGMENTS

We would like to thank the computer center at the Nanjing University for computer time at the SGI 3800 servers.

REFERENCES

[1] J.J. Kipling, *J. Chem. Soc.* **8** (1952) 2858.
[2] J.B. Ng, H.F. Shurvell, *Can. J. Spectrosc.* **30** (1985) 149.
[3] J.B. Ng, H.F. Shurvell, *J. Phys. Chem.* **91** (1987) 496–500.
[4] N. Nishi, K. Yamamoto, *J. Am. Chem. Soc.* **109** (1987) 7353–7361.

[5] K. Yamamoto, N. Nishi, *J. Am. Chem. Soc.* **112** (1990) 549–558.
[6] Y. Akiyama, A. Wakisaka, F. Mizukami, K. Sakaguchi, *J. Chem. Soc., Perkin Trans.* **2** (1998) 95–99.
[7] G. Ruderman, E.R. Caffarena, I.G. Mogilner, E.J. Tolosa, *J. Solution Chem.* **27** (1998) 935.
[8] K. Kosugi, T. Nakabayashi, N. Nishi, *Chem. Phys. Lett.* **291** (1998) 253–261.
[9] U. Kaatze, K. Menzel, R. Pottel, *J. Phys. Chem.* **95** (1991) 324.
[10] N. Nishi, T. Nakabayashi, K. Kosugi, *J. Phys. Chem. A* **103** (1999) 10851–10858.
[11] J.M. Briggs, T.B. Nguyen, W.L. Jorgensen, *J. Phys. Chem.* **95** (1991) 3315.
[12] T. Nakabayashi, K. Kosugi, N. Nishi, *J. Phys. Chem. A* **103** (1999) 8595.
[13] F. Génin, F. Quilès, A. Burneau, *Phys. Chem. Chem. Phys.* **3** (2001) 932–942.
[14] P.R. Rablen, J.W. Lockman, W.L. Jorgensen, *J. Phys. Chem. A* **102** (1998) 3782–3797.
[15] H.-C. Chang, J.-C. Jiang, M.-S. Lin, H.-E. Kao, C.-M. Feng, Y.-C. Huang, S.H. Lin, *J. Chem. Phys.* **117** (2002) 3799.
[16] Q. Gao, K.T. Leung, *J. Chem. Phys.* **123** (2005) 074325.
[17] C. Colominas, J. Teixidó, J. Cemelķ, F.J. Luque, M. Orozco, *J. Phys. Chem. B* **102** (1998) 2269.
[18] A.J.A. Aquino, D. Tunega, G. Haberhauer, M.H. Gerzabek, H. Lischka, *J. Phys. Chem. A* **106** (2002) 1862.
[19] J. Chocholoušová, J. Vacek, P. Hobza, *J. Phys. Chem. A* **107** (2003) 3086–3092.
[20] R. Car, M. Parrinello, *Phys. Rev. Lett.* **55** (1985) 2471–2474.
[21] Gaussian 98, Revision A.7, M.J. Frisch, G.W. Trucks, H.B. Schlegel, G.E. Scuseria, M.A. Robb, J.R. Cheeseman, V.G. Zakrzewski, J.A. Montgomery, Jr., R.E. Stratmann, J.C. Burant, S. Dapprich, J.M. Millam, A.D. Daniels, K.N. Kudin, M.C. Strain, O. Farkas, J. Tomasi, V. Barone, M. Cossi, R. Cammi, B. Mennucci, C. Pomelli, C. Adamo, S. Clifford, J. Ochterski, G.A. Petersson, P.Y. Ayala, Q. Cui, K. Morokuma, D.K. Malick, A.D. Rabuck, K. Raghavachari, J.B. Foresman, J. Cioslowski, J.V. Ortiz, A.G. Baboul, B.B. Stefanov, G. Liu, A. Liashenko, P. Piskorz, I. Komaromi, R. Gomperts, R.L. Martin, D.J. Fox, T. Keith, M.A. Al-Laham, C.Y. Peng, A. Nanayakkara, C. Gonzalez, M. Challacombe, P.M.W. Gill, B. Johnson, W. Chen, M.W. Wong, J.L. Andres, C. Gonzalez, M. Head-Gordon, E.S. Replogle, J.A. Pople, Gaussian, Inc., Pittsburgh PA (1998).
[22] S.F. Boys, F. Bernardi, *Mol. Phys.* **19** (1970) 553.
[23] L.A. Curtiss, D.J. Frurip, M. Blander, *J. Chem. Phys.* **71** (1979) 2703.
[24] J.E. Del Bene, W.B. Person, K. Szczepaniak, *J. Phys. Chem.* **99** (1995) 10705.
[25] D. Hankins, J.W. Moskowitz, F.H. Stillinger, *J. Chem. Phys.* **53** (1970) 4544–4554.
[26] D.J. Frurip, L.A. Curtiss, M. Blander, *J. Am. Chem. Soc.* **102(8)**, (1980) 2610.
[27] S.S. Xantheas, Y.H.J. Dunning, *J. Chem. Phys.* **99(11)**, (1993) 8774.
[28] D.R. Lide (Ed.), *CRC Handbook of Chemistry and Physics*, 85th ed., CRC Press, 2004–2005.
[29] CPMD, Copyright IBM Corp 1990–2004, Copyright MPI für Festkörperforschung, Stuttgart, 1997–2001.
[30] A.D. Becke, *Phys. Rev. A* **38** (1988) 3098.
[31] C. Lee, W. Yang, R.G. Parr, *Phys. Rev. B* **37** (1988) 785.
[32] L.M. Ramaniah, M. Bernasconi, M. Parrinello, *J. Chem. Phys.* **111** (1999) 1587–1591.
[33] M. Sprik, J. Hutter, M. Parrinello, *J. Chem. Phys.* **105** (1996) 1142–1152.
[34] P.L. Silvestrelli, M. Bernasconi, M. Parrinello, *Chem. Phys. Lett.* **277** (1997) 478–482.
[35] J.T. Bulmer, H.F. Shurvell, *J. Phys. Chem.* **77** (1973) 256–262.
[36] G. Seifert, T. Patzlaff, H. Graener, *Chem. Phys. Lett.* **333** (2001) 248–254.
[37] S. Hirabayashi, K.M.T. Yamada, *J. Chem. Phys.* **122** (2005) 244501.
[38] Y. Maréchal, *J. Chem. Phys.* **87(11)**, (1987) 6344–6353.

CHAPTER **22**

Current Situation and Future Development of Discrete Variational Multielectron Method

Kazuyoshi Ogasawara and **Shinta Watanabe**

Contents

Abstracts

The computational procedure and the recent applications of the relativistic discrete variational multielectron (DVME) method are reviewed. The analysis of first-principles calculations of the multiplet energy levels and $4f^n$–$4f^{n-1}5d$ transition spectra of rare-earth ions in $LiYF_4$ crystal, and the analysis of MCD of Cr $L_{2,3}$-edge XANES of CrO_2 are shown as applications to optical and magnetic materials, respectively. Some future plans on the extension of the relativistic DVME calculation program are also mentioned.

Department of Chemistry, Kwansei Gakuin University, 2-1 Gakuen, Sanda, Hyogo 669-1337, Japan
Corresponding author. E-mail: ogasawara@ksc.kwansei.ac.jp

Advances in Quantum Chemistry, Vol. 54
ISSN 0065-3276, DOI 10.1016/S0065-3276(07)00022-6

1. INTRODUCTION

The discrete variational multielectron (DVME) method is an electronic structure calculation method using configuration-interaction (CI) approach based on the discrete-variational Xα (DV-Xα) molecular orbital (MO) method [1]. Within the one-electron approximation, highly accurate electronic structure calculations can be easily performed using commercially available band structure calculation or MO calculation programs. However, for example, multiplet spectra of transition-metal (TM) ions or rare-earth (RE) ions in crystals are still analyzed based on semiempirical approaches such as the ligand-field theory [2] or the crystal field (CF) theory (Judd–Ofelt theory) [3–5] due to the complexity arising from the many-electron (multiplet) effects. In the case of RE ions, the relativistic effects are also significant. Therefore, the situation is more complicated due to the coexistence of the relativistic effects and the multiplet effects. A strong desire to overcome these situations was our motivation to develop the DVME calculation program. In other words, the DVME calculation program was especially designed to perform first-principles calculations of multiplet spectra of RE ions in crystals. The status of the DVME method and the motivation to develop the relativistic DVME method are schematically shown in Figure 22.1.

The non-relativistic version of DVME method was developed in 1998 and was applied to the analysis of multiplet spectra of ruby [6–8]. This method was later applied to the analysis of a variety of TM-doped solid-state-laser materials [9–11]. The relativistic version of DVME method was developed in 2000. However, at that time, it was still difficult to calculate multiplet spectra of RE ions due to the limited performance of available computers. On the other hand, the relativistic

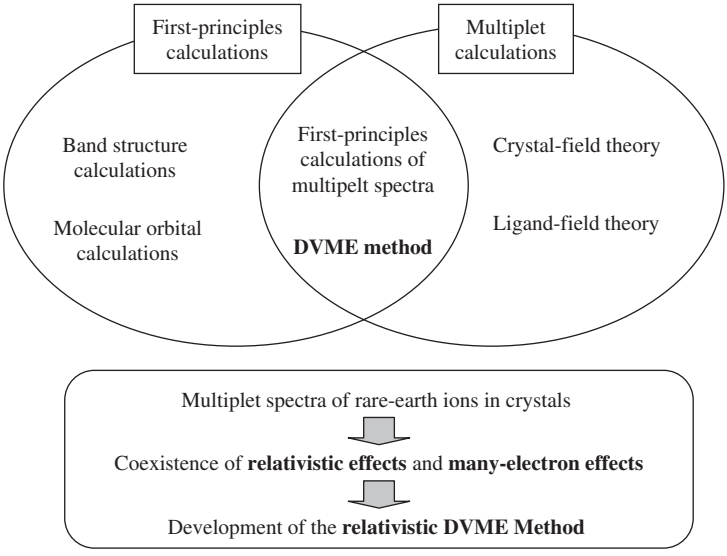

Figure 22.1 Status of the DVME method and the motivation to develop the relativistic DVME method.

DVME method is also quite useful for the analysis of X-ray absorption near-edge structures (XANES) or electron energy-loss near-edge structures (ELNES) at TM $L_{2,3}$-edges since in addition to the significant relativistic effects at the TM 2p core levels, multiplet effects take place due to the interactions among 3d-electrons and the created core hole. Thus, the situation of these spectra is almost the same as the multiplet spectra of RE ions since the major difficulty is the coexistence of the relativistic effects and the multiplet effects. Therefore, we have first applied the relativistic DVME method to the first-principles calculations of TM $L_{2,3}$-edge XANES/ELNES of some TM compounds [12]. Recently, the relativistic DVME method was also utilized to clarify the local electronic structure around Ni ions in $LiNiO_2$ [13].

TM compounds are also important as magnetic materials due to their characteristic spin states. In order to characterize magnetic properties of these materials, it is important to evaluate the spin and orbital moments separately. For this purpose, magnetic circular dichroism (MCD) of XANES is quite useful. When absorption spectrum of a magnetic material is measured using circularly polarized light, slightly different spectra are obtained for the right polarization and for the left polarization depending on the magnetic moments of the measured TM ion [14].

Experimentally, these spin moments can be directly estimated by integrating the experimental MCD spectrum using the appropriate "sum rules" [15,16]. In order to especially determine the spin moments, L_2- and L_3-edges must be integrated separately. However, for some TM compounds, there is a strong mixing between L_2- and L_3-edges, which gives a significant difficulty for the analysis based on the sum rules [17]. In order to overcome these problems, first-principles calculations of MCD spectra and accompanying magnetic moments are strongly desired. Thus, we have recently extended the relativistic DVME method to take into account a magnetic field and circularly polarized light. As a result, first-principles calculations of MCD for absorption spectra are now possible.

Thanks to the rapid development of high-performance computers, the relativistic DVME method can now be applied to the analysis of multiplet spectra of RE ions. We have recently performed a systematic calculations of multiplet energy levels arising from $4f^n$ and $4f^{n-1}5d$ configurations as well as the $4f^n-4f^{n-1}5d$ transition spectra.

In this paper, we first describe the theoretical background of the relativistic DVME method and then in order to demonstrate its wide applicability, its applications to optical and magnetic materials will be shown.

As an application to the optical materials, we will show first-principles calculations of multiplet energy levels and $4f^n-4f^{n-1}5d$ transition spectra of RE ions in $LiYF_4$ (YLF) crystal [18]. As a reference on the energy levels of RE ions, Dieke's diagram is widely known [19,20]. This is a diagram of experimentally observed energy levels of RE^{3+} in $LaCl_3$ obtained up to ca. 40,000 cm^{-1}. Above this energy region, the multiplet states are quite complicated due to the strong configuration interactions and significantly dependent on the host crystals. Our first-principles calculations of multiplet energy levels provide a theoretical

extension of the Dieke's diagram up to ca. 350,000 cm^{-1} as well as unambiguous analysis of $4f^n$–$4f^{n-1}5d$ transition spectra based on the explicitly obtained relativistic many-electron wave functions.

As an application to magnetic materials, we will show the first-principles calculations of the MCD spectra of Cr $L_{2,3}$-edge XANES of CrO_2. The experimental spectra have been reported by Goering et al. [21]. They also measured the anisotropy of MCD spectra by changing the direction of the applied magnetic field and the direction of the incident light. Especially they reported that the MCD even changes sign around L_2-edge between the spectra for **H**//**a** and for **H**//**c** where **H** is the magnetic field vector, and **a** and **c** are lattice vectors of the crystal. In order to investigate the origin of this characteristic anisotropy of the MCD spectra, we have performed first-principles calculations of MCD spectra for different alignments of the applied magnetic field. The relation between the local magnetic moments and the MCD spectra have been also investigated by estimating the expectation values of the spin magnetic moments $\langle S_z \rangle$ and those of the orbital magnetic moments $\langle L_z \rangle$ based on the explicit many-electron wave functions.

2. COMPUTATIONAL PROCEDURE

2.1 The relativistic DV-Xα method

In the relativistic DVME method, first, the relativistic DV-Xα calculation [22] is performed to obtain the fully relativistic four-component MOs used for the CI calculations.

The relativistic MOs and MO energy levels are generally obtained by solving the one-electron Dirac equation [23,24],

$$h\phi_k(\mathbf{r}) = \varepsilon_k \phi_k(\mathbf{r}), H \tag{1}$$

where $\mathbf{r}$ is the position of the electron, and ϕ_k and ε_k are the kth MO and its energy, respectively. h represents the Dirac's one-electron Hamiltonian,

$$\begin{aligned} h &= c\tilde{\boldsymbol{\alpha}}\mathbf{p} + \tilde{\beta}c^2 + V(\mathbf{r}) \\ &= -ic\left(\tilde{\alpha}_x \frac{\partial}{\partial x} + \tilde{\alpha}_y \frac{\partial}{\partial y} + \tilde{\alpha}_z \frac{\partial}{\partial z}\right) + \tilde{\beta}c^2 + V(\mathbf{r}), \end{aligned} \tag{2}$$

where c is the velocity of light, $\mathbf{r}$ and $\mathbf{p} = -\nabla$ the position vector and the momentum operator of the electron, $\tilde{\boldsymbol{\alpha}}$ and $\tilde{\beta}$ the Dirac matrices. The Dirac matrices are represented by the Pauli's spin matrices $\tilde{\boldsymbol{\sigma}}$,

$$\tilde{\sigma}_x = \begin{pmatrix} 0 & 1 \\ 1 & 0 \end{pmatrix}, \tilde{\sigma}_y \begin{pmatrix} 0 & -i \\ i & 0 \end{pmatrix}, \tilde{\sigma}_z = \begin{pmatrix} 1 & 0 \\ 0 & -1 \end{pmatrix} \tag{3}$$

and 2×2 unit matrix $\tilde{I}$ as

$$\tilde{\alpha}_i = \begin{pmatrix} 0 & \tilde{\sigma}_i \\ \tilde{\sigma}_i & 0 \end{pmatrix} (i = x, y, z), \tilde{\beta} = \begin{pmatrix} \tilde{I} & 0 \\ 0 & -\tilde{I} \end{pmatrix} \tag{4}$$

In the relativistic DV-Xα method [22], the potential $V(\mathbf{r})$ in Eq. (2) is expressed using the Slater's Xα potential [25] as

$$V(\mathbf{r}) = -\sum_{v}\frac{Z_v}{|\mathbf{r}-\mathbf{R}_v|} + \int\frac{\rho(\mathbf{r}')}{|\mathbf{r}-\mathbf{r}'|}d\mathbf{r}' - 3\alpha\left\{\frac{3}{4\pi}\rho(\mathbf{r})\right\}^{1/3} + \sum_{\mu}\frac{Z_\mu^{\mathrm{eff}}}{\mathbf{r}-\mathbf{R}_\mu}, \tag{5}$$

where Z_v and $\mathbf{R}_v$ are the atomic number and the position of the vth atom inside the model cluster, respectively, ρ the electron density, Z_μ^{eff} and $\mathbf{R}_\mu$ the effective charge and position of the μth ion outside the model cluster. The first term represents the interaction between electrons and nuclei, the second term represents the Coulomb interaction between electrons, and the third term represents the exchange-correlation potential. The fourth term describes effective Madelung potential created by point charges. In this work, α is fixed to be 0.7, which was found to be an appropriate value for many solid-state systems [26].

2.2 Hamiltonian used in the relativistic DVME method

The eigenstates of a many-electron system (multiplet states for open shell systems) can be obtained by solving the relativistic many-electron equations for relativistic electrons:

$$H\Psi_l = E_l\Psi_l, \tag{6}$$

where H, Ψ_l, E_l are the relativistic many-electron Hamiltonian, the lth many-electron wave function, and the corresponding energy eigenvalue, respectively. In the relativistic DVME method, the so-called Dirac–Coulomb Hamiltonian [27] is used as the relativistic many-electron Hamiltonian which is a simple extension of the one-electron Dirac Hamiltonian to a many-electron system. Due to the limitation of our computational resources, only relevant electrons and relevant MOs are treated explicitly and the other electrons are considered to be frozen. The relativistic many-electron Hamiltonian for explicitly treated n electrons is expressed in atomic units as

$$H = \sum_{i}^{n} h(\mathbf{r}_i) + \sum_{i}^{n}\sum_{j<i}^{n} g(\mathbf{r}_i,\mathbf{r}_j) + H_z(L_z + 2S_z), \tag{7}$$

$$h(\mathbf{r}_i) = c\tilde{\boldsymbol{\alpha}}\mathbf{p}_i + \tilde{\beta}c^2 - \sum_{v}\frac{Z_v}{|\mathbf{r}_i-\mathbf{R}_v|} + V_0(\mathbf{r}_i) + \sum_{\mu}\frac{Z_\mu^{\mathrm{eff}}}{|\mathbf{r}_i-\mathbf{R}_\mu|}, \tag{8}$$

$$g(\mathbf{r}_i,\mathbf{r}_j) = \frac{1}{|\mathbf{r}_i-\mathbf{r}_j|}. \tag{9}$$

The first term of H is the one-electron operators including the potential from the frozen electrons $V_0(\mathbf{r}_i)$,

$$V_0(\mathbf{r}) = \int\frac{\rho_0(\mathbf{r}')}{|\mathbf{r}-\mathbf{r}'|}d\mathbf{r}' + \frac{3}{4}\left[\frac{\rho(r)V_{xc}\{\rho(\mathbf{r})\} - \rho_0(\mathbf{r})V_{xc}\{\rho_0(\mathbf{r})\}}{\rho_1(\mathbf{r})} - V_{xc}\{\rho_1(\mathbf{r})\}\right], \tag{10}$$

where V_{xc} is the Slater's Xα potential, $\rho(\mathbf{r})$ the density of all electrons, $\rho_1(\mathbf{r})$ the density of the explicitly treated n electrons, $\rho_0(\mathbf{r})$ the density of the frozen

electrons [28]. The second term is the two-electron operators representing the Coulomb repulsion interactions among explicitly treated electrons. The third term is the Zeeman term represented by the external magnetic field H_z, the spin and angular momentum operators S_z and L_z. This term is considered only in the situation with applied magnetic field such as calculation of MCD.

2.3 Configuration interaction approach

In the DVME method, the many-electron Hamiltonian is diagonalized based on the CI approach. In this approach, the lth many-electron wave function Ψ_l is represented as a linear combination of the Slater determinants which are constructed from MOs obtained by the relativistic DV-Xα calculations as:

$$\Psi_l = \sum_{j=1}^{K} W_{jl}\Phi_j, \tag{11}$$

$$\Phi_j(\mathbf{r}_1,\ldots,\mathbf{r}_n) = \frac{1}{\sqrt{n!}}\begin{vmatrix} \phi_{j1}(\mathbf{r}_1) & \phi_{j1}(\mathbf{r}_2) & \cdots & \phi_{j1}(\mathbf{r}_n) \\ \phi_{j2}(\mathbf{r}_1) & \phi_{j2}(\mathbf{r}_2) & \cdots & \phi_{j2}(\mathbf{r}_n) \\ \vdots & \vdots & \ddots & \vdots \\ \phi_{jn}(\mathbf{r}_1) & \phi_{jn}(\mathbf{r}_2) & \cdots & \phi_{jn}(\mathbf{r}_n) \end{vmatrix}. \tag{12}$$

In the above equations, W_{jl} is the coefficient of the jth Slater determinant in the lth many-electron wave function and K is the total number of the Slater determinants used for the linear combination. For example, for $4f^2$ electron configuration, such as the ground-state configuration of the Pr^{3+} ion, two f electrons occupy 14 MOs. Therefore, the number of possible combinations is $K = 14!/\{2!(14-2)!\} = 91$.

Using Eq. (11), Eq. (6) can be rewritten in the form of the secular equation,

$$\tilde{H}\tilde{W} = \tilde{W}\tilde{E}. \tag{13}$$

By solving this, the multiplet energies $\tilde{E}$ and the coefficients of the many-electron wave functions $\tilde{W}$ are obtained.

2.4 Configuration analysis of many-electron wave functions

In the relativistic DVME method, the interactions among the states represented by the Slater determinants, i.e., the CI can be analyzed using explicit many-electron wave functions expressed by Eq. (11). From the orthonormality of the Slater determinants, the inner product of the lth many-electron wave function with itself can be expanded as:

$$\begin{aligned}\langle\Psi_l|\Psi_l\rangle &= \left\langle \sum_j W_{jl}\Phi_j \middle| \sum_k W_{kl}\Phi_k \right\rangle = \sum_j\sum_k W_{jl}^* W_{kl}\langle\Phi_j|\Phi_k\rangle \\ &= \sum_j |W_{jl}|^2\langle\Phi_j|\Phi_j\rangle = \sum_j |W_{jl}|^2 = 1.\end{aligned} \tag{14}$$

In this scheme, the contribution of the jth Slater determinant Φ_j within the lth many-electron wave function Ψ_1 can be simply represented as

$$Q_j^l = |W_{jl}|^2. \tag{15}$$

Summing Q_j^l over all possible j yields unity, in accordance with Eq. (14).

2.5 Calculation of theoretical absorption spectra

Since the many-electron wave functions are obtained explicitly as linear combinations of the Slater determinants, the oscillator strengths of an electric dipole transition from the ith state to the jth state for linearly polarized light can be calculated by

$$I_{ij} = 2(E_j - E_i)\left|\left\langle \Psi_j \left| \sum_{k=1}^{n} \mathbf{r}_k \cdot \mathbf{e} \right| \Psi_i \right\rangle\right|^2, \tag{16}$$

where **e** is the unit vector parallel to the electric field vector of the incident light. In the case of circularly polarized light, the oscillator strengths are expressed as:

$$I_{ij}^R = (E_j - E_i)\left|\left\langle \Psi_j \left| \sum_{k=1}^{n} \mathbf{r}_k \cdot (\mathbf{x} + i\mathbf{y}) \right| \Psi_i \right\rangle\right|^2 \tag{17}$$

for right polarization and

$$I_{ij}^L = (E_j - E_i)\left|\left\langle \Psi_j \left| \sum_{k=1}^{n} \mathbf{r}_k \cdot (\mathbf{x} - i\mathbf{y}) \right| \Psi_i \right\rangle\right|^2 \tag{18}$$

for left polarization, where the direction of the incident light is assumed to be in the z-direction, and **x** and **y** are the unit vectors parallel to the x and y directions respectively. For easy comparison with the experimental spectra, the theoretical absorption spectrum can be obtained by convoluting oscillator strengths using a Gaussian function. In this work the width of the Gaussian function is determined so that the calculated spectra are in good agreement with experimental ones.

3. $4f^n$-$4f^{n-1}5D$ TRANSITION SPECTRA FOR TRIVALENT RE IONS IN $LiYF_4$

3.1 Model clusters for trivalent RE ions in $LiYF_4$

The crystal structure of $LiYF_4$ (YLF) is shown in Figure 22.2 [29]. The space group is $I4_1/a$, the crystal system is tetragonal and the lattice constants are $a = 5.171$ Å and $c = 10.748$ Å. Considering the ionic radii, valency, and charge compensation, trivalent RE ions (Ln^{3+}) are expected to substitute for Y^{3+} ions. Therefore, a model cluster consisting of Ln^{3+} ion coordinated with eight fluorine ions was constructed (Figure 22.3). The point group of the Y site is S_4 and the Y–F bond

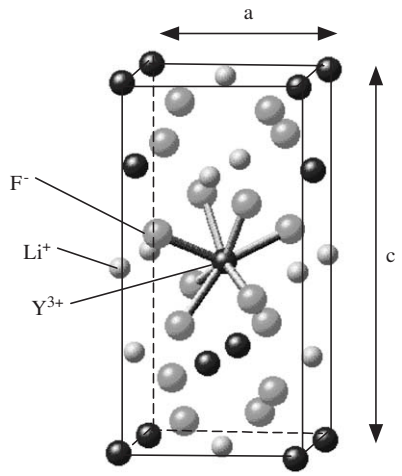

Figure 22.2 Crystal structure of $LiYF_4$. For a colour version of this figure please see the colour plate section near the end of the book.

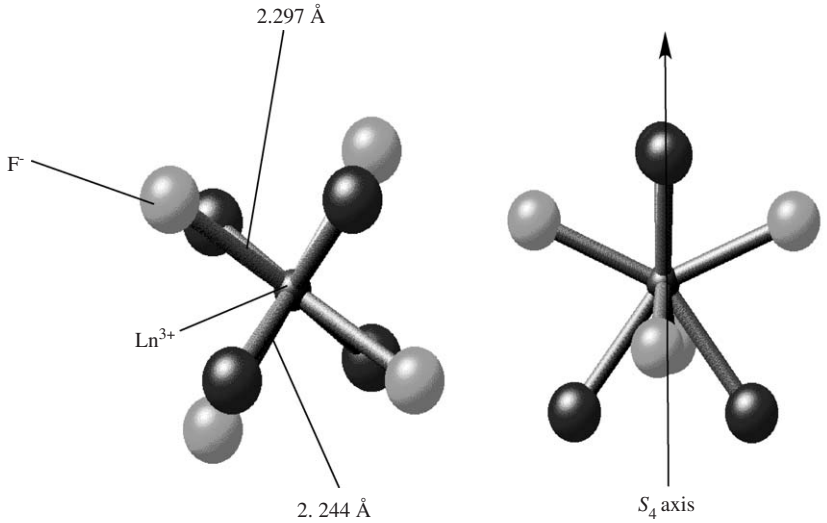

Figure 22.3 Model cluster for trivalent RE (Ln^{3+}) in $LiYF_4$. For a colour version of this figure please see the colour plate section near the end of the book.

lengths are 2.247 Å for four fluorine ions and 2.299 Å for another four. The lattice relaxation by the substitution of Ln^{3+} was not considered. In order to take into account the effects of the surroundings of the model cluster, an effective Madelung potential was considered by locating several thousand point charges at atomic sites outside the cluster. The number of the sampling points was 100,000 and the atomic orbitals (AO) used for the relativistic DV-Xα calculation were from 1s to 6p for Ln and from 1s to 2p for F.

3.2 Molecular orbital energy levels

The MO energy levels for all RE^{3+} ions in YLF are shown in Figure 22.4. Each MO is labeled with the name of the most dominant AO. The valence states mainly consist of F- 2p orbitals while the conduction band is not reproduced because of the lack of the surrounding cations in the present model clusters. The RE 4f orbitals are split due to the spin–orbit interactions and the effects of the CF are seen only in the small Stark splittings. On the other hand, RE 5d orbitals split significantly due to the CF. Here the energy levels are denoted as $a \sim e$ in the order of increasing energy. The splittings of RE 5d state into four groups of levels, a, b, (c and d), and e are due to the CF of S_4 symmetry while the small splitting between c and d is due to the spin–orbit interaction. The energy separation between RE 4f and RE 5d states increases as the atomic number increases.

3.3 Multiplet energy levels for $4f^n$ and $4f^{n-1}5d$ configurations

The results of the relativistic DVME calculations are presented in Figure 22.5, where the energy levels of $4f^n$ and $4f^{n-1}5d$ configurations for each element are shown on the left and right, respectively. In Figure 22.5, the lengths of the lines denote the contribution of each configuration. A short line on the left column indicates a partial contribution of the $4f^n$ configuration and there should be a corresponding short line representing a remaining partial contribution of the $4f^{n-1}5d$ configuration to the state on the right column. Although the short lines on the right columns are buried in a band formed with the full-length lines, we can estimate their contribution from the composition of $4f^n$ configuration. One can note from Figure 22.5 that, in the case of ions in YLF, there exists a significant mixture between $4f^n$ and $4f^{n-1}5d$ configurations, which is absent in the case of

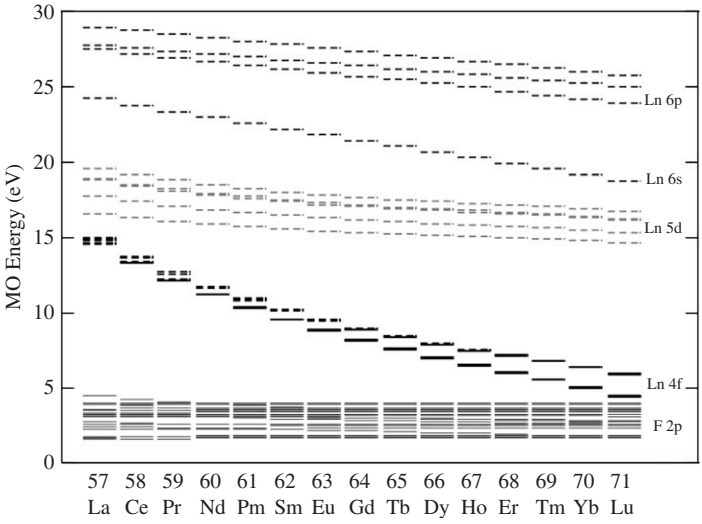

Figure 22.4 Calculated MO energy levels for trivalent RE ions in YLF.

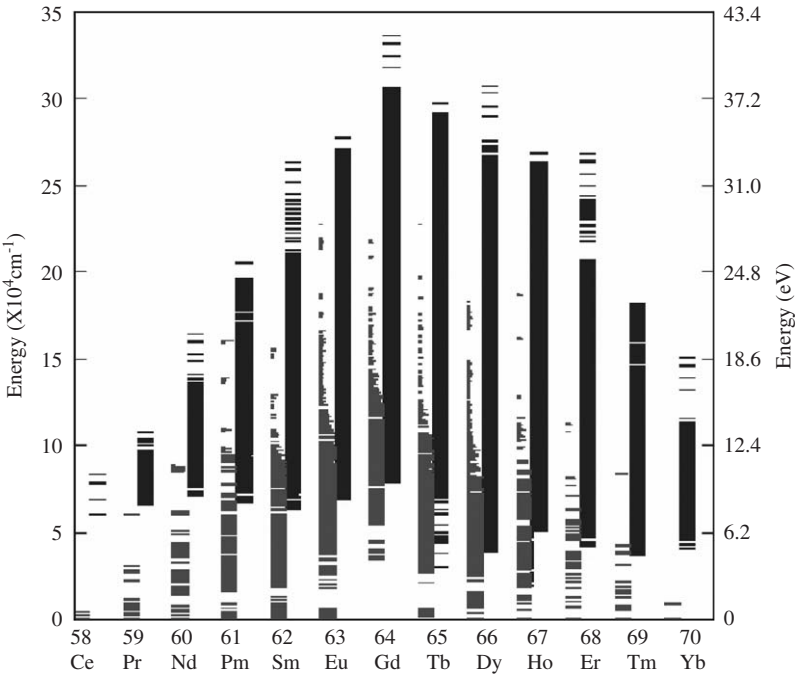

Figure 22.5 Complete $4f^n$ and $4f^{n-1}5d$ energy level diagram for all trivalent RE ions in YLF obtained by the first-principles relativistic CI calculations. For each element, the compositions of the $4f^n$ configurations are shown on the left and those of $4f^{n-1}5d$ configurations are shown on the right, respectively. See text for further explanations.

isolated ions due to the difference in parity [30]. The origin of this mixture is the lack of inversion symmetry in the S_4 point group. The calculated energy levels are overestimated typically by 20–30%. The major reason for this discrepancy is probably underestimation of electron correlations since only the states mainly composed of RE 4f or RE 5d characters were considered in the CI calculations due to our computational limitations. The inclusion of the other orbitals such as the states mainly composed of F 2p character into the CI active space is expected to reduce this overestimation.

Although the energy levels are overestimated in the first-principles method, if we take into account the element-specific scaling factor estimated from the free-ion calculations [30,31], the results of the first-principles method agree well with those of the semiempirical method and also with the experimental data such as the Dieke's diagram.

3.4 $4f^2-4f5d$ transition spectrum of Pr:YLF

In order to analyze the $4f^2-4f5d$ transitions, multiplet structures for the $4f^2$ and 4f5d configurations were calculated by the relativistic DVME method. The MOs mainly consisting of Pr 4f or Pr 5d states were used in the Slater determinants.

The number of states is 91 for the $4f^2$ configuration and 140 for the 4f5d configuration leading to a total of 231 levels as shown in Figure 22.5.

The calculated multiplet energy levels and configuration compositions within each multiplet state are shown in Figure 22.5. All levels within the range 0–7.65 eV correspond to the $4f^2$ configuration and all levels with higher energies correspond to 4f5d configuration. The mixing between the $4f^2$ configuration and the 4f5d configuration is almost negligible, which means there is practically no interaction between the $4f^2$ and 4f5d configurations.

The theoretical ground-state absorption (GSA) spectrum is compared to the experimental spectra [32,33] in Figure 22.6. Although the host crystal for the

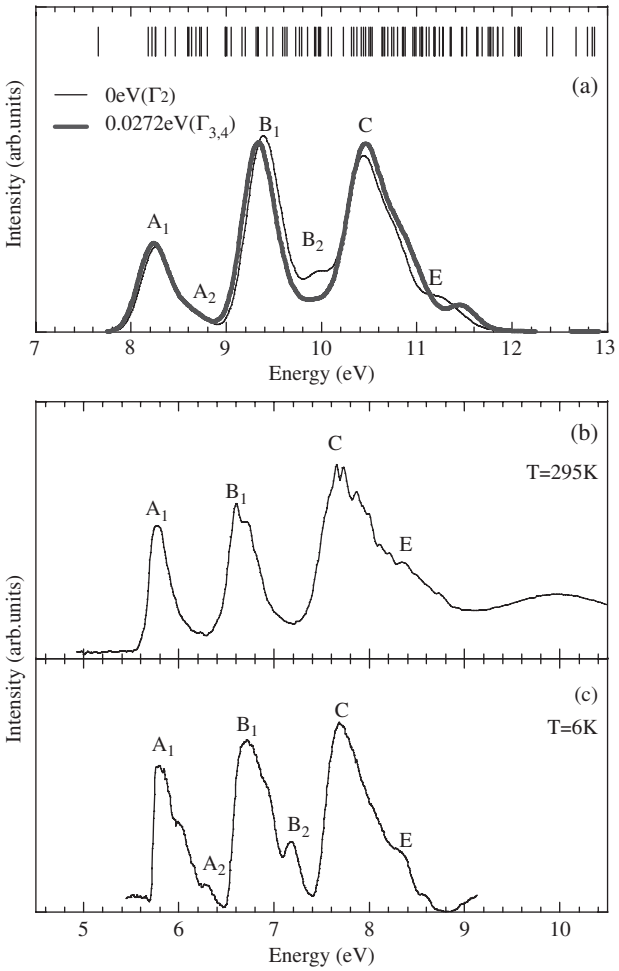

Figure 22.6 Ground-state absorption (GSA) spectrum for Pr^{3+}:$LiYF_4$ or Pr^{3+}:$LiLuF_4$. (a) Theoretical spectra of Pr^{3+}:$LiYF_4$ for 0 eV level (Γ_2)→4f5d and 0.0272 eV level ($\Gamma_{3,4}$)→4f5d; (b) experimental absorption spectrum of Pr^{3+}:$LiLuF_4$ [32]; (c) experimental excitation spectrum of Pr^{3+}:$LiYF_4$ [33].

experimental absorption spectrum is $LiLuF_4$, it can be compared to the theoretical spectrum for YLF, since the crystal structure of $LiLuF_4$ is the same as that of $LiYF_4$ with slightly different lattice parameters. Since the experiment was performed at room temperature, not only the lowest level (at 0 eV) of $^3H_4$ but also the first excited state at 0.0272 eV were considered as the initial states of the transitions because of the thermal population of the latter. The theoretical spectrum was calculated by convoluting the obtained oscillator strengths by a Gaussian function with 0.30 eV FWHM. It is shown on top of Figure 22.6 where the thin line represents the transitions for 0 eV level (Γ_2)→4f5d while the thick line represents transitions for 0.0272 eV level ($\Gamma_{3,4}$)→4f5d. The energy levels for the 4f5d configuration are also shown above the spectrum. The spectra from two different initial states are almost the same, which indicates small temperature dependence of the spectrum. Comparing with the experimental spectrum, peaks A_1, B_1, C, E are seen both in the observed and the theoretical spectra and relative positions and intensities of these peaks are reproduced. The spectrum shown in the bottom panel is the experimental excitation spectrum. Although the calculated intensities cannot be directly compared with the excitation spectrum [33], the positions of the peaks A_1 and A_2 are reproduced in the theoretical spectrum corresponding to absorption from the lowest state (thin line).

According to a detailed configuration analysis of the many-electron wave functions, peak A_1 corresponds to transitions to the $(4f_{5/2})(5d_b)$ configuration, while peak A_2 corresponds to transitions to the $(4f_{7/2})(5d_b)$ configuration. These results indicate that the splitting between peak A_1 and A_2 originate from the spin–orbit splitting of the Pr 4f levels. Similarly, the origin of the splitting between peak B_1 and peak B_2 is also the spin–orbit splitting of Pr 4f levels. In the whole spectra, the results of the configuration analysis indicate that the separations among peaks A, B, C are due to the CF splitting of Pr 5d levels.

3.5 $4f^{10}-4f^9$5d transition spectrum of Ho:YLF

The theoretical $4f^{10}\rightarrow 4f^9$5d absorption spectrum of Ho^{3+} in YLF is calculated and compared with the experimental excitation spectrum [34] in Figure 22.7. Each level was convoluted by a Gaussian function with 0.1 eV FWHM. Although the $4f^{10}-4f^9$5d transition energies are underestimated by about 0.5 eV, the agreement is better than in the case of Pr^{3+}. This is probably due to compensation of the overestimation of the energy intervals between the $4f^{10}$ and $4f^9$5d configurations by the overestimation of the multiplet splitting of the $4f^9$5d configuration. The former would increase the $4f^{10}\rightarrow 4f^9$5d transition energies while the latter would decrease the threshold energy of the $4f^{10}\rightarrow 4f^9 5d$ transitions. The experimental spectrum displays five main and broad bands labeled A, B, C, D, and E. There are characteristic features among the intensities of these peaks. The intensity changes alternately until peak D and peak E is the strongest. These features are also reproduced by CF calculations [35]. According to the first-principles calculations shown in Figure 22.7, the number of energy levels of this configuration is quite large and they almost form a band. However, when the transition probabilities from the ground state to these levels are calculated, only a limited number of states contribute

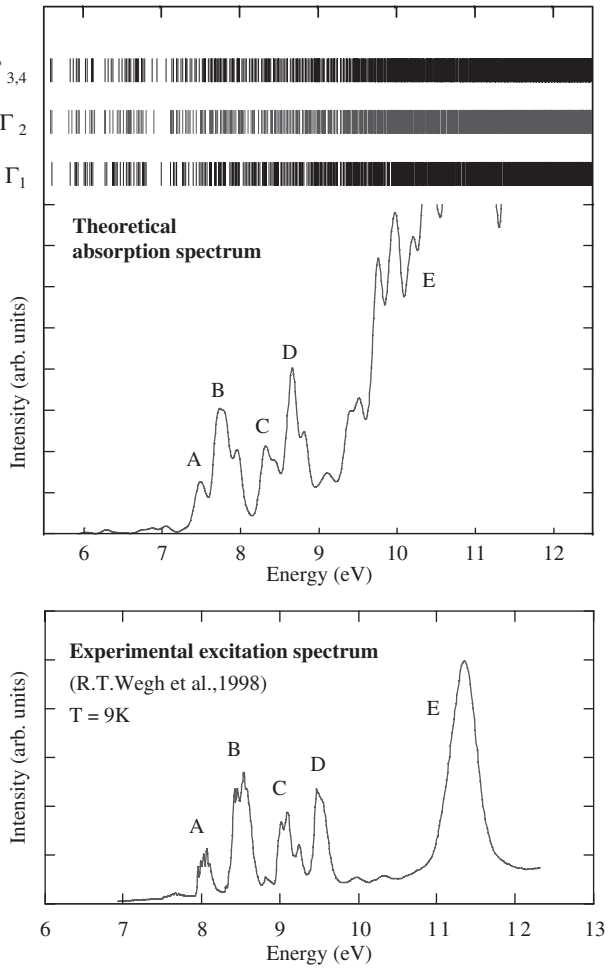

Figure 22.7 Theoretical $4f^{10} \rightarrow 4f^{9}5d$ absorption spectrum (top) and experimental excitation spectrum (bottom) [34] of Ho^{3+} in YLF.

to the transitions. As a result, the characteristic features of the experimental spectrum are well reproduced by the non-empirical relativistic DVME calculation.

3.6 $4f^{12}-4f^{11}5d$ transition spectrum of Tm:YLF

The theoretical $4f^{12}-4f^{11}5d$ absorption spectrum of Tm^{3+} in YLF is calculated and compared with the experimental excitation spectrum [34] in Figure 22.8. Each level is convoluted by a Gaussian function with 0.08 eV FWHM. The $4f^{12}-4f^{11}5d$ transition energies are underestimated by about 2.5 eV in this case. Again, this is probably due to compensation between the overestimation of the energy intervals between the $4f^{12}$ and $4f^{11}5d$ configurations and the overestimation of the multiplet splitting of the $4f^{11}5d$ configuration. In this case, the

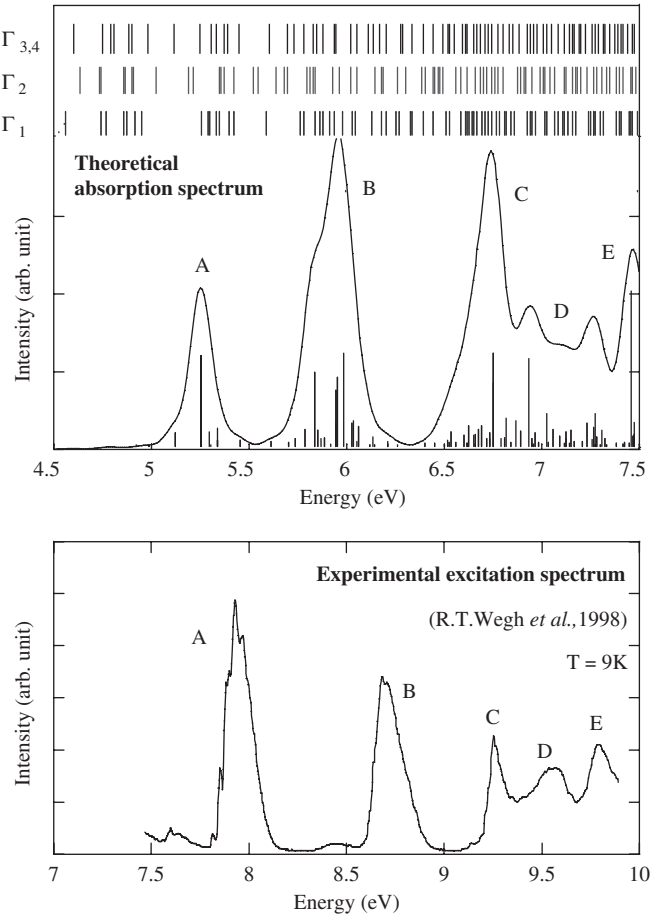

Figure 22.8 Theoretical $4f^{12} \rightarrow 4f^{11}5d$ absorption spectrum (top) and experimental excitation spectrum (bottom) [34] of Tm^{3+} in YLF.

latter is dominant due to the larger number of 4f electrons. Five broad lines labeled A, B, C, D, and E are seen in the experimental spectrum. The intensities of these peaks gradually decrease except the last one (peak E). In the theoretical spectrum, the intensity of peak A is underestimated, for a currently unknown reason. A similar underestimation of the intensity of peak A in CF calculations is also reported by van Pieterson et al. [35]. Therefore, the intensity variation is difficult to reproduce even by the CF calculation. A possible reason for this discrepancy is the effect of broadening. In this work, we have broadened each peak uniformly. However, the peak widths can be different for each peak. The number of energy levels of this configuration is also quite large. However, when transition probabilities from the ground state to these levels are calculated, only a limited number of states contribute to the peaks in the spectrum and the relative peak positions are well reproduced by the non-empirical relativistic DVME calculation.

4. MCD OF Cr $L_{2,3}$-EDGE XANES OF CrO_2

4.1 Model clusters for CrO_2

CrO_2 has a rutile type crystal structure [36]. The space group is $P4_2/mnm$, the crystal system is tetragonal, and the lattice constants are $a = 4.4190$ Å and $c = 2.9154$ Å. The point group of the Cr site is D_{2h} and the Cr–O bond lengths are 1.917 Å for four oxygen ions and 1.871 Å for the other two oxygen ions. In order to take into account the effects of the surroundings of the model cluster, an effective Madelung potential was considered by locating several thousand point charges at atomic sites outside the cluster. The number of the sampling points was 100,000 and the AOs used for the relativistic DV-Xα calculation were from 1s to 4p for Cr and from 1s to 2p for O. The MCD calculations were performed for two different alignments of the magnetic field (**H//a** and **H//c**) as shown in Figure 22.9. The applied magnetic field was 1 (T) for both calculations.

4.2 Theoretical MCD spectra

The theoretical MCD spectra of Cr $L_{2,3}$-edge XANES for **H//a** and **H//c** are shown in Figure 22.10, where I^R and I^L denote the intensities for the right polarization and the left polarization, respectively. In both spectra there are two main broad peaks at around 588 and 592 eV corresponding to the L_3-edge and L_2-edge, respectively. These peak energies are slightly overestimated compared to the experimental values which are 578 eV and 586 eV. In the MCD spectra for **H//a**, I^R is stronger than I^L at L_3 edge while I^L is stronger than I^R at the L_2-edge. On the other hand, in the case of MCD spectra for **H//c**, the I^R became stronger at L_2 edge especially at the lower energy side. As a result, the MCD spectra clearly change sign around L_2 edge depending on the direction of magnetic field.

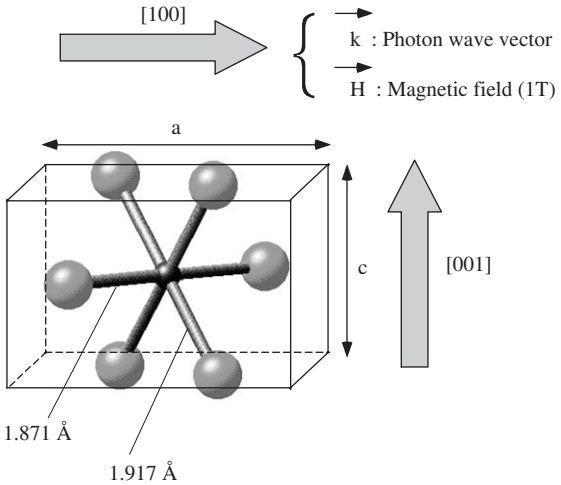

Figure 22.9 Model cluster of CrO_2 and alignments of the magnetic field.

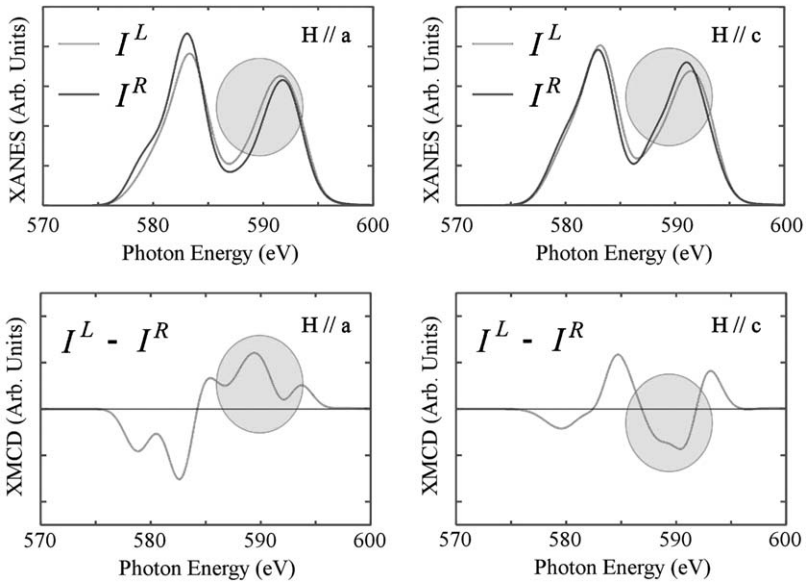

Figure 22.10 The theoretical Cr $L_{2,3}$-edge XANES for circularly polarized light and the corresponding MCD spectra for **H//a** and **H//c**.

Therefore, the characteristic anisotropy of MCD spectra for Cr $L_{2,3}$-edge XANES of CrO_2 was clearly reproduced without introducing any empirical parameters.

In addition to the theoretical MCD spectra we also calculated the expectation values of the spin and the orbital moments of Cr^{4+} ion using the explicitly obtained many-electron wave functions. The calculated magnetic moments are $\langle S_z \rangle = -0.481\mu_B$, $\langle L_z \rangle = 0.040\mu_B$ for **H//a** and $\langle S_z \rangle = -0.744\mu_B$, and $\langle L_z \rangle = 0.066\mu_B$ for **H//c**, where μ_B is the Bohr magneton. Therefore, the characteristic anisotropy of the MCD spectra is probably related to the large difference in $\langle S_z \rangle$.

5. SUMMARY AND PERSPECTIVES

In this paper, a detailed description of the fully relativistic DVME method was given and some recent applications of this method were exhibited.

As an application to the optical materials, we have shown the first-principles calculations of multiplet energy levels and $4f^n - 4f^{n-1}5d$ transition spectra of RE ions in YLF. The calculated energy levels provide a theoretical extension of the well known Dieke's diagram up to ca. 350,000 cm^{-1}. The origins of the peaks in the spectra were clarified based on the configuration analysis of the explicit many-electron wave functions.

As an application to magnetic materials, we have shown the first-principles calculation of the MCD spectra of Cr $L_{2,3}$-edge XANES of CrO_2. By performing the first-principles calculations of MCD spectra for different alignment of the applied magnetic field, the characteristic anisotropy of the MCD spectra has

been reproduced without using any empirical parameters. The spin and orbital magnetic moments were also estimated based on the explicit many-electron wave functions.

Currently, development of new programs for calculation of variety of physical properties such as magnetic dipole transitions, electric quadrapole transitions, etc. are in progress. The algorithm of the program is still constantly improved in order to perform faster and larger calculations. These new programs are expected to further enhance the applicability of the relativistic DVME method to a wide variety of research fields.

ACKNOWLEDGMENT

This work was supported in part by the Industrial Technology Research Grant Program in 2001 from the New Energy and Industrial Technology Development Organization (NEDO) of Japan and in part by the "Open Research Center" Project for Private Universities: matching fund subsidy from MEXT (the Japanese Ministry of Education, Culture, Sports, Science and Technology) and in part by the 2004 Yamada Science Foundation Grant.

REFERENCES

[1] D.E. Ellis, G.S. Painter, *Phys. Rev. B* **2** (1970) 2887.
[2] S. Sugano, Y. Tanabe, H. Kamimura, *Multiplets of Transition-Metal Ions in Crystals*, Academic Press, New York, 1970.
[3] D.J. Newman, B. Ng (Eds.), *Crystal Field Handbook*, Cambridge University Press, 2000.
[4] B.R. Judd, *Phys. Rev.* **127** (1963) 750.
[5] G.S. Ofelt, *J. Chem. Phys.* **37** (1962) 511.
[6] K. Ogasawara, T. Ishii, Y. Ito, H. Ida, I. Tanaka, H. Adachi, *Jpn. J. Appl. Phys.* **37** (1998) 4590.
[7] K. Ogasawara, T. Ishii, I. Tanaka, H. Adachi, *Mat. Trans. JIM* **40** (1999) 396.
[8] K. Ogasawara, T. Ishii, I. Tanaka, H. Adachi, *Phys. Rev.* **B61** (2000) 143.
[9] T. Ishii, K. Ogasawara, H. Adachi, I. Tanaka, *Appl. Phys. Lett.* **78** (2001) 2154.
[10] T. Ishii, K. Ogasawara, H. Adachi, I. Tanaka, *J. Chem. Phys* **115** (2001) 492–508.
[11] T. Ishii, K. Fujimura, K. Ogasawara, H. Adachi, I. Tanaka, *J. Phys. Condens. Matter* **13** (2001) 5757–5784.
[12] K. Ogasawara, T. Iwata, Y. Koyama, T. Ishii, I. Tanaka, H. Adachi, *Phys. Rev. B* **64** (2001) 115413.
[13] H. Ikeno, I. Tanaka, Y. Koyama, T. Mizoguchi, K. Ogasawara, *Phys. Rev. B* **72** (2006) 075123.
[14] G. Van der Laan, B.T. Thole, *Phys. Rev. B* **42** (1990) 6670–6674.
[15] B.T. Thole, P. Carra, F. Sette, G. van der Laan, *Phys. Rev. Lett.* **68** (1992) 1943–1946.
[16] P. Carra, B.T. Thole, M. Altarelli, X. Wang, *Phys. Rev. Lett.* **70** (1993) 694–697.
[17] Y. Teramura, A. Tanak, T. Jo, *J. Phys. Soc. Jpn.* **65** (1996) 1053–1055.
[18] K. Ogasawara, S. Watanabe, H. Toyoshima, T. Ishii, M.G. Brik, H. Ikeno, I. Tanaka, *J. Sol. State Chem.* **178** (2005) 412.
[19] G.H. Dieke, H.M. Crosswhite, *Appl. Opt.* **2** (1963) 675.
[20] G.H. Dieke, *Spectra and Energy Levels of Rare Earth Ions in Crystals*, Wiley Interscience, New York, 1968.
[21] E. Goering, A. Bayer, S. Gold, G. Schutz, *Phys. Rev. Lett.* **88** (2002) 207203.
[22] A. Rosén, D.E. Ellis, *Chem. Phys. Lett.* **27** (1974) 595.
[23] P.A.M. Dirac, *Proc. R. Soc. Lond.* **117** (1928) 610.
[24] P.A.M. Dirac, *The Principles of Quantum Mechanics*, Fourth ed.., Oxford University Press, 1958.
[25] J.C. Slater, *Quantum Theory of Molecules and Solids*, Vol. 4, McGraw-Hill, New York, 1974.
[26] C. Satoko, M. Tsukada, H. Adachi, *J. Phys. Soc. Jpn.* **45** (1978) 1333.
[27] P. Schwerdtfeger (Ed.), *Relativistic Electronic Structure Theory, Part 1 Fundamentals*, Elsevier, Amsterdam, 2002.

[28] S. Watanabe, H. Kamimura, *Mater. Sci. Eng. B* **3** (1989) 313.
[29] A.V. Goryunov, A.I. Popov, *Russ. J. Inorg. Chem.* **37** (1992) 126.
[30] K. Ogasawara, S. Watanabe, Y. Sakai, H. Toyoshima, T. Ishii, M.G. Brik, I. Tanaka, *Jpn. J. Appl. Phys.* **43** (2004) L611.
[31] K. Ogasawara, S. Watanabe, T. Ishii, M.G. Brik, *Jpn. J. Appl. Phys.* **44** (2005) 7488.
[32] E. Sarantopoulou, C. Cefalas, A.M. Dubinskii, A.C. Nicolaides, Y.R. Abdulsabirov, L.S. Korableva, K.A. Naumov, V.V. Semashko, *Appl. Phys. Lett.* **15** (1994) 813.
[33] M.F. Reid, L. van Pieterson, R.T. Wegh, A. Meijerink, *Phys. Rev. B* **62** (2000) 14744.
[34] R.T. Wegh, H. Donker, A. Meijerink, *Electrochem. Soc. Proc.* **97-29** (1998) 284.
[35] L. van Pieterson, M.F. Reid, R.T. Wegh, S. Soverna, A. Meijerink, *Phys. Rev. B* **65** (2000) 045114.
[36] J.K. Burdett, G.J. Miller, J.W. Richardson, Jr.., J.V. Smith, *J. Am. Chem. Soc.* **110** (1988) 8064–8071.

CHAPTER 23

Evaluation of Laboratory Ultra-Soft X-Ray Absorption Spectrometer by Li–K XANES Measurements and Their DV-Xα Calculations

Tsutomu Kurisaki*, Yuichi Nakazono*, Shuji Matsuo, Rupert C.C. Perera***, James H. Underwood***** and **Hisanobu Wakita***

Contents

Abstract

We have built a novel laboratory ultra-soft X-ray absorption (USXA) spectrometer optimized from 50 to 150 eV ultra-soft X-ray (USX) region, which is especially useful for the measurement of the absorption spectra of light elements such as lithium. We have measured the X-ray absorption near edge structure (XANES) spectra of some lithium halides by this spectrometer and evaluated the quality of the observed spectra from comparison with calculated spectra obtained by the discrete variational (DV) Xα molecular orbital (MO) calculation.

* Department of Chemistry, Faculty of Science, Fukuoka University 8-19-1 Nanakuma, Jonan-ku, Fukuoka, 814-0180, Japan
Corresponding author. E-mail: kurisaki@fukuoka-u.ac.jp
** Physical Analysis and Evaluation Department, Electronics Division, KOBELCO Research Institute, Inc., 1-5-5 Takatsukadai, Nishi-ku, Kobe, Hyogo 651-2271, Japan
*** EUV Technology, 6680 Alhambra Avenue #187, Martinez, CA 94553, USA

Advances in Quantum Chemistry, Vol. 54
ISSN 0065-3276, DOI 10.1016/S0065-3276(07)00023-8

1. INTRODUCTION

Inner shell absorption spectroscopy provides a map of unoccupied electronic states (or levels) and the electronic structures of conduction bands in the vicinity of the core-excited atom. The X-ray absorption spectroscopy (XAS) represents a fingerprint of the chemical state of the element. It provides useful means of nondestructive site-dependent chemical analysis of complex systems. Ultra-soft X-ray absorption (USXA) method is categorically interesting for chemical analysis of a variety of complex materials in battery industry, environmental science, and semiconductor industry.

Lithium compounds are used in industrial and commercial applications such as lithium ion batteries, lithium glasses, and medicines of a manic-depressive illness. The USXA method has not been widely used to estimate the characteristic of these materials owing to the low energy (below about 70 eV) of Li–K edge. It is difficult to measure the USXA, although the Li–K edge X-ray absorption near edge structure (XANES) spectra of lithium compounds have been reported previously [1–9]. Tsuji and co-workers [8] have reported the Li–K edge XANES spectra of lithium halides using the synchrotron radiation, and the observed spectra were assigned by using the DV-Xα method. However, in laboratory system spectra of lithium compounds have not been reported in previous studies.

In the present study, we have built a novel laboratory USXA spectrometer optimized for the 50–150 eV ultra-soft X-ray (USX) region and for the sample mounted horizontally. We examine the Li–K XANES spectral measurements of lithium halides using the USXA spectrometer. The obtained experimental XANES spectra are analyzed using the theoretically calculated spectra from the DV-Xα method.

2. OUTLINE OF THE SPECTROMETER

Figure 23.1 shows the schematic picture of our USXA spectrometer. The spectrometer consists of four sub-systems: (i) a laser and focusing optics; (ii) target and target chamber; (iii) monochromator; and (iv) detector system and sample chamber. A vacuum system, a power distribution system, pneumatic controls, and a control system with a computer interface exist. The laser light is focused to a tiny spot on the target, a thin metal tape. The intense pulse of light energy evaporates the metal and heats to a high temperature, so that it becomes ionized plasma that emits extreme ultraviolet light in a continuous spectrum. The laser is a Q-switched Nd:YAG laser which produces about 650 mJ of light at the fundamental (infrared) wavelength of 1064 nm, in a pulse 8 ns long. A frequency doubler converts about 350 mJ of this into light of 532 nm wavelength, and it is this green light that is focused on the target to produce USX radiation. The beam from the laser is first expanded and collimated by a 4 × beam expander. The light is turned from a vertical to a horizontal beam by a 45° mirror at the top of the light tube. A lens then focuses

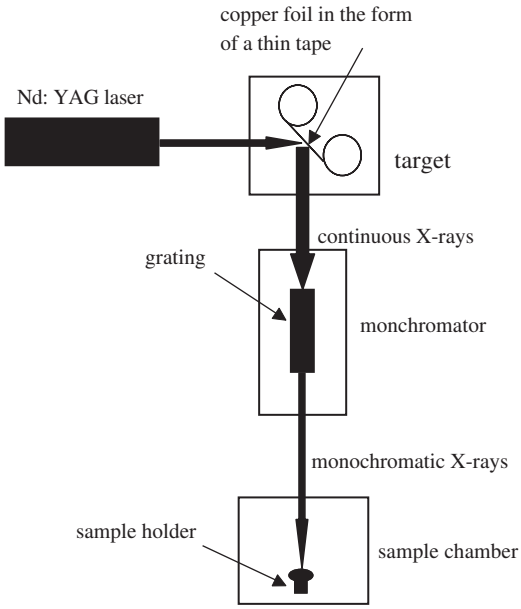

Figure 23.1 Schematic picture of ultra-soft X-ray absorption (USXA) spectrometer.

the light through a glass vacuum window to a tiny spot on the target. As for the detail mechanistic evaluation of this spectrometer, it is under preparation for submitting in another journal.

The spectrum of this radiation is essentially a continuum in the USX region. A small slice of the continuous spectrum from this source is selected by the monochromator and focused on to the sample. By scanning the monochromator, a spectrum of absorption versus wavelength can be obtained.

3. COMPUTATIONAL METHOD

The DV-Xα molecular orbital (MO) calculations were performed to analyze the Li–K XANES spectra of lithium halides powder. The computational details of the DV-Xα method have been previously described [10]. In this method, the exchange-correlation interaction, V_{xc}, between electrons is given by the Slater's Xα potential,

$$V_{XC} = -3\alpha\left[\frac{3}{8\pi}\rho(r)\right]^{1/3} \tag{1}$$

where $\rho(r)$ is the molecular charge density at the position r, α is the Slater exchange limit, fixed at 0.7 throughout the present work. The MO wave function

ϕ is expressed by a linear combination of atomic orbitals (LCAO) as

$$\phi_l = \sum_i C_{il}\chi_i \tag{2}$$

where χ_i denotes ith atomic orbital. The coefficient, C_{il} represents the spread of the ith atomic orbital at the lth molecular orbital. The atomic orbitals as the numerical basis function are obtained by solving the Schrödinger equations for each atomic potential in the molecule.

Cluster models shown in Figure 23.2 were constructed from respective crystal structure [11,12]. The crystal structure of LiX is NaCl-type. The bond lengths of Li–Cl and Li–Br are 2.570 and 2.751 Å, respectively. The calculation is performed for four clusters, $[LiX_6]^{5-}$ for model I, $[Li_{13}X_6]^{7-}$ for model II, $[Li_{13}X_{14}]^{-}$ for mode III, and $[Li_{19}X_{14}]^{5+}$ for model IV. The model clusters were embedded in the

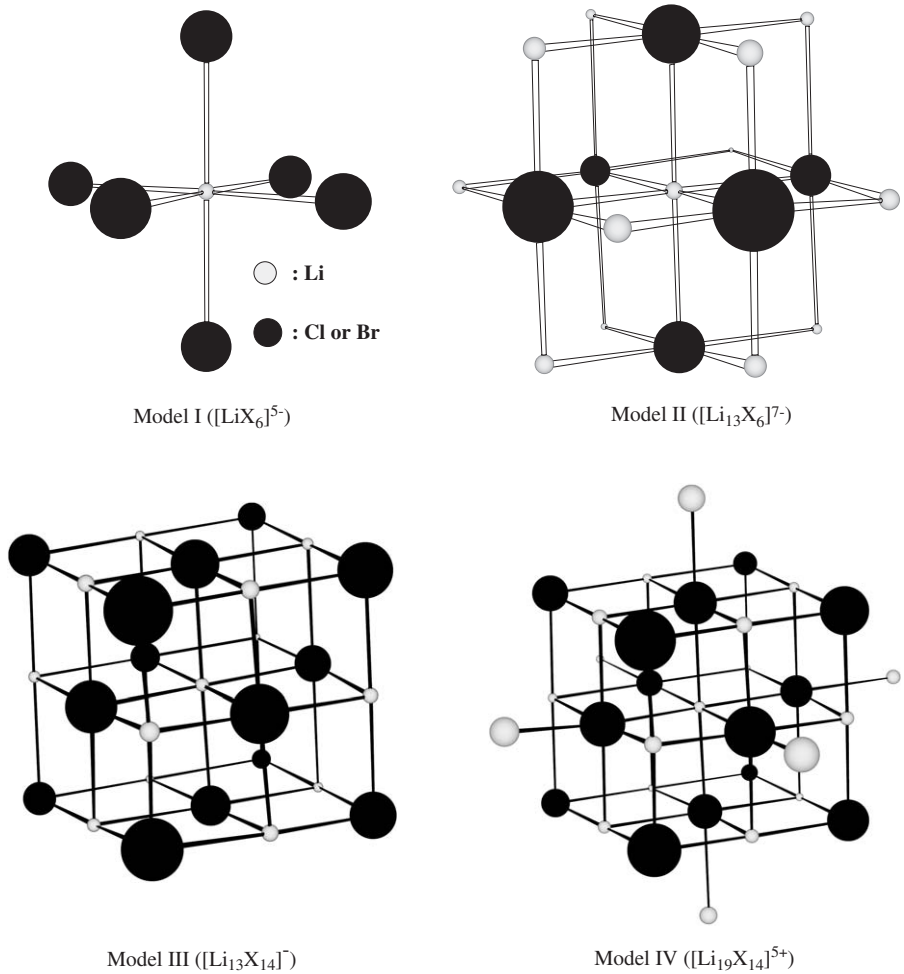

Figure 23.2 Models of lithium chloride and lithium bromide used for DV-Xα calculations.

Madelung potential generated by approximately 1,000 point charges of formal values. Numerical atomic orbitals of 1s to 2p for Li, 1s to 4p for Cl, and 1s to 4d for Br were used as a basis set for the DV-Xα calculations. The sample points used in the numerical integration were taken up to 500 points per atom for each calculation. A self-consistency of within 0.001 electrons was obtained for the final orbital populations. In order to obtain the net charge and the bond overlap population, the Mulliken population analysis was performed [13]. Transition probabilities calculated for each model were convoluted by a Gaussian function with a full width at half maximum (FWHM) of 1.0 eV to make transition peak shapes comparable with experimental XANES spectra. The calculated energy axis was shifted according to the experimental spectra.

4. RESULTS AND DISCUSSION

The measured XANES spectra for lithium chloride and lithium bromide are shown in Figure 23.3(a) together with the spectra measured at BL8B1 of UV-SOR (Figure 23.3(b)). The energy was calibrated by the first peak (60.6 eV) of LiBr. The spectra of lithium chloride and lithium bromide show four and three peaks, respectively. The characteristic peaks are labeled A, B, C, and D in Figure 23.3(a). Further, the energy positions of the absorption edges of measured XANES spectra shift to the lower energy side with the increase of the atomic number of

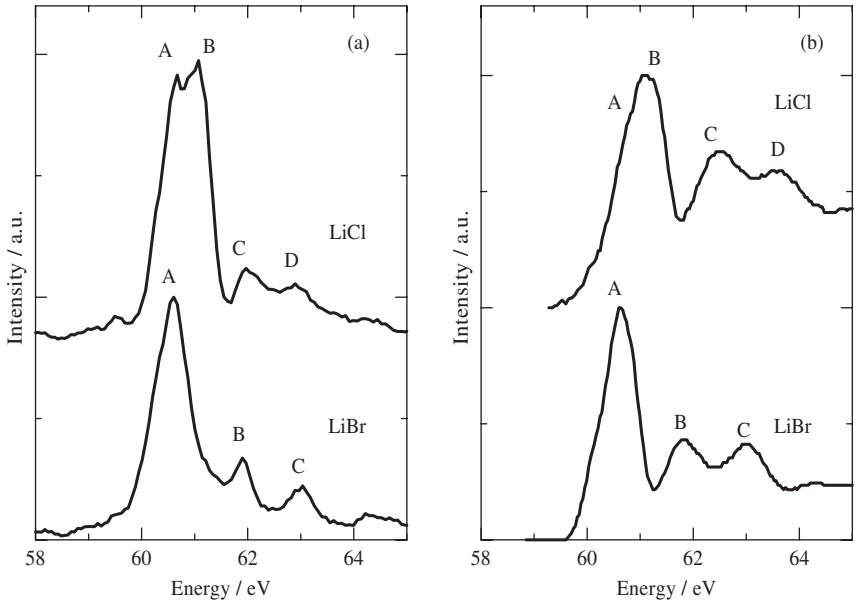

Figure 23.3 Li–K XANES spectra for lithium halides measured by (a) our spectrometer and (b) UV-SOR.

halide ions. These results suggest that we finally could build up a reliable enough spectrometer for our purpose.

Calculated transition probabilities and peaks for the four different models and the observed XANES spectra of lithium chloride and lithium bromide are shown in Figures 23.4 and 23.5. As can be seen from Figures 23.4 and 23.5,

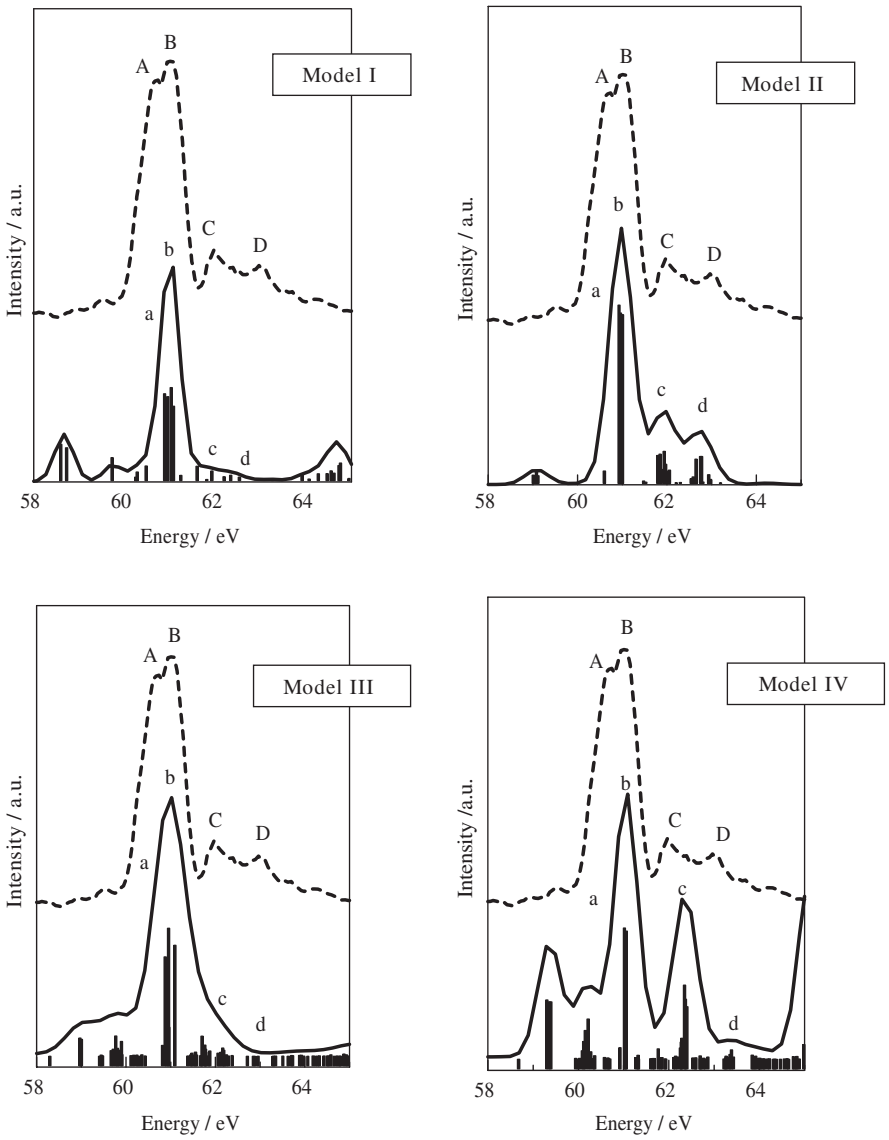

Figure 23.4 Calculated transition peaks (vertical bars) and curves (solid line) for models I–IV. The broken lines are the observed Li–K XANES spectra for lithium chloride.

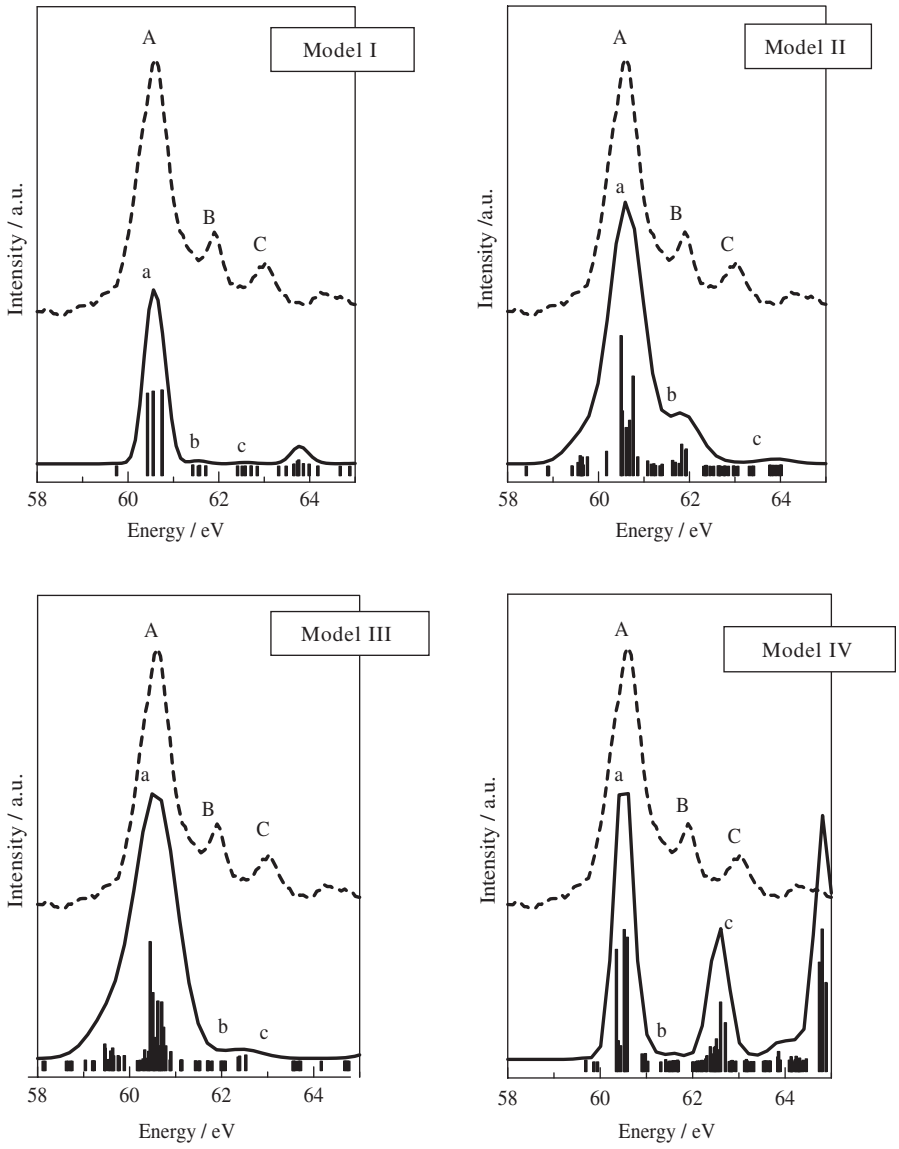

Figure 23.5 Calculated transition peaks (vertical bars) and curves (solid line) for models I–IV. The broken lines are the observed Li–K XANES spectra for lithium bromide.

the transition peaks for each model, I, III, and IV, cannot correctly represent the particular features in the observed XANES spectra, while those of model II are in good agreement. Nevertheless, model II could not explain peak C of lithium bromide. This peak assignment could be done by using DV-ME

calculation under the consideration of the relativistic effect of the bromine element.

The atomic orbitals constituting the molecular orbital of the prominent peaks and their proportions per atom for each atomic species are shown in Table 23.1. It is found that the molecular orbitals of each peak consist of the following orbitals: peak A (LiCl) consists of the neighboring Li 2s and 2p orbitals; peak B (LiCl) of the Li 2s, Li 2p, and Cl 3d orbitals; peaks C and D (LiCl) of the neighboring Li 2p orbital; peak A (LiBr) of the Li 2p orbital; peaks B and C (LiBr) of the neighboring Li 2p orbital.

Table 23.2 shows the net charge of the center lithium ion and the bond overlap population between the center lithium ion and neighboring halide ions obtained for model II. The net charge values decrease with increasing atomic number of halide ion. On the other hand, the bond overlap population values are almost identical. This is probably due to increased electronic charge around the lithium ion.

Table 23.1 The atomic orbitals constituting the molecular orbital of prominent peaks and their proportions

Atomic orbital and its proportion[a] (%)						
LiCl						
Peak	Li 2s	Li 2p	Li 2s[b]	Li 2p[b]	Cl 3d	Cl 4s
A	0	0	25	45	10	15
B	20	25	15	10	25	
C	0	0	25	50	15	
D	0	0	10	65	15	
LiBr						
Peak	Li 2s	Li 2p	Li 2s[b]	Li 2p[b]	Br 4d	
A	20	40	0	20	20	
B	0	0	30	60	0	
C	0	0	0	90	10	

[a]Proportion per atom for atomic species.
[b]The neighboring Li.

Table 23.2 Net charge and bond overlap population

	Net charge of central Li	Bond overlap population of central Li-halide ions (average)
LiCl	0.355	0.139
LiBr	0.280	0.148

5. CONCLUSIONS

We have built a novel laboratory USXA spectrometer and measured the Li–K XANES spectra of lithium halides. The measured spectra were compared with those of the synchrotron instrument. The results indicated the Li–K XANES spectra can be measured by using this spectrometer by the same quality as the synchrotron instrument. The Li–K XANES spectra of lithium chloride and lithium bromide were analyzed by using the DV-Xα calculations. The obtained XANES spectra could be assigned by using $[Li_{13}X_6]^{7-}$ cluster model.

ACKNOWLEDGMENTS

This study was partially supported by a Grant-in-Aid for Scientific Research (B) (17350041) from the Japan Society for the Promotion of Science and the Advanced Materials Institute of Fukuoka University.

REFERENCES

[1] R. Haensel, C. Kunz, B. Sonntag, *Phys. Rev. Lett.* **20** (1968) 262.
[2] F.C. Brown, C. Gahwiller, A.B. Kunz, N.O. Lipari, *Phys. Rev. Lett.* **25** (1970) 927.
[3] A.B. Kunz, J.T. Devreese, T.C. Collins, *J. Phys. C* **5** (1972) 3259.
[4] A.B. Kunz, D.J. Mickish, T.C. Collins, *Phys. Rev. Lett.* **31** (1973) 756.
[5] B.F. Sonntag, *Phys. Rev. B* **9** (1974) 3601.
[6] H. Petersen, *Phys. Rev. Lett.* **35** (1975) 1363.
[7] J. Tsuji, K. Kojima, S. Ikeda, H. Nakamatsu, T. Mukoyama, K. Taniguchi, *Adv. X-Ray Chem. Anal. Jpn.* **31** (2000) 149.
[8] J. Tsuji, K. Kojima, S. Ikeda, H. Nakamatsu, T. Mukoyama, K. Taniguchi, *J. Synchrotron Radiat.* **8** (2001) 554.
[9] J. Tsuji, H. Nakamatsu, T. Mukoyama, K. Kojima, S. Ikeda, K. Taniguchi, *X-Ray Spectrom.* **31** (2002) 319.
[10] H. Adachi, M. Tsukada, C. Satoko, *J. Phys. Soc. Jpn.* **45** (1978) 875.
[11] H. Ott, *Z. Kristallogr.* **63** (1926) 231.
[12] H. Ott, *Physik. Z.* **24** (1923) 209.
[13] R.S. Mulliken, *J. Chem. Phys.* **23** (1955) 1833.

CHAPTER 24

Ab Initio Calculation of the Electronic Structure of ZnO with an Impurity from Li to Bi

Yusuke Kinoshita*, Takayuki Noguchi*, Takeshi Inoue*, Takumi Tomita*[1] and **Yoshinori Hayafuji***

Contents

Abstract

We calculated the electronic structures of ZnO with an impurity atom from lithium to bismuth in the periodic table to study the energy levels of the impurities by the discrete-variational (DV)-Xα method using the program code SCAT. Atomic cluster models used in the calculations were based on two kinds of ZnO clusters: $(Zn_{29}O_{56}X)^{56-}$ and $(Zn_{56}YO_{96})^{78-}$, whose centers were occupied by an X atom located at its O site or by a Y atom located at its Zn site, where the X and Y atoms were impurity atoms from lithium to bismuth. The calculated energy level diagrams for almost all the ZnO cluster

* Graduate School of Science and Technology, Kwansei Gakuin University, 2-1 Gakuen, Sanda, Hyogo 669-1337, Japan
Corresponding author. E-mail: scbc1061@ksc.kwansei.ac.jp

[1] Present address: SHARP Corporation.

Advances in Quantum Chemistry, Vol. 54
ISSN 0065-3276, DOI 10.1016/S0065-3276(07)00024-X

models with the impurity gave us impurity energy levels in the energy gap between the highest occupied and lowest unoccupied molecular orbitals. The results showed that it is likely for a part of group-IA, -IIA, and -VIIA elements in the O site to be shallow donors as well as group-VA elements to be shallow acceptors, and also for a part of group-IA elements in the Zn site to be shallow acceptors as well as group-VIB elements to be shallow donors.

1. INTRODUCTION

Zinc oxide (ZnO) is one of the II–VI compound semiconductors with a wide bandgap of 3.37 eV at room temperature. It is well known that undoped ZnO naturally exhibits high n-type conductivity. This is due to the formation of intrinsic donors by intrinsic defects such as oxygen vacancies or zinc interstitials [1]. Not only the concentration but also the formation mechanisms of the intrinsic donor are not well understood yet, because they are determined in practice by the history of the sample. Such donor formation makes it difficult for us to control carrier concentration in ZnO, especially in p-type ZnO, because it is determined by the net concentration of carriers by the above intrinsic donors and extrinsic n- or p-type impurities. In general, both acceptor- and donor-type impurities may be present simultaneously in practical semiconductor materials. The conductivity type of the semiconductor is then determined by the impurity which is present in the greater concentration. Aluminum and gallium are usually used as donor impurities for the n-type conductive ZnO [1] and also nitrogen and phosphorus as acceptor impurities for the p-type ZnO [2] with a small activation energy of the order of kT at $T = 300$ K, i.e., those with binding energies of 0.025 eV. These are referred to as shallow impurities.

Generally speaking most of the shallow impurity levels which we shall encounter are based on substitution by an impurity atom for one of the host atoms. An atom must also occupy an interstitial site to be a shallow impurity. In fact, interstitial lithium in silicon has been reported to act as a shallow donor level. All of the impurities associated with shallow impurity levels are not always located at the substitutional sites, but a part of the impurities are at interstitial sites. Indeed, about 90% of group-VA elements and boron implanted into Si almost certainly take up substitutional sites; i.e., they replace atoms of the host lattice, but the remaining atoms of 10% are at interstitial sites. About 30% of the implanted atoms of group-IIIA elements except boron are located at either a substitutional site or an interstitial site, and the other 40% atoms exist at unspecified sites in Si [3]. The location of the impurity atoms in the semiconductors; substitutional, interstitial, or other site, is a matter of considerable concern to us, because the electric property depends on whether they are at the substitutional, interstitial, or other sites. The number of possible impurity configurations is doubled when we consider even substitutional impurities in a compound semiconductor such as ZnO and gallium arsenide instead of an elemental semiconductor such as Si [4].

The situation with II–VI semiconductors such as ZnO is similar to the situation with the elemental and the III–V semiconductors in respect of the location of the impurity atoms and their influences on the electric property. It is reported in ZnO that P, As, or S atom replaces either Zn or O site, and a part of them are also located at an interstitial site, as well as at a substitutional site [2,5–7]. The effect of a few kind of impurities such as group-IIIA and -VA elements on the electric property of ZnO was extensively studied, especially when the impurity atoms were located at a substitutional site. The effects of the greater part of elements in the periodic table on the electric property of ZnO are, however, not well understood yet. The purpose of the present study is to calculate energy levels of the impurity atoms; from Li to Bi in the periodic table, to clarify the effect of impurity atoms on the electric property of ZnO. In the present paper, we consider double possible configuration of the impurity atoms in ZnO: an atom substitutes the cation lattice site, while another atom also substitutes the anion sublattice site. The calculations of the electronic structure are performed by the discrete-variational (DV)-Xα method using the program code SCAT [8,9].

2. CLUSTER MODELS AND COMPUTATIONAL PROCEDURE

ZnO crystallizes with the wurtzite structure having space group $P6_3mc$ of hexagonal symmetry with lattice parameters, $a = 3.250$ Å and $c = 5.207$ Å [10]. The wurtzite structure consists of two interpenetrating hexagonal close-packed lattices, shifted by 3/8 of c along the z axis to each other. In this structure, the Zn (or O) atoms are tetrahedrally coordinated with four O (or Zn) atoms 1.992 Å apart from each other. We may choose to regard the structure as composed of two tetrahedral building blocks with one bond along [0 0 1], placed so that the orientation of the remaining bonds differs by rotation by π around the z axis.

Atomic cluster models used in the present study were based on the following two kinds of the ZnO clusters, as shown in Figure 24.1: one was a $(Zn_{29}O_{57})^{56-}$ cluster model whose center was occupied by an O atom, and another one was a $(Zn_{57}O_{96})^{78-}$ cluster model whose center was occupied by a Zn atom. To study energy levels of ZnO with a variety of impurity atoms, electronic structures were calculated using a series of $(Zn_{29}O_{56}X)^{56-}$ and $(Zn_{56}YO_{96})^{78-}$ clusters with an X or a Y impurity atom replacing the O or Zn atoms at the center of the clusters, respectively, where the X and Y atoms were 78 atoms from Li to Bi without radioactive elements. These cluster models with a roughly spherical shape were embedded in a three-dimensional array of approximately 30,000 point charges with the formal charges of +2.00e for the Zn site and −2.00e for the O site. The three-dimensional array of the point charges were located within about 40 Å radius outside the cluster model for considering a Madelung potential inside the cluster as well as in a crystal. The Madelung potential is of central importance in the theory of ionic crystal, which is the total energy of ions, calculated by the summation of the interaction energy between two ions.

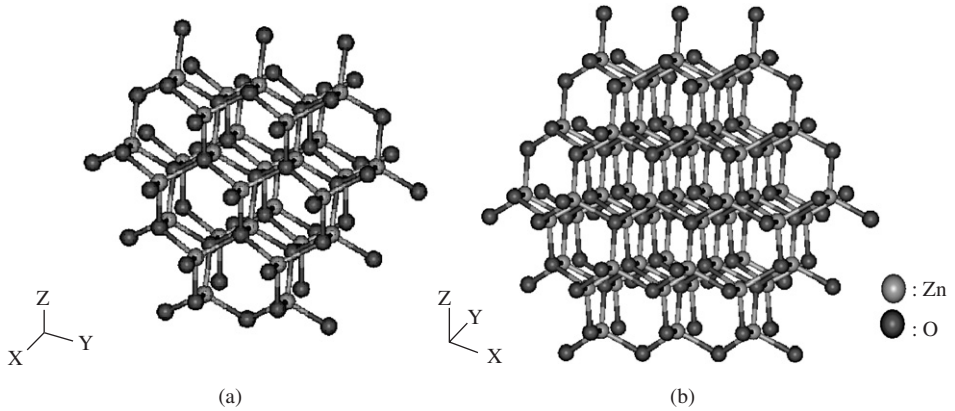

Figure 24.1 Basic cluster models used; (a) the $(Zn_{29}O_{57})^{56-}$ cluster with an O atom at the center of the cluster, and (b) the $(Zn_{57}O_{96})^{78-}$ cluster with a Zn atom at the center of the cluster. For a colour version of this figure please see the colour plate section near the end of the book.

The wave eigenfunctions and energy eigenvalues were obtained by real space electronic state calculations, which were performed by the use of the program code SCAT of the DV-Xα molecular orbital (MO) cluster method with the Hartree–Fock–Slater approximation [8,9]. In the method, the exchange-correlation term V_{xc} in the one-electron Hamiltonian was expressed in terms of the statistical local potential (1),

$$V_{xc}(\mathbf{r}) = -3\alpha\left\{\frac{3}{8\pi}\rho(\mathbf{r})\right\}^{1/3}, \tag{1}$$

where $\rho(\mathbf{r})$ was the local electron density at $\mathbf{r}$, and α was the scaling parameter in the DV-Xα method; α was set to $\alpha = 0.7$ throughout the present work. A random sampling method was used for calculating the matrix elements of the Hamiltonian and the overlap integrals. The number of sampling points for the DV calculation was 1,000 points per atom.

Molecular orbitals (MOs) were constructed using linear combinations of basis functions of atomic orbitals. The MO eigenfunctions were obtained by solving the Schrödinger equations in numerical form, including 1s−(n+1)p, that is to say, 1s, 2s, 2p, –ns, np, nd, (n+1)s, (n+1)p orbitals for elements from n-th row in the periodic table and 1s–2p orbitals for O, where $n-1$ corresponded to the principal quantum number of the valence shell.

A Mulliken overlap population analysis [11] was employed to analyze the atomic orbital components in the energy levels caused by the impurities and to estimate the net charges of ions. The net charge ΔQ_X, for example, for the atom X with an atomic number Z was defined by the following equations:

$$\Delta Q_X = Z_X - Q_X, \tag{2}$$

$$Q_X = \sum_X Q_i, \tag{3}$$

$$Q_i = \sum_l Q_i^l, \tag{4}$$

$$Q_i^l = \sum_j Q_{ij}^l. \tag{5}$$

The quantity $Q_{ij}^l = n_l c_{ij} c_{jl} S_{ij}$ was the partial overlap population, namely, electron population of the overlapped region between the atomic orbitals χ_i and χ_j in the MO ϕ_l, where n_l is the number of electrons in the MO ϕ_l (usually $n_l = 2$), c_{il} and c_{jl} the contribution of atomic orbitals, and S_{ij} the overlap integral.

3. RESULTS

3.1 Estimations of the net charge of O and Zn atoms

The calculated net charges ΔQ_O and ΔQ_{Zn} were obtained to be −1.07e and +1.07e for the centered O atom and the first nearest-neighbor Zn atoms, respectively, in the $(Zn_{29}O_{57})^{56-}$ cluster model, and to be −1.09e and +1.09e for the centered Zn atom and the first nearest-neighbor O atoms, respectively, in the $(Zn_{57}O_{96})^{78-}$ cluster model, almost independent of the number of point charges with ±2.00e in the three-dimensional array. These calculated net charges differed fairly from the formal net charges of −2.00e and +2.00e, but agreed closely with the experimental values of −1.06e and +1.06e, respectively. Thus, the number of point charges in the three-dimensional array was fixed at the formal charges of +2.00e for the Zn site and −2.00e for the O site through the whole course of this study. The experimental and calculated net charges ΔQ_O and ΔQ_{Zn} are shown in Table 24.1 for the experimental [12] and calculated values, respectively.

3.2 Energy levels of the O-substitutional impurities for $(Zn_{29}O_{56}X)^{56-}$

The calculated band gap energy for the $(Zn_{29}O_{57})^{56-}$ cluster model was obtained to be 3.95 eV, which was relatively larger than the experimentally obtained value

Table 24.1 Experimental and calculated net charges in e

		Effective net charges (e)	
		ΔQ_O	ΔQ_{Zn}
Experimental		−1.06	+1.06
Calculated	$(Zn_{29}O_{57})^{56-}$	−1.07	+1.07
	$(Zn_{57}O_{96})^{78-}$	−1.09	+1.09

of 3.37 eV [1]. The disagreement between the calculated and experimental band gap energies may be due to the size effect of the small $(Zn_{29}O_{57})^{56-}$ cluster model.

Figure 24.2 shows energy levels for the $(Zn_{29}O_{56}X)^{56-}$ cluster model with the impurity X at the O substitutional site.

We consider that the monovalent substitutional impurities generate one localized energy level in the band gap. When the number of valence electrons of the polyvalent impurities differs from that of the host atoms by two or more, the excess electrons, or holes if there is a deficiency of valence electrons, generate two or more localized energy levels in the band gap. For simplicity, however, we plotted in Figure 24.2 only the shallowest donors or acceptors among such two or more localized energy levels in the band gap for the polyvalent impurities. Along the horizontal direction of this figure, the data are all arranged according to the atomic number of the impurity element in the periodic table. The upper and lower solid lines are the energy levels of the lowest unoccupied molecular orbital (LUMO) and the highest occupied molecular orbital (HOMO), respectively. The region in energy gap between the LUMO and the HOMO corresponds to the energy band gap in the ZnO crystal. The energy levels for the impurities were measured from the top of the HOMO. Three symbols: —, ◆, ▲ denote a single donor and/or an acceptor, a double donor, and a double acceptor, respectively.

The monovalent substitutional impurities of group-VA element such as N, P, As, Sb, or Bi produced single shallow acceptor levels with the ionization energy of 0.087 eV for N, 0.140 eV for P, 0.064 eV for As, 0.277 eV for Sb, and 0.632 eV for Bi from the level of the HOMO, namely, above the upper edge of the valence band, respectively, by substituting host O atoms. These acceptor energy levels were shallower than all the energy levels produced by other impurities used in this study. The acceptor energy levels of the group-VA impurities became deeper

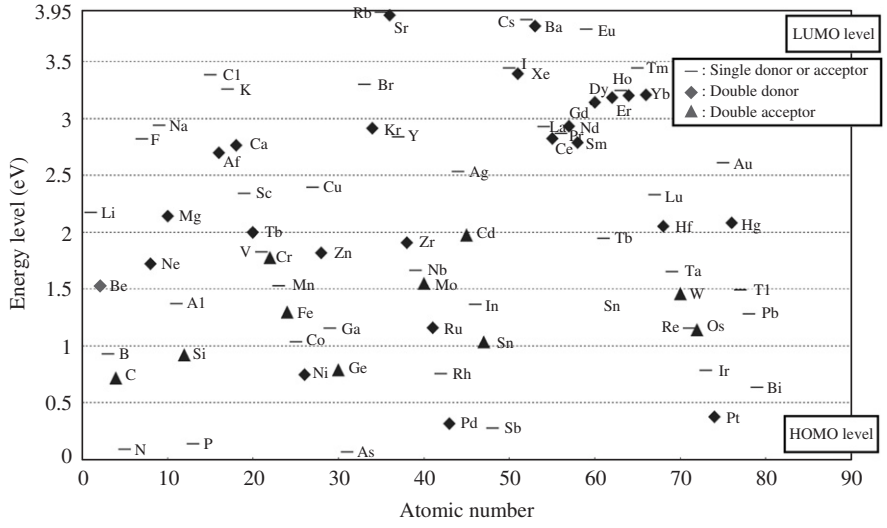

Figure 24.2 Impurity energy levels in the gap for $(Zn_{29}O_{56}X)^{56-}$ with the impurity at the O substitutional site.

as the row number of the periodic table increased. Some monovalent substitutional impurities of another type of group-VIIA elements such as F, Cl, Br, or I produced single shallow donor level with the ionization energy of 1.132 eV for F, 0.568 eV for Cl, 0.655 eV for Br, and 0.511 eV for I from the LUMO, namely, below the lower edge of the conduction band, respectively, by substituting the host O atom.

The bivalent substitutional impurities of group-IVA elements such as C, Si, Ge, Sn, or Pb also produced double shallow acceptor levels with the ionization energy of 0.721 eV for C, 0.919 eV for Si, 0.792 eV for Ge, 1.034 eV for Sn, and 1.283 eV for Pb, respectively. Some bivalent substitutional impurities of another type of group-VIIIA elements such as Ne, Ar, Kr, or Xe did not produce any energy levels in the band gap by the substituting host O atom. As expected, the acceptor levels produced by the impurities of group-VA and -IVA elements at the O site were single or double acceptors, respectively. Quantitave analysis of these shallow acceptors produced by the monovalent and bivalent substitutional impurities will be made in Section 4.2.

Some impurity elements of group-IA such as K, Rb, or Cs, and of group-IIA such as Sr or Ba, at the O site produced shallow donors in an energy range of 0.016–1.124 eV below the lower edge of the conduction band. These donor energy levels of group-IA and IIA impurities became almost shallower within the same group as the row number increased, contrary to the behavior of the acceptors.

Although it has been found that even isovalent atoms may act as electrically active impurities in compound semiconductors such as GaP, isovalent atoms of group-VIA such as S, Se, and Te replacing the O atoms in ZnO did not produce any energy levels in the band gap. It is also worth noting that the depth of the energy levels of the impurities in the same row in the periodic table, measured from the upper edge of valence band became smaller as a distance between the columns of O atom: sixth column and the column of the impurity atoms decreased.

3.3 Energy levels of the Zn-substitutional impurities for $(Zn_{56}YO_{96})^{78-}$

The calculated band gap energy for the $(Zn_{57}O_{96})^{78-}$ cluster model was obtained to be 2.91 eV, which crudely agreed with the experimental value of 3.37 eV. The difference was only 0.4 eV. This agreement showed that the computational procedure was reliable to a certain extent and the size effect of the small $(Zn_{57}O_{96})^{78-}$ cluster model could be negligible on calculation.

Figure 24.3 shows energy levels for the $(Zn_{56}YO_{96})^{78-}$ cluster model with the impurity Y at the Zn substitutional site. Along the horizontal direction of this figure, the data are also arranged according to the atomic number of the impurity elements. The symbols and the horizontal solid lines used in this figure are the same as in Figure 24.2.

The monovalent substitutional impurities of group-IIIA element such as B, Al, Ga, In, or Tl produced single, relatively shallow donor levels with the ionization energies of 0.930 eV for B, 0.806 eV for Al, 0.820 eV for Ga, 0.872 eV for In, and 0.867 eV for Tl below the lower edge of the conduction band, respectively, by

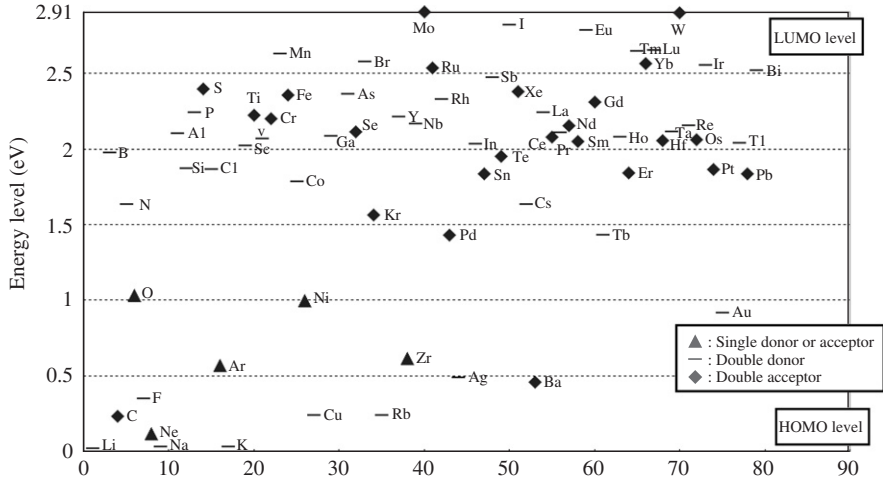

Figure 24.3 Impurity energy levels in the gap for $(Zn_{56}\ YO_{96})^{78-}$ with the impurity Y at the Zn substitutional site. The meanings of the symbols used in this figure, —, ◆, and ▲ are the same in Figure 24.2.

substituting the host Zn atom. Some monovalent substitutional impurities of other type of group-IA elements such as Li, Na, K, and Rb, except Cs, produced very shallow, single acceptor levels with the ionization energies of 0.020 eV for Li, 0.030 eV for Na, 0.028 eV for K, 0.239 eV for Rb, and 2.062 eV for Cs above the upper edge of the valence band, respectively, by substituting the host Zn atoms.

Some monovalent substitutional impurities of group-IB elements such as Cu, Ag, and Au did not produce shallow acceptor levels. The bivalent impurity atoms of group-IVA and -VIII substituting Zn atoms did not produce any shallow energy levels but deep levels, in marked contrast to the case of the bivalent impurity atoms substituting O atoms. The isovalent atoms of group-IIA such as Be, Mg, Ca, Sr, or Ba replacing the Zn atoms also did not produce any energy levels in the band gap. It is very interesting that the impurities of group-VIB elements such as Cr, Mo, or W produced very shallow double donors with the ionization energies of 0.704 eV for Cr, 0.0001 eV for Mo, 0.0009 eV for W, respectively.

4. DISCUSSION

4.1 Electrical behavior and lattice positions of impurities in ZnO [13]

ZnO is an important material for next-generation short-wavelength optoelectronic devices and has been recently investigated extensively for optoelectronic applications. To realize these device applications, ZnO has several disadvantages, including lack of reproducible and high-quality p-type material. ZnO has the asymmetric doping limitation, i.e., it can be an easily doped high-quality n-type,

but it is difficult to dope to p-type due to the self-compensating effect from native defects: vacancies at O sites, V_O, and Zn interstitial atoms, Zn_i. n-type ZnO is easily realized via Al, Ga, or In doping, while p-type doping ZnO has proven difficult to achieve. Recent research in p-type impurities, therefore, has focused on group-V elements substituted at the O site.

4.1.1 n-type ZnO

ZnO exhibits naturally n-type conductivity through electron doping via defects, originating from Zn_i and V_O in the ZnO lattice [14]. The concentration of the intrinsic defects was estimated to be normally of the order of $10^{18}\,cm^{-3}$. The intrinsic defect levels that led to n-type doping was reported to lie approximately 0.05 eV [14] or about 0.2 eV [15] below the conduction band. In the concentration range of the order of $10^{18}\,cm^{-3}$ [16], however, the intrinsic defect donor band was considered to most likely arise from intrinsic lattice defects.

The fabrication of n-type ZnO is easily realized, while the fabrication of p-type ZnO is rather difficult due to the self-compensating effect from intrinsic defects. Additional electron carriers can be produced normally via doping of group-IIIA substitutional elements such as B, Al, Ga, In, or Tl with impurity concentration over the order of $10^{18}\,cm^{-3}$, which act as shallow donors. Many papers are published in the studies on the fabrication of n-type ZnO. We can find few papers describing the electronic structures of ZnO with group-IIIA substitutional elements. In high doping concentration over $10^{18}\,cm^{-3}$, the impurity energy levels also may form impurity donor band. The impurity donor band, the intrinsic defect donor band, and conduction band were reported to merge at increasing carrier concentration by doping group-IIIA substitutional elements [17]. This is one of the reasons that there is a lack of the detailed information of the electronic structure including the energy levels of group-IIIA substitutional elements in ZnO.

4.1.2 p-type ZnO

Recently many groups tried to grow p-type ZnO. Some groups succeeded to fabricate p-type N-doped ZnO, which was reasonable because N had a similar ionic radius as O and was easily substitutable. Look et al. reported [18] that the analysis of photoluminescence spectra showed the acceptor energy levels of N to be in the range of 0.170–0.200 eV in N-doped p-type ZnO at a $9 \times 10^{16}\,cm^{-3}$ hole concentration.

Hwang et al. [19] reported that the acceptor energy level of the phosphorus (P) impurity was estimated to be located at 0.127 eV above the valence band on the study of the free electron to the acceptor transition at 3.310 eV from the photoluminescence spectra of P-doped p-type ZnO films grown by rf-frequency magnetron sputtering. They also suggested that the emission lines at 3.310 and 3.241 eV of the photoluminescence spectra could be attributed to a conduction band to the P-related acceptor transition and a donor to the acceptor pair transition, respectively.

Ryu et al. [20] reported that the experimentally obtained ionization energy of the As acceptor was in the range of 0.115–0.164 eV using As-doped p-type ZnO

grown by hybrid beam deposition and the calculated As-acceptor ionization energy was 0.130 eV on the assumption that As was a hydrogen-like acceptor in ZnO with $m^* = 0.73\,\mathrm{m}$ and $\varepsilon = 8.75$ for ZnO [21]. They described in the paper that the electrical behavior of As-doped ZnO films changed from intrinsic n-type induced by the net of donor defect Zn_i and acceptor defect Zn vacancy (V_{Zn}) to highly conductive p-type with increased As impurity concentration. Recently, Limpijumnong et al. proposed [22] a new doping mechanism for As and Sb impurities in ZnO based on a first-principles calculation. And they suggested that As (Sb) would substitute for Zn instead of O and then produce two corresponding Zn vacancies, which was a As_{Zn}–$2V_{Zn}$ (Sb_{Zn}–$2V_{Zn}$) complex. Look et al. [5] reported that in strongly p-type As-doped ZnO by an evaporation/sputtering process substitutional As atoms produced an impurity energy level with an ionization energy of 0.133 eV for low acceptor concentration region. This ionization energy E_{A_0} at low acceptor concentration was estimated from the screening formula:

$$E_{\mathrm{A}} = E_{\mathrm{A}_0} - \beta N_{\mathrm{A}}^{1/3}, \tag{6}$$

where E_{A} was the ionization energy of 0.090 eV at high acceptor concentration N_{A} of $10^{19}\,\mathrm{cm}^{-3}$ and β the specific parameter for ZnO to be $2 \times 10^{-5}\,\mathrm{meV\,cm}$. Although the microscopic structure of the As-related acceptor was not clear, two possible structures were proposed by Look et al. [5]. The simplest structure would be As atoms at the O site, As_O; another possibility, recently presented, was that the structure was much more complex, namely, As_{Zn}–$2V_{Zn}$, in which the As is substituted on the Zn site, forming a donor, but that it induced two Zn-vacancy acceptors.

Xiu et al. [16] reported on photoluminescence study of Sb-doped p-type ZnO films by molecular-beam epitaxy that from free electron to acceptor transition, the Sb acceptor ionization energy of 0.14 eV above the valence band was determined, which was in good agreement with analytical results of the temperature-dependent photoluminescence measurements. They also described that with the complete activation of Sb impurities at the annealing temperature of 800°C or above; heavy Sb doping facilitated the formation of more Zn vacancies than light Sb doping. Owing to the large size of the Sb atom, instead of replacing an O atom an Sb imputity was predicted to substitute a Zn atom and simultaneously connected to two Zn vacancies to form a Sb_{zn}–$2V_{zn}$ complex, which was a shallow acceptor, where Sb_{zn} was a Sb atom substituting host Zn atom and V_{zn} was a vacancy at the Zn site. However, Zn vacancy V_{zn} did not play important roles in p-type conductivity since they were relatively deeper acceptors than the complex Sb_{zn}–$2V_{zn}$.

Xiu et al. [23] reported in Bi-doped ZnO films by molecular-beam epitaxy that Bi-induced acceptor ionization energy was estimated to be 0.185–0.245 eV by photoluminescence measurements based on the donor–acceptor pair peak position in the Bi-doped ZnO films; Bi in ZnO films had positive charge state determined by X-ray photoelectron spectroscopy measurements, indicating that Bi_{Zn} at Zn sites, rather than Bi_O at O sites, was formed in the films. Bi_{Zn} itself, however, is a donor. The origin of the shallow acceptor states was, therefore, identified as a donor–acceptor pair such as Bi_{Zn}–V_{Zn}–O_i or Bi_{Zn}–$2V_{Zn}$ complexes.

4.1.3 ZnO doped with group-IV elements

Norton et al. [24] suggested in the study of ferromagnetism in Mn-implanted ZnO with Sn that as a +4 valence cation, Sn should behave as a doubly ionized donor, thus introducing deep states in the energy gap. This means that Sn would be at Zn substitutional site. They described none of electronic behavior of Sn in ZnO.

4.1.4 Transition metal-doped ZnO

Transition metal impurities usually occupy the lattice interstitial site. A few examples of transition metal impurities are known to be located in the substitutional site and to replace a Zn host atom in ZnO [17]. Recent theoretical and experimental works in ZnO predicted that ZnO normally was n-type, when doped with magnetic transition impurities. Despite intensive efforts on transition metal-doped ZnO, however, the theoretical and experimental results on the electronic structure of ZnO with transition impurities did not converge on a definite conclusion [25,26]. We will not, therefore, discuss about electronic behavior of ZnO with transition impurities further.

4.2 Spherical hydrogenic models and other models for monovalent impurities [27]

In general, the shallow impurity states associated with monovalent donors and acceptors give rise to weakly bound states of electrons and holes. Although there is some confusion due to lack of a full understanding and quantitative prediction, of these weakly bound states, the energy levels of these impurities can be estimated by the impurity-independent hydrogenic-state model, namely spherical hydrogenic models, for the electron-hole binding energy [28]. The most-important difference between free hydrogen atoms in vacuum and impurity atoms in the crystal is that the crystal is polarizable, so that at long distances the Coulomb interaction in vacuum

$$V_{\text{coulomb}} = -\frac{e^2}{\mathbf{r}} \tag{7}$$

is replaced by the modified interaction

$$V_{\text{coulomb}} = -\frac{e^2}{\varepsilon \mathbf{r}}, \tag{8}$$

where ε is the static dielectric constant which should describe the reduction in field between the extra particle (electron or hole) and the ionic impurity in the crystal. The second difference concerns the kinetic energy of the extra particle in the crystal. In general, kinetic energy E_{kinetic} is described in term of the relationship between the energy of the particle in the absence the Coulomb field of the ion, and the momentum p of the particle. For an electron in vacuum the kinetic energy is simply

$$E_{\text{kinetic}} = E_0 + \frac{p^2}{2m}, \tag{9}$$

where E_0 is the zero of energy and m the electron mass. In the crystal, the extra particle should be thought of as a wave packet which travels with the usual group velocity. One approach to describe the kinetic energy of the wave packet is to continue to use Eq. (9), but to replace m by the effective electron mass m^* in the crystal, where $(m^*)^{-1}$ is a suitably weighted average of the coefficients of $(p-p_0)^2/2$ in applying the effective mass theory. The extra particle that interacts with the impurity ion has the energy of an electron bound to a proton, but with e^2 replaced by e^2/ε and m replaced by m^*. This gives rise to a hydrogenic set of energy levels, with the binding energy E_{1s} of the 1s ground state given by

$$E_{1s} = \frac{m^*}{m}\frac{1}{\varepsilon^2}E_H, \tag{10}$$

where E_H is 13.6 eV, equal to the ionization potential of the free hydrogen atom. The effective mass m^*/m is quite small in group-IV and III–V semiconductors, and is still small (0.2–0.3) even in II–VI semiconductors such as ZnSe and ZnO. According to Eq. (10), the ionization energy associated with monovalent donors is small in all compound semiconductors except GaP. In GaP crystal, the effective mass ionization energy for donors in GaP is about twice as large as for donors in Si, because of smaller dielectric constant for GaP.

Corresponding to the use of Eq. (10) with $\varepsilon = 8.75$ and $m_h^* = 0.73m$ for ZnO [26], the acceptor ionization energy for a hole was obtained to be 0.130 eV. This value agrees closely but not exactly with experimental values of 0.170–0.200 eV for N, 0.127 eV for P, 0.115–0.164 eV for As, 0.14 eV for Sb, and 0.185–0.245 eV for Bi, and also agrees closely with calculated values. As already mentioned above, whether the spherical hydrogenic models provide an appropriate calculation of estimated ionization energies or not, may be dependent on lattice strain effects due to an atomic size of the impurities.

Using Eq. (10) with $\varepsilon = 8.75$ and $m_e^* = 0.28m$ [10] for ZnO, the donor ionization energy for an electron is obtained to be 0.050 eV. The value of the donor ionization energy for an electron is about one third of the value for the hole, proportional to m_e^*/m_h^*. The experimental donor ionization energies of the impurities for the monovalent impurities such as B, Al, Ga, In, or Tl were not determined precisely, because of the difficulty of their measurements due to formation of the impurity band merging into the conduction band at high impurity concentrations. The estimated value of 0.05 eV above is consistent with the phenomena that the impurity band merges with the conduction band.

4.3 Comparison between experimental and calculated ionization energies

We roughly attempted to compare the acceptor ionization energies between the experimental and calculated values, for the monovalent substitutional impurities of group-VA elements at the host O site. The comparison was made for group-VA elements because of the existence of the most reliable data for them. The experimental values [20,22,29–31] of the acceptor activation energies for group-VA elements were already described in Section 4.1 to be 0.170–0.200 eV for N,

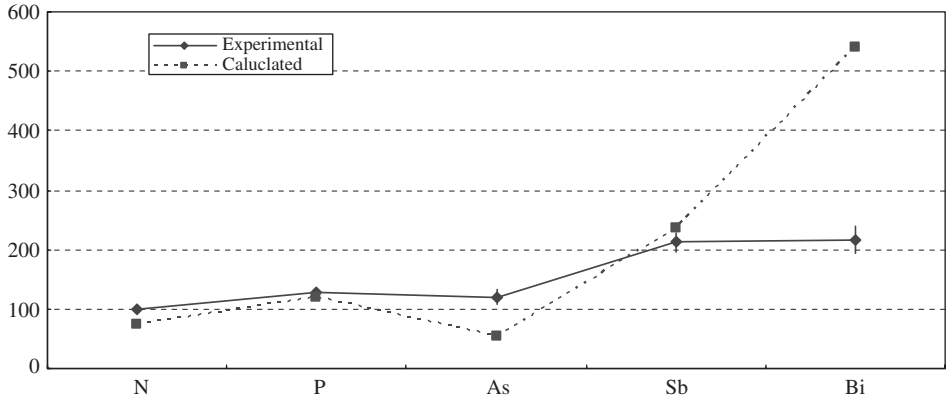

Figure 24.4 Experimental [20,23,29–31] and calculated activation energies for the group-V impurities in ZnO.

0.127 eV for P, 0.115–0.164 eV for As, 0.14 eV for Sb, and 0.185–0.245 eV for Bi above the upper edge of the valence band. The calculated values were also listed in Section 3.2 to be 0.074 eV for N, 0.119 eV for P, 0.055 eV for As, 0.237 ev for Sb, and 0.237 eV for Bi. Figure 24.4 shows a brief sketch of the comparison of acceptor ionization energies for group-VA impurities. In this sketch, the values of the calculated acceptor ionization energies were normalized in such a way that the calculated gap energy was in exact accordance with the experimentally obtained gap energy of ZnO. We can see a good agreement among the values for group-VA impurities except Bi, as shown in Figure 24.4. The acceptor ionization energy of the group-VA elements appears to become larger within group-VA as the row number increase. The tendency of the increase in acceptor ionization energy against the increase of row number also agreed on the experimental and calculated values. The reason why this tendency occurs is already mentioned in Section 4.1: this tendency in behavior of the group-V monovalent-impurity ionization energies is explained by a simple model based on a hydrogenic state and strain charges upon impurity charging.

We have to make a comparison of the donor ionization energies between the experimental and calculated values, at least, for the monovalent substitutional impurities of group-IIIA elements at the host Zn site. It is, however, difficult due to a lack of detailed information of the experimentally obtained energy levels.

5. CONCLUSIONS

In conclusion, we briefly summarize the chief points made in this report. We calculated the electronic structures of ZnO with impurity atoms from Li to Bi without radioactive elements to study impurity energy levels. Atomic cluster models used in the calculations were based on the $(Zn_{29}O_{56}X)^{56-}$ cluster with an X atom located at its O site and on the $(Zn_{56}YO_{96})^{78-}$ cluster with a Y atom

located at its Zn site. The calculated energy level diagrams for almost all impurities except isovalent impurities in the ZnO cluster models gave us impurity energy levels in the energy gap. The results showed that it is likely for a part of group-IA, -IIA, and -VIIA elements in the O site to be a shallow donor as well as group-VA elements to be a shallow acceptor, and also for a part of group-IA elements in the Zn site to be a shallow acceptor as well as group-IIIA elements to be a shallow donor.

The calculated shallow acceptor ionization energies of group-VA elements and some elements of group-IA elements agreed satisfactorily but not exactly with experimental values of group-VA elements and some elements of group-IA elements, respectively, and also had wide agreement with the estimated shallow acceptor ionization energies by spherical hydrogenic models for monovalent substitutional impurities.

The isovalent atoms of O of group-VIA such as S, Se, and Te replacing the O atoms and the isovalent atoms of group-IIA such as Be, Mg, Ca, Sr, and Ba and of group-IIB such as Cd, Ag, and Au replacing the Zn atoms did not produce any energy levels in the band gap.

REFERENCES

[1] T. Minami, *MRS Bull.* **25** (2000) 38.
[2] S.J. Pearton, D.P. Norton, K. Ip, Y.W. Heo, T. Steiner, *J. Vac. Sci. Technol.* **B22(3)**, (2004) 932.
[3] L. Eriksson, G. Fladda, K. Björkqvist, *Appl. Phys. Lett.* **14** (1969) 195.
[4] J.C. Phillips, *Bonds and Bands in Semiconductors*, Academic Press, New York and London, 1973, p. 221.
[5] D.C. Look, G.M. Renlund, R.H. Burgener, II., J.R. Sizelove, *Appl. Phys. Lett.* **85** (2004) 5269.
[6] Y.-Z. Yoo, Z.-W. Jin, T. Chikyow, T. Fukumura, M. Kawasaki, H. Koinuma, *Appl. Phys. Lett.* **81** (2002) 3798.
[7] C. Cruz-Vázquez, F. Rocha-Alonzo, S.E. Burruel-Ibarra, M. Inoue, *Superficies Vacío* **13** (2001) 89.
[8] H. Adachi, M. Tsukada, C. Satoko, *J. Phys. Soc. Jpn.* **45** (1978) 875.
[9] D.E. Ellis, H. Adachi, F.W. Averill, *Surf. Sci.* **58** (1976) 497.
[10] W. Martienssen, et al., *Landolt–Bornstein Numerical Data and Functional Relationships in Science and Technology, New Series*, Springer, Berlin, 1996, p. 162.
[11] R.S. Mulliken, *J. Chem. Phys.* **23** (1955) 1841.
[12] R.J. Collins, D.A. Kleinman, *J. Phys. Solids* **11** (1959) 190.
[13] J.C. Phillips, *Bonds and Bands in Semiconductors*, Academic Press, New York and London, 1973, p. 240.
[14] D.C. Look, J.W. Hemsky, J.R. Sizelove, *Phys. Rev. Lett.* **82** (1999) 2552.
[15] V. Gavryushin, G. Raciukaitis, D. Juodzbalis, A. Kazlauskas, V. Kubertavicius, *J. Cryst. Growth* **138** (1994) 924.
[16] F.X. Xiu, Z. Yang, L.J. Mandalapu, D.T. Zhao, J.L. Liu, *Appl. Phys. Lett.* **87** (2005) 252102-1.
[17] K. Osuch, E.B. Lombardi, W. Gebicki, *Phys. Rev.* **B73** (2006) 075202.
[18] D.C. Look, F.C. Reynolds, C.W. Litton, R.L. Jones, D.B. Eason, G. Cantwell, *Appl. Phys. Lett.* **81** (2002) 1830.
[19] D.K. Hwang, H.S. Kim, J.H. Lim, J.Y. Oh, J.H. Yang, S.J. Park, K.K. Kim, D.C. Look, Y.S. Park, *Appl. Phys. Lett.* **86** (2005) 151917.
[20] Y.R. Ryu, T.S. Lee, H.W. White, *Appl. Phys. Lett.* **83** (2003) 87.
[21] O. Madelung, *Data in Science and Technology, Semiconductors Other Than Group IV Elements and III–V Compounds*, Springer, Berlin, 1992.
[22] S. Limpijumnong, S.B. Zhang, S.H. Wei, C.H. Park, *Phys. Rev. Lett.* **92** (2004) 155504.

[23] F.X. Xiu, L.J. Mandalapu, Z. Yang, J.L. Liu, G.F. Liu, J.A. Yarmoff, *Appl. Phys. Lett.* **89** (2006) 052103.
[24] D.P. Norton, S.J. Pearton, A.F. Hebard, N. Theodoropoulou, L.A. Boatner, R.G. Wilson, *Appl. Phys. Lett.* **82** (2003) 239.
[25] K. Sato, H. Katayama-Yoshida, *Jpn. J. Appl. Phys.* **39** (2000) L555.
[26] T. Dietl, H. Ohno, F. Matsukura, J. Gibert, D. Ferrand, *Science* **287** (2000) 1019.
[27] J.C. Phillips, *Bonds and Bands in Semiconductors*, Academic Press, New York and London, 1973, p. 227.
[28] J.M. Luttinger, W. Kohn, *Phys. Rev.* **97** (1955) 869.
[29] A. Tsukazaki, A. Otomo, M. Kawasaki, *Oyo Butsuri* **74** (2005) 1359.
[30] K.K. Kim, D.C. Look, Y.S. Park, *Appl. Phys. Lett.* **86** (2005) 151917.
[31] F.X. Xiu, Z. Yang, L.J. Mandalapu, D.T. Zhao, J.L. Liu, W.P. Beyermann, *Appl. Phys. Lett.* **87** (2005) 152101.

CHAPTER 25

First-Principles Investigation of Dimethyl Ether Steam Reforming

Kimichika Fukushima

Contents

Abstract

This paper reports the investigation of dimethyl ether (DME) steam reforming and related processes. The study uses the Xα molecular orbital theory, which has been successfully applied to analyze material properties. It was found that, when H_2O approaches Al on a surface of Si oxides (and pure Al_2O_3), charge transfer between H_2O and the surface destabilizes the H_2O. Approach of the destabilized H to a CH_3OCH_3 molecule then produces CH_3OH. Finally, injection of CO_2, by-produced in the reforming, to coal seam was shown to increase the CH_4 production by substitution.

1. INTRODUCTION

This paper deals with metal oxide catalysts for the dimethyl ether (DME) steam reforming [1,2]. The study used the DV-Xα molecular orbital theory, which has been successfully applied to analyze properties of metals, semiconductors, and so on [3]. DME is expected as a next-generation fuel with properties similar to liquefied petroleum gas (LPG) and light oil. There is a plan to transport DME from a producing country to a consuming country for an additional energy resource as shown in Figure 25.1. DME is reformed by steam by absorbing

AITEL Corporation, 8, Shinsugita-cho, Isogo-ku, Yokohama, 235-8523, Japan
E-mail: kimichika1a.fukushima@glb.toshiba.co.jp

Advances in Quantum Chemistry, Vol. 54
ISSN 0065-3276, DOI 10.1016/S0065-3276(07)00025-1

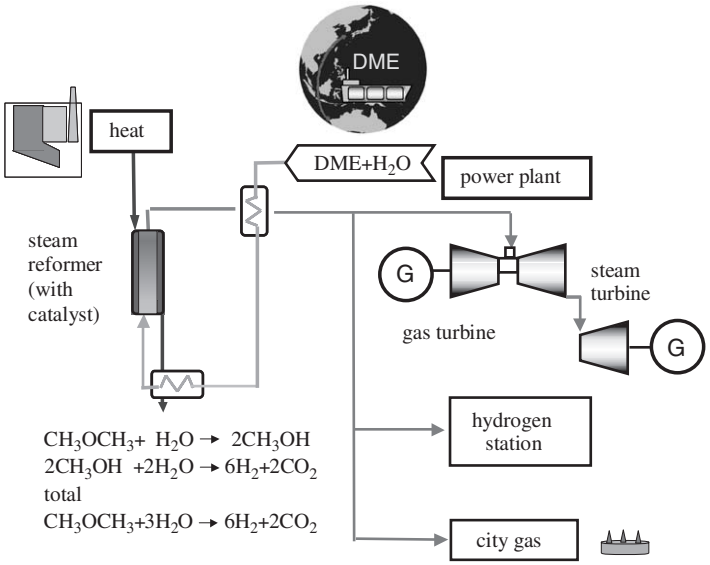

Figure 25.1 Hydrogen production system by the DME steam reforming.

(waste) heat, and H_2 is produced from DME through methanol. Equations of reaction are described as:

$$CH_3OCH_3 + H_2O \rightarrow 2CH_3OH, \tag{1}$$

$$2CH_3OH + 2H_2O \rightarrow 6H_2 + 2CO_2, \tag{2}$$

that is, totally

$$CH_3OCH_3 + 3H_2O \rightarrow 6H_2 + 2CO_2. \tag{3}$$

Produced H_2 will be used for power plants, hydrogen stations, city gases, and so on.

The by-product CO_2 in the DME reforming process may be used for the methane increased production by CO_2 injection to coal seam (Figure 25.2). The produced methane will be used for the DME synthesis with CO_2 as shown in Figure 25.2. Issues this paper addresses are concerned with: (1) processes of DME steam reforming as well as catalyst properties, where DME is transformed to methanol and methanol produces hydrogen; (2) mechanism of methane increased production by CO_2 injection to coal seam. Investigation was performed via first-principle calculations using the DV-Xα molecular orbital method. These reaction processes and catalyst properties have not yet been fully revealed theoretically. We will investigate here the DME hydrolysis to methanol by catalytic metal oxides, and will examine the mechanism of CO_2 substitution for methane on a coal surface.

It is suggested that, DME is transformed to methanol in the steam reforming. We will first deal with a transformation of DME to methanol by hydrolysis on a catalyst surface. (Surface may be different between dynamic and static states.)

For this transformation process, two catalysts were considered. The first catalyst was Si oxide containing Al, and the second one was Al_2O_3. To help evaluations of following models, calculations were performed for a model of a bulk host Si oxide. A model cluster for Si oxide surface was then derived by removing atoms out of the bulk Si oxide surface. A surface of Si oxide containing Al was then simulated by substituting Si atom by an Al atom at the surface. It was assumed that a surface of the Si oxide containing Al is supplied with additional electrons. It is reasonable to expect that H_2O will become active by adsorbing on a catalyst surface and exchanging charges with the catalyst surface. This expectation is based on the fact that bonding orbitals of H_2O are all occupied by electrons and H_2O may be destabilized by exchanging charges with a catalyst surfaces. The destabilization possibility of H_2O was examined using a model where H_2O is adsorbed on a surface of Si oxide with Al at a surface. In this examination, two different geometries of adsorbed H_2O were taken into account. The destabilization possibility of adsorbed H_2O was also investigated in the case of an Al_2O_3 surface without containing Si.

The next investigation concerns a subsequent hydrolysis process of DME, where DME (CH_3OCH_3) is transformed to methanol (CH_3OH) possibly caused by the destabilized H_2O. After the H_2O destabilization mentioned above, there is a possibility that H approaches O in CH_3OCH_3. It is then expected that, if a bond-breaking between CH_3O and CH_3 in CH_3OCH_3 occurs by an approach of H, CH_3OH may be produced, and the remaining OH of H_2O and CH_3 of CH_3OCH_3 will produce CH_3OH as shown in Figure 25.3. Based on this expectation, the author investigated a system where H approaches O in CH_3OCH_3, and examined a process of a transformation of DME to methanol.

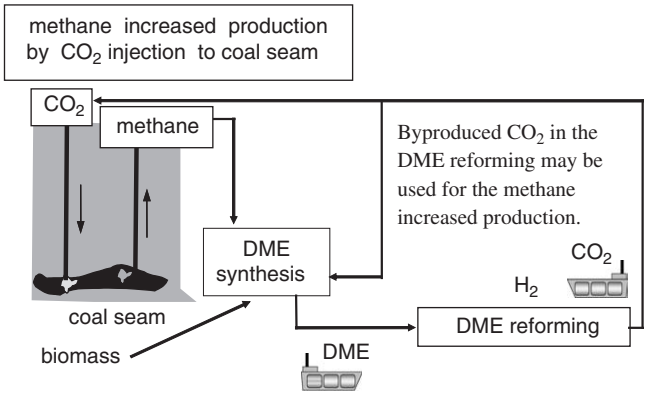

Figure 25.2 A plan of DME cycle.

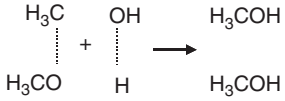

Figure 25.3 A possible transformation of DME to methanol by hydrolysis.

In the DME steam reforming, CO_2 is by-produced. If necessary, this CO_2 may be injected to coal seam, and then CO_2 will be substituted for CH_4 on coal. We finally evaluated an interaction strength of CO_2 with a coal surface, and compared with the case of CH_4 on coal to see an effectiveness of this substitution.

In this paper, Section 2 is devoted to describe calculational procedures and models. Section 3 presents calculated results for the DME steam reforming and related processes. Section 4 summarizes the results.

2. CALCULATIONAL PROCEDURE AND MODELS

Molecular orbital calculations of the DME steam reforming and the methane production increased by CO_2 injection to coal seam was performed by the DV-Xα method. The equation for the wave function $\psi_i(\boldsymbol{r})$ at a space point $\boldsymbol{r}$ in atomic units is denoted as

$$\left[-\frac{1}{2}\nabla^2 + V(\boldsymbol{r})\right]\psi_i(\boldsymbol{r}) = \varepsilon_i\psi_i(\boldsymbol{r}), \tag{4}$$

where ε_i is the energy of an electron, and the potential $V(\boldsymbol{r})$ at a point is given by

$$V(\boldsymbol{r}) = V_{\mathrm{N}}(\boldsymbol{r}) + V_{\mathrm{C}}(\boldsymbol{r}) + V_{\mathrm{X}\alpha}(\boldsymbol{r}). \tag{5}$$

In the expression above, $V_{\mathrm{N}}(\boldsymbol{r})$ and $V_{\mathrm{C}}(\boldsymbol{r})$ are the Coulomb potentials produced by nuclei and by electrons, respectively. The Xα potential $V_{\mathrm{X}\alpha}(\boldsymbol{r})$, corresponding to the exchange interaction potential, in the Xα scheme is presented by

$$V_{\mathrm{X}\alpha}(\boldsymbol{r}) \propto \alpha[\rho(\boldsymbol{r})]^{1/3}. \tag{6}$$

where $\rho(\boldsymbol{x})$ is the electron charge, and usually a value of 0.7 is set to α. In the molecular orbital theory, each electron wave function (molecular orbital) for a hydrogen-like molecule, for instance, is expanded in terms of normalized atomic orbitals $\chi_j(\boldsymbol{r})$, which belong to atom j (j=1,2), as

$$\psi_i(\boldsymbol{r}) = c_{i1}\chi_1(\boldsymbol{r}) + c_{i2}\chi_2(\boldsymbol{r}). \tag{7}$$

Mulliken populations are useful to evaluate chemical bonds and ionic states. The overlap charge between atomic orbitals is defined as

$$q_{i12} = 2n_i c_{i1} c_{i2} \int d\boldsymbol{r}\chi_1^*(\boldsymbol{r})\chi_2(\boldsymbol{r}), \tag{8}$$

where n_i is the electron number of the orbital wave function $\psi_i(\boldsymbol{r})$. The orbital charge belonging to the atom j=1 becomes

$$q_{i11} = n_i[c_{i1}c_{i1}\int d\boldsymbol{r}\chi_1^*(\boldsymbol{r})\chi_1(\boldsymbol{r}) + c_{i1}c_{i2}\int d\boldsymbol{r}\chi_1^*(\boldsymbol{r})\chi_2(\boldsymbol{r})]. \tag{9}$$

For an examination of the H_2O destabilization on the Si oxide surface containing Al which possibly promote a transformation of DME to methanol in the steam reforming process, model clusters employed are shown in Figures 25.4–25.8. A cluster shown in Figure 25.4 is a model of a bulk Si oxide, which is a reference material here. In this cluster, Si atoms are located at (0,0,0),

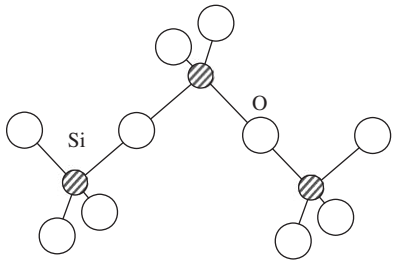

Figure 25.4 Model of a bulk Si oxide.

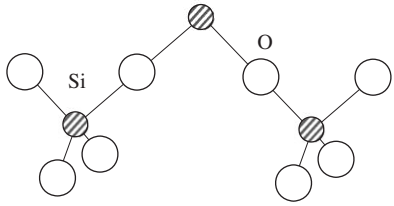

Figure 25.5 Model of Si oxide surface.

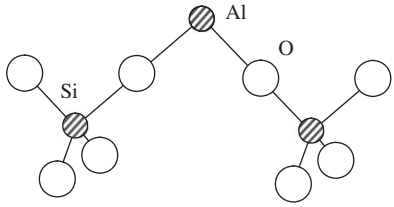

Figure 25.6 Model of Si oxide surface with Al.

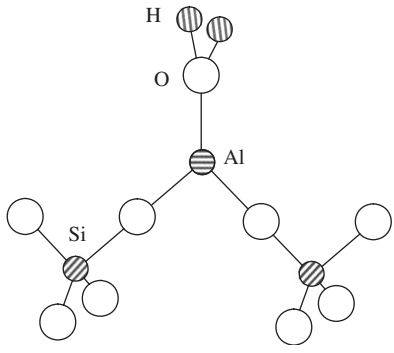

Figure 25.7 Model of H_2O adsorbed on Si oxide surface with Al.

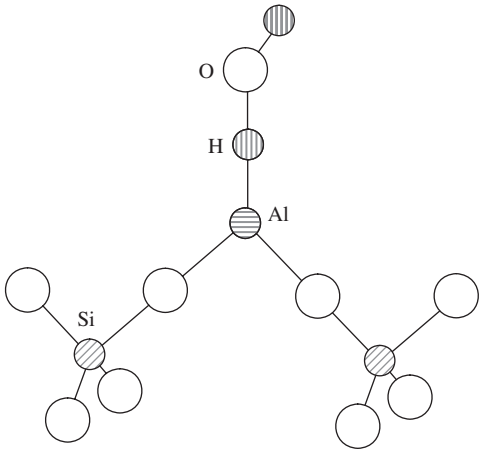

Figure 25.8 Another model of H_2O adsorbed on Si oxide surface with Al.

(–2*a*,–2*a*,–2*a*), and (2*a*,2*a*,–2*a*), and O atoms are at (–3*a*,–*a*,–3*a*), (–*a*,–3*a*,–3*a*), (*a*,3*a*,-3*a*), (3*a*,*a*,–3*a*), (–3*a*,–3*a*,–*a*), (3*a*,3*a*,–*a*), (–*a*,–*a*,–*a*), (*a*,*a*,–*a*), (–*a*,*a*,*a*) and (*a*,–*a*,*a*) where *a* is 0.0895 nm. Next cluster shown in Figure 25.5 is an ideal surface model of the Si oxide, which was derived by removing O atoms positioned at (–*a*,*a*,*a*) and (*a*,–*a*,*a*) in the bulk model in Figure 25.4. A substitution of an Al atom for the Si atom at (0,0,0) in the Si oxide surface in Figure 25.5 results in a model of an Al-containing Si oxide surface indicated in Figure 25.6. We then arrive at a model of H_2O adsorption on the Si oxide with Al shown in Figure 25.7, by adding H_2O on the surface, where the O atom of H_2O is just on the Al atom in the cluster indicated in Figure 25.6. A value set to the Al–O distance was 0.205 nm. The O–H axis in H_2O is normal to the Si–Al axis in Figure 25.7. The atomic configurations in H_2O were those in a vacuum, that is, the O–H distance is 0.09578 nm and the H–O–H angle is 104.478° [4]. Figure 25.8 is another model, where the geometrical configuration of adsorbed H_2O is different from that in the Figure 25.7 case mentioned above. The H atom of H_2O is just on the Al atom and the H–O axis is normal to the Al–Si axis. A value of the Al–H distance was 0.173 nm. A similar material, Al_2O_3, was also considered with the help of a surface model shown in Figure 25.9. In this model, positions of Al atoms are (0,0,0) as well as (0.5*b*,0.5*b*,–1.5*b*), and O atoms are at (–*b*,0,0), (0,–*b*,0), (*b*,0,0), (0,*b*,0), (0,0,–*b*), (*b*, *b*,–*b*), (b,0,–2*b*), (0,*b*,–2*b*), where a value set to *b* was 0.198 nm. For Al_2O_3, we also considered two different geometrical configurations of H_2O adsorbed on the surface. In the case of Figure 25.10, the O atom of H_2O is just on the Al atom, and (*x*,*y*) components of vectors connecting O and H are directed to (1,−1) or (−1,1). A value set to the Al–O distance was 0.220 nm. Figure 25.11 shows another model, where H_2O has a geometrical configuration different from that in Figure 25.10. The H atom of H_2O is just on the Al atom with an Al–H distance of 0.188 nm, and (*x*,*y*) components of the vector connecting O and the terminal H are directed to (−1,−1).

In the next examination for the transformation of DME, shown in Figure 25.12, to methanol by hydrolysis, a model employed is illustrated in Figure 25.13,

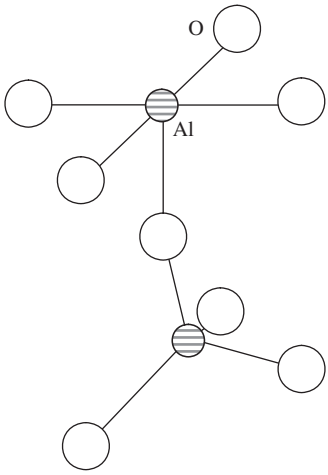

Figure 25.9 Model of an Al_2O_3 surface.

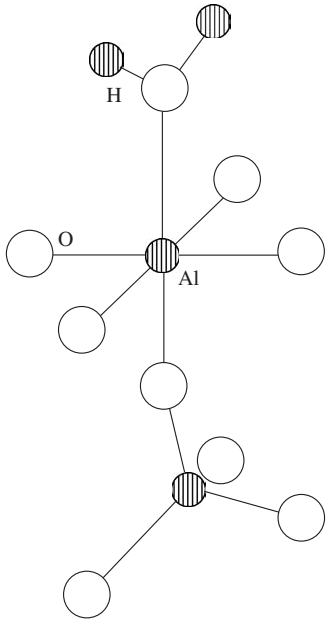

Figure 25.10 Model of adsorbed H_2O on Al_2O_3.

where H approaches DME. As to DME shown in Figure 25.12, C–H and C–O distances are 0.1121 and 0.1416 nm, respectively, and HCH and COC angles are 108 and 112°, respectively. A value set to the interatomic distance from the approaching H to O of CH_3OCH_3 was 0.0963 nm.

In the final analysis for the methane production increase from the coal seam by CO_2 injection, a simple model cluster of coal surface adopted is depicted in

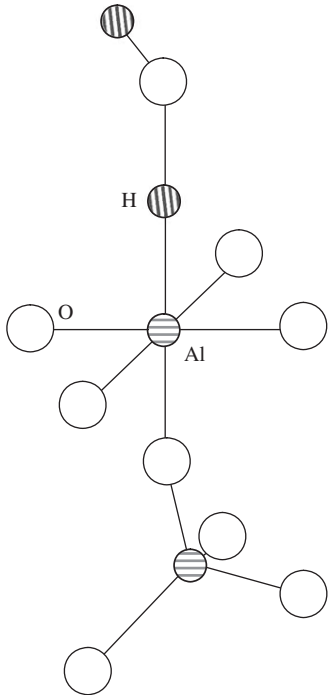

Figure 25.11 Another model of adsorbed H_2O on Al_2O_3.

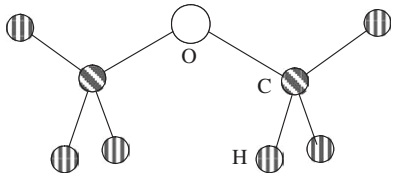

Figure 25.12 Atomic configuration of DME.

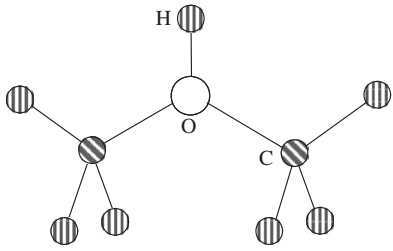

Figure 25.13 Model of H approaching O of DME.

Figure 25.14. In this model, C atoms are positioned at (0,0,0), (–*c*,0,0), and (*c*,0,0), where a value set to *c* was 0.1541 nm. H atoms, which form hydrocarbon are located at (0,–*d*,0), (0,*d*,0), (–*c*,–*d*,0), (–*c*,*d*,0), (–*c*–*d*,0,0), (*c*,–*d*,0), (*c*,*d*,0), and (*c*+*d*,0,0), where a value set to *d* was 0.109 nm. Using this coal surface model, we considered adsorbed methane on a coal surface by employing a model in Figure 25.15, where an H atom of CH_4 was adsorbed just on the C atom of the coal surface, and a value set to C–H distance was 0.109 nm. The distance between C and H of CH_4 used was 0.10870 nm. CO_2 adsorption on a coal surface was also evaluated with the help of a model shown in Figure 25.16, where a model for the coal surface is the same as in the CH_4 adsorption case. The O atom of CO_2 was adsorbed just on

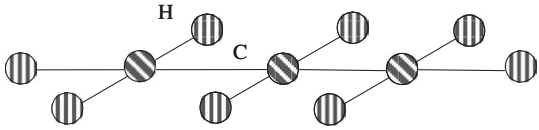

Figure 25.14 Simple model of a coal surface.

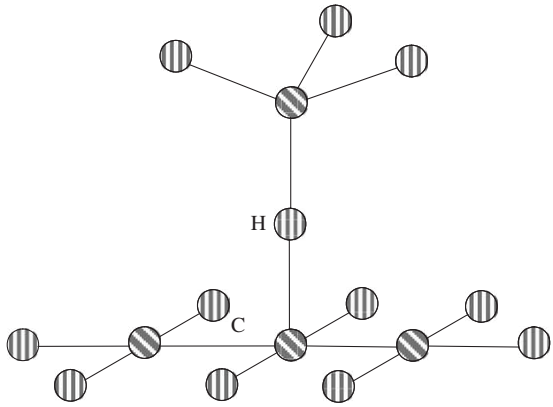

Figure 25.15 Model of adsorbed CH_4 on a coal surface.

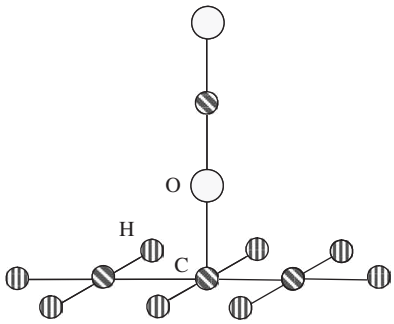

Figure 25.16 Model of adsorbed CO_2 on a coal surface.

the C atom of the coal surface, and a value set to the distance from C at the surface to O of CO_2 was 0.143 nm. The C–O distance of CO_2 used was 0.11600 nm.

Other details of molecular orbital calculations were as follows: A numerical basis set used was 1*s* atomic orbital for H, 1*s*–2*p* for C and O, and 1*s*–3*p* for Al and Si. The formal charges of oxide elements in iterations were +3*e* for Al, +4*e* for Si, −2*e* for O and those of the other molecule elements were neutral. The DV sampling points for numerical integration were 500–1000 per atom. For molecular orbitals, point group was not taken into account.

3. RESULTS AND DISCUSSION

We begin with calculated results of the H_2O destabilization by Si oxides including Al in the process of the DME transformation to methanol by hydrolysis. Before describing a destabilization possibility of H_2O adsorbed on a catalyst surface, it may be worthy to examine the host material of the catalyst. Figure 25.17 is a molecular orbital energy level diagram for the model of a bulk Si oxide in Figure 25.4 where energy of molecular orbitals is measured from the energy of highest occupied molecular orbital (HOMO). In the figure for the bulk Si oxide, there appear valency states below HOMO as well as conduction states above lowest unoccupied molecular orbital (LUMO), and an energy gap is seen between the top of the valency states and the bottom of the conduction states. As is expected, energy levels indicate that the Si oxide has an insulating property. Figure 25.18 is a molecular orbital energy level diagram for the model of the Si oxide ideal surface shown in Figure 25.5. In this figure, energy levels arising from

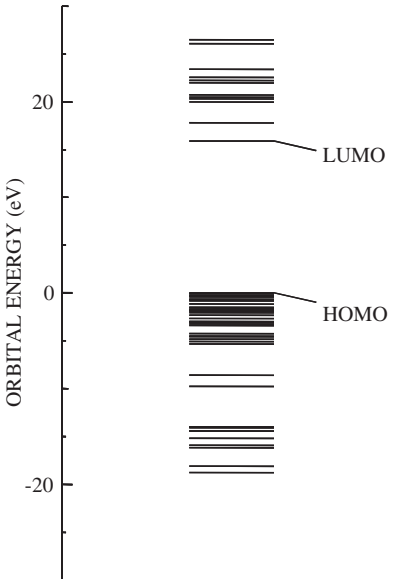

Figure 25.17 Energy levels of a bulk Si oxide.

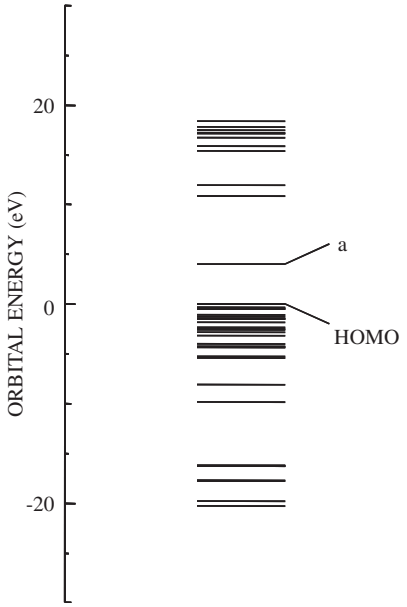

Figure 25.18 Energy levels of Si oxide surface.

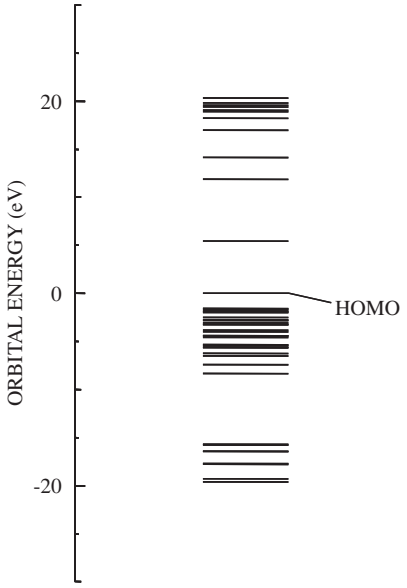

Figure 25.19 Energy levels of Si oxide surface containing Al.

dangling bonds on a surface, such as an energy level expressed with symbol *a*, appear in the energy gap. Figure 25.19 is a molecular orbital energy level diagram for the model cluster in Figure 25.6, where Si atom at a surface was replaced by Al atom, and it was assumed that an additional electron was supplied.

In Figure 25.19, HOMO with a predominant Al-s*p* character is occupied by one electron. From this energy level diagram, it is expected that, when H_2O approaches this surface, electron may be supplied to H_2O.

Calculations were then performed for a system, where the O atom of H_2O adsorbed on a substituted Al site of the Si oxide surface as shown in the model cluster in Figure 25.7. Figure 25.20 is a derived molecular orbital energy level diagram. Energy of the orbital, which contains a predominant O-s*p* contribution from H_2O is lower than the HOMO energy. The Mulliken overlap charge between the H atom and the O atom of the adsorbed H_2O has a reduction by 0.105 for one electron addition (and negative value for two electrons addition) compared to 0.648 for H_2O in a vacuum as shown in Table 25.1. This decrease in the Mulliken

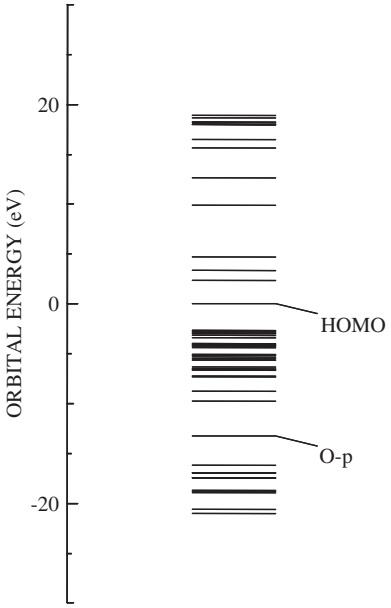

Figure 25.20 Energy levels of adsorbed H_2O on a bulk Si oxide surface containing Al.

Table 25.1 Mulliken overlap charge between H and O atoms of adsorbed H_2O on catalysis

Geometrical configuration	Mulliken overlap charge (H–O of adsorbed H_2O)
H_2O in a vacuum	0.648
H_2O adsorbed on Si oxide with Al (Figure 25.7)	
One electron addition	0.105
Two electrons addition	Negative value
H_2O adsorbed on Si oxide with Al (Figure 25.8)	0.253
Adsorbed H_2O on Al_2O_3 (Figure 25.10)	Negative value
Adsorbed H_2O on Al_2O_3 (Figure 25.11)	Negative value

overlap charge implies that H_2O adsorbed on a substituted Al site of the Si oxide surface is destabilized. In order to see the electronic state in a different geometrical configuration of H_2O adsorbed on a substituted Al site at the surface of the Si oxide, calculations were done for the model cluster displayed in Figure 25.8, where the H atom of H_2O is adsorbed on a substituted Al site of the Si oxide surface. Calculated molecular orbital energy level diagram is depicted in Figure 25.21, and the energy of the orbital whose main component is H-*s* of H_2O is lower than HOMO. The Mulliken overlap charge between the H and O atoms of H_2O adsorbed on the surface have a value of 0.253 decreased from a corresponding value 0.648 in H_2O in a vacuum as shown in Table 25.1. Therefore, H_2O adsorbed on a surface of Si oxides containing Al, is destabilized both for two different geometrical configurations.

Since similar phenomena are expected to occur on Al_2O_3, we considered adsorbed H_2O on an Al atom at an Al_2O_3 surface. Before considering adsorption, calculations were carried out for the model cluster of an Al_2O_3 surface without adsorption shown in Figure 25.9. This cluster has an Al atom at an octahedral site and at a tetrahedral site, and Figure 25.22 shows a molecular orbital energy level diagram for this cluster. Even energy levels of the model of an Al_2O_3 surface have an energy gap between the HOMO energy and the LUMO energy. We then carried out calculations for the model cluster in Figure 25.10, where H_2O was adsorbed on the surface of the Al_2O_3. Figure 25.23 shows a molecular orbital energy level diagram for this model. The energy of the orbital comprised mainly of the O-*p* (including O-*s*) atomic orbital belonging to H_2O is lower than the

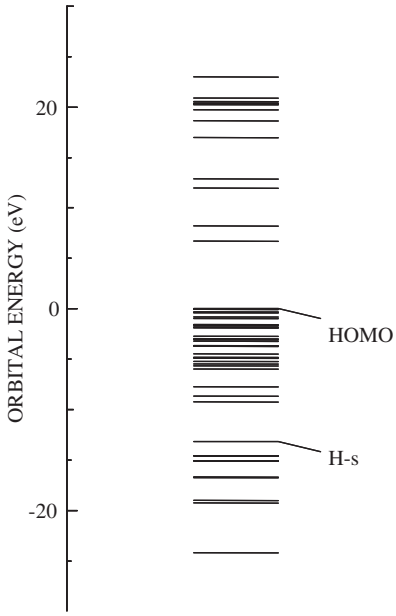

Figure 25.21 Energy levels of adsorbed H_2O on Si oxide surface containing Al in another geometrical configuration.

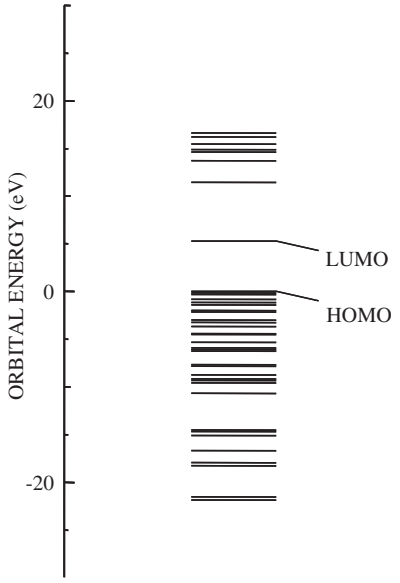

Figure 25.22 Energy levels of an Al_2O_3 surface.

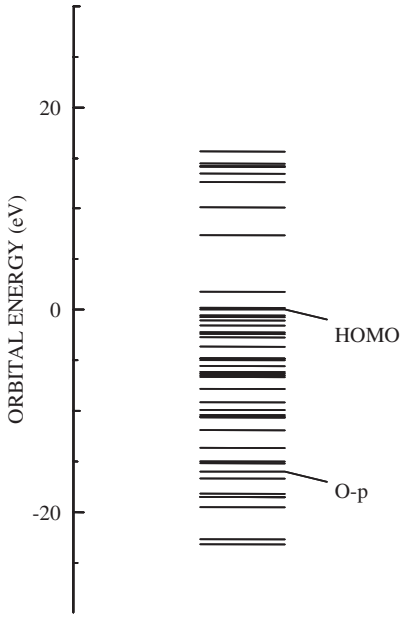

Figure 25.23 Energy levels of adsorbed H_2O on an Al_2O_3 surface.

HOMO energy. Due to a charge transfer between H_2O and Al_2O_3, the O–H overlap charge in H_2O molecule has a reduced small negative value from 0.648 for H_2O in a vacuum as shown in Table 25.1. H_2O molecule adsorbed on a surface on Al_2O_3 thus also becomes destabilized. Calculations were performed for

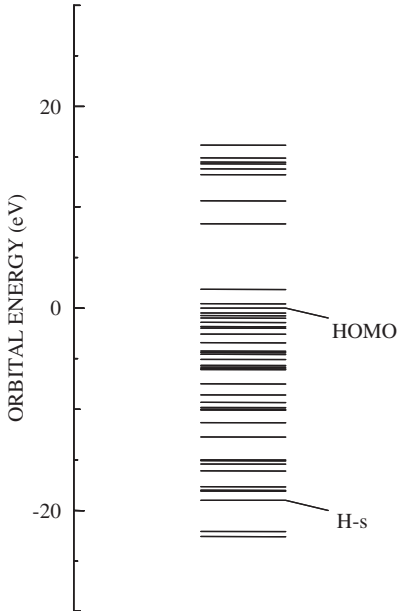

Figure 25.24 Energy levels of H_2O adsorbed on an Al_2O_3 surface in another H_2O geometrical configuration.

another geometrical configuration of H_2O adsorption as shown in Figure 25.11, where the H atom of H_2O is adsorbed on an Al_2O_3 surface. Figure 25.24 shows a molecular orbital energy level diagram for this case. The energy originated from the H-*s* atomic orbital of H_2O is lower than that of HOMO. Due to a charge transfer between H_2O and the Al_2O_3 surface, overlap charge between the H atom absorbed on the Al_2O_3 surface and the O atom of the H_2O molecule is deduced to a small negative value from 0.648 for H_2O in a vacuum as shown in Table 25.1. This indicates that the destabilization of H_2O also occurs for a different geometrical configuration on an Al_2O_3 surface.

Based on calculations derived above, we next examined a transformation mechanism of DME to methanol. An energy level diagram calculated for a DME molecule in Figure 25.12 is shown in Figure 25.25. Calculations were then done for the case where H approaches a DME molecule as shown in Figure 25.13. A molecular orbital energy level diagram for this case is shown in Figure 25.26, and the energy of the orbital with a significant contribution from the 1*s* atomic orbital of the H approaching the DME molecule is lower than the HOMO energy. The overlap charge between the O atom and the C atom of DME has a value of 0.110 decreased from a corresponding geometrical configuration value (0.627) in a vacuum as shown in Table 25.2. The results indicate that the bond between an O atom and a C atom of DME is broken by an approach of H. Then, CH_3O of DME makes a bond with the approaching H forming a methanol CH_3OH. The remaining CH_3 of the DME molecule and OH of the H_2O molecule will form another methanol CH_3OH as shown in Figure 25.3.

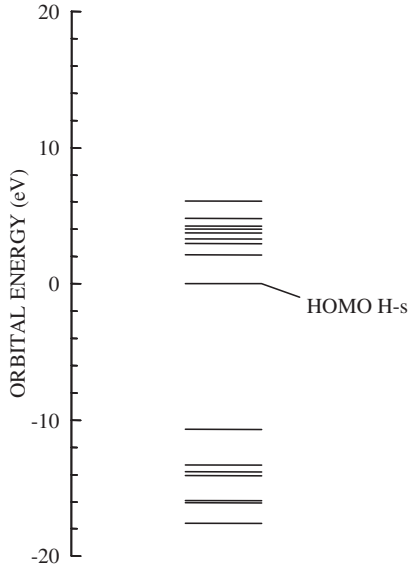

Figure 25.25 Energy levels of DME.

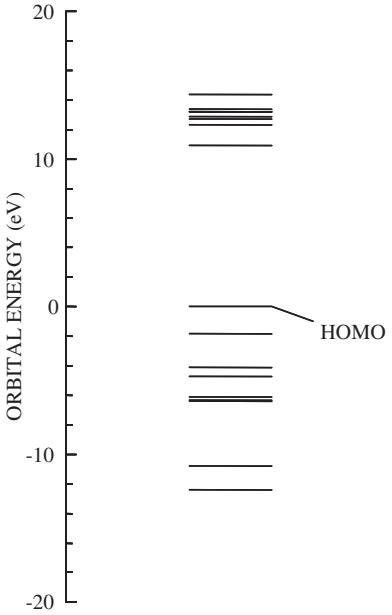

Figure 25.26 Energy levels of a system where H is approaching DME.

Calculations were finally performed to investigate a mechanism of the methane production increase by CO_2 injection to coal seam. Coal includes carbon, hydrogen, and other elements, as Figure 25.14 depicted a simple model of a coal surface. Figure 25.27 shows a molecular orbital energy level diagram for this

Table 25.2 Mulliken overlap charge between O and C atoms of CH_3OCH_3 to which H is approaching

Geometrical configuration	Mulliken overlap charge (O–C of CH_3OCH_3)
CH_3OCH_3 in a vacuum	0.627
CH_3OCH_3 to which H is approaching	0.110

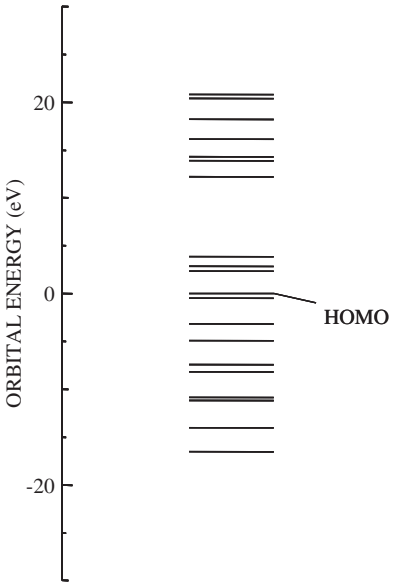

Figure 25.27 Energy levels of a simple coal surface model.

simple coal surface model. By using the coal surface model cluster, two adsorption cases were considered; CH_4 and CO_2 were adsorbed on a coal surface as shown in Figures 25.15 and 25.16, respectively. Figure 25.28 shows a molecular orbital energy level diagram of the model cluster for CH_4 on a coal surface. The energy of a molecular orbital consisting mainly of *s* atomic orbital of the H atom adsorbed on the coal surface is lower than the HOMO energy. Figure 25.29 shows a molecular orbital energy level diagram of the model for CO_2 adsorption. The energy of a molecular orbital comprising mainly *p* (and *s*) atomic orbitals of the O atom adsorbed on the coal surface is also lower than the HOMO energy. An overlap charge between the O atom of CO_2 and the C atom on the coal surface take a value of 0.306, and larger than the corresponding value of 0.101 between the H atom of CH_4 on the C atom of the coal surface as shown in Table 25.3. From the result of the stronger interaction of CO_2 with a coal surface compared to the CH_4 adsorption case, it is expected that CO_2 will be substituted for CH_4. Therefore, methane production will be enhanced by injection of CO_2 to the coal seam.

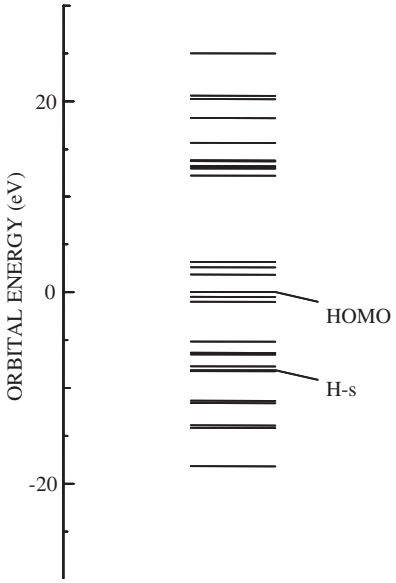

Figure 25.28 Energy levels of adsorbed CH_4 on a coal surface.

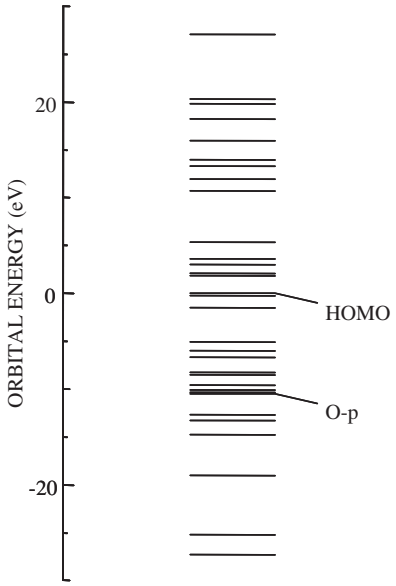

Figure 25.29 Energy levels of adsorbed CO_2 on a coal surface.

4. CONCLUSIONS

This paper reported analysis concerning DME steam reforming and related processes with the use of (waste) heat, as well as catalytic properties for reforming. The Xα molecular orbital theory has been successfully applied to

Table 25.3 Mulliken overlap charge between atoms of CO_2 and CH_4 on a coal surface

Geometrical configuration	Mulliken overlap charge
CO_2 on a coal surface	0.306 (O–C[coal])
CH_4 on a coal surface	0.101 (H–C[coal])

analyze material properties. In the DME steam reforming, DME is transformed to methanol, and methanol produces hydrogen by hydrolysis. Furthermore, CO_2 by-product may be injected to coal seam to enhance CH_4 production, and CH_4 with CO_2 is used for the DME synthesis. In the analysis, the author carried out electronic state calculations to examine a destabilization of H_2O on a surface of catalytic Si oxides containing Al. Calculations showed that charges are transferred between H_2O and the surface, when H_2O approaches Al. Since bonding orbitals of H_2O are all occupied by electrons, the bond strength between H and O is weakened by the charge transfer between H_2O and the surface, which results in a destabilization of H_2O. This destabilization of H_2O was also seen on Al_2O_3. We next investigated hydrolysis of DME, where DME (CH_3OCH_3) is transformed to methanol (CH_3OH). After the H_2O destabilization mentioned above, there is a possibility that H approaches O of CH_3OCH_3. Calculations for this model indicated that the bond between O and C in CH_3OCH_3 becomes weak. The bond-breaking in CH_3OCH_3 caused by H will produce CH_3OH and CH_3. Then, the remaining OH of H_2O and CH_3 of CH_3CH_3 will form CH_3OH. In the DME steam reforming, CO_2 is by-produced. If necessary, this CO_2 is injected to coal seam. Calculations were performed for CO_2 and CH_4 on coal. It was found that the bond strength between CO_2 and coal is stronger than that between CH_4 and coal. This indicates that the injection of CO_2 to coal seam leads to CO_2 substitution for CH_4 on coal and an increased production of CH_4.

REFERENCES

[1] K. Fukushima, T. Ogawa, *JSME Int. J. B Fluids Therm. Eng.* **47** (2004) 340.
[2] K. Fukushima, T. Ogawa, N. Segawa, S. Makino, K. Yamada, In: Proceeding of 15th World Hydrogen Energy Conference, HESS, NEDO, 2004, 30D-03.
[3] H. Adachi, M. Tsukada, C. Satoko, *J. Phys. Soc. Jpn.* **45** (1978) 875.
[4] The Chemical Society of Japan (Ed), *Kagaku Binran* (several editions of chemical handbook in Japanese, Maruzen, until 1993).

SUBJECT INDEX

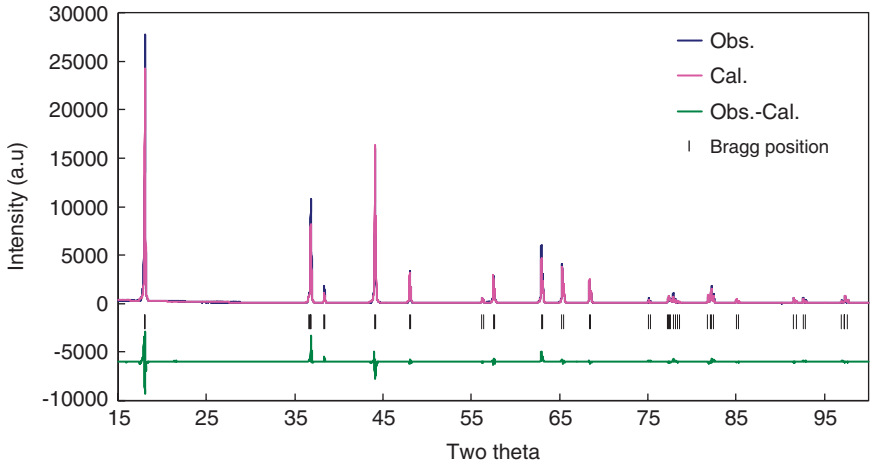

Figure 3.1 The XRD profiles of $Li_{1.1}V_{0.9}O_2$ after the Rietveld refinement (a) x=0.1, (b) 0.2, and (c) 0.3.

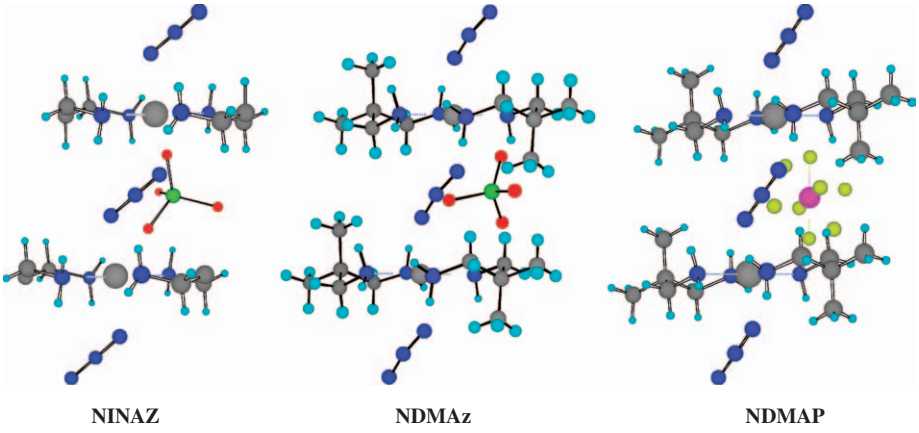

Figure 4.4 Cluster model N_3–$Ni(tn)_2$–N_3–$Ni(tn)_2$–N_3 of NINAZ (left), N_3–$Ni(dmpn)_2$–N_3–$Ni(dmpn)_2$–N_3 of NDMAZ (center) and N_3–$Ni(dmpn)_2$–N_3–$Ni(dmpn)_2$–N_3 of NDMAP (right). Counter anions ClO_4^- and PF_6^- are excluded for the DV-Xα calculations.

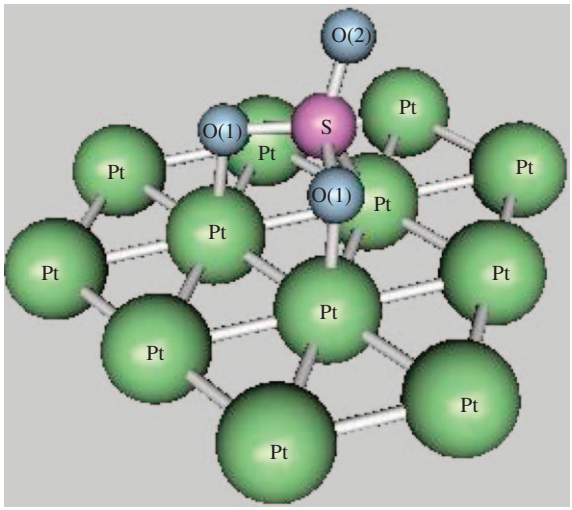

(a) Suzuki *et al.*

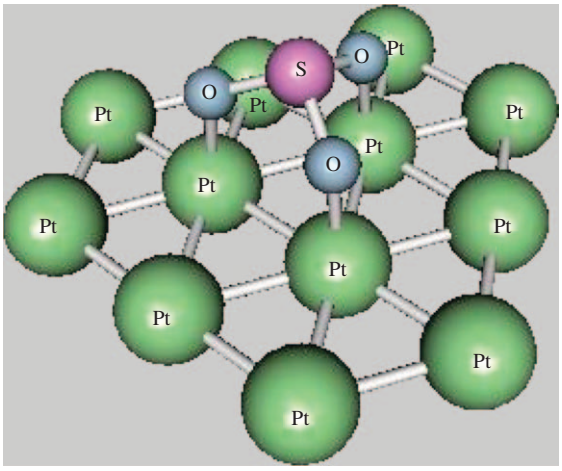

(b) Suzuki *et al.*

Figure 6.1 SO_3Pt_{12} cluster models used for the calculation with DV-Xα method. (a) Configuration A, (b) configuration B.

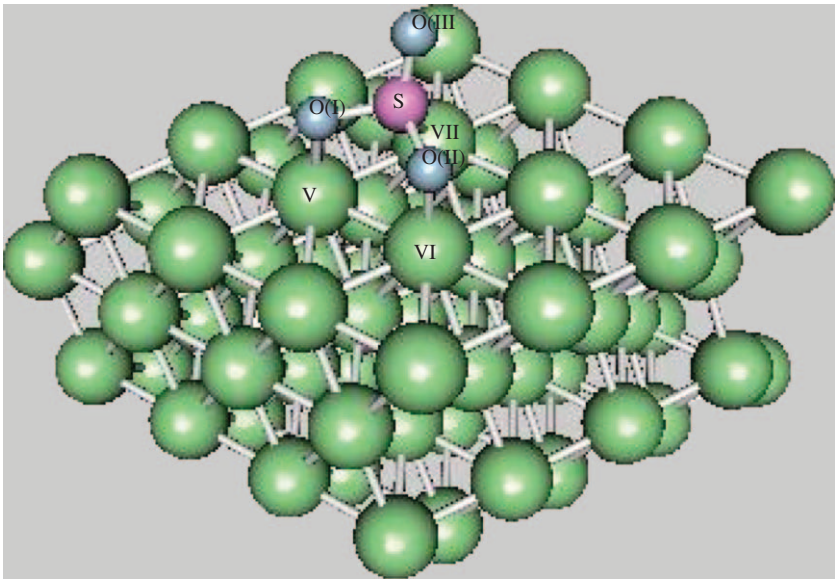

(a) Suzuki *et al.*

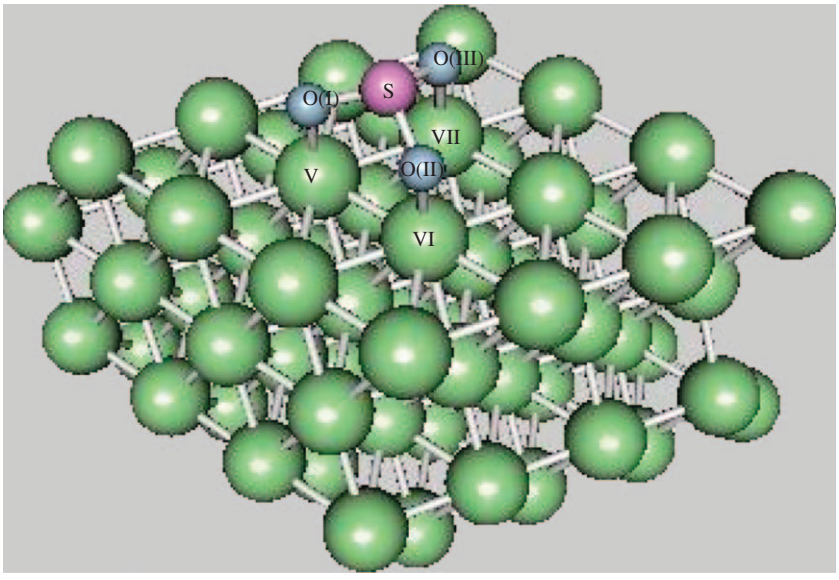

(b) Suzuki *et al.*

Figure 6.2 Calculated adsorbed SO_3 configuration on Pt surface. (a) Configuration A (b) configuration B.

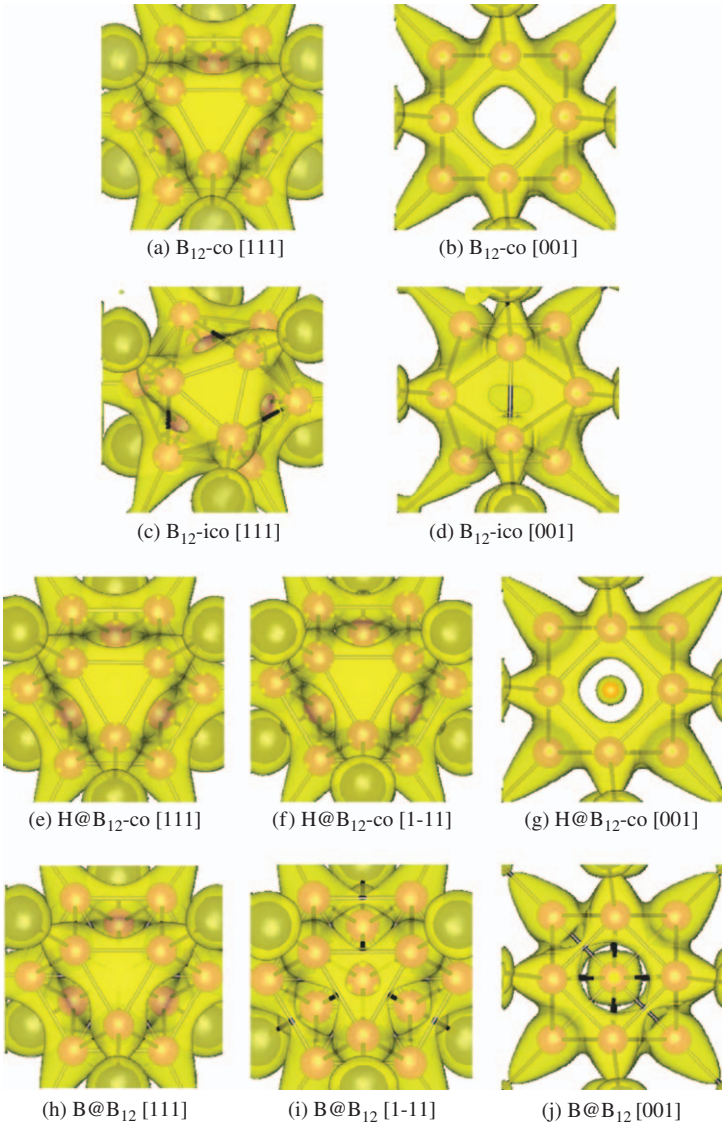

Figure 8.10 Iso-surfaces of electron densities (density level: 0.1/Å^3) calculated for (a, b) B_{12}-co, (c, d) B_{12}-ico, (e, f, g) H@B_{12}-co, and (h, i, j) B@B_{12} clusters with their nearest-neighbor silicon atoms. (a, c, e, and h) are viewed along the [111], (b, d, g, and j) are along the [0 0 1], and (f) and (i) are along the [1 –11] direction of the cluster.

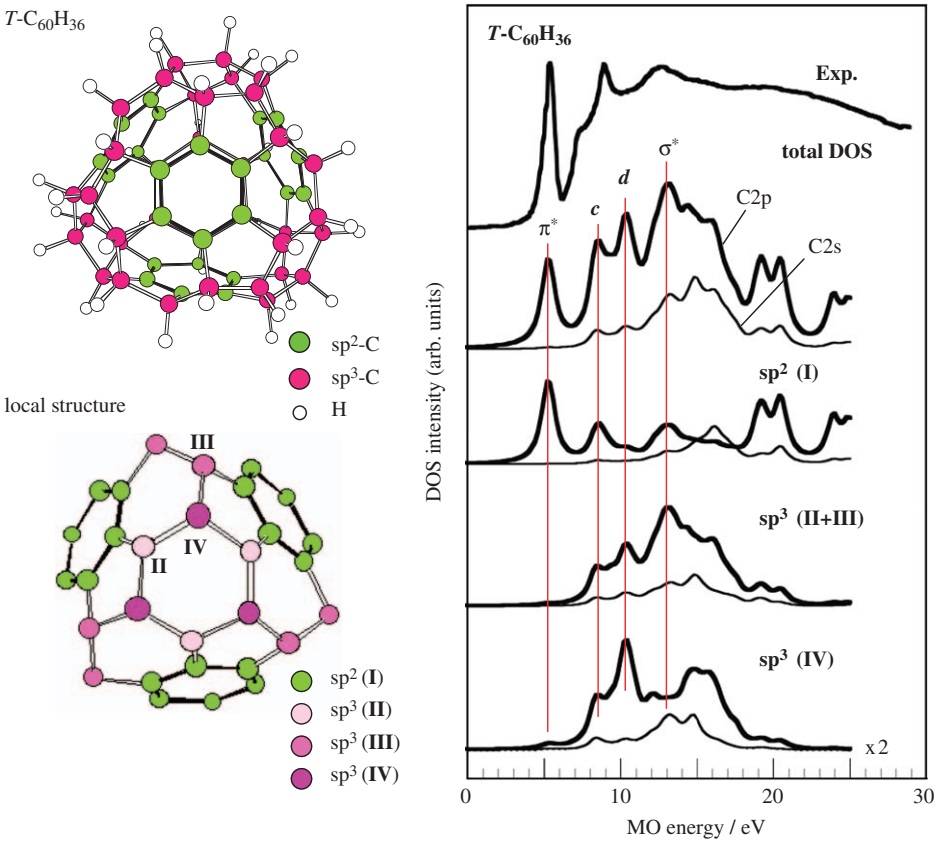

Figure 16.2 Left panel shows the molecular and local structure of *T*-$C_{60}H_{36}$. Right panel shows the unoccupied C 2s-DOS and C 2p-DOS of *T*-$C_{60}H_{36}$. The measured X-ray absorption spectrum (Exp.) of $C_{60}H_{36}$ is described on the total DOS.

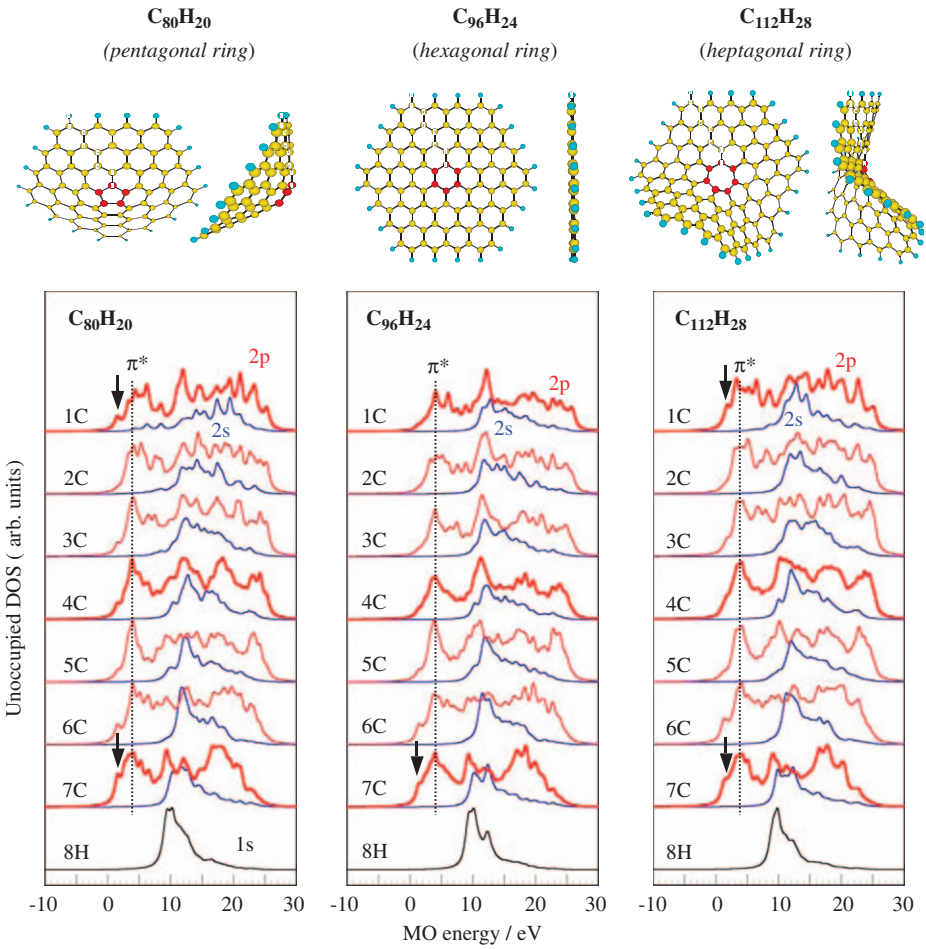

Figure 16.4 Upper panel shows a benzenoid cluster model ($C_{96}H_{24}$) and nonbenzenoid models ($C_{80}H_{20}$, $C_{112}H_{28}$). Lower panel shows the unoccupied C 2p-DOS and C 2s-DOS of carbon atoms in the cluster models. Carbon atoms from the centered atoms to the edged atoms are numbered as 1C–7C, respectively. Hydrogen atoms terminating the edged-carbon atoms are numbered as 8H. The lower-energy DOS portions at the π^* peak positions of 1C and 7C are denoted by arrows.

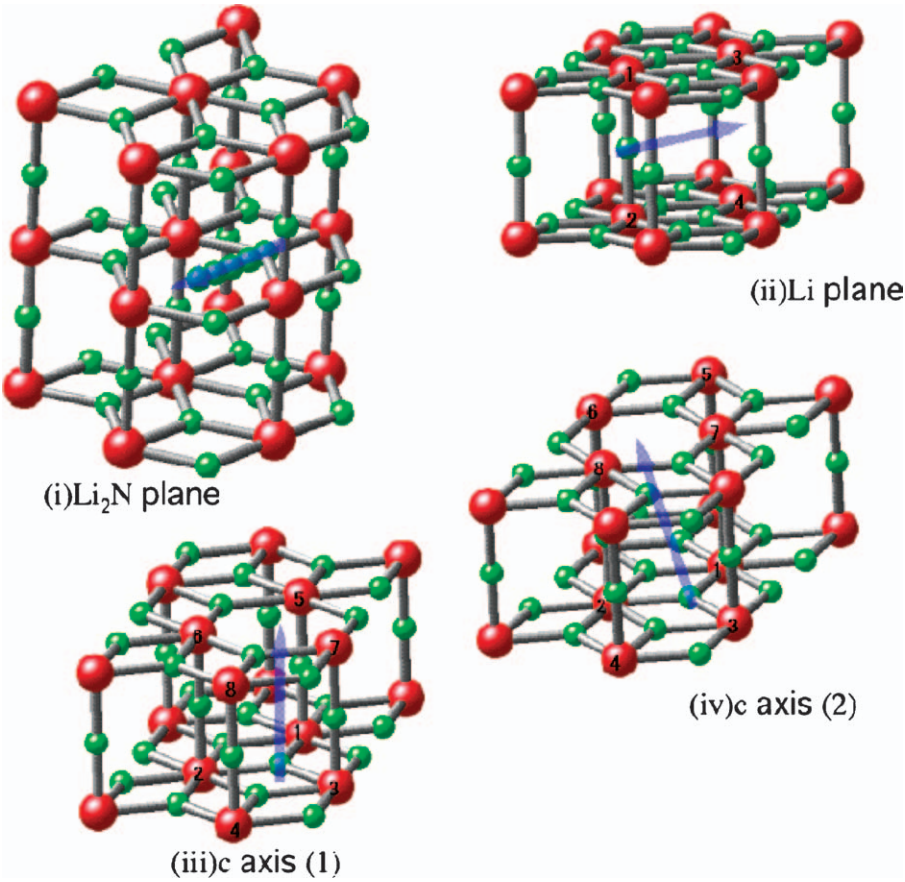

Figure 20.1 Schematic diagram of the Li_3N model clusters.

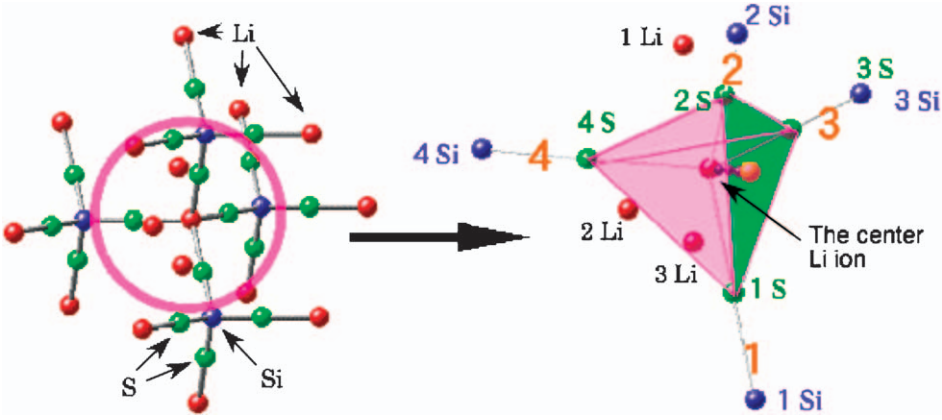

Figure 20.6 Schematic diagram of the $Li_{16}Si_4S_{16}$ model cluster.

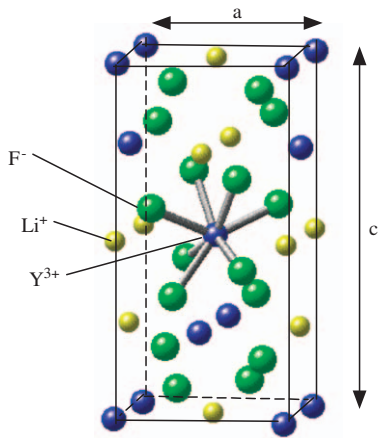

Figure 22.2 Crystal structure of $LiYF_4$.

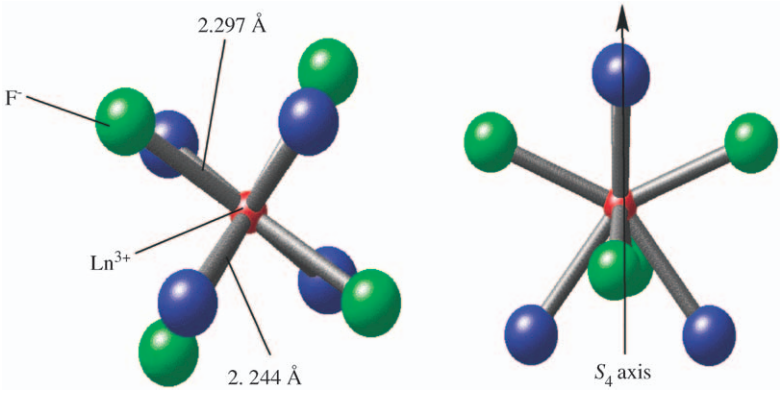

Figure 22.3 Model cluster for trivalent RE (Ln^{3+}) in $LiYF_4$.

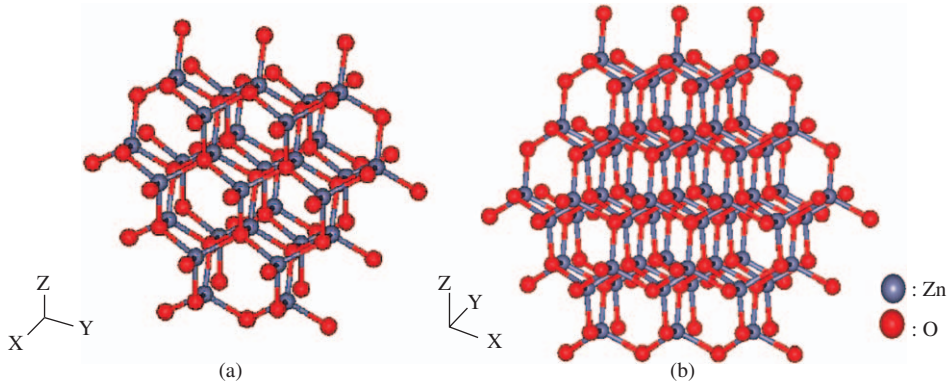

Figure 24.1 Basic cluster models used; (a) the $(Zn_{29}O_{57})^{56-}$ cluster with an O atom at the center of the cluster, and (b) the $(Zn_{57}O_{96})^{78-}$ cluster with a Zn atom at the center of the cluster.